Optimization and Valuation of Reconfigurable Satellite Constellations Under Uncertainty

by

Robert Scott Legge Jr.

Sc.B., Brown University (2006)

S.M., Massachusetts Institute of Technology (2008)

Submitted to the Department of Aeronautics and Astronautics
in partial fulfillment of the requirements for the degree of

Doctor of Philosophy

at the

MASSACHUSETTS INSTITUTE OF TECHNOLOGY

September 2014

Author . . . .
Department of Aeronautics and Astronautics
August 19, 2014
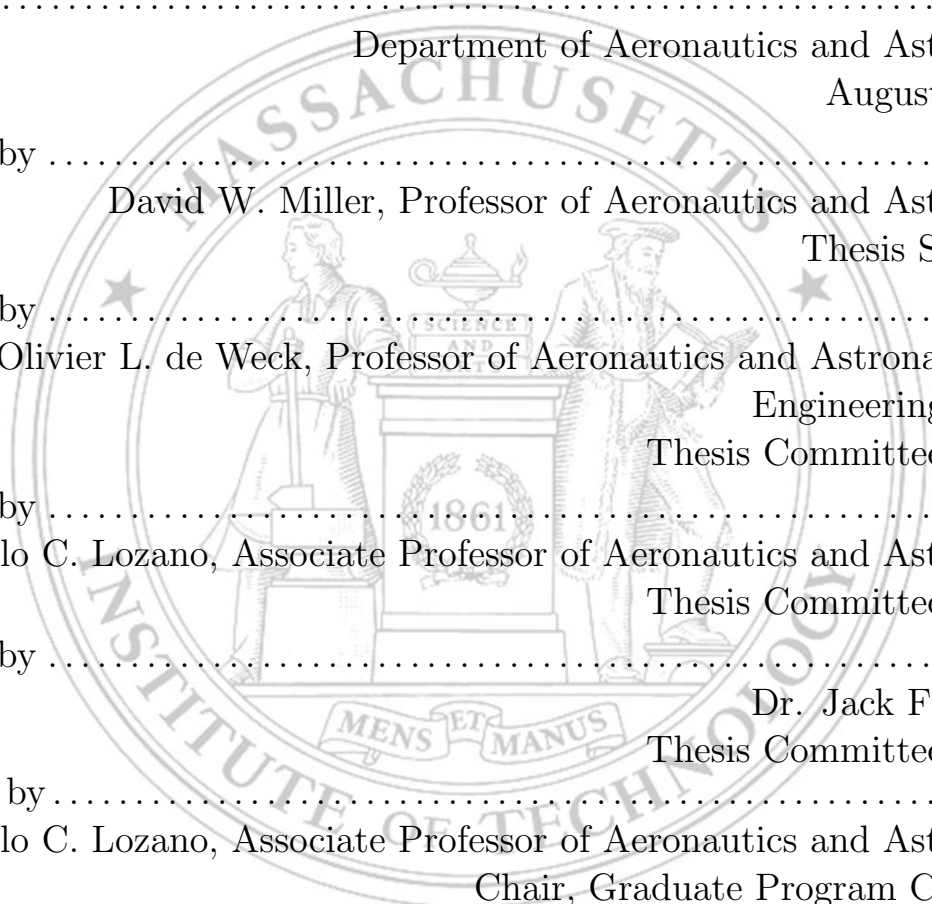
Certified by . . . .
David W. Miller, Professor of Aeronautics and Astronautics
Thesis Supervisor

Certified by . . . .
Olivier L. de Weck, Professor of Aeronautics and Astronautics and
Engineering Systems
Thesis Committee Member

Certified by . . . .
Paulo C. Lozano, Associate Professor of Aeronautics and Astronautics
Thesis Committee Member

Certified by . . . .
Dr. Jack Fleischman
Thesis Committee Member

Accepted by . . . .
Paulo C. Lozano, Associate Professor of Aeronautics and Astronautics
Chair, Graduate Program Committee

Optimization and Valuation of Reconfigurable Satellite Constellations Under Uncertainty

by

Robert Scott Legge Jr.

Submitted to the Department of Aeronautics and Astronautics
on August 19, 2014, in partial fulfillment of the
requirements for the degree of
Doctor of Philosophy

Abstract

Space-based persistent surveillance provides decision makers with information necessary to effectively respond to both natural and man-made crises. This thesis investigates a *reconfigurable* constellation strategy that utilizes on-demand, maneuverable satellites to provide focused regional coverage with short revisit times at greatly decreased cost when compared to traditional static satellite constellations.

The thesis develops and demonstrates a general framework to guide the design and optimization of reconfigurable satellite constellations specifically tailored to stakeholder objectives while considering requirement uncertainty. The framework is novel in that it avoids many of the assumptions and simplifications of past research by: 1. explicitly considering uncertainty in future operating conditions; 2. concurrently optimizing constellation pattern design, satellite design, and operations design; and, 3. investigating layered and asymmetric patterns. The framework consists of three elements: a detailed simulation model to compute constellation performance and cost for a variety of architectures and patterns, Monte Carlo simulation to determine how well each design performs under uncertain future conditions, and a parallel multi-objective evolutionary algorithm developed from the ϵ-NSGA-II genetic algorithm to find designs that maximize performance while simultaneously minimizing cost. Additionally, a new performance metric is developed to measure directly how well a design meets desired temporal and spatial sampling requirements and a decision model and optimal assignment process is developed to determine how to employ the option of reconfigurability to respond to specific regional events.

The framework was used to perform 85 optimization runs selected to compare the cost-effectiveness of several constellation architectures over varied operating conditions and coverage requirements. All optimization runs were performed in less than three months, demonstrating that parallel computing coupled with sophisticated optimization routines enable rapid spiral development of satellite constellations. Results show that reconfigurable constellations cost 20 to 70% less than similarly performing static constellations for the scenarios studied. The cost savings grows with increasingly demanding coverage requirements. Results from optimizing a fully asymmetric constellation pattern led to two the development of new 'quasi'-asymmetric patterns that were found to significantly outperform symmetric patterns

for providing discontinuous coverage. Additionally, results show that the sun-synchronous and rapid launch architectures are the least cost-effective approaches.

Thesis Supervisor: David W. Miller, Professor of Aeronautics and Astronautics
Title: Thesis Supervisor

Thesis Supervisor: Olivier L. de Weck, Professor of Aeronautics and Astronautics and Engineering Systems
Title: Thesis Committee Member

Thesis Supervisor: Paulo C. Lozano, Associate Professor of Aeronautics and Astronautics
Title: Thesis Committee Member

Thesis Supervisor: Dr. Jack Fleischman
Title: Thesis Committee Member

Acknowledgments

Contents

Nomenclature

Constants

μ	Earth gravitational constant	$398600.43560\ km^3\,s^{-2}$
$\omega_\oplus$	Earth spin rate	$7.29211585530 \times 10^{-5}\,rad\,s^{-1}$
g	Mean acceleration due to Earth's gravity at the surface	$9.80665\,m\,s^{-2}$
J_2	Earth oblateness constant	0.0010826269
$R_\oplus$	Earth equatorial radius	$6378.137\ km$
T_s	Sidereal year duration	$365.25636\,days$

Variables

α	Decision model weight variable	$-$
α_0	Initial decision model weight variable	$-$
$\bar{P}$	Mean performance	$-$
Δalt	Altitude difference between ROM and GOM orbits	km
ΔD	Decimal days from vernal equinox	$days$
Δh_D	Difference between drift orbit altitude and GOM altitude	km
ΔM	Parameter controlling M spacing of satellites in adjacent orbit planes	deg
ΔM_{max}	Maximum M spacing in SSO orbit plane without coverage gaps	deg
ΔM_{SSO}	Parameter controlling M spacing of satellites in same SSO orbit plane	deg
ΔV	Change in velocity	$m\,s^{-1}$
ΔV_R	Total reconfiguration ΔV	$m\,s^{-1}$
$\Delta V_{deorbit}$	De-orbit ΔV	$m\,s^{-1}$
ΔV_{dep}	Deployment ΔV	$m\,s^{-1}$
ΔV_{drag}	ΔV required for aerodynamic drag makeup	$m\,s^{-1}$
ΔV_{LV}	ΔV required to correct for launch vehicle injection errors	$m\,s^{-1}$
ΔV_{recon}	Reconfiguration ΔV	$m\,s^{-1}$
ΔV_{sat}	Remaining satellite propulsive capability	$m\,s^{-1}$
ΔV_{SK}	ΔV required for other stationkeeping maneuvers	$m\,s^{-1}$
ΔV_T	Total satellite ΔV	$m\,s^{-1}$
δ	NIIRS scaling factor	$-$

ϵ	Non-dominated front resolution parameter	*varied*
η	Boresight angle	*deg*
η_T	Thruster efficiency	—
η_{max}	Boresight angle at zero ground elevation angle	*deg*
η_{pack}	Launch vehicle volumetric packing efficiency	—
Λ	RGT ground track angle	*deg*
λ	Earth central angle	*deg*
λ	Longitude	*deg*
λ_{max}	Earth central angle at zero ground elevation angle	*deg*
λ_s	Optical sensing wavelength	*m*
ν	True anomaly	*deg*
Ω	Right ascension of the ascending node	*deg*
ω	Argument of perigee	*deg*
Φ	Constellation orbital state	—
ρ_a	Atmospheric density	$kg\,m^{-3}$
ρ_{sc}	Stowed spacecraft density	$kg\,m^{-3}$
τ	Time since last observation	*hr*
θ	Mean time	*deg*
$\tilde{P}$	Median performance	—
ε	Satellite ground elevation angle	*deg*
ε_{min}	Minimum satellite ground elevation angle constraint	*deg*
φ	Latitude	*deg*
Υ	Vernal equinox	—
ξ_Ω	Parameter controlling Ω extent of 'quasi'-asymmetric constellation	—
ξ_p	Propulsion system dry mass fraction	—
ξ_R	Fraction of satellites available for reconfiguration	—
ξ_{pay}	Payload RE cost as a fraction of payload NRE cost	—
ξ_{sc}	Satellite RE cost as a fraction of satellite NRE cost	—
a	Semi-major axis	*km*
b	Learning curve factor	*kg*
BC	Ballistic coefficient	$kg\,m^{-2}$
C_{FPA}	Focal plane array cost	$M FY2010
C_L	Total launch cost	$M FY2010
C_{NRE}	Total constellation non-recurring cost	$M FY2010
C_{OTA}	Optical telescope assembly cost	$M FY2010
C_{pay}	Payload cost	$M FY2010

C_{RE}	Total constellation recurring cost	$M FY2010
$C_{sc,NRE}$	Spacecraft non-recurring cost	$M FY2010
$C_{sc,TFU}$	Spacecraft theoretical first unit cost	$M FY2010
D	Aperture diameter	m
e	Eccentricity	$-$
F	Constellation phasing parameter	$-$
F	Thrust	N
G_{DM}	Decision model gain	$-$
h	Altitude	km
i	Inclination	deg
I_{SP}	Specific impulse	s
L	Satellite to ground slant range	km
L_{max}	Satellite to ground slant range at zero ground elevation angle	km
M	Mean anomaly	deg
$M_{d,sc}$	Spacecraft dry mass without propulsion system	kg
M_d	Spacecraft wet mass	kg
M_{LV}	Launch vehicle payload capacity by mass	kg
M_{prop}	Propellant mass	kg
M_P	Propulsion system wet mass	kg
M_w	Spacecraft wet mass	kg
n	Mean motion	$rad\,s^{-1}$
N_d	Number of days	#
N_o	Number of orbits	#
N_p	Number of orbit planes	#
N_T	Total number of satellites	#
N_{calls}	Number of calls that the master makes to slave processors	#
$N_{cluster}$	Number of slave processors in computational cluster	#
N_{pop}	Evolutionary algorithm population size	$-$
N_{sp}	Number of satellites per orbit plane	#
P	Orbital period	s
P	Power	W
p	Perifocal distance	km
p	Temporal utility curve shape parameter	$-$
P_E	Performance for a single event response	$-$
P_{max}	Ideal performance	$-$
PU	Pattern Unit	deg

T	Desired temporal resolution	hr
t	Time	s
t_R	Total reconfiguration time	s
t_{fp}	Time to first pass	s
T_{life}	System lifetime	$years$
U	Utility	$-$
V	Velocity	$m\,s^{-1}$
V_{LV}	Launch vehicle payload capacity by volume	m^3
X	Desired spatial resolution	m
X	Satellite orbital state	$-$
x	Ground sample distance	m

Acronyms

$DARPA$	Defense Advanced Research Projects Agency
$ECEF$	Earth centered Earth fixed
FPA	Focal plane array
GEO	Geosynchronous Earth orbit
$GIQE$	General Image Quality Equation
$GMST$	Greenwich mean sidereal time
GMT	Greenwich mean time
GOM	Global operational mode
GPS	Global Positioning System
GSD	Ground sample distance
LEO	Low Earth orbit
LMT	Local mean time
LV	Launch vehicle
MEO	Medium Earth orbit
$MOEA$	Multi-objective evolutionary algorithms
$NICM$	NASA Instrument Cost Model
$NIIRS$	National Imagery Interpretability Rating Scale
NRE	Non-Recurring engineering
ORS	Operationally Responsive Space
OTA	Optical Telescope Assembly
RCO	Repeat coverage orbit
RE	Recurring engineering
RGT	Repeating ground track
ROM	Regional operational mode

SAR	Synthetic aperture radar
$SSCM$	Small Satellite Cost Model
SSO	Sun-synchronous orbit
STK	Systems Tool Kit
UAV	Unmanned aerial vehicle
$USCM$	Unmanned Spacecraft Cost Model
VoR	Value of reconfigurability

List of Figures

17

List of Tables

Chapter 1

Introduction

New thinking is needed to design, develop and implement cost-effective persistent surveillance satellite constellations. Rather than finding the 'best' static design that meets fixed requirements based on projected future needs, a flexible approach gives operators the ability to actively adapt the system to actual future needs. This thesis develops a flexible, reconfigurable constellation strategy that utilizes maneuverable satellites to give operators the option to actively change the constellation pattern to focus system resources in times of need. The ability to change the constellation pattern increases satellite utilization and results in dramatically improved system cost-effectiveness, even after accounting for the cost of increased satellite propulsive capability. In this thesis, these new reconfigurable constellations are compared to traditional static constellations using a comprehensive constellation design and optimization framework that avoids many of the assumptions and simplifications made in past research. The framework utilizes detailed simulation models, Monte Carlo sampling, advanced multi-objective optimization techniques, and parallel computing to find the set of efficient designs that simultaneously maximizes performance while minimizing cost and incorporating uncertainty in the future operating context. Results obtained using this framework show that for the same level of performance, reconfigurable designs cost 20 to 70% less than similarly performing traditional static designs, and asymmetric constellation patterns significantly outperform traditional symmetric patterns for the scenarios studied.

The reconfigurable constellation approach is enabled by several factors. First, recent advances in small satellite propulsive technology significantly lowers the cost of implementing

maneuverable satellites. Second, increasing satellite autonomy and automated satellite oper-ations enables frequent satellite reconfiguration maneuvers with minimal added operational overhead. Third, advanced computational capability allows for improved design and opti-mization of satellite constellations that prevents arbitrary restriction of the design space and allows for the discovery of more cost-effective designs. And, finally, a new constellation cov-erage metric is developed in this thesis that directly measures persistence and is not skewed by statistical outliers, avoiding the situation where outliers drive the overall optimization process.

The remainder of this chapter is organized into six sections. Section 1.1 motivates the need for space-based persistent surveillance. Section 1.2 then presents an overview of past literature focused on satellite constellation design and optimization, as well as satellite con-stellation reconfiguration. Section 1.3 introduces how flexibility is engineered into a system and how to quantify the economic benefit of incorporating flexibility. Section 1.4 lists specific gaps in current literature that are addressed in this thesis. Section 1.5 formally outlines the research objectives and expected contributions of this thesis. Section 1.6 gives an overview of the specific optical imaging scenario investigated in this thesis and the chapter concludes by providing an outline for the rest of the thesis in Section 1.7.

1.1 The Need for Space-Based Persistent Surveillance

Access to timely persistent surveillance data products enables decision makers to effectively respond to crises, either natural or man-made, and the increasing risk posed by natural disasters increases the need for this data. World-wide population growth has increased population exposure and, as a result, 2013 was the sixth costliest year since 2000 (USD192 Billion) and the seventh costliest year since 1950 in terms of total global economic losses [9]. Persistent surveillance data is used to improve situational awareness, provide initial damage assessment, improve resource allocation and logistics, and allow for response planning [164].

Ground-based systems provide local high resolution imagery, but damage to local in-frastructure can significantly reduce the mobility and effectiveness of these systems dur-ing disaster response. Air-based systems, including aircraft and unmanned aerial vehicles

(UAVs), provide local and regional high resolution imagery, but cannot cover extended areas without frequent refueling and are also unable to operate in denied environments. Additionally, airborne systems may suffer from poor responsiveness unless they happen to be based close to the disaster event. They also need local airfields and air traffic control capability, which may be unavailable due to damage to local infrastructure caused by the disaster event. The Defense Advanced Research Projects Agency (DARPA) Vulture Program is focused on developing a solution to the air-basing problem: ultra-long duration airborne surveillance platforms that could remain on-station for years and provide re-taskable pseudo-satellite coverage [146]. While this concept relieves the refueling and airport needs, airborne systems are still are unable to provide coverage in areas without air traffic control and significant reliability problems arise when trying to operate ultra-long endurance vehicles [7].

Space-based systems provide persistent surveillance capability without many of the limitations encountered with the other approaches. These systems can be broken down into three broad architectures: rapid launch, ad-hoc, and dedicated. In the rapid launch architecture, fully functional, ready for launch satellites are stored on the ground, to facilitate quick response to an urgent space capability need [178]. The Air Force's Operationally Responsive Space (ORS) program is developing technologies and systems to support emerging military needs in relevant time frames. Part of the program is attempting to enable the rapid deployment of disposable space assets with response times on the order of a two week testing and launch time line [178] or, more aggressively, a $24hr$ launch vehicle integration and $24hr$ on-orbit deployment time [110]. In another effort, the DARPA SEEME program is focusing on developing low-cost, disposable satellites that could be rapidly deployed to provide 60 to 90 days of enhanced regional coverage to directly support ground operations when needed [18]. The rapid launch architecture suffers from two flaws: 1. responsiveness is limited to a few weeks given current and near-term satellite integration and launch vehicle technology, and limited launch facility availability; 2. and once satellites are launched to an orbit that provides good coverage to the current disaster event, the satellites will likely provide poor coverage for another disaster event located in another region, essentially making these satellites one-time-use-only. Despite these flaws, the rapid launch architecture is analyzed in more detail in Section 6.6. In the ad-hoc constellation architecture, satellites, owned and operated

by individual external stakeholders, volunteer persistent surveillance data products to support disaster response. One example of this approach is the International Charter for Space and Major Disasters[1] which is an organization that coordinates voluntary contributions of remote sensing products from government and commercial entities for disaster response. The downside to this approach is that cooperation is not guaranteed, and coverage will likely be bunched together at either mid-morning or mid-afternoon local time, since existing Earth observation satellites typically use sun-synchronous orbits.

Dedicated in-space constellations, comprised of a deployed constellation of satellites tailored to provide responsive persistent surveillance, exhibit increased responsiveness when compared to rapidly launched assets and increased persistence when compared with ad-hoc constellations. However, traditional earth observation satellite constellations, capable of providing persistent surveillance with short revisit times, have proven to be too costly to implement – a trend that will only worsen as budgetary constraints force increased scrutiny on future expenditures. Inefficient satellite utilization is the fundamental cost driver of these systems and is caused by a variety of contributing factors including: static constellation patterns that are unable to effectively respond to uncertain future needs; overly conservative designs due to performance metrics (maximum revisit time, average revisit time) that are skewed by worst case statistical outliers; and uncertainty in future regional surveillance needs that lead to broad partial global coverage requirements. As proposed in this thesis, reconfigurable satellite constellations are an alternative strategy to significantly improve cost-effectiveness, making effective space-based surveillance affordable in the future.

1.2 History of Constellation Design and Optimization

The fundamental tradeoff for space-based remote sensing systems is the balance between orbital altitude and payload/bus capability. Higher altitudes enable larger satellite ground footprints and lead to smaller constellation sizes for fixed coverage requirements. However, in order to achieve the same ground sensing performance as the altitude increases, the payload capability must also increase. For optical payloads, aperture diameter must increase with

---

[1]http://www.disasterscharter.org/web/charter/home, Accessed 5/13/2014

increasing altitude to produce the same spatial resolution on the ground, which leads to higher satellite cost. For example, a satellite at $860km$ has twice the ground footprint diameter as a satellite at $400km$; however, to maintain the same ground sensing performance, the aperture would need to increase by a factor of 2.15. This basic tension between many small, cheap satellites at lower altitudes and fewer larger, and more expensive satellites at higher altitudes is central to the satellite constellation optimization problem.

Further complicating analysis, satellite coverage patterns are constrained by orbital dynamics. Besides altitude and assuming circular orbits, the designer also has control over the right ascension of the ascending node and the inclination; two factors that together specify the satellite's orbital plane. If the target location is at the poles or on the equator, an orbit can be selected so that the satellite provides a period of coverage on each orbit. For any other case, and, if the target location is known *a priori*, an orbit can be selected to synchronize orbital precession with the Earth's rotation rate. This ensures the satellite will follow the same ground track with, at best, a daily revisit period. However, these repeating ground track (RGT) orbits typically do not provide coverage for ground locations far from the ground track, and cannot be used if the target location is either unknown or uncertain. In these cases, the satellite orbit is limited to be non-synchronous to provide wide-area zonal coverage. This limitation reduces the coverage provided by a single satellite for any given ground location, and therefore the satellite is used inefficiently. Later in this thesis I will show that reconfigurable constellations combine the benefits of repeating ground track orbits with the ability to respond to uncertain target locations by allowing system operators to move this focused coverage area.

Inclination determines the range of latitudes covered by a constellation. Generally, coverage is best around the ground latitude corresponding to the inclination of the constellation and diminishes to a minimum at the equator. No coverage is provided to ground locations with latitudes greater than the inclination and outside of the ground footprint swath. Therefore, the smaller the defined target region, the more likely that the constellation can be designed to focus coverage and maximize individual satellite coverage efficiency. The Repeat Coverage Orbit (RCO) concept introduced by Wertz [218] is an example of a method where satellite coverage is tailored for a small geographical region known prior to launch.

In an RCO, the satellite is launched into an orbit with the inclination a little higher than the latitude of the region to be covered, allowing a single satellite to have several periods of coverage per day. RCO orbits are considered as part of a rapid launch architecture later in this thesis (Section 6.6).

In a constellation containing many satellites, designers can also tailor the relative phasing between satellites to produce beneficial ground coverage patterns. The ensemble phasing and relative placement between satellites in a constellation is called the constellation pattern. Each satellite's position is described fully by six orbital parameters creating combinatorial design variable growth and a rapidly intractable design space. Even when both the altitudes and inclinations are common throughout the constellation, there are still $2N_T$ variables specifying the right ascension and mean anomaly, where N_T is the number of satellites. To overcome this computational problem, traditional constellation design methods (e.g. the Walker and streets-of-coverage patterns described in more detail in the next section) have utilized symmetry to reduce the number of design variables. Past research has shown that these symmetric and near-symmetric constellation patterns provide near optimal continuous global or zonal coverage [207, 126, 201, 212, 213, 139, 140]; but, asymmetric constellations provide better discontinuous coverage [82, 120]. Continuous coverage refers to providing uninterrupted coverage to the ground point of interest, while discontinuous coverage refers to providing intermittent coverage.

Discontinuous coverage performance is traditionally measured by either percent coverage or revisit time (maximum or average). Percent coverage is the percentage of time that the constellation provides coverage of the target. Maximum and average revisit time correspond to the maximum and average time between coverage periods, respectively. Williams et al. [224, 225] has shown these two figures of merit to be in tension, and improving average revisit time usually degrades maximum revisit time. These traditional metrics tend to mask the underlying coverage statistics [219] and do not provide a good way of assessing persistence. A better metric would measure how close coverage matches the desired temporal resolution, and would not be skewed by outliers. A new persistence metric, developed in this thesis, assigns coverage utility based on time since the last observation within a specified daily time window. This metric is easily adapted to various mission objectives and

allows inclusion of spatial resolution effects, illumination constraints for optical imagery, and observation discounting as the time after the event increases.

The remainder of this section provides a comprehensive history of constellation design and optimization literature relevant to this thesis work. Literature dedicated to constellation design and optimization has a long history. The earliest research on the subject was focused on determining the minimum amount of satellites needed to provide either continuous global or continuous zonal coverage. Later research explored constellation designs that provide global, zonal, and regional discontinuous coverage. Only within the last decade have researchers looked at satellite constellation reconfiguration or the coupled satellite design and constellation pattern optimization problem. This thesis work investigates the concurrent optimization of satellite design and constellation pattern design for discontinuous regional coverage with both symmetric and asymmetric patterns, and, therefore, builds on much of this previous work. Sections 1.2.1, 1.2.2, and 1.2.3 provide an overview of previous work focused on continuous coverage, discontinuous coverage, and regional coverage, respectively. Section 1.2.5 touches on the limited prior work on the coupled satellite design and constellation pattern optimization and Section 1.2.6 details previous work on satellite reconfiguration.

1.2.1 Continuous Global or Zonal Coverage

Early work [207, 126, 201] developed several symmetric constellation patterns, which reduced the number of design variables in the problem and made constellation design and analysis computationally tractable. Vargo [207] found the minimum number of satellites necessary to provide continuous global coverage for two types of patterns: a constellation with multiple planes at the same inclination spread out in right ascension ($L - type$); and a constellation with multiple planes with the same right ascension and spread out in inclination ($\lambda - type$). Vargo also found that both offered similar numbers of satellites for a given orbital altitude, but mentioned that launch considerations favored $L - type$ constellations. Vargo also found that $L - type$ constellations provided excess coverage at higher latitudes while $\lambda - type$ provided excess coverage at lower latitudes. Luders [126] found the minimum number of satellites to provide single continuous global and zonal coverage using symmetric equatorial, polar, and inclined constellations. The polar constellations that he developed were the genesis

of the streets-of-coverage method. Later research by Ullock et al. [201], built on Luders'
polar constellations work, and further reduced the minimum number of satellites needed for
continuous zonal coverage above a certain latitude. He achieved this by introducing a slightly
asymmetric polar constellation that featured smaller spacing between the counter-rotating
adjacent planes than the spacing between planes moving in the same direction.

Pursuing the development of symmetric inclined constellations, Walker [212, 213, 214]
developed the 'star pattern' and 'delta pattern' representations. Both patterns feature satel-
lites in circular orbits with common inclination and semi-major axis. The star pattern
features satellites in orbits with all ascending nodes in one hemisphere, while the delta pat-
tern features satellites spread with equal spacing in Ω and M. Following convention, for
the remainder of this thesis, the delta pattern is referred to as the Walker pattern. Walker
constellations rely on symmetric geometry and circular orbits to describe a constellation
in only three variables corresponding to the number of planes, the number of satellites in
each plane, and an inter-plane phasing parameter. The constellation geometry is similar to
the $L - type$ constellations developed earlier by Vargo [207]. Walker constellations provide
partial global coverage by covering a range of latitudes roughly equal to plus and minus its
inclination, and the pattern is an efficient configuration for wide area continuous coverage. A
contemporary of Walker, Mozhaev [139, 140, 141] proposed similar symmetric constellations,
also described by three variables (not the same as with Walker patterns), that he developed
using a mathematical derivation based on symmetry groups. Ballard [17] extended and gen-
eralized Walker constellations into what he termed Rosette constellations and confirmed the
results provided by both Walker and Mozhaev.

The literature presented thus far has introduced two constellation patterns used for pro-
viding continuous global coverage: the Walker Delta Pattern based on symmetric inclined
orbits and the streets-of-coverage pattern based on polar (or near polar) orbits. Subsequent
literature focused on generating efficient designs using these patterns, determining condi-
tions when each pattern performed best, and also compared their performance with several
asymmetric and eccentric orbit design approaches.

Several authors have investigated efficient Walker designs. Lang [117, 118] used sin-
gle objective full-factorial optimization to optimize Walker-type constellations of up to 100

satellites for single through four-fold continuous global coverage. The term n-fold coverage means that all locations within the area of interest are in view of n satellites simultaneously. Lang found the Walker pattern parameters, including number of planes, number of satellites per plane and phasing parameter, that gave the smallest satellite footprint for different constellation sizes (number of satellites). Smaller satellite ground footprints translate to lower altitudes and smaller, less costly optics for fixed ground spatial resolution. Other literature developed analytical techniques to guide design and reduce the computational burden caused by full-factorial optimization. Hanson [96] developed analytic methods to find efficient Walker patterns for zonal coverage, and, later, Turner [199] developed axiomatic rules to guide the selection of Walker phasing parameters for both zonal and regional coverage.

Other authors investigated efficient streets-of-coverage designs, and much research has focused on the phasing between adjacent orbit planes. Beste [20] found that streets-of-coverage constellations with non-uniform plane phasing required 10-20% fewer satellites than the uniform spacing designs found earlier by Luders [126]. Rider [167] built on this work and developed analytical tools to determine the optimal inter-plane phasing for streets-of-coverage constellations for both global coverage and zonal coverage above a certain latitude. He found that designs with optimized phasing were more efficient than designs with arbitrary phasing, however, the improvement rapidly diminished with increasingly redundant coverage. Adams [4] compared streets-of-coverage patterns with both optimal and arbitrary phasing using higher precision analytical methods than earlier research. The optimization procedure used an iterative approach to minimize the ground footprint for different constellation sizes. The results showed that previous techniques by Beste [20] and Rider [167] overestimated the number of satellites required for n-fold coverage. Ulybyshev [202] showed that near polar constellations outperform strictly polar constellations for double continuous global coverage and that these orbits allow for a range of inclinations to be used without significantly changing orbital altitude.

Other literature focused on determining when Walker or streets-of-coverage patterns yield more efficient designs. Luders [126] found that polar constellations are preferred over inclined constellations for complete global coverage. However, he found that inclined constellations performed better than polar constellations when the problem was restricted to specific zones

31

bounded by latitude. This is caused by better coverage provided for latitudes close to the inclination. Later research indicated that Walker patterns are more efficient for small constellation sizes while streets-of-coverage patterns are more efficient for large constellation sizes. Ballard [17] showed that Walker constellations outperform (provide a smaller constellation size for continuous coverage) the best streets-of-coverage constellations reported earlier by Walker [212] and Beste [20] for configurations up to 15 satellites with the benefit diminishing with increasing constellation size. Lang [118] later showed that for single and multi-fold global coverage with less than 20 satellites, symmetric inclined Walker type constellations outperform the asymmetric streets-of-coverage based polar constellations.

Both the Walker and streets-of-coverage patterns mandate that all the satellites are in circular orbits with common altitude and inclination. These simplifications arbitrarily restrict the design space and potentially lead to sub-optimal solutions. This observation led some researchers to investigate more general approaches. Palmerini found that eccentric streets-of-coverage constellations could provide longer coverage periods for certain ground locations [153, 154]. Ely [64, 65] also investigated eccentric streets-of-coverage constellations for zonal coverage through the use of a single objective genetic algorithm. The approach was to maintaining continuous zonal coverage and minimize both the constellation altitude and total number of satellites. The authors found that for either low or high numbers of satellites, the circular approach was best, and, for moderate numbers of satellites the elliptical approach was more efficient. A different approach is to allow satellites in the constellation to have different inclinations and/or different orbital altitudes. In this thesis, these types of constellations are referred to as layered constellations. Beste [20] compared polar constellation patterns to a layered approach using three orthogonal planes: two polar and one equatorial. He found the polar constellation pattern to be superior for the cases studied. Yuan [60] proposed using a layered constellation approach comprised of a streets-of-coverage constellation and a Walker constellation in order to provide global coverage with a better balance of coverage between polar and mid-latitude regions. The authors showed that the approach was less efficient (larger constellation sizes) than a strictly streets-of-coverage constellation and more efficient (smaller constellation sizes) than a strictly inclined constellation. Asvial et al. [11, 12, 13, 14] found that layered communication constellations

with satellites in LEO, MEO and GEO provided better global coverage than single layer constellations.

Recently, the Flower Constellation framework was introduced as a new way to systematically describe and generate constellations patterns, and the framework is more general than traditional Walker and streets-of-coverage methods [135, 222]. Flower constellations contain satellites that have identical semi-major axis, inclination and eccentricity and the semi-major axis can be set so that they are compatible with a rotating axis (e.g.Earth's rotation to set up repeating ground track orbits). For constellations that are compatible with the Earth-centered Earth-fixed coordinate frame (ECEF), these orbits are then repeating ground tracks; however, the constellations could also be made compatible with other rotating frames [132]. Initial comparisons showed that flower constellation designs can outperform Walker constellation designs [22]. Further work on flower constellations extended the analytic techniques available [134, 223, 30] and simplified the theory by creating the 2D lattice theory for the special case of uniform symmetric constellation designs [16]. These uniform and symmetric constellations were termed harmonic flower constellations and could be represented by three integer variables plus altitude, eccentricity, and inclination for any number of satellites. The theory was also generalized to be independent of any rotating frame. Harmonic flower constellations provide a more general framework for optimization and can also fully describe Walker constellations. Further research extended the 2D theory to form 3D lattice theory, which allows for elliptical and J_2 compatible orbits [42]. Applications investigated with flower constellations include: navigation systems [197, 31], interferometry [197], Earth observation [1, 22, 2, 3], telecommunications [133], space surveillance [131], and planetary exploration [132].

1.2.2 Discontinuous Global or Zonal Coverage

Later literature examined the design and optimization of constellations that provide discontinuous or intermittent coverage. Historically, researchers have optimized discontinuous coverage constellations by finding pattern designs that maximize the percentage of time that ground locations are covered, or minimize either the average or maximum gap time between coverage periods. Most early literature on discontinuous coverage constellations was focused

on finding constellation designs that minimized the maximum revisit time. Lang [121] created a computer-based tool to minimize the maximum revisit time for a set of targets spread in latitude using symmetric constellations. The approach used a full factorial search of all combinations of planes and number of satellites per plane to minimize a cost function based on the deviation of desired and computed maximum revisit time. Hayes [99] investigated extending the analysis to include asymmetric constellation designs. She found that constellations designed to minimize the maximum revisit time were generally symmetric in the rotating Earth frame, but not in an inertial frame. She also found that constellations with good maximum revisit time performance for ground targets at one latitude could perform poorly for targets in another latitude. Other authors studied using repeating ground track orbits to provide efficient discontinuous coverage. Hopkins [100] studied small constellations of satellites in repeat ground-track orbits to determine the best inclination and spacing between ground-tracks to produce desired maximum revisit times. Hanson [94, 95] developed procedures aimed at finding constellations that would meet coverage requirements with minimum inclination (aimed at reducing launch cost), minimum number of satellites, and a minimum maximum revisit time. The results showed that repeat-ground-track orbits performed better than non-repeating orbits and asymmetric constellation designs generally outperformed Walker constellations. Similarly, Ma [127] used computer-based optimization to find efficient designs that met revisit time requirements, while minimizing the total number of satellites and using the lowest inclination. These authors recognized that constellation design is inherently multi-objective in nature and not just a matter of minimizing the number of satellites in a constellation. However, the emphasis on minimizing inclination to reduce launch cost is misdirected since the real objective is to reduce overall cost, and higher inclinations may lead to fewer satellites.

Other research focused on finding when asymmetric constellations outperform Walker constellations for discontinuous coverage. George [82] used single objective genetic algorithms to show that Walker type constellations provide the best solutions when the maximum revisit time requirement is less than around 0.8 times the orbital period; however, for longer desired revisit times, the asymmetric designs can significantly outperform Walker constellations. Similarly, Lang [120] used a brute force enumeration approach on the problem

and concluded that asymmetric constellations provide more efficient solutions than Walker constellations when the desired revisit times approach the orbital period. Pegher [157] also used a single objective generic algorithm to compare the performance of Walker constellations to asymmetric constellations in terms of average revisit time, maximum revisit time, and percent coverage. The authors found that the asymmetric constellations either outperformed or matched the performance of Walker constellations in all cases tested. They also found that the performance difference between symmetric and asymmetric constellations increased as the number of satellites in the constellation decreased. Crossley et al. [38] used both simulated annealing and genetic algorithms to minimize the maximum revisit time for three and five satellite constellations.

While most early literature focused on minimizing the maximum revisit time, later literature looked at minimizing both maximum and average revisit time. Williams et al. [224, 225] used a multi-objective genetic algorithm, based on two-branch tournament selection [37], to investigate the design tradeoff between minimizing the maximum revisit time and minimizing the average revisit time. Surprisingly, they found that the two objectives are often competing. Their major findings were: as the number of satellites increased, the average and maximum revisit time tradeoff diminished; retrograde constellations generally outperformed prograde constellations; and asymmetric constellations generally outperformed symmetric constellations. Lang [119] also studied the maximum and average revisit time tradeoff with genetic algorithms. He found that asymmetric constellations performed better for three and four satellite constellations and Walker constellations performed better with five and six satellite constellations. Lang also found that retrograde orbits provided lower average revisit times, while prograde orbits provided the smallest maximum revisit time. Other research looked at the performance of layered constellations for providing discontinuous coverage. Jackson [102] showed that meshed-comb constellations, comprised of both prograde and retrograde satellites, generally exhibit smaller maximum revisit times and smaller, more consistent average revisit times. These references show that constellation coverage is inherently multi-objective with many possible objectives (GSD, average, maximum revisit time), and that unconventional patterns such as retrograde and layered patterns can perform better when considering multiple objectives.

1.2.3 Regional Coverage

Limited research has addressed the problem of optimizing local coverage, and existing literature has focused on providing coverage for a specific region or a specific set of target locations. Abdelkhalik [1] used a genetic algorithm and a gradient based method to find efficient natural orbits to best cover a set of multiple ground locations, known *a priori*. The author used two objective functions: one that attempted to maximize the resolution for all targets; and, one that maximized the overall percent coverage for all targets. Later research by Vtipil et al. [210] built on this work by considering eccentric orbits and adding altitude to the design vector. The authors found that eccentric orbits provided the most efficient solutions. Others have looked at finding efficient orbital patterns to provide coverage for a specific region. Frayssinhes [80] used genetic algorithms to find asymmetric constellations that outperformed Walker constellations for sparse, regional coverage over the continental United States. The analysis used a pattern that was symmetric in right ascension of the ascending node, but varied the mean anomaly during optimization. Ferringer et al. [71] furthered this work by investigating the tradeoff between minimizing both average and maximum revisit time for a three satellite constellation providing coverage in the continental United States, using an asymmetric pattern. Investigating a different tradeoff, Pontani [160] used repeating ground track orbits to maximize the percent coverage and minimize the maximum gap time for a coverage to a single target latitude. The authors developed an analytical approach to determine efficient designs that reduced computational complexity compared to heuristic optimization algorithms. In a similar effort, Ulybyshev [203, 204] presented a new geometric method based on visibility regions to design symmetric constellations for continuous or partial coverage.

1.2.4 Current and Historic Satellite Constellations

This section provides an overview of the pattern design for current and past satellite constellations. Most constellations launched to date provide wide area communications and navigation services. These systems are fundamentally different that the optical Earth observations systems investigated in this thesis because they can use high altitude orbits to

increase each satellite's footprint without large increases in payload capability.

Communications and navigation constellations generally provide continuous multi-fold zonal coverage. Several systems utilize symmetric constellations. The IRIDIUM communication constellation, fully deployed in 1998, consists of 66 active satellites in 6 orbital planes ($h = 780km$, $i = 86°$) and use a circular polar pattern, proposed by Adams et al. , where the orbital planes have their points of intersection near the poles and their greatest distance above the equator [4, 105]. The European Union's Galileo global navigation satellite system will use a Walker 27/3/1 pattern ($h = 23222km$, $i = 56°$) [172, 27]. Russia's GLONASS global navigation satellite system uses a Walker 24/8/1 pattern ($h = 19100km$, $i = 64.8°$), and has 31 total operational satellites including spares as of May 2012 [27]. The Globalstar communications constellation utilizes a Walker 48/8/1 pattern ($h = 1400km$, $i = 52°$) [59].

Several other constellations use mixed patterns consisting of satellites at different inclination and altitude. China's Compass Satellite Navigation Experimental System (BeiDou-1) started out providing regional coverage with 4 GEO, 5 inclined GEO at $i = 55°$, and 2 MEO satellites launched as of 2012 [231]. The BeiDou-2 constellation (named the Compass Navigation Satellite System), currently in deployment, will consist of 5 inclined GEO and 30 MEO satellites at $a = 21500km$ and $i = 55°$ to provide global coverage [27]. This approach allowed the system to initially provide regional coverage of Asia and then transition to fully global coverage. The Orbcomm communications constellation consists of two satellites at $i = 70°$ and $h = 741km$, three planes of eight satellites, spread out in Ω by 135°, at $i = 45°$ and $h = 815km$, and a fourth plane of two satellites at $i = 108°$ and $h = 830km$ [128, 228].

The U.S. Global Positioning System (GPS) has a unique history when it comes to pattern design. The system was initially designed using a Walker 24/3/4 pattern at $h \approx 20200km$ and $i = 55°$, and featured repeating ground tracks. Due to budget concerns, the system was later transitioned during testing of Block I satellites to an 18 satellite Walker 18/6/2 pattern. Further research conducted at The Aerospace Corporation found that the symmetry of the constellation caused a loss of precision in the case of failed satellites. When increased funding allowed for an increase in satellites to 21, Aerospace proposed a 21 satellite, six plane asymmetric constellation, also at $i = 55°$. This asymmetric pattern significantly improved performance in the case of a lost satellite. Through 2002, Aerospace continued optimization

of the GPS pattern and found a further optimal 24 satellite asymmetric pattern and a 27 satellite asymmetric pattern [130]. This example shows one instance in which optimized asymmetric patterns can provide better coverage for no additional space segment cost.

There are few examples of high resolution Earth observation constellations. The Disaster Monitoring Constellation consists of 4-8 satellites in a loose constellation pattern. Each satellites resides in a sun-synchronous orbit with a 10am equatorial crossing time [39], and the system as a whole provides global daily revisit. The RapidEye constellation provides daily revisit time and consists of five satellites in a single sun-synchronous orbital plane with an 11am equatorial crossing time and $h = 620km$ [200]. The Pléiades constellation consists of two satellites (Pléiades-1 & 2) in a single $695km$ sun-synchronous orbit plane with a 10:30am descending equatorial crossing time providing daily revisit with a minimum ground elevation angle of $45°$ and $0.7m$ nadir GSD [85].

1.2.5   Coupled Constellation Geometry and Satellite Optimization

While there is plentiful literature dedicated to separate constellation coverage optimization and satellite design optimization [136, 137, 138, 166], little prior work has touched on the coupled optimization of constellation design and satellite design. Budianto et al. [25, 23, 24] used collaborative optimization to find the minimum cost Walker constellation design that would provide single-fold global coverage with a constraint on minimum resolution. The collaborative optimization model incorporated three subsystem optimizations: pattern design, satellite design, and launch. This research showed that sophisticated multidisciplinary optimization techniques can be used to find globally efficient solutions to complex constellation design problems; however, the constellation geometry was limited to Walker patterns. Jilla [103] also investigated the multidisciplinary, multi-objective optimization of satellite constellations. He used multi-objective simulated annealing optimization to find efficient designs for three distributed satellite systems: a distributed interferometry mission, a space-based radar constellation, and a commercial broadband communications satellite constellation. While the analysis successfully coupled the satellite and constellation optimization, the constellation design space was also limited to symmetric streets-of-coverage and Walker patterns. Recently, Krueger et al. [114] utilized multidisciplinary system design optimization techniques

to find efficient designs for a LEO-based small satellite constellation. The coupled satellite and orbit model simulated the interactions between the satellites's subsystems, and Systems Tool Kit (STK) was used to propagate orbits and generate coverage statistics. The authors demonstrated coupled analysis, but the orbital tradespace was limited to symmetric patterns.

1.2.6   Constellation Reconfiguration

Recently, the topic of constellation reconfiguration has gained significant attention. Ferguson [70] defines a "reconfigurable system" as "one in which the configurations can be changed repeatedly and reversibly." Siddiqi [175] added that reconfigurable systems "achieve a desired outcome within acceptable reconfiguration time and cost." For satellite constellations, reconfiguration time is usually dictated by astrodynamics and phasing, while the cost is a combination of lost revenue during reconfiguration maneuvers and expended consumables (e.g. propellant). Both time and cost form a reconfiguration efficiency tradeoff [75]. Historically, constellation reconfiguration literature has focused on three topics: recovering from satellite failures; allowing for staged deployment of constellations over time; and, changing coverage characteristics.

Early literature studied the problem of optimizing reconfiguration between two predefined orbital patterns. Ahn [8] studied how to optimally reconfigure satellites from a six satellite formation to a five satellite formation after a satellite failure. The authors developed tools to determine the optimal assignment of satellites to open slots in order to minimize total propellant use and to distribute propellant use evenly across all satellites. Scialom [174] studied the reconfiguration of a constellation to enable staged deployment. The goal was to develop a framework to minimize both constellation cost and transfer time, when a small initial constellation transformed into a larger one, with both patterns known *a priori*. He identified two main steps in the framework: 1. assign all of the current assets to new orbital slots; and then 2. plan the launches and transfers of the new satellites to the unfilled slots. The reconfiguration framework was then expanded in later research [49, 32] to investigate the value of the staged deployment scenario. The authors found that, from an economic perspective, the flexible option of staged deployment allows the system to perform

39

much better over a range of unexpected future operating conditions. Siddiqi et al. [176, 177] separately studied the reconfiguration of constellation geometry and the reconfiguration of satellite hardware to support staged deployment of a communications constellation. The objective of the constellation reconfiguration was to minimize the cost (a combination of additional satellites needed and additional propellant required for reconfiguration), while meeting a performance constraint. De Weck et al. used part of the framework developed by Scialom [174] to study the staged deployment of a communications constellation [51]. The authors used the auction algorithm to optimally assign satellites to maneuver to open slots in the new constellation, so that the overall propellant usage is minimized. The authors mentioned that settling for a suboptimal constellation design, either initial or final, might greatly reduce the cost and complexity of reconfiguration. Therefore, in order to find best global designs, the reconfiguration strategy should be co-optimized with the constellation pattern design. De Weck et al. also stated that possible extensions of their work were to minimize the variance of ΔV capacity left for the satellites at the end of reconfiguration, and to look at using space tugs or fuel depots to allow the constellation to repeatedly reconfigure.

More recent literature focuses on reconfiguring a constellation to provide better coverage. In this case, the reconfiguration maneuver and the final orbits are optimized together. Lamassoure [116] investigated adding the flexible options of maneuverable satellites and propellant replenishment to LEO radar constellations. This would allow the constellation to actively focus coverage on specific, but uncertain, ground locations. Kim et al. [107, 106] used genetic algorithms to study the problem of maneuvering existing, on-orbit satellites to minimize the average revisit time for a specific ground location for 30 days, while satisfying stringent ΔV constraints. The authors found that the average revisit time over the ground location could be cut in half for ΔV values of around $100m/s$ for a constellation of four satellites. Similarly, Co et al. [35] investigated the feasibility of using chemical and electric propulsion to change the ground track of a single satellite in order to provide enhanced coverage of different regions of the Earth. Others have studied using Lorentz forces [159], aero-assisted orbital transfer [161], and electric propulsion [87] to enable satellites to adjust their coverage patterns responsively. Eves et al. [67, 69] also suggest that a small satellite could maneuver to lower its altitude in times of crises to provide better resolution. Ferringer

[75, 76, 72] developed a framework and an *a posteriori* decision support methodology to allow for an idealized 24 satellite GPS constellation to increase performance after the loss of a single satellite or a single plane. The approach reconfigured the constellation into a new, but previously unknown, optimized pattern and utilized multi-objective genetic algorithms to evaluate the reconfiguration problem in terms of six competing objectives. The competing objectives included maximizing two performance metrics: average daily visibility time and worst case daily visibility time for the global grid of ground points. The four cost objectives to be minimized were: the total time of flight; the largest ΔV required by any satellite; the variance of propellant usage among the satellites that maneuver; and, the number of satellites to be maneuvered.

A small amount of literature has touched on optimizing both constellation pattern design and reconfiguration strategy. Nann [142] investigated the use of reconfiguration to allow a 4 to 8 micro-satellite constellation orbiting Mars to take radio occultation measurements of the Martian atmosphere and to serve as a navigation aid for future Mars spacecraft. The author used Monte Carlo based tradespace exploration to highlight good candidate orbital patterns that would allow the system to reconfigure with constraints on propellant use. Davis [43] independently studied both the problem of optimizing constellation design and optimizing the reconfiguration of a constellation from one static design to another. He mentioned that future work should address the combined optimization of constellation design and reconfiguration and the optimization of constellation designs with uncertain mission requirements. Initial work on the ReCon concept laid the foundations for some of the research in this thesis. Paek investigated the combined optimization of satellite constellation patterns, reconfiguration strategy, and satellite design to enable a reconfigurable satellite constellation to provide on-demand, responsive coverage [152].

1.3 Flexible Design: An Active Approach to Manage Uncertainty

Over the past decade, much work focused on defining the nomenclature relating to systems that change over time. Changeability embodies a system's ability to be changed easily and is broken down into four categories: robustness, agility, adaptability, and flexibility [81]. Ryan et al. defines flexibility as "the measure of how easily a system's capabilities can be modified in response to external change" and adaptability as "the measure of how effectively a system can modify its own capabilities in response to change after it has been fielded" [170]. Flexibility differs from adaptability in that - in adaptable systems - the change must happen automatically without external intervention [170], and - for flexible systems - the change is initiated external to the system [169]. In contrast, robustness is defined as "the ability to remain 'constant' in parameters in spite of system internal and external changes" [169] and the "ability to be insensitive towards changing environments" [81]. Agility is related to flexibility and is "the measure of how quickly a system's capabilities can be modified in response to external change" [170]. Therefore, robust systems do not change, adaptable systems automatically change without external intervention, and flexible systems actively change with external intervention to respond to uncertainties in operating context.

Traditional engineering design often ignores uncertainty by fixing requirements early in the design process based on an expected operating context [50]. This practice simplifies the design process, but "these restrictions channel designers toward a fixed, static view of the problem" and can severely limit the system's future value while operating under different operating contexts [47]. The Iridium satellite constellation is a clear example of this limitation. This constellation was a technological success that revolutionized satellite mass production, but it was designed to a fixed expected market size. The system was unable to adapt when a much smaller actual market materialized, leading the company to bankruptcy [49, 50]. Had the designers considered market uncertainty, the system could have been designed to mitigate the impact of a much smaller market (e.g. potentially through staged deployment [49]). Much recent literature has focused on classifying typical uncertainties faced in complex system development. Earl et al. [34] divides uncertainty into two groups, 'unknown'

and 'known' uncertainty, which are present in two forms, descriptions and data. Known uncertainty is quantifiable from past experience and may be bounded and represented by distribution functions. Unknown uncertainty is comprised of unpredicted events that can either be in the system or outside of the system. In some literature known uncertainty is referred to as aleatory uncertainty and unknown uncertainty is referred to as epistemic uncertainty [227]. De Weck et al. [50] and Lin [124] further classify unknown uncertainty into three main groups: endogenous, exogenous, and hybrid. Endogenous uncertainty originates from within a system and includes performance uncertainty and system component reliability. Exogenous uncertainty originates from the external environment, is outside of the direct control or influence of the system designers, and, therefore, cannot be reduced at the source. Examples of exogenous uncertainty are government regulations, market fluctuations, and operational context uncertainty. Hybrid uncertainty results from a combination of endogenous and exogenous factors. Examples of hybrid uncertainty include schedule and contractual uncertainty. The three approaches to manage uncertainty are to: 1. control it by investing in uncertainty reduction through better forecasting or technology development and testing to increase reliability; 2. take a reactive approach by designing for robustness; 3. take a proactive approach by embedding real options or flexibility into the system design [124].

Lin cites two ways to achieve flexibility in a system, coincidental flexibility and design flexibility [124]. Coincidental flexibility refers to flexibility that is not intentionally designed for, and design flexibility is intentionally embedded into the system by the designers. This thesis is focused on design flexibility by intentionally embedding flexibility (or real options) in systems to limit downside risk and take advantage of upside opportunity. The major challenge is to decide where to embed flexibility within the system [45].

Lin [124] also developed a taxonomy of flexible options for large, capital intensive systems and classifies flexibility into three types as shown in Table 1.1: strategic level flexibility, tactical level flexibility, and operational level flexibility. Flexibility at the strategic level refers to flexibility in the systems' technology concept and high level configurations. Strategic level flexibility is comprised of technology concept flexibility (where there is flexibility in choosing technology and development concepts), and architectural flexibility (where there is flexibility

to modify system architectures or configurations over time). Flexibility at the tactical level refers to the flexibility to modify the behavior or performance of individual nodes or connections. Tactical level flexibility is comprised of facility flexibility, (where the facility can be easily modified to produce different products as inputs or the environment change), and capacity flexibility (where the facility can easily expand or contract production capacity). Flexibility at the operational level refers to flexibility to modify ways to operate a system without changing the systems' configuration or design. Reconfiguration provides tactical flexibility by allowing constellation operators to continually adjust the constellation pattern to optimize performance and recover from satellites failures to maximize expected future cost-effectiveness. Reconfiguration also provides operational flexibility by giving operators the ability to change the constellation pattern to focus coverage on regions of interest.

Table 1.1: Classification of Flexibility

Type of Flexibility		Application to Satellite Constellations
Strategic	Technology Concept	
	Architectural	➤Staged Deployment (expandable)
		➤Modular Payload (upgradable)
Tactical	Facility	➤Software Upgrades (upgradable)
		➤Reconfiguration (reconfigurable)
	Capacity	➤Refueling (replenishable)
Operational		➤Reconfiguration (reconfigurable)

Design for flexibility attempts to intelligently embed flexibility into systems to give decision makers the option to adapt to circumstances that develop to "cut losses by avoiding undesirable outcomes, and increase gains by taking advantage of new opportunities" [45]. First developed in the field of finance, an option is the right, but not the obligation, to take some course of action in the future. When an option is a physical entity it is called a real option [44]. The ability to expand a building as capacity demand increases is an example of a real option. This option must be enabled by initially spending more money to over-design and over-construct the building foundation so that it can support later expansion.

Flexibility derives its value from uncertainty and is most valuable when uncertainty is high [45]. Literature distinguishes between two types of options: options on systems that treat the system design as a black box and options in systems in which the system is specifically designed to be flexible [215]. For flexibility in systems, "flexibility is achieved intentionally by design, which not only mitigates downside risk but also allows systems to capture upside opportunities" [124]. A wide range of complex systems have been shown to benefit significantly from flexible design including: oil extraction [124, 97], satellite constellation reconfiguration [49, 32], satellite constellation design [98], aircraft families [155], and even highway transportation systems [46]. Cardin et al. proposed a nine step method to guide flexible design [29, 28]. The methodology starts out by identifying major uncertainties facing the system, then computes the deterministic performance of an initial inflexible design. Next, additional flexible options are introduced and the system's expected performance is compared with the performance of the inflexible system over the expected distribution of uncertain parameters. The comparison uses expected net present value and value at risk and gain curves as comparison metrics.

1.3.1 Valuation of Flexibility

Embedding flexibility in systems typically increases total life cycle costs and can cause compromises in system performance. Therefore, it is important to correctly determine the value of the flexible options to see if the investment makes sense and increases overall system value. Some literature has even found that flexible options can reduce the initial investment capital expenditure in a project by deferring costs over time [47]. Often, the flexible designs generate value in non-traditional areas of the design space. This has led to significant research in finding the correct value proposition for flexible designs that includes the value of flexibility [125, 171]. Several methods have been developed to investigate the value of flexibility. Viscito et al. used multi-attribute tradespace exploration with epoch era analysis to quantify system's ability to adapt to different 'epochs' that represent changes in operating context [208, 209]. Instead of quantifying the value of flexibility, this analysis quantified the amount of flexibility given by specific designs. Monte Carlo analysis with simulation models has also been used in the past to quantify the value of flexibility [45, 215, 216]. Monte Carlo analysis,

45

used to sample the distributions of uncertain parameters and then uses simulation models to compute the resulting system performance, is the approach taken in this thesis.

1.3.2   Flexible Constellation Architectures

Roos et al. [168] states that the success of complex engineering systems is often significantly affected by uncertainties and "an emphasis on strategies to deal with uncertainty - such as flexibility or robustness - may lead designers to different solutions than those that focus on optimization to meet specific criteria or specifications." There are several types of uncertainty encountered when operating satellite constellations. Satellite failure rate is an example of endogenous uncertainty. In the case of an Earth observation constellation, exogenous uncertainty encompasses uncertainty in: the event ground locations; the rate at which event response is needed; and the utility of collected data. An example of hybrid uncertainty is the cost to design, produce, deploy and operate the system. Lin [124] states that there are three main ways to manage uncertainty. The first is to try to control uncertainty by investing in better forecasting of the exogenous and endogenous uncertainties. An example of this method is to improve reliability through better control of satellite design and production processes. However, this approach is limited, since it is often impossible to produce better forecasts and it has proven to be very costly to improve satellite reliability. The second approach to manage uncertainty is to design the system to be robust to changing contexts. While this reactive approach often mitigates the downsides of uncertainty, it is not able to take advantage of the potential upsides [45]. The third approach to manage uncertainty is to be proactive and design the system to be flexible. Embedding flexible options in a system design typically costs more upfront; therefore, designers must ensure that the value generated by flexibility exceeds the additional cost. Earlier studies have shown a 20% increase in the total system value for a communications constellation deployed flexibly, in two stages. This increase in value occured despite an increase in satellite propulsion system complexity to allow for on-orbit reconfiguration [49]. It is expected that flexibility will yield similar improvements for reconfigurable earth observation satellite constellations.

Several flexible options have been identified to mitigate uncertainty in future operating context for satellite constellations. These include satellite constellation designs that are:

- Reconfigurable: The use of maneuverable satellites makes the constellation reconfigurable and allows satellites to alter their placement in the constellation. This facilitates on-demand, focused coverage for specific regions, which mitigates target location uncertainty. This flexible option also allows the constellation to actively respond to satellite failures by adjusting the constellation pattern to re-optimize coverage in the degraded state.

- Retaskable: A satellite with the ability to perform a number of different functions allows it to be retasked when needed providing another form of reconfigurability. Retaskable systems could satisfy multiple mission requirements or could mitigate market uncertainty by giving system operators several ways of generating revenue.

- Replenishable: The ability to replenish satellites allows satellite consumables, such as propellant, to be restocked. Besides linearizing the rocket equation and allowing for deferred launch costs for additional propellant, it gives operators the option to increase maneuver capability to mitigate event response rate uncertainty.

- Expandable: The ability to expand the system allows the constellation size to grow over time through staged-deployment, which lessens the impact of uncertainty in the remote sensing market. If the market utility of remote sensing data provided by the constellation meets or exceeds expectations, more capital can be invested to increase constellation size. If the market is lower than expectations, the option to not expand the constellation limits downside risk.

- Upgradable: The ability to upgrade the satellites allows for new technology to be inserted into the constellation to improve or alter surveillance capability and respond to uncertainties in remote sensing market demand. Upgrades could be changes to satellite software or hardware through on-orbit servicing or by introducing upgraded satellites during staged deployment.

This thesis focuses on the flexible option of reconfigurability and will leave analysis of the other options for future work. Retasking and replenishment are direct extensions of this work, and should be investigated in future work.

The Reconfigurable Constellation (ReCon) concept consists of a constellation with two operational modes: global observation mode (GOM) and regional observation mode (ROM). GOM features a constellation pattern allowing the satellites to provide coverage within a latitude band equal to the orbit inclination, and is similar to traditional static constellations. ROM features repeating ground track (RGT) orbits where the Earth nodal day and the satellite period are synchronized so that the ground paths repeat and the satellites provide enhanced regional coverage. The ReCon constellation normally resides in GOM providing partial global coverage. When a disaster event requiring additional coverage occurs, a subset of the constellation would maneuver, via an altitude change and proper phasing, into ROM to meet a desired level of persistence. Figure 1-1 shows the unfocused zonal coverage provided in GOM mode (left) and the focused regional coverage provided in ROM mode (right) for an eight satellite constellation. The ReCon concept employs the flexible option of reconfigurability to allow the constellation to provide both partial global coverage and on-demand focused regional coverage. This allows for increased satellite utilization which reduces the total number of satellites needed in the constellation. ReCon is also easily expanded and exhibits graceful degradation.
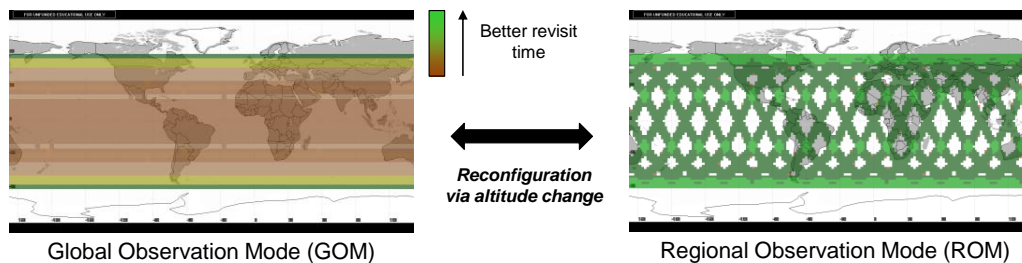
Figure 1-1: The ReCon concept features two operational modes: GOM provides wide-area partial global coverage and ROM features focused regional coverage

1.4 Open Issues in Constellation Design and Optimization

The design and optimization of satellite constellations is challenging due to immense computation demands associated with computing coverage statistics, and the combinatorial nature

of the design space. These difficulties have led previous researchers to simplify the problem in various ways including: decoupling pattern design from satellite design; only considering symmetric patterns; ignoring uncertainty; not considering satellite reconfiguration as a way to improve system cost effectiveness; and, not concurrently optimizing reconfiguration strategy and pattern/satellite design. These five gaps in current literature, summarized below, are directly addressed in this thesis.

1. **Satellite design and pattern design must be treated as a coupled problem**

   Despite significant coupling between satellite design and pattern design, these two elements are often optimized separately. Several exceptions to this statement include Budianto et al. [24], Jilla [103], and Krueger et al. [114]; however, these references only considered simple symmetric constellation patterns. Many researchers studying pattern design have chosen to summarize satellite design considerations by a combination of one or more of the following objectives: minimizing altitude (easier launch and smaller optics); minimizing inclination (easier launch); and minimizing the total number of satellites in the constellation. While these objectives do capture several effects of satellite design and deployment, they do not capture the intricacies of the problem. For instance, the quantization associated with fitting several spacecraft into a launch vehicle, often makes launch cost independent of inclination. As we will see later in this thesis, launch cost is actually driven by the number and type of launch vehicles needed, which is a function of launch vehicle capacity, the number of satellites, the size of the satellites, and the number and spacing of orbit planes in the constellation pattern. Additionally, the objective of minimizing the total number of satellites in the constellation is also misguided. In many cases in this thesis, the lowest cost designs are often comprised of many small satellites in lower orbits rather than fewer satellites in higher orbits. These examples illustrate why the design and optimization of satellite constellations must be treated as a multi-disciplinary multi-objective problem that accounts for the coupling between pattern design and satellite design.

2. **The design space must be expanded to consider asymmetric and layered patterns**

   While previous research has shown that asymmetric constellation patterns outperform

symmetric patterns for providing discontinuous coverage [94, 95, 82, 120, 157], most litera-ture still only considers traditional symmetric patterns. In 1996, Frayssinhes summarized his results, which showed that asymmetric patterns outperform symmetric patterns for discontinuous regional coverage, should help eliminate the "systematic use of symmetri-cal Walker constellations outside their appropriate context [continuous global coverage]". However, the continued use of symmetric patterns is likely due to a combination of sev-eral factors. First, many recent researchers have been more focused on optimizing the satellite design rather than the pattern design; and, therefore, elect to use well-known symmetric patterns. Second, optimization of asymmetric patterns requires significantly more computational effort, and only recently has computing technology advanced enough to accomplish the task in a rigorous way. In 2006, Ferringer [71] investigated a regional coverage asymmetric constellation using parallel multi-objective genetic algorithms, but the constellation size was limited to three satellites due to computational constraints. However, as will be seen in this thesis, modern optimization techniques and comput-ing capability coupled with asymmetric and layered patterns can significantly improve constellation cost-effectiveness.

3. **Uncertainty in requirements must be addressed to find truly resilient designs**
Previous satellite constellation literature does not explicitly consider uncertainty in future requirements or operating conditions. Most pattern research assumes the need for wide-area coverage, which implicitly incorporates uncertainty in the locations where coverage is needed. Some of the reconfiguration literature focuses on recovering from uncertain satellite failures, and staged deployment to allow for the constellation to expand if uncer-tain market demand materializes; instead, constellations should be optimized for actual uncertain parameter distributions. This accomplishes two goals: 1. the constellation can be tailored to actual estimated distributions instead of taking an overly conservative approach, and 2. the constellation can be designed to be resilient to the uncertainty.

4. **Reconfigurable satellites must be investigated to improve cost-effectiveness**
As presented in the introduction, reconfigurable constellations can focus coverage on spe-cific regions, which improves satellite utilization and leads to improved cost effectiveness. While previous research has investigated using reconfigurable satellites to recover from

failures and to enable staged deployment, there has not been significant research addressing the repeated use of satellite reconfiguration to improve overall cost-effectiveness and to mitigate uncertainty. This thesis presents an alternative reconfiguration strategy that does not consume large amounts of propellant and can, therefore, operate without complex and costly on-orbit refueling.

5. **Reconfiguration strategy must be concurrently optimized with satellite design and pattern design**

   In order to maximize efficiency, the reconfiguration strategy, for a reconfigurable architecture, should be concurrently optimized with the pattern design and satellite design. Concurrent optimization can lead to more efficient results by settling for a compromise between maximizing coverage in the two patterns, while minimizing reconfiguration cost. The sole reference that looked in concurrent optimization of reconfiguration and pattern designs was Nann et al., who concurrently optimized a single reconfiguration maneuver between two orbital states for a small constellation, but the research was limited to a single reconfiguration.

1.5 Research Objectives

The preceding sections alluded to the great difficulties in designing and optimizing constellations. Recognizing the inherent uncertainties in the future operating environment of a system designed to last decades only makes this task harder. The core problems are: how do we find good designs without arbitrarily restricting the design space; and, how do we find designs that that perform well over an uncertain operating context? My hypothesis for the proposed research is that a general methodology incorporating flexible design strategies with multidisciplinary system design optimization can find cost-effective reconfigurable satellite constellations and calculate the value of reconfigurability. When compared with traditional static designs, I believe these systems are more cost-effective and resilient to future operating conditions.

Therefore, the primary thesis objective is to develop and demonstrate a methodology to guide the design of cost-effective reconfigurable satellite constellations through the use of

integrated life cycle models while accounting for uncertainty in the future operating context. This objective is broken down into the following four sub-objectives:

1. Develop and demonstrate a comprehensive framework for optimizing reconfigurable satellite constellations that perform well under uncertain future operating conditions

2. Develop and validate an integrated, multidisciplinary model to compute the performance and cost of satellite constellations providing persistent regional coverage

3. Identify and characterize efficient reconfigurable constellation architectures and quantify the value of reconfigurability

4. Compare the cost-effectiveness of reconfigurable satellite constellations to other concepts including sun-synchronous constellations and rapid launched satellites

1.6   Specific Optical Imaging Scenario Investigated

This thesis considers an optical imaging constellation that must 1. provide enhanced coverage for a series of events during the system lifetime, and 2. must provide partial global coverage between -60 and 60° latitude with a $24hr$ maximum revisit time when not responding to an event. The desired event coverage is specified by the spatial resolution, temporal resolution, location, time of event, and the duration for the desired event coverage. As we will see in Section 4.2.3, all the events that occur during the system lifetime comprise the 'target deck', and each event in the target deck can have a different location, time, and desired coverage characteristics. Table 1.2 shows the values used in this thesis. The framework and tools presented in this thesis are easily modified to investigate other mission scenarios and, therefore, can serve as a basis for future work on other specific missions. The performance metric introduced in Section 3.6 measures how well a constellation meets the desired spatial and temporal resolutions, and the location and timing of events are modeled as uncertain parameters as explained in Section 4.2.

Table 1.2: Event properties for the scenario investigated in this thesis

Event Parameter	Values Investigated
Desired temporal resolution	0.5, $1hr$ from 6am to 6pm local time
Desired spatial resolution	0.5, $1m$
Location	sampled from PDF (see Chapter 4)
Time of event	sampled from PDF (see Chapter 4)
Event duration	14 days

1.7   Thesis Roadmap

The thesis is organized as follows. First, Chapter 2 introduces the constellation design and optimization framework. Chapter 3 provides an extensive overview of the detailed multi-disciplinary simulation model, which computes the performance and cost of static and reconfigurable satellite constellations. Chapter 4 introduces the Monte Carlo sampling implementation and Chapter 5 introduces a novel multi-objective evolutionary optimization algorithm implemented on a large computer cluster. Chapter 6 discusses results obtained for symmetric, layered and asymmetric constellations; and compares the static and reconfigurable architectures to traditional sun-synchronous orbit constellations, and rapidly launched architectures. Conclusions and recommendations for future research are given in Chapter 7.

Chapter 2

Constellation Design and Optimization Framework

The first thesis objective is to develop and demonstrate a comprehensive constellation design and optimization framework capable of optimizing reconfigurable satellite constellations. In order to find globally efficient constellation designs and avoid the limitations of previous research, the framework must: 1. use detailed multidisciplinary models that capture important linkages between subsystems; 2. explicitly consider uncertainty in the future operating context; and 3. eliminate artificial constraints that only serve to arbitrarily limit the design space. This thesis explicitly incorporates all three of these ideas into a unified framework capable of rapidly generating results using currently available computing resources. This chapter lays out the objectives of the framework, describes the framework in detail, and concludes by discussing how to use the framework output.
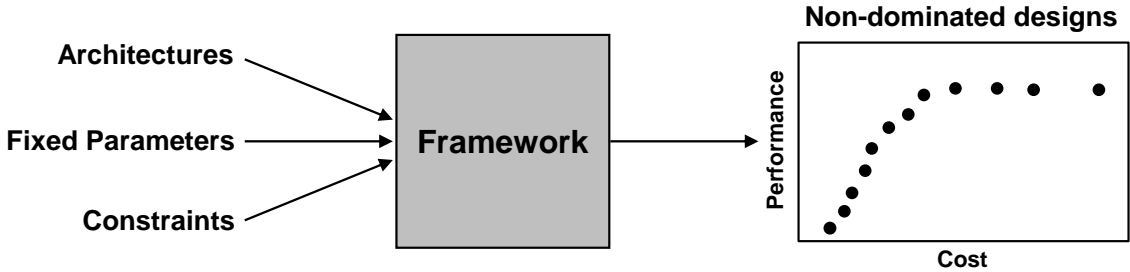
Figure 2-1: Desired inputs and outputs for the constellation design and optimization framework

Figure 2-1 shows the desired inputs and outputs for the constellation design and optimization framework. Prior to optimization, the user selects the architecture, a set of fixed parameters, and constraints. Several architectures are considered in this thesis including: static, reconfigurable, sun-synchronous, and rapid launched; however, the framework could handle almost any constellation architecture with only small modifications. Additional details on the four architectures studied in this thesis are provided in Chapter 6. Fixed parameters specify system properties and are not varied during optimization (e.g. satellite ballistic coefficient or propulsion system specific impulse), and constraints bound the optimization process by either specifying limits on constellation properties or placing bounds on design variables (e.g. minimum altitude, maximum optical aperture size). Additional details on the parameters, constraints, and bounds are provided in Chapter 5. Based on these user inputs, the framework finds the set of designs that form the optimal tradeoff between maximizing performance and minimizing cost. The designs that form the optimal tradeoff are termed non-dominated designs and, for these designs, increasing performance mean increasing cost.

The remainder of this chapter provides an overview of the constellation design and optimization framework and is organized into two major sections. Section 2.1 introduces three analysis layers that comprise the framework including the simulation layer, the Monte Carlo layer, and the multi-objective optimization layer. Section 2.2 explains how the non-dominated fronts output by the framework are used to: compare the cost-effectiveness of different constellation architectures, determine the value of incorporating reconfiguration into satellite constellations, and quantify the sensitivity of changing parameters.

2.1   The Three Framework Layers

The constellation design and optimization framework, shown in Figure 2-2, consists of three analysis layers: the simulation layer, the Monte Carlo layer, and the multi-objective optimization layer. The simulation layer is comprised of a multidisciplinary campaign-based simulation model that computes the life-cycle performance and cost of constellation designs. The performance is rated by the extent the constellation meets desired coverage of a specific set of ground events that are distributed in space and in time. The cost is the sum of
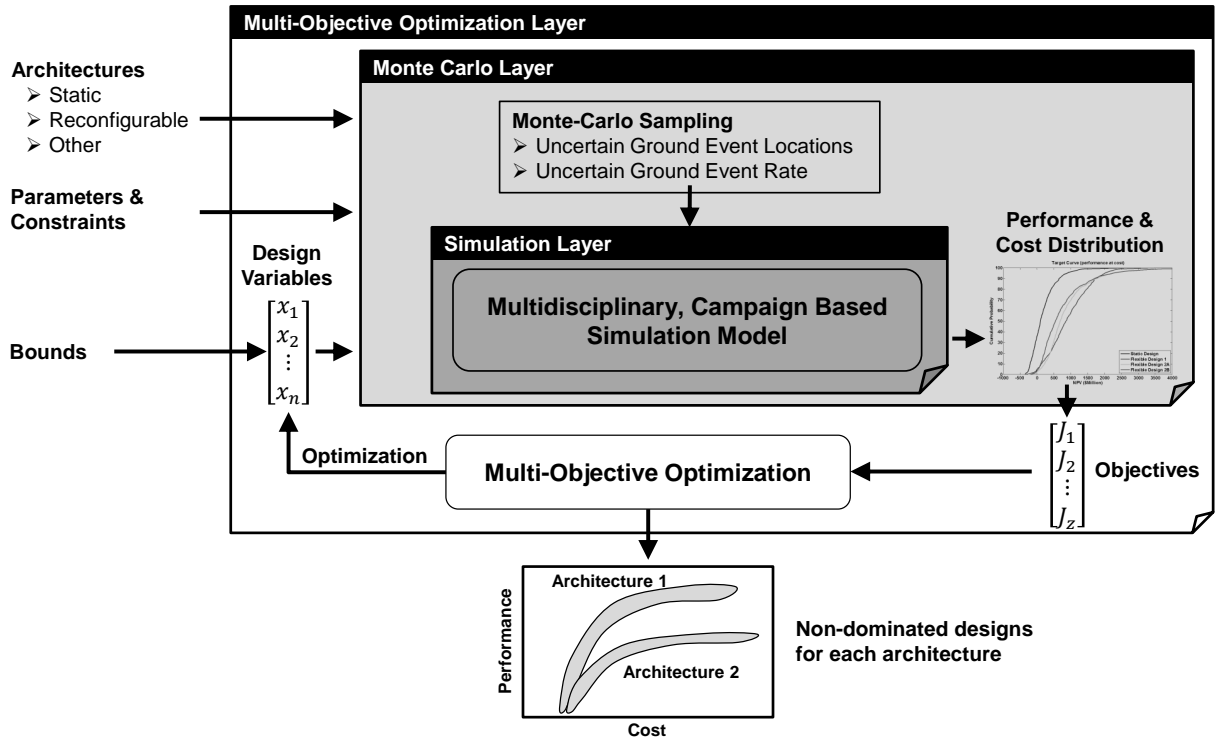
Figure 2-2: Constellation design and optimization framework

the non-recurring and recurring development, production, and launch cost. Operations and retirement cost is not modeled. Wrapped around the simulation layer is the Monte Carlo layer. By running the simulation model for different parameters sampled from the uncertain parameter distributions, this layer determines the performance distribution for a specific constellation design. The performance will vary given different sets of event locations and timing for a given future operating context. System cost is modeled in this thesis as deterministic. Given that the simulation model is non-linear and to avoid the 'flaw of averages' [173], Monte Carlo analysis is needed to perform the mapping from uncertain parameter distributions to a distribution of system performance. Wrapped around the Monte Carlo layer is a multi-objective optimization layer. This layer uses a multi-objective genetic algorithm to find non-dominated designs that form the optimal tradeoff between maximizing performance and minimizing cost. The Monte Carlo layer outputs a distribution of performance for each design, and the median is used as the performance for the optimization routine. The user also specifies bounds on the design variables and system property constraints to control the feasible design space for optimization. The non-dominated fronts are compared to determine

the cost-effectiveness of different architectures. Chapters 3, 4, and 5 of this thesis describe the simulation, the Monte Carlo, and the multi-objective optimization layers in more detail.

2.2 How is the Framework Useful?

The non-dominated fronts output by the framework can be used to: compare the cost-effectiveness of different constellation architectures, calculate the value of incorporating reconfiguration into satellite constellations, and quantify the sensitivity of the value of reconfigurability to changing parameters.

2.2.1 Finding Efficient Designs

The direct output from the constellation design and optimization framework are the actual non-dominated designs themselves. These designs represent the optimal tradeoff of the two competing objectives of maximizing performance and minimizing cost. Typically, in traditional single objective optimization, these two objectives would be combined into a single objective with a weighting function applied *a priori*, masking the actual tradeoff between objectives. Instead, the output from this framework gives designers constellation designs that represent the direct tradeoff of multiple competing objectives and enables more informed decisions. An example strategy of how a decision maker could select a design from the non-dominated front using a variety of data generated by the framework is given in Section 6.5.1.

2.2.2 Architecture Comparison and Computing the Value of Reconfigurability

The non-dominated fronts output from the framework can be easily compared to assess the cost-effectiveness of different constellation architectures. Additionally, the non-dominated fronts for the reconfigurable and static architectures can be directly compared to quantify the benefit of a reconfigurable system. While it may seem counter-intuitive at first, reconfigurable satellite constellations cost less than similarly performing traditional static constellations.

The combined effects of increased satellite utilization and the ability to perform well over uncertain future operating conditions create this cost benefit. As presented in Chapter 6, reconfigurable constellations require fewer satellites than static constellations to generate the same performance. The reconfigurable architecture is more cost-effective because the reduction in constellation size outweighs the increase in cost caused by additional propulsive capability. The value of flexibility, introduced previously in Section 1.3.1, is used to quantify the generated value of embedding flexibility into a system. The value of reconfigurability is defined as the reduction in total system cost for the same performance level by incorporating reconfigurability into the system. This metric provides a quantitative way to measure the benefit of incorporating reconfigurability and is found by comparing the non-dominated sets of designs for reconfigurable and static architectures.

2.2.3 Sensitivity Analysis

The framework can also be used to perform two types of sensitivity analysis: determining the sensitivity of the value of reconfigurability to changing parameters (or constraints) and determining the sensitivity of individual design performance and cost to changing parameters. In the former case, the framework finds non-dominated fronts for both static and reconfigurable designs using each combination of parameters. The difference between iso-performance designs is the new value of reconfigurability. In the second case, only the simulation and Monte Carlo layers are used to determine how the performance and cost of a specific system changes with changing parameters. Sections 6.1.3 and 6.1.4 quantifies the value of reconfigurability sensitivity to a few parameters and Section 6.5.3 quantifies the performance and cost sensitivity for a specific design to a few parameters.

Chapter 3

Simulation Model

To enable tradespace exploration and optimization, simulation models must accurately predict system response for a wide variety of designs and architectures . Modeling detail must be sufficient to capture all relevant system interactions. However, given the many functional evaluations needed by multi-objective optimization techniques it must also be limited to ensure computational efficiency. The purpose of the simulation model in this thesis is to evaluate the life-cycle performance and life-cycle cost of both static and reconfigurable constellation architectures. Inputs to the simulation model include design variables, parameters, and the choice of architecture to be studied (static or reconfigurable, and constellation pattern type) as shown in Figure 3-1. The design variables specify details of the pattern, the spacecraft and operations for reconfigurable systems. These values are varied by the optimization process in order to find efficient designs that simultaneously maximize performance and minimize cost. Semi-fixed quantities, called parameters, are also inputs to the simulation model and represent aspects of the system that are not varied during the optimization process. Some parameters are classified as uncertain. The uncertain parameters considered in this thesis include the timing and locations of ground events. Monte Carlo sampling then samples these parameters from input probability distributions and uses the simulation model to generate the corresponding system performance distribution. The model outputs consist of the two optimization objectives of performance and cost and a set of constraint violations that determine when optimization constraints are violated. The constraints ensure that the optimization process focuses in on the feasible region within the design space. More details

are given about the Monte Carlo sampling (Chapter 4) and optimization process (Chapter 5) later in this thesis.
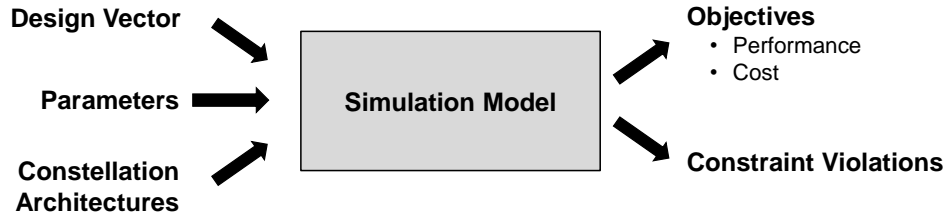
Figure 3-1: The simulation model computes the performance and cost of a constellation design given a context specified by parameters

The simulation model consists of five primary modules, shown in Figure 3-2, including simulation setup, spacecraft, cost, astrodynamics and performance. The simulation setup module generates the initial constellation pattern and initializes the uncertain operating parameters. The spacecraft module sizes the payload, spacecraft bus, and propulsion system based on the design vector. The spacecraft dry mass and launch volume are modeled as a function of aperture diameter based on historical optical Earth observation satellites. The propulsion system propellant mass and dry mass are a function of the spacecraft dry mass and ΔV requirements. The cost module computes the system life-cycle cost by aggregating the cost of the optical payload, the spacecraft, and the launch as well as applying quantities of scale effects. The astrodynamics module tracks the orbital state of the constellation throughout its lifetime and computes coverage in GOM and ROM. For reconfigurable systems, the simulation model employs a decision model that mimics the behavior of a decision maker in order to determine how to use the reconfigurable option for each event (how many satellites should be reconfigured and how fast should they be reconfigured). The simulation model then tracks both the performance as well as depletion of individual satellite ΔV over time. The final module is the performance module which computes the overall life-cycle performance of the system (the mean performance generated during all regional events). This performance model is tailored to rate how well the system provided the desired level of temporal and spatial resolution coverage for each regional event.

The remainder of this chapter provides an in-depth overview of the simulation model
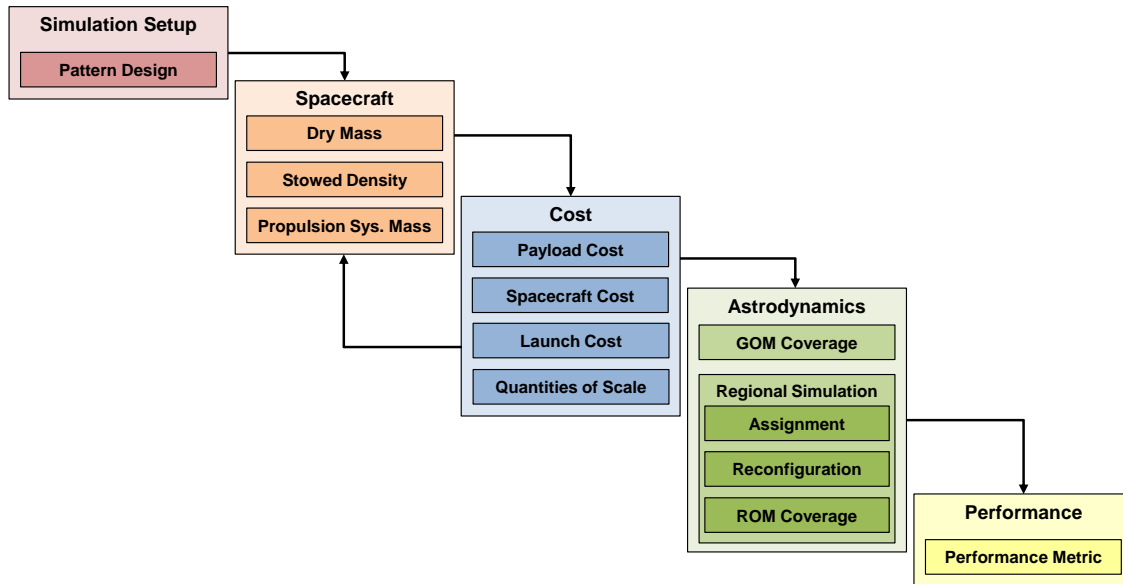
Figure 3-2: The simulation model is comprised of five modules arranged to minimize feedback and maximize computational efficiency

and is organized as follows. First, Section 3.1 gives an introduction to some fundamental astrodynamics relationships that are critical to understanding model construction. This is followed by detailed explanations of the five simulation modules described previously: simulation setup (Section 3.2), spacecraft properties (Section 3.3), cost modeling (Section 3.4), astrodynamics (Section 3.5), and performance (Section 3.6). This discussion is then followed by model validation (Section 3.7) and a summary of simulation model efficiency and computational run time (Section 3.8).

3.1 Astrodynamics Introduction

This section provides an overview of three fundamental astrodynamics relationships that are critical to understanding details of simulation model construction starting with a brief overview of orbital elements. Next, an introduction to repeating ground track (RGT) orbits and a discussion on how pass times are calculated for any given RGT orbit. The section concludes by introducing the fundamental satellite based observation geometry that governs ground coverage and spatial resolution.
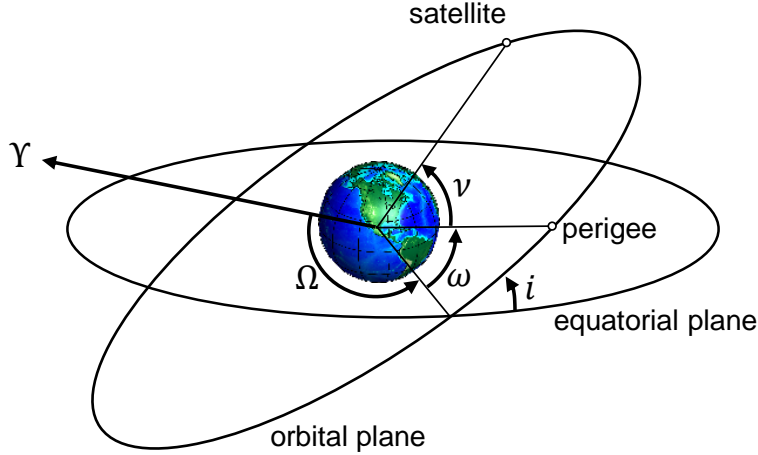
Figure 3-3: Diagram showing how the four angular elements are defined

A satellite's position is classically described by six orbital elements. The semi-major axis (a) and the eccentricity (e) describe the orbit's shape and size while the right ascension of the ascending node (Ω) and inclination (i) specify the orbital plane orientation. The last two orbital parameters, the argument of perigee (ω) and true anomaly (ν), specify the location of the satellite in the orbit plane. The four angular elements are shown in Figure 3-3. i is the angle between the orbit plane and equatorial plane and Ω is the angle from the vernal equinox to the location where the orbit crosses the equatorial plane on the ascending pass. ω is the angle from the ascending node to perigee which is the closest approach of the satellite to the central body, and ν is the angle from perigee to the satellite's current position. A Keplerian orbit is an orbit in which gravity is the only force and the central body is represented as a point mass. The first five orbital parameters (a,e,i,Ω,ω) are time invariant in a Keplerian orbit while only the true anomaly changes, accounting for satellite motion. In this thesis, the mean anomaly (M) is used in the place of the true anomaly. The mean anomaly is defined as an angle measured from perigee with constant angular rate corresponding to the satellite's mean motion (n) defined below in Equation 3.2. For circular orbits, $M = \theta$. Under these assumptions, the satellite state is then given as:

$$X(t) \quad = \quad (a_0, e_0, i_0, \Omega_0, \omega_0, M_0 + nt) \tag{3.1}$$

where the mean motion (n) is a function of Earth's gravitational constant (μ) and a:

$$n = \sqrt{\mu/a^3} \tag{3.2}$$

Satellites encounter deviations from Keplerian motion by two types of perturbations, secular and cyclic. Secular perturbations build up over time, while cyclic perturbations have zero net effect over the course of a complete orbit. The analysis in this thesis accounts for secular perturbations only. The primary cause of secular perturbations for low earth orbit satellites (LEO) is the J_2 zonal effect caused by Earth's gravitational bulge at the equator. The J_2 perturbation causes orbital precession which leads to a time rate of change for Ω, ω and M given as [221]:

$$\dot{\Omega} = \frac{3nR_\oplus^2 J_2}{2p^2} \cos i \tag{3.3}$$

$$\dot{\omega} = \frac{-3nR_\oplus^2 J_2}{4p^2} \left(5\cos^2 i - 1\right) \tag{3.4}$$

$$\dot{M} = \frac{-3nR_\oplus^2 J_2}{4p^2} \left(3\cos^2 i - 1\right) \sqrt{1 - e^2} \tag{3.5}$$

Where the parameter (p) is given as: $p = a(1 - e)$. The inclusion of J_2 effects modifies Equation 3.1 to give the state of the satellite as a function of time (t) as:

$$X(t) = (a_0, e_0, i_0, \Omega_0 + \dot{\Omega}t, \omega_0 + \dot{\omega}t, M_0 + \dot{M}t + nt) \tag{3.6}$$

The rate of orbital precession is primarily a function of inclination and altitude (see Figure 3-4). $\dot{\Omega}$ is equal to zero at an inclination of 90° and is negative for prograde orbits and positive for retrograde orbits. $\dot{\omega}$ is equal to zero at the critical inclinations of 63.435° and 116.565° and is positive for inclinations higher between those critical inclinations, and negative otherwise. Later in this thesis, we will see that these precession rates greatly affect initial constellation deployment (Section 3.3.2) and coverage (Section 3.1.2).
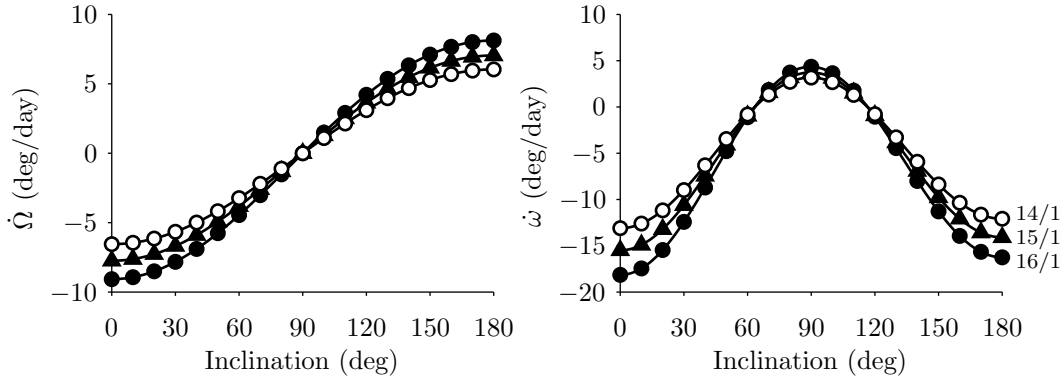
Figure 3-4: Orbital precession, causing $\dot{\Omega}$ and $\dot{\omega}$, is primarily affected by inclination and altitude

3.1.1 Repeating Ground Track Orbits

Repeating ground track (RGT) orbits are specialized orbits where the satellite ground track repeats every N_o integer orbits in N_d integer sidereal days. This is accomplished by synchronizing orbital motion (including perturbations) with the Earth's rotation rate ($\omega_\oplus$). Setting up a RGT orbit involves two main steps. First, we must solve for the semi-major axis that satisfies the compatibility criterion, and, second, we must phase the spacecraft properly to place the ground track over a specific ground position. The second order anomalistic period that satisfies the RGT compatibility criterion is given by Mortari et al. [134] as:

$$T \;=\; \frac{2\pi N_d}{\omega_\oplus N_o}\left(1 + 2\xi\frac{n}{\omega_\oplus}\cos i\right)^{-1}\chi \tag{3.7}$$

Where:

$$\chi \;=\; 1 + \xi\left[4 + 2\sqrt{1-e^2} - \left(5 + 3\sqrt{1-e^2}\right)\sin^2 i\right]$$
$$\xi \;=\; \frac{3R_\oplus^2 J_2}{4a^2\left(1-e^2\right)}$$
$$T \;=\; \frac{2\pi}{n}$$

The semi-major axis is then found by solving Equation 3.7 and the RGT altitude increases as the inclination increases (see Figure 3-5). This second order relation is sufficient for the

work in this thesis since the simulation model only propagates the RGT orbit over a few weeks, however more detailed analysis that includes the J_2^2 and J_4 terms is given by Vtipil et al. [211].
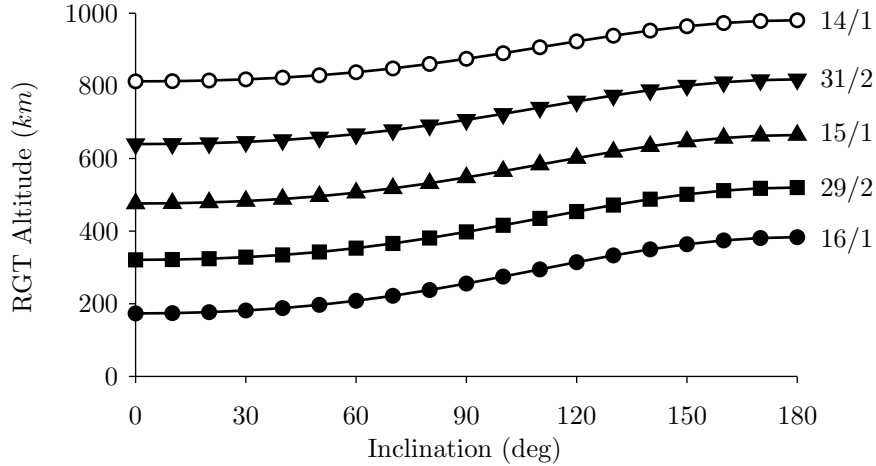
Figure 3-5: RGT altitude increases with increasing inclination and with decreasing N_o/N_d ratio

Once the semi-major axis is found that synchronizes the orbital period with Earth's inertial rotation period, we must then find the specific RGT orbit that passes over a specific ground position. One way to accomplish this is to use Flower Constellation theory by introducing an angle that specifies the shift in longitude of the ground track (Λ)[16]:

$$\Lambda = N_o\Omega + N_d M \tag{3.8}$$

Figure 3-6 shows two repeating ground tracks corresponding to $\Lambda = 0°$ (solid) and $\Lambda = 90°$ (dashed). Here we see that the angle shifts the repeating ground track to the east on the interval $(0 - 360°)$ and the ground track for $\Lambda = 0°$ is the same as $\Lambda = 360°$. It should be noted that, given the static nature of a RGT ground trace, the only way to change the specific RGT that a satellite is in is to either modify Ω or M. The typical way to accomplish this is to change orbital altitude which causes a difference in mean motion and allows M to change relative to the intended RGT slot. Ω can also be changed by differential orbital precession after an altitude change, or using propulsion at great propellant expense. Additionally, by changing Λ, it is possible to pass over a specific ground location with two

different RGT orbits. One pass occurs when the satellite is ascending in latitude coverage
(termed ascending pass coverage in this thesis) and one occurs when the satellite is descending
in latitude coverage (termed descending pass coverage in this thesis).
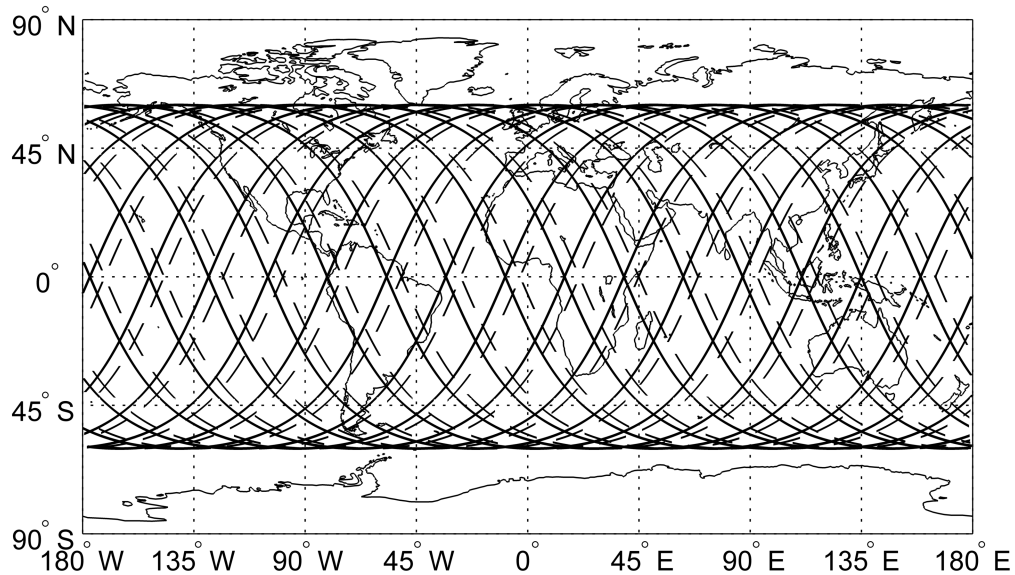
Figure 3-6: The RGT ground track is adjusted in longitude by the phasing angle Λ. RGT
orbits are plotted with $\Lambda = 0°$ (solid) and $\Lambda = 90°$ (dashed)

3.1.2 Determining RGT Pass Time

Solar illumination conditions often affect the quality of space based optical imagery. Images
taken early in the morning or late in the evening will be dim and will include shadows that
reduce overall information content. This means that in a reconfigurable constellation, only
those assets that can provide coverage within desired illumination constraints should be
reconfigured. This section explains how to predict the local solar time of a pass for a given
RGT orbit. This pass time is a function of the ground location (φ, λ), the satellite's orbital
plane (i, Ω), and time of year. Figure 3-7 shows the geometry for computing pass time for
the ascending pass coverage case. We must find the Greenwich mean sidereal time (θ_{GMST})
that ensures a nadir pass over the target location on the RGT denoted by 'P'. Figure 3-7
shows that the ground location's λ and θ_{GMST} are equal to the satellite's Ω and the $\Delta\lambda$

quantity since these two sets of angles are referenced to the vernal equinox (Υ). Taking the ascending pass case first, the balance equation is as follows:

$$\theta_{GMST} + \lambda \ = \Omega + \Delta\lambda \tag{3.9}$$

Here we see that the Greenwich mean sidereal time θ_{GMST} is added to the target longitude (λ) and must equal the satellite's right ascension of the ascending node Ω added to the longitude shift from the ascending node to the target ($\Delta\lambda$).
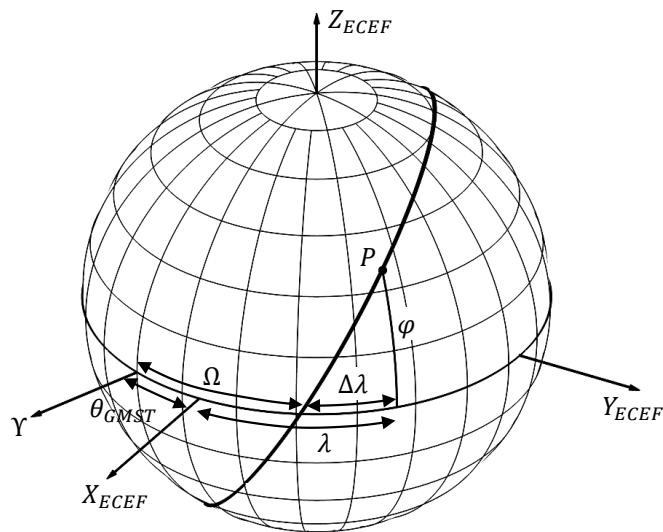
Figure 3-7: The local time of an ascending pass is calculated by solving an angle balance in longitude. The mean sidereal time plus the target longitude must equal the satellite Ω plus the drift in longitude during the ascending portion of the orbital arc.

This equation, solved for θ_{GMST}, yields the solution for the pass time for an ascending pass case (Equation 3.10a), and similarly for the pass time for an descending pass case (Equation 3.10b).

$$\theta_{GMST}\,(ascending) = \Omega + \Delta\lambda - \lambda \tag{3.10a}$$

$$\theta_{GMST}\,(descending) = \Omega - \Delta\lambda - \lambda - \pi \tag{3.10b}$$

The $\Delta\lambda$ term can be approximated by assuming that the triangle formed by $\Delta\lambda$, φ and the

ground track is a right spherical triangle:

$$\Delta\lambda = \arcsin\left(\tan\varphi / \tan i\right)$$

Once θ_{GMST} is determined, then the sidereal time needs to be converted to solar time and then converted to the local time at the target longitude. Sidereal time is referenced inertially (to the stars) whereas solar time is referenced to the sun. Since both the Earth's orbit around the sun and the Earth's rotation are counter-clockwise, there is one extra sidereal day for every solar year. Greenwich mean solar time θ_{GMT} is solar time referenced to the prime meridian. The conversion between θ_{GMST} and θ_{GMT} is given as:

$$\theta_{GMT} = \theta_{GMST} - \frac{2\pi}{T_s}\Delta D + \pi \tag{3.11}$$

Where, ΔD is the decimal days of the year referenced to the vernal equinox, and T_s is the sidereal year duration in days. The added factor of π is caused by Greenwich mean time being referenced to local noon. The solar time is then converted to local mean time θ_{LMT} according to the target longitude λ as:

$$\theta_{LMT} = \theta_{GMT} + \lambda \tag{3.12}$$

θ_{LMT} is then converted from degrees to hours and combining these relations together yields final relations that predict local time of coverage based on orbital parameters and ground location:

$$\theta_{LMT,a} = \Omega + \arcsin\left(\frac{\tan\varphi}{\tan i}\right) - \frac{2\pi}{T_s}\Delta D + \pi \tag{3.13a}$$

$$\theta_{LMT,d} = \Omega - \arcsin\left(\frac{\tan\varphi}{\tan i}\right) - \frac{2\pi}{T_s}\Delta D \tag{3.13b}$$

Here we can see how the various parameters affect the pass time. The most noticeable feature is that the ground longitude (λ) canceled out, so that ground coverage time is only a function of the target latitude (φ). Additionally as ΔD increases, the pass time moves backward and as Ω increases the pass time moves ahead. Therefore, since Ω changes in time

due to orbital precession and ΔD changes with time, the pass time is likely to change as a function of time. Figure 3-8 shows the pass time drift in hours per day as a function of inclination for three different N_o/N_d ratios. We see that pass time drift is largest for low inclination prograde orbits and high inclination retrograde orbits, and is zero around polar orbits. Also, the pass time drift rate increases with decreasing RGT altitude. For sun-synchronous orbits, the ΔD induced shift cancels the Ω induced shift yielding time-invariant pass time. The inclinations for sun-synchronous, RGT orbits are 96.560° for $N_o/N_d = 16/1$, 97.635° for $N_o/N_d = 15/1$ and 98.982° for $N_o/N_d = 14/1$.
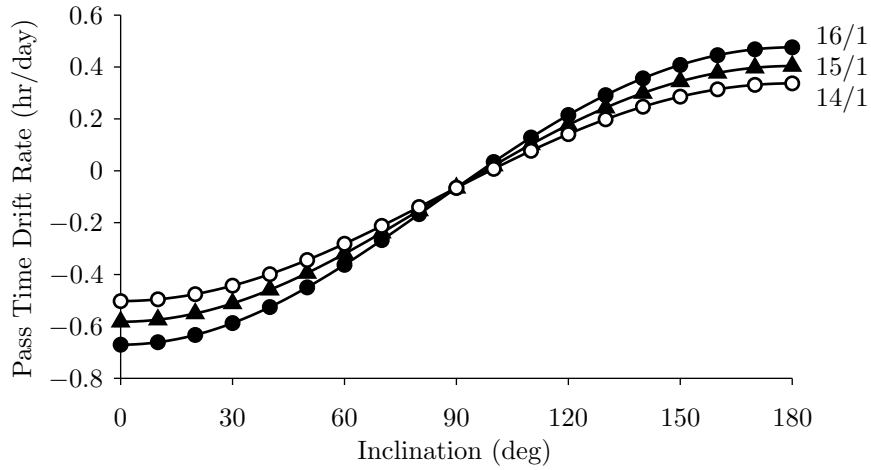
Figure 3-8: The pass time drift rate is strongly affected by inclination and increases with larger N_o/N_d ratios

As was discussed earlier, each satellite can provide either ascending or descending pass coverage in RGT, each of which will likely have different pass times. The difference in pass times give system operators options in providing the best coverage. The difference between ascending and descending pass coverage times is given as:

$$\theta_{LMT,a} - \theta_{LMT,d} = 2 \arcsin\left(\frac{\tan\varphi}{\tan i}\right) + \pi \qquad (3.14)$$

This relation shows that the ascending and descending pass times differ in a π phase shift along with the *arcsin* term which is a function of the inclination and target latitude. If the orbit inclination is equal to the target latitude, then the arcsin term is equal to π and the term cancels out on the interval 2π. This means that difference in θ_{LMT} for ascending and

71

descending pass coverage is π which is equivalent to 12 hours. If the target latitude is greater than the inclination (ignoring any satellite footprint extent), then there is no coverage. If the target latitude is less than the inclination, then the pass time difference decreases as the arcsin term gets smaller. Figure 3-9 shows the minimum pass time separation between ascending and descending passes as a function of inclination and target latitude.
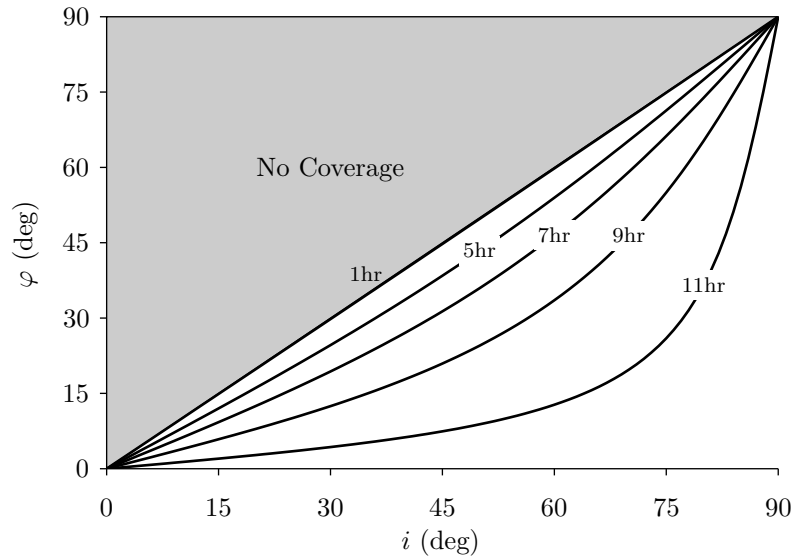
Figure 3-9: The time difference between ascending and descending passes is small when $i \approx \varphi$, approaches 12 hours when $i >> \varphi$, and no coverage is provided when $i < \varphi$ and the target is outside of the satellite ground footprint

Figure 3-10 shows a snapshot of the latitudinal coverage as a function of Ω for passes between 6am and 6pm local time (left) and 8am and 4pm local time, with ascending pass coverage (shaded light), descending pass coverage (shaded medium) and both (shaded dark). The plots were produced with $i = 60°$ and $\Delta D = 0$. Here we see that the latitude band for coverage in the desired time period varies with Ω. For $0° \leq \Omega \leq 60°$ and $300° \leq \Omega \leq 360°$, the satellite has wide coverage with an ascending pass RGT while for $120° \leq \Omega \leq 240°$, the satellite has wide coverage with an descending pass RGT. For $60° \leq \Omega \leq 120°$ and $240° \leq \Omega \leq 300°$, there is coverage provided from ascending and descending RGT orbits for some latitudes and no coverage for other latitudes. Additionally, the width of each band is proportional to the fraction of the day of the desired coverage time period. In this case, the desired time period is 12 hours, which is half of a day so the width of the coverage band is

72

180°. As the desired time period decreases, the coverage bands also decrease in size, leading to a smaller range of orbit planes that can provide coverage.
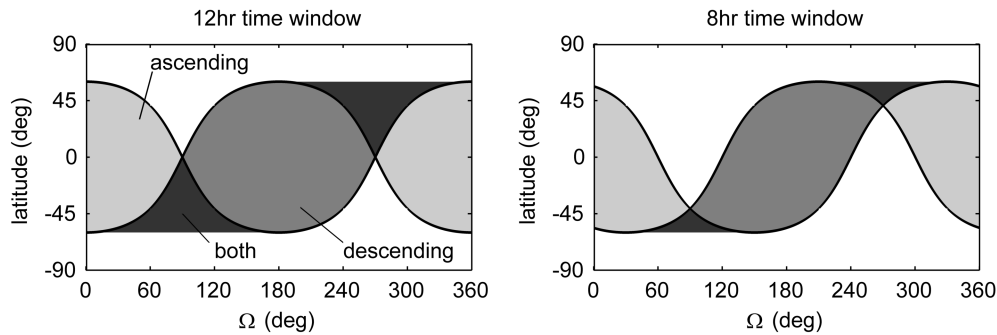
Figure 3-10: The range of latitudes serviced by a satellite in a RGT orbit within a fixed daily time window is only a function of Ω

The coverage plot displayed in Figure 3-10 varies with time due to both orbital precession (causing $\dot{\Omega}$) and the ΔD term in Equation 3.13. As was described earlier in this section and shown in Figure 3-4, Ω can vary between -10 to 10 degrees per day depending on inclination and orbital altitude. This will shift the satellite Ω to the right or left in the plot. The ΔD term causes a shift of coverage to the right with a one year repetition period. Figure 3-11 shows the change in coverage for a 12 hour desired time period (subplots a,c,e) and an 8 hour desired time period (subplots b,d,f). The times displayed are 0 months (subplots a,b), 2 months (subplots c,d) and 4 months (subplots e,f). The constant changing of the ground coverage coupled with the distribution and randomness of target location in longitude generally removes any preference for absolute Ω positioning of satellites in the constellation. However, the relative positioning, controlled by the pattern design, has a large effect on overall performance and is a focus of this thesis.

3.1.3 Earth Observation Geometry

The 'satellite ground footprint' refers to the instantaneous area on the Earth's surface covered by an orbiting satellite. Two footprints exist: the maximum footprint representing coverage from horizon to horizon; and the smaller effective footprint which includes minimum ground elevation angle constraints. This section introduces viewing relations for both cases, and then discusses how ground sampling distance (GSD) is calculated.

73
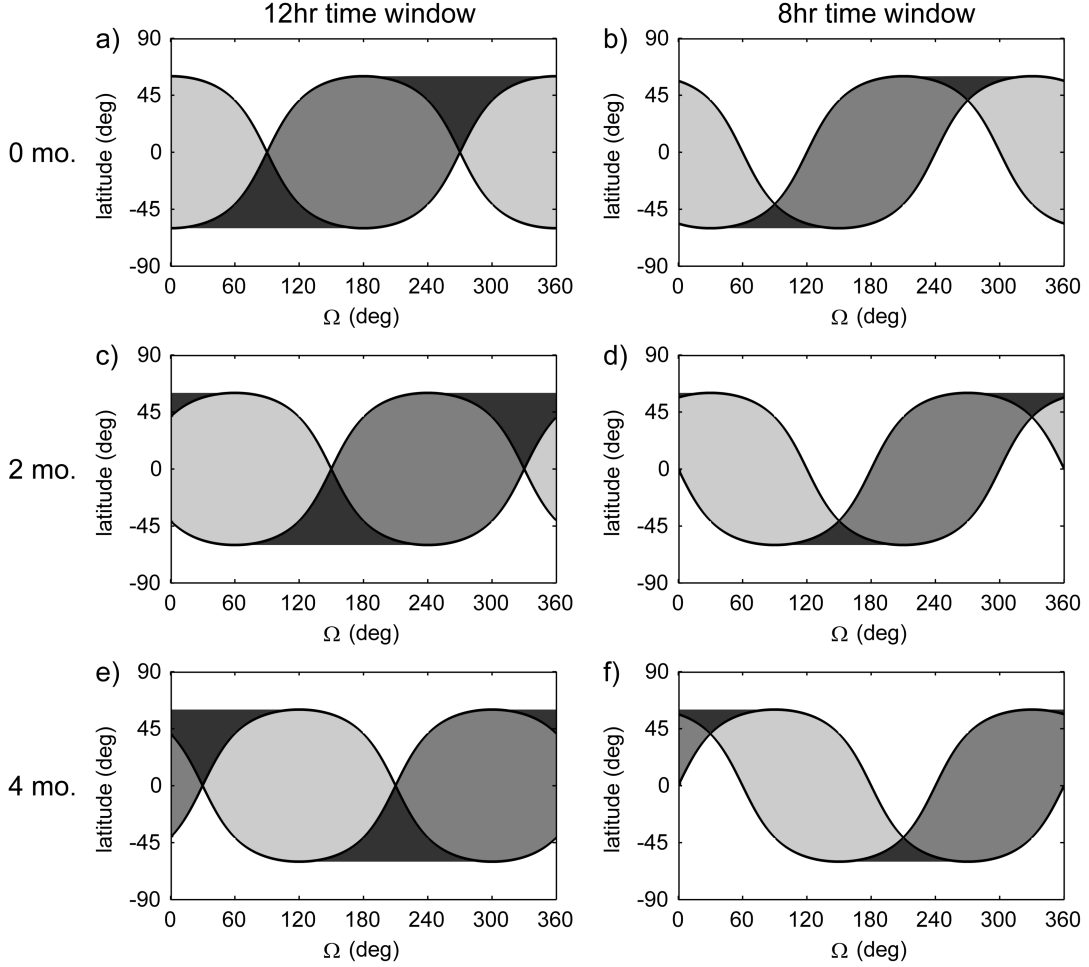
Figure 3-11: The latitudinal coverage band shifts in Ω over time due to orbital precession and changing ΔD

The satellite, located at point P in Figure 3-12, provides a maximum ground coverage footprint with an Earth central angle of λ_{max}. The maximum boresight angle η_{max} is defined as the angle off nadir to the horizon and the maximum slant range (at λ_{max}) is L_{max}. Relations for η_{max}, L_{max}, and λ_{max} are given as follows [221, 206]:

$$\eta_{max} = \arcsin\left(\frac{R_\oplus}{R_\oplus + h}\right) \tag{3.15}$$

$$\lambda_{max} = \frac{\pi}{2} - \eta_{max} \tag{3.16}$$

$$L_{max} = R_\oplus \left(\sin\lambda_{max}/\sin\eta_{max}\right) \tag{3.17}$$
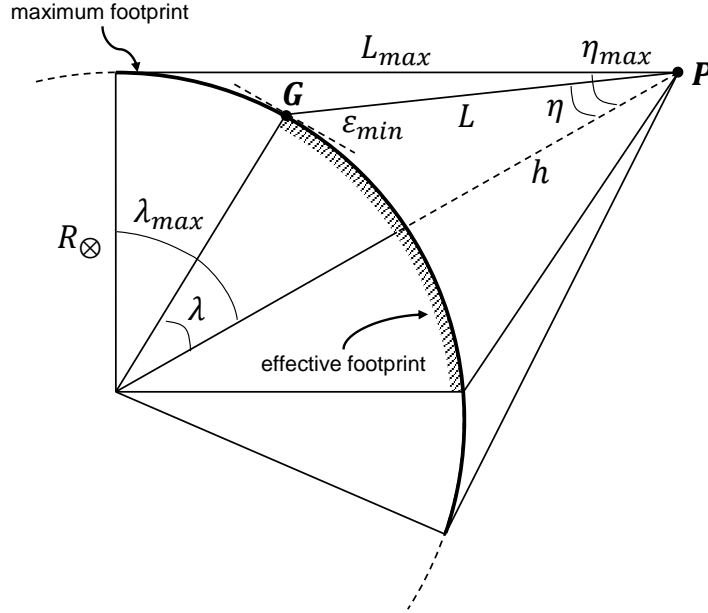
Figure 3-12: Satellite to Earth observation geometry

In general, there will be some minimum satellite elevation angle ε_{min} necessary for useful observation. ε is the angle measured from ground between the local horizontal and the vector to the satellite's position. For optical imagery, large ε is desired to avoid obscuration from tall objects and improve both GSD and radiometric accuracy. However, as ε_{min} increases, the satellite's effective ground footprint shrinks, reducing overall coverage.

Ground location G, located at the edge of the effective ground footprint, will have an elevation angle of ε_{min}. In this case, the earth central angle λ, boresight angle η, and slant range L are given as [221, 206]:

$$\eta = \arcsin\left(\cos\varepsilon_{min}\sin\eta_{max}\right) \tag{3.18}$$

$$\lambda = \tfrac{\pi}{2} - \varepsilon_{min} - \eta \tag{3.19}$$

$$L = R_\oplus\left(\sin\lambda/\sin\eta\right) \tag{3.20}$$

As ϵ_{min} increases the satellite footprint shrinks considerably, shown in Figure 3-13, and therefore overall coverage will be reduced. For ground points contained nearer to the center of the effective ground footprint will have larger ε, leading to smaller η, smaller λ and

75

therefore smaller L.
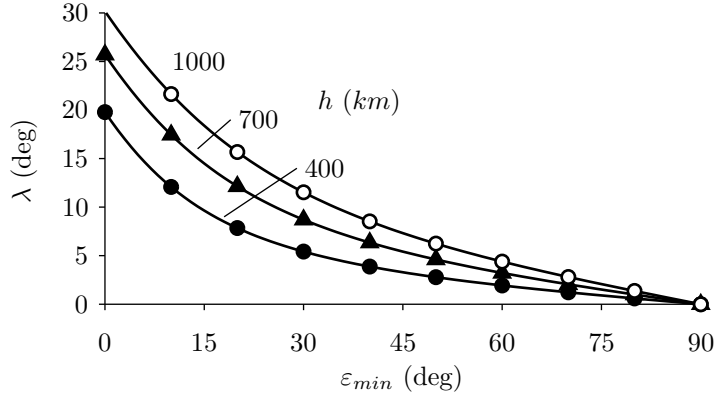
Figure 3-13: Both decreasing altitude and increasing ε_{min} requirements lead to smaller effective ground footprints and therefore significantly reduced coverage

The GSD (spatial resolution) of an optical sensor is fundamentally limited by diffraction to the Ralyleigh limit. For nadir viewing, this limit is a function of the observation wavelength λ_s, orbital altitude h and aperture diameter D as follows:

$$x_{nadir} = \frac{1.22\lambda_s h}{D} \tag{3.21}$$

For off-nadir viewing, the resolution along-boresight (x_a) and cross-boresight (x_c) will be different and are given by:

$$x_a = \frac{1.22\lambda_s L}{D \sin \varepsilon} \tag{3.22}$$

$$x_c = \frac{1.22\lambda_s L}{D} \tag{3.23}$$

For this thesis (and consistent with current practice) [123], I take the geometric mean of the along and cross track resolutions to determine the overall ground sample distance (x):

$$x = \sqrt{x_a x_c} = \frac{1.22\lambda_s L}{D\sqrt{\sin \varepsilon}} \tag{3.24}$$

x is minimized (for fixed h and D) when the ground points of interest are close to the satellite's ground track. In the case where the ground point lies on the satellite's ground track, then $x = x_{nadir}$. As the ground point moves further away from the ground track, ε

decreases and x increases dramatically, as shown in figure 3-14.
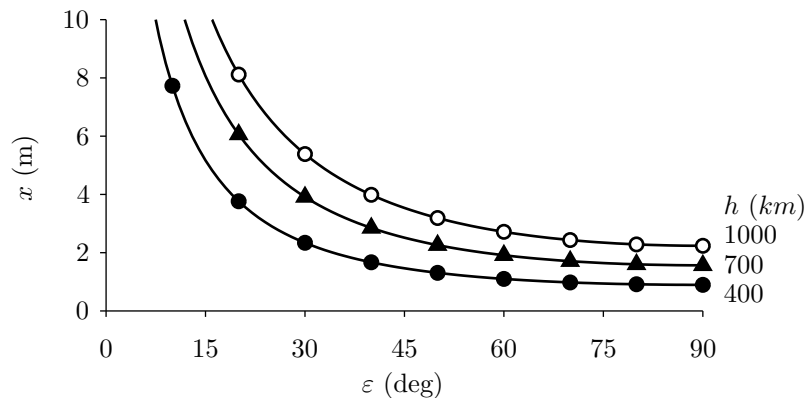
Figure 3-14: The $1/\sqrt{\sin \varepsilon}$ term in Equation 3.24 causes GSD to be relatively independent of ε when $\varepsilon > 45°$ (values calculated with $D = 0.3m$)

Therefore, there are three way to decrease x. Lowering h reduces the slant range L and decreases x but also reduces the effective satellite ground footprint. Increasing D reduces x, but will increase payload cost. Ensuring nadir, or close to nadir, passes increases ε and therefore reduces x, but often requires orbital maneuvers to change the satellite's ground track.

3.2   Simulation Setup Module
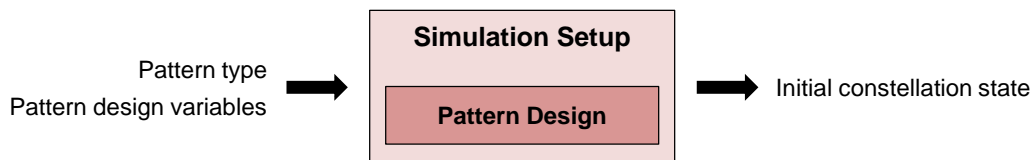
Figure 3-15: The simulation setup module computes the initial constellation state given a constellation pattern type and a set of pattern design variables

The simulation setup module initializes the constellation pattern by computing the initial satellite orbital positions. Various pattern designs are considered in this thesis including: a single symmetric pattern identical to the Walker Delta pattern; a two-layer pattern that combines two symmetric patterns shifted in i, Ω, and M; an asymmetric pattern with common i and h, but with free range of Ω and M for each satellite; two 'quasi'-asymmetric patterns

(the restricted asymmetric and asymmetric Walker pattern) that combine the benefits of a fully asymmetric pattern with some regular spacing rules to reduce design variables; and an asymmetric layered pattern, which is similar to the layered pattern but consists of two asymmetric Walker patterns. In addition to these patterns, the thesis also considers sun-synchronous and rapid launched architectures. Section 6 describes the individual patterns in more detail before presenting results.

3.3 Spacecraft Module
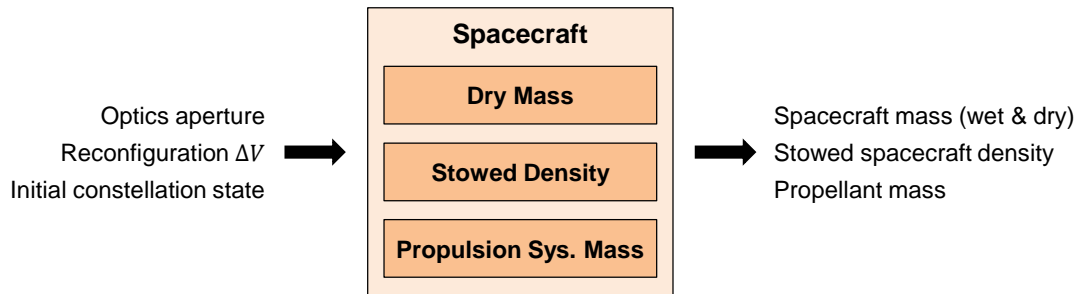
Figure 3-16: The spacecraft properties module computes the size and weight of the satellites given several input design variables

The spacecraft module computes payload, spacecraft bus and propulsion system properties. These properties are used by the cost model to determine payload, spacecraft, and launch cost. This section details how the payload and spacecraft bus mass and stowed volume are estimated and summarizes sizing of the propulsion system.

3.3.1 Payload and Bus Design

Spacecraft mass and volume are estimated in the simulation model by fitting curves to the properties of existing optical Earth observation satellites. This ensures that the estimates are consistent with currently fielded technology and eliminates the need for a complicated satellite model that would be difficult to validate. Table 3.1 lists the aperture size, wet mass, satellite dry mass, stowed dimensions, stowed volume, and stowed density of ten high resolution optical Earth observation satellites with apertures from 14.5 cm to 110 cm.

Figure 3-17 plots the satellite dry mass (top) and stowed satellite density (bottom) as a function of aperture diameter. There appears to be one outlier (the WorldView-1 spacecraft) in the satellite dry mass data which clearly does not fit the visual trend and has been omitted from the curve fitting process. One explanation for why WorldView-1 is an outlier is that it represents a intermediate capability between the QuickBird satellites and WorldView-2. All four of these satellites were produced by Ball Aerospace of Boulder, Colorado. QuickBird 1 and 2 and Worldview-1 share a similar instrument while WorldView-1 and WorldView-2 share a similar bus with increased capability [66]. Therefore, the WorldView-1 weighs considerably more than the QuickBird satellites and has similar aperture size. A second order polynomial curve fit for satellite dry mass as a function of aperture diameter accounts for over 93% of the data variation. The simulation model uses this curve fit to calculate the satellite dry mass as a function of aperture diameter to size the propulsion system and determine overall satellite cost. We see that with increasing aperture size, the satellite dry mass increases at a faster than linear rate. A linear curve fit for stowed satellite density as a function of aperture diameter accounts for around 42% of the data variation and captures the basic trend where the satellite density decreases with increasing aperture. This relationship makes sense since larger apertures will require larger optical telescope assemblies that contain a lot of empty volume. The fit only accounts for 42% of the variation and, therefore, extra margin is added when this estimated density is used to estimate stowed spacecraft volume in the launch vehicle cost model (see Section 3.4.3).

3.3.2   Propulsion System Design

The propulsion system is sized to provide the necessary satellite maneuvering capability for initial deployment and phasing, station-keeping, aerodynamic drag makeup, constellation reconfiguration (for reconfigurable designs) and end-of-life disposal. The following section details how each ΔV requirement is determined and then describes how propellant mass and total propulsion system mass are calculated.

Table 3.1: Properties of Selected Optical Earth Observation Satellites

Spacecraft	D	M_w	$M_{d,sc}$	Stowed Size	Stowed Volume	ρ_{sc}	References
	cm	kg	kg	m, m, m	m^3	kg/m^3	
RapidEye	14.5	166.4	154.4	1.17, 0.78, 0.94	0.858	193.9	[66, 151]
EROS-A	30	260	230	2.23, 1.2, 1.2	3.21	81.0	[66]
NigeriaSat-2	38.5	286	274	0.79, 1.2, 1.2	1.456	188.2	[66, 185, 41]
FormoSat-2	60	746	665	2.4, 1.6, 1.6	6.14	121.4	[66, 33]
WorldView-1	60	2500	2090	3.6, 2.5, 2.5	22.5	111.1	[66, 193]
Quickbird 1,2	61	951	911	3.0, 1.6, 1.6	7.68	123.8	[113, 193, 62]
Pléiades 1B	65	1015	940	3.0, 2.5, 2.5	12	84.6	[66, 85]
Ikonos 1,2	70	728	658†	1.83, 1.57, 1.57	4.51	161.4	[66]
GeoEye-1	110	1955	1811	4.35, 2.7, 2.7	31.7	61.7	[66]
WorldView-2	110	2800	2390	5.7, 2.5, 2.5	35.6	78.6	[66, 193]

† Estimated using $\Delta V = 300 m/s$ and $I_{SP} = 300s$

ΔV Requirements

Propulsive capability is required for initial deployment, to correct for launch vehicle injection errors, to properly phase the satellites to achieve proper placement in the constellation pattern, and for disposal through de-orbiting at end-of-life. Table 3.2 shows typical 3σ injection errors for four contemporary launch vehicles including the Pegasus [148], Minotaur IV [150], Falcon 9 [181], and Delta IV Heavy [149], which represent a variety of available launch vehicle sizes and technologies. A Monte Carlo simulation then sampled from a Gaussian distribution of injection errors, calibrated to the data in Table 3.2 assuming that the errors are uncorrelated, to estimate the launch vehicle correction ΔV (ΔV_{LV}). Figure 3-18 shows a cumulative distribution plot of ΔV_{LV} for the four launch vehicles. Here we see that ΔV_{LV} is less than 22 m/s with 80% confidence for the worst launch vehicle and, therefore, ΔV_{LV} is set to a constant value of 22 m/s in the simulation model.

Phasing relates to the situation where several satellites are launched together that will ultimately reside in different orbital slots in the constellation pattern. These satellites will either need to spread out in M if they ultimately will reside in the same orbit plane, or Ω if they will reside in different orbit planes. Changing M separation is trivial, since a small change in altitude between two satellites will cause a difference in mean motion, and, therefore, M separation. Changing Ω is much harder and can be accomplished via costly
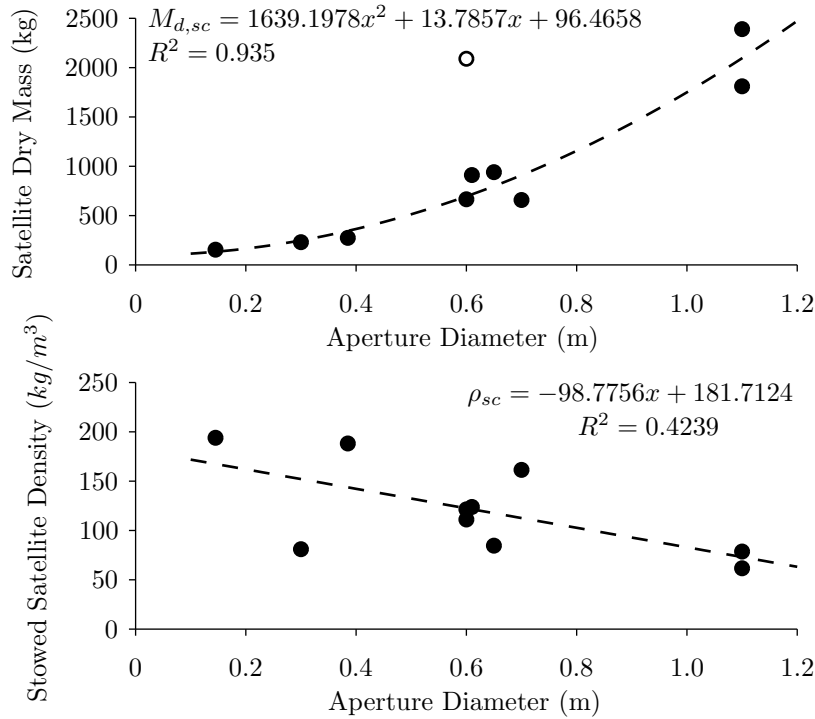
Figure 3-17: The satellite dry mass and stowed density both show correlation with aperture diameter

propulsive maneuvers or orbital precession. Differential orbital precession, caused primarily by the Earth J_2 gravity variation, can then be harnessed to slowly change the relative Ω of satellites over time.

In this model, the satellites are launched to an altitude lower than the intended GOM altitude to allow for phasing. A lower altitude harnesses the effect of staging, effectively using the satellite's on-board propulsion system as the final launch stage. The relative drift rate ($\dot{\Omega}_{rel}$) is a function of the altitude difference between the launch orbit semi-major axis (a_{launch}), the final GOM altitude (a_{GOM}), and inclination:

$$\dot{\Omega}_{rel} = \dot{\Omega}_{deploy} - \dot{\Omega}_{GOM} \qquad (3.25)$$

81

Table 3.2: Launch Vehicle LEO Insertion Accuracies

Launch Vehicle	Apse 1 km	Apse 2 km	Inclination deg
Pegasus XL	10	80	0.15
Minotaur IV	18.5	92.6	0.2
Falcon 9	10	10	0.1
Delta IV Heavy	11	12	0.03
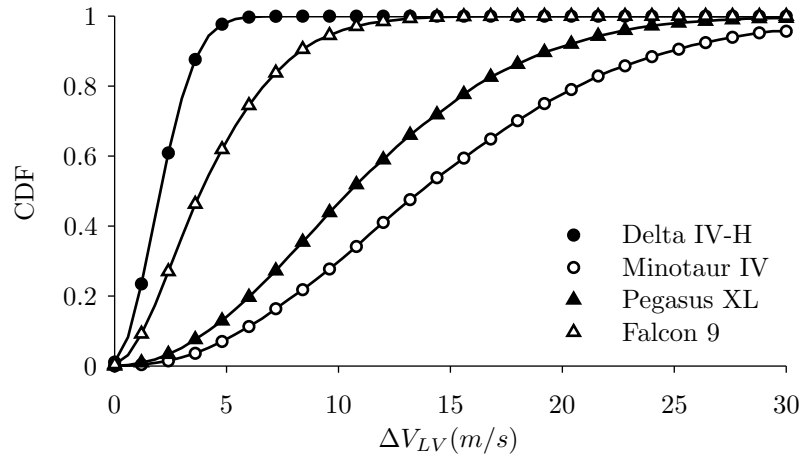
Figure 3-18: ΔV_{LV} is approximately $5m/s$ for liquid propellant launch vehicles (Delta IV-H, Falcon-9) and approximately $20m/s$ for solid propellant launch vehicles (Pegasus XL, Minotaur IV)

Using the relation for $\dot{\Omega}$ including only J_2 effects (Equation 3.3), Equation 3.25 becomes:

$$\dot{\Omega}_{rel} = -\frac{3}{2}J_2R_\oplus^2\sqrt{\mu}\cos i \left(\frac{1}{(a_{GOM} + \Delta a_{deploy})^{7/2}} - \frac{1}{a_{GOM}^{7/2}} \right) \qquad (3.26)$$

Here we clearly see that the phasing rate (assuming circular orbits) is a function of inclination and the deployment altitude difference from GOM altitude (Δa_{deploy}), where $\Delta a_{deploy} = a_{launch} - a_{GOM}$. This altitude difference is, in turn, a function of how much ΔV is allocated to deployment, and, therefore, how much the spacecraft is able to change its orbital altitude. If the transfer from the launch orbit to GOM orbit is modeled as a Hohmann transfer, then the relationship between ΔV_{deploy} and the phasing rate is shown in Figure 3-19. This figure shows the tradeoff between propellant use and the ability to phase satellites after sharing

a launch. The more ΔV available for deployment, the greater the altitude offset between launch altitude and GOM altitude, and the greater $\dot{\Omega}_{rel}$. Inclination also plays a significant role. Near polar inclinations feature little Ω precession, so that satellites traveling to different orbital planes will need separate launches, which ultimately increases launch cost. In the simulation model, Δa_{deploy} is a free internal variable selected to minimize overall constellation cost. This process is explained in more detail during discussion of the launch cost model in Section 3.4.3.
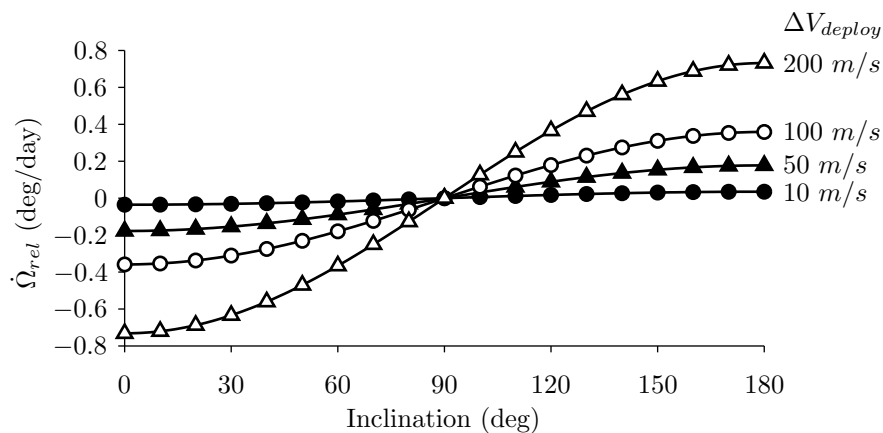
Figure 3-19: The Ω phasing rate ($\dot{\Omega}_{rel}$) is affected by the inclination and amount of deployment ΔV (ΔV_{deploy}) used (values calculated for a $500km$ GOM orbit altitude)

LEO satellite constellation station-keeping consists of correcting several perturbations including: gravitational variation caused by the non-spherical Earth, third body interactions, aerodynamic drag, and solar radiation pressure. Previous research has shown that absolute station-keeping, where each satellite stays in its own station-keeping box, is more efficient than relative station-keeping, where the relative positions referenced to a key satellite are maintained [220]. In this thesis, I partition station-keeping requirements into aerodynamic drag (ΔV_{drag}) and other station-keeping (ΔV_{SK}), which corrects for perturbations caused by the non-spherical Earth, third body interactions and solar radiation pressure. ΔV_{SK} is independent of altitude and inclination and is modeled as a constant 10 m/s per year to control cross-track position to within $10km$ [220]. ΔV_{drag} is a strong function of altitude and

is determined by the following relation:

$$\Delta V_{drag} \quad = \quad \frac{1}{2}V^2 \left(\frac{\rho_a}{BC}\right) T_{life} \tag{3.27}$$

Where ρ_a is the atmospheric density, $V = \sqrt{\mu/a}$ is the orbital velocity, BC is the ballistic coefficient and T_{life} is the satellite lifetime. Both the atmospheric density and orbital velocity increase with decreasing altitude and lead to higher ΔV_{drag}. The atmospheric density is implemented as a function of altitude for solar mean using interpolated data from Wertz et al. [221], and a constant ballistic coefficient (BC) of 75 kg/m^3 is used [221]. While in ROM, the satellites will encounter different aerodynamic drag forces, and an increase or decrease in ΔV_{drag} is accounted for by adjusting the ΔV available for reconfiguration (ΔV_{recon}) accordingly. At the end of the constellation's lifetime, the satellites will need to be responsibly decommissioned quickly by de-orbiting. The required $\Delta V_{deorbit}$ is calculated to lower the perigee altitude to 50 km ensuring quick disposal. While this model assumes propulsive de-orbit, it should be noted that other techniques such as tethers or aerodynamic drag devices could be employed in the future to reduce overall propulsive requirements. Also, an alternative disposal strategy could boost the altitude to a graveyard orbit in the radiation belts. Figure 3-20 shows ΔV_{drag} and $\Delta V_{deorbit}$ as a function of orbital altitude for a 5 year lifetime. Here we see that these two factors are oppositely affected by altitude, and that there is an altitude for minimum $\Delta V_{drag} + \Delta V_{deorbit}$.
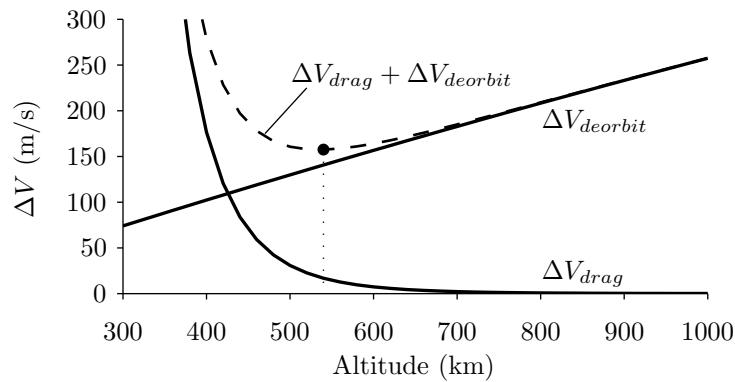
Figure 3-20: There is tension between minimizing ΔV_{drag} and minimizing $\Delta V_{deorbit}$. As T_{life} increases, ΔV_{drag} increases and the minimum ΔV altitude increases. (values calculated with $T_{life} = 5yr$)

The total amount of ΔV required by each satellite is then the sum of all individual ΔV requirements:

$$\Delta V_T = \Delta V_{LV} + \Delta V_{dep} + \Delta V_{drag} + \Delta V_{SK} + \Delta V_{deorbit} + \Delta V_{recon} \tag{3.28}$$

In summary, the total ΔV budget is derived from many requirements. Table 3.3 lists a summary of how each ΔV component is modeled. ΔV_{LV} and ΔV_{SK} are modeled as fixed parameters, ΔV_{drag} and $\Delta V_{deorbit}$ are determined as a function of orbital altitude and satellite properties, ΔV_{dep} is solved for to minimize overall constellation cost and ΔV_{recon} is a design variable for reconfigurable designs.

Table 3.3: ΔV Requirements Summary

ΔV Component	Value
ΔV_{LV}	22 m/s
ΔV_{dep}	internal variable
ΔV_{drag}	function of altitude
ΔV_{SK}	10 m/s/yr
$\Delta V_{deorbit}$	function of altitude
ΔV_{recon}	design variable

Propulsion System Model

Once ΔV_T is known, then the propellant mass (M_{prop}) and propulsion system total mass (M_P) can be calculated. Using the rocket equation, the propellant mass is:

$$M_{prop} = -M_{d,sc}\left(\frac{\zeta - 1}{\xi_p\,(\zeta - 1) - 1}\right) \tag{3.29}$$

$M_{d,sc}$ is the spacecraft bus dry mass not including dry mass associated with the propulsion system, ξ_p is the propulsion system dry mass fraction (propulsion system dry mass as a fraction of the total propulsion system wet mass), I_{SP} is the specific impulse and $\zeta = \exp\left(\Delta V_T/gI_{SP}\right)$. In this thesis ξ_p is set to 0.2 based on previous research [229] that indicated that the dry mass of hydrazine monopropellant systems is roughly 20% of the total propulsion

system wet mass. The total propulsion system mass is then:

$$M_P = \frac{M_{prop}}{(1 - \xi_p)} \tag{3.30}$$

And the total spacecraft wet mass is:

$$M_w = M_{d,sc} + M_P \tag{3.31}$$

Both ΔV_T and I_{SP} affect the size, and ultimately the cost attributed to the propulsion system. Figure 3-21 shows the propulsion system mass fraction (M_P/M_w) as a function of ΔV_T for several values of I_{SP}. I_{SP} is a measure of the propellant efficiency of a propulsion system. Higher I_{SP} systems require less propellant mass for fixed ΔV_T than lower I_{SP} systems. I have chosen to limit analysis to chemical monopropellant systems due to their heritage, long-term storability, and the ability to generate high thrust for fast and efficient maneuvers. These systems have typical I_{SP} values of $220s$ for traditional hydrazine propellant [221] and up to $260s$ for newer 'green' monopropellants [61, 182]. For this analysis, I chose to set I_{SP} to $240s$ as a representative value for monopropellant systems. Additionally, in order to eliminate infeasible designs, I implemented a constraint that limits the propulsion system mass fraction to less than 0.42.
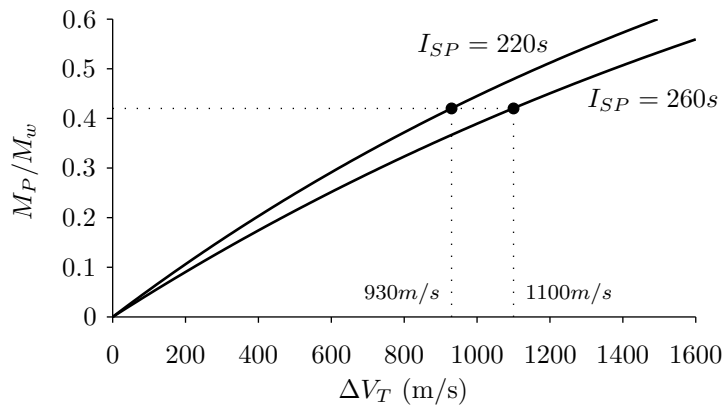
Figure 3-21: Higher I_{SP} propulsion systems allow for greater ΔV_T while satisfying the maximum propulsion system mass fraction constraint of $M_P/M_w \leq 0.42$. (values calculated with $\xi_p = 0.2$)

Why not use electric propulsion?

Electric propulsion provides increased propellant efficiency at the cost of increased power consumption and reduced thrust. Greater propellant efficiency means that less propellant is needed to complete maneuvers and potentially leads to reduced cost or increased ΔV capability. However, the reduced thrust can affect the responsiveness of the reconfigurable constellation concept. The thrust provided by an electric propulsion thruster is a function of the I_{SP}, the input electrical power (P) and the thruster efficiency (η_T) as follows:

$$F = \frac{2P\eta_T}{gI_{SP}} \tag{3.32}$$

For example, consider a $1000kg$ satellite equipped with a hall thruster ($\eta_T \approx 0.5$, $I_{SP} \approx 1600s$ [129]), with $1000W$ of available power for the thruster. This yields a maximum thrust of only $0.064N$ and conducting a $20m/s$ ΔV maneuver would take almost 87 days. Adding to the problem, the low thrust altitude increase maneuver takes more ΔV to accomplish than the near impulsive chemical maneuvers. The maneuver time would be reduced for smaller spacecraft due to their lower overall mass, but smaller spacecraft would likely require additional solar panel area and power processing equipment to generate the additional $1000W$ of power, which could negate the mass savings of electric propulsion. Electo-thermal propulsion such as resisto-jets and arc-jets might be considered since they provide higher thrust at the expense of lower I_{SP}. An alternative strategy could use an electric propulsion system to perform the maneuvers that are not time sensitive like deployment, station-keeping, drag makeup, deorbit, and returning to GOM after an event response while a chemical system would be used for the reconfiguration maneuver. One promising concept that should be looked into in the future is to simply augment the monopropellant chemical system with either a resistojet or arcjet that uses the same propellant. This would increase the I_{SP} for the non-time sensitive maneuvers leading to reduced propellant mass.
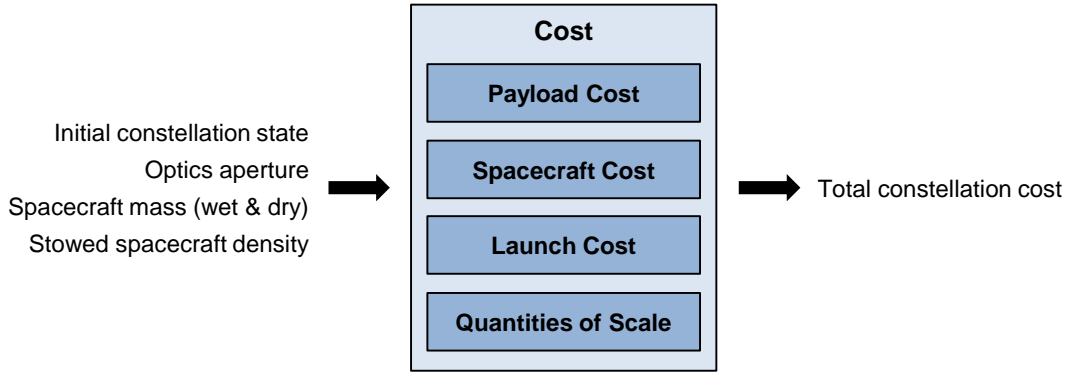
Figure 3-22: The cost module computes the total constellation cost given several spacecraft properties and the initial constellation state

3.4 Cost Model

The cost model computes the total lifecycle cost of the satellite constellation. This total cost is comprised of four primary elements: payload cost, spacecraft cost, launch cost, and quantities of scale effects. Operations cost is not modeled in this thesis. This section provides an overview of how cost is modeled for each of these elements, starting with payload cost.

3.4.1 Payload Cost

The payload for an Earth optical remote sensing satellite includes the optical telescope assembly (OTA) and the imaging sensor. Two approaches are commonly used to parametrically model OTA cost. The first uses the aperture diameter as the independent variable, while the second uses OTA mass as the independent variable. Early work on developing parametric cost models for terrestrial telescopes found that the cost of such systems scaled primarily with aperture diameter raised to the powers of 2 - 3 [186]. Recent research, however, has shown that these models do not accurately extend to space telescopes [186, 190, 189, 188, 187]. Instead, recently developed models indicate that space OTA cost scales with aperture diameter raised to the power of 1.4 to 2.0 power [187].

The NASA Instrument Cost Model (NICM) [88] is a commonly used mass based parametric model. NICM uses the optical subsystem mass to estimate OTA cost and uses detector mass to estimate CCD sensor cost. Habib et al. [89] recently modified NICM to create the NASA Explorer Class Instrument Cost Model (NICM-E), which takes into account the lower

costs incurred by NASA class D missions. This modified model is likely more representative of commercial space costs than the original NICM model. I have decided to use a combination of the Stahl OTA cost model [186, 190, 189, 188, 187] and the NICM sensor cost model after comparing several options. The four approaches that I compared are:

1. NICM Earth-Orbiting Optical Instrument Sensor Cost Model
2. NICM-E Earth-Orbiting Optical Instrument Sensor Cost Model
3. Stahl OTA Cost Model with estimated sensor cost
4. Stahl OTA Cost Model with NICM CCD Cost Model

A full comparison of all four approaches showed that all candidate models exhibited similar trends in estimating cost as a function of aperture size; however, I decided to implement model 4 due to the voluminous recent work by Stahl et al.. Additionally, aperture diameter is a design variable in this thesis work while OTA mass is not. A mass based parametric model would require an estimated OTA mass, which would introduce further error. It was also important to include the sensor cost as it typically constitutes around 25% of total Earth observation optical spacecraft cost [187].

The modeled OTA cost as a function of aperture diameter in thousands of FY2010 dollars is [187]:

$$C_{OTA} = 38000D^{1.6} \qquad (3.33)$$

The modeled focal plane array (FPA) cost is a function of FPA mass (M_{FPA}) in kg [88] and is:

$$C_{FPA} = 1983M_{FPA}^{0.89} \qquad (3.34)$$

Absent available FPA mass data for existing Earth observation satellites, M_{FPA} is estimated by scaling the mass of the Kodak Model 1000 Camera System by aperture diameter [221]. This instrument was used on the IKONOS spacecraft and had an aperture size of $0.7m$ and a FPA mass of $16kg$ [113]. I estimate that M_{FPA} will scale with the cube of the scaling ratio,

which is a ratio of the aperture diameter to $0.7m$ as follows:

$$R \quad = \quad \frac{D}{0.7m} \tag{3.35}$$

$$M_{FPA} \quad = \quad 16kg \times R^3 \tag{3.36}$$

Section 6.1.4 looks at the sensitivity of the value of reconfigurability to the FPA mass scaling ratio exponent. This FPA mass estimate should be refined in future work. The total payload cost is then the sum of the OTA and FPA cost:

$$C_{pay} \quad = \quad C_{OTA} + C_{FPA} \tag{3.37}$$

Additionally, since C_{FPA} is based on M_{FPA}, which is in turn based on aperture diameter, C_{FPA} can then be expressed directly in terms of aperture diameter, and the total payload cost is then:

$$C_{pay} \quad = \quad 38000D^{1.6} + 60615D^{2.67} \tag{3.38}$$

Figure 3-23 shows how C_{OTA} and C_{FPA} scales with aperture size. Here we see that the OTA cost dominates for small aperture sizes and the FPA cost dominates for large aperture sizes.
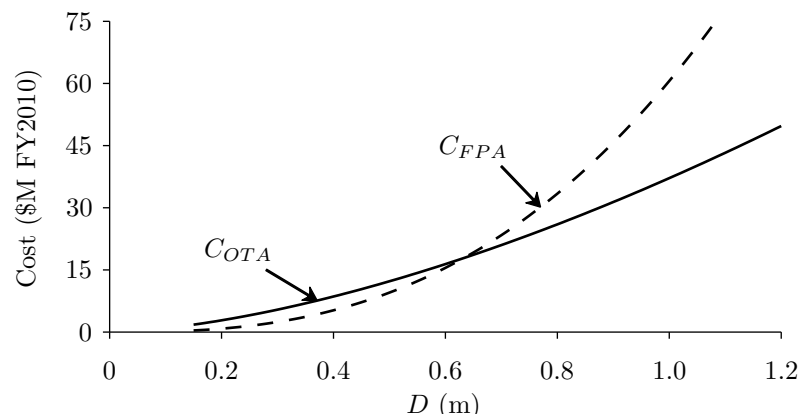
Figure 3-23: FPA cost is lower than OTA cost for apertures less than around $0.6m$

90

3.4.2 Spacecraft Cost

The cost of the complete satellite is also estimated through parametric relations. I have chosen to model the bus cost by blending the estimates from the Small Satellite Cost Model (SSCM) [221] for $M_d \leq 400kg$ and the Unmanned Spacecraft Cost Model (USCM8) [221] for $M_d \geq 200kg$. In the range where the models overlap, I implemented a linear blending scheme with a linear blending parameter $y = (M_d - 200)/(400 - 200)$:

$$C_{sc,NRE} = yC_{sc,NRE}^{SCCM} + (1 - y)C_{sc,NRE}^{USCM} \tag{3.39}$$

$$C_{sc,TFU} = yC_{sc,RE}^{SCCM} + (1 - y)C_{sc,RE}^{USCM} \tag{3.40}$$

I use the satellite dry mass M_d, which includes the propulsion system dry mass, as the mass for cost model calculations, since the cost models are not calibrated for highly maneuverable satellites.

Unmanned Spacecraft Cost Model 8

The USCM8 spacecraft bus system cost estimating relationship (CER) estimates the cost of the spacecraft bus and is optimized for larger spacecraft. This bus cost is then added to the payload cost C_{pay} estimated earlier, and then wrap factors are included for: integration, assembly and test, program level, and aerospace ground equipment. The USCM8 model partitions the bus cost into a non-recurring engineering cost (NRE) and recurring engineering cost (RE). The NRE cost includes the cost of development and build of one qualification unit, and RE is an estimate of the manufacturing cost of the first flight unit. Since the payload cost is not partitioned into NRE and RE, an estimate of this breakdown is made using the following relations:

$$C_{pay,NRE} = \left(\frac{1}{\xi_{pay} + 1}\right) C_{pay} \tag{3.41}$$

$$C_{pay,RE} = \left(\frac{\xi_{pay}}{\xi_{pay} + 1}\right) C_{pay} \tag{3.42}$$

91

Where ξ_{pay} is a parameter representing the cost of RE compared to NRE. For this work, I have set $\xi_{pay} = 0.4$ assuming that the RE is 40% of the total NRE cost.

Small Satellite Cost Model

The SSCM spacecraft bus system CER estimates the total NRE cost of the spacecraft bus and is focused on small satellites with masses less than $400kg$. Similar to the USCM8 model, this bus cost is then added to the payload cost C_{pay}, and then wrap factors are included for: integration, assembly and test, program level, and ground support equipment. Since the SSCM only estimates the NRE cost, a second parameter is introduced (ξ_{sc}) which represents the RE cost fraction of NRE cost, similar to ξ_{pay}. For this work, I have also set $\xi_{sc} = 0.4$ assuming that the spacecraft RE is 40% of the total spacecraft NRE cost.

Blended Total Spacecraft Cost

Figure 3-24 illustrates the blending process. The top plot shows the SSCM (solid) and USCM (dotted) estimated NRE and RE cost as a function of aperture diameter while holding all other spacecraft variables constant. The NRE cost curves are located above while the RE cost curves are located below. We see that the SSCM generally predicts lower costs than USCM8 for small spacecraft while the USCM8 model predicts lower costs than SSCM for large spacecraft. Also shown in the plot is the region where the models are blended, corresponding to spacecraft dry mass between 200 and $400kg$. The plot shows that this is the region where both models show the most agreement and therefore the blended curves (Figure 3-24 bottom) are fairly smooth.

3.4.3   Launch Cost

Launch cost is often a significant fraction of total space system costs and must be modeled in a detailed manner. Simple launch cost models use a fixed cost per unit mass (e.g. $5000 per kg to LEO) to estimate launch cost. These simplistic approaches do not capture the effect of orbital altitude, inclination and the number of orbit planes on launch cost. They also generally do not account for both mass payload and volumetric constraints for specific

92
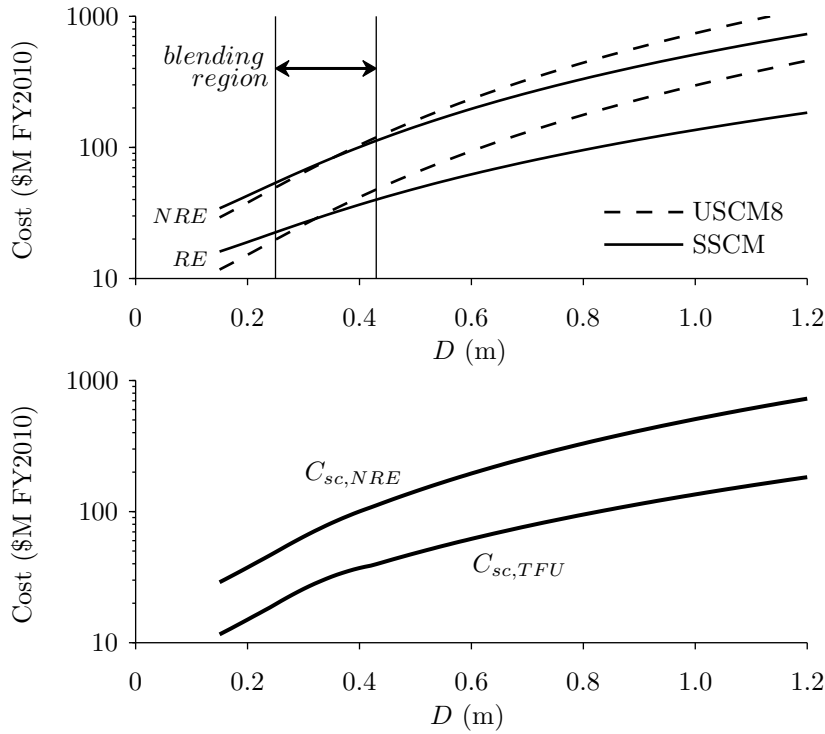
Figure 3-24: The spacecraft cost model for both NRE and RE is a blended combination of two cost models. The SSCM and USCM8 cost models cross over within the blending region yielding a smooth blended model

launch vehicles. In this thesis I am optimizing over altitude, inclination and the number of orbit planes, so it is important to model all of these factors that can significantly effect launch cost. Additionally, optical satellites with large OTA assemblies tend to have large volumetric footprints causing launch vehicle performance to be limited by volume rather than mass. This thesis uses an approach that assigns individual satellites to specific launch vehicles selected from a database of existing U.S. launch vehicles to minimize total launch cost subject to mass and volume constraints. Multiple satellites can share a launch vehicle, however, if the satellites must achieve a different orbit plane in the final constellation pattern, then the satellites must be able to utilize differential orbital precession to achieve their final orbit slot within a fixed deployment time constraint.

In this section, I describe the launch and deployment strategy and introduce the compiled database of existing U.S. launch vehicles. Next, I describe the minimum cost assignment process employed to assign satellites to specific launch vehicles subject to deployment time

constraints. Lastly, I discuss the overall launch cost optimization process which analyzes the trade between increasing spacecraft propulsive capability that increase space segment costs but can reduce launch cost. For example, increasing satellite deployment ΔV could allow more satellites with diverse final orbit planes to be launched on the same launch vehicle.

Launch Strategy and Modeled Launch Vehicles

The launch and deployment model assumes that the spacecraft will be launched to an orbital altitude lower than the intended GOM altitude (a_{GOM}). The satellites will then remain in this orbit until they achieve the correct phasing with their intended GOM orbital slot. This phasing is achieved through differential mean motion and orbital precession. The initial launch semi-major axis (a_{launch}) is lower than a_{GOM} to harness the effect of staging. A higher launch altitude requires the launch vehicle to lift the spacecraft's deployment propellant mass to a higher orbit, and leads to lower overall launch vehicle capability with no additional benefit. A larger altitude difference between a_{launch} and a_{GOM}, allows more change of the satellite's relative Ω during the constrained deployment period; therefore, more satellites might share launch vehicles which could reduce launch cost. However, this reduction in launch cost must be traded with the increase in satellite costs caused by increased propulsive capability. The amount of differential Ω that a satellite can achieve during deployment is a function of the differential precession rates and the maximum time allowed for deployment (T_{dep}):

$$\Delta\Omega_{dep} \quad = \quad \left(\dot{\Omega}_{dep} - \dot{\Omega}_{GOM} \right) T_{dep} \tag{3.43}$$

Using relations for $\dot{\Omega}$ from Section 3.1, Equation 3.43 is expanded to:

$$\Delta\Omega_{dep} \quad = \quad -\frac{3}{2} J_2 R_\oplus^2 \sqrt{\mu} \cos i \left(\frac{1}{(a_{GOM} + \Delta a_{dep})^{7/2}} - \frac{1}{a_{GOM}^{7/2}} \right) T_{dep} \tag{3.44}$$

Where $\Delta a_{dep} = a_{launch} - a_{GOM}$. Here we see that $\Delta\Omega_{dep}$ is a function of GOM altitude and inclination as well as the deployment time and the altitude difference between the launch orbit and GOM orbit. The relation between ΔV_{dep} and Δa_{dep}, assuming a single Hohmann

94

transfer is utilized to change the satellite's semi-major axis from a_{launch} to a_{GOM} is:

$$\Delta V_{dep} = \left(\sqrt{\frac{2\mu}{a_{launch}} - \frac{\mu}{a_{launch} + \frac{1}{2}\Delta a_{dep}}} - \sqrt{\frac{\mu}{a_{launch}}} \right)$$
$$+ \left(\sqrt{\frac{\mu}{a_{GOM}}} - \sqrt{\frac{2\mu}{a_{GOM}} - \frac{\mu}{a_{launch} + \frac{1}{2}\Delta a_{dep}}} \right) \quad (3.45)$$
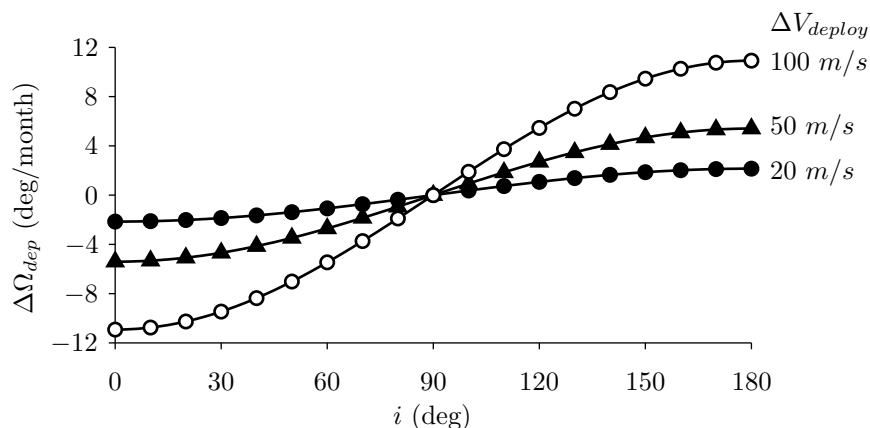
Figure 3-25: The relative Ω drift rate during deployment increases with increasing ΔV_{deploy} and with inclinations closer to equatorial, either prograde or retrograde. Near polar orbits feature little precession. Values calculated for a $500km$ GOM orbit altitude.

Given ΔV_{dep}, Equation 3.45 can then be solved to find Δa_{dep} for use in Equation 3.44. Figure 3-25 shows $\Delta\Omega_{dep}$, in degrees per month, as a function of orbital inclination and ΔV_{dep} for $a_{GOM} = 500$km. Increasing ΔV_{dep} leads to a larger altitude difference Δa_{dep} and increased deployment drift range $\Delta\Omega_{dep}$. Additionally, $\Delta\Omega_{dep}$ is higher for low inclinations, diminishes to zero for polar inclinations, and then increases as retrograde inclinations increase. This means that for fixed ΔV_{dep}, low inclination prograde and high inclination retrograde orbits allow satellites launched in the same launch vehicle to achieve more diverse orbit planes. Conversely, satellites with near-polar inclinations cannot change their orbit planes as effectively, which may lead to more launches and higher launch cost. Therefore, inclination can play a major role in determining launch cost.

Table 3.4 shows the performance and cost of current and near-future U.S. launch vehicles. The performance data has been taken from the respective launch vehicle user guides while

the cost data has been derived from various sources as indicated. It should be noted here that these costs can vary widely given current economic conditions, the number of launches in a particular year and negotiated block purchases experienced when launching a constellation. These costs can and should be adjusted with any additional cost data when the framework is used in future work. Notice the quantities of scale savings where the cost per kg decreases with increasing launch vehicle payload capacity. Five of the launch vehicles (starred in Table 3.4) were chosen to be included in the simulation model since they form the set of non-dominated options for maximizing payload mass capacity and minimizing cost.

Table 3.4: Properties of Selected U.S. Launch Vehicles

Launch Vehicle	LEO Performance[†] kg	Cost $M (FY10)	Cost per kg $k (FY10)	Payload Volume m^3	References
Pegasus XL*	443	30	67.7	1.87	[148, 143]
Athena Ic*	700	41	58.6	14.5	[15]
Taurus XL	1380	54	39.1	13.0	[147]
Minotaur IV*	1650	50	30.3	11.4	[150]
Athena IIc	1730	65	31.5	11.4	[15, 217]
Falcon 9* v1.1	10450	56.7	5.43	146	[181, 180]
Atlas 5	18814	161.8	11.1	121	[205, 221]
Delta IV Heavy	22560	214.3	19.3	233	[149, 221]
Falcon Heavy*	53000	100	1.89	146	[180]

[†] Payload mass to 28.5° inclination, $200km$

* Included in launch vehicle assignment

The payload mass performance given in Table 3.4 is for insertion into a $200km$ altitude circular orbit at 28.5° inclination. Launching to higher altitudes and higher inclinations results in lower payload mass performance. The launch cost model utilizes recently published response surfaces [77, 115] that compute the payload mass performance as a function of launch altitude and inclination. The orbital cost function (OCF) is then defined as the launch vehicle performance to a reference orbit at 28.5° inclination and $200km$ altitude divided by the performance given by the response surfaces as shown in Equation 3.46. The orbital cost function measures the relative difficulty in launching to various orbits with difficulty increasing with increasing OCF.

$$OCF = \frac{M_{LV}\left(200, 28.5°\right)}{M_{LV}\left(h, i\right)} \qquad (3.46)$$

I made several assumptions to enable the use of the published response surfaces over the full range of inclinations and launch vehicles included in the simulation model. First, orbital inclination is limited to the range of 30° to 150°. Since all the launch vehicles can be launched from a latitude less than 30°, the launch vehicles do not need to execute plane changes during ascent. Additionally I assume that there are no launch azimuth restrictions that would further reduce launch vehicle performance by introducing dog-leg maneuvers, and I extrapolate the performance response surfaces since the published response surfaces only cover prograde and sun-synchronous inclinations. Figure 3-26 shows the orbital cost function for the Minotaur IV launch vehicle generated by the response surfaces. The shaded part of the surface ($i \leq 103.9°$) is directly given by the response curves [77], while the non-shaded part of the surface is extrapolated. We see that the effect of increasing inclination reduces payload performance much more than the effect of increasing launch altitude. Earth's rotation decreases launch ΔV requirements for prograde orbits, and increases launch ΔV requirements for retrograde orbits.

Published performance response surfaces were not available for the Athena Ic and Falcon Heavy launch vehicles. I decided to use the OCF for the Athena I launch vehicle to model the Athena Ic since the vehicles are nearly identical. I also used the Delta IV Heavy OCF to model the Falcon Heavy launch vehicle OCF. This model may overestimate the performance impact for Falcon Heavy given that the payload performance of the Falcon Heavy is nearly twice that of the Delta IV Heavy. I use the published 200km and 28.5° published performance for both the Athena Ic [15] and Falcon Heavy launch vehicles [180]. Figure 3-27 shows the orbital cost function for the remaining four modeled launch vehicles. The data shows that as the capacity of the launch vehicle increases, the effect of increased inclination and altitude is less pronounced on payload performance. The OCF curves have been capped at 8 in the plot for the Pegasus XL and Athena Ic launch vehicles. The OCF for these vehicles increases sharply at high altitude and high inclination because these situations come close to the zero
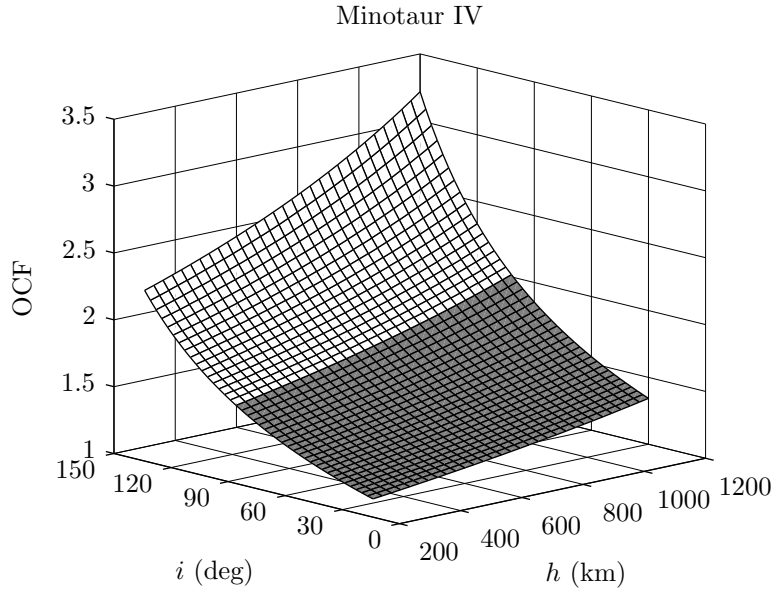
Figure 3-26: Orbital cost function for the Minotaur IV launch vehicle with the published response surface (shaded dark) [77, 115] and extrapolated data (shaded light)

payload performance of the vehicles.

Launch Vehicle Assignment

Now that we have a list of available launch vehicles (in the database), and we know how much Ω drift each satellite can achieve during deployment, we must now determine set of launch vehicles that will minimize cost. This assignment process is detailed in this section and consists of three steps: 1) calculate how many inertial launch bins are necessary given $\Delta\Omega_{dep}$; 2) determine the minimum launch cost assignment of launch vehicles to service these inertial launches; and 3) find the minimum total constellation cost by varying ΔV_{dep}. The launch assignment process is allowed to choose a combination of different launch vehicles (e.g.three Minotaur IV and one Falcon 9 launch vehicles) that can launch all satellites in the constellations for the lowest total cost. While designing satellites to accommodate multiple launch vehicles might increase design, test and integration effort, it is not clear whether cost would increase substantially. For example, the 93 satellite IRIDIUM constellation, which featured a per-satellite cost of approximately $13M FY2005, was launched on 22 total launch vehicles including: twelve Delta-2, six Long March, three Proton, and one EUROCKOT [101, 191]. Additionally, using multiple types of launch vehicles to deploy a
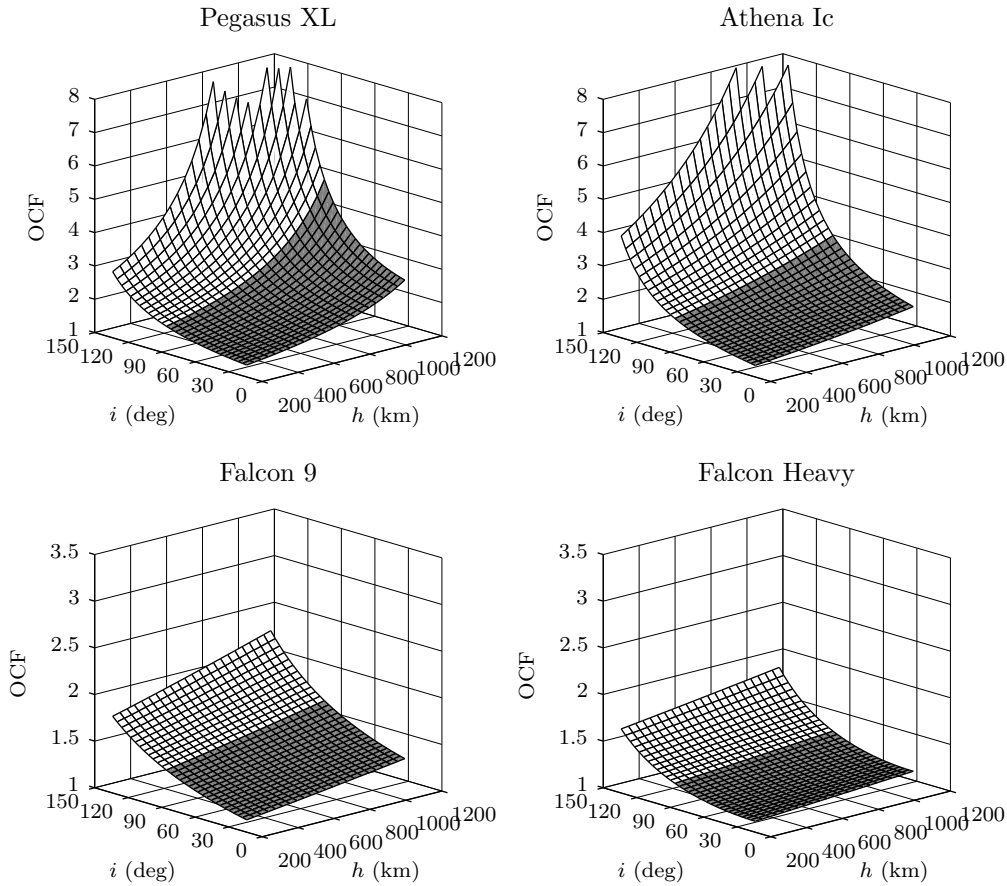
Figure 3-27: Orbital cost functions for the remaining four modeled launch vehicles

constellation can shorten the launch campaign and reduce the risk that a launch failure for one launch vehicle type would cause significant delays in deploying the remaining satellites in the constellation.

The first step in the launch vehicle assignment process calculates how many inertial launch bins are necessary given the satellite's deployment range $\Delta\Omega_{dep}$. An inertial launch bin is defined as the range in Ω that satellites can move to during the deployment period. For example, if $\Delta\Omega_{dep} = 15°$, then a launch vehicle could potentially launch any number of satellites that are intended to achieve final orbit planes within 15° of each other in Ω, subject to launch vehicle capability constraints. The problem is simply stated as: what is the minimum number of bins (with bin width of $\Delta\Omega_{dep}$) required to populate all Ω slots in the GOM constellation pattern? The procedure is illustrated in Figure 3-28 for a 10 satellite
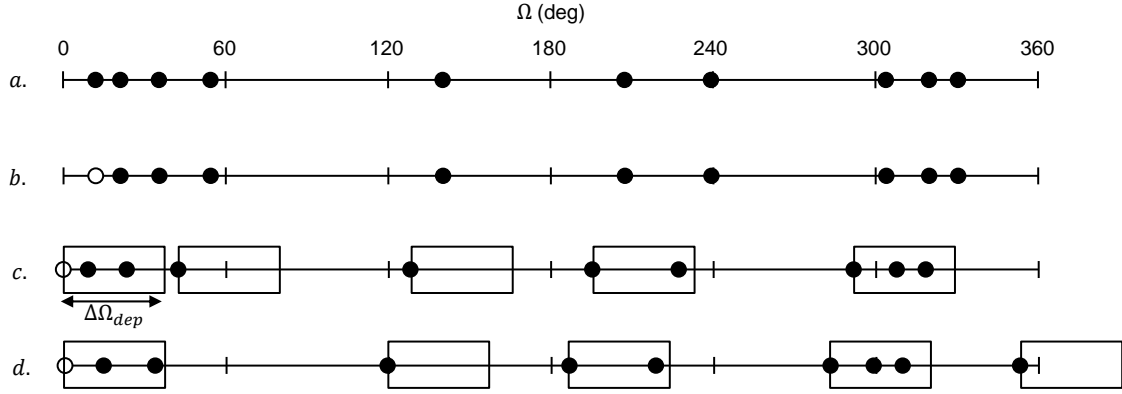
Figure 3-28: Illustration of process to determine minimum number of launch bins including: the defined Ω positions (a), reference satellite selection (b), angular shift and bin placement (c), and repetition of the process with each satellite assigned as the reference satellite (d).

constellation. The satellites in the constellation will each be placed in orbit planes specified by Ω. Subplot a shows the Ω for each satellite in the constellation pattern and, in this case, each satellite has a unique orbit plane. The next step in the process selects a single satellite as reference, and converts the remaining satellite Ω values to an angular difference with respect to the reference Ω on the interval $0 \rightarrow 360°$. Subplot b shows the initial reference satellite as the white filled dot, and subplot c shows the Ω values converted to angular differences with the reference satellite set to $0°$. Next, starting with the reference satellite, launch bins with width $\Delta\Omega_{dep}$ are placed sequentially until all satellites have been assigned to a bin. The binning process is repeated using each satellite as the reference (subplot d shows the second satellite as the reference) to find the configuration that provides the minimum total number of bins. This minimum number of bins corresponds to the minimum number of individual launches required to launch the constellation. The binning process is given in pseudo-code in Algorithm 1.

Once the minimum number of bins have been determined, then the problem shifts to finding the minimum cost assignment of specific launch vehicles for each unique bin size. The number of satellites contained in each bin is referred to as the bin size, N_B. Figure 3-28c shows that a total of five bins are required, with two containing three satellites ($N_B = 3$), one containing two satellites ($N_B = 2$), and two containing a single satellite ($N_B = 1$). We can determine the minimum cost launch assignment for each bin size and then multiply

Algorithm 1 Determine minimum number of launch bins

1: Compute list of unique Ω values ($\vec{\Omega}$)
2: **for all** i ← all $\vec{\Omega}$ **do**
3: $\quad$ $N_{bin,i} = 0$
4: $\quad$ Set $\Omega_0 \leftarrow \vec{\Omega}_i$
5: $\quad$ Compute ascending distance from reference, $\Delta\vec{\Omega} = \left(\vec{\Omega} - \Omega_0\right) \bmod 2\pi$
6: $\quad$ Set $j \leftarrow 1$
7: $\quad$ **while** $j \leq$ length $\vec{\Omega}$ **do**
8: $\quad\quad$ Find number of values (N) that are contained in a bin starting at $\vec{\Omega}_j$
9: $\quad\quad$ $N_{bin,i} = N_{bin,j} + 1$
10: $\quad\quad$ $j = j + N$
11: $\quad$ **end while**
12: **end for**
13: Compute minimum number of bins, $N_{bin} = \min_i N_{bin,i}$

this cost by the number of bins that correspond to that size. For each unique N_B, we then calculate the minimum number of launches required to populate each bin using each launch vehicle exclusively.

$$N_{s,LV} = \min\left[\min\left(\left\lfloor\frac{M_{LV}}{M_w}\right\rfloor, \left\lfloor\frac{V_{LV}\eta_{pack}}{M_w/\rho_{sc}}\right\rfloor\right), N_B\right] \tag{3.47}$$

V_{LV} is the payload volume of the launch vehicle, η_{pack} is the volumetric packing efficiency, and ρ_{SC} is the spacecraft density (from Section 3.3.1). Here the $\lfloor M_{LV}/M_w \rfloor$ term represents the capacity by mass of the launch vehicle in terms of number of satellites, and $\lfloor (V_{LV}\eta_{pack})/(M_w/\rho_{sc}) \rfloor$ represents the capacity by volume of the launch vehicle in terms of number of satellites. $N_{s,LV}$ is also capped at a max of N_B to speed the optimization process. This procedure is performed for each of the five modeled launch vehicles to yield a set of the number of each type of launch vehicle that can be assigned for each bin size:

$$S_i = \{0, 1, \cdots, N_{s,LV_i}\} \tag{3.48}$$

Next, we take the Cartesian product of these sets to generate the set $\mathcal{S}$ of possible launch vehicle assignments. For example, one such assignment is $s = [1, 0, 1, 0, 0]$ where $s \in \mathcal{S}$.

This specific assignment is comprised of one Pegasus XL, zero Athena Ic, one Minotaur IV, and zero Falcon 9 and Falcon Heavy launch vehicles. The size of set $\mathcal{S}$ is $\prod_i (N_{s,LV_i} + 1)$. Next, all of the combinations not able to accommodate N_B satellites are filtered out as infeasible solutions, and the remaining assignment options are assigned a cost by summing the individual launch vehicle costs. The assignment with the lowest cost is then selected and the process is repeated for the next bin size. After each bin size has a specific launch vehicle assignment, then the total launch cost is the cost of each launch vehicle type times the total number times that LV type was assigned over all bin sizes. Algorithm 2 provides pseudo-code for this process.

Algorithm 2 Determine minimum cost launch vehicle assignment

1: **for** k ← all unique N_B **do**
2:     **for** i ← all launch vehicle types **do**
3:         compute number of launches to populate bin, N_{s,LV_i}
4:         $S_i \leftarrow \{0, 1, \cdots, N_{s,LV_i}\}$
5:     **end for**
6:     $\mathcal{S} \leftarrow$ Cartesian product of S_i over i
7:     **for all** s $\in \mathcal{S}$ **do**
8:         **if** $\sum N_{s,LV_i} < N_B$ **then**
9:             s $\leftarrow \varnothing$
10:        **end if**
11:        compute cost of s
12:    **end for**
13:    determine minimum cost assignment in set $\mathcal{S}$
14: **end for**
15: total launch cost is sum of minimum assignments over all unique N_B

I will now present an example to clarify the process. Let's assume that we are interested in launching a 24 satellite constellation and want to know the effect of the number of orbit planes (N_p) on launch cost. All of the satellites have a common inclination so each orbit plane is characterized fully by Ω. Further, assuming that the constellation is symmetric, then the spacing between adjacent plans is uniform and is equal to $360°/N_p$. For small N_p, many satellites could be launched on a single launch vehicle reducing launch cost, given enough launch vehicle capability. As the number of planes increases, the plane spacing in Ω decreases; however, this is not initially helpful because the plane spacing is larger than the maximum bin width $\Delta\Omega_{dep}$. Therefore more launch vehicles will be needed to service all

orbit planes. As the number of orbit planes grows larger, the plane spacing will eventually fall to less than the maximum bin width, the number of launch vehicles required will stop increasing, and may even be reduced.
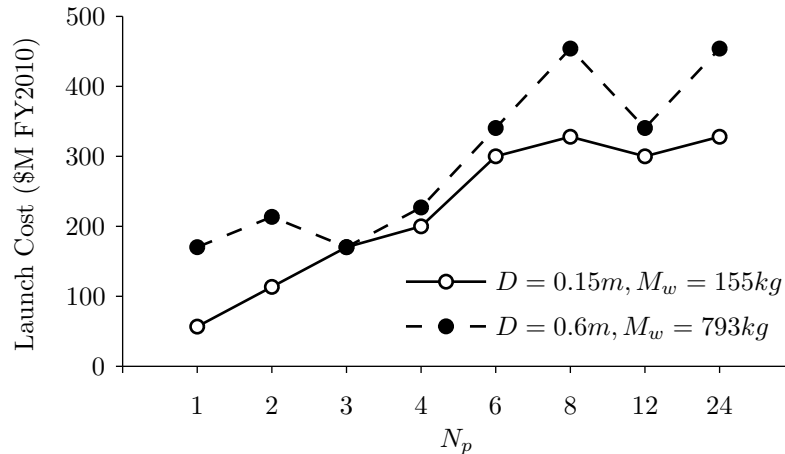
Figure 3-29: Contrary to what simplistic launch cost models would predict, launch cost does not always increase with increasing number of orbit planes due to launch vehicle quantization effects. Using a constant $30k FY2010 per kg, the launch costs would be independent of N_p and would be $112M and $571M FY2010 for the $D = 0.15$ and $D = 0.6m$ constellations, respectively

Figure 3-29 shows the launch cost for two 24 satellite constellations with different size spacecraft as a function of increasing N_p. The general trend is that launch cost increases with increasing number of orbit planes and that larger satellites will cost more to launch (both intuitive trends). However, there are some interesting dynamics as evidenced by the non-smooth nature of the curves. Table 3.5 shows more detail, including the orbit plane spacing and the launch vehicle assignment for the scenario shown in Figure 3-29. Here we see that for the constellation with smaller spacecraft ($D = 0.15m, M_w = 155kg$), with $N_p = 1$ the entire constellation could be launched with one Falcon 9 launch vehicle. As N_p increases to 2 and 3, the constellation would need two and three total Falcon 9 launch vehicles since smaller launch vehicles cannot accommodate 12 and 8 spacecraft, respectively. This increases launch costs tremendously. As N_p increases further, smaller launch vehicles are utilized and the growth in total launch cost slows. For the constellation with larger spacecraft ($D = 0.6m, M_w = 793kg$), the same general trend holds. However there is an

interesting dynamic between $N_p = 1, 2, 3$. For $N_p = 1$ three Falcon 9 launch vehicles are required to lift all 24 satellites into the common orbital plane at a cost of \$170M. For $N_p = 2$, there are two orbital planes spread 180° apart. A single Falcon 9 cannot launch all 12 satellites, so a second, smaller, Minotaur IV launch vehicle is needed as well. This means that a total of two Minotaur IV and two Falcon 9 launch vehicles are required for a cost of \$214M. For $N_p = 3$, there are three orbit planes spread 120° apart. Since a single Falcon 9 can lift 8 satellites, we are back to using 3 Falcon 9 launch vehicles and the total launch cost has dropped back down to \$170M. These launch cost quantization effects are important to model in order to find cost-effective constellation designs, and cannot be captured by more simplistic launch cost models. Additionally, the launch vehicle assignment process can be easily updated with the latest launch vehicle cost data to provide up-to-date estimates.

Table 3.5: Launch cost and assignment for a 24 satellite constellation as a function of spacecraft aperture and number of orbit planes

N_p #	Plane Spacing deg	$D = 0.15m$ Assignment	C_L \$M FY2010	$D = 0.6m$ Assignment	C_L \$M FY2010
1	–	[0,0,0,1,0]	57	[0,0,0,3,0]	170
2	180	[0,0,0,2,0]	114	[0,0,2,2,0]	214
3	120	[0,0,0,3,0]	170	[0,0,0,3,0]	170
4	90	[0,0,4,0,0]	200	[0,0,0,4,0]	227
6	60	[0,0,6,0,0]	300	[0,0,0,6,0]	341
8	45	[0,8,0,0,0]	328	[0,0,0,8,0]	454
12	30	[0,0,6,0,0]	300	[0,0,0,6,0]	341
24	15	[0,8,0,0,0]	328	[0,0,0,8,0]	454

Launch Cost vs. Spacecraft Cost Optimization

This launch assignment process is then repeated for different ΔV_{dep} values to find the global minimum constellation cost. Figure 3-30 shows the launch cost, space segment cost and total constellation cost as a function of ΔV_{dep} for an example case. Here we see that as ΔV_{dep} increases, the launch cost is dramatically reduced with very little increase in the space segment cost. This situation typically arises for small satellites, where the increase in total space segment cost is small compared to the reduction in launch cost. Again, the reduction

104

in launch cost is caused by an increase in the ability for satellites to change their orbit planes during deployment, which results in fewer total launch vehicles. In the simulation model, the maximum ΔV_{dep} is capped at $200m/s$ and the launch altitude is subject to minimum altitude constraints. Additionally, the overall propellant mass fraction constraint may also play a role in limiting ΔV_{dep} as it may yield a more cost-effective constellation to lower ΔV_{dep} to allow for higher ΔV_{recon}.
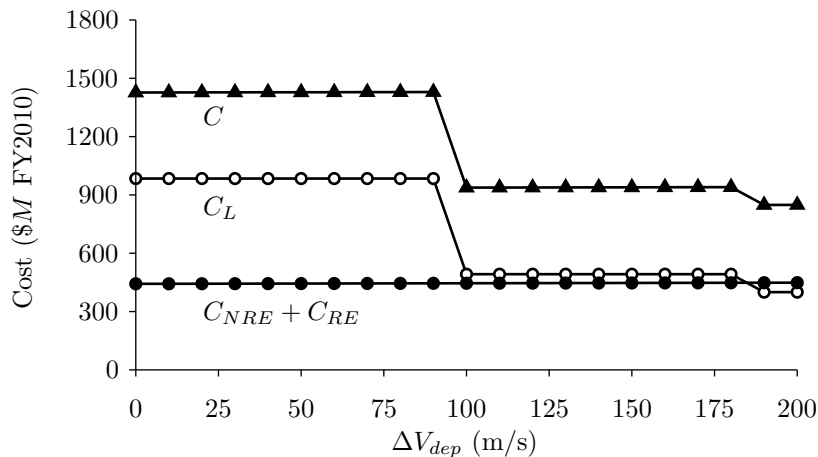
Figure 3-30: For small satellite constellations, it is often better to increase ΔV_{deploy} in order to reduce launch cost substantially. In this case, the increase in space segment cost is small compared to the reduction in launch cost. Values calculated for a 24 satellite constellation.

3.4.4 Economies of Scale and Total Constellation Cost

The cost model also includes two cost improvement effects: amortization of NRE, and the learning curve effect. As the number of satellites in the constellation increases NRE remains a fixed quantity, and the NRE cost per satellite decreases. This is referred to as amortization. The learning curve effect attempts to model the efficiency gain of producing multiple copies of a complex product. Efficiency gains are caused by many factors including: volume purchasing, improved and streamlined processes, reuse of manufacturing and test equipment, and reduced testing on later spacecraft. The learning curve equation to calculate the nth

satellite production cost, using the unit curve formulation [144], is:

$$C_{sc,RE,n} = C_{sc,TFU} X^{\log b/\log 2} \tag{3.49}$$

Where b is the learning curve factor which represents the fractional reduction in unit cost for every doubling of unit production. While there are limited examples of large scale production of space systems, a good rule of thumb for complex aerospace systems is to assume a learning curve of 85 to 90%, so $0.85 \leq b \leq 0.9$ [144]. This means that the second unit will cost 85 to 90% of the cost of the first unit, and the fourth unit will cost 85 to 90% the cost of the second unit and so on. I implement a learning curve of 90% for the work presented in this thesis. The total constellation RE cost is then given as:

$$C_{RE} = \sum_{n=1}^{N_T} C_{sc,RE,n} \tag{3.50}$$

And the total constellation NRE cost is given as:

$$C_{NRE} = C_{sc,NRE} \tag{3.51}$$

The total system cost (excluding operations and retirement cost) is the sum of the total constellation RE cost, the total constellation NRE cost and the total launch cost:

$$C = C_{NRE} + C_{RE} + C_L \tag{3.52}$$

3.5 Astrodynamics

The astrodynamics module first computes partial global GOM coverage and then proceeds to model the constellation's sequential response to a series of regional events distributed geographically and distributed in time. For reconfigurable architectures, the system has the option to maneuver satellites into ROM to provide enhanced coverage; while for static architectures, the system provides regional event coverage from GOM. The campaign-based simulation propagates the satellites' orbital state and accounts for propellant depletion.
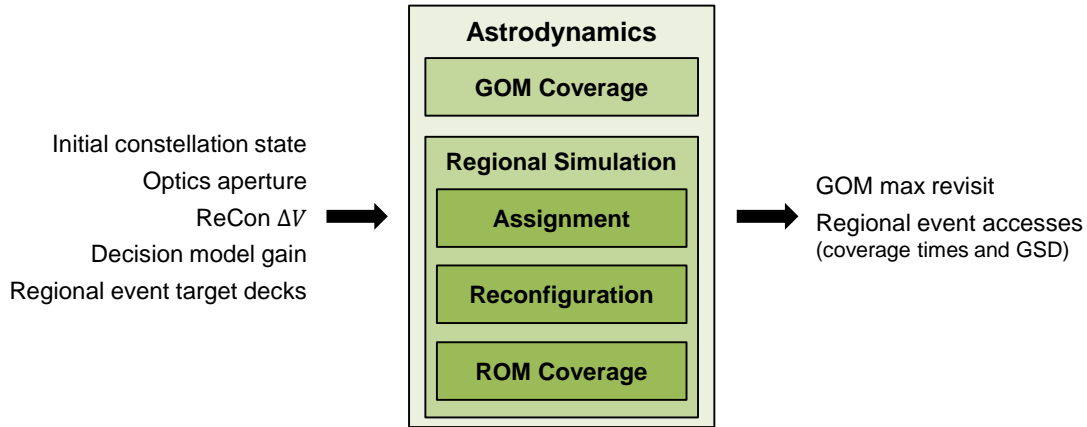
Figure 3-31: The astrodynamics module computes coverage statistics in GOM and ROM based on a variety of inputs

3.5.1 GOM Simulation

While the primary objective of this constellation is to support regional disaster response, it must also provide utility in between events. This capability is imposed as a constraint on the maximum revisit time for partial global coverage within a latitude band. The GOM simulation propagates the initial satellite constellation for 48 hours with a timestep of 30 seconds and computes access times from the constellation to a set of ground points to assess partial global coverage. Since we are only interested in ensuring that the 24 hour maximum revisit time constraint is satisfied, propagation for 48 hours is sufficient. The 30 second timestep was chosen as a compromise between computational efficiency and accuracy, and during validation, produced errors generally less than 1% (see details on model validation in Section 3.7). To reduce the computational time, the ground points are restricted to one-eighth of the partial global surface area. This simplification is possible due to symmetry in the problem. The target points are constructed by selecting latitude values with a fixed step on the interval $0° \leq \varphi \leq \varphi_{max}$, and then assigning longitude randomly on the interval $0° \leq \lambda \leq 90°$. This method ensures sampling of the entire latitude range and gives diversity to the sampled longitudes, which is essential to prevent the optimization process from finding solutions that 'game' the system and to provide good coverage for evaluated ground points. Figure 3-32 shows the ground target points with a latitude granularity of 0.25°. A comparison with detailed STK coverage analysis which showed that this granularity provided maximum

revisit time estimates with 0.144% median error (also see Section 3.7 for more validation information).
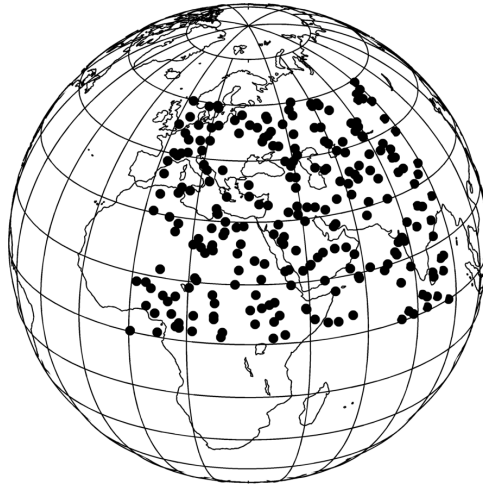
Figure 3-32: 241 ground target locations distributed in the range $0° \leq \varphi \leq \varphi_{max}$ and $0° \leq \lambda \leq 90°$ are used to evaluate the maximum GOM revisit time constraint.

Once the accesses to each ground point is found, then the average and maximum revisit times for each point is calculated over the 48 hour analysis period. The maximum GOM revisit time is then computed as the largest of all ground point maximum revisit times.

3.5.2   Campaign-Based Regional Event Response Simulation

After GOM coverage is computed, the next step in the modeling process quantifies the coverage provided by the constellation for a series of regional events distributed both geographically and in time. This is accomplished through the use of a campaign-based simulation model which tracks the constellation through a sequence of event responses over its life cycle. The campaign-based simulation process flow is depicted in Figure 3-33. The constellation is initially deployed into GOM through the launch and deployment process previously explained in Section 3.4.3. While in GOM, the simulation model propagates the constellation, including orbital precession effects, and accounts for station-keeping and drag makeup ΔV. When the first regional event occurs, the simulation model goes through an optimal assignment process to determine which satellites should be reconfigured into ROM. This process determines how many satellites need to reconfigure, which specific satellites should be reconfigured, and how fast each satellite should be reconfigured. The final part of the assignment
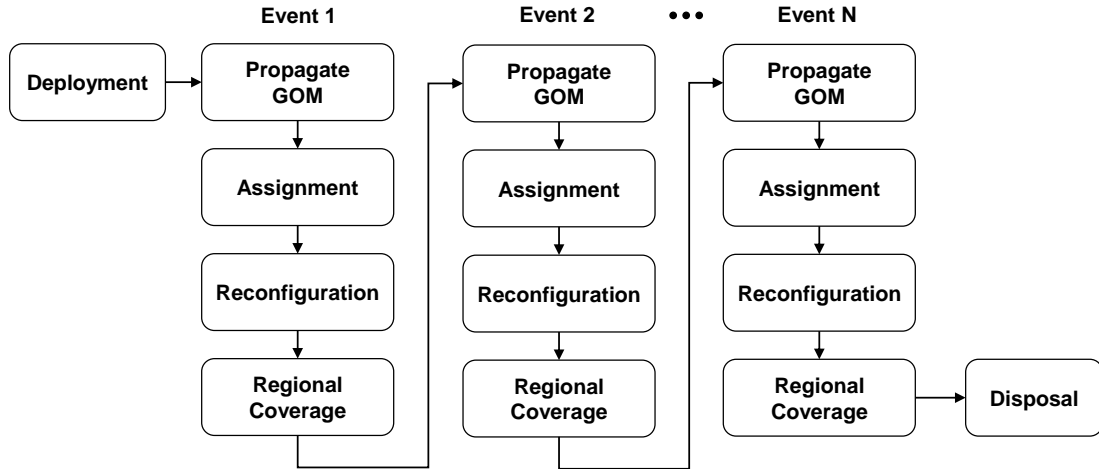
Figure 3-33: A campaign-based lifecycle simulation tracks how the system responds to an uncertain number of regional events. For each event response the simulation: uses an assignment process to determine how many and which specific satellites are reconfigured, models the reconfiguration maneuver and computes the resulting coverage for the event.

process employs a decision model to mimic decision-maker preferences and select how many satellites should be reconfigured for the specific event. Following this decision, the assigned satellites are reconfigured and access times are computed for the duration of the event. After the event is over, the satellites in ROM return to GOM to await the next event. The reconfiguration maneuver (Section 3.5.3), optimal assignment (Section 3.5.4), decision model (Section 3.5.5), and ROM simulation (Section 3.5.6) processes are described in more detail in the following sections.

3.5.3 Reconfiguration Maneuver Model

The goal of reconfiguration is to move satellites from GOM to a specific orbital slot in ROM that provides coverage to a specific ground location. The maneuver consists of an altitude change in addition to proper phasing to achieve the correct ROM orbit. The maneuver is modeled as either a single Hohmann transfer or double Hohmann transfer. The double Hohmann transfer places the satellite in a drift orbit, with a greater altitude difference from ROM, to speed phasing with the desired ROM orbital slot. All maneuvers are modeled as in-plane and impulsive. Propulsive plane changes are restricted due to their immense ΔV cost, and, contrary to intuition, they have not been seen to significantly improve performance.

109

Modeling the maneuvers as impulsive implies chemical propulsion. Low thrust, high I_{SP} electric propulsion could be used for the reconfiguration maneuver, however this thesis is focused on quick response to short duration events and therefore chemical propulsion systems are more appropriate. However, the return to GOM after event response could potentially utilize electric propulsion for higher propulsive efficiency.
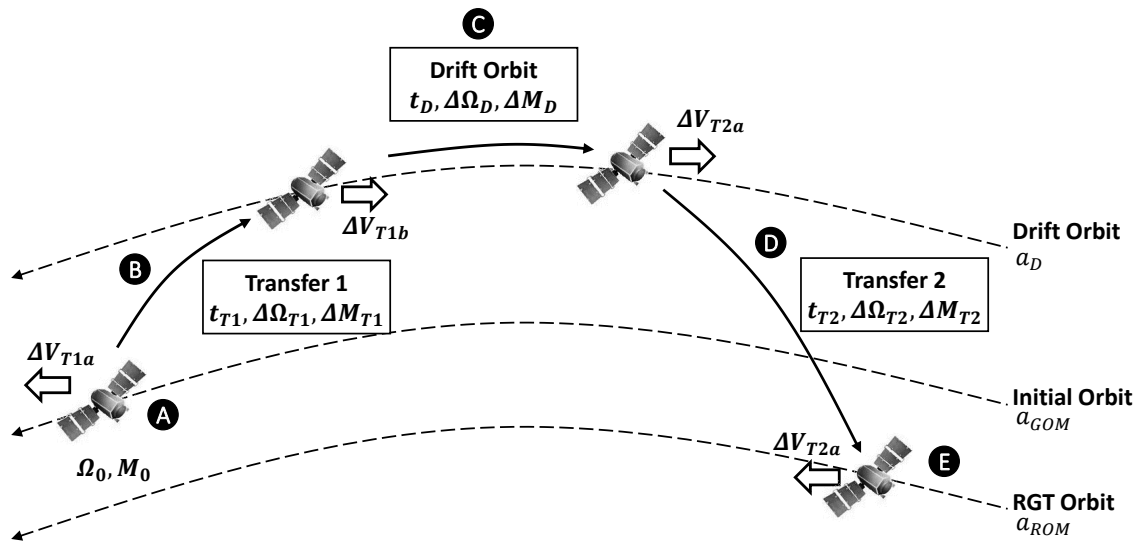
Figure 3-34: The satellite reconfiguration strategy involves two in-plane Hohmann-transfers: one to move the satellites into a drift orbit for faster phasing with the desired ROM orbital slot (labeled B), and one to move the satellites into ROM (labeled D).

Figure 3-34 shows the reconfiguration strategy in more detail. The satellite starts off (label A) with an initial orbital position described by Ω_0, M_0, and a_{GOM}. The satellite then performs a Hohmann transfer (label B) with initial propulsive maneuver ΔV_{T1a} and final propulsive maneuver ΔV_{T1b} to achieve a new semi-major axis of $a_D = a_{GOM} + \Delta h_D$. The transfer has a duration of t_{T1} during which time the orbital state changes by $\Delta\Omega_{T1}$ and ΔM_{T1} by J_2 induced orbital precession and mean motion, respectively. The satellite then waits in the drift orbit (label C) for duration t_D during which time the orbital state changes by $\Delta\Omega_D$ and ΔM_D. When proper orbital phasing occurs, the satellite then performs a second Hohmann transfer (label D) with initial propulsive maneuver ΔV_{T2a} and final propulsive maneuver ΔV_{T2b} to achieve the RGT orbit (label E) with semi-major axis a_{ROM}. The second transfer has a duration of t_{T2} during which time the orbital state changes by $\Delta\Omega_{T2}$

and ΔM_{T2}. The total reconfiguration time is $t_R = t_{T1} + t_D + t_{T2}$. The rest of this section explains how the drift time t_D is computed to ensure proper phasing to place the satellite into a ROM orbit that provides RGT coverage for a specific ground location.

Section 3.1.1 introduced how each RGT orbit can be described by the unique angle Λ, which is a function of the satellite's orbital state and the RGT type (an integer number of orbits repeating in an integer number of days):

$$\Lambda = N_o\Omega + N_d M \tag{3.53}$$

For any satellite in GOM, with given Ω, this equation specifies the mean anomaly needed to achieve the correct RGT as specified by Λ. Additionally, Λ changes with time due to the effects of mean motion and orbital precession as follows:

$$\Lambda_f = \Lambda_0 + \left[N_o\dot{\Omega}_{ROM} + N_d \left(n_{ROM} + \dot{M}_{ROM} + \dot{\omega}_{ROM} \right) \right] t_R \tag{3.54}$$

Where Λ_0 is the initial RGT angle, and Λ_f is the RGT angle at the end of the reconfiguration maneuver. Using Λ_f in Equation 3.53, and rearranging for M yields:

$$M_f = \frac{(\Lambda_f - N_o\Omega_f)}{N_d} \tag{3.55}$$

Where Λ_f is the RGT angle at $t = t_f$ and Ω_f is the satellite's Ω at time $t = t_f$. This relation gives the necessary M to achieve the correct ROM orbit including J_2 orbital precession effects. The satellite's final orbital state (Ω_f and M_f) is dictated by the reconfiguration maneuver strategy and is determined by the following relations:

$$\Omega_f = \Omega_0 + \Delta\Omega_{T1} + \Delta\Omega_D + \Delta\Omega_{T2} \tag{3.56}$$

$$M_f = M_0 + \Delta M_{T1} + \Delta M_D + \Delta M_{T2} \tag{3.57}$$

Where Ω_0 and M_0 is the satellite's original state, $\Delta\Omega_{T1}$ and ΔM_{T1} is the change in orbital parameters during the first Hohmann transfer, $\Delta\Omega_D$ and ΔM_D change in orbital parameters during time spent in the drift orbit, and $\Delta\Omega_{T2}$ and ΔM_{T2} is the change in orbital parameters

during the second Hohmann transfer. Equations 3.56 and 3.57 can then be expanded to:

$$\Omega_f = \Omega_0 + \dot{\Omega}_{T1} t_{T1} + \dot{\Omega}_D t_D + \dot{\Omega}_{T2} t_{T2} \tag{3.58}$$

$$M_f = M_0 + \left(n_{T1} + \dot{\omega}_{T1} + \dot{M}_{T1}\right) t_{T1} + \left(n_D + \dot{\omega}_D + \dot{M}_D\right) t_D$$
$$+ \left(n_{T2} + \dot{\omega}_{T2} + \dot{M}_{T2}\right) t_{T2} \tag{3.59}$$

Where t_{T1} and t_{T2} are the transfer times for Hohmann transfer 1 and 2 respectively which are equal to $\frac{1}{2}$ the orbital period of the eccentric transfer orbits. Relations for n, $\dot{\Omega}$, $\dot{\omega}$, and $\dot{M}$ were previously given in Equations 3.2, 3.3, 3.4, and 3.5. Given known i, a_{GOM} and a_{ROM}, and Δh_D, then the only remaining variable in the problem is the drift orbit duration t_D. The problem is then reduced to finding the minimum t_D that satisfies Equation 3.55. Selecting different drift orbit altitudes (through the internal variable Δh_D) will change t_D, and will also change the total round-trip reconfiguration ΔV cost given by:

$$\Delta V_R = \Delta V_{T1a} + \Delta V_{T1b} + \Delta V_{T2a} + \Delta V_{T2b} + \Delta V_{T3a} + \Delta V_{T3b} \tag{3.60}$$

Where ΔV_{T3} is the return to GOM ΔV. These ΔV costs are given by:

$$\Delta V_{T1a} = \left| \sqrt{\frac{2\mu}{a_{GOM}} - \frac{\mu}{a_{T1}}} - \sqrt{\frac{\mu}{a_{GOM}}} \right| \quad \Delta V_{T1b} = \left| \sqrt{\frac{2\mu}{a_D} - \frac{\mu}{a_{T1}}} - \sqrt{\frac{\mu}{a_D}} \right|$$

$$\Delta V_{T2a} = \left| \sqrt{\frac{2\mu}{a_D} - \frac{\mu}{a_{T2}}} - \sqrt{\frac{\mu}{a_D}} \right| \quad \Delta V_{T2b} = \left| \sqrt{\frac{2\mu}{a_{ROM}} - \frac{\mu}{a_{T2}}} - \sqrt{\frac{\mu}{a_{ROM}}} \right|$$

$$\Delta V_{T3a} = \left| \sqrt{\frac{2\mu}{a_{ROM}} - \frac{\mu}{a_R}} - \sqrt{\frac{\mu}{a_{ROM}}} \right| \quad \Delta V_{T3b} = \left| \sqrt{\frac{2\mu}{a_{GOM}} - \frac{\mu}{a_R}} - \sqrt{\frac{\mu}{a_{GOM}}} \right|$$

and where:

$$a_{T1} = \left(2a_{GOM} + \Delta alt\right)/2$$

$$a_{T2} = \left(a_{ROM} + a_{GOM} + \Delta alt\right)/2$$

$$a_R = \left(a_{ROM} + a_{GOM}\right)/2$$

Additionally, the time to first pass t_{fp} in ROM can be calculated as total reconfiguration

time t_R plus the amount of time it takes for the satellite to pass over the event location after achieving ROM. Therefore, at the expense of higher propellant expenditure operators can choose a larger Δalt for faster phasing. These tradeoffs are shown in more detail in the following section.

Why not consider eccentric orbits?

Eccentric RGT orbits can provide improved GSD imagery for the same aperture size due to a lower altitude near perigee. Additionally, reconfiguring the satellites into an eccentric RGT does not need to circularize the orbit and therefore might require less maneuvers. However, there are several drawbacks to eccentric RGT orbits. First, phasing is much harder since, not only do the satellites need to be placed into the correct RGT to provide coverage for the event, but perigee also needs to be placed close to the event location. The difficulty associated with phasing is a function of the type of GOM orbit used. This phasing is simple if the GOM orbit is circular, but it is very difficult if the GOM orbit is eccentric. The second drawback is that the perigee location along the RGT will drift due to orbital precession unless the inclination is set to one of two critical inclinations ($i = 63.435°$, $i = 116.565°$) where $\dot{\omega} = 0$ in Equation 3.4. For other inclinations, the perigee will drift away from the event location, and the benefits of using an eccentric orbit will be lost.

Figure 3-35 illustrates some of the tradeoffs associated with eccentric RGT orbits. The example scenario considered starts with a satellite in a circular GOM orbit with semi-major axis $a_{GOM} = a_{ROM} + \Delta alt$. This satellite then is placed directly into an eccentric RGT orbit with semi-major axis a_{ROM} to satisfy the RGT compatibility criterion in Equation 3.7. The plot shows contours of the percent improvement of GSD between a circular RGT orbit and the eccentric RGT orbit as a function of inclination and Δalt. The figure also shows the round trip ΔV_R for reconfiguration and shows the two inclination regions where the perigee location drifts less than 1° per day. Here it takes a considerable amount of ΔV to achieve significant GSD improvement, and the inclination range to reduce perigee drift is small. For comparison, most efficient circular RGT designs have Δalt values between 1 and $10 km$.

An eccentric RGT orbit can also provide longer dwell time by imaging at apogee. Here, the increased dwell time potentially allows for more imaging during a single pass but requires
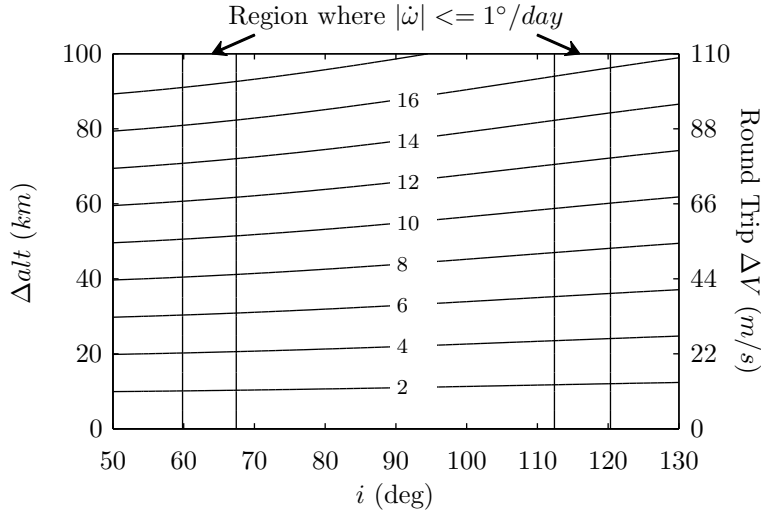
Figure 3-35: Contour plot showing the GSD percent improvement (contours) as a function of inclination and Δalt. Large round-trip ΔV is needed for significant GSD improvement, and the inclination range is severely restricted to keep perigee over the event location.

larger optics to provide imagery with the same spatial resolution. Again, assuming that the GOM orbit is circular (to allow for quick phasing for reconfiguration), Figure 3-36 shows the dwell time, aperture size, and round-trip reconfiguration ΔV for increasingly eccentric ROM orbits with $\varepsilon_{min} = 60°$ and $N_o/N_d = 15/1$. As the eccentricity increases, the dwell time increases, but the round-trip reconfiguration ΔV and aperture size also increase. In this case, an eccentric orbit with $e = 0.0131$ increases the dwell time by 16% ($65.9s \rightarrow 76.5s$), but must also increase aperture diameter by 18% ($0.308m \rightarrow 0.363m$) to maintain $1m$ GSD and requires $99m/s$ to complete each round-trip reconfiguration maneuver.

Therefore, while eccentric RGT orbits have the potential to improve the GSD provided for a given aperture size during perigee viewing or improve the dwell time during apogee viewing, they require significant increases in ΔV, severely limit possible inclinations, increase aperture size for apogee viewing, and pose additional phasing constraints. For these reasons, only circular orbits are considered in this thesis. Future work could further consider the mission flexibility allowed by eccentric orbits by considering the following scenario. The reconfigurable constellation could normally utilize circular ROM orbits, but when specific event responses need either lower GSD or higher dwell time (at the expense of GSD), then the system could use eccentric ROM orbits.
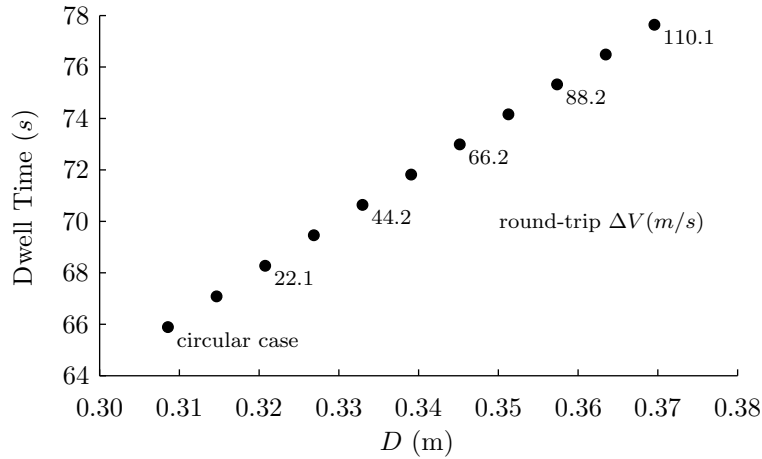
Figure 3-36: Apogee viewing in an eccentric ROM orbit increases dwell time as the cost of increased aperture size and increased round-trip reconfiguration ΔV

3.5.4 Satellite Assignment

The satellite assignment problem must determine for each event response: 1. how many satellites to reconfigure; 2. which specific combination of satellites to reconfigure; 3. how fast should the satellites be reconfigured (selection of drift orbit altitude); and 4. which RGT orbit should each reconfigured satellite be placed in (selection of ascending or descending pass coverage). Additionally, the assignment process should penalize assignment of satellites that have less than the average amount of propellant left in the constellation (to avoid premature propellant depletion of some satellites) and should prevent assignment of satellites that have run out of reconfiguration propellant or satellites that have failed.

In order to find globally optimal solutions, I have developed an optimization strategy that optimizes assignment while also concurrently accounting for all of the previously listed factors. The output from assignment is the direct tradeoff between regional coverage performance and total constellation propellant use for each event. This information is then used to aid decision makers when determining the appropriate level of response, or in the case of this simulation model, to feed a decision model that mimics the response of a human decision maker. The decision model is explained in detail in Section 3.5.5. Figure 3-37 shows the options available for each satellite in the constellation for each event response. Each satellite can remain in GOM, or can be reconfigured into either an ascending or descending

pass RGT orbit. If the satellite is reconfigured, then there are many options for the drift orbit altitude, which is a balance between minimizing fuel use (ΔV_R) and minimizing time to first pass (t_{fp}). The difficulty in solving the assignment problem is the immense size of the decision space. Each satellite has many reconfiguration options, and any combination of satellites along with their reconfiguration options leads to an extraordinarily large decision space.
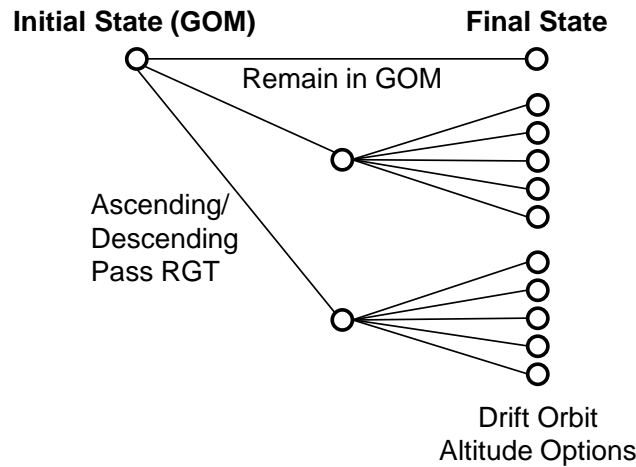
Figure 3-37: There are many reconfiguration options available to each satellite in the constellation

The assignment optimization process that I have developed is depicted in Figure 3-38. Inputs to the process include the satellites' current orbital state, propellant levels and the event location (φ, λ). The next few sections will detail each of the process steps.

Step 1: Compute Pass Times

The first step in the process involves computing the pass times for ascending and descending pass coverage for each satellite. This is a function of the satellite Ω and details for this process were previously provided in Section 3.1.2.

Steps 2 & 3: Determine Non-dominated Satellite Reconfiguration Options

The second step in the assignment process is to calculate the total time to first pass t_{fp} vs. ΔV_R tradeoff curves. The process begins by constructing a vector of possible drift
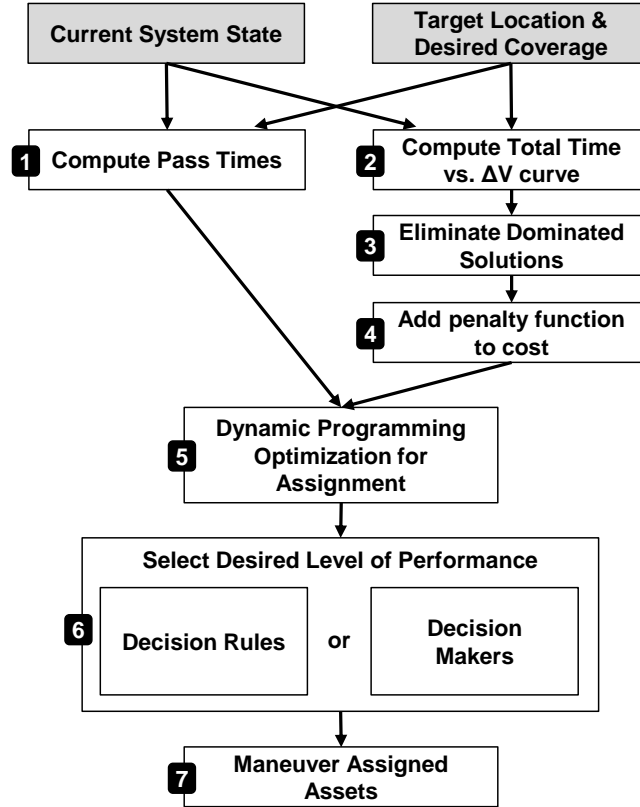
Figure 3-38: Satellite assignment process diagram

orbit altitudes $\overrightarrow{\Delta h_D}$, guided by parameters controlling the maximum altitude offset and granularity. For this thesis these values have been fixed at $\pm 100 km$ and $10 km$, respectively, yielding $\overrightarrow{\Delta h_D} = [-100 : 10 : 100]$. Next, several filtering steps remove infeasible options. If the drift orbit lies between GOM and ROM, then this will provide longer t_{fp} for the same ΔV_R (since phasing will be slower) and is removed from $\overrightarrow{\Delta h_D}$. Also, if the resulting a_D is greater than the maximum altitude constraint, or if a_D is less than the minimum altitude constraint, then the option will also be removed from $\overrightarrow{\Delta alt}$. Once the pre-filtering steps are complete then t_{fp} and ΔV_R are found for each value in $\overrightarrow{\Delta h_D}$ for both ascending and descending pass RGT coverage. Section 3.5.3 described how t_{fp} and ΔV_R are determined given the satellite state, the target location, and the drift orbit altitude.

Example curves for a case where a_{GOM} is $20 km$ higher than a_{ROM} are displayed in Figure 3-39. The ROM orbital altitude is plotted as a vertical dashed line at $\Delta h_D = -20 km$. In the top plot, which shows drift time (t_D) vs. Δh_D, we see that the drift orbits lower than ROM provide faster phasing for ascending RGT orbits and drift orbits higher than ROM provide
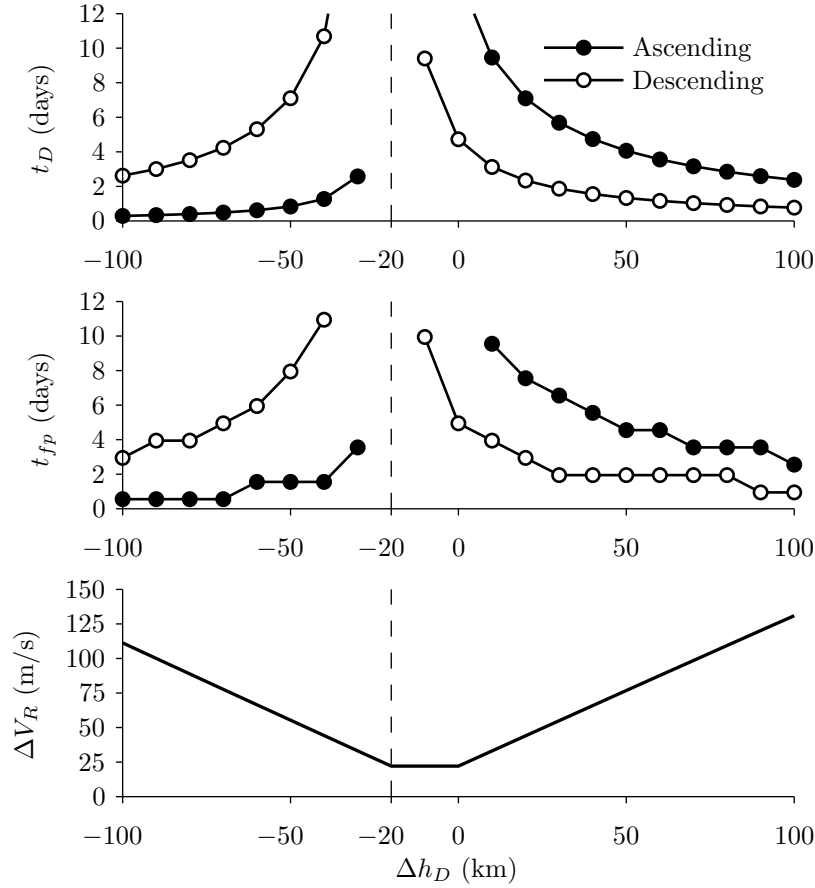
Figure 3-39: The drift time (t_D), time to first pass (t_{fp}) and ΔV_R as a function of Δh_D for ascending and descending pass RGT orbits for an example case where a_{GOM} is $20 km$ higher than a_{ROM}

faster phasing for descending RGT orbits. The middle plot shows time to first pass (t_{fp}) vs. Δh_D. Here we see that in some cases, increasing Δh_D decreases t_D but does not decrease t_{fp} and, therefore, consumes more ΔV with no added benefit. t_D and t_{fp} are different for ascending and descending RGT orbits since the satellites must achieve different orbital slots during phasing. In the bottom plot, we see that ΔV_R is nearly a linear function with Δh_D and has a constant bottom value between a_{GOM} and a_{ROM}. This bottom value of ΔV_R is simply the amount of ΔV required to go from GOM to ROM and back. It is also clear from these plots that there is no benefit for placing the drift orbit in between GOM and ROM since phasing will be slower for no reduction in ΔV_R, and, therefore, these options are

filtered out in the pre-filtering step explained previously.

The third step in the assignment process is to eliminate the dominated solutions in the t_{fp} vs. ΔV_R tradeoff. A dominated solution is one where another option provides either the same or lower t_{fp}, while simultaneously providing the same or lower ΔV_R. This process is illustrated in Figure 3-40. The top plot shows t_{fp} vs. ΔV_R for all reconfiguration options shown previously in Figure 3-39, and the bottom plot shows only the non-dominated reconfiguration options. This process is then repeated for all satellites in the constellation to create a list of all non-dominated satellite reconfiguration options.
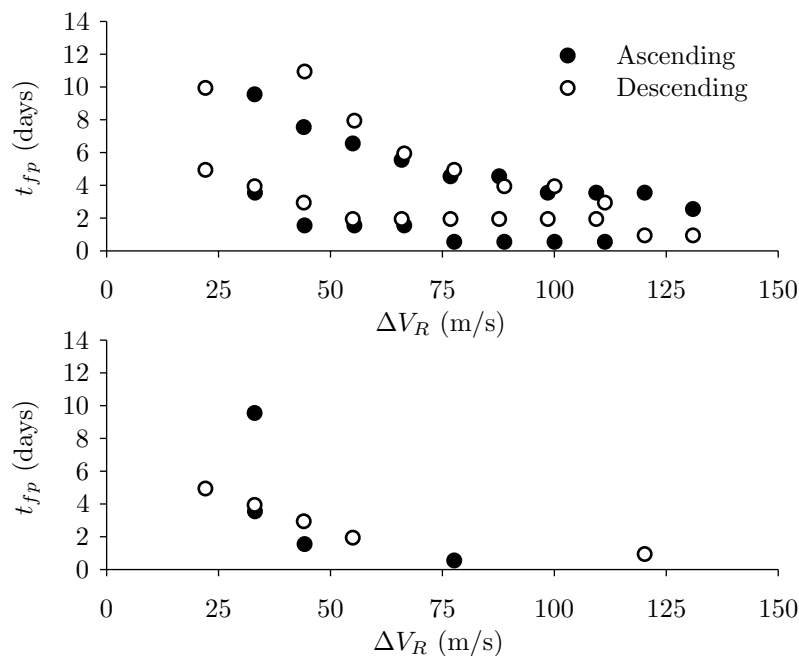
Figure 3-40: Tradeoff between minimizing time to first pass and minimizing reconfiguration propellant usage. The top plot shows all options, while the lower plot only shows non-dominated options for the ascending and descending RGT orbits.

Step 4: Add Penalty Function

The fourth step in the assignment process applies a penalty function to penalize assignment of satellites that have less than the average propellant remaining in the constellation. It also blocks assignment for satellites that have run out of reconfiguration propellant or have experienced failures. The reconfiguration cost is defined as the sum of the reconfiguration

ΔV and a penalty term:

$$C_R = \Delta V_R + \Delta V_{pen} \tag{3.61}$$

$$\tag{3.62}$$

Where ΔV_{pen} is governed by the following penalty function:

$$\Delta V_{pen,i} = -\min\left(0, \ \Delta V_{sat,i} - \frac{1}{N_T}\sum_{k=1}^{N_T}\Delta V_{sat,k}\right)G_{pen} \tag{3.63}$$

$$\tag{3.64}$$

Where $\Delta V_{sat,i}$ is the ith's satellite remaining reconfiguration ΔV and G_{pen} is a penalty function gain which is set to 0.1. G_{pen} can be used to control how tightly satellites are kept at the same propellant level. The penalty function works by increasing the satellite reconfiguration cost proportional to the difference in its remaining reconfiguration ΔV compared to the average remaining reconfiguration ΔV in the constellation. Additionally, no penalty is applied for satellites with higher than the average propellant left. With $G_{pen} = 0.1$, the applied penalty is 10% of the difference between the satellite's remaining reconfiguration ΔV and the average reconfiguration ΔV of the satellites in the constellation.

Step 5: Solve Optimum Assignment Problem

The fifth step in the assignment process is to determine the optimum assignment of satellites to be reconfigured. The problem to be solved is what is the best combination of m satellites, out of N_T total satellites in the constellation that provides the minimum cost to benefit ratio for providing coverage of the regional event. Additionally, each satellite has many reconfiguration options including the type of RGT (ascending or descending) and drift orbit altitude. This decision space is extremely large. Without filtering out dominated solutions, the number of reconfiguration options for each satellite is equal to $(1 + 2N_{\Delta h_D})$, where $N_{\Delta h_D}$

is the size of $\overrightarrow{\Delta h_D}$. The total decision space for reconfiguring k of N_T satellites is then:

$$N_{D,k} = (1 + 2N_{\Delta h_D})^k \binom{N_T}{k} \tag{3.65}$$

Where $\binom{N_T}{k}$ are the complete set of combinations for choosing k satellites out of N_T total satellites and is equal to $\frac{N_T!}{k!(N_T - k)!}$. For example, if we wanted to only reconfigure one satellite, the size of the decision space would be equal to the number of reconfiguration options for each satellite times the constellation size. If $\overrightarrow{\Delta h_D} = [-100 : 10 : 100]$ then $N_{\Delta h_D} = 21$ and the number of reconfiguration options for each satellite is 43. The total decision space for reconfiguring any number of satellites out of N_T is then:

$$N_D = \sum_{k=1}^{N_T} \left[(1 + 2N_{\Delta h_D})^k \binom{N_T}{k} \right] \tag{3.66}$$

The size of the decision space increases rapidly as the constellation size increases as shown in Table 3.6. In practice, after filtering dominated options, the decision space will be smaller. However, even if the number of non-dominated solutions is around 5 total per satellite (if $(1 + 2N_{\Delta h_D}) = 5$), the total non-dominated decision space $N_{D,nd}$ is much smaller as shown in Table 3.6, yet still unpractical for enumeration (brute force) based optimization schemes.

Table 3.6: Decision space size as a function of constellation size

N_T	N_D	$N_{D,nd}$
2	1935	35
4	3.8×10^6	1300
8	1.4×10^{13}	1.7×10^6
12	5.3×10^{19}	2.2×10^9
24	2.8×10^{39}	4.7×10^{18}
48	7.7×10^{78}	2.2×10^{37}

A dynamic programming based optimization approach was developed to overcome this immense computational burden. Essentially, dynamic programming performs enumeration, but greatly improves computational efficiency by not evaluating branches in the full-factorial tree that are known to be dominated. This process is called 'implicit enumeration', which

means that the entire decision space is searched implicitly. The algorithm is guaranteed to find the global optimum when correctly implemented. Dynamic programming breaks the optimization process down into simpler subproblems that are solved sequentially, and results from earlier subproblems are used to solve later subproblems. More background on dynamic programming can be found in published literature [19].

The basic building blocks of dynamic programming are stages and states. Each stage corresponds to a separate subproblem and contains a set of states, which are particular assignments. For the satellite assignment problem, the stages are how many of the satellites in the constellation are to be reconfigured (index k in Equation 3.66). At each stage, the goal is to minimize the reconfiguration cost (C_R) divided by the predicted utility generated during event response (U). This utility is the predicted performance due to persistence without GSD effects (see Section 3.6.1). Table 3.7 shows the reconfiguration options for a three satellite example. The options are a combined list of all non-dominated reconfiguration options for each satellite. The options list contains the option identifier in the first column, the satellite ID number, the type of RGT orbit (ascending or descending), the initial pass time θ_{LMT} in local solar time for the event location, the time to first pass t_{fp}, and the reconfiguration cost C_R from Equation 3.61.
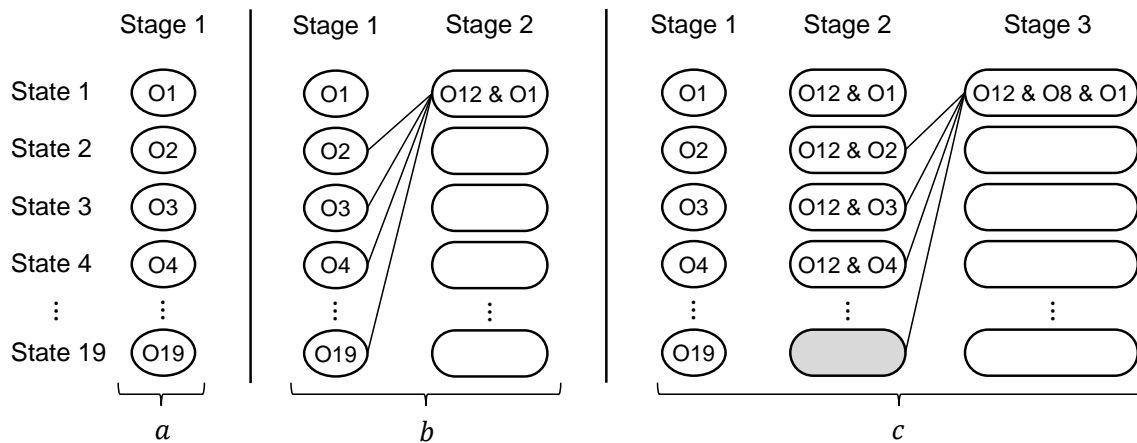
Figure 3-41: Dynamic programming optimization breaks the problem into a series of simpler subproblems to dramatically reduce computational complexity

The dynamic programming optimization starts off in stage 1 where the goal is to select one satellite from the constellation that minimizes C_R/U. Figure 3-41 illustrates the process

Table 3.7: Dynamic programming states for a 3 satellite example

Option	Satellite	RGT Type	θ_{LMT} hr	t_{fp} hr	C_R	C_R/U	ΔV_R m/s
O1	1	A	0.97	24.97	11.10	-	11.10
O2	1	D	7.70	7.70	44.57	22.28	44.57
O3	1	D	7.70	31.70	11.10	11.10	11.10
O4	2	A	8.95	104.95	26.47	26.47	25.36
O5	2	A	8.95	80.95	37.51	18.75	36.39
O6	2	A	8.95	56.95	48.52	16.17	47.41
O7	2	A	8.95	32.95	81.41	20.35	80.30
O8	2	D	15.69	111.69	26.47	2.94	25.36
O9	2	D	15.69	87.69	37.51	3.75	36.39
O10	2	D	15.69	63.69	48.52	4.41	47.41
O11	2	D	15.69	39.69	70.47	5.87	69.36
O12	3	A	16.95	112.95	25.36	2.82	25.36
O13	3	A	16.95	88.95	36.39	3.64	36.39
O14	3	A	16.95	64.95	47.41	4.31	47.41
O15	3	A	16.95	40.95	69.36	5.78	69.36
O16	3	D	23.69	119.69	25.36	-	25.36
O17	3	D	23.69	71.69	36.39	-	36.39
O18	3	D	23.69	47.69	58.39	-	58.39
O19	3	D	23.69	23.69	102.11	-	102.11

for a three satellite constellation example. The algorithm utilizes the states in the previous stage as a starting point to determine the collection of states comprising the current stage. Initially, the first stage is populated with each reconfiguration option as shown in Figure 3-41a, and the number of states is equal to the number of reconfiguration options. In stage 2, the goal is find the minimum cost to utility assignment by combining the states in stage 1 with each of the reconfiguration options. In stage 2, the algorithm starts off with state 1 where it evaluates the cost and performance of combining each state in stage 1 with reconfiguration option 1. The combination with the minimum $\Sigma C_R/U$ is then selected to be state 1 in stage 2. The cost is defined as the sum of each satellite's reconfiguration cost $\sum C_R$ and the utility is a function of the predicted pass times and is computed using the method explained in Section 3.6, without the GSD term. Additionally, satellites can only be assigned once and therefore some states are not valid and are excluded from the decision space. Figure 3-41b shows that the minimum cost assignment for state 1 in stage 2 for the three satellite example is to use reconfiguration options O12 and O1. This process is

repeated for all remaining states in stage 2 and then all stages in the assignment problem.

Table 3.8 shows the completed dynamic programming state space including the cost, performance, and $\Sigma C_R/U$ ratio for the three satellite example problem. States that are not valid are denoted by dashes and we see that the number of valid states diminishes as the stages increase. Once the dynamic programming optimization is complete, and the states are found for each stage, then the state in each stage that has the minimum $\Sigma C_R/U$ value is the optimal assignment for the stage. Table 3.8 shows that the minimum $\Sigma C_R/U$ value of the optimum assignment increases with increasing stages. For stage 1, the minimum $\Sigma C_R/U$ is 2.8, for stage 2 it is 2.9 and for stage 3 it is 3.3. This diminishing returns effect is intuitive since the best satellites will be assigned earlier and as more satellites must be assigned, efficiency will decrease.

Table 3.8: Dynamic programming states for a 3 satellite example

State		Stage 1				Stage 2				Stage 3		
		U	ΣC_R	$\Sigma C_R/U$		U	ΣC_R	$\Sigma C_R/U$		U	ΣC_R	$\Sigma C_R/U$
1	O1	0.0	11.1	-	O12,O1	9.0	36.5	4.1	O12,O8,O1	18.0	62.9	3.5
2	O2	2.0	44.6	22.3	O12,O2	11.0	69.9	6.4	O12,O8,O2	20.0	96.4	4.8
3	O3	1.0	11.1	11.1	O12,O3	10.0	36.5	3.6	O12,O8,O3	19.0	62.9	3.3
4	O4	1.0	26.5	26.5	O12,O4	10.0	51.8	5.2	-	-	-	-
5	O5	2.0	37.5	18.8	O12,O5	11.0	62.9	5.7	-	-	-	-
6	O6	3.0	48.5	16.2	O12,O6	12.0	73.9	6.2	-	-	-	-
7	O7	4.0	81.4	20.4	O12,O7	13.0	106.8	8.2	-	-	-	-
8	O8	9.0	26.5	2.9	O12,O8	18.0	51.8	2.9	O12,O3,O8	19.0	62.9	3.3
9	O9	10.0	37.5	3.8	O12,O9	19.0	62.9	3.3	O12,O3,O9	20.0	74.0	3.7
10	O10	11.0	48.5	4.4	O12,O10	20.0	73.9	3.7	O12,O3,O10	21.0	85.0	4.0
11	O11	12.0	70.5	5.9	O12,O11	21.0	95.8	4.6	O12,O3,O11	22.0	106.9	4.9
12	O12	9.0	25.4	2.8	O8,O12	18.0	51.8	2.9	-	-	-	-
13	O13	10.0	36.4	3.6	O8,O13	19.0	62.9	3.3	-	-	-	-
14	O14	11.0	47.4	4.3	O8,O14	20.0	73.9	3.7	-	-	-	-
15	O15	12.0	69.4	5.8	O8,O15	21.0	95.8	4.6	-	-	-	-
16	O16	0.0	25.4	-	-	-	-	-	-	-	-	-
17	O17	0.0	36.4	-	-	-	-	-	-	-	-	-
18	O18	0.0	58.4	-	-	-	-	-	-	-	-	-
19	O19	0.0	102.1	-	-	-	-	-	-	-	-	-

The output of the dynamic programming process is then condensed into a plot showing the cost and predicted utility corresponding to the lowest $\Sigma C_R/U$ assignment for each stage. Figure 3-42 shows these results for a 12 satellite assignment. The plot includes the optimal assignment of each stage as well as the option to not reconfigure any satellites giving zero predicted utility and zero reconfiguration cost. As the number of satellites reconfigured increases, the total reconfiguration ΔV increases steadily while the increase in utility starts

leveling off. This is caused by the situation where satellites able to provide the best coverage are assigned first and as more satellites are assigned, the ability of these additional satellites to provide coverage is reduced creating diminishing returns. A decision maker can then utilize this information to determine the appropriate balance between performance and cost to respond to the given event. Alternatively, in the place of a decision maker, a decision model equipped with decision rules can automatically select the assignment. This process is discussed in Section 3.5.5.
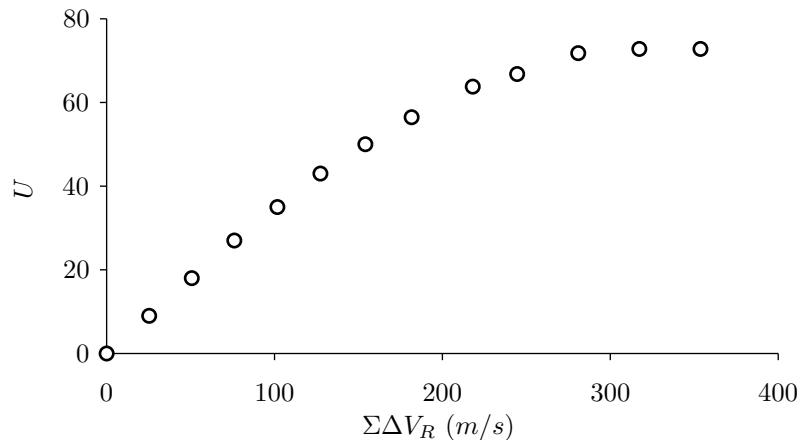
Figure 3-42: Dynamic programming output for a 12 satellite example constellation

The dynamic programming-based optimization approach significantly reduces computational complexity. Table 3.9 shows the time it takes to solve for the optimal assignment with enumeration and dynamic programming as a function of constellation size for $(1 + 2N_{\Delta alt}) = 5$ on an Intel Core i5-2410M processor. Enumeration is faster for small constellation sizes due to computational overhead required to set up dynamic programming. However, as the constellation size increases, dynamic programming provides a significant reduction in computation time while still ensuring that the global optimal solutions are found. The dynamic programming assignment process is validated through comparison with enumeration for small constellation sizes in Section 3.7.

125

Table 3.9: Dynamic programming optimization drastically reduces computational complexity

N_T	Enumeration	DP
2	0.006s	0.019s
4	0.24s	0.026s
8	314s	0.059s
12	4.7hr	0.12s
24	2.7×10^7yr	1.5s
48	1.3×10^{26}yr	23s

Steps 6 & 7: Select Desired Level of Performance and Maneuver Assigned Satellites

For each event response, the dynamic programming optimization process gives decision makers the optimal tradeoff (for each event response) of generating utility for the current event and preserving constellation capability for later events. Using this information, the decision makers must then select the appropriate level of response (step 6) and then reconfigure the assigned assets (step 7). To enable optimization, a decision model is implemented to mimic decision maker preferences. Details on the decision model are provided next in Section 3.5.5.

3.5.5 Decision Rules for When and How to use Flexibility

In an operational system, human decision makers would use the dynamic programming output to decide how many satellites to reconfigure for each event. However, this decision making process needs to be automated in order to support the optimization process. In this thesis, an automated weight-based decision model is utilized to mimic decision maker preferences and allow for rapid assignment in the simulation model. This section details how the decision model is implemented.

Two characteristics of the decision making process are captured in the decision model. The first recognizes that there are two primary competing objectives facing the decision maker: providing coverage for the current event and conserving system resources (propellant) for later event responses. The second recognizes that the decision maker will likely alter their preferences based on the current state of the system and changes in the future outlook. The decision model converts the two competing objectives (coverage now vs. conserving

propellant) into a single objective function using a weighting variable. This objective, to be maximized, is then written as:

$$J = -\alpha \sum (\Delta V_R) + (1 - \alpha) U \tag{3.67}$$

Where J is the objective, $\sum (\Delta V_R)$ is the total reconfiguration ΔV across all satellites, U is the total event utility, and α is the decision model weight variable. In an operational system, the decision maker would have to balance the use of resources so that the system would not run out of propellant early, or have unused propellant at the end of the design lifetime. The α variable is similar. Very high α values place too much emphasis on conserving propellant, likely leaving unused propellant in the satellites at system end of life. This will correspond to lost opportunity for generating utility. Conversely, very small α values place too much emphasis on generating utility. This will cause the system to run out of propellant early and the system will then be unable to effectively respond to later events. To avoid selecting α *a priori*, I decided early on to include α in the design vector letting the optimization process select the appropriate α for a given design optimized for a specific mission scenario. In this way, the optimization process will likely select α so that most of the reconfiguration propellant is used for event response.

The second characteristic that the decision model needed to capture was that as information regarding propellant use becomes known during the system lifetime, the decision maker might change their preferences. To model this behavior, α is continuously adapted during the regional simulation based on propellant use. Assuming that the propellant would be used at a constant rate during the system's lifetime then the adapted α is given as:

$$\alpha = \begin{cases} \min\left[(-\delta_P G_{DM} + 1)\,\alpha_0, 1\right] & \delta_P \geq 0 \\ \alpha_0 / (\delta_P G_{DM} + 1) & \delta_P < 0 \end{cases}$$

δ_P is related to the difference between the predicted and actual remaining propellant, G_{DM} is a gain term controlling how responsive the decision maker is to changing α based on new information, and α_0 is the initial weighting which is a design variable in the decision vector.

δ_P is calculated by comparing the actual remaining propellant with an estimate of how much propellant should be remaining. This estimate is based on assuming a constant depletion of propellant during the system's lifetime. If $\delta_P > 0$ then the system is using propellant at a slower rate than expected and α can be decreased for future events to avoid having excess propellant at the end of the system lifetime. If $\delta_P < 0$ then the system is using propellant faster than expected and α should be increased so that the system does not run out of propellant early. δ_P, normalized to the interval -1 to 1 is given as:

$$\delta_P = \frac{\left(\overline{\Delta V_{sat}} - \kappa \Delta V_{recon}\right)}{\Delta V_{recon}} \tag{3.68}$$

Where $\overline{\Delta V_{sat}}$ is the average satellite reconfiguration propellant remaining, ΔV_{recon} is the starting reconfiguration propellant, and κ is the fractional remaining lifetime of the constellation. Figure 3-43 shows how α varies as a function of δ_P for three different gains with $\alpha_0 = 0.5$. Here we see that when the constellation is using propellant faster than predicted (corresponding to $\delta_P < 0$), α is increased to place more emphasis on conserving ΔV. When the constellation is using propellant slower than predicted (corresponding to $\delta_P > 0$), α is decreased to place more emphasis on generating event response performance. We also see that as the gain increases, the model changes α more dramatically which results in the propellant use more closely matching a constant depletion rate. I have set $G_{DM} = 3$ for the work in this thesis.

Once α is determined, then the decision model objective function can be calculated using Equation 3.67. Figure 3-44 shows J for three different α weightings for the assignment output introduced in Figure 3-42. In this example, when $\alpha = 0.08$, J is maximized when 10 satellites are reconfigured. As α increases, and more emphasis is placed on conserving propellant, the number of satellites that maximizes J reduces. When $\alpha = 0.4$, zero satellites are reconfigured and regional coverage is only provided from GOM.

The design variable α_0 is part of the constellation design and should inform the decision maker as to what weightings should be used operationally in order to maximize system performance. The reasoning behind this is that the optimization process designed the system to perform well over the range of uncertain parameters with the specific value of α_0. In the
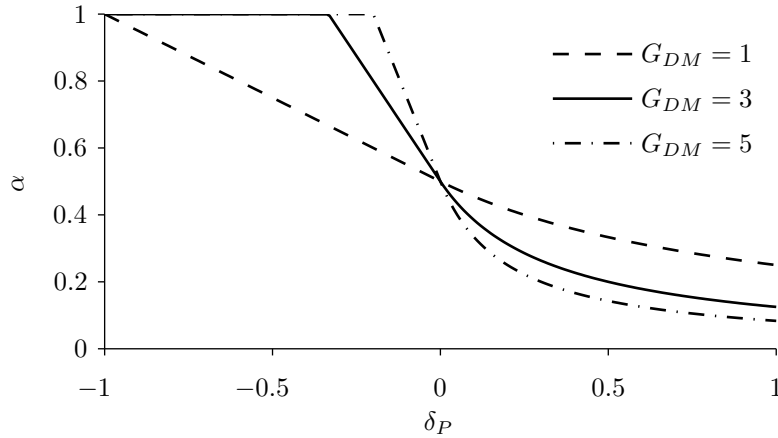
Figure 3-43: The decision model gain controls how closely the constellation follows the linear propellant depletion. Large gain means that α will be adjusted more to ensure that the constellation is using propellant at a constant rate throughout the lifetime

case where no additional information is gathered, changing α_0 will only yield sub-optimal system performance. It is likely, that new information regarding the system and future event probabilities will arise, in which case a new optimization should be performed to determine the new α_0 weighting that should be used. Additionally, the optimal α_0 for a given design is only applicable to the specific mission scenario considered during optimization. If a different mission scenario is investigated, the system will need to be re-optimized, likely changing the value of α_0.

3.5.6 ROM Simulation & Return to GOM

After satellite assignment, the satellite reconfiguration maneuvers are modeled and regional event access times by the constellation are computed for the duration of the event response. Numerical propagation and access calculations were the same as was used for GOM coverage calculations (Section 3.5.1) except that a timestep of 20 seconds was used to keep errors generally less than 0.3% (see model validation in Section 3.7).

After the event response is over, the satellites are then returned to GOM via a single Hohmann transfer to await the next regional event response. In most cases, some satellites will have remained in GOM and will have experienced different orbital precession rates. When returning to GOM, the satellites return back to their original M position; however,
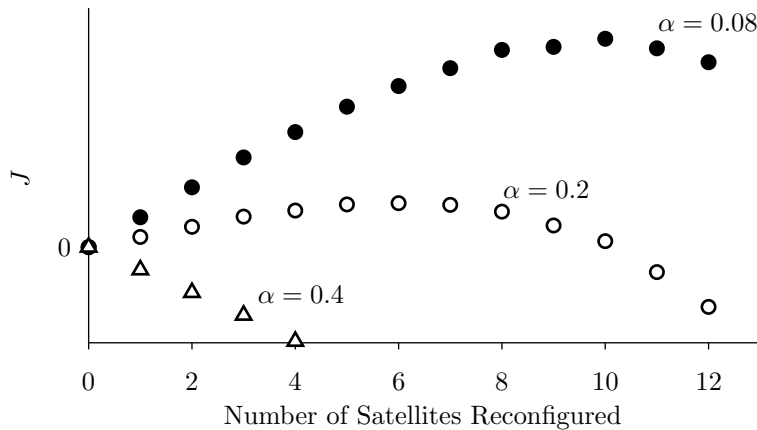
Figure 3-44: The decision model weight directly affects how many satellites should be reconfigured to minimize the objective J. In this example, $\alpha = 0$ results in zero satellites reconfigured while $\alpha = 0.08$ results in 10 satellites reconfigured.

the difference in Ω will be left uncorrected. This will cause the initial constellation pattern to decay slightly over time. This approach is used for two reasons: 1. the Ω drift is small, and 2. restoring the satellites to their initial position would cost additional propellant use. Since differential orbital precession is limited by the short time spent in ROM, the Ω difference is guaranteed to be small. Also, each of the satellites will eventually execute many reconfigurations, and, therefore, the Ω differences will tend to cancel out. Correcting for Ω differences would require a net increase in ΔV since the ROM satellites would need to maneuver to a drift orbit that would exhibit $\dot{\Omega}$ with a reversed sign. This means that if the ROM altitude were lower than GOM, then the drift orbit would have an altitude higher than GOM to restore the satellites to their initial GOM position. Figure 3-45 shows the Ω drift of twelve satellites through 20 regional responses. The Ω shift is the difference between the current satellite Ω and the Ω that would preserve the initial GOM constellation pattern, referenced to the key satellite. It should be noted there that the entire GOM constellation pattern will be shifted slowly over time. We see that the satellites stay within a few degrees of their initial GOM position with minimal performance degradation.

130
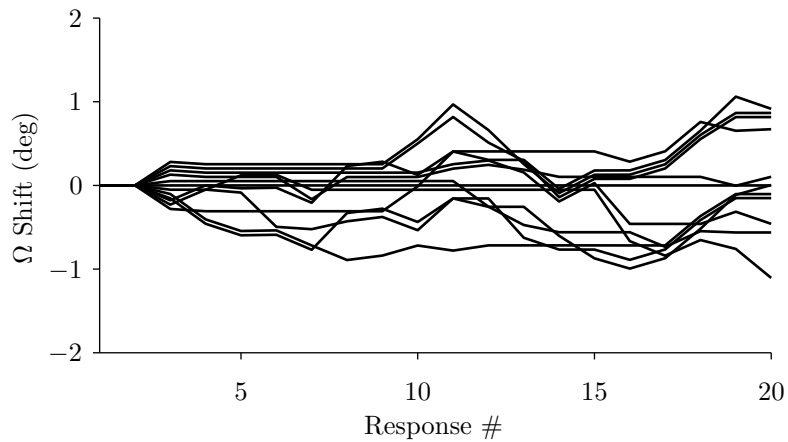
Figure 3-45: The amount of drift in Ω caused by not correcting for relative orbital precession during event responses is small

Why not just stay in ROM to await the next event?

An alternative strategy would leave the reconfigured satellites in ROM to await the next regional event. If the next event happened to be covered by the current RGT, then the satellite would already be in position to provide coverage with no propellant expenditure. While this sounds attractive, there are several drawbacks to this approach. The first drawback is that the partial global coverage provided by the constellation when not responding to an event would likely degrade. The second drawback is that the satellites will then be at different orbital altitudes for a significant amount of time. This will cause large relative drift (in terms of Ω), which would likely cause bunching of satellites in Ω. This would result in less diversity in pass time options for future event responses, which would lead to worse persistence. The third drawback is that it is unlikely that the next regional event location will be on the current RGT. In one case there is still coverage provided, but at off nadir viewing angles and therefore lower resolution. In a second case, there is no coverage provided by the current RGT and the satellite will need to maneuver to a drift orbit to allow for proper phasing, which diminishes any propellant savings by remaining in ROM in the first place. It is because of these drawbacks that the strategy employed in this thesis is to have all reconfigured satellites return to GOM after the event response is complete.

3.6 Performance

Regional event accesses
(coverage times and GSD)

Desired persistence & GSD

Performance

Performance Metric
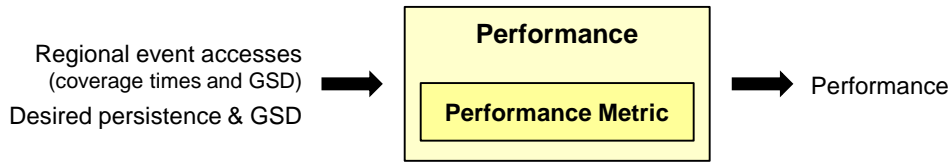
Performance

Figure 3-46: The performance module computes the constellation's aggregate performance given the computed ROM coverage statistics and the desired persistence and GSD

The objective of the Earth observing optical satellite constellations investigated in this thesis is to provide persistent coverage of regional events, where persistence is defined as long-term, continuing coverage with a specified frequency of observation. Therefore, a performance metric must capture how well the constellation matches the desired persistence. If the provided coverage under-samples with respect to the desired persistence, then some temporal event dynamics will be missed, and overall performance should decrease. If the provided coverage over-samples with respect to the desired persistence, then all the temporal event dynamics will be captured, but little or no additional utility may be gained for oversampling. In this case the performance should not increase beyond ideal sampling. Additionally, the performance metric must also account several other factors influencing optical imaging quality including solar illumination and spatial resolution. This section will first motivate the need for a new performance metric tied directly to persistence and then will detail how the metric is constructed.

Statistical metrics such as average and maximum revisit time are often used to evaluate the performance of discontinuous coverage satellite constellations. However, these metrics exhibit several undesirable traits stemming from their statistical underpinnings that make them poor measures of persistence. Previous literature [224, 225, 119, 74] has shown that the two objectives of average and maximum revisit time are often in tension and that optimizing one often degrades the other. This basic tension illustrates how these statistical measures fail in measuring persistence. Minimizing average revisit time involves simply increasing the number of observations in some fixed time window regardless of when they occur. The maximum revisit time simply measures the longest gap in coverage and does not account for

any of the other coverage information. Recently, response time, which measures the mean time to access in a given time period, has been proposed as a better measure of persistence [165]. This metric provides significant improvements over average and maximum revisit time, but it is still statistical in nature and, therefore, cannot easily incorporate additional factors like spatial resolution. Instead, I propose a new metric that takes a micro-scale approach to measuring persistence and can easily incorporate illumination constraints and spatial resolution effects. The new performance metric, which I term the 'Persistence Metric', is comprised of two utility functions: the first measures how well the desired persistence is met; and the second measures how well the desired spatial resolution is met. I will first describe the persistence (temporal resolution) term in Section 3.6.1 and then I will introduce the spatial resolution term in Section 3.6.2.

3.6.1 Persistence Metric
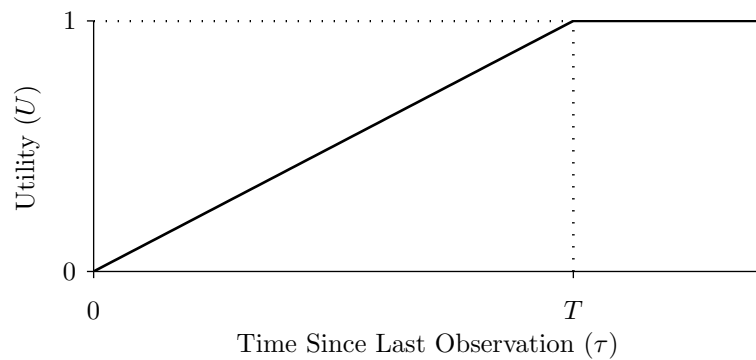
Figure 3-47: The temporal utility function term in the persistence metric assigns utility for a specific observation based on how well the time since the last observation matches the desired time between observations

The temporal term in the persistence metric is comprised of a utility function based on the time elapsed since the last observation. The utility function is described mathematically by:

$$U_\tau = \min\left(\left[\frac{\tau}{T}\right], 1\right) \tag{3.69}$$

133

Where T is the desired temporal resolution and τ is the time since last observation. This utility function, shown in Figure 3-47, starts off at 0 when $\tau = 0$ and ramps up to a maximum value of 1 when τ is equal to the desired characteristic time constant T. Therefore, if the scene was recently sampled, then the utility for the current observation would be low. If $\tau \geq T$, then the utility for the current observation is set to 1 regardless of the size of τ. While this may seem counterintuitive, there is an opportunity cost associated with undersampling, since the objective is to maximize the utility generated in a fixed time period. Any period where the utility is not accumulating is, therefore, lost opportunity in terms of maximizing the total utility generated during an event. The total utility for n observations is then given as the sum of each individual observation utility $U_{\tau,i}$:

$$U_\tau = \sum_{i=1}^{n} (U_{\tau,i}) \tag{3.70}$$
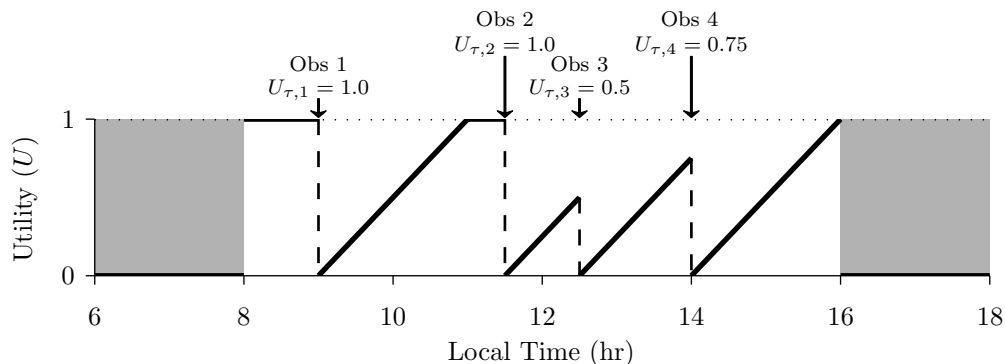
Figure 3-48: The persistence utility function changes throughout the day based on when observations occur

Figure 3-48 shows an example that illustrates how coverage performance is calculated for four observations made in one day with a desired revisit time of $T = 2hr$. The plot shows utility as a function of local time of day. For this example, only coverage between 8am and 4pm is desired for solar illumination reasons and, therefore, any coverage outside of this time window has zero utility. The allowable observation window is a function of the type of information collected by the satellites and future work can change or eliminate this window when considering infrared and synthetic aperture radar missions. Additionally, the

effect of weather on observation utility is not modeled and should be investigated in future work. The first observation occurs at 9am and, since this is the first observation of the day and τ is undefined, the utility is set to 1 giving $U_1 = 1$. After the first observation, the utility for subsequent coverage increases until $\tau = 2hr$ at which time it levels out at 1, which occurs at 11am. The second observation occurs at 11:30am giving $\tau_2 = 2.5hr$ and, therefore, $U_2 = 1$. The third observation occurs shortly after at 12:30pm giving $\tau_3 = 1hr$ and $U_3 = 0.5$. The last observation for the day occurs at 2pm giving $\tau_4 = 1.5hr$ and $U_4 = 0.75$. The total utility is then $U_{tot} = U_1 + U_2 + U_3 + U_4 = 3.25$ out of a maximum of 5 if there were five observations starting at 8am and spaced every 2 hours. In this way, the persistence metric takes a micro-scale approach to measuring how well coverage matches the desired observation frequency.
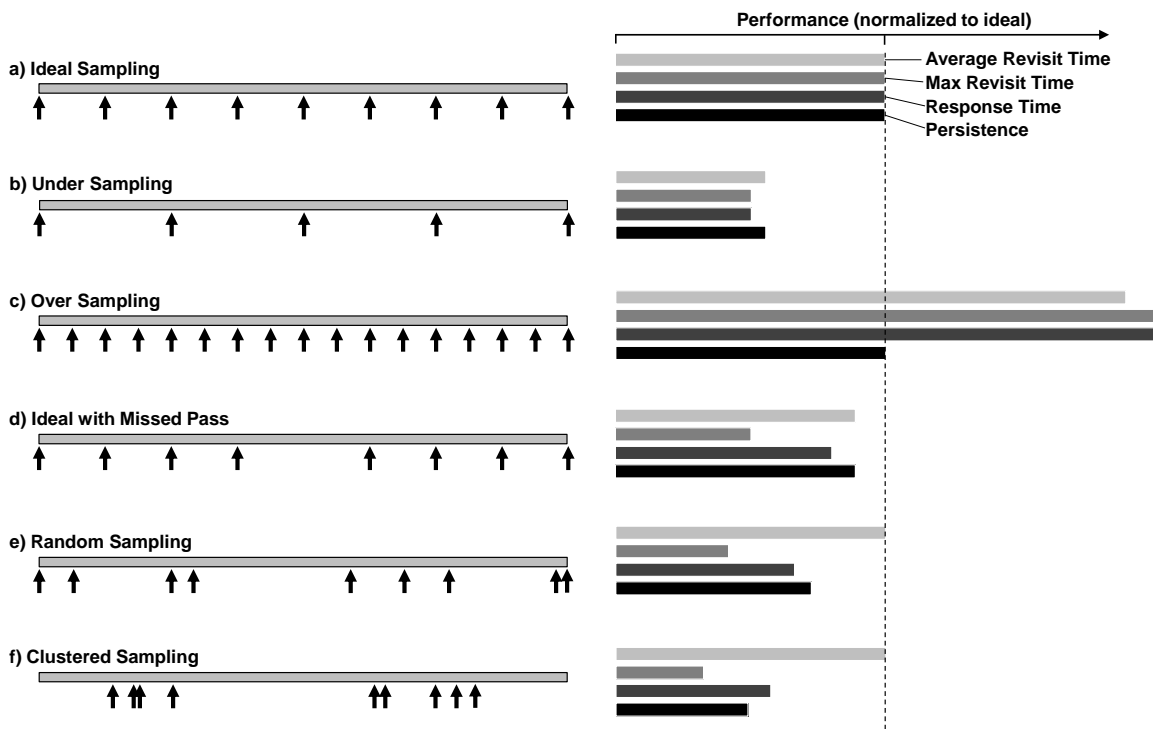
Figure 3-49: The persistence metric is not skewed by statistical outliers that plague traditional metrics like average and maximum revisit time

I now compare this new persistence metric with the traditional metrics of average revisit time, maximum revisit time, and response time. Average revisit time (including end gaps) is given by: T_{samp}/n where n is the number of observations and T_{samp} is the time period

duration. Maximum revisit time (including end gaps) is given by the longest gap in coverage during T_{samp}. The response time metric measures the mean time to access in a given time period and is based on the probability density function of the gap times [165], and mean response time is given as: $\bar{x} = \frac{1}{2T_{samp}} \sum_{i=1}^{n} (\tau_i^2)$.

Figure 3-49 shows a comparison of the four metrics for a number of different daily observation scenarios. The first scenario (a) is the ideal coverage scenario where observations are made with a time between observations of $\tau = T$ as shown to the left of the figure. The performance, given by the four metrics, is displayed on the right side of the figure and is normalized to the ideal sampling scenario. The larger the horizontal bar, the better the performance given by the respective metric. For the ideal scenario, all metrics give the same value due to normalization. For the second scenario (b), where the scene has been under sampled and $\tau = 2T$, the four metrics all give roughly half the ideal performance. In the third scenario (c), where the scene has been over sampled and $\tau = \frac{1}{2}T$, the first three metrics give roughly twice the ideal performance, while the persistence metric gives the same performance as the ideal scenario. This highlights the first flaw of the traditional metrics, which is that they overestimate performance for oversampling. The fourth scenario (d) is identical to the ideal scenario, except that one of the observations is missing. For this case, performance would be expected to be slightly lower than ideal performance given that coverage with the desired persistence is provided for most of the day. While most of the metrics show this trend, the maximum revisit time metric gives greatly reduced performance. Here we see the flaw with the maximum revisit time metric, in that it is only governed by the largest gap in coverage and ignores the rest of the observations entirely. The last two scenarios (e and f) show what happens when the times of 9 observations are randomized. Both show the major flaw of average revisit time that it is only governed by the number of observations in a fixed time period. This is why the average revisit time performance for these two scenarios is identical to the ideal scenario despite the significant clustering of observations, and, therefore, less than ideal persistence.

Overall, these examples show how macro-scale statistical metrics like average and maximum revisit time are often misleading in terms of measuring persistence. The response time metric displays a response similar to the persistence metric with the exception of the over-

sampling case. While this could be corrected for, the primary advantage of the micro-scale persistence metric over the macro-scale response time metric is its potential for extensibility. The persistence metric can be tailored in many ways including: a) modifying the curve to reward over sampling; b) scaling utility as a function of solar elevation angle; and c) adding in a term for spatial resolution. I will briefly discuss a and b as possible extensions to this thesis work before going into detail on c (in Section 3.6.2) which is implemented in this thesis.

Modifying the utility function to reward over sampling

The implicit assumption in the persistence metric is that all of the temporal information content is acquired when sampling at the desired observation period T and no additional information is gathered in the case of over-sampling. This is the case when the entire target area can be imaged during a single observation. However, in the case where there is some additional utility for over-sampling, the persistence metric can be modified by adding a parameter p which alters the utility curve as follows:

$$U_\tau = \min \left(\left[\frac{\tau}{T}\right]^p, 1 \right) \tag{3.71}$$

The value of p can be determined by finding the marginal increase in utility ΔU for over sampling by a factor of two as follows:

$$p = \frac{\ln \left(0.5 + 0.5\Delta U\right)}{\ln \left(0.5\right)} \tag{3.72}$$

$P \approx 0.8$ when $\Delta U = 0.15$, which corresponds to a 15% increase in utility for doubling the sampling frequency. The utility curves with p values of 1, 0.8 and 0.3 are shown in Figure 3-50. The analysis in this thesis is limited to $p = 1$ and leaves the investigation of other p values for future work.
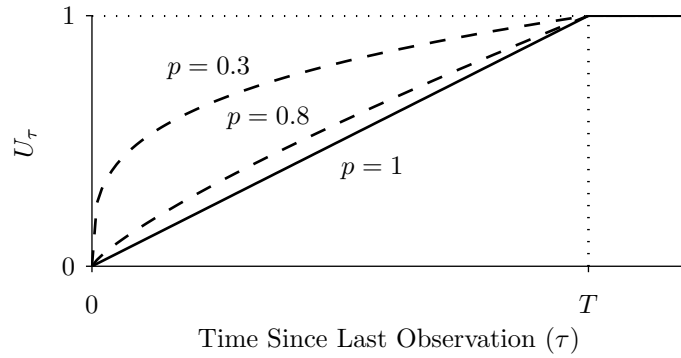
Figure 3-50: The parameter p causes the persistence utility curve to shift upward to reward oversampling

Scaling utility as a function of solar elevation angle

The second potential extension of the persistence metric would account for the effect of solar elevation angle on observation quality, and, therefore, utility. Solar elevation angle is the angle difference between the sun vector and the local horizontal. Larger solar elevation angles yield better imagery by increasing illumination intensity and reducing shadows. Figure 3-51 shows two potential solar elevation angle utility curves. The window function, where observations only have utility in a fixed time window, was used earlier and is shown as the shaded regions in Figure 3-48. A second method uses a utility curve based on the cosine of the solar elevation angle, which corresponds to the intensity of the solar illumination. This utility function is shown as the dashed curve in Figure 3-51. An example of four observations (similar to what was presented in Figure 3-48) using this solar utility curve is shown in Figure 3-52. The analysis in this thesis is limited to the rectangular window case and leaves investigation of the solar elevation angle utility for future work. Additionally, future work could also construct other solar illumination utility functions to accommodate other mission scenarios (e.g.missions where imagery with near-constant shadow conditions that allow analysts to better characterize imagery).

138
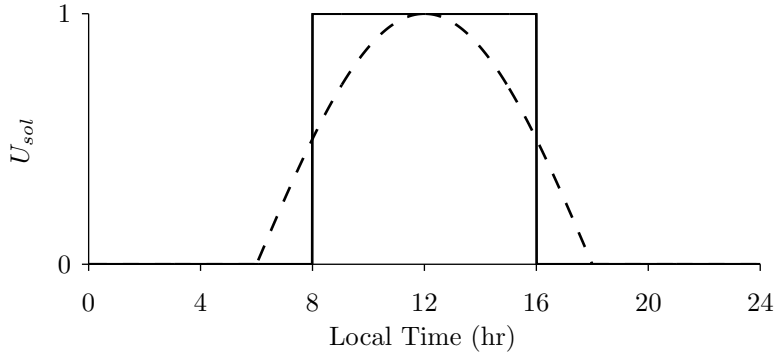
Figure 3-51: While the rectangular window function is used in this thesis, a more detailed window function based on solar elevation angle could be easily implemented to reward observations made around local noon
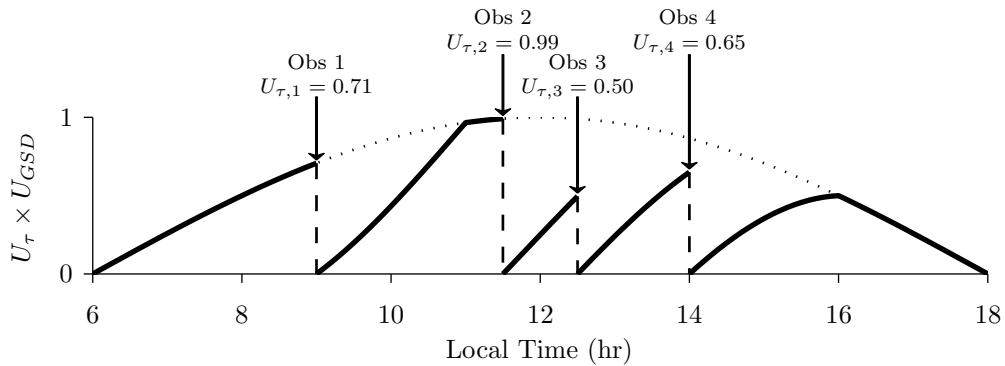
Figure 3-52: Same four observations as plotted in Figure 3-48 with the solar elevation angle window function applied

3.6.2   Persistence Metric with GSD

The third extension of the persistence metric accounts for differences in spatial resolution also known as ground sample distance (GSD). Most literature on satellite constellation design does not account for GSD differences, other than imposing fixed requirements. The analysis in this thesis, however, deals with satellites at different altitudes (caused by the GOM and ROM modes of operation and layered constellations) and also satellites that ensure nadir passes in ROM (for reconfigured satellites). Therefore, it is important to include the effect of GSD on performance.

GSD affects the information content contained in optical imagery. Similar to an event

139

having a desired sampling rate, the event will also have a desired GSD which will be driven by the end data product. Rather than the usual method of enforcing strict GSD requirements, I introduce a GSD based utility function matched to the degradation in the optical information content as GSD increases past the desired GSD. This degradation is matched to the change in the National Imagery Interpretability Rating Scale (NIIRS) as predicted in the General Image Quality Equation (GIQE) [123, 196]. The GIQE predicts that the change in NIIRS based on increasing GSD (assuming good sharpness) is given by [196]:

$$\Delta_{\text{NIIRS}} = -3.32 log_{10} \left[\frac{x}{X} \right] \tag{3.73}$$

Where X is the desired GSD and x is the actual achieved GSD. The GSD utility function is then given as a function of Δ_{NIIRS} as follows:

$$U_{GSD} = \min \left(\max \left(1 - \frac{\Delta_{\text{NIIRS}}}{\delta}, 0 \right), 1 \right) \tag{3.74}$$

Where δ is a scaling parameter that maps the drop in U_{GSD} to the drop in NIIRS, so that $U_{GSD} = 0$ when $x \geq 2^{\delta} X$. For this thesis I use $\delta = 2$ meaning that $U_{GSD} = 0$ when $x/X = 4$. This means that the utility is zero when actual GSD is four times greater than desired GSD. Figure 3-53 shows the GSD utility curve as a function of x/X. The plot shows that $U_{GSD} = 1$ when $x \leq X$ and $U_{GSD} = 0$ when $x \geq 4X$. When $X \leq x \geq 4X$, the utility is governed by the scaled NIIRS relation. This spatial resolution utility function exhibits similar behavior to the persistence utility function with no additional utility generated through spatial over-sampling.

The temporal and spatial resolution terms (Equations 3.71 & 3.74, respectively) are then combined to form the complete persistence metric with GSD effects, which can be written for the *ith* observation as:

$$U\left(\tau_i, x_i\right) = U_{\tau,i} \times U_{GSD,i} \tag{3.75}$$

The combined persistence utility surface (in terms of τ/T and x/X) is shown in Figure 3-54. Here we see that: the utility is 1 when $x \leq X$ and $\tau \geq T$; the utility is 0 when $x \geq 4X$

140
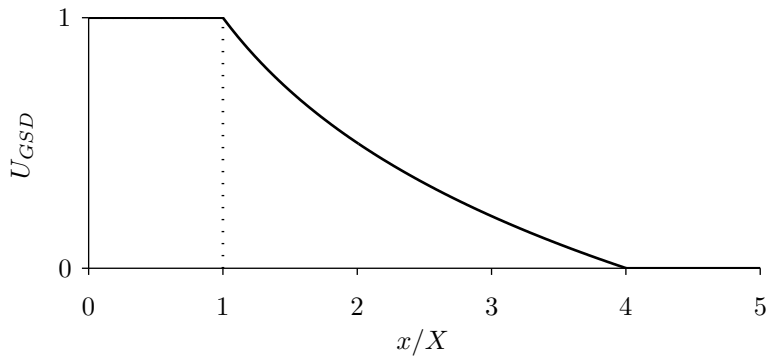
Figure 3-53: The GSD utility function is a function of the ratio of the actual to desired spatial resolution. The curve is plotted for $\delta = 2$

or $\tau = 0$; and the utility is on the interval $0 \rightarrow 1$ otherwise.
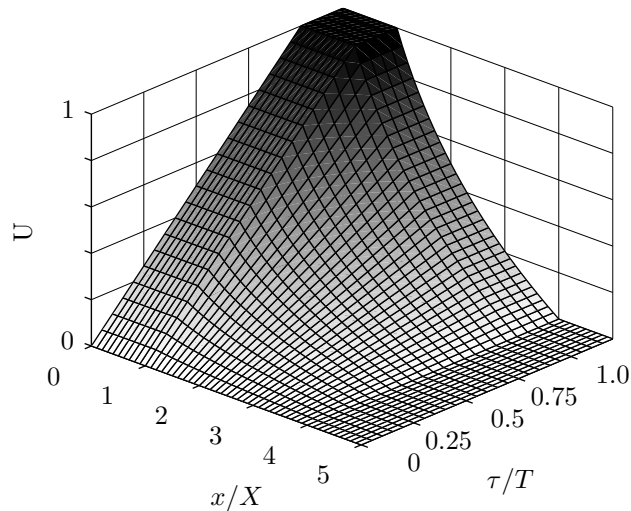
Figure 3-54: Combining the persistence utility function with the GSD utility function creates a two dimensional utility surface

Ensuring Symmetry

There is an inherent problem in combining the temporal and GSD utility curves, explained with an example illustrated in Figure 3-55. The example consists of two observation scenarios providing coverage for a target that has a desired revisit time of 1hr and desired GSD of 1m. The first scenario contains two observations (A and B) as plotted on the utility surface in
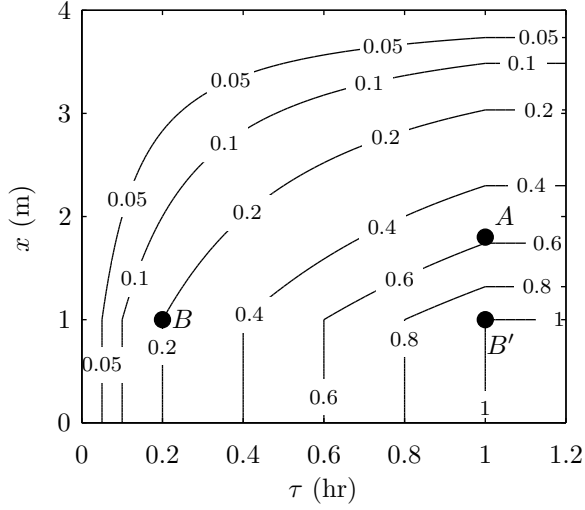
Figure 3-55: Three observations (A, B, B') plotted on the persistence utility surface (left) and observation details (right)

Figure 3-55 (left). Observation A provides 1.8m GSD while observation B occurs 0.2hr later and provides 1.0m GSD. Since A is the first observation of the day, the temporal utility is 1 while the spatial utility is less than 1 given that $x > X$. Observation B occurs shortly after A, meaning that the temporal utility will be low, however it provides much better GSD than A. The total utility for the first scenario is then given as $U_{tot} = U_A + U_B = 0.58 + 0.2 = 0.78$ as shown in Figure 3-55 (right). However, the second scenario shows that if only the second observation occurred, the total utility would be $U_{tot} = U_{B'} = 1.0$. It does not make sense that adding an observation would actually reduce total utility. This situation arises because the temporal utility function is artificially depressing the utility of the second observation and does not take into account the fact that the second observation provides significantly better GSD.

To fix this problem, a dynamic correction term is added to Equation 3.75. This dynamic correction term augments U_τ in the case that later observations provide better GSD. The persistence utility function with the correction term ΔU is given as:

$$U\left(\tau_i, x_i\right) = \left(U_{\tau,i} + \Delta U_i\right) \times U_{GSD,i} \tag{3.76}$$

Where $U_{\tau,i}$ and $U_{GSD,i}$ are given in Equations 3.71 & 3.74, respectively, and ΔU_i is the

142

following correction factor:

$$\Delta U_i = \max \left[0, U\left(\tau_{i-1}, x_i, \Delta U_{i-1}\right) - U\left(\tau_{i-1}, x_{i-1}, \Delta U_{i-1}\right) \right] \times \left(\frac{1 - U_{\tau,i}}{U_{GSD,i}} \right) \qquad (3.77)$$
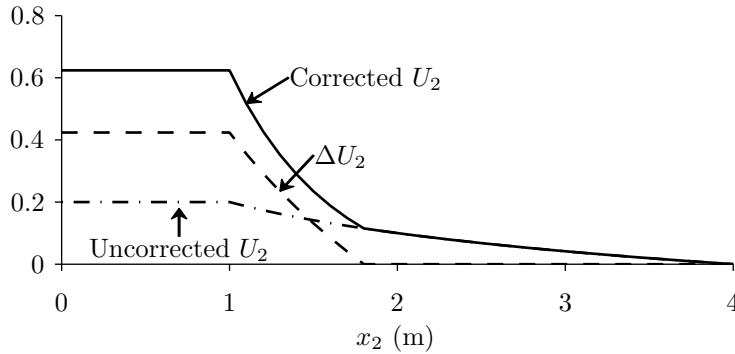
Figure 3-57: The utility correction function ΔU adds utility for a subsequent observation with better GSD than the first observation. This ensures that persistence is independent of observation order

The correction factor provides an increase in U_τ based on the difference in utility between the last observation utility $U\left(\tau_{i-1}, x_{i-1}\right)$ and a hypothetical utility for the last observation using the current observation GSD $U\left(\tau_{i-1}, x_i\right)$. The $\left(\frac{1 - U_\tau}{U_{GSD}} \right)$ term normalizes the result to ensure that the total utility is the same if the order of observations is reversed. For example, if the observation GSD values were switched, the total utility should be the same. A simple example will illustrate this process. Figure 3-57 shows the utility curve as a function of x_2 corresponding to a second observation 0.2 hours after an initial observation with $x_1 = 1.8m$, $X = 1m$ and $T = 1hr$. The uncorrected utility curve for U_2 (dash-dot) shows the utility generated by Equation 3.75. Here we see that U_2 is very low even when the second observation provides better GSD than the first observation. The utility correction factor ΔU_2 for the second observation (dashed) given by Equation 3.77 is positive for GSD values lower than the first observation GSD of 1.8m. This term is applied to the corrected utility curve (Equation 3.76) to generate the corrected utility curve (solid) which provides an increase in utility for second observations that provide better GSD.

The example discussed earlier and showed in Figure 3-55 can now be revisited with the inclusion of the utility correction factor. Figure 3-58 (left) shows the persistence utility
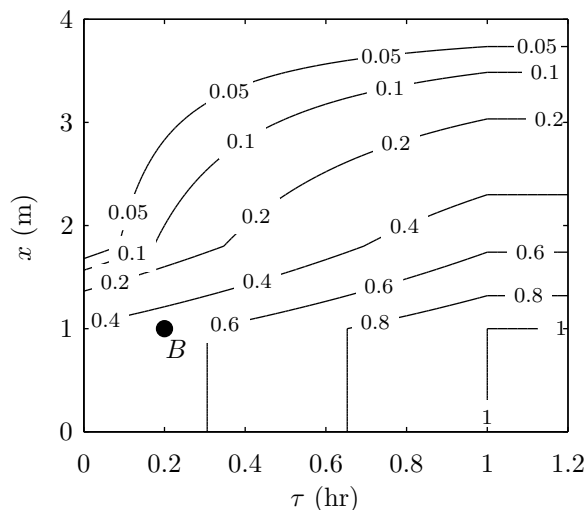
	Initial		Reversed	
	A	B	A"	B"
τ	–	0.2hr	–	0.2hr
x	1.8m	1.0m	1.0m	1.8m
ΔU	0	0.34	0	0
U_τ	1.0	0.54	1.0	0.2
U_{GSD}	0.58	1.0	1.0	0.58
U_i	0.58	0.54	1.0	0.12
ΣU_i	1.12		1.12	

Figure 3-58: Persistence utility surface with corrected U_τ showing observation B (left) and observation details using the corrected utility surface (right)

surface for the second observation including the correction factor ΔU in U_τ. This utility surface, when compared with the uncorrected utility surface in Figure 3-55, shows increased utility for new observations with better than 1.8m GSD. Figure 3-58 (right) shows that the corrected total utility for scenario 1 is 1.12, which is greater than the utility with just observation B, showing that the problem is fixed. Furthermore, the last two columns show the results when the GSD of the observations is switched. When $x_1 = 1.0m$ and $x_2 = 1.8m$, the total utility is still equal to 1.12, and, therefore, the utility surface is independent of observation order.

Figure 3-60 shows the persistence utility surface for a second observation parametrized by the GSD ratios x_1/X and x_2/X for four time since the last observation was made (τ_2). Here we see the symmetry in the surfaces which guarantees order independence. Additionally, we see that the correction factor diminishes with increasing time.

3.6.3 Calculating Constellation Performance

Performance for a constellation providing persistent surveillance to a regional event is defined as the sum of the persistence utility generated by all observations. This is written mathematically as the sum of the utility generated over all observations during each day and
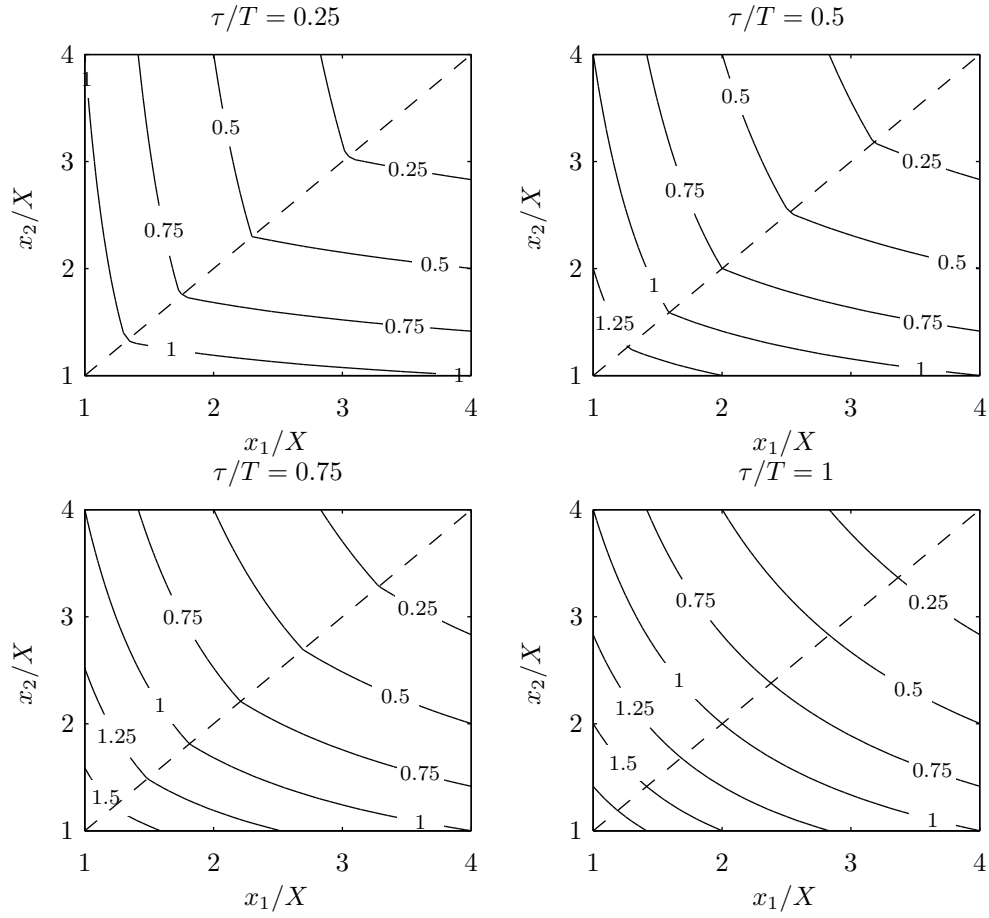
Figure 3-60: Contours of the two-dimensional persistence utility function for two consecutive observations parametrized by x/X and τ/T

then summed over all the days during the event response:

$$P_E = \sum_{days} \left(1 + \sum_{i=2}^{N_{obs}} U\left(\tau_i, x_i\right) \right) \tag{3.78}$$

Where N_{obs} is the number of daily observations and $U\left(\tau_i, x_i\right)$ is given in Equation 3.76. Additionally, the mean performance, denoted by P is calculated to represent the aggregate performance of the constellation while responding to all events during its lifetime.

One benefit of this performance formulation is that there is a maximum possible performance (called the 'ideal' performance, P_{max}) for a an event with a specified duration, a specified daily time window and a desired persistence and GSD. For example, if the event

145

duration was set to 14 days, the daily time window was set to 6am to 6pm, and $T = 1hr$, $X = 1m$, then the best performance would occur if an observation (each with $x = 1m$) was made every hour on the hour from 6am to 6pm. This results in 13 observations per day with $\tau = 1hr$, giving a total utility of 13 per day, and the ideal performance is then 14 days times 13 utility per day which equals 182. The performance for all results presented in this thesis are normalized to P_{max}.

3.7 Model Validation

If the simulation model does not accurately represent the system being optimized, then the results of the optimization process are invalid and misleading. Therefore, detailed model validation is essential to gaining confidence that the simulation model accurately represents the cost and performance of a given constellation design. Table 3.10 details how the major elements of the simulation model were validated. The spacecraft bus and payload sizing is tied directly to the properties of existing systems through parametric models. This ensures that these elements are grounded in reality. Systems Toolkit (STK), a commercially available modeling software, was then used to validate several critical elements in the astro-dynamics module including: orbit propagation, reconfiguration maneuvers, and both GOM and ROM coverage statistics. The dynamic programming based assignment optimization is then validated by comparing the output with an enumeration approach for small constellation sizes. Lastly, the cost model is validated by comparing it's output to cost information gathered from existing Earth observation optical satellites. This section provides details of the validation process and quantifies modeling error.

3.7.1 Astrodynamics Validation

The astrodynamics module validation was focused on ensuring the accuracy of the orbit propagation, RGT targeting of specific event locations, reconfiguration maneuver and coverage calculations. Validation was performed by comparing the output from the simulation model to the output from STK. Figure 3-61 shows how STK tools were integrated into the simulation model for validation purposes. This integration allowed certain calculations to be

Table 3.10: Simulation model validation strategy

Module/Model	Validation Strategy
Satellite	
Satellite mass & area	Tied directly to existing EO satellites
Astrodynamics	
Orbit propagation	Comparison with STK
GOM coverage	Comparison with STK Coverage module
Reconfiguration maneuver	Comparison with STK Astrogator module
ROM coverage	Comparison with STK Access module
Assignment optimization	Comparison with enumeration (full factorial search)
Cost	
Satellite cost	Comparison with the cost of existing EO satellites

seamlessly switched to the external STK software, while keeping the rest of the simulation model constant. The simulation model first sets up the constellation pattern by calculating the initial system state. GOM coverage is then calculated with the STK Coverage tool and results are sent back to MATLAB. The MATLAB simulation model then: determines the target position; propagates the constellation to the time of the next event; computes the propellant remaining on the satellites; solves the assignment problem; and uses the decision model to select the appropriate course of action. Then, given each satellite's drift orbit altitude and drift time, STK Astrogator is used to numerically solve for the reconfiguration maneuvers. Then STK Access is used to propagate the constellation, including reconfiguration maneuvers, and compute access periods to the event ground location. This process was repeated for all events during the system lifetime. The STK-MATLAB interface allowed for STK to be seamlessly integrated into the simulation model to automate all of these tasks and to allow for direct comparison with the simulation model code. The STK augmented model is called the STK validation model. One might ask why the STK model isn't just used at the actual simulation model for optimization. The fast MATLAB simulation model was created for two reasons: simulation runtime and licensing. Since the simulation model will be run hundreds of thousands of times for a single optimization run, it must be as efficient as possible and the MATLAB simulation model is approximately 1000 times faster than the STK validation model. Also, licensing with STK on parallel compute nodes would have been prohibitively costly.
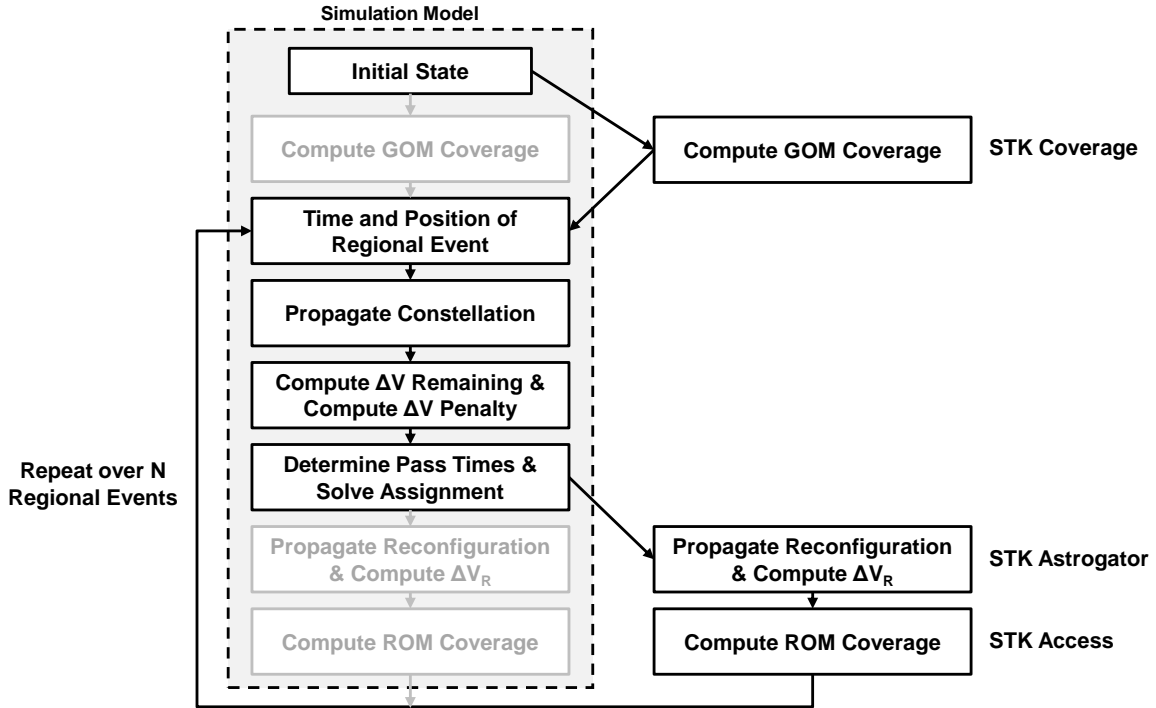
Figure 3-61: The simulation model uses STK to propagate the constellation, perform the reconfiguration maneuvers and compute coverage during the model validation process

The astrodynamics validation section is organized as follows. First the GOM coverage is compared to quantify the error between the simulation model and the STK validation model. Next, ROM performance is compared for a single constellation responding to a single target location. Following this initial validation, the model output was compared in a Monte Carlo simulation with different target decks and a fixed constellation design to quantify how the error varies over a distribution of uncertain parameters. Then, the model output was compared for a wide range of constellation designs to assess modeling error over the entire design space. A secondary goal of the validation process was to determine the appropriate numerical time step to use in the simulation model, which is essentially a tradeoff between simulation model run-time and modeling error.

GOM Maximum Revisit Time

The first validation effort focused on the effect of simulation model timestep on GOM maximum revisit time error. The modeling error is defined as the difference between the simulation model output and the STK validation model output as a percentage of the STK

validation model value. Figure 3-62 shows the GOM maximum revisit time error as a function of constellation size for different simulation model timesteps. As expected we see that the simulation model timestep decreases, the modeling error generally decreases. Also as the number of satellites in the constellation increase, the errors also tend to increase. This is likely caused by the decrease in the maximum revisit time for larger constellations, so any absolute errors are magnified when converted to a percentage. Simulation model timesteps less than $30s$ generally provide modeling errors less than 1%, while increasing the timestep to $40s$ increases the error significantly, and the error also becomes less predictable as evidenced by the spikes. Therefore, a $30s$ timestep was determined to be a good balance between simulation run-time and modeling error and is used in the thesis for computing GOM coverage.
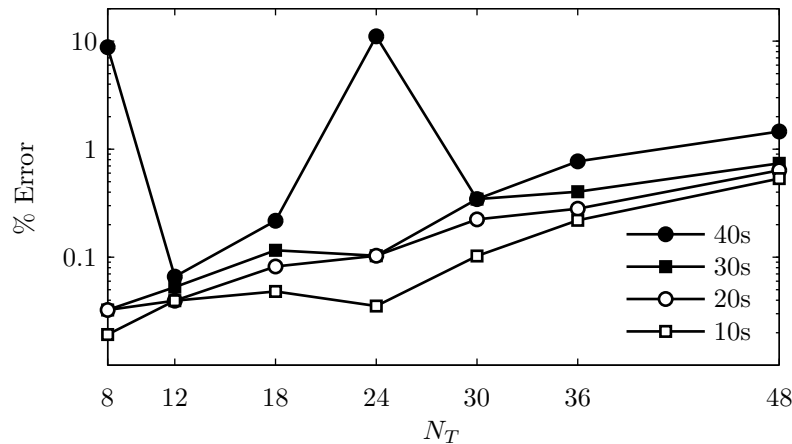
Figure 3-62: A $30s$ timestep for calculating the GOM maximum revisit time is a good compromise between minimizing error and maximizing computational efficiency

Figure 3-63 shows the GOM maximum revisit time predicted by the MATLAB model (crosses) and STK validation model (circles) for various constellation sizes using the $30s$ timestep. The lower plot shows the percent difference between the two models in greater detail than Figure 3-62. Here we see that the error is generally less than 0.1% for smaller constellations and approaches a maximum of 0.6% for a constellation of 48 satellites. Additionally, 88 random samples were taken from the design space to assess GOM maximum revisit time modeling error throughout the design space. Using a $30s$ timestep, the median

error was 0.144% with an interquartile range of 0.1% to 0.37%.
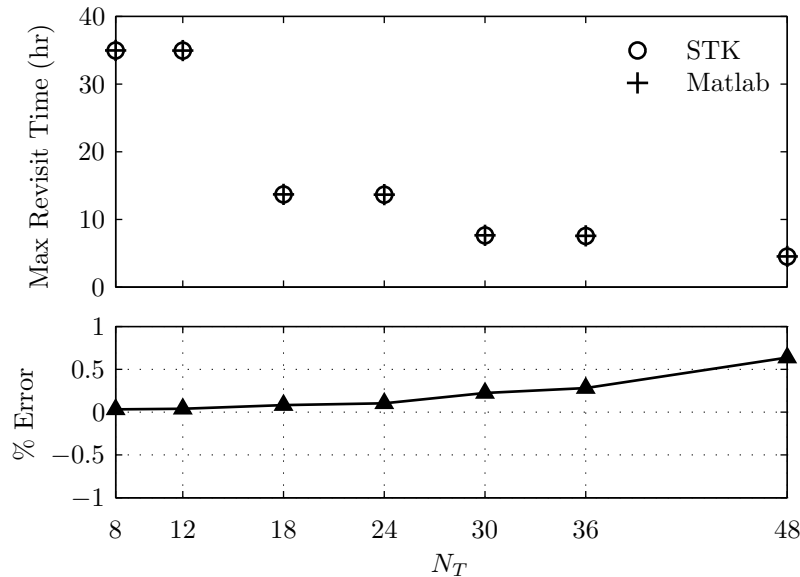
Figure 3-63: A $30s$ timestep results in errors of 0.1% for small constellations and 0.6% for large constellations

ROM Coverage

The second validation effort focused on the effect of simulation model timestep on total performance generated for regional response over the system lifetime. Figure 3-64 shows the total performance error as a function of constellation size and simulation model timestep during ROM simulation. Here we see that the the modeling error increases with increasing timestep and is not a strong function of constellation size. A ROM simulation timestep of $20s$ gives modeling errors generally less than 0.3% and is used in this thesis as a good balance between run-time and modeling error. The small error for total performance validates that many aspects of the simulation model are modeled correctly including: orbit propagation; RGT targeting; the reconfiguration maneuver and phasing; and coverage calculations. If any of these aspects were not modeled correctly, the satellites would not be properly aligned with the target in the STK validation model and the resulting system performance calculated by the two models would be substantially different.

I decided to also compare propagation error during a reconfiguration maneuver. Figure 3-65 shows the absolute range difference between the simulation model and the STK validation
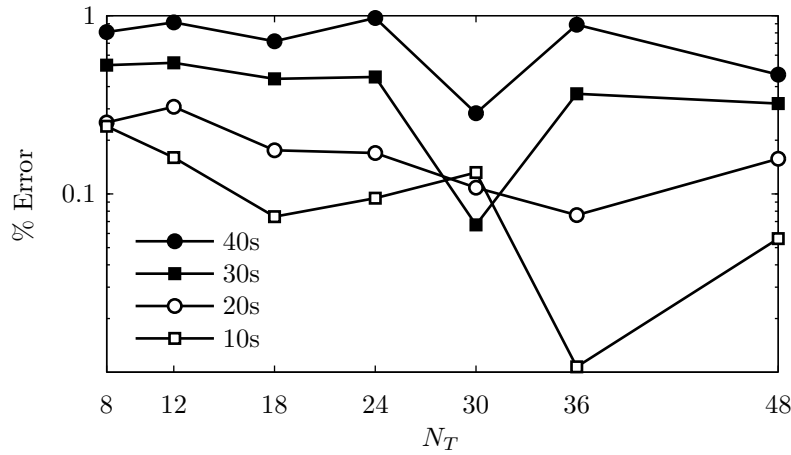
Figure 3-64: A 20s timestep results in errors of less than 0.3% for predicting total constellation performance

model using the J_2 propagator. The satellite initially starts in GOM, executes the first Hohmann transfer, then sits in the drift orbit before executing the second Hohmann transfer into ROM. The discontinuities in the range error correspond to the two Hohmann transfers. Overall this error, which is largely in-track, remains quite small over the 14 day ROM duration. Errors are on the order of 10-20km in-track, corresponding to a 2-3s shift in pass time, which is much smaller than the simulation timestep and does not introduce further error.
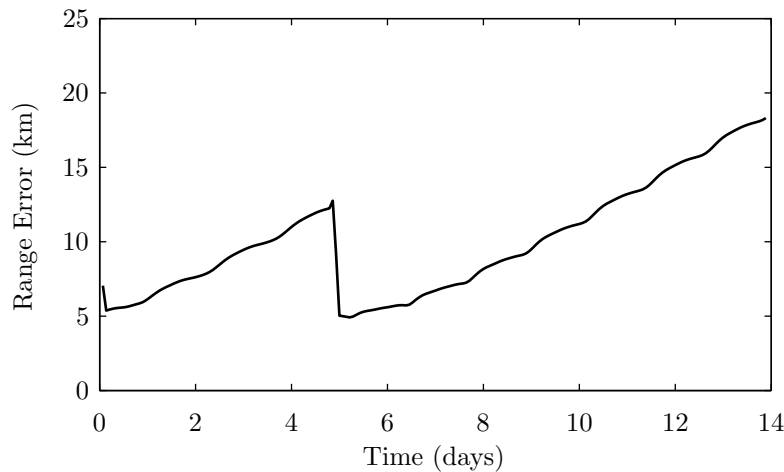
Figure 3-65: The total satellite position error between STK and MATLAB after 14 days of propagation is less than 20km

151

Additionally, the coverage predicted by the simulation model and the STK validation model were compared for a single regional response for a static and a reconfigurable constellation, both with 12 satellites. Figure 3-66 shows the GSD and access times for the static (top) and reconfigurable (bottom) constellations with the STK validation model plotted as circles and the simulation model plotted as crosses. We see very close agreement between the two models, which again demonstrates that the simulation model correctly calculates targeting, reconfiguration maneuvers and coverage (including GSD). The only observed difference between the models is that the STK validation model, since it uses a much smaller timestep than the MATLAB coverage model, picks up a few additional passes at high grazing angle. We also see the clear advantage for reconfigurable systems in that they ensure nadir passes which provides the best achievable GSD.
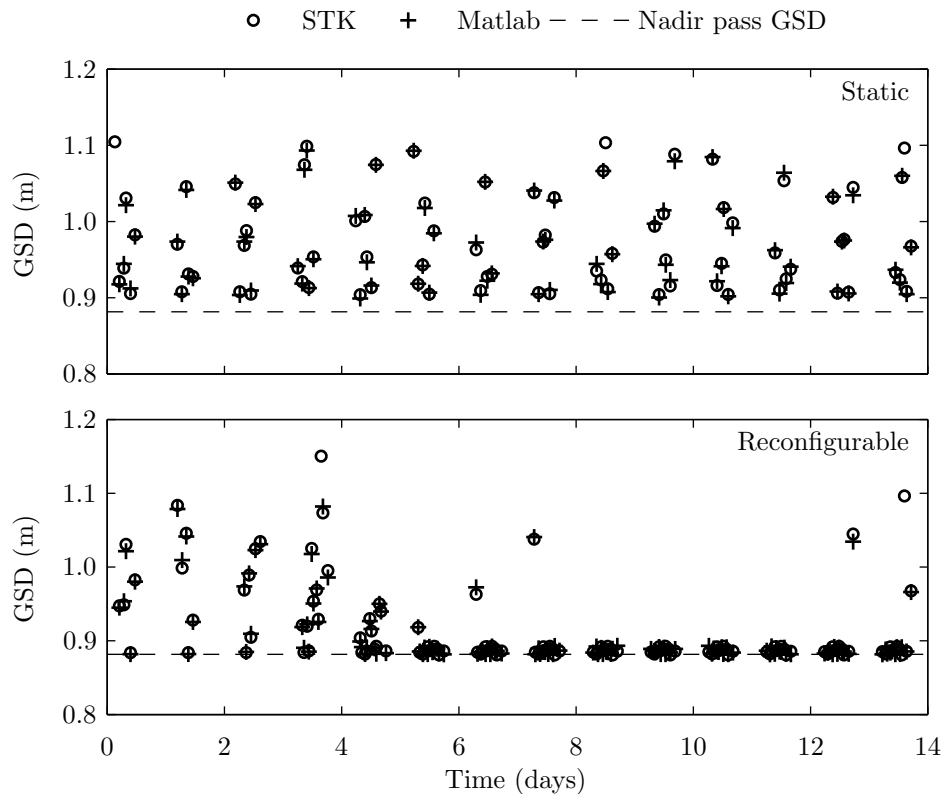
Figure 3-66: The MATLAB simulation model and STK validation model predict nearly identical ROM coverage

The modeling error was also quantified for a fixed, 8-satellite constellation design, in a

Monte Carlo simulation comprised of 65 different target decks. Figure 3-67 shows the modeling error as a function of model timestep for three model outputs. Remaining propellant is the average difference in the propellant remaining for each of the 8 satellites at the end of each event response. Event utilities is the average difference in the performance for each regional event, while total performance is the difference in the average performance over each event. The boxes show the interquartile range with the median value plotted as the horizontal line. The mean is plotted as a white filled circle while the bars show the 20th and 80th percentile values and the outliers are plotted as black dots. We see that the remaining propellant error is very low showing that the propulsive aspect of the reconfiguration maneuver is modeled accurately. For a 20s simulation timestep the individual event performance median error is 0.23% with an interquartile range of 0.15% to 0.38% and the total performance median error is 0.23% with an interquartile range of 0.14% to 0.36%.
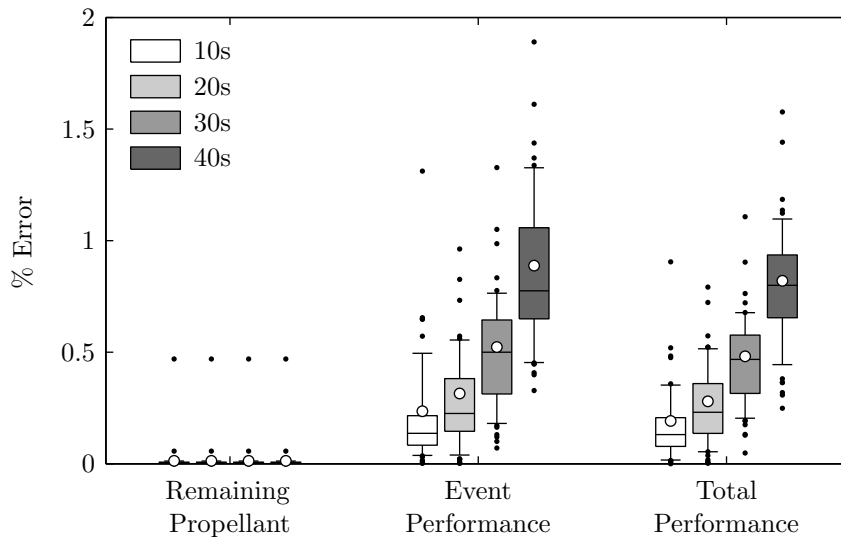
Figure 3-67: Model error as a function of timestep over 65 random target decks

The modeling error was also quantified over a wide range of constellation designs in the design space. 88 designs were randomly sampled from the design space. Figure 3-68 shows the modeling error as a function of timestep for these 88 designs. Here we see that the modeling errors are higher that those reported in Figure 3-67, but are generally less than 1% using a 20s timestep. We also see that the 10s timestep does not provide significantly lower

error than the 20s timestep. Based on all of these results a 20s timestep was determined to be a good balance between run-time and modeling error for the ROM simulation and is used in the thesis for computing ROM coverage. For a 20s simulation timestep, the individual event performance median error is 0.76% with an interquartile range of 0.52% to 1.17% and the total performance median error is 0.80% with an interquartile range of 0.54% to 1.16%.
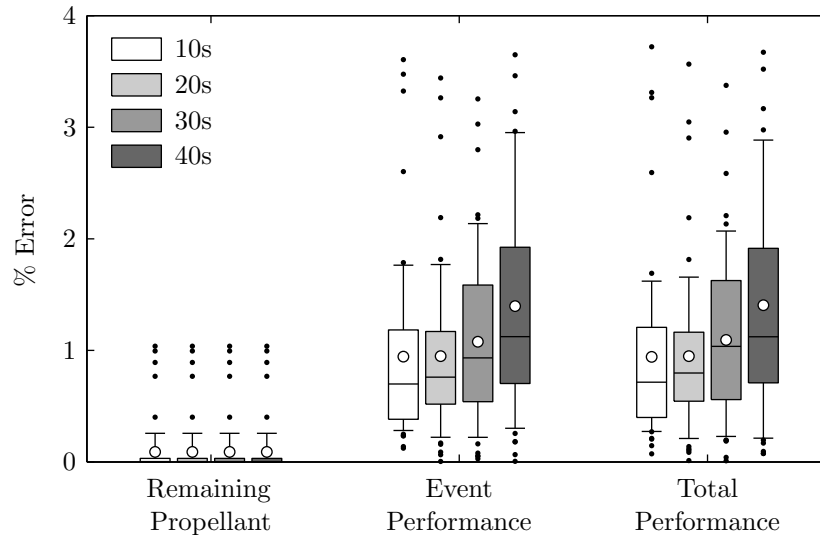
Figure 3-68: Model error as a function of timestep over 88 random designs

3.7.2 Assignment Validation

An enumeration approach was taken to validate the dynamic programming based assignment optimization process detailed in Section 3.5.4. This approach compared the output between a full factorial search and the dynamic programming optimization. This comparison was only feasible for constellation sizes up to 12 satellites due to the computational complexity of full factorial search. For comparison, the runtime for the 12 satellite full factorial search was around 2.5 hours, and the estimated runtime for a 13 satellite full factorial search is around 18 hours. Figure 3-69 shows the suite of non-dominated assignment options for four 8 satellite constellation assignments (leftmost four plots) and for two 12 satellite constellation assignments (right plots). The output from the full factorial search is plotted as open circles and the output from the dynamic programming optimization is plotted as crosses. Here we

see that the dynamic programming optimization found the globally optimal solutions for all six cases tested.
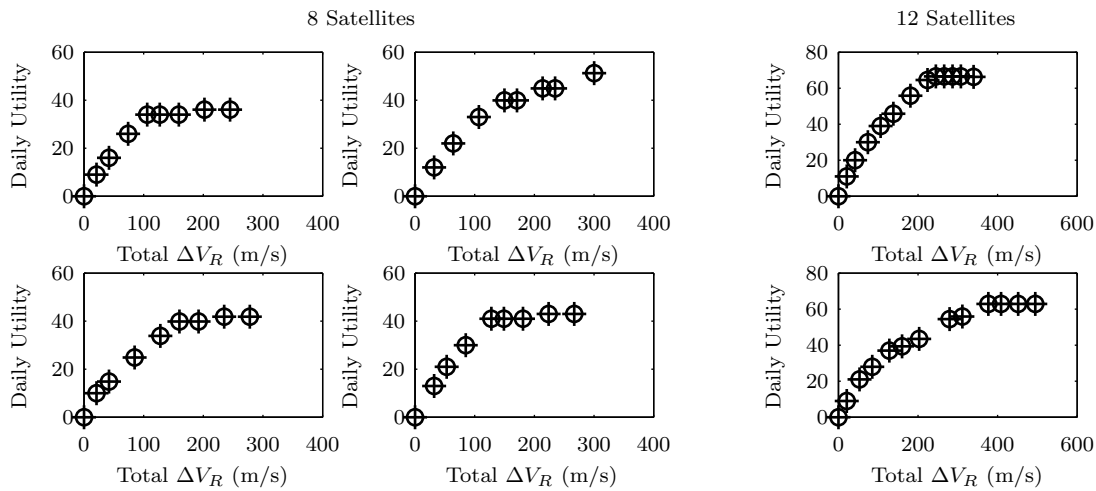
Figure 3-69: The dynamic programming optimization yields the same result as a full factorial search for four 8-satellite cases (leftmost four plots) and two 12-satellite cases (right plots)

3.7.3   Cost Model Validation

The cost model was validated by comparing its output to the estimated cost of existing optical Earth observation satellites. Figure 3-70 shows the spacecraft NRE, RE and total (NRE + RE) cost generated by the cost model plotted as lines along with estimates of the cost of six existing satellites plotted as individual data points. This estimated cost was compiled from information gathered from many sources. The RapidEye constellation is comprised of five satellites based on the SSTL-150 satellite bus. They each feature 14.5cm optics and were launched in 2008. The total system along with ground station is reported to have cost a total of $150M FY2008 [179]. Assuming a ground station cost of $20M and adjusting to FY2010 dollars, each satellite is estimated to cost $26.96M. The NigeriaSat-2 satellite is based on the SSTL-300 platform and is reported to cost 32M GBP FY2008 [26] and $55M FY2010 [5]. Converting to FY2010 USD, these estimates are then $53.23 and $53.92M which is in between the RE and NRE model estimates. This is partially explained since SSTL leveraged many existing components and designs from previous programs which would lower overall costs. The Quickbird satellite has been reported to cost $60M FY2000 [158], $100M

FY2008[68], and \$200M FY2001 [62] which when converted to FY2010 dollars is \$82.2M, \$103.7M, and \$264.2M respectively. The larger estimates are based off the insured value and possibly include additional coverage for lost revenue and launch. The lower values most likely represent the cost of the spacecraft. The GeoEye-1 satellite has an optical aperture size of 1.1m and is reported to cost \$520.57M FY2010 (\$502M FY2008) [83]. The successor spacecraft, GeoEye-2, also has a 1.1m aperture and is reported to have cost \$835M FY2010 [48] including launch on an Atlas V and insurance. Assuming 20% for insurance and \$172M FY2010 for the Atlas V launch [221], the spacecraft cost was then \$552.5M FY2010. The 1.1m aperture Worldview-2 spacecraft is reported to cost \$511.5M FY2010 (\$500M FY2009) [104].
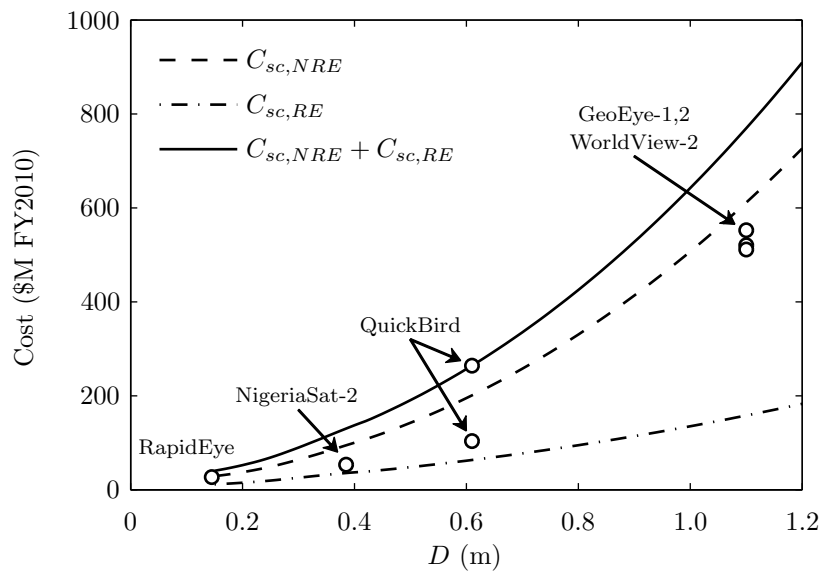
Figure 3-70: Comparison of modeled cost to estimated cost of six existing satellites

The cost model matches the general trend of the existing satellite cost quite well, however, it seems to consistently over predict the total cost by roughly 30%. One explanation for this is that the cost provided for existing satellites might not include some of the NRE cost associated with the satellite. For instance, when building the RapidEye and NigeriSat-2 spacecraft, SSTL used an existing satellite bus design and likely reused previous designs for the major subsystems from other small satellites that they previously produced, which would reduce overall cost.

156

3.8 Model Efficiency

Throughout construction of the simulation model there has been tension between adding detail and reducing model runtime. From the outset I was determined to avoid some of the simplifications made in previous research in order to capture as many interrelated effects as possible. However, since I am attempting to optimize the system over uncertainty, computational efficiency is also extremely important. Optimization over uncertainty means that the simulation model is essentially embedded within two nested loops, a Monte Carlo loop that maps uncertain operating parameter distributions to system performance distributions and an optimization loop that finds efficient designs. This nested loop approach amplifies the computational burden of the simulation model. The total optimization time is a function of the simulation model run time, the number of Monte Carlo samples, and the number of functional evaluations needed for the optimization process to converge. For example, with a $60s$ simulation model runtime, 24 Monte Carlo samples, and 20,000 functional evaluations, then the total optimization time is 340 days. Therefore, any reduction in the simulation model runtime translates to a 480,000X reduction in overall optimization time. Several approaches were taken to construct an efficient simulation model without causing a substantial loss in detail and are listed below.

1. Avoid external software calls: The simulation model was written entirely in MATLAB with no function calls to external software. While MATLAB isn't the fastest language, it was chosen to speed the coding and debugging process. While STK is very efficient at orbit propagation and coverage calculations, early testing showed that the communication overhead and problem set-up time negated any overall speed advantage with incorporating STK into the simulation model. Also, this would complicate efforts to run the simulation model in parallel due to license restrictions.

2. Take advantage of MATLAB vectorization and avoid loops: Significant focus was places at implementing a vectorized approach wherever possible since MATLAB is very efficient at solving vectorized equations. Several areas in the simulation model benefited significantly from vectorization including orbit propagation, coverage calculations, and implementing the assignment dynamic programming optimization.

3. Avoid numerical solvers: While numerical solvers are easy to implement in MATLAB, they are computationally inefficient and unnecessary in many cases. When direct solution could not be implemented, another approach was taken that leveraged MATLAB's vectorized math capability. The calculation of the minimum reconfiguration maneuver drift time was one example of this. This problem is difficult because while there are many drift times that satisfy the phasing equation (Equation 3.55), we are only interested in the smallest drift time. Additionally, the problem involves many variables that are modulo 2π. Initially, the simulation model used MATLAB's 'fminsearch' numerical solver to solve Equation 3.55. This approach correctly found the minimum phasing drift time, but 'fminsearch' had an total runtime of $44s$ for a 24 satellite constellation over 20 regional event responses. Instead, a vectorized approach was taken that combined the satellite state (Ω, M) and options for Δalt, ascending / descending RGT and a variable that searched over a modulo range into a concatenated 4D array. This 4D array then solved for the error in satisfying Equation 3.55 in one step to find the minimum drift time solution with a run time of $0.16s$, which is roughly 300 times faster than using 'fminsearch'. This is just one example of how the same problem can be solved in a different way with significant simulation speedup.

4. Use MATLAB profiler to identify bottlenecks and slow functions: The MATLAB profiler function was used extensively to identify and fix slow code. It also allowed me to identify which built in functions were inefficient. The find function is one example of an inefficient built in function and can be avoided entirely using MATLAB's logical indexing feature.

5. Clear unused variables to reduce memory usage: The last major effort was focused on managing memory use to avoid bottlenecks, by clearing unused variables. Efficient memory management has allowed continuous optimization runs lasting over two weeks without memory problems.

Figure 3-71 shows the simulation model execution time as a function of constellation size for 20 regional event responses, each with a 14 day duration. The upper plot shows a comparison of model runtime for reconfigurable and static constellations. Additionally, the amount of time that the dynamic programming assignment optimization takes for the reconfigurable constellation is indicated as a dashed line. For small constellation sizes, the

reconfigurable constellation takes only a little more time to run than the static constellation. For larger constellation sizes, the reconfigurable constellation has significantly longer execution time, with the increase driven by the additional assignment optimization. The lower plot shows the execution time breakdown for the reconfigurable constellation in terms of: assignment optimization, GOM propagation and coverage, ROM propagation and coverage, and all other routines. Here we see that the propagation and coverage calculations dominate the execution time for small constellation sizes while the assignment optimization dominates execution time for large constellation sizes.
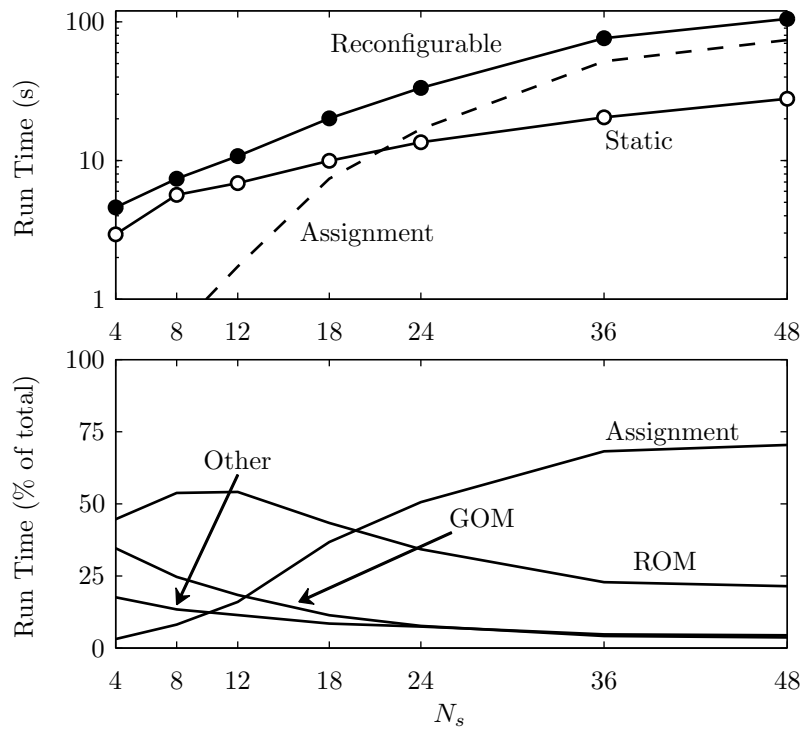
Figure 3-71: Simulation run time breakdown for reconfigurable and static constellations over 20 regional event responses

Chapter 4

Monte Carlo Sampling

This chapter introduces the Monte Carlo analysis layer of the constellation design and optimization framework, which uses Monte Carlo sampling to map input distributions of uncertain parameters to distributions of system performance for specific constellation designs. This chapter outlines the need for Monte Carlo simulation, provides details on the types of uncertain parameters considered, and describes the Monte Carlo simulation implementation.

4.1   Monte Carlo Sampling
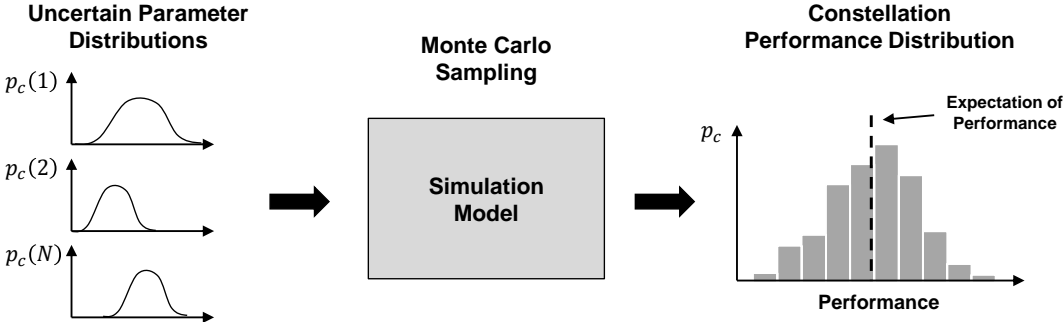
Figure 4-1: The Monte Carlo layer maps uncertain parameter distributions to a distribution of system performance

The Monte Carlo analysis process maps uncertain parameter distributions into performance distributions through Monte Carlo sampling as illustrated in Figure 4-1. A simple strategy to perform this mapping might simply use the expected values of the uncertain

parameters and assume that this will produce a good estimate of the expected system performance. However, the simulation model is non-linear, which means that the simulation model response using expected values of the uncertain parameters will not give the correct expected value of system performance due to the flaw of averages [173]. Therefore, Monte Carlo analysis is needed to perform this mapping by sampling over the entire uncertain parameter distribution. The flaw of averages written as a mathematical inequality is given in Equation 4.1.

$$f\left(E\left(x\right)\right) \neq E\left(f\left(x\right)\right) \tag{4.1}$$

A simple example illustrates the flaw of averages. Consider the function $f\left(x\right) = x^2$, with a uniform distribution of x on the interval $0 \leq x \leq 1$. The expected value of x is $E\left(x\right) = 0.5$ which yields $f\left(E\left(x\right)\right) = \left(0.5^2\right) = 0.25$. However, the actual expected value of $f\left(x\right)$ when the entire distribution is sampled is $E\left(f\left(x\right)\right) \approx 0.33$. Therefore, sampling the distribution of uncertain parameters is necessary to correctly approximate the expected performance of a non-linear system response while operating under uncertainty.

4.2 Uncertain Parameters

There are many uncertain operating parameters associated with the responsive Earth observation satellite constellation investigated in this thesis. Three important uncertainties are: *1)* the event ground locations specified by latitude (φ) and longitude (λ); *2)* the time between events; and *3)* the satellite failure rate. This thesis focuses on the event location and event rate uncertainty and leaves investigation of the satellite failure rate for future work. The rest of this section describes how the distributions for event locations and event rate were developed and then describes how the two uncertain parameters combine to create a set of target decks used by the Monte Carlo simulation.

4.2.1 Uncertain Event Location

The location of future disaster events is highly uncertain. I investigate two different distributions in this thesis: a uniform zonal probability distribution function (PDF) with event locations contained within latitude bounds, and a more complex PDF generated from natural disaster risk data. These two distributions represent different levels of knowledge for the future operating context of the system. It should be noted that the methodology developed in this thesis was designed to be flexible and can easily accommodate any event location PDF (e.g.a specific region, several regions, or another global PDF).
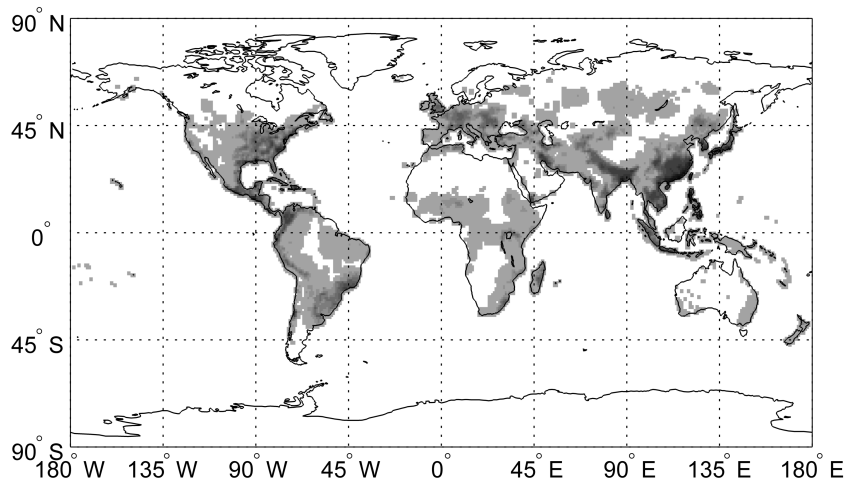
Figure 4-2: Natural disaster event location PDF with increasing probability indicated by darker shading

The uniform distribution is comprised of a uniform PDF between the latitudes of $-40°$ and $+60°$. These latitude limits were chosen to cover more than 99.6% of the world's population [79]. The natural disaster risk PDF is based on an estimated distribution of future disaster events published by The World Bank [60]. The distribution is normalized by estimated total economic loss risk for a number of disaster types including: cyclones, earthquakes, floods, and volcanoes. The input data is a 2.5-minute grid of global multi-hazard total economic loss risks with equal weighting between the four disaster types. The resulting natural disaster event location PDF is shown in Figure 4-2, where increasing event probability is indicated by darker shading. Figure 4-3 shows 1000 randomly sampled locations from

163

the uniform (left) and natural disaster (right) event location PDFs.
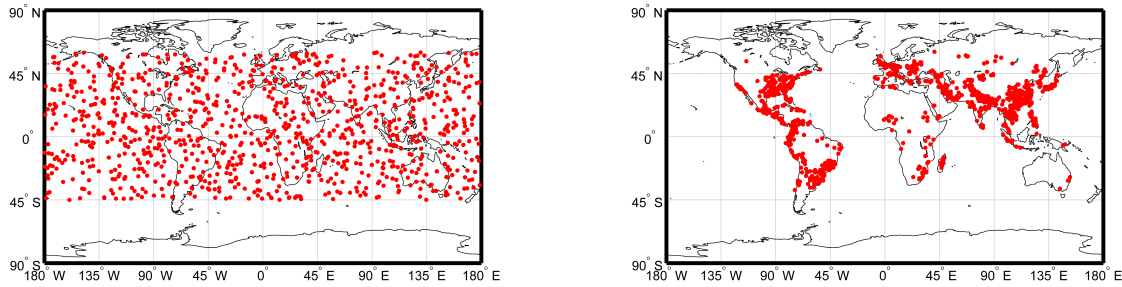
Figure 4-3: 1000 samples drawn from the uniform (left) and disaster (right) distributions

4.2.2   Uncertain Event Rate

The number and specific timing of events during the constellation lifetime is also highly uncertain. I have modeled this uncertainty of the time between disaster events as a normal distribution. Two parameters representing the mean time between events and the standard deviation of the time between events control the shape of the distribution, and these two parameters should be tailored to specific stakeholder goals and objectives. For the purposes of this thesis, I assume that the mean time between events is 3 months and the standard deviation is 1 month. These sample values should be tailored to specific mission scenarios in future work. The minimum time between events is constrained to 2.5 weeks to ensure that events do not overlap given a 14-day event duration. While overlapping events is not a focus of this thesis, it is an important topic for future research since the availability of resources must then be split between the two events. In this case, decision makers would have to consider the possibility of leaving satellites in GOM as a reserve in case a second event were to occur during the current event response. The resulting distribution of the time between events over 10^6 samples, is shown in Figure 4-4, and the small spike in the distribution for small times is caused by the 2.5 week constraint. It should be noted here that the time between events distribution coupled with the constellation lifetime together specify the total number of events that occur during the constellation lifetime. The number of events will affect the utility of a reconfigurable satellite constellation. In the extreme cases where there are few events or many events, a reconfigurable constellation will have limited

utility. Section 6.1.4 investigates how performance and cost vary with a doubling of the constellation lifetime, which is similar to doubling the event rate.
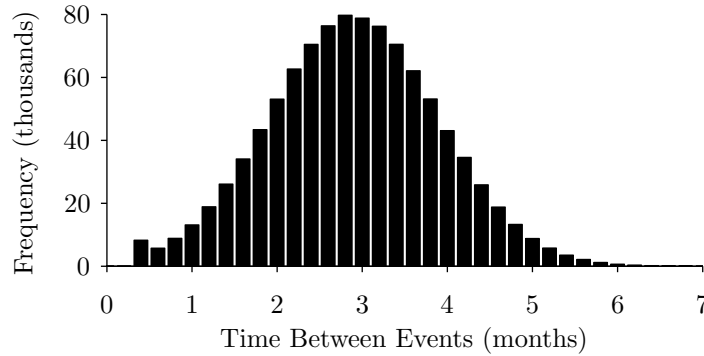
Figure 4-4: The distribution for the time between event distribution is modeled as a normal distribution with a mean of three months and a standard deviation of one month

4.2.3 Constructing Target Decks

The uncertain event locations and uncertain event rate are sampled together to construct a single target deck for each Monte Carlo simulation run. Each target deck, comprised of a list of ground locations (φ and λ) and the time of each event, represents one possible future operating context for the system. The number of events in the target deck is determined by sampling the event rate distribution to see how many events occur within the system lifetime. The process starts by randomly sampling the event rate PDF to determine the time of the first event. Next, another random sample is taken from the event rate PDF that corresponds to the elapsed time between the first and second events. Therefore, the time of the second event is the cumulative sum of the first two samples. This process continues until the cumulative sum exceeds the system lifetime (T_{life}). This target deck generation process leads to target decks of varying size. Figure 4-5 shows the distribution of target deck sizes for 5 and 10 year constellation lifetimes over 10^5 samples.

Once the list of event times is constructed and any times that exceed T_{life} are excluded, then the event location distribution is sampled for each event. Figure 4-6 shows three example target decks with differing size. Each target deck contains the latitude and longitude of the events, the time of the events, and additional parameters that specify desired coverage for

165
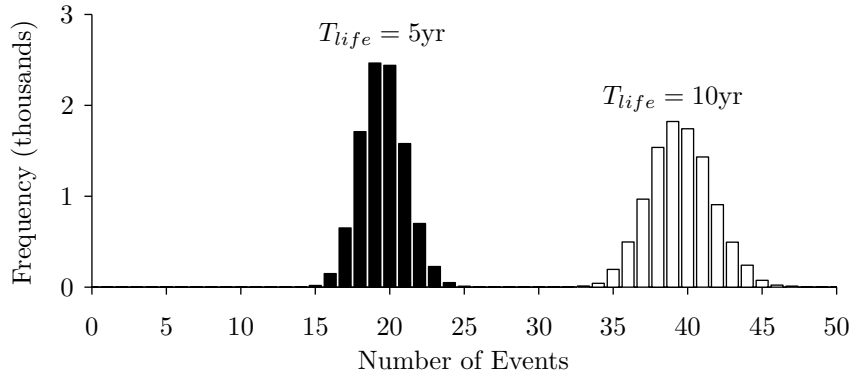
Figure 4-5: Target deck size distribution for 5yr and 10yr system lifetime

each event. These additional parameters include: the event duration, the desired persistence (T), the desired GSD (X), and the local time window constraint described by the starting time θ_{LMT}^S and ending time θ_{LMT}^E. The analysis in this thesis assumes that these additional parameters are the same for each event; however, future work could relax this assumption to include different classes of events, each with different desired observation characteristics. For example, each event could have a threshold NIIRS where imagery with worse NIIRS would provide zero utlity. The work presented in this thesis uses 14-day event durations and a time window of 6am to 6pm (in local time) for all events. Section 3.6.1 previously described examples of how future work could modify the time window to better account for solar illumination constraints. Each Monte Carlo sample uses a different target deck that represents a different operational context for the system.

4.3 Monte Carlo Implementation

The goal of Monte Carlo simulation in this thesis is to determine the distribution of system performance over the distribution of uncertain parameters previously described. This system performance distribution is then condensed into a single statistical performance measure to represent design fitness during optimization. This performance measure could be the average, median or a percentile of the performance distribution generated through Monte Carlo sampling and the choice should be based on stakeholder objectives and needs. Since they can be skewed by outliers, averages are often misleading, and, therefore are not recommended.

Target Deck 1

Event #	φ deg	λ deg	Time years	Duration days	T hr	X m	θ_{LMT}^{S} hr	θ_{LMT}^{E} hr
1	32.188	126.701	0.161	14	1	1	6	18
2	31.558	106.223	0.486	14	1	1	6	18
3	27.567	118.193	0.804	14	1	1	6	18
4	-7.404	-76.613	1.018	14	1	1	6	18
5	11.604	109.977	1.230	14	1	1	6	18
6	30.665	30.320	1.472	14	1	1	6	18
7	30.508	39.495	1.830	14	1	1	6	18
8	29.667	48.295	2.047	14	1	1	6	18
9	35.338	-93.837	2.268	14	1	1	6	18
10	8.296	105.431	2.523	14	1	1	6	18
11	-0.368	123.740	2.712	14	1	1	6	18
12	17.223	118.234	2.902	14	1	1	6	18
13	17.485	114.481	3.101	14	1	1	6	18
14	12.392	87.998	3.312	14	1	1	6	18
15	31.243	140.672	3.545	14	1	1	6	18
16	12.392	110.352	3.848	14	1	1	6	18
17	-26.569	112.437	4.174	14	1	1	6	18
18	46.575	19.143	4.328	14	1	1	6	18
19	25.152	119.110	4.593	14	1	1	6	18
20	-5.251	-83.828	4.947	14	1	1	6	18

Target Deck 2

Event #	φ deg	λ deg	Time years	$\cdots$
1	0.315	-89.583	0.326	
2	-7.981	124.866	0.604	
3	32.503	106.557	0.869	
4	38.174	39.745	1.044	
5	12.340	88.123	1.265	
6	32.030	42.206	1.452	
7	20.163	77.280	1.746	
8	26.517	132.831	2.006	
9	24.417	112.354	2.279	
10	12.340	106.766	2.534	
11	39.224	26.316	2.811	
12	-3.256	-74.110	3.097	
13	8.296	84.537	3.286	
14	27.252	116.024	3.561	
15	34.131	72.692	3.875	
16	-27.095	113.397	4.001	
17	-4.568	39.411	4.319	
18	7.509	82.660	4.744	

Target Deck 3

Event #	φ deg	λ deg	Time years	$\cdots$
1	31.453	34.782	0.343	
2	32.975	27.567	0.673	
3	1.103	-91.001	0.982	
4	34.498	-74.819	1.151	
5	13.547	109.101	1.278	
6	27.252	110.769	1.607	
7	48.203	94.504	1.825	
8	11.079	69.648	2.136	
9	5.986	-66.687	2.518	
10	0.315	-89.750	2.877	
11	48.938	6.798	3.236	
12	27.620	133.457	3.515	
13	0.630	103.054	3.618	
14	12.865	91.460	3.841	
15	27.305	-77.905	3.959	
16	-12.602	-75.403	4.105	
17	19.691	110.811	4.381	
18	12.707	115.315	4.668	
19	33.763	28.568	4.989	

Figure 4-6: Three example target decks containing event locations and desired coverage characteristics

The median measures the middle of the distribution, while a percentile value could incorporate some of the distribution spread in the overall system fitness. The analysis presented in this thesis uses median values; however, this section provides also provides details on both mean and percentile values to aid in future work.

The law of large numbers states that as the number of samples of a random process increases, the difference between true mean and sampling mean decreases [63]. This means that the Monte Carlo sampling error will decrease with increasing numbers of samples. The sampling mean and variance of the mean with n samples is given as [226]:

$$\bar{P} = \frac{1}{n} \sum_{i=1}^{n} P_i \tag{4.2}$$

$$s^2 = \frac{1}{n-1} \sum_{i=1}^{n} \left(P_i - \bar{P} \right)^2 \tag{4.3}$$

Where $\bar{P}$ is the mean performance and s is the standard deviation of the performance. The basic Monte Carlo technique, without applying variance reduction strategies, converges with

the inverse square of the number of samples n, and the standard error of the mean is:

$$s_{\bar{P}} = \frac{s}{\sqrt{n}} \qquad (4.4)$$

The one sigma (68%) confidence interval for the mean is given by $\bar{P} \pm s_{\bar{P}}$, and the error of the mean for arbitrary confidence level is:

$$s_{\bar{P}} = \frac{s}{\sqrt{n}} \Phi^{-1}\left(\frac{1+\alpha}{2}\right) \qquad (4.5)$$

Where α is the desired confidence level (e.g. $\alpha = 0.975$ for 95% confidence), and $\Phi^{-1}(\cdot)$ is the inverse normal cumulative distribution function. This method assumes a normal distribution for x; however, it also provides a good approximation for non-normal distributions [195]. Figure 4-7 shows the performance of a single constellation design for 500 Monte Carlo samples plotted as crosses, each using a different target deck. The mean performance is shown as a solid line, and the 68% and 95% confidence intervals are shown as dark and light shaded areas, respectively. Here we see that as expected the mean performance stabilizes with increasing number of samples.
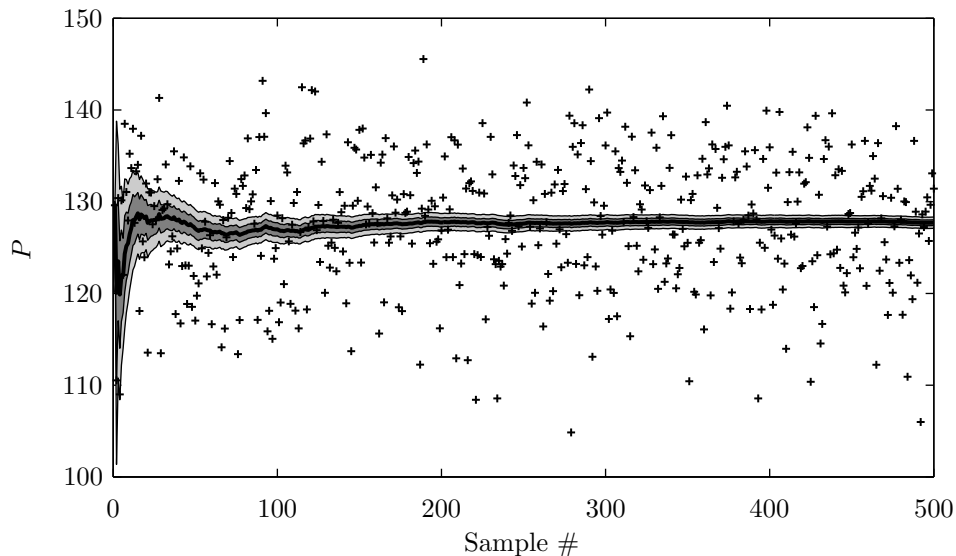
Figure 4-7: Mean performance (solid) as a function of number of samples showing 68% confidence interval (dark shaded) and 95% confidence interval (light shaded)

Quantifying the confidence interval for percentile values is more difficult. I have chosen to implement a distribution-free method based on order statistics. I do not explain this technique in detail here, but more information is provided in the following references [84, 93]. Figure 4-8 shows the median (upper curves) and 20th percentile (lower curves) values for the same 500 Monte Carlo samples as in Figure 4-7. Again, the median and 20th percentile performance is shown as a solid line, and the 68% confidence interval and 95% confidence interval are shown as a dark and light shaded areas, respectively. By comparison with Figure 4-7, we see that the confidence interval for median is larger than the confidence interval for the mean, and the confidence interval increases for percentiles further away from the median. This means that more samples will be needed to maintain the same confidence interval size for fixed confidence level as we move from mean to median and from median to percentiles away from the median.
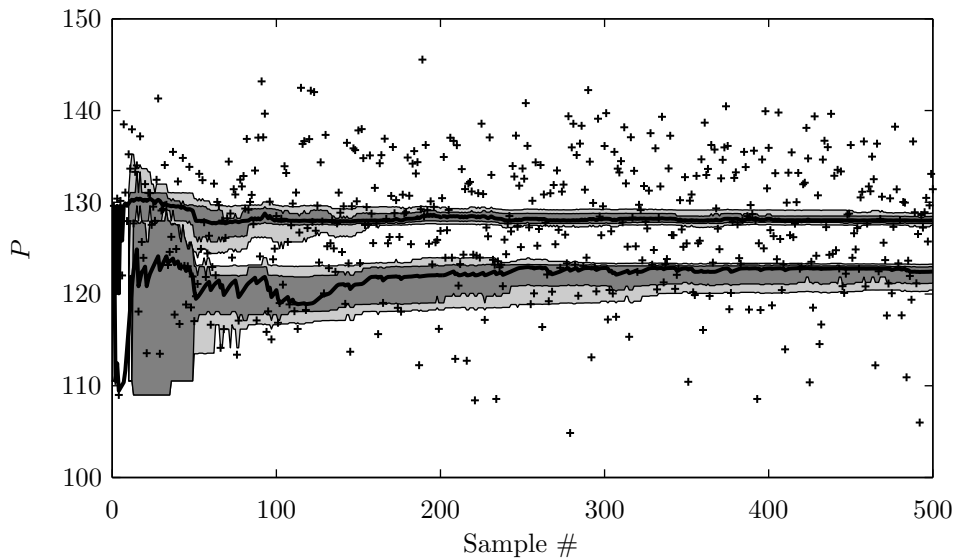
Figure 4-8: Median (upper curves) and 20th percentile (lower curves) performance as a function of number of samples showing 68% confidence interval (dark shaded) and 95% confidence interval (light shaded). Top curves are for median and lower curves are for 20th percentile

Figure 4-9 shows the 68% and 95% confidence interval size for the median as a function of number of samples averaged over 20 different constellation designs. The confidence interval size is expressed as a percent of the median value. For the results presented in this thesis,

available computational resources limited the maximum number of Monte Carlo samples to no more than 24, which gives a 68% confidence interval size of around 3% of median value. Therefore, the actual median performance value is within ±1.5% of the performance value used to determine the population fitness with 68% confidence.
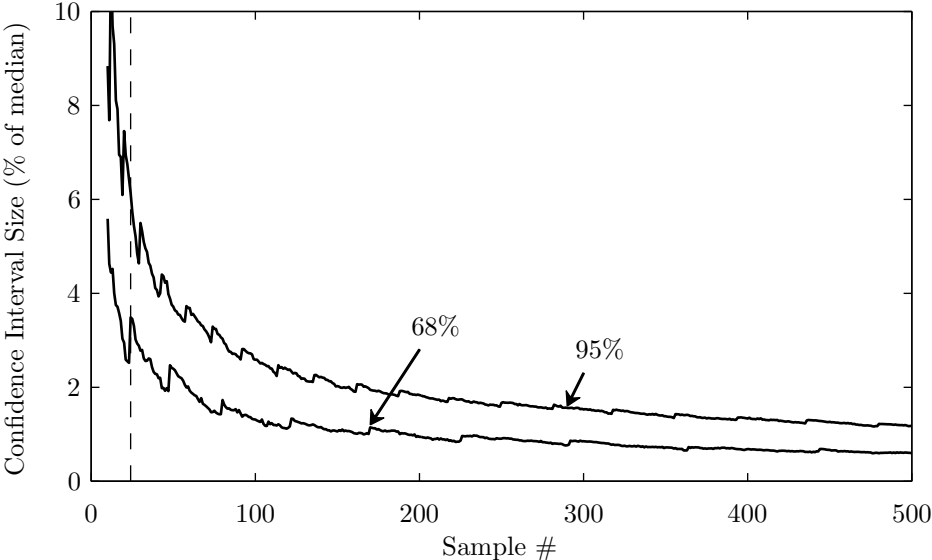
Figure 4-9: Confidence interval as a function of number of samples averaged over 20 designs

Chapter 5

Multi-Objective Optimization

Traditional optimization techniques attempt to find the single "globally optimal" design that best achieves a single objective like maximizing performance or minimizing cost. However, complex, real-world systems often contain multiple competing objectives and focusing on only one objective often leads to suboptimal designs. In these cases, multi-objective optimization attempts to find the set of non-dominated designs where improving one objective always results in worsening another. Absent further information or stakeholder preferences, one non-dominated design cannot be determined to be better than another. Therefore, the goal of multi-objective optimization is not to output the "best" design, but to give designers more information about the direct tradeoff of multiple competing objectives, hopefully leading designers to better-informed decision making. The goal of multi-objective optimization in this thesis is to find the non-dominated set of designs that simultaneously maximize median system performance over uncertain operating conditions, while minimizing total system cost. The satellite constellation optimization problem investigated in this thesis presents a difficult optimization problem for a variety of reasons, including:

1. the objective space is discontinuous and non-linear

2. the design vector contains continuous, integer, and discreet (categorical) variables

3. functional evaluations are computationally expensive

For these reasons, I chose to implement heuristic optimization as the primary optimization strategy. Heuristic optimization uses randomness and "heuristic rules" to guide the optimization process. These techniques are able to handle mixed design variable types easily

while avoiding premature convergence to local optima. However, heuristic optimization does not guarantee convergence to the global optima and is typically less efficient in terms of functional evaluations than gradient-based or gradient-free methods. When using heuristic methods, we must recognize that the output will likely not be the true Pareto front, but will instead be a set of non-dominated designs close to the true Pareto front. Therefore, in order to avoid confusion, the term non-dominated front will be used instead of Pareto front in this thesis.

This chapter is organized as follows. First an overview of multi-objective evolutionary algorithms (MOEAs) is provided in Section 5.1. Next, a new MOEA method is presented in Section 5.2 that builds on the well established ϵ-NSGA-II algorithm by incorporating several additional features that improve convergence, minimize computational effort, and provide a means to measure both progress and termination criteria. Section 5.3 then describes how the algorithm was modified to allow for large cluster parallel computing and introduces the 1024 processor grid computing resource utilized to perform optimization. The chapter concludes in Section 5.4 by formally stating the optimization problem including objectives, constraints, design variables, bounds, and parameters.

5.1 Multi-Objective Evolutionary Algorithms

Early MOEA optimization methods used weighting functions to convert problems with multiple objectives into a set of single objective problems. These single objective problems were then solved with well-established single objective optimization methods, and the resulting designs would each represent a single point on the non-dominated front. Examples of these methods are: weighted sum, adaptive weighted sum [108], and normal boundary intersection [40]. These techniques have difficulty dealing with complex Pareto front geometry, and the procedures are computationally inefficient since each optimization run yields only one non-dominated design [74]. These limitations are particularly severe with non-linear systems and computationally expensive models, both encountered in this thesis.

The development of MOEA methods over the past decade has alleviated many of the problems encountered with traditional single objective methods and have been used widely

for aerospace applications [10]. MOEA methods attempt to approximate the Pareto front by simultaneously trying to advance the non-dominated front while imposing an additional objective of spreading the non-dominated points out to capture the extent of the non-dominated front in a single run. The difference between single objective optimization using weighting between different objectives and multi-objective optimization techniques is shown in Figure 5-1. Here we see that the single objective optimization technique seeks one non-dominated point that lies on the objective vector corresponding to the specified weighting for every optimization run. The multi-objective scheme attempts to directly find the front by introducing an additional objective (in addition to the original objectives J_1 and J_2) of increasing the spacing between non-dominated points. This strategy is able to find and approximate complex Pareto front geometry and is much more computationally efficient.
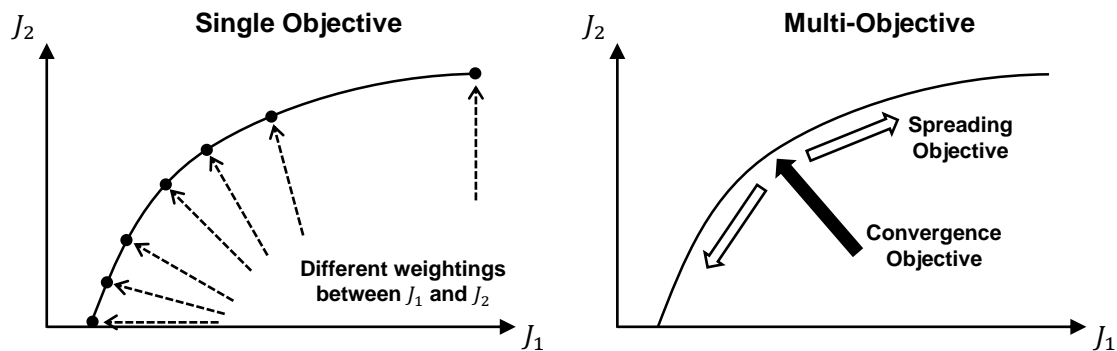
Figure 5-1: Single objective optimization with a weighted combination of objectives (left) vs. true multi-objective optimization (right)

Several notable first generational MOEA algorithms are MOGA [78] and NSGA [183]. These algorithms proved to be quite effective by combining non-domination sorting to rank the population and niching to maintain population diversity. Niching refers to the idea that population members close together must compete for resources, which artificially reduces their overall fitness, and, therefore, implicitly favors well spread out solutions. However, these algorithms tend to become trapped in local optima and required an additional sharing parameter to be assigned prior to optimization. These drawbacks led to the development of several second generation algorithms including SPEA [233], PAES [111], and NSGA-II [57]. Both SPEA and PAES incorporate a second archived population of non-dominated designs with a maximum archive size. They differ in the way the archive is managed when

the maximum size is reached. SPEA uses clustering to eliminate closely spaced solutions, while PAES uses a density measure to replace existing archive members while ensuring a good spread of solutions. The NSGA-II algorithm approached elitism differently by combining the parent and offspring populations of equal size and then using both non-domination sorting and sorting based on crowding distance to select the next population. Over the past decade, NSGA-II has proven to be effective for a diverse set of applications and, therefore, serves as the foundation for the optimization methodology employed in this thesis. A more detailed history of MOEAs can be found in the extensive literature survey papers by Coello et al. [36] and Zhou et al. [230].
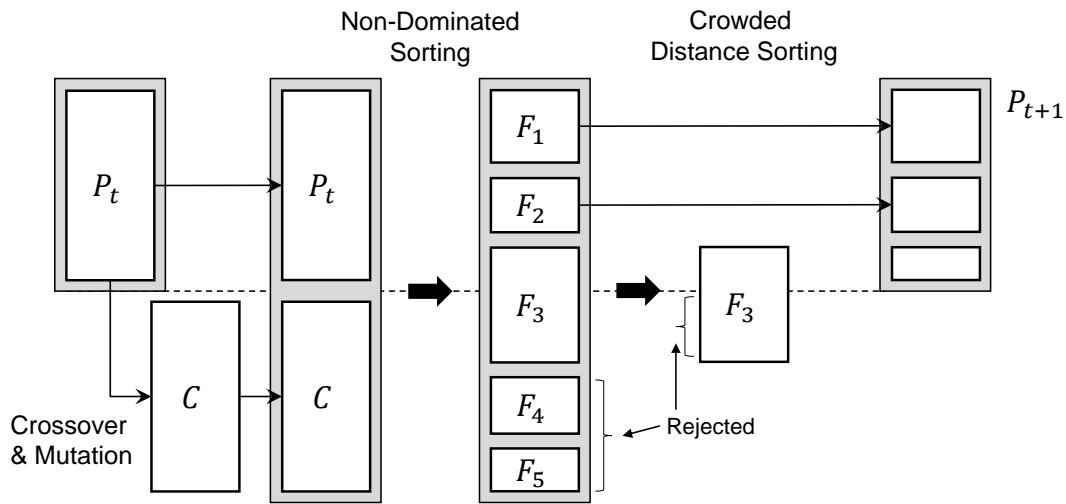
Figure 5-2: NSGA-II Algorithm Process (adapted from [57])

Figure 5-2 shows the NSGA-II optimization process for one generation. At the start of the generation, the current population P_t of size N_{pop} creates an offspring population C of size N_{pop} through selection, crossover and mutation. The combined population of size $2N_{pop}$ is then sorted into non-dominated fronts $F_1, F_2, \cdots$, etc. The process first finds the population members comprising the actual non-dominated front. These members become front F_1 and are removed from the population. The next non-dominated front is then found from the remaining population and comprises front F_2. This process is continued until all population members are assigned to a front. In the example shown in Figure 5-2 there are five fronts corresponding to five different ranks. The new generation population P_{t+1} of size N_{pop} is

then formed by adding members of the combined population, front by front, until there is no room to accommodate the entire population of the next front. When this happens, crowding distance sorting determines the members that are included in the next population based on how spaced out along the front they are. In the example shown in Figure 5-2, fronts F_1 and F_2 are selected for the next generation, sorting determines which members of front F_3 are selected or rejected, and fronts F_4 and F_5 are entirely rejected. This optimization routine repeats until convergence is observed or a specified number of generations are completed.

5.2 Modified ϵ-NSGA-II Algorithm

The second generation MOEAs (SPEA, PAES and NSGA-II) attempt to simultaneously maintain convergence and diversity. These two conflicting goals are difficult to balance and improving one will often result in the worsening of the other. The emphasis on preserving diversity leads to the problem of deterioration [122]. Deterioration occurs when a fixed population size forces the algorithm to remove non-dominated designs [91] and can eventually lead the algorithm to sacrifice convergence for diversity. Additionally, Ferringer et al. [74] discovered that the non-dominated fronts found by NSGA-II for a satellite constellation problem were sensitive to the initial random seed, indicating that the algorithm became trapped in different local optima. This led Ferringer et al. to take the best designs from 10 consecutive NSGA-II runs in order to mitigate the initial seed dependence effect and generate a good approximation of the true Pareto front. A more desirable algorithm would not deteriorate and will reliably converge close to the true Pareto front.

The search for solutions to both the deterioration and premature stagnation problems has led to a third generation of algorithms including ϵ-MOEA [122], ϵ-NSGA-II [162, 112], SPEA-2 [232], and Borg-MOEA [92]. The optimization algorithm employed in this thesis builds on ϵ-NSGA-II by adding several additional features from ϵ-MOEA and Borg-MOEA. The following sections describe these additional features (listed below) and rationale for including them.

1. ϵ-dominance archiving to avoid deterioration (adapted from ϵ-MOEA)
2. ϵ-progress to efficiently measure convergence speed (adapted from Borg-MOEA)

3. adaptive population sizing to reduce initial computational effort (adapted from ϵ-NSGA-II)

4. time continuation to escape from premature population stagnation with ϵ-progress and population size imbalance restarts (adapted from Borg-MOEA)

5. multiple recombination operators to improve convergence and handle complex design variable interactions (adapted from Borg-MOEA)

6. real time archive use to improve convergence speed (adapted from ϵ-MOEA)

ϵ-Dominance Archiving, and ϵ-Progress

Laumanns et al. [122] introduced the ϵ-dominance archiving concept to solve the deterioration problem by preserving diversity and guaranteeing convergence. ϵ-dominance allows the decision maker to specify a desired resolution for each objective, denoted by ϵ. This effectively divides the objective space into rectangular boxes with side length ϵ. In order for a solution to dominate another solution, it must occupy an ϵ-box that is better in one or more of the objectives. If two solutions occupy the same ϵ-box, only the solution closer to the lower left corner (assuming minimization) is saved, while the other is eliminated. This process directly ensures that solutions do not bunch close together on the Pareto front. The selection of ϵ values also directly corresponds to the maximum number of permitted non-dominated solutions ensuring that computational cost is commensurate with the desired resolution of the final non-dominated front. Using notation from Hadka et al. [92], a given solution with fitness vector $\boldsymbol{u}$ ϵ-box dominates another solution with fitness vector $\boldsymbol{v}$ (denoted by $\boldsymbol{u} \prec_\epsilon \boldsymbol{v}$) if:

1. $\left\lfloor \frac{\boldsymbol{u}}{\epsilon} \right\rfloor \prec \left\lfloor \frac{\boldsymbol{v}}{\epsilon} \right\rfloor$, or

2. $\left\lfloor \frac{\boldsymbol{u}}{\epsilon} \right\rfloor = \left\lfloor \frac{\boldsymbol{v}}{\epsilon} \right\rfloor$ and $\left\| \boldsymbol{u} - \epsilon \left\lfloor \frac{\boldsymbol{u}}{\epsilon} \right\rfloor \right\| < \left\| \boldsymbol{v} - \epsilon \left\lfloor \frac{\boldsymbol{v}}{\epsilon} \right\rfloor \right\|$

Where ($\lfloor \cdot \rfloor$) is the floor function. The first statement states that solution $\boldsymbol{u}$ dominates another solution $\boldsymbol{v}$ only if it resides in a different ϵ-box that is better in terms of at least one objective. The second statement takes care of the situation when the two solutions reside in the same ϵ-box. In this case, the algorithm saves the solution that is closer to the lower left corner of the box (assuming minimization) and eliminates the other.

The ϵ-Archive concept, first implemented in ϵ-MOEA [122], solves the deterioration problem by maintaining an archive of ϵ-box non-dominated solutions external to the normal population. This ensures preservation of the best solutions and mitigates deterioration. ϵ-NSGA-II uses the ϵ-Archive to seed a new population after restart while ϵ-MOEA and Borg-MOEA use the ϵ-Archive to generate one of the parents during recombination. Hadka et al. [92] introduced ϵ-Progress as an efficient method for measuring convergence using ϵ-Dominance. During the ϵ-Archive update process, a counter tracks how many solutions are accepted into the archive that reside in new ϵ-boxes (satisfies statement 1 in the ϵ-Dominance definition above). This effectively uses ϵ as a minimum threshold for measuring improvement. The number of new ϵ-boxes added to the archive is tracked for each generation. ϵ-Progress is then defined as the cumulative number of new ϵ-boxes added to the archive over the most recent five generations divided by the archive size. When the ϵ-Progress metric drops below a specified value (0.2 is used in this thesis), then the optimization algorithm is determined to have stagnated and optimization is restarted. The archive is maintained by the process outlined in Algorithm 3.

Algorithm 3 ϵ-Archive Update and ϵ-Progress

Input: new solution $\boldsymbol{x}$
1: progress $\leftarrow$ `false`
2: **for all** solutions $\boldsymbol{y}$ in archive **do**
3:     **if** $\boldsymbol{x} \prec_\epsilon \boldsymbol{y}$ **then** $\triangleright$ if $\boldsymbol{x}$ ϵ-dominates $\boldsymbol{y}$
4:         remove $\boldsymbol{y}$ from archive
5:         **if** $\left\lfloor \frac{\boldsymbol{x}}{\epsilon} \right\rfloor \neq \left\lfloor \frac{\boldsymbol{y}}{\epsilon} \right\rfloor$ **then**
6:             progress $\leftarrow$ `true` $\triangleright$ ϵ-Progress has occurred
7:         **end if**
8:     **else if** $\boldsymbol{y} \prec_\epsilon \boldsymbol{x}$ **then**
9:         **return** $\triangleright$ $\boldsymbol{x}$ is ϵ-dominated by $\boldsymbol{y}$
10:     **end if**
11: **end for**
12: add $\boldsymbol{x}$ to archive $\triangleright$ $\boldsymbol{x}$ is an ϵ-non-dominated solution

---

While ϵ-Dominance and the ϵ-Archive significantly improves diversity and convergence, stagnation can still occur. Time continuation has been proposed [86, 184] as a way of recovering from stagnation. Traditional evolutionary optimization techniques employ a single large population until termination. In the time continuation paradigm, the optimization

process is split between many 'epochs'. When the population in one epoch stagnates, a new epoch is started by seeding the new population with a diverse set of good performing members of the last epoch.

Early research on time continuation kept the population size constant between epochs; however, recent research has found that maintaining the population size proportional to archive size improved convergence for complex problems [194]. Therefore, the population size is allowed to vary from epoch to epoch based on archive size in the modified ϵ-NSGA-II scheme implemented in this thesis. A 4:1 population size to archive size ratio is used, since it has been shown to perform well in previous research [112]. Smaller populations will converge faster than larger populations, but have a higher propensity to stagnate. Adaptive population sizing allows the optimization routine to start with a small initial population that is computationally efficient at performing a coarse search of the objective space. As the archive grows, the population size also grows and the optimization transitions from coarse search to refined search close to the true Pareto front. Additionally, the population size can decrease if the archive size decreases. Eventually, when the archive size stabilizes, the population size also stabilizes and the optimization process turns into classical time continuation. The next section explains the restart procedure used to transition from one epoch to the next in the modified ϵ-NSGA-II scheme implemented in this thesis.

Restarts

This section describes the restart process employed by the modified ϵ-NSGA-II algorithm introduced in this thesis. The restart procedure is triggered when either stagnation is detected via ϵ-Progress or when the population to archive size ratio differs from 4:1 by more than 25%. When a restart is triggered, the new population size is calculated to best achieve a 4:1 ratio, and the population is regenerated through a modified injection scheme. The original injection scheme proposed for ϵ-NSGA-II [112] added all of the archive members to the new population and then the remaining slots were populated with random solutions. Instead, I use a modified injection scheme introduced by Hadka et al. [92] for Borg-MOEA where the remaining population slots are filled by mutating randomly selected archive members using uniform mutation with a probability of $1/n$, where n is the number of design variables[92].

This strategy maintains a higher level of elitism than simple random generation of new population members. Additionally, the crossover tournament size is adjusted to keep the tournament size proportional to the population size as is done in Borg-MOEA[92]. Figure 5-3 shows the overall modified ϵ-NSGA-II optimization process. The main loop is similar to the original NSGA-II algorithm with the exception of the offline archive and the restart and termination criterion. Also depicted is the restart process, which restarts the main loop with a new population with adaptive population size.
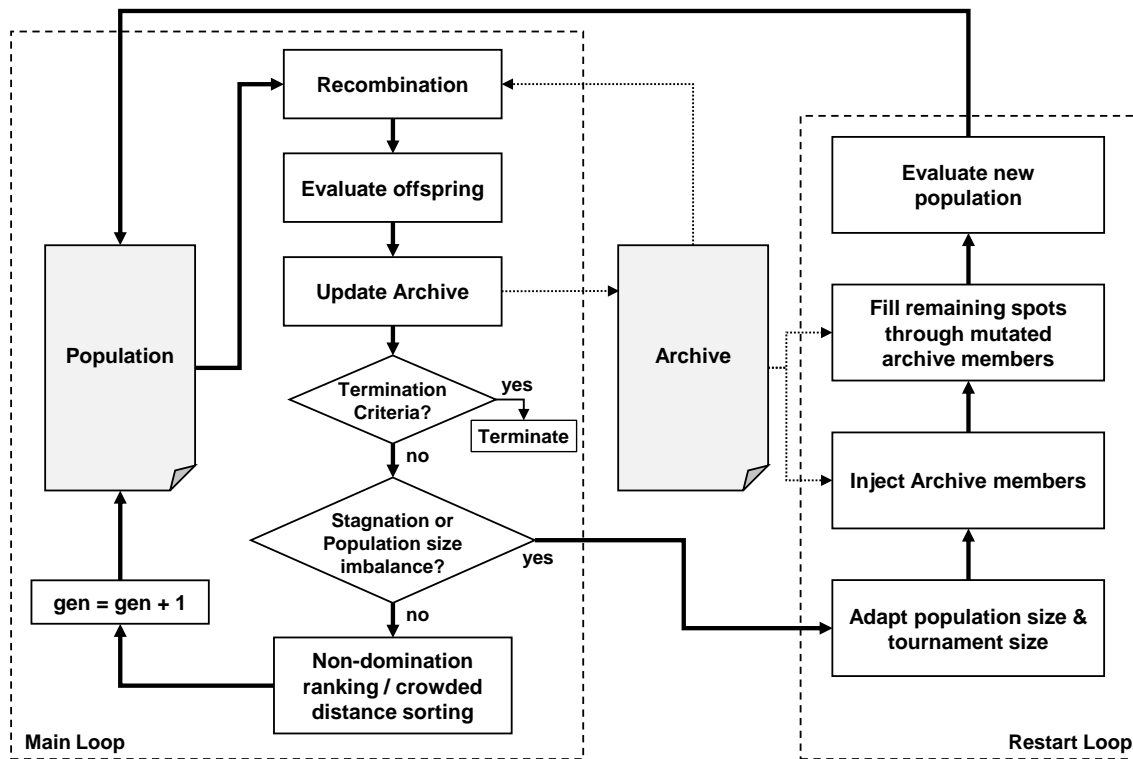
Figure 5-3: Modified ϵ-NSGA-II optimization process

Crossover and Mutation Operators

The recombination operator is the primary search mechanism for evolutionary algorithms and is crucial to the success of the optimization process. Deb et al. [53] classified crossover operators into two categories: variable-wise and vector-wise operators. Variable-wise operators treat each variable separately and, therefore, do not perform well for problems with significant linkage between design variables. Vector-wise operators use linear combinations

of the parents' entire variable vectors to create an offspring variable vector. This strategy preserves the linkage between variables and performs well for problems with coupled variables [58]. Crossover operators can also use a single parent, two parents or many parents to create offspring. Recent research has shown that multi parent operators can improve convergence for complex problems [156]. Given these factors, I decided to implement a random multi-operator approach where the optimization algorithm randomly selects an operator when producing each offspring. This approach is similar to the approach taken in Borg-MOEA, but I have chosen not to implement the adaptive scheme where the probability of selecting different operators is adjusted based on the historical success of the offspring generated by each operator. Nebro et al. [145] showed that the adaptive scheme did not provide significant advantages over the random approach for bi-objective problems. The diverse set of operators implemented in the modified ϵ-NSGA-II optimization routine are listed in Table 5.1 along with the settings used. Polynomial mutation is also applied to all offspring except those produced by uniform mutation using recommended settings from Deb et al. [52]: distribution index of 100 and a mutation probability of $1/n$ where n is the number of design variables.

Table 5.1: Set of crossover operators incorporated in the modified ϵ-NSGA-II algorithm. The settings values are provided in the nomenclature found in the references.

Operator	Settings	Ref.
Uniform mutation (UM)	$P_c = 1/n$, 1 parent	
Simulated binary crossover (SBX)	$\lambda = 20$, $P_c = 0.9$, 3 parents	[6, 55]
Unimodal normal distribution (UNDX)	$\sigma_\zeta = 0.5$, $\sigma_\eta = \frac{0.35}{\sqrt{n}}$, 3 parents	[109]
Parent-centric crossover (PCX)	$\sigma_\zeta = \sigma_\eta = 0.1$, 3 parents	[54]
Differential evolution (DE)	$CR = 0.6$, $F = 0.5$, 4 parents	[192]
Simplex crossover (SPX)	$\varepsilon = \sqrt{n+1}$, $n+1$ parents	[198]

5.2.1 Termination Criteria

The optimization routine continues until the rate of improvement drops below a specified threshold. The rate of improvement is defined as the number of archive updates per 100 functional evaluations, averaged over the last 2500 functional evaluations, as a percentage of the archive size. This improvement rate is similar to ϵ-Progress introduced previously, however,

it adds in a smoothing term to overcome spikes in convergence. The rate of improvement I, described mathematically, is:

$$I = \frac{\sum\limits_{2500} (\text{archive updates})}{2500} \times \frac{100}{N_{archive}} \times 100 \tag{5.1}$$

Where $\sum\limits_{2500} (\text{archive updates})$ is the cumulative number of archive updates made in the last 2500 functional evaluations and $N_{archive}$ is the archive size. Averaging over a large number of functional evaluations is necessary to smooth out spikes in convergence typically observed during optimization. Figure 5-4 (top) shows the cumulative number of archive updates as a function of total functional evaluations for an example optimization run. The bottom plot shows I with smoothing carried out for 500, 1000 and 2500 functional evaluations. 2500 functional evaluations was selected as a good balance between overcoming convergence spikes while still being able to terminate the algorithm as soon as the rate of improvement slows to below the specified threshold. Interpreting the meaning of I is straightforward. $I = 5$ means that the optimization algorithm has improved 5% of the archive for every 100 functional evaluations, when averaged over the last 2500 functional evaluations. The optimization process was terminated when I dropped below 2.5, which gave a common stopping condition for all of the optimization runs presented in this thesis.

5.3   Parallel Implementation and Computing Resources

I recognized early on that parallel computation was needed to overcome the long functional evaluation time encountered in the reconfigurable satellite constellation problem. Parallel processing refers to using multiple processors in parallel to share the computational burden and reduce overall processing time. The least complex parallel implementation is the master-slave approach. The master-slave approach utilizes a master processor that is responsible for all of the optimization functions (recombination, archiving, restarts...) and communicates with a set of slave processors to perform functional evaluations. For small clusters with limited resources, the master processor also performs functional evaluations. For large clusters, the master processor only handles communication and optimization routine implementation.
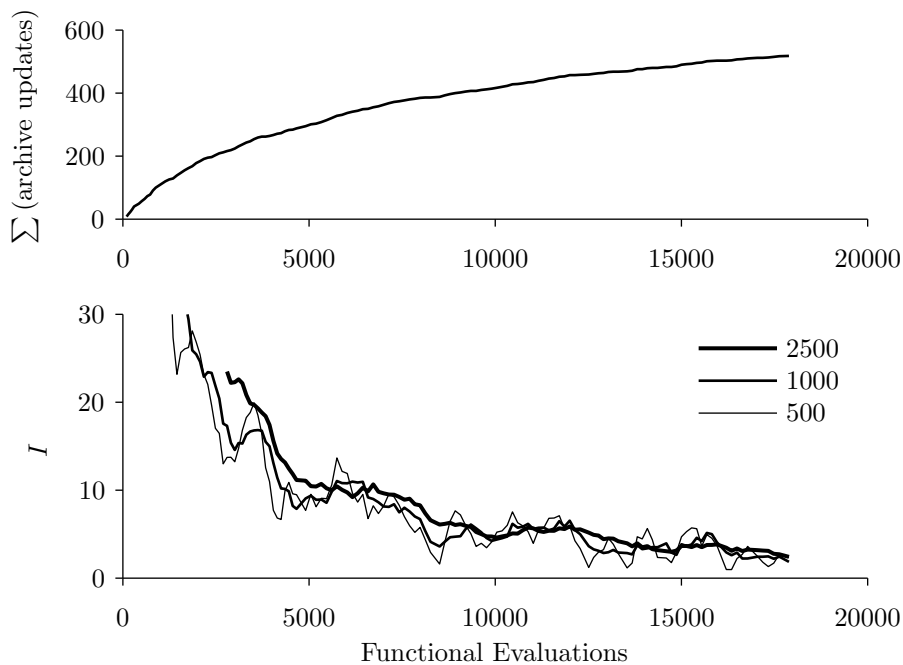
Figure 5-4: The cumulative archive updates (top) and improvement metric (bottom) with various smoothing ranges as a function of total functional evaluations during a sample optimization run.

Ideally, the overall speedup provided by the parallel processing approach should increase linearly with the available number of processors (cluster size), but this is often not the case in practice. Practical limitations reduce parallel efficiency due to increased overhead associated with master to slave communication and slave idle time. Communication time refers to the time that is required to pass messages between computer resources and generally increases with cluster size. Computational bottlenecks and generational synchronization are the primary causes of resource idle time. In parallel processing applications, assuming memory is not an issue, computational bottlenecks occur when slave processors must wait for messages from the master processor in order to execute additional tasks. This often occurs when an overloaded master processor delays sending additional instructions to slave processors. Generational synchronization idle time is caused by the fact that all current generation functional evaluations must be complete in order for the master processor to move on to the next generation, and, during this time, finished slave processors sit idle. Previous research has shown that the master-slave approach suffers significant loss in efficiency due

to generational synchronization with heterogeneous computational systems [73, 163]. This is caused by the situation where faster processors must wait for slower processors to finish execution, which effectively slows all resources down to the slowest processor. This behavior is also encountered for systems with functional evaluations of varying computational time like the simulation model considered in this thesis.

Several solutions have been proposed to reduce both communication time and idle time. Instead of the master-slave approach, the multiple-population approach executes separate optimization runs on each processor or a small cluster of processors, and periodically exchanges population information between the sub-populations. The implementation of this approach is much more complex, but it has been shown to reduce both communication time and overall processor idle time by effectively reducing cluster size [71]. Additionally, asynchronous execution has also been proposed to alleviate the generational synchronization problem. One asynchronous execution method allows the master processor to move to the next generation before all previous generation functional evaluations are complete, allowing for increased resource utilization. This technique uses a variable length offspring population and functional evaluations from the last generation that complete during the current generation are added to the current generation offspring population. This approach is implemented in the LC-ϵ-NSGA-II algorithm [163, 75, 76]. Another asynchronous execution method moves away from generational optimization to a stationary process that is inherently asynchronous and eliminates idle time caused by generational synchronization. The stationary approach is used in ϵ-MOEA [56] and Borg-MOEA [92]. In this approach, the master processor produces one offspring for each slave resource and, as the slave resources complete their functional evaluations, the master sends them more work [90].

The parallel approach that I have taken in this thesis is to use the simple master-slave model with synchronous execution. This decision was driven primarily by the large functional evaluation time difference between different constellation designs. Figure 3-71 illustrated this time difference and a 4-satellite constellation takes around 5 seconds to evaluate while a 36-satellite constellation takes around 80 seconds to evaluate. This time difference is further complicated by the fact that each design needs to be evaluated for many Monte Carlo samples. This large time difference would cause an asynchronous algorithm to preferentially

evaluate more designs in the low performance (smaller constellation size) regime. Instead, I have implemented a novel batch processing approach, which attempts to even out the computational burden sent to each slave processor during each generation. This process splits up the total computational task for each generation into a set of discrete evaluation blocks, each with similar computational burden. Figure 5-5 shows the evaluation set generation process.
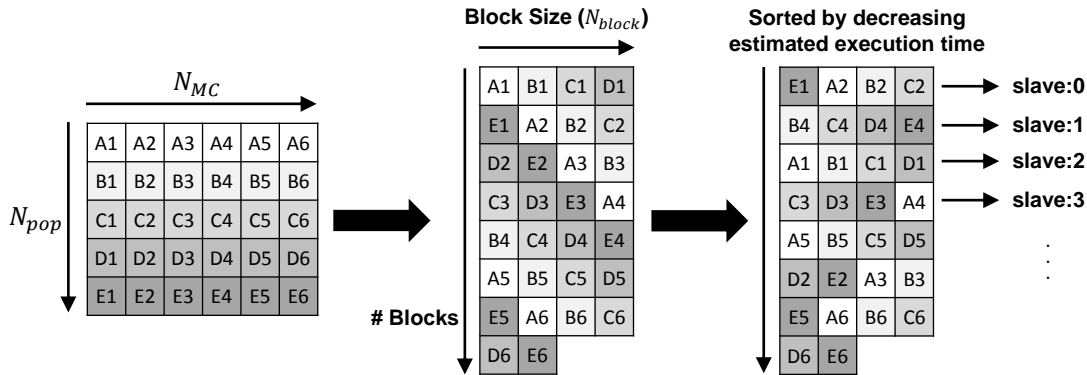
Figure 5-5: Evaluation set generation process

First, a population of offspring (labeled A to E in Figure 5-5) is generated through recombination for each generation. Each of these offspring population members will need to be evaluated for a number of Monte Carlo samples (labeled 1-6 in Figure 5-5). Therefore the total number of evaluations for each generation is given by the offspring population size times the Monte Carlo sample size ($N_{pop} \times N_{MC}$). The second step in the process breaks up the set of functional evaluations into evaluation blocks with a specified block size. This is accomplished by assigning individual functional evaluations to evaluation blocks by looping first through all Monte Carlo samples and then through all offspring population members. By looping through the Monte Carlo samples in the outer loop, the individual offspring designs are distributed amongst different evaluation blocks which helps average out block evaluation time. Next, to further reduce idle time, an expected execution time is computed for each block and then the blocks are sorted in terms of decreasing estimated execution time. The estimated block execution time is based on the number of satellites for a given design as shown in Figure 3-71. The master processor then sends out the individual blocks to slave processors for execution. The batch processing approach alleviates idle time by:

184

- reducing communication time by sending multiple functional evaluations at a time to each slave processor
- reducing execution time variation by mixing different offspring population members in each evaluation block
- reducing generational synchronization time by sending out blocks with longer estimated processing times first so that blocks with shorter processing times can later be sent to slave processors that have completed their previous evaluation block

The block size (N_{block}) is chosen based on a user supplied desired number of calls to each slave processor and is determined through the following relation:

$$N_{block} = \max\left(\left\lfloor \frac{N_{pop}\,N_{MC}}{N_{calls}\,N_{cluster}} \right\rfloor, 2\right) \tag{5.2}$$

Where $N_{cluster}$ is the number of slave processors in the computational cluster, N_{calls} is the average number of calls that the master will make to each slave processor to evaluate the entire offspring population, and $\lfloor\cdot\rfloor$ is the floor function. Increasing N_{calls} will reduce communication time, but will generally increase synchronization idle time since it is harder to even out block execution time. For this reason, N_{calls} is set to eight for reconfigurable architectures while N_{calls} is set to six for static architectures since static architectures show less variation in execution time as a function of constellation size.

The parallel master-slave implementation is depicted in Figure 5-6 from the perspective of the master processor (left) and slave processors (right). For the master, once the list of offspring is generated through recombination, the offspring and their Monte Carlo samples are divided into evaluation blocks and sorted by descending estimated computational time. The master then sends one evaluation block to each slave for evaluation using the MatlabMPI message passing implementation included in pMatlab [21]. When each slave receives an evaluation block in a message from the master, it performs the simulation model evaluations contained in the evaluation block and then sends the results back to the master. After one evaluation block is sent to each slave, the master then waits for messages from the slaves indicating that they have completed their task. When the master receives a message, the results are stored and then the master will perform one of three actions depending on the

Master Processor **Slave Processors**

| Offspring to be evaluated | → | Create set of evaluation blocks | → | Send $N_{cluster}$ blocks to slave processors |

Wait for slave processor message

Receive result from slave:x

All results received?

All blocks sent?

Unsort / rearrange results

Offspring fitness ← **Compute objective statistics** ← **Send next set to slave:x**

Wait for message from master

Receive evaluation block from master

Perform simulation model evaluations

Send result to master

Figure 5-6: Master-slave parallel function evaluation process for the master (left) and slave (right) processors

current evaluation state. If there are more evaluation blocks to be evaluated, then the next evaluation block is sent to the now idle slave. If all evaluation blocks have been sent, but not all results have been received, then the master will continue to wait for additional results from the slaves. If all results have been received, then the master processor unsorts the results and computes the bi-objective fitness (median performance and cost) for each offspring over the Monte Carlo samples. The master then returns to the MOEA algorithm process to move on to the next generation.

All optimization runs were performed on MIT Lincoln Laboratory's LLGrid [21] computing cluster running MATLAB R2014a. While I had access to 1024 processors in total, each optimization run was limited to 256 processors in order to minimize the generational synchronization efficiency loss. This efficiency loss is caused by the reduction in both the number and size of evaluation blocks which makes it harder for the algorithm to even out computational load. Limiting each optimization run to 256 processors allowed four optimization runs to be performed in parallel to utilize the full 1024 processor capability. In total, 85 optimization runs were completed over a span of three months, requiring almost

40 million simulation model calls. Without parallel computing, this effort would have taken approximately 151 years of non-stop computation by a modern computer processor (an Intel Core i5-2410M was used as reference). Post processing included performing a 96 sample Monte Carlo simulation on the final non-dominated fronts using a 16 core Dell T7200 Precision workstation equipped with two E5-2665 eight core processors running Ubuntu 12.04 and MATLAB R2014a.

5.4 Problem Formulation

The formal multi-objective problem formulation is expressed as:

$$\min \mathbf{J}\left(\mathbf{x}, \mathbf{p}\right) =$$
$$\text{subject to: } \mathbf{g}\left(\mathbf{x}, \mathbf{p}\right) \leq 0$$
$$\mathbf{h}\left(\mathbf{x}, \mathbf{p}\right) = 0$$
$$x_{i,LB} \leq x_i \leq x_{i,UB} \ \left(i = 1, \ldots, n\right)$$

Where $\mathbf{J}$ are the objectives to be minimized, $\mathbf{g}$ are inequality constraints, $\mathbf{h}$ are equality constraints, $\mathbf{p}$ are fixed parameters, and $\mathbf{x}$ is the design vector of design variables with bounds $x_{i,LB}$ and $x_{i,UB}$. The following sections will provide details on the objectives, constraints, design variables, and parameters for the satellite constellation design problem.

5.4.1 Objectives

The optimization objectives are to maximize median constellation performance $\tilde{P}$ (over all Monte carlo samples) while simultaneously minimizing total constellation cost C. The objectives vector, written as a minimization problem, is then:

$$\mathbf{J} = \begin{bmatrix} -\tilde{P} \\ C \end{bmatrix}$$

5.4.2 Constraints

Throughout development of the optimization methodology, I took great care to avoid unnecessarily constraining the optimization process. This emphasis resulted in only four inequality constraints and no equality constraints. The four inequality constraints implemented are: a minimum altitude constraint; a maximum propulsion system mass fraction constraint; a maximum GOM revisit time constraint; and a constraint on the maximum number of satellites in the constellation. The minimum altitude h_{min} was constrained to be greater than $300km$ during all phases of system life cycle including ROM, GOM, and drift orbits for both deployment and reconfiguration. The propulsion system mass fraction $\frac{M_P}{M_w}$ was constrained t be less than 42% of the total satellite wet mass. The maximum revisit time for GOM partial global coverage T_{rev} must be less than or equal to 24 hours to provide overall system utility in between event responses. Due to computational time limitations, the total number of satellites in the constellation N_s is also constrained to less than or equal to 36 or 48 satellites depending on the desired level of persistence. While cost should naturally limit the maximum constellation size, the computational time increases dramatically and becomes impractical for greater than 48 satellites. Section 6.4.1 investigates how this maximum satellite constraint affects the value of reconfigurability. When a design violates these any of these four constraints, the fitness is penalized and the optimization process naturally tries to satisfy all constraints. These constraints can be changed easily and should be aligned with stakeholder objectives. The constraints vector is then written as:

$$\mathbf{g} = \begin{bmatrix} 300\text{km} - h_{min} \\ \frac{M_{prop}}{M_w} - 0.42 \\ T_{revisit} - 24\text{hr} \\ N_T - 36 \end{bmatrix} \leq 0$$

Additionally, the design variables are constrained within specified bounds. These bounds are discussed further for the varied architectures studied in Chapter 6.

5.4.3 Design Vector

One of the central objectives of this thesis work was to perform concurrent optimization of the constellation pattern design, the satellite design, and the operational design. Therefore, there are three categories of design variables in the multidisciplinary constellation design problem studied in this thesis: constellation pattern design variables; satellite design variables; and operational design variables. The complete set of design variables is called the design vector $\mathbf{x}$ and is expressed as:

$$
\mathbf{x} = \begin{bmatrix} x_1 \\ \vdots \\ x_n \end{bmatrix}
$$

This design vector will have a varying number of design variables n depending on whether the constellation is static or flexible, and which type of constellation pattern is being considered. The work in this thesis considers five unique constellation patterns: a symmetric pattern with common inclination; a layered pattern comprised of two symmetric layers at different inclinations; an asymmetric pattern with common inclination; and two different restricted asymmetric designs with common inclination. Additionally, two other architectures are optimized for comparison with the reconfigurable approach including: a traditional polar sun-synchronous constellation and a rapid launch architecture utilizing responsive orbits [218]. Chapter 6 elaborates on the design vector setup for each of these constellation patterns, including the list of design variables and variable bounds, prior to presenting optimization results.

5.4.4 Parameters

Parameters are semi-fixed quantities that define the operational context under which the systems are optimized. Table 5.2 lists all of the parameters contained in the simulation model and provides their nominal values as well as the section in this thesis where the parameters were introduced in detail. Many of these parameters were varied as part of two sensitivity studies presented in Sections 6.1.4 and 6.5.3.

Table 5.2: Master table of parameters

Parameter	Symbol	Value	Units	Section
Pattern				
Eccentricity	e	0	-	-
Satellite				
Ballistic coefficient	BC	75	kg/m^2	3.3.2
LV correction ΔV	ΔV_{LV}	22	m/s	3.3.2
Stationkeeping ΔV	ΔV_{SK}	20	$m/s/yr$	3.3.2
Maximum deployment ΔV	$\Delta V_{dep,max}$	200	m/s	3.4.3
Deployment ΔV granularity	-	10	m/s	3.4.3
Maximum deployment time	T_{dep}	90	$days$	3.4.3
De-orbit perigee altitude	-	75	km	3.3.2
Maximum field of regard	ρ_{max}	45	deg	3.1.3
Lifetime	T_{life}	5	yr	-
Propulsion specific impulse	I_{sp}	240	s	3.3.2
Propulsion system dry mass fraction	ξ_p	0.2	-	3.3.2
Propellant penalty function gain	G_{pen}	0.1	-	3.5.4
Maximum reconfiguration altitude offset	-	80	km	3.5.4
Reconfiguration altitude granularity	-	5	km	3.5.4
Maximum reconfiguration time	-	6	$days$	3.5.4
Launch vehicle packing factor	η_{pack}	0.5	-	3.4.3
Learning rate	b	0.9	-	3.4.4
Decision model gain	G_{DM}	3	-	3.5.5
Observation				
Minimum elevation angle	ε_{min}	60	deg	3.1.3
Observation wavelength	λ_s	500	nm	3.1.3
Temporal utility power	P	1	-	3.6.1
Spatial utility scaling parameter	δ	2	-	3.6.2
Desired Persistence	T	1	hr	3.6.1
Desired GSD	X	1	m	3.6.2

Chapter 6

Results
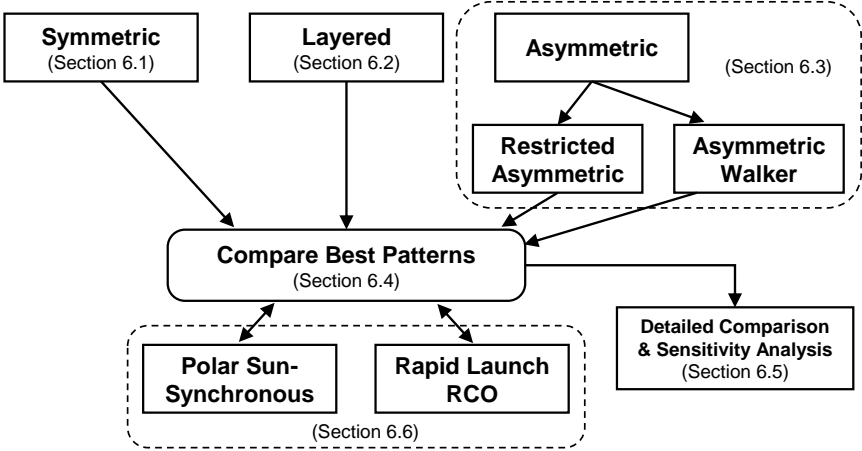
Figure 6-1: Graphical organization and mapping of the results presented in Chapter 6

This chapter presents the results from 85 optimization runs conducted using eight different constellation patterns and four architectures, comprising over 1.64 million functional evaluations and almost 40 million simulation model calls. Scenarios were chosen to investigate the effectiveness of different constellation patterns and to assess the sensitivity of the results to changes in selected parameters. Figure 6-1 graphically depicts the organization of the chapter. Section 6.1 presents optimization results for both static and reconfigurable architectures using traditional symmetric constellation patterns. Results for the nominal scenario ($1hr$ desired persistence, $1m$ spatial resolution, and event locations drawn from the natural disaster PDF) are presented first. For this scenario, optimization run-data are provided and data post processing activities are discussed. The static and reconfigurable

191

non-dominated design fronts are then directly compared and the value of reconfigurability is calculated. Following this, design details of the static and reconfigurable non-dominated designs are compared to assess trends and identify major differences between the two architectures. A sensitivity analysis is then conducted to determine how both the non-dominated designs and value of reconfigurability are affected by changes to the desired sampling resolution (temporal and spatial) and other important parameters and constraints.

Following the symmetric pattern analysis, Section 6.2 presents the optimization results for the layered pattern for scenarios 1 through 4. The layered pattern was found to significantly improve the efficiency of the static architecture but had little effect on the efficiency of the reconfigurable architecture. The asymmetric pattern results, presented in Section 6.3, show increased efficiency over symmetric designs for both architectures, but suffered from slow convergence caused by the large increase in the number of design variables. Post-optimization analysis found that this increase in efficiency was caused by the ability to position satellites closer together in Ω. Two quasi-asymmetric patterns are then introduced that allow for this clustering design freedom, but use regular spacing in Ω and M to vastly reduce the number of design variables needed to describe the pattern. The results from these two new patterns show that they significantly outperform the symmetric pattern. Section 6.4 then compares the results from all pattern designs and compiles combined non-dominated fronts for static and reconfigurable architectures. Section 6.5 looks at how system designers and stakeholders might select specific designs from the non-dominated fronts, and then compares the performance of a single reconfigurable design and an iso-cost static design. Section 6.6 then compares optimized static and reconfigurable designs to optimized designs for two other proposed architectures: the polar sun-synchronous pattern and a rapid launch architecture using repeat coverage orbits. Section 6.7 then looks at how restricting the number of satellites available to respond to a single event affects the non-dominated front for the reconfigurable architecture. The chapter concludes by summarizing all results in Section 6.8. Design variable details for selected non-dominated designs for all runs are provided in Appendix A.

6.1 Symmetric Pattern

This section presents the symmetric constellation pattern optimization results for the static and reconfigurable architectures and also presents details of the: optimization process, data post-processing and sensitivity of optimization results to changes in parameters and constraints. The section is organized as follows. Section 6.1.1 provides details for the symmetric pattern construction and design variables for each architecture. Next, Section 6.1.2 presents details of the optimization process, a comparison of the reconfigurable and static non-dominated fronts, and describes how the value of reconfigurability is computed for the nominal scenario. Section 6.1.3 then investigates the effect of increased temporal and spatial resolution requirements on the non-dominated designs and value of reconfigurability. Section 6.1.4 further investigates how varying several other parameters affects the value of reconfigurability.

6.1.1 Symmetric Pattern Design

A single symmetric constellation is comprised of satellites in circular orbits with common a and i that are divided into N_p equally spaced orbit planes, each containing N_{sp} satellites. This gives a total number of satellites in the constellation as $N_T = N_p N_{sp}$. Additionally, the satellites in each plane are spaced equally in M, and the difference in M for satellites in adjacent orbit planes is controlled by a phasing parameter F. The Walker Delta Pattern is one method of constructing a symmetric constellation and is based on the pattern unit, $PU = 2\pi/(N_T)$ [214, 221]. Using the pattern unit the orbit planes are then spaced in Ω by $N_{sp} \times PU$ increments and the satellites within each orbit plane are spaced in M by $N_p \times PU$ increments. Satellites in adjacent orbit planes are shifted in M by $F \times PU$, where $F = 0, \cdots, (N_p - 1)$ is the phasing parameter. The pattern design process starts off by determining the orbital state of a 'key satellite' (Ω_{key} and M_{key}). The initial orbital states

193

of the remaining satellites are then given as:

$$\Omega_{kl} = \frac{2\pi k}{N_p} + \Omega_{key} \tag{6.1}$$

$$M_{kl} = \frac{2\pi l}{N_{sp}} + \frac{2\pi k F}{N_p N_{sp}} + M_{key} \tag{6.2}$$

Where $k = 0, \cdots, (N_p - 1)$ and $l = 0, \cdots, (N_{sp} - 1)$. Figure 6-2 shows the effect of F on a 9 satellite constellation with $N_p = 3$, $N_{sp} = 3$, $\Omega_{key} = 0°$, and $M_{key} = 0°$. In this case the pattern unit $PU = 360°/9 = 40°$. We see that the three orbital planes are separated in Ω by $N_{sp} \times PU = 120°$ and the three satellites in each orbital plane are separated in Ω by $N_p \times PU = 120°$. For $F = 0$ (top left), the satellites in adjacent planes have the same M. For $F = 1$, satellites in adjacent planes are shifted in M by one PU. When $F = N_p = 3$ the pattern repeats since F is on the interval 0 to $N_p - 1$. The initial constellation orbital state for the symmetric pattern is then given as the orbital elements for each satellite, $X_i = (a, e, i, \Omega_i, \omega, M_i)$. The initial state of the whole 9 satellite constellation Φ is then given as:

$$\Phi = \begin{vmatrix} X_1 \\ X_2 \\ \vdots \\ X_{N_T} \end{vmatrix} = \begin{vmatrix} a & 0 & i & \Omega_1 & 0 & M_1 \\ a & 0 & i & \Omega_2 & 0 & M_2 \\ \vdots & \vdots & \vdots & \vdots & \vdots & \vdots \\ a & 0 & i & \Omega_{N_T} & 0 & M_{N_T} \end{vmatrix}$$

The complete set of design variables for the symmetric pattern is shown in Table 6.1 for both the reconfigurable and static architectures. Starting first with the reconfigurable architecture (subtable a), there are nine total design variables. Design variables x_1 to x_6 define the constellation pattern; design variables x_7 and x_8 define the satellite design; and design variable x_9 defines the operational decision maker preferences as explained in Section 3.5.5. There are three types of variables in this problem including continuous (cont.), integer (int.), and categorical (cat.). Table 6.1 shows that for the reconfigurable architecture, there are five continuous, three integer and one categorical design variables. Also shown are the bounds of the design variables used in the optimization process. The static architecture design vector differs from the reconfigurable architecture design vector in two ways. First, the N_o/N_d and Δalt design variables are collapsed into a single design variable for the
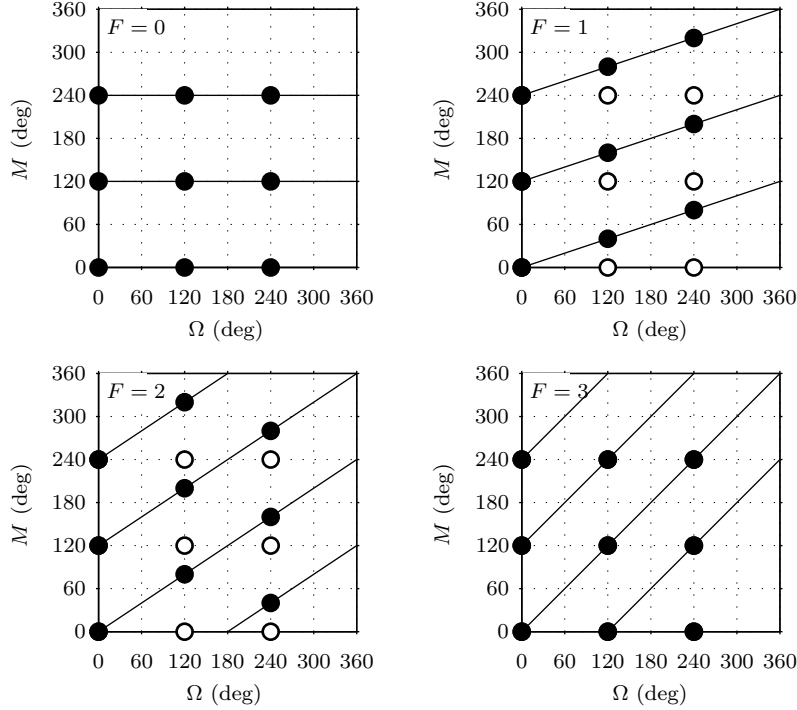
Figure 6-2: The Walker phasing parameter F controls the M spacing of satellites in adjacent orbit planes. For reference, the open circles show the $F = 0$ case

GOM altitude h_{GOM}. Second, the ΔV_{recon} and α_0 design variables are eliminated since the satellites will not be reconfigured. While the design vector could have been left the the same for the static architecture by allowing the combination of N_o/N_d and Δalt to specify h_{GOM} and setting ΔV_{recon} and α_0 to zero, reducing the design space improved optimization convergence for the static architecture.

6.1.2 Symmetric Pattern Scenario 1 Results

Various scenarios were considered in order to investigate how changing parameters and constraints would affect the cost effectiveness of static and reconfigurable architectures and the value of reconfigurability. Scenario 1 is the nominal scenario considered in this thesis. An ideal design for scenario 1 would provide persistent coverage with $1hr$ temporal resolution and $1m$ spatial resolution over a 5 year lifetime for event locations drawn from the natural disaster PDF. Table 5.2 lists the rest of the parameter values used in scenario 1.

Table 6.1: Symmetric constellation pattern design variables for (a) reconfigurable and (b) static architectures

(a) Reconfigurable Architecture

#	Variable Name	Symbol	Type	Bounds	
x_1	RGT type	N_o/N_d	cat.	$[\frac{31}{2}, \frac{15}{1}, \frac{29}{2}, \frac{14}{1}, \frac{27}{2}, \frac{13}{1}]$	
x_2	GOM altitude offset	Δalt	cont.	-50 to 50 km	
x_3	Number of orbit planes	N_p	int.	1 to 36 (or 48)	Pattern
x_4	Number of satellites per plane	N_{sp}	int.	1 to 24	
x_5	Inclination	i	cont.	$50°$ to $130°$	
x_6	Phasing parameter	F	int.	0 to $N_p - 1$	
x_7	Aperture size	D	cont.	0.1 to 1.2 m	Satellite
x_8	ReCon ΔV	ΔV_{recon}	cont.	0 to 1000 m/s	
x_9	Decision model weight	α_0	cont.	0 to 1	Operations

(b) Static Architecture

#	Variable Name	Symbol	Type	Bounds	
x_1	GOM altitude	h_{GOM}	cont.	300 to 1000 km	
x_2	Number of orbit planes	N_p	int.	1 to 36 (or 48)	
x_3	Number of satellites per plane	N_{sp}	int.	1 to 24	Pattern
x_4	Inclination	i	cont.	$50°$ to $130°$	
x_5	Phasing parameter	F	int.	0 to $N_p - 1$	
x_6	Aperture size	D	cont.	0.1 to 1.2 m	Satellite

Optimization Run Data & Convergence

Various data was collected to measure optimization progress and this run data for scenario 1 is shown in Figure 6-3 for the reconfigurable (left) and static (right) architectures. The top plots show the population to archive size ratio and ϵ-Progress as a function of the number of completed functional evaluations. These two metrics determine when to trigger the population restart procedure in the optimization algorithm, as was previously explained in Section 5.2. A restart is triggered when the population to archive size ratio deviates from 4 by more than 25% or when ϵ-Progress drops below 0.2. These trigger thresholds are depicted in the figure by horizontal dashed lines and the triggering events are depicted by filled in data markers. The middle set of plots show the population size and archive size as a function of the number of completed functional evaluations. Here we see that initially the population size grows with growing archive size. This growth period then transitions to a period where the archive size and, therefore, the population size is nearly constant. For all

| | (a) Reconfigurable | (b) Static |
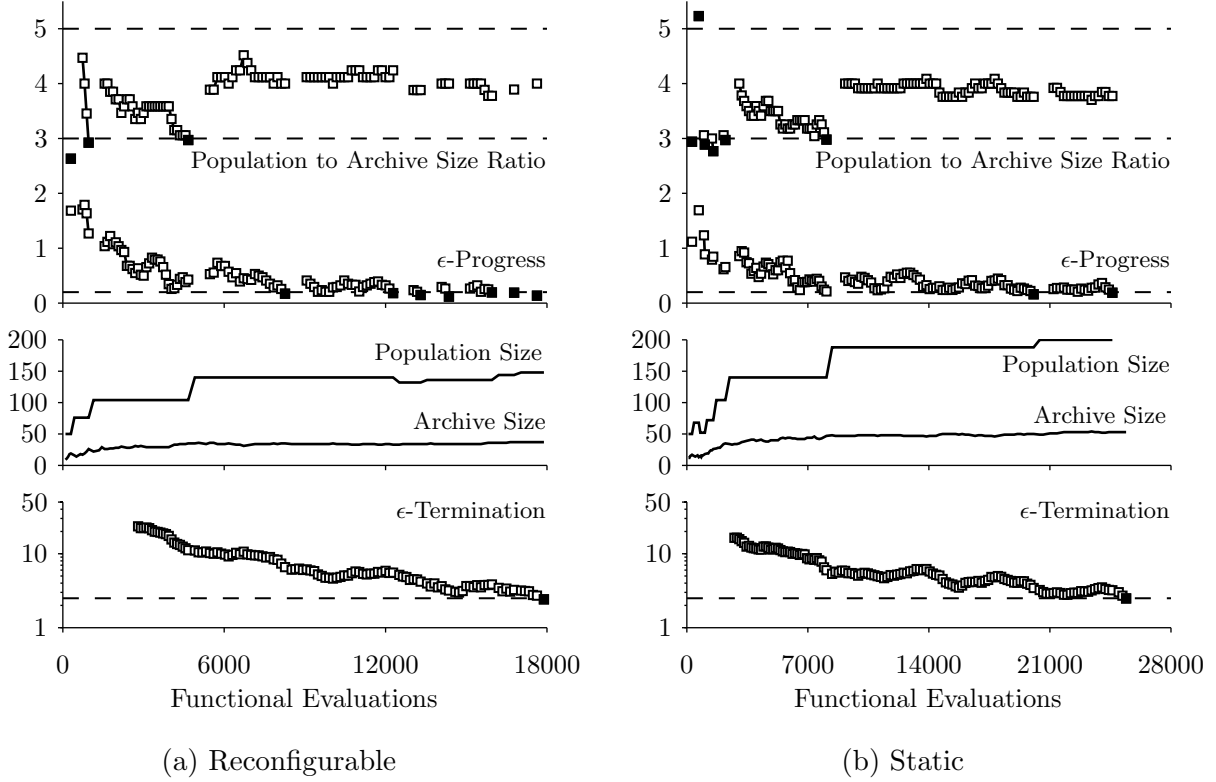
Figure 6-3: Symmetric pattern scenario 1 optimization run data and convergence

optimization runs in this thesis, this generally occurred when the archive size was around 30 to 50 and the population size was around 120-200. The lower plots show ϵ-Termination as a function of the number of completed functional evaluations. An ϵ-Termination value of 2.5 was used as the termination criterion for all optimization runs in this thesis. For scenario 1, the reconfigurable architecture optimization terminated after 17,887 functional evaluations (427,288 simulation model calls with a Monte Carlo sampling size of 24), while the static architecture optimization terminated after 25,405 functional evaluations (609,720 simulation model calls).

Table 6.2 shows run statistics for the 77 optimization runs presented in this thesis. The static and reconfigurable architectures both took, on average, around 20,000 functional evaluation for optimization termination, and the static designs had an a mean simulation model execution time of $121s$ versus $126s$ for reconfigurable designs. In Section 3.8 we saw that the simulation model runtime for reconfigurable designs is much longer; however, efficient

197

reconfigurable designs feature fewer satellites than static designs and the overall mean model runtime is similar. The SSO and rapid launch architectures took fewer functional evaluations to converge. The estimated computational time for a single modern processor and 256 modern processors are also listed in Table 6.2. In total, over 151 years worth of calculations (on a single Intel Core i5-2410M processor) were completed over the course of three months using a 1024 processor computing cluster broken up into four, simultaneous, 256 processor optimization runs.

Table 6.2: Optimization run statistics for the 85 optimization runs presented in this thesis

			Computation Time		
	# Runs	Mean Functional Evaluations	Mean Sim s	1 core[†] years	256 cores* days
Static	37	19,540	120.8	57.7	110.1
Reconfigurable	40	20,374	126.3	72.3	148.9
SSO	4	15,079	125.8	5.8	11.0
Rapid	4	9,493	18.4	0.5	1.0
Total	85	–	–	151.2	287.3

[†] Intel Core i5-2410M

* 1.5 times faster than Intel Core i5-2410M, 50% parallel efficiency

Non-dominated Fronts & Computing the Value of Reconfigurability

Several post-processing steps prepared the data for analysis and comparison following optimization termination. First, a non-domination sort procedure was used to find the set of non-dominated designs encountered over all functional evaluations performed during optimization. For scenario 1 there were 245 unique non-dominated designs for the reconfigurable architecture and 263 unique non-dominated designs for the static architecture. These unique non-dominated designs are plotted in Figure 6-4 as solid markers for the reconfigurable (colored black) and static (colored gray) architectures. Roughly 40 to 50 designs were selected through ϵ-domination sorting for further evaluation with a 96 sample Monte Carlo simulation. This additional sampling solved two problems. First, due to computational time limitations, the Monte Carlo sampling size used in the optimization routine was limited to 24 samples giving a 68% confidence interval size for the median performance of around 3%.

198
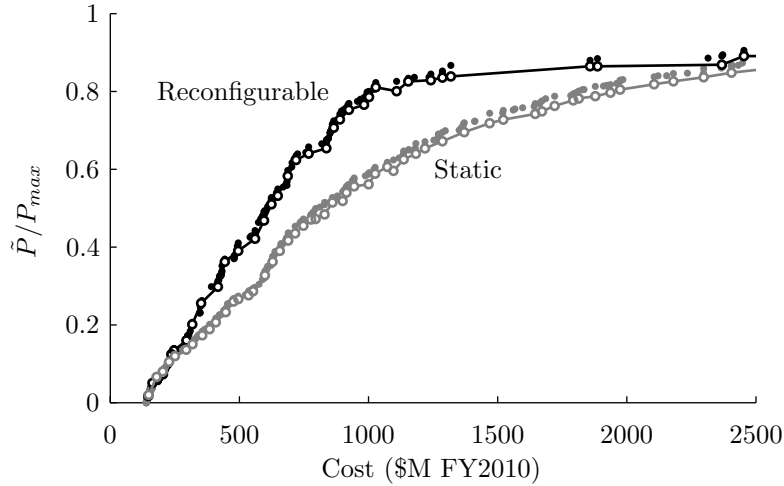
Figure 6-4: The reconfigurable non-dominated front (colored black) completely dominates the static non-dominated front (colored gray) in terms of maximizing performance while minimizing cost

Increasing the sample size to 96 halved this to around 1.5%. Second, since the optimization process was evaluating designs over several independent Monte Carlo simulations, it is prone to identify 'favorable' Monte Carlo sample draws. For example, if we perform two 24 sample Monte Carlo simulation runs with the same design, the optimization process will select the higher of the two median performance values and, as the optimization process proceeds, this estimate of the median will drift further away from the true median value. The median performance over 96 Monte Carlo samples is shown as a line with open circle markers in Figure 6-4 for 37 reconfigurable designs and 53 static designs. As expected, the performance of the designs given by the optimization routine is higher due to the 'optimization' of Monte Carlo sample draws previously explained. This post-processing process with 96 Monte Carlo samples is repeated for all results presented in this thesis. Additionally, the median performance $\tilde{P}$ is normalized by the ideal performance for the scenario P_{max}, which is described in more detail in Section 3.6.2. The full design variable values for selected designs from both fronts are listed in Appendix A.

Direct comparison of the reconfigurable and static non-dominated fronts shows that reconfigurable designs completely dominate the static designs in terms of maximizing performance while minimizing cost. The value of reconfigurability (VoR) was previously defined as the reduction in total system cost, while maintaining the same performance, made possible

199

by adopting the more efficient reconfigurable architecture. VoR is determined by computing the horizontal distance between the reconfigurable and static non-dominated fronts in Figure 6-4. Additionally, a bootstrap re-sampling procedure (with replacement) is used to capture some of the effects of sampling error into the VoR calculation. 1000 bootstrap samples are generated for each non-dominated design to construct 1000 different splines representing the reconfigurable and static non-dominated fronts. VoR (the horizontal distance between the non-dominated fronts) is then calculated from these splines. Figure 6-5 shows the mean VoR (thick line) as well as the high and low 3σ VoR values (thin lines). The top plot shows VoR in terms of FY2010 dollars while the lower plot shows VoR in terms of a percentage of the static architecture cost. Here we see that VoR is between 20 to 50%, meaning that the reconfigurable architecture is 20 to 50% less expensive than a static architecture for the same performance level. Also, we see that VoR generally increases with increasing performance.
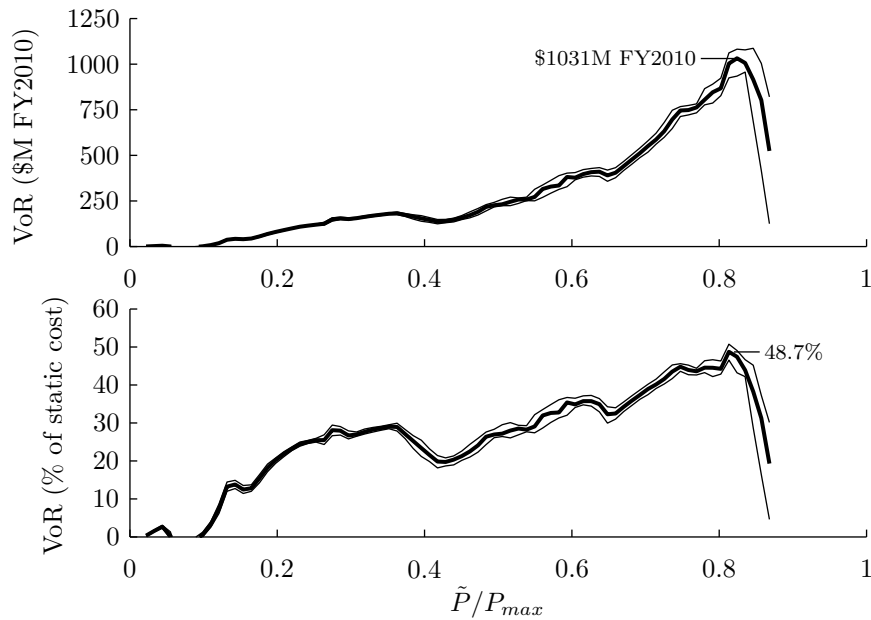
Figure 6-5: The value of reconfigurability, which is equal to how much cheaper the reconfigurable designs are when compared to iso-performance static designs, is 20-50% of the static architecture cost

Non-dominated Front Design Details

Figure 6-6 shows details of the reconfigurable (colored black) and static (colored grey) non-dominated designs as a function of normalized performance. The plotted design details include: the total number of satellites (N_T), aperture size (D), GOM altitude (h_{GOM}), inclination (i), number of orbit planes (N_p), number of satellites per orbit plane (N_{sp}), total ΔV (ΔV_T), and total number of launches to deploy the constellation. Here we see that the non-dominated designs for the two architectures are significantly different. In the low performance region ($\tilde{P}/P_{max} < 0.6$), static designs tend to feature more satellites at a lower altitude when compared to reconfigurable designs. However, despite the lower altitude, static designs feature similar aperture sizes, since static designs must have larger apertures to maintain good spatial resolution for off-nadir passes, while reconfigurable designs ensure nadir viewing. The reduction in the number of satellites for reconfigurable designs is caused by increased per-satellite utilization enabled by the ability to reconfigure. This is the fundamental cost reduction driver for reconfigurable architectures. In the higher performance region ($\tilde{P}/P_{max} > 0.6$), the static architecture runs up against the maximum satellite constraint which is set to 36 for scenario 1. Therefore, to improve performance for static designs, altitude and aperture size must increase, inflating overall system cost.

Reconfigurable designs, except for very low performance designs that feature small numbers of satellites, tend to feature prograde inclinations of around 60° and a single satellite per orbit plane. This difference is likely caused by the tension between minimizing launch cost and maximizing performance. For small numbers of total satellites, it is difficult for two satellites to share a single launch because the orbit planes are too far apart in Ω to be serviced by the differential orbital precession during the three month deployment period. Therefore, a dedicated launch for each satellite is needed, which increases launch cost. However, the time of pass for a specific event location in an RGT orbit for the reconfigurable architecture is a function of Ω only, and greater diversity in Ω leads to better persistence, as was seen in Section 3.1.2. This explains why high performance reconfigurable designs tend to feature only one satellite per orbit plane. Static designs tend to feature multiple satellites per orbit plane, fewer total orbit planes, and retrograde inclinations of around 120°. Therefore,
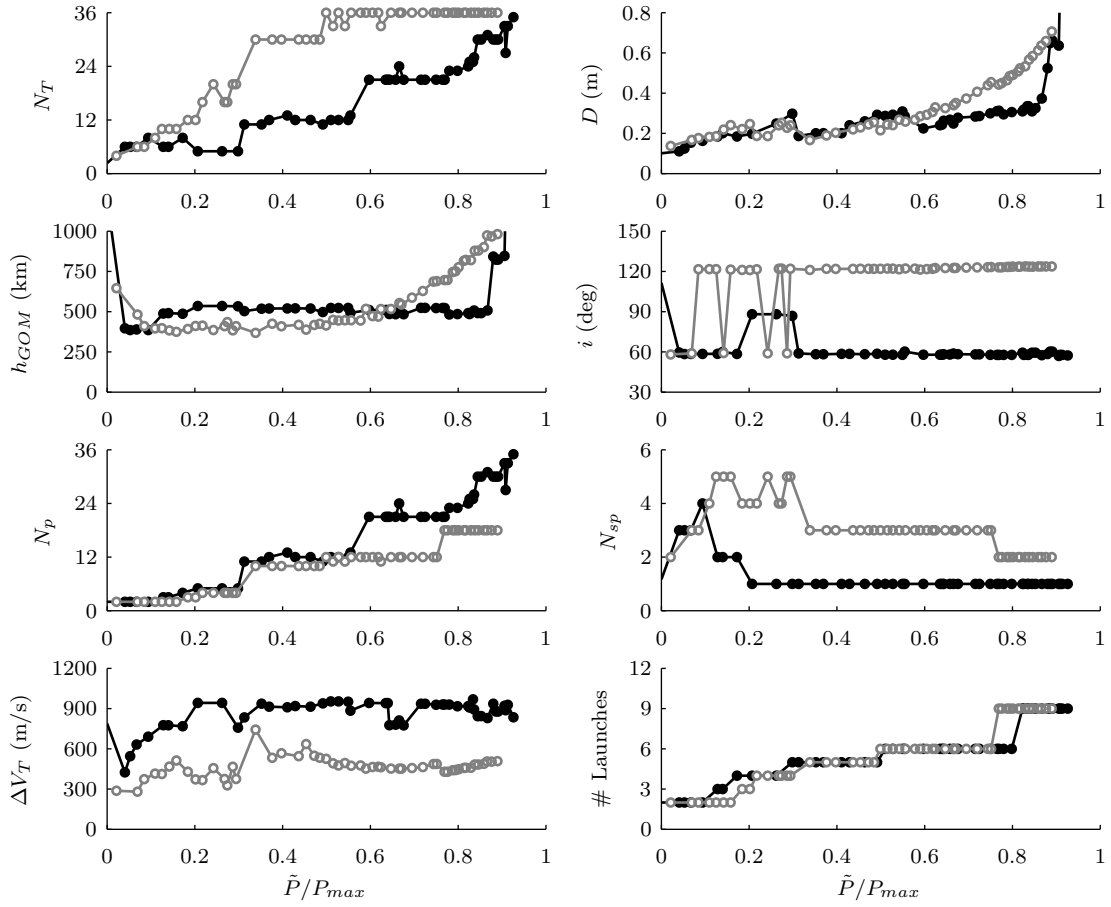
Figure 6-6: Design details for the reconfigurable (colored black) and static (colored gray) non-dominated fronts

for these static designs, the performance benefits of retrograde inclinations must outweigh the increase in launch cost to launch to higher inclinations for retrograde designs to be on the non-dominated front. There is, however, some chatter between prograde and retrograde inclinations for low performing static designs, which indicates that the performance difference between prograde and retrograde designs is small. This chatter phenomenon between prograde and retrograde inclinations in static designs was observed in many of the scenarios studied in this thesis. Additionally, the effect of inclination bounds is studied later in Section 6.1.4. Reconfigurable designs also feature nearly twice the total propulsive capability of static designs in order to support reconfiguration maneuvers. The maximum propulsion system mass fraction constraint (set to 42% which corresponds to around $980m/s$ using the

parameters specified in Section 3.3.2) is active for many non-dominated reconfigurable designs and relaxing this constraint will increase the value of reconfigurability, as we will also see in Section 6.1.4.

Performance Comparison with Traditional Metrics

The performance metric used in this thesis directly measures both temporal and spatial resolution for persistent surveillance and alleviates some of the problems encountered with traditional satellite coverage metrics. However, it is useful to see how the static and reconfigurable non-dominated designs found using the new performance metric compare in terms of the traditional metrics. Figure 6-7 shows a comparison of the static and reconfigurable non-dominated designs in terms of average and maximum revisit time, mean response time and mean GSD as a function of overall system cost. The traditional metric values plotted are the median metric value over all event responses during the system lifetime and over the 96 Monte Carlo samples. The metric value for each event response is defined as the daily value averaged over days 4 to 14 of the event response. Only counting days 4 through 14 gives the reconfigurable system time to complete the reconfiguration maneuvers and the performance during days 1 through 3 are investigated later in Figure 6-9. The desired metric values are plotted as horizontal dashed lines. Figure 6-7 shows that the reconfigurable architecture provides better average revisit time and mean response time and significantly better maximum revisit time. However, the static architecture provides better mean GSD for low-cost designs. This likely means that, for static designs, it is less costly to increase aperture size and therefore increase spatial resolution than to increase temporal resolution. Consequently, the optimization process places more emphasis on providing better mean GSD for these designs. This comparison shows that the traditional metrics tend to show the same trends as the new persistence metric introduced in this thesis.

Table 6.3 shows the details of one reconfigurable design (labeled design R) chosen close to the 'knee' in the non-dominated front. Two static designs were also chosen, one that features similar cost as design R (labeled design S1) and one that features similar performance as design R (labeled design S2). These selected designs are shown on the non-dominated fronts in Figure 6-8. The performance metrics shown here are the same as for those plotted in
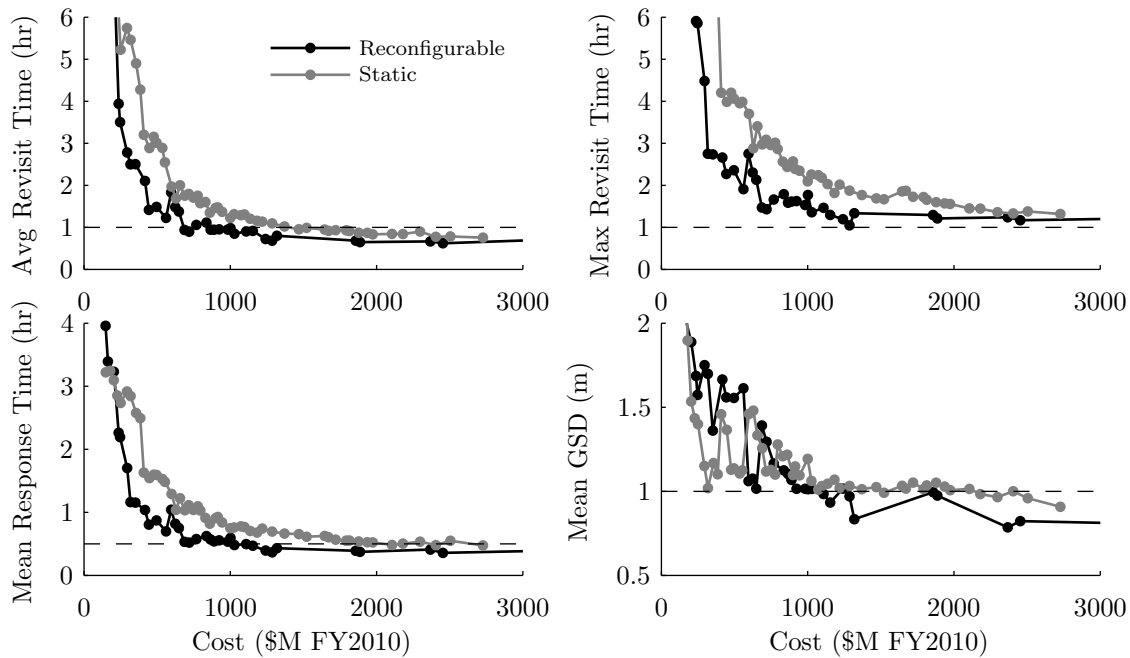
Figure 6-7: When compared with traditional figures of merit, non-dominated reconfigurable designs (colored black) generally outperform iso-cost non-dominated static designs (colored gray)

Figure 6-7 except that they are averaged over all days during the event response. Here we see that the performance for the reconfigurable design is significantly better than the performance of the iso-cost static design for all five metrics. When compared to the iso-cost static design, the reconfigurable design has a slightly larger aperture, significantly fewer total satellites, a lower GOM altitude and roughly twice the total ΔV. In this case, the increase in cost for the reconfigurable design is due to increased total ΔV, slightly increased aperture size and increased number of orbit planes and is offset by the increase in cost for the static design due to significantly more satellites at a higher inclination. While the performance between the reconfigurable design and iso-performance static design is nearly the same, the static design costs almost twice as much as the reconfigurable design. For this case, the value of reconfigurability is around 47%.

While Figure 6-7 showed the metric values averaged over days 4 to 14 during the event response, it is also important to look at how coverage varied from day to day. This will show the performance as a function of time during event response, illustrating the response time
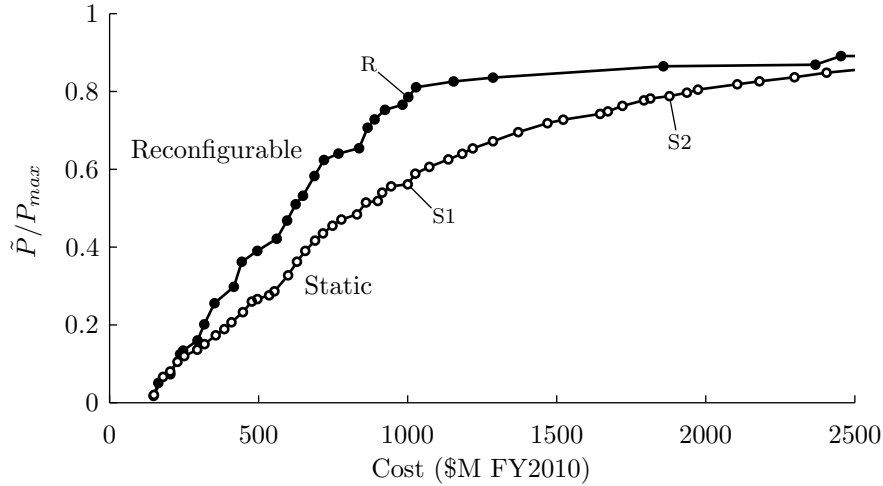
Figure 6-8: The symmetric pattern non-dominated fronts with selected designs R, S1 and S2 shown

Table 6.3: Performance and design details comparison between a reconfigurable design and one iso-performance static design and one iso-cost static design

	Cost $M	$\tilde{P}$ -	Avg. Revisit hr	Max Revisit hr	Mean Response hr	Mean GSD m	i deg	D m	N_T -	h_{GOM} km	ΔV_T m/s
R	1002	142.7	0.86	1.12	0.46	1.00	57.73	0.31	23	484.9	917
S1	1000	102.2	1.05	1.83	0.67	1.20	121.37	0.29	36	517.6	453
S2	1878	143.4	0.71	1.31	0.46	1.05	123.55	0.51	36	816.3	458

for the reconfigurable architecture. Figure 6-9 shows the traditional performance metrics as a function of days during event response for designs R, S1 and S2. The performance is calculated as the average daily performance over all event responses and then averaged over the 96 Monte Carlo samples. The vertical bars indicate the extent of the interquartile range averaged over all event responses and averaged over the 96 Monte Carlo samples. The coverage provided by the reconfigurable design initially starts off poor, but steadily improves as satellites maneuver into ROM, and surpasses the coverage provided by the static designs after three to four days. Additionally, the interquartile range for the reconfigurable design is larger initially than the static designs, but becomes smaller after the satellites move into ROM. This analysis shows that the response time for the reconfigurable architecture is on the order of a few days. This response time can potentially be decreased by increasing the drift orbit altitude to allow for faster phasing at the cost of additional propellant use; however,

this would lead to a less efficient overall system design given the objectives investigated in this thesis. Future work could consider changing the performance metric to reward quick response times for missions where the time to first image is critical.
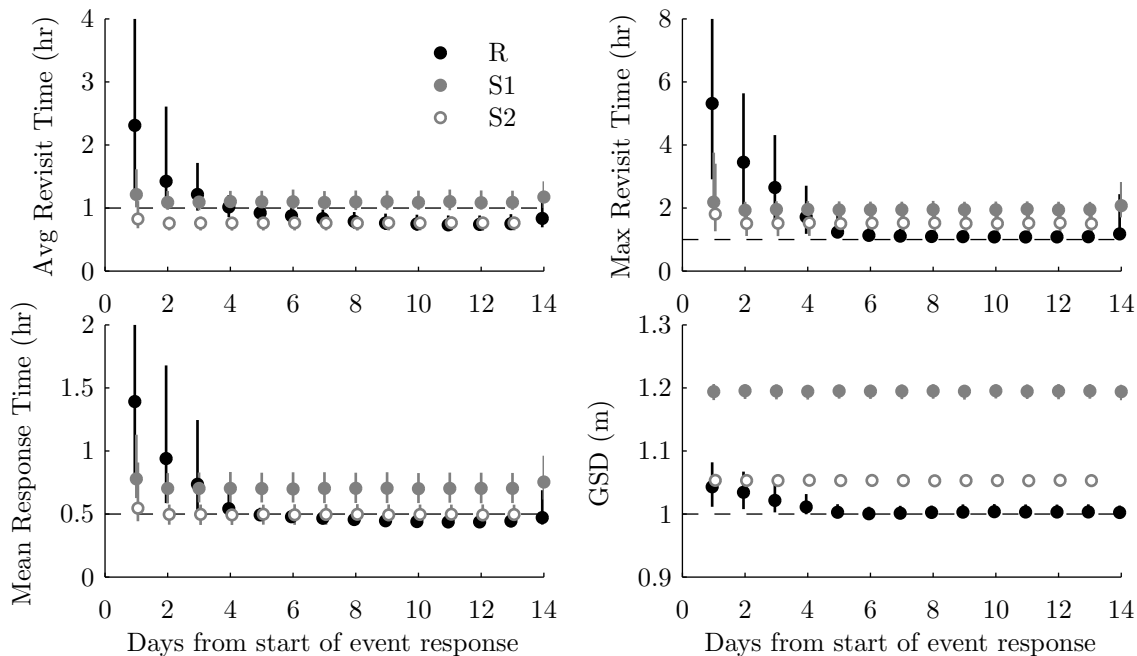
Figure 6-9: Daily traditional metric comparison for a reconfigurable design (black), an iso-cost static designs (filled gray), and an iso-performance static design (unfilled gray)

6.1.3 Effect of Increased Temporal and Spatial Resolution

Scenarios 2 through 4 investigate how increasing temporal and spatial resolution requirements affect the value of reconfigurability. Scenarios 2 and 4 increase the spatial resolution requirement to $0.5m$, while scenarios 3 and 4 increase the temporal resolution requirement to $0.5hr$. For the cases with increased temporal resolution, the constraint on the maximum total number of satellites was also increased to 48, since increased persistence generally requires more satellites. Figure 6-10 shows the non-dominated fronts for scenarios 1-4. The non-dominated fronts for scenarios 2-4 show the same type of trends as was seen for scenario 1. As the temporal and spatial resolution requirements increase, the cost of the non-dominated designs for a given normalized performance level also increases. However, static costs increase faster than reconfigurable costs, which leads to increased VoR. Figure 6-11 shows that

VoR generally increases with increasing temporal and spatial resolution requirements and is more sensitive to increased temporal resolution. This indicates that the reconfigurable architecture is better able to handle increased temporal resolution requirements due to its more efficient use of satellites. The mean VoR over the normalized performance range of $0.5 \leq \tilde{P}/P_{max} \leq 1$ is 36.5% for scenario 1, 46.7% for scenario 2, 48.5% for scenario 3, and 55.4% for scenario 4.
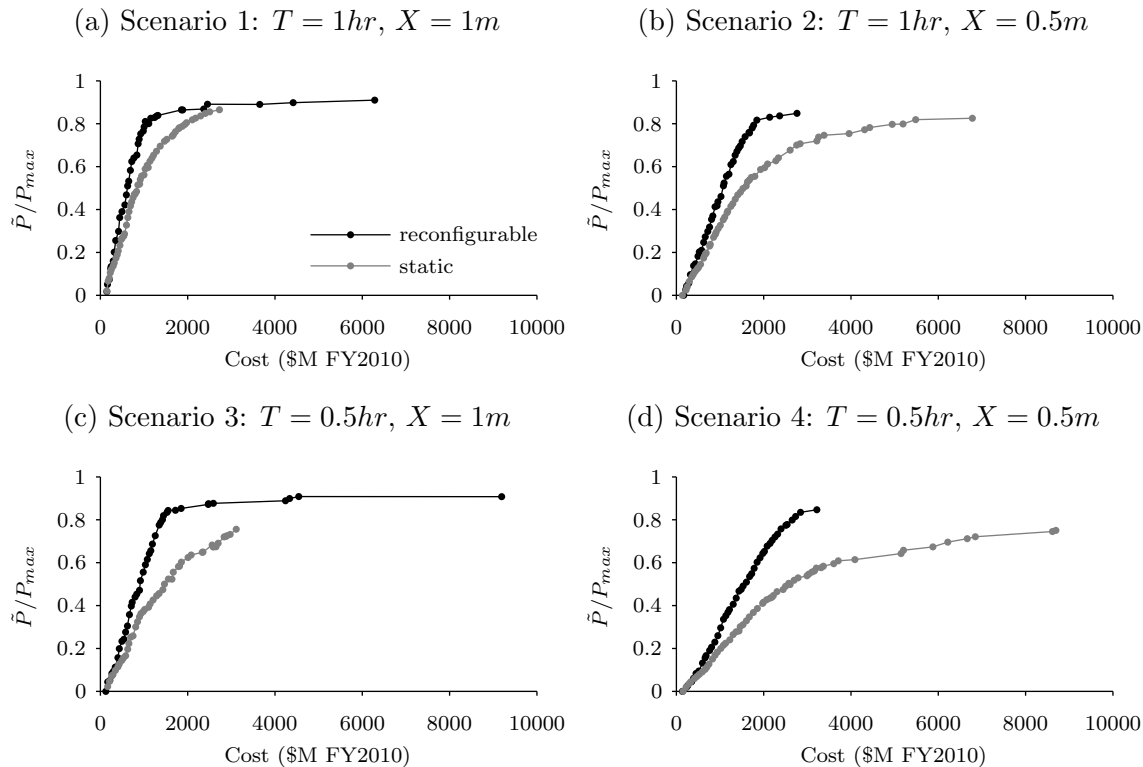
Figure 6-10: Symmetric pattern non-dominated front comparison for scenarios 1 through 4

6.1.4 Value of Reconfigurability Sensitivity to Other Parameters

In addition to varying the desired temporal and spatial resolution, several other parameters and constraints were varied to assess their effects on static and reconfigurable architecture cost effectiveness and the value of reconfigurability. Table 6.4 lists the parameters and constraints used for scenarios 1 through 11, and highlights the changes with respect to the nominal scenario. The resulting value of reconfigurability curves as a function of normalized performance are shown in Figure 6-12.
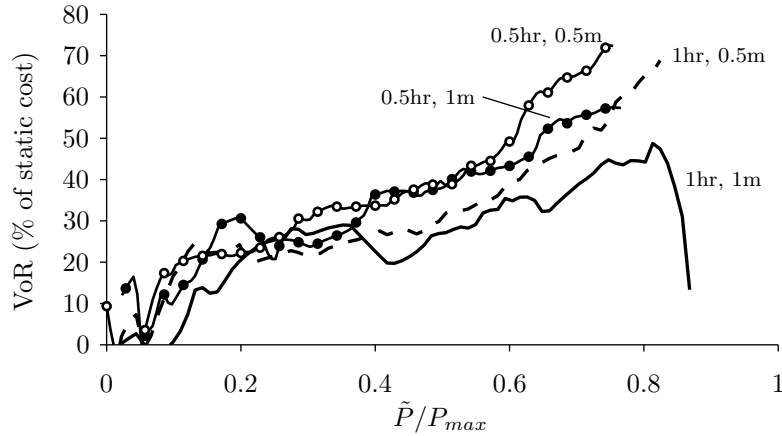
Figure 6-11: The value of reconfigurability increases with increasing coverage requirements

Table 6.4: Parameters values used in scenarios 2 through 11 to investigate the sensitivity of the value of reconfigurability to changes in parameters

Scenario #	T hr	X m	Event PDF	Lifetime yr	b	ε_{min} deg	i deg	N_T	$\frac{M_P}{M_w}$
1	1	1	Disaster	5	0.9	60°	50−130	≤36	≤0.42
2	1	0.5	Disaster	5	0.9	60°	50−130	≤36	≤0.42
3	0.5	1	Disaster	5	0.9	60°	50−130	≤48	≤0.42
4	0.5	0.5	Disaster	5	0.9	60°	50−130	≤48	≤0.42
5	1	1	Uniform	5	0.9	60°	50−130	≤36	≤0.42
6	1	1	Disaster	10	0.9	60°	50−130	≤36	≤0.42
7	1	1	Disaster	5	1.0	60°	50−130	≤36	≤0.42
8	1	1	Disaster	5	0.9	45°	50−130	≤36	≤0.42
9	1	1	Disaster	5	0.9	60°	50−100	≤36	≤0.42
10a	1	1	Disaster	5	0.9	60°	50−130	≤12	≤0.42
10b	1	1	Disaster	5	0.9	60°	50−130	≤24	≤0.42
11	1	1	Disaster	5	0.9	60°	50−130	≤36	≤0.50

Subplot (a) shows the effect of temporal and spatial resolution described previously in Section 6.1.3. Subplot (b) shows that VoR is not a strong function of the event location PDF. One reason for this is that both the disaster and uniform distributions studied in this thesis contain distributions that are spread globally in longitude and have similar latitude ranges. I would suspect that VoR might change as the input distributions were to become focused on smaller, more localized regions. This investigation is left for future work. Subplot (c) shows that increasing the system lifetime T_{life} from 5 to 10 years (while maintaining the same event rate) decreases VoR. This effect is primarily caused by insufficient propellant for reconfigurable designs to service twice as many event responses since the maximum

208

(a) Temporal & Spatial Resolution

(b) Event Location Distribution

(c) Constellation Lifetime

(d) Learning Curve

(e) Minimum Ground Elevation Angle

(f) Inclination Bounds

(g) Maximum # Satellites Constraint

(h) Maximum Propulsion System Mass Fraction
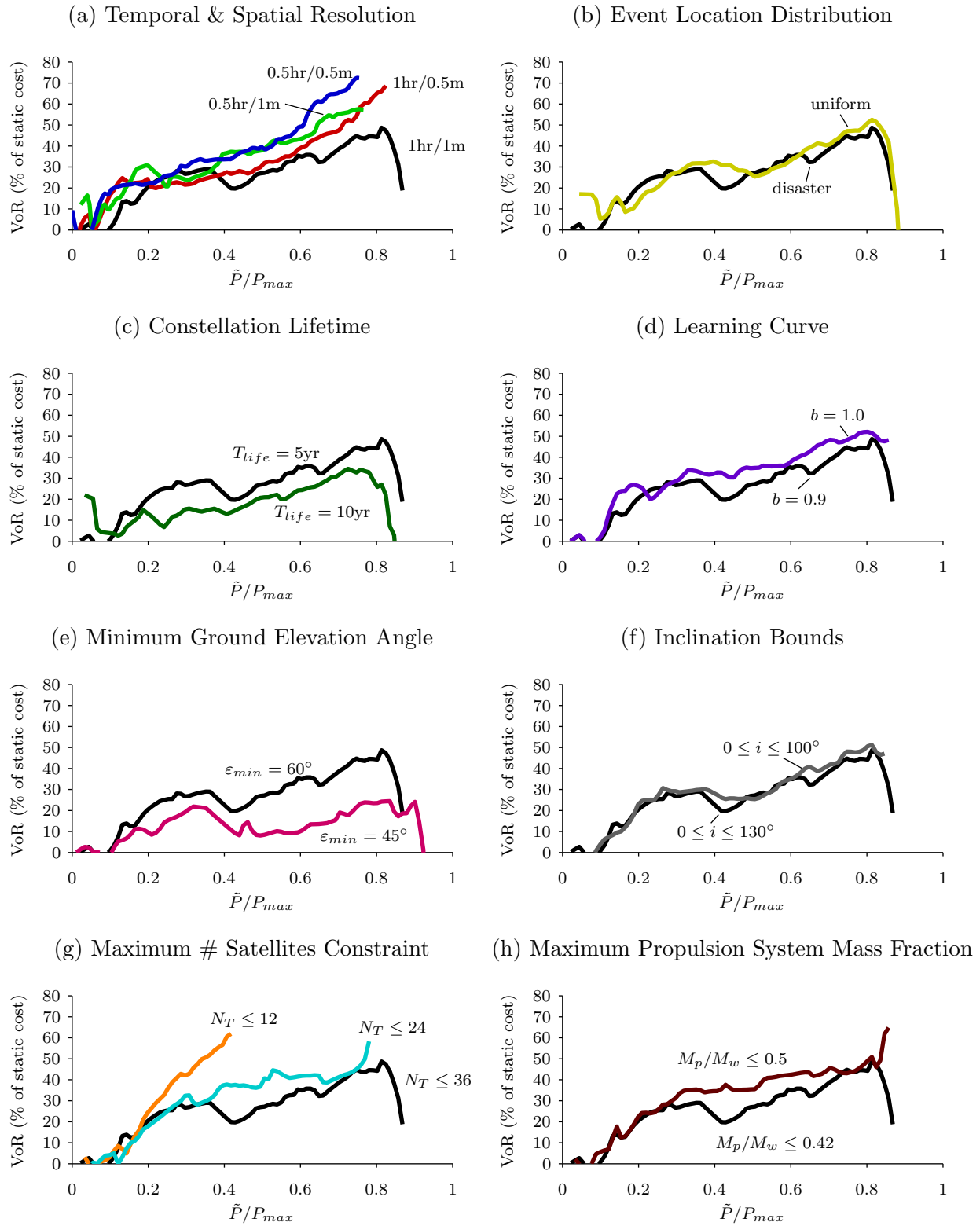
Figure 6-12: Value of reconfigurability sensitivity to changing parameters in scenarios 1 through 11

propulsion system mass fraction constraint is already active for scenario 1. Doubling the lifetime also increases the stationkeeping and drag makeup ΔV requirements, which further reduces ΔV_{recon}. Subplot (d) shows that the VoR is inversely correlated with the learning curve effect. This trend is intuitive since static designs typically have more satellites and, therefore, eliminating the learning curve ($b = 1.0$) increases the cost of static designs more than reconfigurable designs. Subplot (e) shows that reducing the minimum ground elevation angle (ε_{min}) constraint significantly decreases VoR. Reducing ε_{min} significantly increases the satellite ground footprint and improves the coverage provided by static designs. It is hypothesized that increasing ε_{min} would have the reverse effect and would significantly increase VoR. For space based optical imagery, a ε_{min} value of at least $60°$ is generally needed to avoid obscuration for areas with high relief and tall buildings. Subplot (f) shows that VoR increases by a small amount if the inclination is kept smaller than a typical sun-synchronous orbit. As static designs prefer retrograde inclinations, an increase in VoR was expected. This is an important finding since launch restrictions typically make highly retrograde inclinations harder to achieve. Subplot (g) shows that reducing the maximum satellite constraint causes substantial increases to VoR. This is caused by the increased number of satellites needed in static designs to overcome poor satellite utilization. When the maximum satellite constraint is reached, the only alternative for increasing performance is to increase orbital altitude, which improves coverage, but results in larger apertures and higher launch cost. Additionally, as the maximum satellite constraint is reduced, the maximum performance of the static architectures is substantially reduced as evidenced by the shortened horizontal extent of the VoR curve. Therefore, not only does the reconfigurable architecture provide a larger cost reduction, but it also allows for higher performing designs. Subplot (h) shows that increasing the maximum propellant mass fraction increases VoR, especially for the mid-performance region. It was expected that VoR would increase with an increase in the mass fraction constraint since the constraint was active on the reconfigurable designs for scenario 1. Allowing the satellites to have more propellant, allows each satellite to respond to more events that increases per-satellite utilization and overall system cost effectiveness.

The normalized VoR sensitivity to the eight changes to parameters and constraints that were parametrically varied, excluding the event location PDF, is shown in Figure 6-13. The
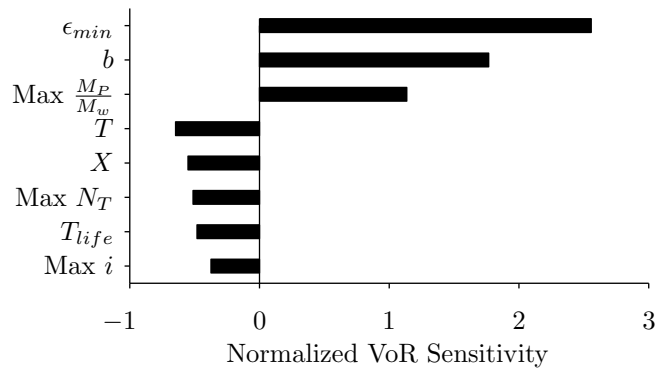
Figure 6-13: Normalized value of reconfigurability sensitivity to selected parameters

normalized sensitivity captures the relative sensitivity of changes to different parameters and is defined as the % change in objective per % change in the parameter value.[1] Positive sensitivity values indicate a positive correlation between the parameter or constraint value and VoR (increasing the value will cause an increase in VoR). The sensitivity magnitude indicates how much VoR changes with a change in the parameter or constraint value. The plot lists the parameters and constraints in order of descending VoR sensitivity and shows that VoR is most sensitive to the minimum ground elevation angle ε_{min} constraint and that increasing ε_{min} will increase VoR.

6.1.5 Value of Reconfigurability Sensitivity to Cost Model Parameters

The value of reconfigurability sensitivity to several cost model parameters was also investigated. Table 6.5 lists the changes made to the OTA cost, FPA cost and FPA mass relations previously introduced in Section 3.4. Scenario 1 is the base scenario. Scenario 12 reduces the OTA cost model exponent on D by 10%. Scenario 13 reduces the FPA cost model exponent on the FPA mass by 10% and scenario 14 reduces both the OTA and FPA cost model exponents by 10%. Scenario 15 reduces the FPA mass model exponent on the scaling ratio (R) from 3 to 2, which effectively changes the FPA mass growth from cubic to quadratic in terms of aperture size. The last column of Table 6.5 shows the mean VoR over the nor-

---

[1]de Weck, O. and Willcox, K. "Gradient Calculation and Sensitivity Analysis", ESD.77 Lecture Notes, MIT, 2012

malized performance range of $0.5 \leq \tilde{P}/P_{max} \leq 1$, and Figure 6-14 compares the value of reconfigurability curves for scenario 1 to scenarios 12, 13, 14 and 15.

Table 6.5: Parameters values used in scenarios 12 through 15 to investigate the sensitivity of the value of reconfigurability to changes in cost model parameters

Scenario	OTA Cost	FPA Cost	FPA Mass	$\bar{VoR}$ for $\tilde{P}/P_{max} \geq 0.5$
1	$C_{OTA} \propto D^{1.6}$	$C_{FPA} \propto M_{FPA}^{0.89}$	$M_{FPA} \propto R^3$	43.6%
12	$C_{OTA} \propto D^{1.44}$	$C_{FPA} \propto M_{FPA}^{0.89}$	$M_{FPA} \propto R^3$	32.1%
13	$C_{OTA} \propto D^{1.6}$	$C_{FPA} \propto M_{FPA}^{0.801}$	$M_{FPA} \propto R^3$	38.0%
14	$C_{OTA} \propto D^{1.44}$	$C_{FPA} \propto M_{FPA}^{0.801}$	$M_{FPA} \propto R^3$	46.9%
15	$C_{OTA} \propto D^{1.6}$	$C_{FPA} \propto M_{FPA}^{0.89}$	$M_{FPA} \propto R^2$	34.6%

In general, the comparison in Figure 6-14 shows that the parametric cost model changes do not significantly change VoR, showing that the VoR values presented in this thesis are robust to small changes in the cost model. One reason for this stability is that VoR is essentially the difference between static and reconfigurable design cost. Therefore, changes to the cost model affect the cost of both architectures without causing a large difference in VoR. Future work should work to further refine the cost models and assess their impact on non-dominated static and reconfigurable designs.

6.1.6   Summary of Symmetric Pattern Results

Section 6.1 introduced optimization run and convergence details and described the data post-processing procedure used on all optimization runs. We also saw that the optimization framework coupled with a new persistence metric yielded well-balanced designs that were not skewed by the statistical outliers that can occur when using traditional metrics. The results show that the reconfigurable constellation architecture provides significant value (20 to 50% reduction in cost for scenario 1) when compared to traditional static constellations and that this value increases with increasing temporal and spatial resolution requirements.
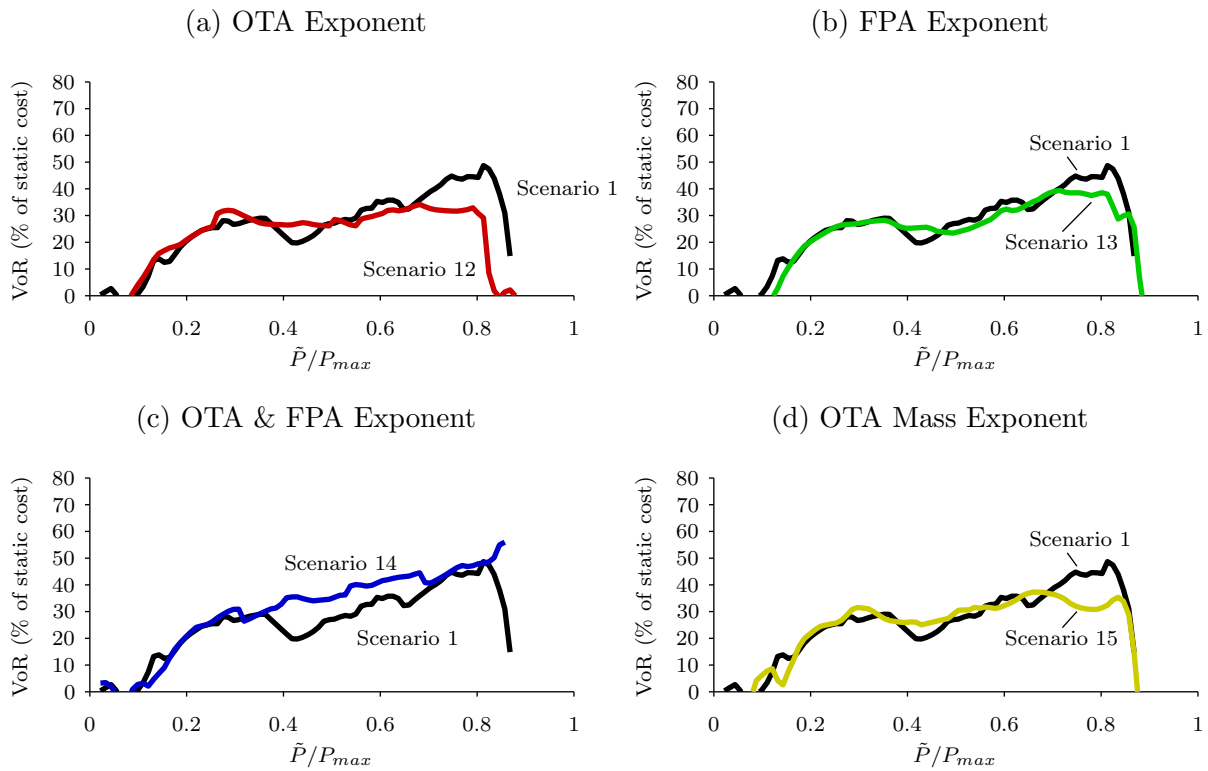
Figure 6-14: Value of reconfigurability sensitivity to changing cost model parameters in scenarios 12 through 15.

6.2 Layered Pattern

This section presents the layered constellation pattern optimization results for the static and reconfigurable architectures. First, the symmetric pattern construction and design vector for each architecture is provided in Section 6.2.1. This is followed by a comparison of the non-dominated designs for scenario 1 in Section 6.2.2 and then for scenarios 1 through 4 in Section 6.2.3.

6.2.1 Layered Pattern Design

The layered pattern considered in this thesis consists of satellites divided into two symmetric Walker patterns. Each symmetric pattern can have a different inclination and a different number of satellites. Additionally, two phasing variables $\Delta\Omega_{key}$ and ΔM_{key} specify the phasing in Ω and M between the key satellites in each symmetric constellation. The two symmetric sub-constellations, labeled with superscripts 1 and 2, are comprised of N_p^1, N_p^2 orbit planes and N_{sp}^1, N_{sp}^2 satellites per orbit plane, giving a total number of satellites in each sub-constellation as N_T^1, N_T^2, and a total number of satellites in the constellation as $N_T = N_T^1 + N_T^2$. The key satellite of the second sub-constellation is referenced from the key satellite of the first sub-constellation as follows:

$$\Omega_{key}^2 = \Omega_{key}^1 + \Delta\Omega_{key} \tag{6.3}$$

$$M_{key}^2 = M_{key}^1 + \Delta M_{key} \tag{6.4}$$

Where the design variables $\Delta\Omega_{key}$ and ΔM_{key} are both on the interval $0 \to 360°$ and Ω_{key}^1 and M_{key}^1 are both set to $0°$. Each of the two sub-constellations have independent phasing parameters $F^1 = 0, \cdots, \left(N_p^1 - 1\right)$ and $F^2 = 0, \cdots, \left(N_p^2 - 1\right)$ which allow for each pattern to be designed by Equations 6.1 and 6.2. The orbital state of the constellation is the combination

214

of the sub-constellation states, Φ^1 and Φ^2 as follows:

$$\Phi = \begin{vmatrix} \Phi^1 \\ \Phi^2 \end{vmatrix} = \begin{vmatrix} a^1 & 0 & i^1 & \Omega_1^1 & 0 & M_1^1 \\ \vdots & \vdots & \vdots & \vdots & \vdots & \vdots \\ a^1 & 0 & i^1 & \Omega_{N_{T1}}^1 & 0 & M_{N_{T1}}^1 \\ a^2 & 0 & i^2 & \Omega_1^2 & 0 & M_1^2 \\ \vdots & \vdots & \vdots & \vdots & \vdots & \vdots \\ a^2 & 0 & i^2 & \Omega_{N_{T2}}^2 & 0 & M_{N_{T2}}^2 \end{vmatrix}$$

Here we see that the semi-major axis a of the two sub-constellations are different. This is caused by the difference in inclination, which leads to different RGT altitudes.

The design variables and variable bounds for the layered pattern are shown in Table 6.6 for the reconfigurable architecture. Here we see that the total number of design variables has increased to 16 from 9 that described the reconfigurable symmetric pattern. Design variables 2 to 6 describe the first layer; variables 7 to 11 describe the second layer; and variables 12 and 13 define the phasing between the key satellites of the two patterns. The static architecture (not shown) features 13 total design variables, and again combines the N_o/N_d and Δalt design variables into a single design variable for the GOM altitude h_{GOM} and eliminates the ΔV_{recon} and α_0 design variables.

6.2.2   Layered Pattern Scenario 1 Results

The post-processing procedure presented for the symmetric patterns in Section 6.1.2 was used to find all non-dominated designs discovered during optimization and re-evaluate a subset of these designs with a 96 sample Monte Carlo simulation. Figure 6-15 shows the non-dominated fronts from the 96 sample Monte Carlo simulation for the static (gray) and reconfigurable (black) architectures. The solid lines show the symmetric pattern non-dominated fronts from Section 6.1.2 and the lines with markers are the layered pattern non-dominated designs. Here we see that the layered pattern provides better static architecture designs, but provides no improvement to reconfigurable architecture designs. The next few paragraphs identify why the layered pattern improves static designs and does not improve reconfigurable

Table 6.6: Layered constellation design variables for reconfigurable designs

#	Variable Name	Symbol	Type	Bounds	
x_1	RGT type	N_o/N_d	cat.	$[\frac{31}{2}, \frac{15}{1}, \frac{29}{2}, \frac{14}{1}, \frac{27}{2}, \frac{13}{1}]$	
x_2	Inclination	i_1	cont.	$0°$ to $180°$	Layer 1 Design
x_3	GOM altitude offset	Δalt_1	cont.	-50 to 50 km	
x_4	Number of orbit planes	$N_{p,1}$	int.	1 to 36	
x_5	Number of satellites per plane	$N_{sp,1}$	int.	1 to 24	
x_6	Phasing parameter	F_1	int.	0 to $N_{p,1} - 1$	
x_7	Inclination	i_2	cont.	0 to $180°$	Layer 2 Design
x_8	GOM altitude offset	Δalt_2	cont.	-50 to 50 km	
x_9	Number of orbit planes	$N_{p,2}$	int.	1 to 36	
x_{10}	Number of satellites per plane	$N_{sp,2}$	int.	0 to 24	
x_{11}	Phasing parameter	F_2	int.	0 to $N_{p,2} - 1$	
x_{12}	Ω offset	$\Delta\Omega_{key}$	cont.	$0°$ to $360°$	Phasing
x_{13}	M offset	ΔM_{key}	cont.	$0°$ to $360°$	
x_{14}	Aperture size	D	cont.	0.1 to 1.2 m	
x_{15}	ReCon ΔV	ΔV_{recon}	cont.	0 to 1000 m/s	
x_{16}	Decision model weight	α_0	cont.	0 to 1	

designs.

Figure 6-16 shows the number of satellites in each of the layers for the static (gray) and reconfigurable (black) non-dominated designs. Here we see that for the reconfigurable architecture, the smaller layer contains zero satellites for the majority of the non-dominated front. When the second layer contains zero satellites, the layered pattern reverts back to the single layer symmetric pattern. Therefore, the optimization process indicates that the symmetric pattern is more cost effective than the layered pattern for the reconfigurable architecture. While initially confusing, this outcome makes sense upon further analysis. Since more coverage is provided to latitudes close to the inclination of a satellite, a layered pattern with multiple inclinations provides a better distribution of coverage over latitude. However, for the reconfigurable architecture, ROM coverage is independent of latitude negating the potential benefits of a layered pattern. Additionally, the pass time of a RGT orbit for a specific ground location is a function of the satellite's Ω (see Section 3.1.2 for more details). If satellites in the constellation have different inclinations, this leads to a difference in a to satisfy the RGT criterion, both of which lead to differential orbital precession. This difference in orbital precession causes the relative spacing between the satellites in Ω to drastically change as a function of time causing periodic clustering in Ω (situations where satellites oc-
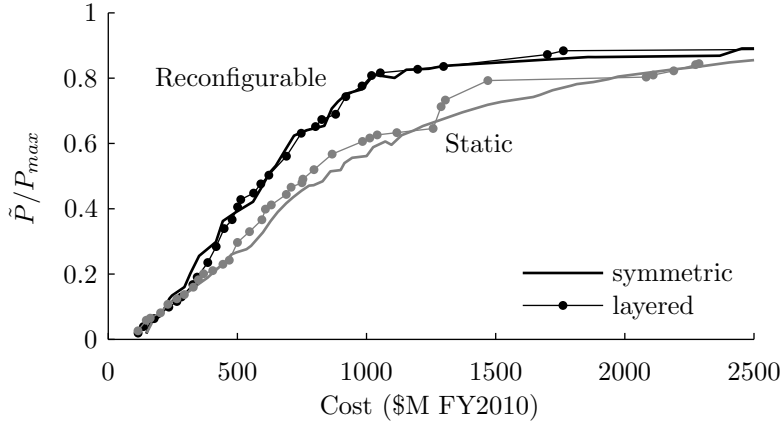
Figure 6-15: Layered pattern yields better static designs, but does not improve reconfigurable designs
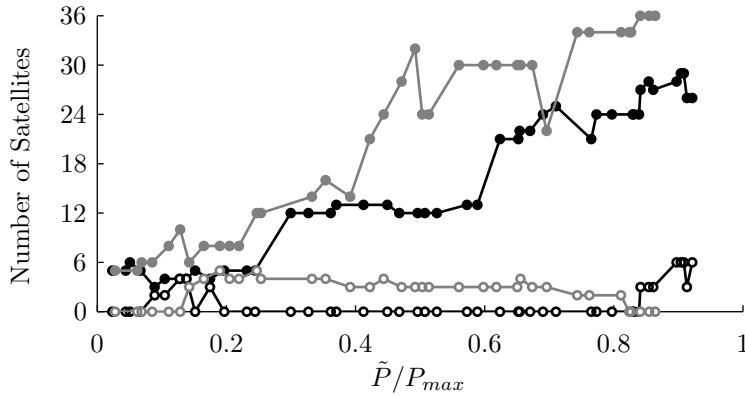
Figure 6-16: The static designs (grey) feature one large layer and one small layer, while for reconfigurable designs (black), the optimization chose to revert back to the symmetric pattern by allocating zero satellites for one layer

cupy similar Ω). Figure 6-17 shows an example 12 satellite reconfigurable constellation with two layers, six satellites at $i = 60°$ (filled markers) and six satellites at $i = 130°$ (open markers). As time progresses, the satellites in different inclinations are subjected to differential Ω precession, which causes periodic clustering of the two layers.

This clustering reduces the ability of a reconfigurable constellation to provide well-spaced coverage periods in ROM to satisfy persistence requirements. Additionally, the difference in a for the two layers causes each layer to provide different nadir spatial resolution and, therefore, one of the layers will be forced to exceed the spatial resolution requirement. The combination of the lack of benefit provided by a layered pattern and poor pass separation
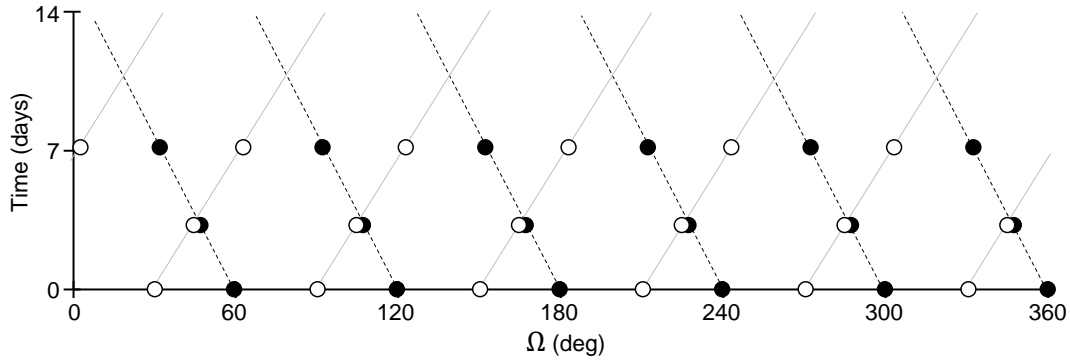
Figure 6-17: Layers at different i and/or different a will be subjected to different orbital precession causing periodic clustering of satellites in Ω

caused by bunching in Ω make the layered pattern perform worse than the symmetric pattern for the reconfigurable architecture.
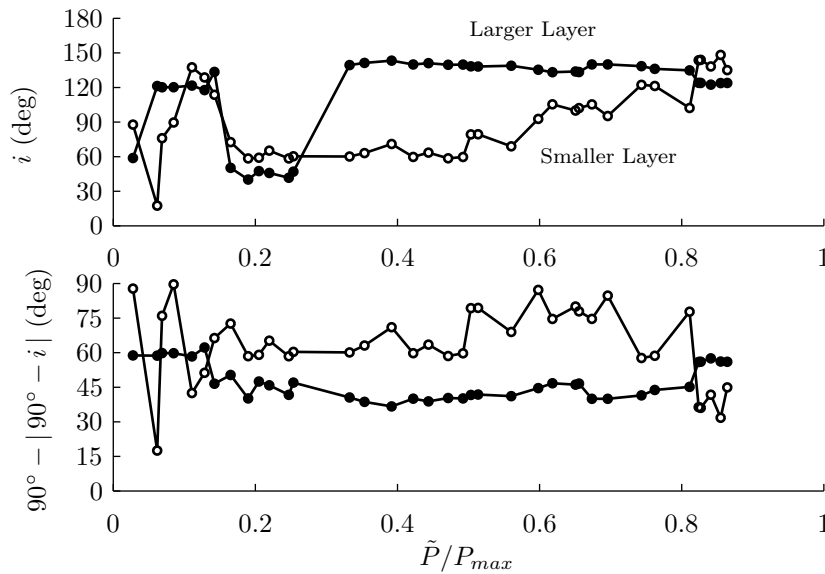
Figure 6-18: The static designs features a large layer providing peak coverage for latitudes from $35° \rightarrow 45°$ and a smaller layer at higher inclination providing coverage up to a latitude of 60°to meet the global maximum revisit time constraint.

On the contrary, static architectures significantly benefit from spreading out the latitudinal coverage with multiple layers. Figure 6-18(top) shows the two layer inclinations for the non-dominated static designs. The bottom plot shows the maximum latitude of the sub-satellite point, which is equal to the prograde inclination and the retrograde inclination

218

is transformed by the following relation: $90° - |90° - i|$. This essentially gives the latitude of the greatest coverage provided by each layer. Here we see that the non-dominated static designs typically feature a larger layer with 5-34 satellites at an inclination of around 135° providing highest coverage at 45° latitude, and a smaller layer with 3-5 satellites at an inclination of between 60° and 120° to provide coverage for latitudes up to 60° to service high latitude regional events and meet the global maximum revisit time constraint. Figure 6-19 shows the benefits of such an arrangement for the static architecture. The plot shows the normalized PDF and CDF of the event location $|\varphi|$ for the natural disaster PDF. Also plotted are the general peak coverage regions for the two static architecture layers described above. The large layer is tuned to provide peak coverage for the upper end of the main distribution and also provides coverage for all lower latitudes as well. The small layer fills in the coverage for the upper tail of the distribution and satisfies the $24hr$ GOM maximum revisit time constraint for latitudes up to 60°.
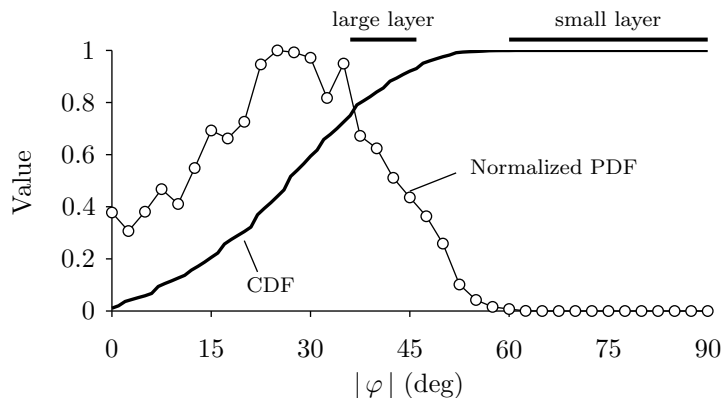
Figure 6-19: The large layer provides peak coverage for the upper end of the main event latitude distribution, while the smaller layer fills in coverage for the upper tail of the distribution and satisfies the GOM maximum revisit time constraint

6.2.3 Layered Pattern Scenarios 1 to 4 Results

The non-dominated fronts for scenarios 1-4, plotted in Figure 6-20, show the same trends observed with scenario 1. The static architecture benefits from the layered pattern while the reconfigurable architecture does not. For scenarios 3 and 4, in the reconfigurable architecture the layered pattern performs much worse than the symmetric pattern at high performance

levels. This is likely an artifact of the optimization process having a hard time zeroing out the second layer size to revert back to the single symmetric pattern.

(a) Scenario 1: $T = 1hr$, $X = 1m$

(b) Scenario 2: $T = 1hr$, $X = 0.5m$

(c) Scenario 3: $T = 0.5hr$, $X = 1m$

(d) Scenario 4: $T = 0.5hr$, $X = 0.5m$
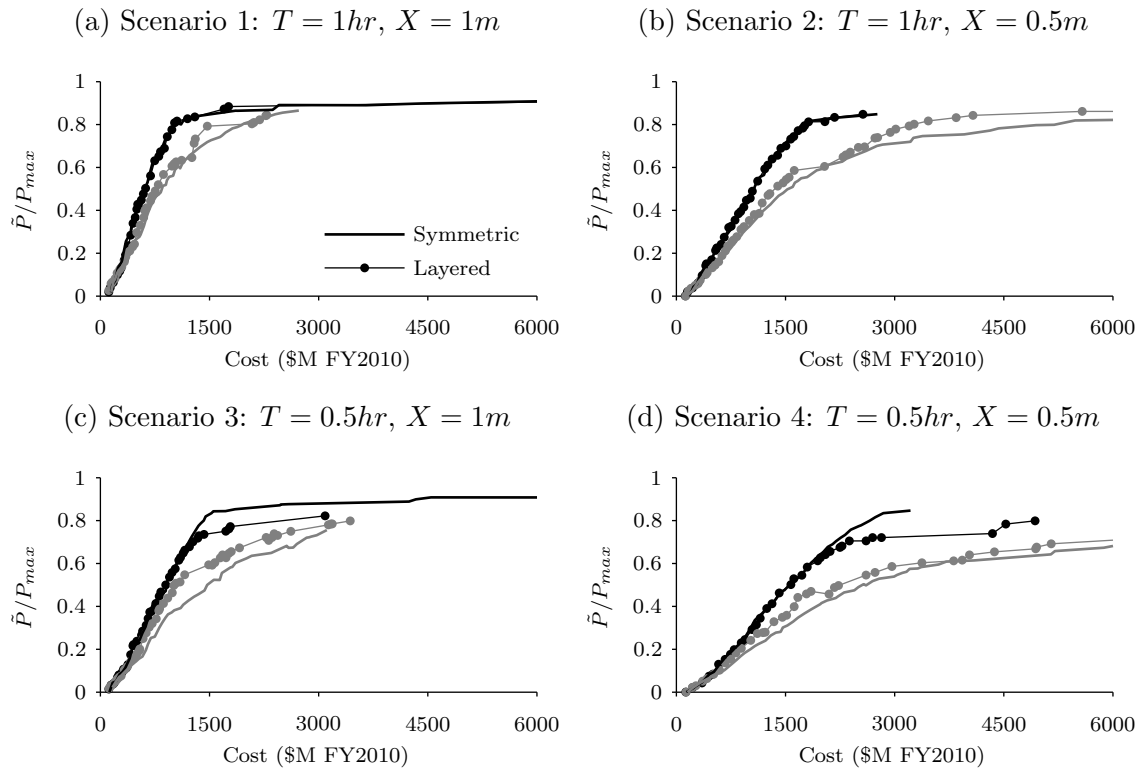
Figure 6-20: Layered pattern non-dominated fronts for scenarios 1-4 compared to the symmetric pattern non-dominated fronts for reconfigurable (black) and static (grey) architectures.

6.3 Asymmetric Pattern

This section presents optimization results for several asymmetric patterns. First, a fully asymmetric pattern was investigated which produced designs with improved cost-effectiveness but suffered from poor optimization convergence. However, these results led to the discovery of two new quasi-asymmetric patterns which combine the benefits of an asymmetric pattern with a vastly reduced number of design variables. Additionally, a layered asymmetric pattern was investigated to see if this would improve cost-effectiveness.

6.3.1 Asymmetric Pattern Design

In the fully asymmetric pattern considered in this thesis, all satellites reside in circular orbits with common a and i. No restrictions are placed on the relative phasing between satellites in Ω and M, freeing the optimization process to select any possible configuration. The abandonment of symmetry can lead to more efficient designs, but also considerably expands the design space and increases optimization difficulty. For the asymmetric pattern, two variables are needed to specify Ω and M for each satellite in the constellation.

Preliminary testing with the optimization routine showed that slightly modifying the design variable construction improved optimization convergence and alleviated premature stagnation. The first problem encountered with the asymmetric pattern is that the number of design variables is a function of the number of satellites in the constellation. This causes the genetic population to have different design vector lengths. To enable genetic operations, dummy variables were introduced to make all designs have the same number of variables. However, since these meaningless dummy variables are then used in genetic operations, the optimization process significantly loses efficiency. To overcome this problem, the asymmetric optimization problem was broken up into several subproblems, each with a fixed total number of satellites N_T, creating the same number of design variables for the genetic population. The second problem encountered was that allowing Ω and M for each satellite to vary freely between 0 and 360° led to non-unique solutions which produced very slow convergence. This problem was alleviated by fixing the satellite order in Ω and re-formulating the Ω design variables to instead describe the separation in Ω between adjacent spacecraft. This reformulation reduced the design vector by one variable, without shrinking the design space, and eliminated the possibility of non-unique solutions. The new design variables $\vec{x}_\Omega$ of length $N_T - 1$ fully define the initial satellite positioning in Ω with the recursive algorithm shown in Algorithm 4.

Algorithm 4 Compute initial satellite Ω from $\vec{x}_\Omega$

1: $\Omega_1 \leftarrow 0°$
2: **for** i $\leftarrow$ 2 to N_T **do**
3:      $\Omega_i \leftarrow (360° - \Omega_{i-1})x_{\Omega,i} + \Omega_{i-1}$
4: **end for**

Where the design variables $\vec{x}_\Omega$ have bounds $0 \to 1$. The design vector for the asymmetric pattern is shown in Table 6.7. In this case, the three design variables that describe the symmetric constellation pattern (N_p, N_{sp}, and F) are replaced by a fixed variable specifying the total number of satellites N_T, $N_T - 1$ variables specifying Ω for each satellite, and N_T variables specifying M for each satellite. Therefore, the design vector length depends on the total number of satellites N_T.

Table 6.7: Asymmetric constellation design variables for reconfigurable designs

#	Variable Name	Symbol	Type	Bounds
x_1	RGT type	N_o/N_d	cat.	$[\frac{31}{2}, \frac{15}{1}, \frac{29}{2}, \frac{14}{1}, \frac{27}{2}, \frac{13}{1}]$
x_2	GOM altitude offset	Δalt	cont.	-50 to 50 km
x_3	Inclination	i	cont.	$50°$ to $130°$
x_4	Number of satellites	N_T	int.	Fixed
x_5	Aperture size	D	cont.	0.1 to 1.2 m
x_6	ReCon ΔV	ΔV_{recon}	cont.	0 to 1000 m/s
x_7	Decision model weight	α_0	cont.	0 to 1
x_8 to $x_{8+(N_T-1)}$	Satellite Ω spacing	$x_{\Omega, 1\,\text{to}\,(N_T-1)}$	cont.	0 to 1
$x_{9+(N_T-1)}$ to x_{8+2N_T-1}	Satellite M	$M_{1\,\text{to}\,N_T}$	cont.	$0°$ to $360°$

Figure 6-21 shows the results from four asymmetric optimization runs (with $N_T = 8, 12, 16, 24$) for the reconfigurable (top) and static (bottom) architectures. The maximum total number of satellites was restricted to 24 due to optimization convergence problems with many design variables. The results show that the asymmetric pattern produced more cost-effective designs than the symmetric pattern for the low performance region for both the static and reconfigurable architectures. The asymmetric pattern would likely outperform the symmetric pattern in the higher performance region if N_T could be increased. Nonetheless, the asymmetric pattern results reinforce previous observations [94, 95, 82, 120, 157], by showing that relaxing the constellation pattern symmetry constraint can yield better designs for partial coverage satellite constellations.

Significant emphasis during data post processing focused on finding why the asymmetric pattern out performed the static pattern. The extent of the spread of satellites in Ω is likely one of the driving factors. Figure 6-22 shows this trend by plotting the initial satellite Ω placement for each non-dominated design. The plots are interpreted as follows, as one sweeps up the non-dominated front from Figure 6-21, the performance increases and number of satel-
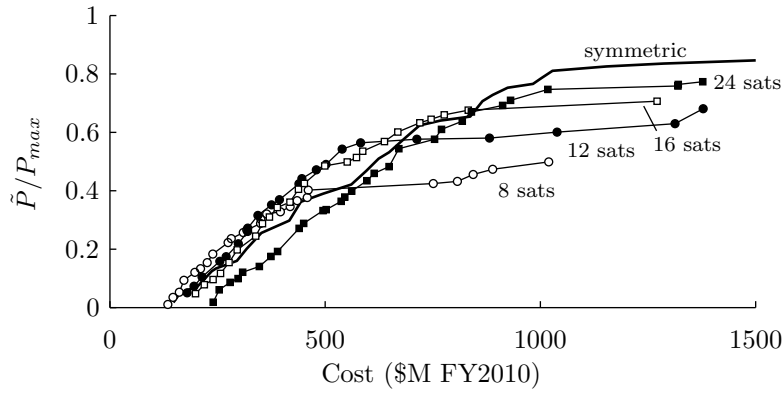
(a) Reconfigurable
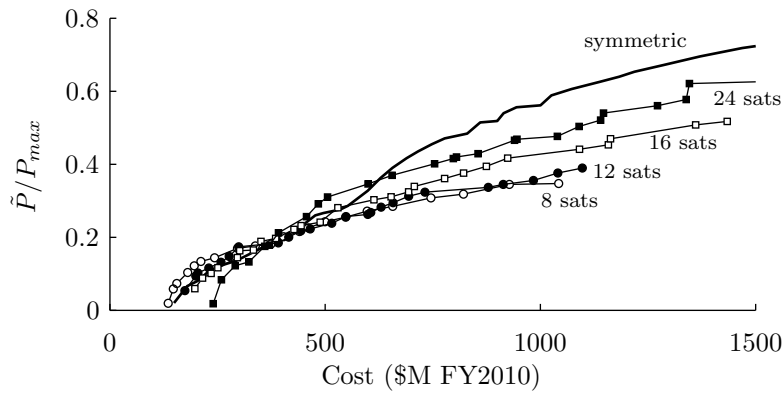
(b) Static

Figure 6-21: By outperforming the symmetric pattern in the low performance region for static and reconfigurable architectures, the asymmetric pattern results show that relaxing symmetry constraints can yield better designs

lites increases, and Figure 6-22 shows the initial Ω placement for each satellite. Therefore, each row of dots in the figure depict the satellite positions for a single non-dominated design. The left two plots show the initial Ω for all non-dominated symmetric designs. Here we see that the satellites are spread out to occupy the whole Ω range due to the construction of the symmetric pattern, which distributes planes evenly in the Ω space. The right plots show the initial Ω range (with Ω shifted to minimize the maximum satellite Ω) for all non-dominated asymmetric pattern designs and only asymmetric designs that outperform symmetric designs are shown. Here we see a clear trend that efficient asymmetric designs contain satellites that are clustered closer together in Ω and only utilize a small range in the $360°$ total Ω space.
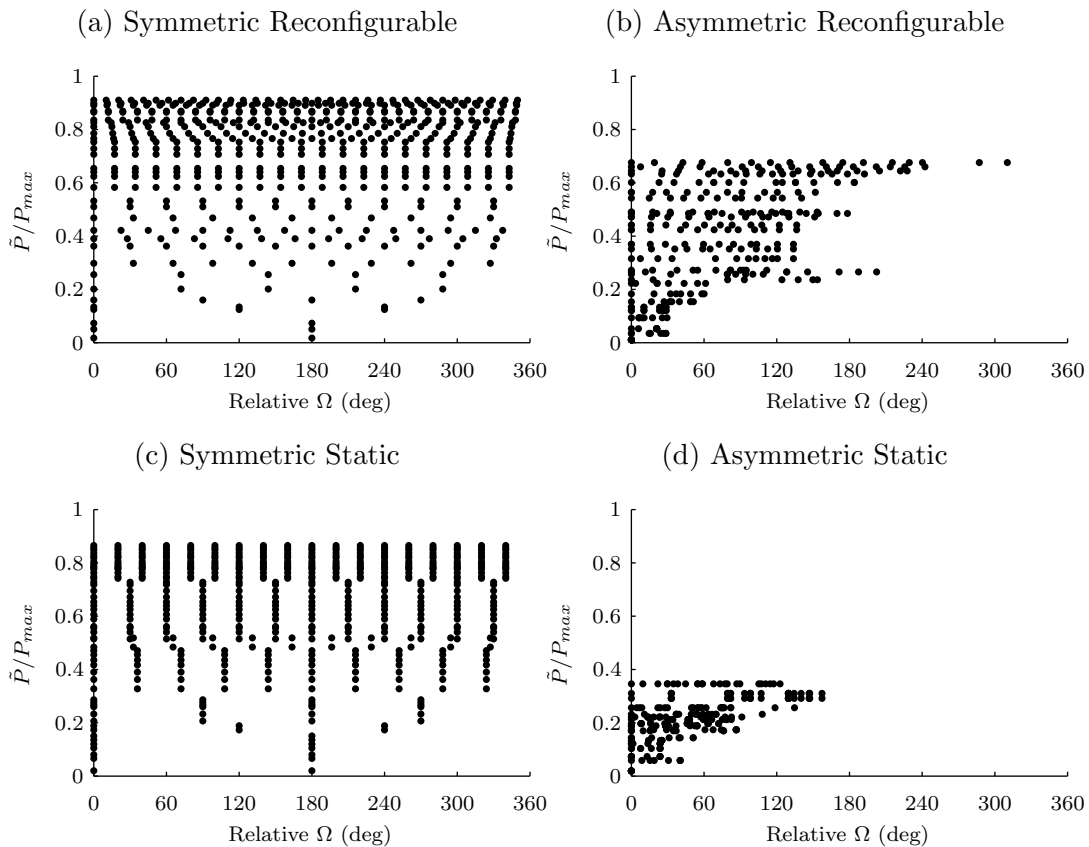
Figure 6-22: Efficient asymmetric pattern designs place satellites in only a fraction of the total Ω space, while symmetric designs, by definition, distribute satellites uniformly in Ω space

This observation makes sense for reconfigurable designs. As was previously explained in Section 3.1.2, the Ω of a satellite in a RGT orbit determines the local pass time for a given event location, and the difference in Ω between two satellites dictates the difference in local

pass times for those two satellites. A 15° difference in Ω translates into a $1hr$ difference in pass time. Additionally, the satellite can provide coverage for an event with either an ascending or descending pass via selection of two different RGT orbits that pass over the event location. These two options provide different local pass times which are spread apart by up to 12 hours. Therefore, reducing the spacing in Ω improves persistence by allowing for smaller spacing between pass times, and restricting the Ω extent from 360° to around 180° doesn't cause large gaps in ground coverage because of the choice of ascending and descending pass coverage. The observation that allowing satellites to only occupy a subset of the total Ω space led to the development of two new 'quasi-asymmetric' patterns. These patterns allow for a shortened Ω extent while also using some equal spacing rules to dramatically reduce the number of design variables in order to improve optimization. These two patterns are explained in the next section.

6.3.2   Quasi-Asymmetric Patterns

Observations made on the fully asymmetric results led to the development of two new asymmetric patterns that combine the benefits of vastly reduced number of design variables with the ability of the pattern to populate only a small region in Ω space.

Restricted Asymmetric Pattern

The first quasi-asymmetric pattern is called the restricted asymmetric pattern and features regular satellite spacing in Ω and M. This allows the constellation to populate only a small region of the Ω and M space. Two variables specify this regular spacing amount for both Ω and M. The ξ_Ω variable, with bounds $0 \rightarrow 1$, specifies the total extent of the constellation in Ω space and the ΔM variable, with bounds $0 \rightarrow 360°$, specifies the M spacing between satellites in adjacent Ω slots. The ξ_Ω variable effectively specifies what fraction of the Ω space is populated with satellites and then the satellites are distributed evenly in Ω within that range. The initial orbital state of the constellation is then determined as follows. The first satellite is set to $[\Omega_1 = 0°, M_1 = 0°]$ and then the ith satellite's state is then determined

by the following relations:

$$\Omega_i = \Omega_{i-1} + \xi_\Omega \left(\frac{360°}{N_T} \right) \tag{6.5}$$

$$M_i = M_{i-1} + \Delta M \tag{6.6}$$

Asymmetric Walker Pattern

The second quasi-asymmetric pattern is called the asymmetric Walker pattern and uses the ξ_Ω design variable to alter the Ω extent of a regular symmetric Walker pattern. The benefit of this pattern over the restricted asymmetric pattern is that it allows for multiple satellites to share the same orbit plane. Equation 6.1, from the symmetric pattern section, is modified as follows:

$$\Omega_{kl} = \xi_\Omega \left(\frac{2\pi k}{N_p} \right) + \Omega_{key} \tag{6.7}$$

Where $k = 0, \cdots, (N_p - 1)$ and $l = 0, \cdots, (N_{sp} - 1)$. The design vector is then the same as what was shown in Table 6.1 with the exception that an additional continuous design variable is added for ξ_Ω with bounds of $0 \to 1$.

6.3.3   Scenario 1 Quasi-Asymmetric and Symmetric Comparison

Figure 6-23 shows the restricted asymmetric pattern (black markers) and asymmetric Walker pattern (white markers) non-dominated fronts for the reconfigurable (top plot) and static (bottom plot) architectures. Also plotted are the symmetric and asymmetric pattern non-dominated designs for scenario 1. Here we see that the two new quasi-asymmetric patterns significantly outperform the symmetric and asymmetric patterns. The asymmetric Walker pattern performs better for the static architecture and the restricted asymmetric pattern performs better for the reconfigurable architecture. This observation was also seen in the optimization results for scenarios 2 through 4. This makes intuitive sense, because the major difference between the two patterns is that the asymmetric Walker pattern allows multiple satellites per orbit plane (Ω slot). This ability improves coverage and reduces launch cost for
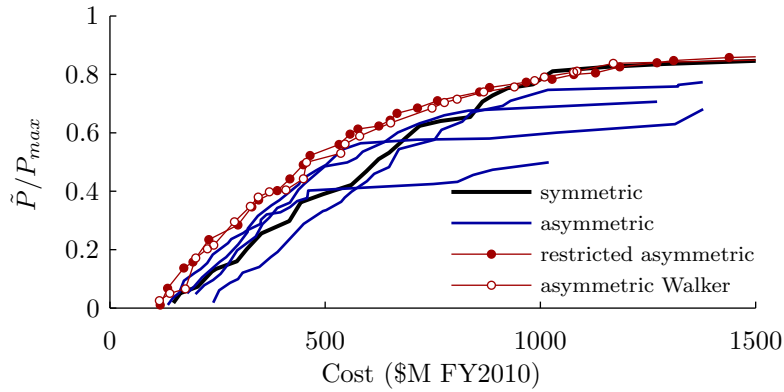
(a) Reconfigurable
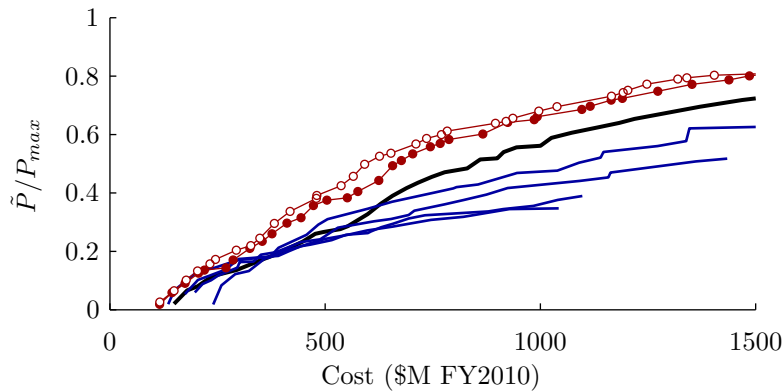
(b) Static

Figure 6-23: Designs using the two 'quasi'-asymmetric patterns outperform symmetric and asymmetric designs. The restricted asymmetric pattern performs best for reconfigurable designs while the asymmetric Walker pattern performs best for static designs

the static architecture, but reduces the pass time options and, therefore, reduces performance for the reconfigurable architecture. While, the optimization process could set the number of satellites per orbit plane to one for the reconfigurable architecture, this requires one extra design variable and slows convergence. Therefore, the restricted asymmetric pattern, by assuming one satellite per orbit plane, converges faster than the asymmetric Walker pattern and, since reconfigurable designs tend to favor a single satellite per orbit plane, this assumption does not eliminate efficient designs.
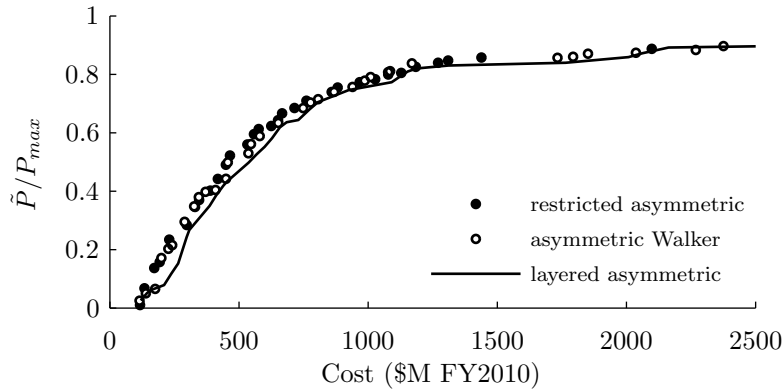
(a) Reconfigurable
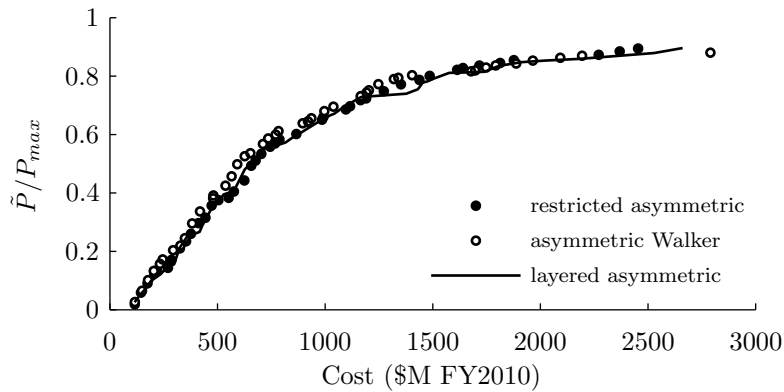
(b) Static

Figure 6-24: The layered asymmetric pattern does not outperform the two 'quasi'-asymmetric patterns for the reconfigurable architecture, and does not outperform the asymmetric Walker pattern for the static architecture

6.3.4   Layered Asymmetric Pattern

A layered pattern consisting of two asymmetric Walker sub-patterns at different inclination was not found to provide increased cost-effectiveness when compared to the 'quasi'-asymmetric patterns. Figure 6-24 shows a comparison of the layered asymmetric pattern with the restricted asymmetric and asymmetric Walker patterns. Here we see that the restricted asymmetric pattern outperforms the layered asymmetric pattern for the reconfigurable architecture, and the asymmetric Walker pattern outperforms the layered asymmetric pattern for the static architecture.

6.4 Comparing All Pattern Results

The results presented so far in this thesis have investigated a wide variety of constellation patterns. This section now takes a broader view by determining which patterns perform best under different circumstances for the static and reconfigurable architectures. Figure 6-25 shows the non-dominated fronts for the reconfigurable (left) and static (right) architectures using the symmetric, layered, restricted asymmetric and asymmetric Walker patterns for scenario 1. Here we see that the restricted asymmetric pattern generally performs the best for the reconfigurable architecture while the asymmetric Walker pattern performs the best for the static architecture. This trend was described previously in Section 6.3.3.
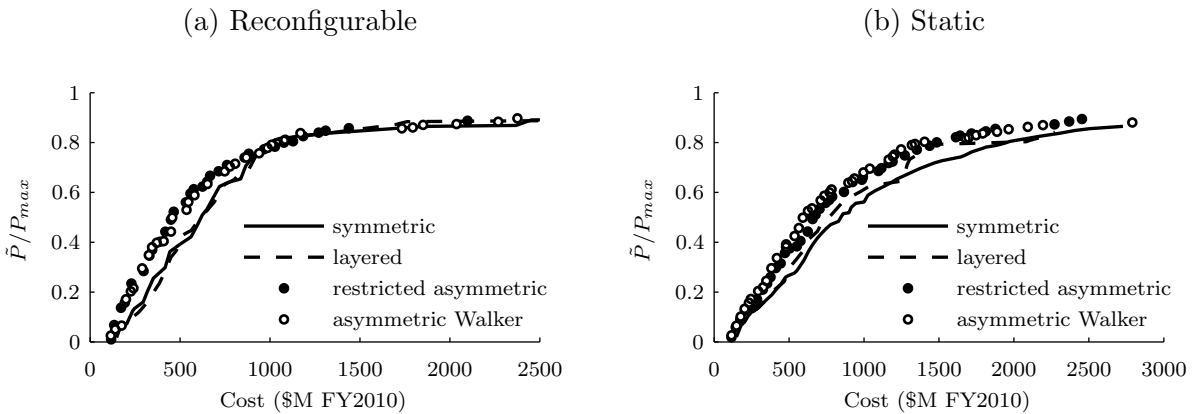
Figure 6-25: Comparison of symmetric, layered, restricted asymmetric, and asymmetric Walker pattern non-dominated fronts

Figure 6-26 shows the range in normalized performance where each pattern performed within 3% of the combined non-dominated front performance. This validates the visible trend in Figure 6-25 that the reconfigurable architecture performs best with the restricted asymmetric pattern, and the static architecture performs best with the asymmetric walker pattern. All patterns perform well in the high performance region for reconfigurable designs and the symmetric pattern performs the best in a very small high performance band for static designs.

Another factor to consider is the performance variability given by each of the patterns. Figure 6-27 shows the performance standard deviation, as a percentage of the median value, for the four patterns over 96 Monte Carlo samples for the reconfigurable (top) and static

(a) Reconfigurable
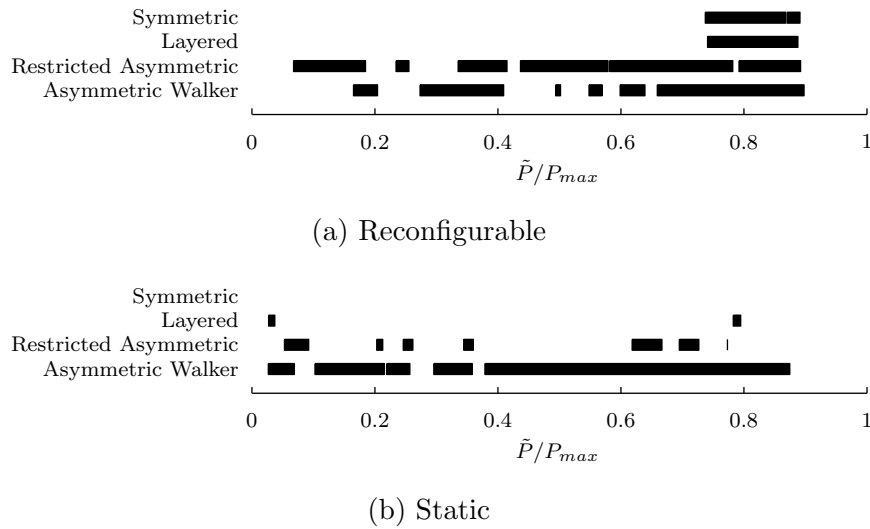
(b) Static

Figure 6-26: The restricted asymmetric pattern generally yields the best reconfigurable designs, while the asymmetric Walker pattern generally yields the best static designs

(bottom) architectures. In the reconfigurable case, the symmetric pattern provides the smallest performance variability and the two asymmetric patterns provide the highest variability, although the variability difference is small for normalized performance over 0.7. In the static case, the symmetric pattern and both asymmetric patterns provide the smallest variability while the layered pattern gives the highest variability. For normalized performance over 0.4, the symmetric, restricted asymmetric, and asymmetric Walker patterns provide almost identical performance variability. These results provide additional insight into the characteristics of the different patterns. For reconfigurable designs, the greatly improved performance provided by the restricted asymmetric pattern when compared to the symmetric pattern likely outweighs the increase in performance variability. For static designs, the layered and asymmetric Walker patterns provide similar performance (see Figure 6-25 bottom) for normalized performance between 0.7 and 0.8, but the layered pattern has twice the performance variance. This may lead to a decision to select the asymmetric Walker pattern over the layered pattern.

Similar trends are observed in Figure 6-28 for scenarios 2 through 4. The gap between the reconfigurable and static non-dominated curves grows with increasing spatial and temporal resolution requirements; and, the maximum achievable performance for the static architecture drops with increased temporal resolution requirements. These observations are quanti-
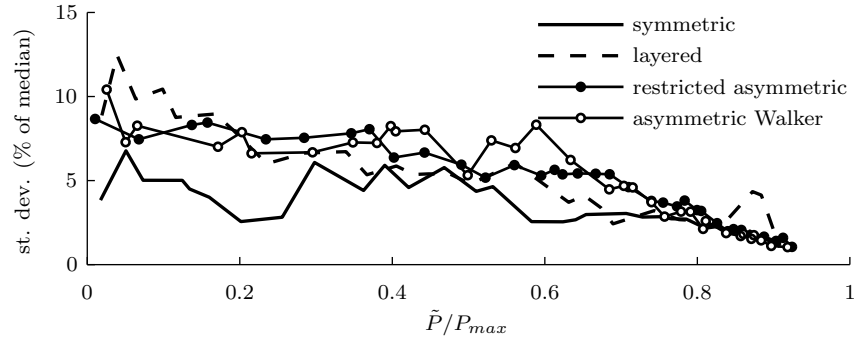
(a) Reconfigurable
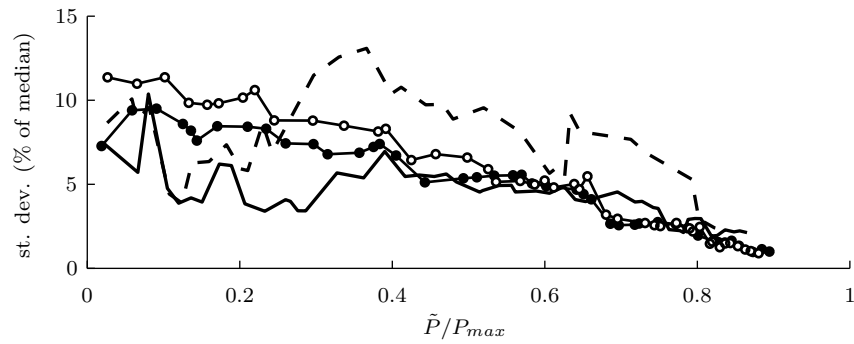
(b) Static

Figure 6-27: Comparison of constellation performance variability (standard deviation as a percentage of median performance value) as a function of pattern type

fied in Figure 6-29 which plots the value of reconfigurability for the four scenarios computed with the combined non-dominated fronts. The mean VoR over the normalized performance range of $0.5 \leq \tilde{P}/P_{max} \leq 1$ is 27.5% for scenario 1, 40.2% for scenario 2, 48.4% for scenario 3, and 59.1% for scenario 4. Table 6.8 shows a comparison of the combined pattern VoR values and the symmetric pattern VoR values that were presented previously in Section 6.1.3. By introducing the layered and asymmetric patterns, the value of reconfigurability remained nearly constant. VoR decreased for scenarios 1 and 2, which means that the more complex patterns provided greater benefits to the static architecture than they provided to the reconfigurable architecture. However, the VoR remained constant for scenario 3, and increased slightly for scenario 4, meaning that the reconfigurable architecture benefited more with the more complex patterns.

(a) Scenario 1: $T = 1hr$, $X = 1m$

(b) Scenario 2: $T = 1hr$, $X = 0.5m$

(c) Scenario 3: $T = 0.5hr$, $X = 1m$

(d) Scenario 4: $T = 0.5hr$, $X = 0.5m$
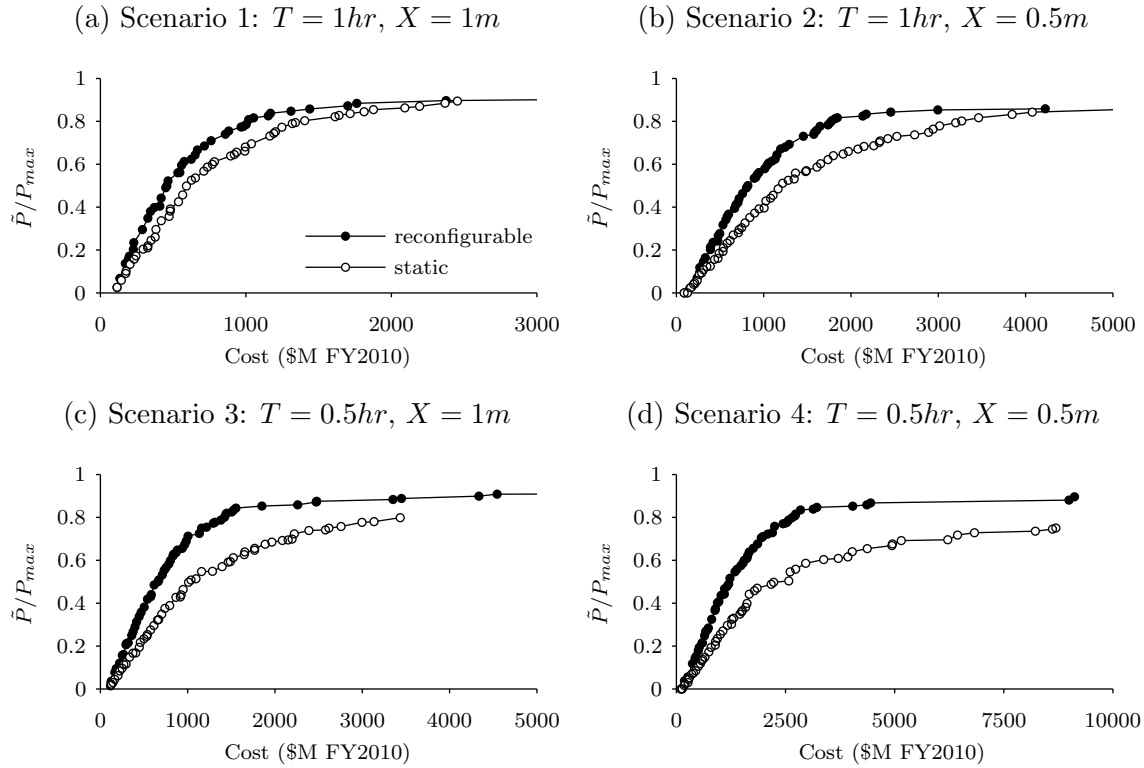
Figure 6-28: Best non-dominated static and reconfigurable fronts, using designs from all patterns, for scenarios 1-4

Combined Non-dominated Front Design Details

Figure 6-30 shows details of the combined non-dominated designs as a function of normalized performance. The plotted design details include: the total number of satellites (N_T), aperture size (D), GOM altitude (h_{GOM}), inclination (i), total ΔV (ΔV_T), and total number of launches to deploy the constellation. Despite the fact that most of the designs are asymmetric, the general design trends are similar to those observed for the symmetric pattern in Section 6.1.2. Again, we see that the non-dominated designs for the two architectures are significantly different. In the low performance region ($\tilde{P}/P_{max} < 0.6$), static designs tend to feature more satellites at a lower altitude when compared to reconfigurable designs. Despite the lower altitude, static designs feature similar aperture sizes to reconfigurable designs. This is caused by the fact that there is no guarantee of nadir pass for static constellations, and consequently, the satellites must have larger apertures to maintain good spatial resolution for off-nadir passes. The reduction in the number of satellites for reconfigurable designs is
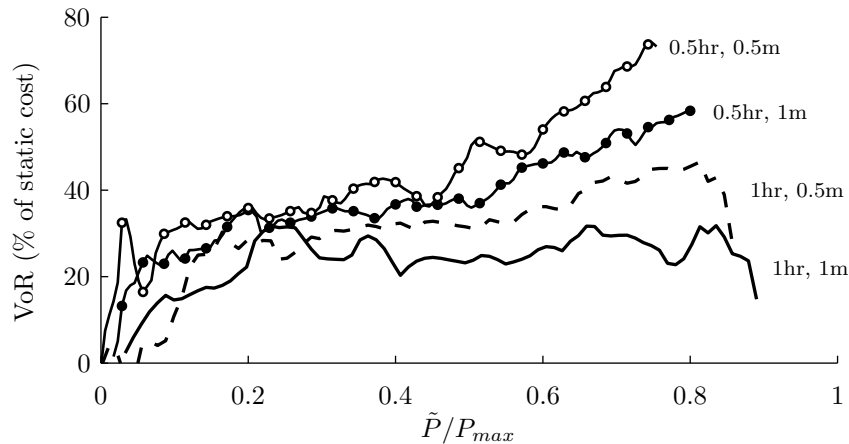
Figure 6-29: Value of reconfigurability for scenarios 1 to 4 using the best static and reconfigurable designs from all patterns

Table 6.8: Value of reconfigurability between the non-dominated symmetric pattern designs and best combined pattern designs, as a percentage of static cost, for scenarios 1-4

	Scenario			
	1	2	3	4
Symmetric only	36.5	46.7	48.5	55.4
Combined patterns	27.5	40.2	48.4	59.1

caused by increased per-satellite utilization enabled by the ability to reconfigure. This is the fundamental cost reduction driver for reconfigurable architectures. At around $\tilde{P}/P_{max} = 0.5$, the static architecture runs up against the maximum satellite constraint, which is set to 36. Therefore, to improve performance for static designs past this point, the altitude must increase to improve per-satellite coverage. Consequently, the aperture size must increase to preserve the desired spatial resolution, and these two factors significantly increase overall system cost.

Reconfigurable designs tend to feature prograde inclinations of around 60° while static designs feature retrograde inclinations around 120°. The chatter for static designs between prograde and retrograde that was observed for the symmetric pattern results is not observed for the combined pattern results. Again, the choice of retrograde inclination is an interesting result given that the performance benefits of retrograde inclinations must outweigh the increase in launch cost to launch to higher inclinations for retrograde designs to be on the

233
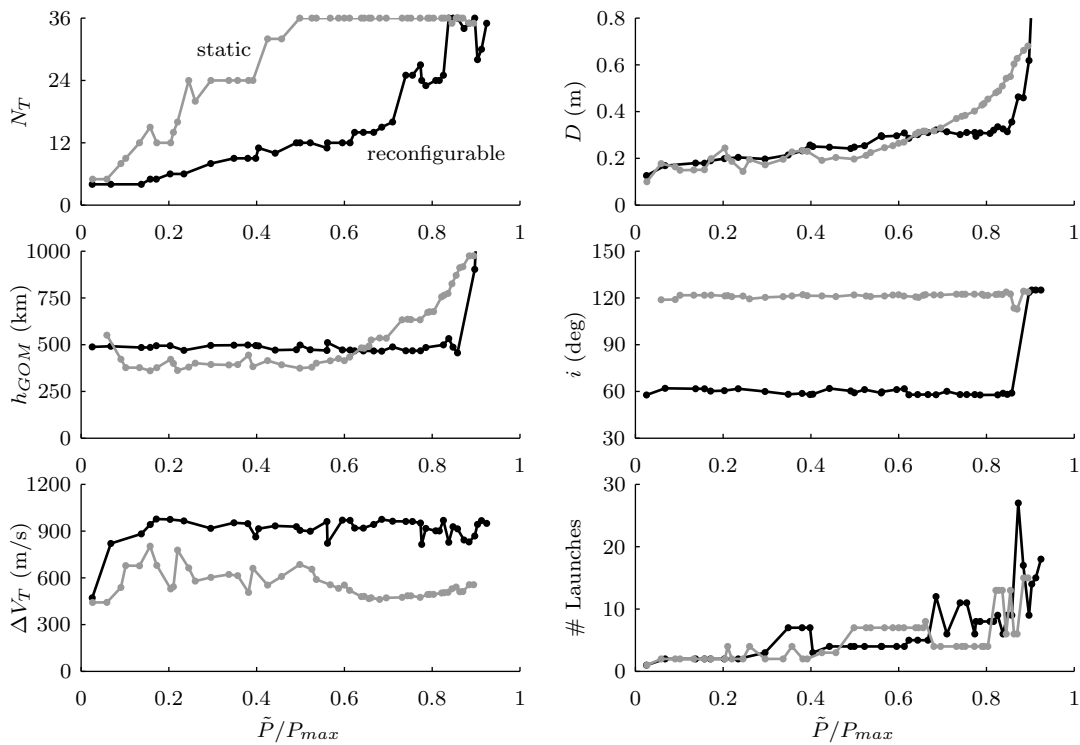
Figure 6-30: Design details for the best static and reconfigurable designs from all patterns for scenario 1 ($T = 1hr$, $X = 1m$)

non-dominated front . Reconfigurable designs also feature nearly twice the total propulsive capability of static designs in order to support reconfiguration maneuvers. The maximum propulsion system mass fraction constraint (set to 42% which corresponds to around 980 m/s using the parameters specified in Section 3.3.2) is active for many non-dominated reconfigurable designs and relaxing this constraint will likely increase the value of reconfigurability, similar to what was observed for the symmetric pattern in Section 6.1.4. Additionally, both architectures feature similar total number of launches to deploy the constellation.

6.4.1 Factors That Determine Non-Dominated Front Shape and Maximum Performance

This thesis has presented many non-dominated fronts that share the same overall shape. I now discuss some of the factors that affect front shape and determine the maximum performance achievable by reconfigurable and static designs. Each front exhibits three regions.

Starting with low-performing and low-cost designs, the non-dominated front shows a near linear increase in performance as cost increases. This transitions to a region of diminishing performance increase and the fronts then approach an asymptote where an increase in performance is not possible regardless of cost. We saw previously, in Figures 6-6 and 6-30, that the transition from the linear relationship to the diminishing returns region occurred when the maximum constellation size constraint became active. This indicates that the temporal term of the persistence metric controls both the diminishing return effect and the maximum achievable performance. This observation makes sense, given that providing coverage with a repeatable revisit time is difficult for satellites that must obey orbital dynamics. When the maximum constellation size constraint is reached, the optimizer must then increase altitude and aperture diameter at great expense in order to improve overall coverage. These greatly increased costs lead to the diminishing returns effect.

Several optimization cases were performed for scenario 1 with different maximum constellation size constraints to further investigate this effect. Figure 6-31 shows non-dominated fronts for the reconfigurable architecture with maximum constellation sizes of 12, 24, 36, and 48 satellites; and the static architecture with maximum constellation sizes of 12, 24, 36, 48, and 60 satellites. Here we see that the static architecture is significantly affected by the constellation size constraint, while the reconfigurable architecture is less affected. This difference is caused by two factors: the reconfigurable architecture uses satellites more efficiently leading to smaller constellation sizes; and, the reconfigurable architecture features controlled and predictable observation times for satellite's in ROM, which improves temporal coverage. The static architecture does not use reconfiguration to focus coverage and, therefore, must rely on uncontrolled and intermittent observations. This increases the number of satellites needed to produce a certain level of performance. Since increasing the maximum number of satellites constraint benefits the static architecture more, the value of reconfigurability changes. Figure 6-32 shows how the maximum number of satellites constraint affects the value of reconfigurability. Here we see that VoR generally decreases with increasing maximum total number of satellites. The mean VoR over the normalized performance range of $0.5 \leq \tilde{P}/P_{max} \leq 1$ is 46.7% for $N_T \leq 24$, 26.7% for $N_T \leq 36$, 14.1% for $N_T \leq 48$, and 12.2% for $N_T \leq 48$ for reconfigurable designs and $N_T \leq 60$ for static designs. Computational
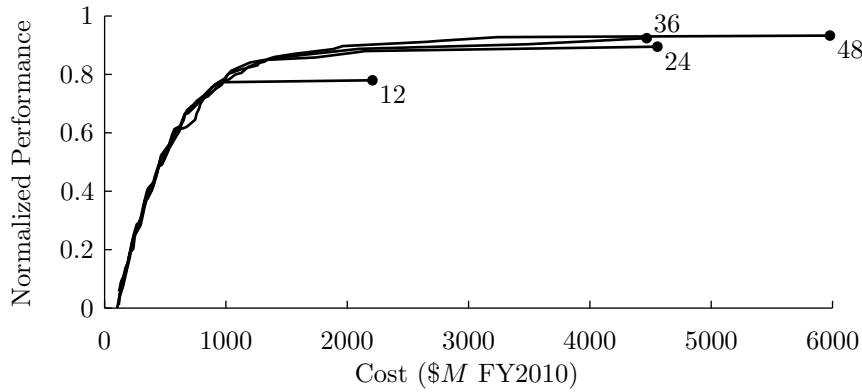
(a) Reconfigurable
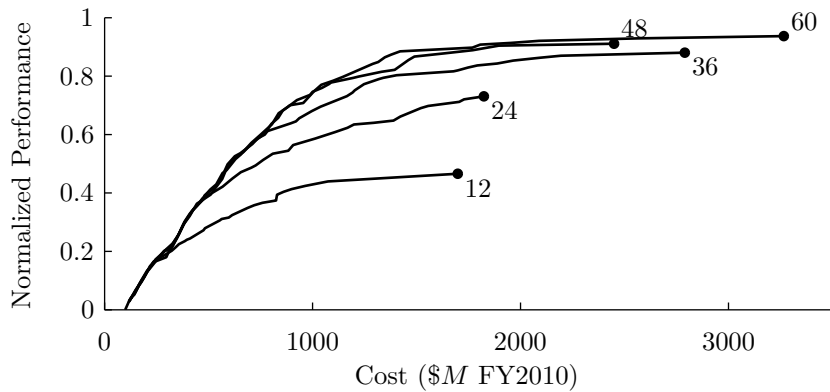
(b) Static

Figure 6-31: The maximum number of satellites constraint has a greater effect on the static architecture

constraints during reconfiguration assignment optimization limited reconfigurable designs to less than 48 satellites. It should be noted that while static designs tend to favor large constellation sizes, this may result in increased operations cost, which has not been modeled.

The asymptotes, where increasing cost stops increasing performance, is caused by two effects. First, active constraints block the optimizer from increasing constellation size and/or altitude, which prevents improvement in temporal coverage. Second, construction of the performance metric is very sensitive to temporal coverage, and when compared to the ideal performance, any coverage gaps longer than the desired revisit time results in decreased performance. For example, assuming ideal GSD, the ideal daily performance for one hour desired revisit time between 6am and 6pm is $P_{max} = 13$. To achieve this, the first observation must occur at exactly 6am, the last observation must occur at exactly 6pm, and the other
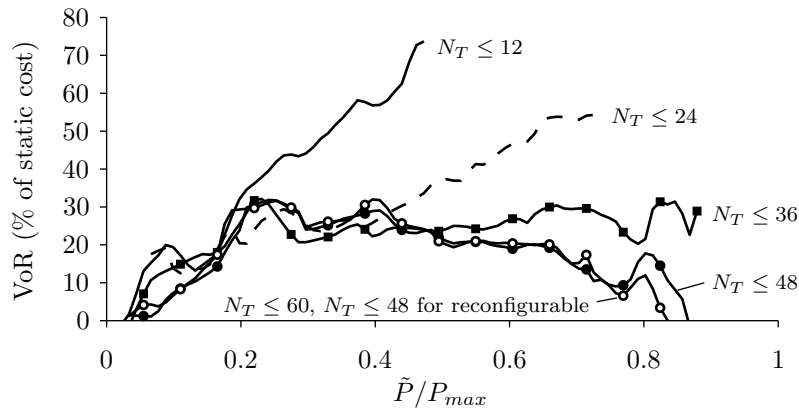
Figure 6-32: The value of reconfigurability is reduced as the maximum number of satellites constraint increases until $N_T \approx 48$.

11 observations must occur hourly on the hour. If the first observation is late or the last observation is early, the performance will decrease. If the first observation is early or the last observation is late, the performance will decrease by a large amount because these observations are outside of the viewing time window and do not generate utility. If variation with a standard deviation of only two minutes is introduced to the 13 observations, then the median normalized performance over 10,000 trials is $P/P_{max} = 0.9065$. This indicates that it is very hard to find designs that perform close to the ideal performance, and it is remarkable that the optimization process can find designs with normalized performance above 0.9.

6.5 Single Design Comparison & Sensitivity Analysis

One the optimization process is complete, stakeholders must then determine which specific design best meets their goal and objectives. Section 6.5.1 first presents some of the considerations that should be made to select the proper design using data generated during optimization. Section 6.5.2 then compares the performance of the selected reconfigurable design to the performance of an iso-cost static design for scenario 1, statistically over many target decks, over one specific target deck, and for one event response. Section 6.5.3 compares the performance and cost sensitivity for the static and reconfigurable designs to changes in model parameters. Section 6.5.4 then presents a summary of reconfigurable and iso-cost

static designs chosen using the previously described process for scenarios 2 through 4.

6.5.1 Selecting the 'Right' Design

The optimization process introduced in this thesis generates a set of non-dominated designs that simultaneously maximize performance and minimize cost. This information gives decision makers the direct tradeoff of these two primary objectives and avoids applying *a priori* weights. The next step in the process is determine which design best meets decision maker and stakeholder needs. Using the restricted asymmetric pattern optimized for scenario 1, Figure 6-33 shows several performance measures and design details for the reconfigurable architecture. The leftmost plots show several measures of performance including: the normalized performance metric, the average revisit time, the maximum revisit time, the mean response time, and the mean GSD. All performance measures, except the normalized performance, are averaged over each day (for days 4 through 14 giving the reconfigurable system time to complete the reconfiguration maneuvers) of the regional event response, then averaged over all event responses during the constellation lifetime, and then the median of this value is taken over the 96 Monte Carlo samples. The vertical bars indicate the interquartile range of the performance measure. The rightmost plots show five of the most important design details for the system including: the total number of satellites, the aperture diameter, GOM altitude, inclination, and total ΔV.

6.5.2 Comparison between Selected Reconfigurable and Iso-cost Static Design for Scenario 1

Given the information contained in Figure 6-6, decision makers must then decide the proper tradeoff between maximizing performance and minimizing cost. The vertical gray line indicates a hypothetical selection located at the 'knee' in the normalized performance curve, and matches the desired performance ($1hr$ revisit and $1m$ GSD) in terms of average revisit time, mean response time, and mean GSD. Higher cost designs improve maximum revisit time by first increasing the number of satellites and then increasing altitude and aperture diameter. Table 6.9 shows the details of the selected reconfigurable design and an iso-cost

238
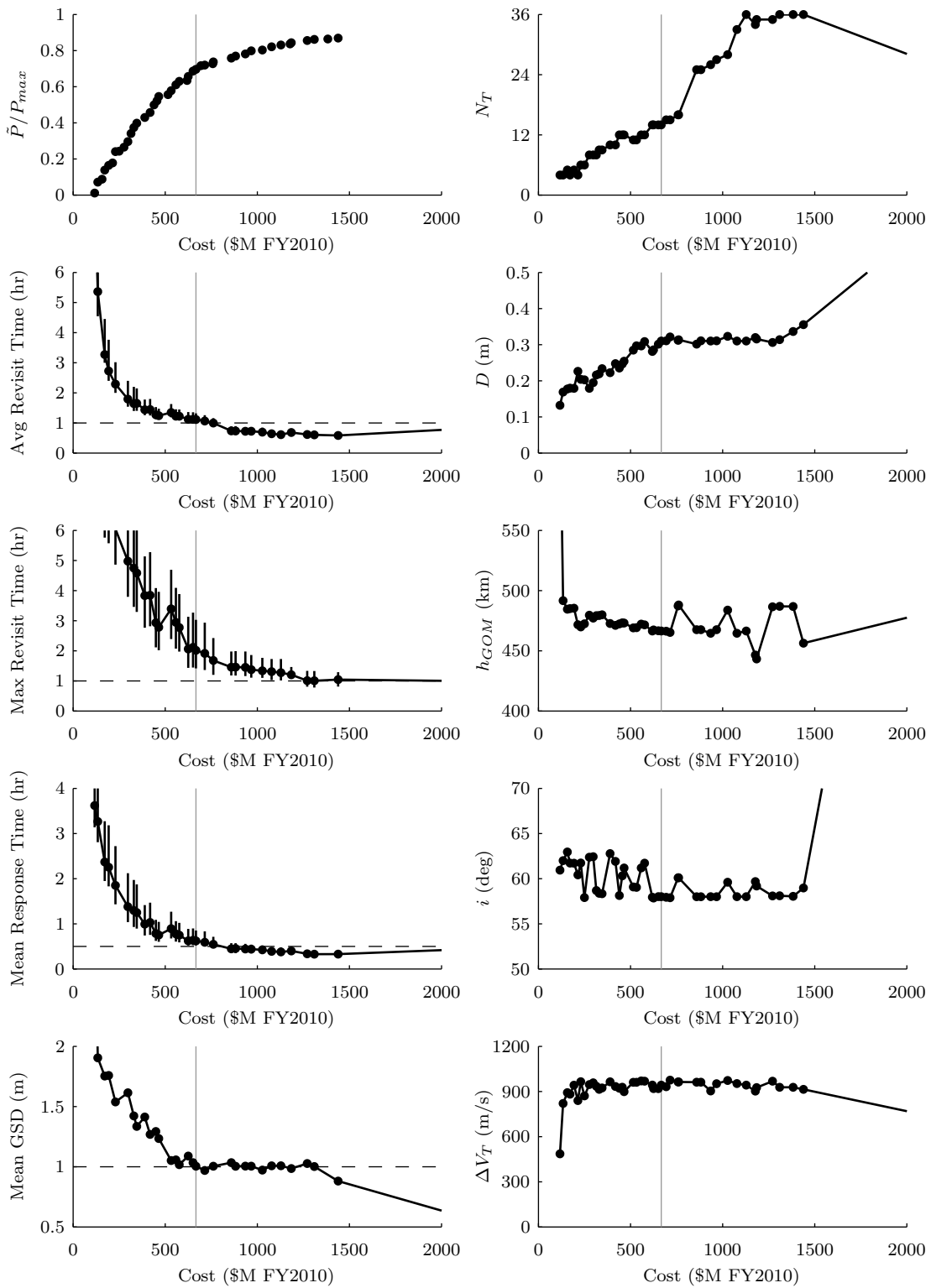
Figure 6-33: Both performance and design details can influence which design best meets stakeholder goals and objectives. The vertical line illustrates one design that balances both cost and performance.

static design using the asymmetric Walker pattern. The reconfigurable design provides better performance for all performance measures, and uses 14 higher capability satellites compared with 36 lower capability satellites for the static architecture. Figure 6-34 shows a histogram of the average performance over all event responses generated by the reconfigurable (black) and static (white) designs over 500 Monte Carlo samples.

Table 6.9: Selected reconfigurable design and iso-cost static design

	Cost $M	$\tilde{P}$ -	Avg. Revisit hr	Max Revisit hr	Mean Response hr	Mean GSD m	i deg	D m	N_T -	h_{GOM} km	ΔV_T m/s
R	666.8	122.3	1.12	2.00	0.62	1.0	58.01	0.310	14	466.5	943
S	652.7	97.7	1.65	2.99	0.93	1.18	120.92	0.225	36	401.1	590
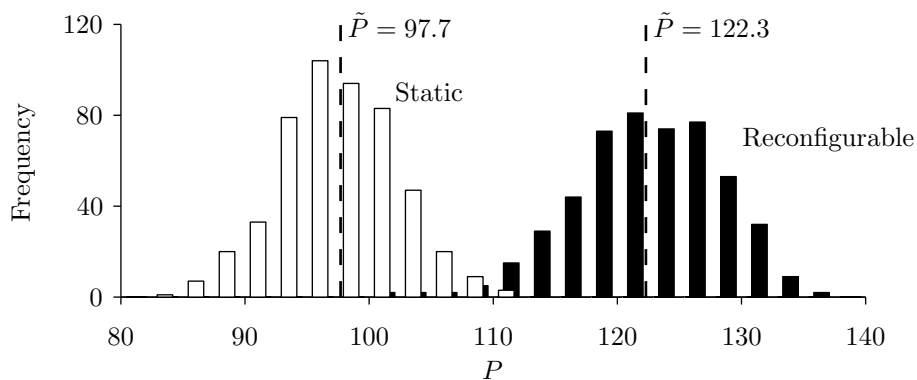
Figure 6-34: Performance distribution comparison between selected reconfigurable and iso-cost static design over 500 Monte Carlo samples

Figure 6-35 shows how the coverage provided by the two designs varied from day to day during the event response. The performance is calculated as the average daily performance over all event responses and then averaged over the 500 Monte Carlo samples. The vertical bars indicate the extent of the interquartile range averaged over all event responses and averaged over the 500 Monte Carlo samples. Here we see that the reconfigurable design initially starts off with worse temporal coverage than the static design, but provides better coverage within 2 to 4 days as reconfiguration maneuvers are completed. These results are similar to the symmetric pattern results presented in Section 6.1.2. The reconfigurable design provides significantly better spatial resolution, which improves as the spacecraft are
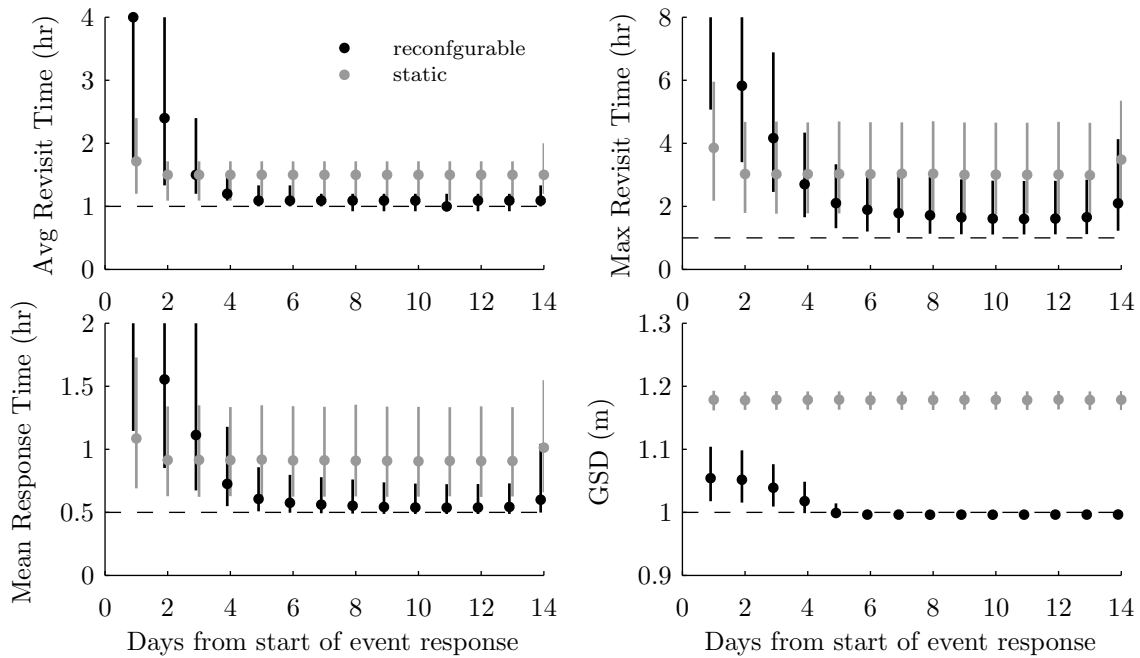
Figure 6-35: The reconfigurable design initially starts off providing worse coverage due to less than half the number of satellites as the static design. After satellites are reconfigured, the reconfigurable design significantly outperforms the static design in all four performance metrics.

reconfigured.

Figure 6-36 shows details of one specific future operating scenario. The map shows the locations for 18 events comprising the target deck. For each of the 18 events, details of the event response are provided under the map, where each row corresponds to a specific event response. The boxes indicate which of the 14 satellites remained in GOM (white) or were reconfigured (black), and the satellites are utilized frequently for this design. The ΔV_{recon} bar plot is like a fuel gauge and shows statistics of the remaining reconfiguration propellant for satellites in the constellation. The filled area indicates the interquartile range, and the horizontal lines show the min and max propellant range. The remaining propellant for the satellites stays fairly uniform due to the adaptive decision model (described in Section 3.5.5), which attempts to even out the propellant expenditure throughout the constellation. For this target deck, the constellation has significant $\Delta V recon$ capability remaining after all event responses. This is likely due to the fact that this specific target deck only has 18 events, while the average target deck will have 20 events, and some will have significantly
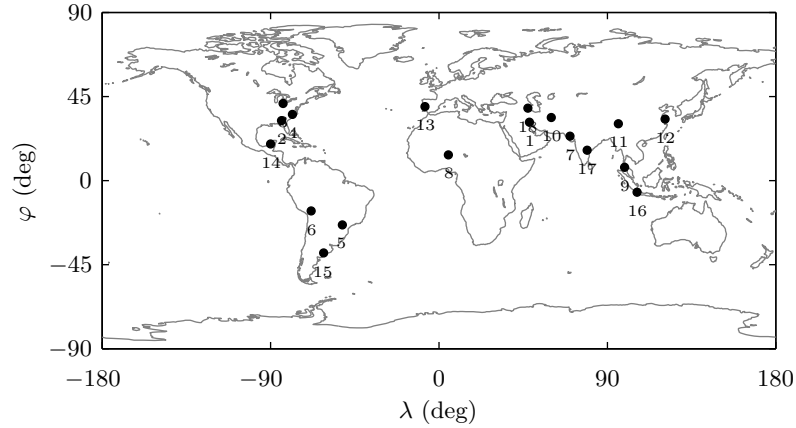
241

	Satellites Reconfigured	ΔV_{recon} Remaining	ΔV	P_E/P_{max} Recon	P_E/P_{max} Static		Satellites Reconfigured	ΔV_{recon} Remaining	ΔV	P_E/P_{max} Recon	P_E/P_{max} Static
1.			318	0.768	0.516	10.			383	0.710	0.684
2.			197	0.681	0.683	11.			207	0.563	0.487
3.			397	0.550	0.389	12.			351	0.795	0.433
4.			384	0.736	0.470	13.			188	0.477	0.398
5.			121	0.734	0.417	14.			210	0.810	0.430
6.			176	0.712	0.473	15.			231	0.779	0.700
7.			271	0.597	0.638	16.			232	0.705	0.508
8.			229	0.683	0.544	17.			230	0.721	0.497
9.			364	0.717	0.512	18.			251	0.621	0.592

Figure 6-36: Details of the reconfigurable and iso-cost static design response for a specific target deck

more. Also shown are the total constellation ΔV expenditure during event response and the performance provided by the reconfigurable and static designs. The reconfigurable design generally provides better performance with less than half of the satellites of the static design.
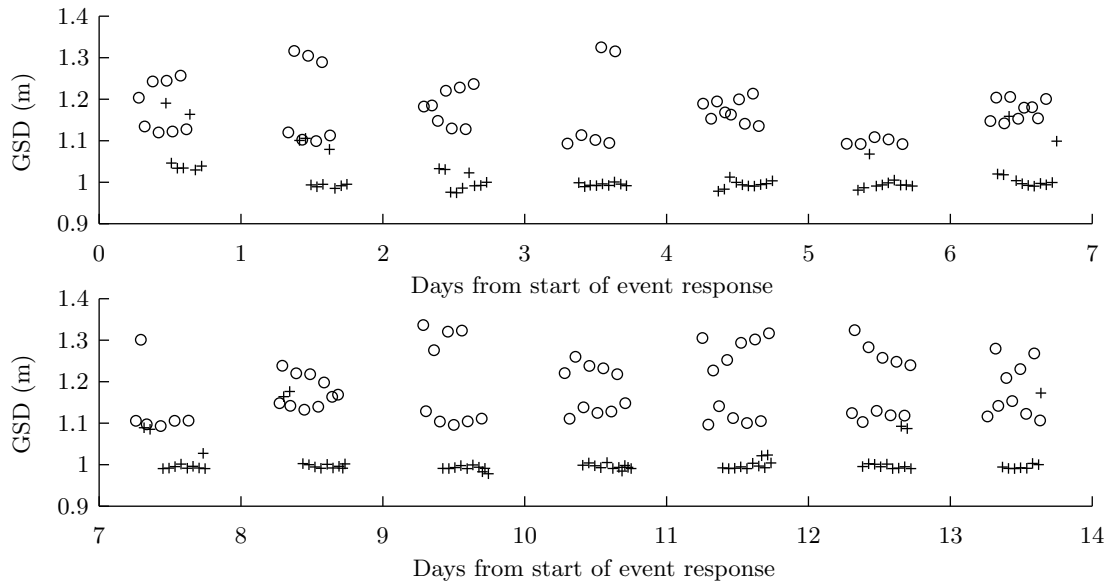
Figure 6-37: Reconfigurable designs (plotted as crosses) provide observations with better temporal and spatial resolution than iso-cost static designs (plotted as circles)

Figure 6-37 shows the coverage provided by the static (plotted as circles) and reconfigurable (plotted as crosses) designs for the 5$^{\text{th}}$ event response from Figure 6-36. Here we see that the reconfigurable design provides more repeatable coverage with significantly better and consistent GSD. For this case, the reconfigurable design provided 138 observations with a mean GSD of $1.01m$, while the static design provided 117 observations with a mean GSD of $1.18m$. During the first two days, when 11 satellites were transitioning from GOM to ROM, the GSD and frequency of observation steadily increased. In the reconfigurable case, the three satellites that remain in GOM provide the small amount of high GSD observations after day three. The static GSD is highly variable due to varying slant ranges from satellite to ground location, while the reconfigurable GSD is consistent since ROM ensures nadir viewing.

243

(a) Performance Sensitivity   (b) Cost Sensitivity
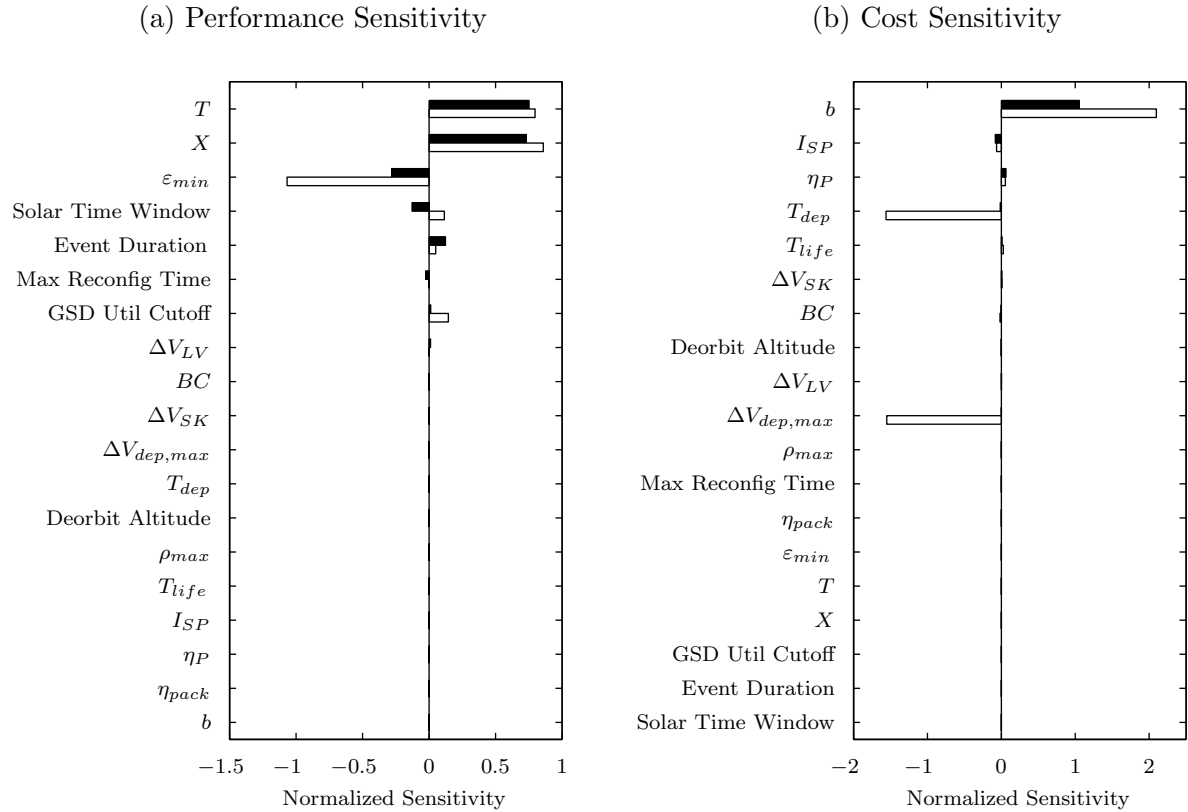
Figure 6-38: Performance and cost sensitivity to changing parameters for the reconfigurable (solid bar) and static (open bar) designs

6.5.3 Sensitivity Analysis

A parametric sensitivity analysis was conducted to quantify the sensitivity of performance and cost to changing parameter values. 96 Monte Carlo samples were performed for the reconfigurable and static designs selected in the previous section (details provided in Table 6.9), while varying nineteen parameters. The sensitivity was then normalized as a percent change in the objectives (cost and median performance) to a percent change in parameter value. This allows for the comparison of the relative sensitivity of all parameters. Figure 6-38 shows the sensitivity for median performance (left) and cost (right). The parameters are listed in order of decreasing reconfigurable design sensitivity. Positive sensitivity values indicates positive correlation, where increasing the parameter value increases the objective value. The figure shows that, for the reconfigurable design, performance is most sensitive to the spatial (X) and temporal (T) resolution, and that increasing the desired resolution

significantly increases performance. The static design is also sensitive to these parameters, but is most sensitive to the minimum ground elevation angle (ε_{min}) parameter. Decreasing ε_{min}, significantly increases the satellite ground footprints, and leads to vastly improved coverage, and, therefore, performance for the static design. The reconfigurable design is much less sensitive to ε_{min} because the reconfigurable architecture ensures nadir passes in ROM. However, there is still some sensitivity because satellites remaining in GOM see improved coverage with smaller ε_{min}. Interestingly, increasing the solar time window leads to increased performance for the static designs and decreased performance for the reconfigurable design.

In terms of cost sensitivity, both designs are most sensitive to the learning curve factor (b), and increasing b lessens learning curve cost savings, which leads to larger cost. The static design is more sensitive since it feature more than twice as many satellites as the reconfigurable design. The static design is also very sensitive to the deployment time (T_{dep}) and maximum deployment ΔV ($\Delta V_{dep,max}$). This is likely caused by a situation in which, the static design could utilize fewer launch vehicles by increasing either T_{dep} or $\Delta V_{dep,max}$ by a small amount.

6.5.4 Comparison between Selected Reconfigurable and Iso-cost Static Design for Scenarios 1 through 4

Table 6.10 shows a comparison between a selected reconfigurable design and an iso-cost static design for scenarios 1 through 4. The reconfigurable design for scenarios 2 through 4 were selected that balances performance and cost using the process outlined previously in Section 6.5.2. Here we see that reconfigurable designs typically feature smaller constellations with larger, more capable satellites, while static designs feature larger constellations with smaller, less capable satellites. The reconfigurable designs provide better performance in all performance measures than iso-cost static designs.

245

Table 6.10: Properties of selected reconfigurable and iso-cost static designs for scenarios 1 through 4

	Scenario 1 (1hr,1m)		Scenario 2 (1hr,0.5m)		Scenario 3 (0.5hr,1m)		Scenario 4 (0.5hr,0.5m)	
	R	S	R	S	R	S	R	S
Total Cost ($M)[†]	666.8	652.7	1131	1166	1005	1015	2201	2275
Satellite Cost ($M)[†]	27.8	13.4	60.5	27.7	22.9	16.6	51.5	40.3
Launch Cost ($M)[†]	277	170.3	283.8	170.3	340.5	220.3	397.3	340.5
$\tilde{P}/P_{max}$	0.672	0.537	0.629	0.489	0.711	0.459	0.732	0.470
Avg. Revisit (hr)	1.12	1.65	1.12	2.07	0.55	0.88	0.49	0.99
Max Revisit (hr)	2.00	2.99	2.14	4.96	1.49	4.22	1.15	3.15
Mean Response (hr)	0.62	0.93	0.64	1.49	0.35	1.03	0.30	0.82
Mean GSD (m)	1.00	1.18	0.54	0.62	1.01	1.37	0.52	0.59
h_{GOM} (km)	466.5	401.1	469.3	356.0	476.5	577.9	490.2	496.1
i (deg)	58.0	120.9	58.1	121.3	61.8	122.6	59.1	119.9
N_T	14	36	14	36	29	48	35	48
ξ_Ω	0.61	0.44	0.58	0.38	0.60	0.34	0.75	0.40
D (m)	0.31	0.225	0.57	0.38	0.31	0.28	0.61	0.56
ΔV_T (m/s)	943	590	866	812	937	455	948	396
M_W (kg)	435	251	1038	536	432	289	1208	759
Launch Vehicles*	1c,4d	3d	5d	3d	6d	1c,3d	7d	6d

[†] Cost in FY2010 dollars

* a-Pegasus XL, b-Athena Ic, c-Minotaur IV, d-Falcon 9, e-Falcon Heavy

6.6 Comparison with Sun Synchronous and Rapid Launch Architectures

Several other constellation architectures have been proposed to provide space-based persistent surveillance. In this section, I compare the cost-effectiveness of the reconfigurable and static architectures to the cost-effectiveness of a polar sun-synchronous constellation architecture and a rapidly launched architecture. In order to perform a meaningful comparison, the constellation optimization framework developed in this thesis was also applied to optimize both the SSO and rapid launch architectures. Sections 6.6.1 and 6.6.2 introduce the two architectures and provide details on how they were modeled and optimized. Section 6.6.3 presents a comparison of the non-dominated fronts for the reconfigurable, static, SSO and rapid launch architectures.

6.6.1 Sun Synchronous Constellation

Many existing Earth observing spacecraft utilize near polar sun-synchronous orbits. Sun-synchronous orbits (SSOs) preserve the orientation of the orbital plane with respect to the Sun by matching orbital precession with the Sun's apparent motion. This allows for the satellites to provide imagery with consistent ground illumination conditions. The compatibility condition is given as:

$$\dot{\Omega} = \frac{360°}{T_s} \tag{6.8}$$

Where $\dot{\Omega}$ is the rate of change of Ω due to orbital precession in degrees per day (given in Equation 3.3) and T_s is the length of the sidereal year in days. SSOs effectively sacrifice the amount of coverage provided by the satellites in order to maintain consistent solar illumination. A satellite in an SSO will provide coverage for up to two times during the day, one for the ascending pass and one for the descending pass, and these times are given by Equation 3.13. Typically, SSO satellites provide coverage within a few hours of local noon to provide good illumination conditions and reduce ground shadows. SSO satellites are described by the local time of coverage provided. For instance, the WorldView-2 currently resides in a $770km$ SSO with 10:30am (local time) descending node coverage[2], while the Worldview-3 satellite planned for launch in 2014 will use a $617km$ SSO with 1:30pm (local time) descending node coverage[3].

A single SSO satellite can provide global coverage (with a potential small gap at the poles) with a revisit time of several days. The revisit time is largest at the equator and diminishes with increasing latitude. Increasing the satellite ground footprint, caused by increasing altitude or decreasing the minimum ground elevation angle, also improves revisit time, and multiple satellites can be deployed in a constellation to improve this revisit time. In order to provide coverage with the same local time, these satellites must have common Ω. Then, the relative spacing in M then defines the spacing between consecutive pass ground swaths. Figure 6-39 shows a single pass ground swath for three satellites in a $500km$ SSO

---

[2]WorldView-2 Datasheet, http://www.satimagingcorp.com/satellite-sensors, Accessed: 05-7-2014
[3]WorldView-3 Datasheet, http://www.satimagingcorp.com/satellite-sensors, Accessed: 05-7-2014
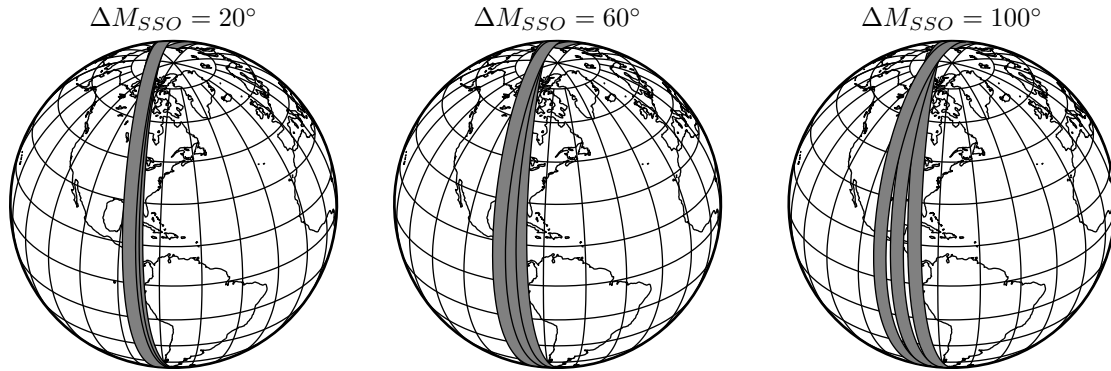
Figure 6-39: The difference in mean anomaly between satellites in a common SSO plane controls the separation of the ground tracks

as a function of the mean anomaly separation. As the mean anomaly separation increases, the swaths move apart. This effect is caused by the increased amount of time between satellite passes coupled with the Earth's rotation underneath the satellite's orbit plane. The minimum number of satellites required for daily coverage is determined by finding the maximum permissible M spacing without creating coverage gaps at the equator, given by the following relation:

$$\Delta M_{max} = \frac{2\lambda}{\omega_\oplus}n \tag{6.9}$$

Where λ is the Earth central angle of the ground footprint and n is the mean motion. In the case of a $500km$ SSO with a minimum ground elevation angle of $60°$, $\Delta M_{max} = 72.15°$. When the actual M spacing is larger than ΔM_{max}, there will be gaps in coverage between adjacent satellite ground swaths as shown in the rightmost plot in Figure 6-39.

The ΔM_{max} calculation also specifies the minimum number of satellites needed in a single plane to ensure that the constellation provides daily coverage. Basically, there needs to be satellites populating the entire M range of $0 \rightarrow 360°$ with a maximum satellite spacing in M of less than ΔM_{max}. This means that the minimum number of satellites is then $\lceil 360°/\Delta M_{max} \rceil$, where $\lceil \cdot \rceil$ is the ceiling function. For the example above, the minimum number of satellites is 5, since $(360°/72.15) \approx 4.99$. Figure 6-40 shows the effect of not having this minimum number of satellites. The leftmost plot shows the coverage provided
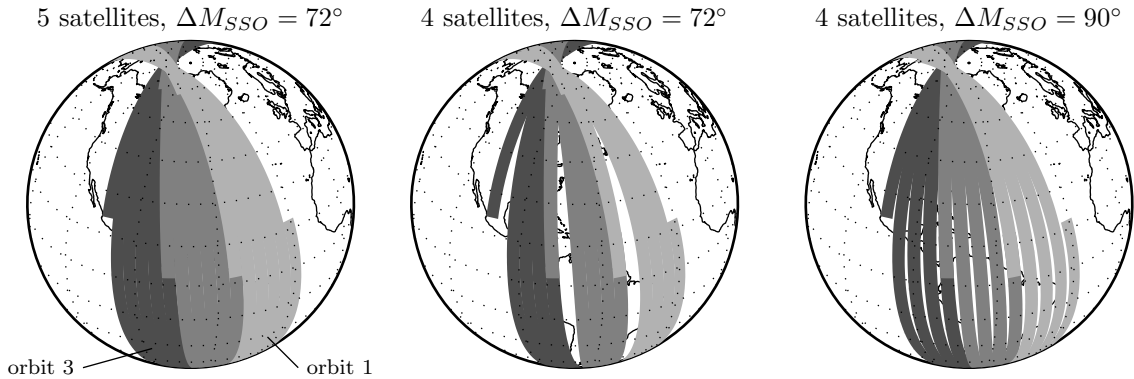
Figure 6-40: The number and spacing of satellites in a SSO plane determines if there are daily coverage gaps

by five satellites with $\Delta M_{SSO} = 72°$ over three consecutive orbits shaded differently. Here we see that there are no coverage gaps between adjacent orbits and therefore coverage will be provided twice a day (one on the ascending pass and one on the descending pass). The center plot shows the case where only four satellites are in the constellation, but the spacing remains at $\Delta M_{SSO} = 72°$. Here we see that the missing satellite causes one large coverage gap per orbit cycle, and therefore, coverage will not be provided every day. The right plot shows what happens if there are only four satellites, but the spacing is changed to provide uniform spacing in M, giving $\Delta M_{SSO} = 90°$. Here we see that the large coverage gap is replaced by several small coverage gaps, and will not be guaranteed everyday. One example of an SSO constellation is the planned SkyBox constellation which will consist of 24 satellites[4] in four orbital planes at $500km$ altitude[5] providing $0.9m$ GSD coverage 4-5 times a day with a per satellite design, build, and launch cost of \$50M[6].

The constellation design and optimization methodology was also used to optimize SSO constellations for persistent surveillance allowing for a direct comparison with static and reconfigurable designs. The SSO constellation design space consists of four design variables as shown in Table 6.11. The inclination is determined from the altitude by solving Equation

---

[4]Henry, Caleb., "Skybox Imaging Exec Discusses Constellation Plans", Via Satellite, 02-11-2014 http://www.satellitetoday.com, Accessed: 05-7-2014

[5]Ferster, Warren "News from Satellite 2014 — To Provide Propulsion for Skybox Satellite Fleet", SpaceNews, 03-11-2014, http://spacenews.com/article/financial-report/39822news-from-satellite-2014-to-provide-propulsion-for-skybox-satellite, Accessed: 08-10-2014

[6]Perry, Tekla S. "Start-up Profile: Skybox Imaging", IEEE Spectrum article, 05-01-2013, http://spectrum.ieee.org/at-work/innovation/startup-profile-skybox-imaging, Accessed: 08-10-2014

Table 6.11: SSO constellation design variables

#	Variable Name	Symbol	Type	Bounds
x_1	Altitude	h	cont.	300 to 1000 km
x_2	Aperture size	D	cont.	0.1 to 1.2 m
x_3	Number of planes	N_p	int.	1 to 36
x_4	Number of satellites per plane	N_{sp}	int.	1 to 36

6.8, and the mean anomaly spacing in each orbital plane is determined as follows. If there are enough satellites to ensure no coverage gaps (i.e. $N_{sp} \geq \lceil 2\pi/\Delta M_{max} \rceil$), then $\Delta M = 2\pi/N_{sp}$. If there are not enough satellites to ensure no coverage gaps (i.e. $N_{sp} < \lceil 2\pi/\Delta M_{max} \rceil$), then $\Delta M_{SSO} = \Delta M_{max}$. Since Ω determines the local time of coverage for each plane, Ω is set for the N_p orbital planes to distribute the local time of coverage evenly throughout the target's local time window constraint, which is set to 6am to 6pm for all events in this thesis (see Section 4.2.3 for more details). Therefore, if $N_p = 5$, then the five orbital planes are set to provide pass times of 8am, 10am, 12pm, 2pm, and 4pm.

6.6.2 Rapidly Launched Satellites

Rapidly launching satellites in times of need has been proposed as an alternative strategy for providing responsive space-based surveillance. This concept involves quickly integrating and launching satellites that have been stored on the ground. Proponents of this strategy point to several benefits. One benefit is that satellites stored on the ground will degrade much slower than those stored in space, thereby giving each satellite a longer period of capability. Also, each satellite can be treated as single-use only, which reduces the need for highly reliable parts and should reduce cost. Another benefit is that satellites can be placed in an orbit that maximizes coverage to the region of interest. However, there are downsides to this concept as well. Integrating and launching satellites on the order of days or even weeks has proved very difficult with current technology, and the number and availability of launch facilities is currently also a limiting factor. There is also the problem of providing coverage for subsequent regional event responses. Since the satellite was placed in an orbit to maximize coverage for the first event, the satellite will likely provide poor or even no coverage for another event. Third, each satellite needs a dedicated launch vehicle to quickly

Figure 6-41: The repeat coverage orbit, where inclination is matched to the target latitude, can provide coverage on successive orbits

place each satellite into different orbit planes to provide coverage spread out in time, which further increases the cost of the concept.

The rapid launch strategy investigated in this thesis considers a system that will provide coverage to regional events by placing satellites into LEO Repeat Coverage Orbits (RCO), which have been proposed as way to provide periodic persistent surveillance by Wertz [218]. The RCO is a LEO orbit with the inclination set a little higher than the target latitude. This allows the satellite to provide coverage during a period of successive orbits which repeats daily. Figure 6-41 shows the coverage provided by a satellite in an RCO orbit over three consecutive passes in the Earth fixed coordinate frame. The relative rotation of the satellite's orbit is caused by a combination of Earth's rotation and orbital precession affecting Ω.

The constellation design and optimization methodology was also used to optimize the rapid launch architecture in order to compare its cost-effectiveness to the other architectures studied in this thesis. I consider a system that is capable of launching up to four satellites for each event response. Optimistic values for launch cost and responsiveness were used to represent potential future capability. The launch time (time from the start of the event response to placement of the satellite into its final orbit) was set to 24 hours and the cost of each launch was set to $10M FY2010. Despite these very optimistic assumptions for

251

responsiveness and cost, we will see that the rapid launch architecture performs poorly when compared to both the reconfigurable and static architectures. This indicates that the rapid launch architecture is not a cost-effective solution for providing responsive persistent surveillance for multiple events distributed geographically. The satellites in the rapid launch architecture are spread out in Ω based on how many satellites will be launched for each event and are distributed uniformly in M. The first satellite is set to have its last pass of the day be at 4:00pm local time, ensuring that the first pass of the day (assuming three passes covering the target per day) will be around 11:30am. Since we are only considering prograde orbits, this time of pass will shift earlier for every day during the event response; therefore, it is desirable to start off providing coverage towards the end of the time window. If additional satellites are launched for the event response, then they are separated in Ω in order to fill in the time gaps. If two satellites are launched to respond to an event, the 2$^{\text{nd}}$ satellite will be placed to have its last pass of the day half of the orbit period earlier than the first satellite at approximately 3:15pm local time. This will give coverage roughly every 45 minutes from 10:45am to 4:00pm which will shift earlier by around 20 minutes per day (see Section 3.1.2 for more details). For four total satellites, there could be coverage every 23 minutes from 10:23am to 4:00pm. Additionally, the satellites remain in orbit to provide coverage for later events.

The rapid launch architecture design space consists of five design variables as shown in Table 6.12. The inclination offset design variable specifies the difference between the target latitude and the inclination using the following relation:

$$i = \varphi + \Delta i \times \lambda \tag{6.10}$$

Where φ is the event latitude and λ is the Earth central angle of the satellite ground footprint (see Section 3.1.3 for more details on Earth observation geometry). Therefore, the Δi design variable allows the inclination to vary from $\varphi - \lambda$ to $\varphi + \lambda$.

Table 6.12: Rapid Launch constellation design variables

#	Variable Name	Symbol	Type	Bounds
x_1	Altitude	h	cont.	300 to 1000 km
x_2	Aperture size	D	cont.	0.1 to 1.2 m
x_3	Total number of satellites	N_T	int.	1 to 36
x_4	Number of satellites per event response	N_E	int.	1 to 4
x_5	Inclination offset	Δi	cont.	-1 to 1

6.6.3 Non-dominated Front Comparison

Figure 6-42 shows the non-dominated fronts for the combined reconfigurable, combined static, SSO, and rapid launch architectures for scenarios 1-4. The reconfigurable architecture completely dominates the static, SSO and rapid launch architectures, except for the very low performance region where the rapid launch architecture is most cost-effective.

Given that SSO constellations are nearly a subset of the asymmetric walker pattern, it is not surprising that the static architecture dominates SSO architecture. The orbit planes are spaced close together and the inclination and altitude are set to satisfy the sun-synchronous condition in the SSO pattern. The only difference between the two patterns is in how the satellites are distributed in M within each orbit plane. The SSO pattern spaces the satellites in M to ensure no coverage gaps in successive satellite passes and the Walker pattern evenly distributes satellites in M. If there are enough satellites per orbit plane to ensure no coverage gaps, then the SSO pattern evenly distributes satellites in M similar to the Walker pattern. Shrinking the design space available for optimization can have different effects on the quality of the final non-dominated fronts. If the removed portion of the design space does not contain efficient designs, then the final non-dominated front is not affected, and the final front can even be better since the optimization process will have an easier time converging in the smaller design space. If the removed portion of the design space does contain efficient designs, then the final non-dominated front will be affected, since the optimization process will not be able to identify those designs. For the SSO pattern, the reduced design space eliminates efficient designs causing the SSO non-dominated front to be outperformed by the asymmetric Walker pattern.

Two primary factors reduce the effectiveness of SSO patterns for providing persistent

(a) Scenario 1: $T = 1hr$, $X = 1m$

(b) Scenario 2: $T = 1hr$, $X = 0.5m$

(c) Scenario 3: $T = 0.5hr$, $X = 1m$

(d) Scenario 4: $T = 0.5hr$, $X = 0.5m$
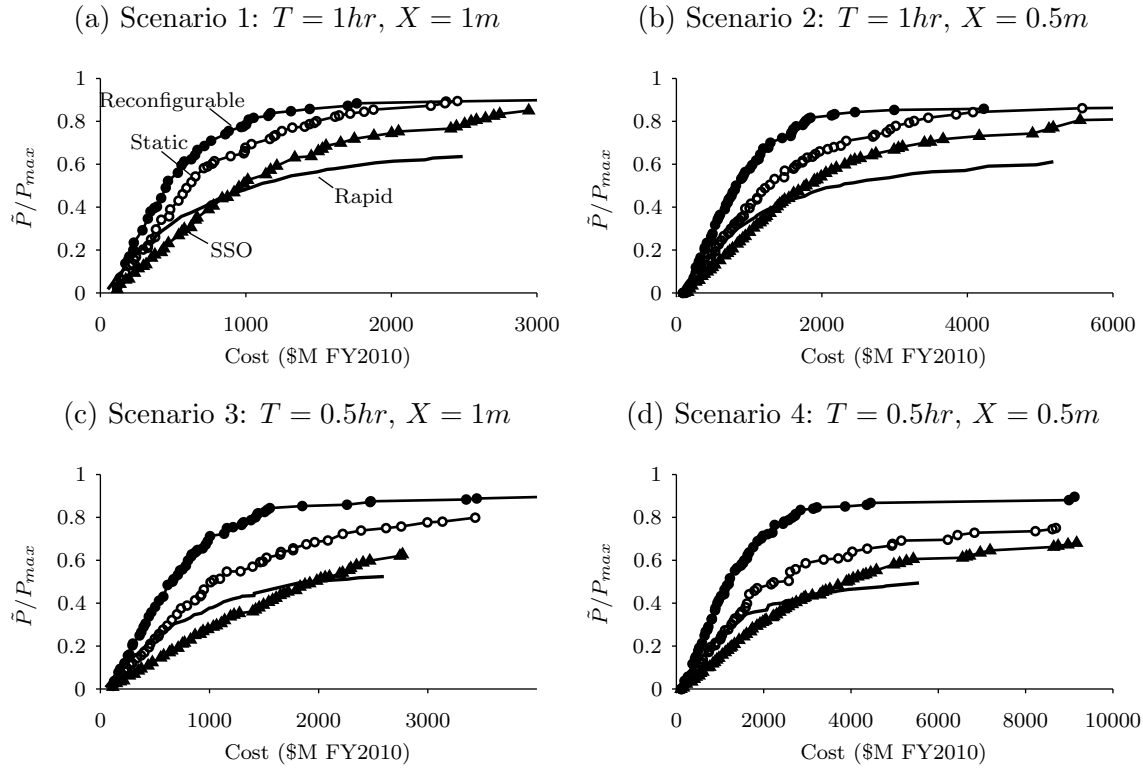
Figure 6-42: Both the reconfigurable and static architectures are more cost-effective than the SSO and rapid launch architectures are

surveillance. The near polar inclination increases launch cost due to lack of ability to conduct plane changes during deployment, and the near polar inclination means that the SSO pattern does not benefit from the coverage amplification for inclinations close to event latitude. Despite the poor cost-effectiveness provided by the SSO pattern, this architecture ensures imaging with nearly constant solar illumination. However, any constellation that provides persistent surveillance with short coverage gaps will provide daily imaging with similar solar illumination. As an example, Figure 6-43 shows the coverage provided by a reconfigurable constellation, and static constellation and a SSO constellation drawn from the non-dominated fronts shown in Figure 6-42a with similar total cost. The dots indicate each time the event $(\varphi = 30°, \lambda = -70°)$ is imaged between $6am$ and $6pm$ local time over the 14 day event duration.

The reconfigurable constellation[7] features 16 satellites in a restricted asymmetric pattern

---

[7]$N_o/N_d = 15/1$, $\Delta alt = 12.05km$, $i = 60.1°$, $N_T = 16$, $D = 0.314m$, $\Delta V_{recon} = 500.9m/s$, $\alpha_0 = 0.004$, $\xi_\Omega = 0.65$, $\Delta M = 294°$
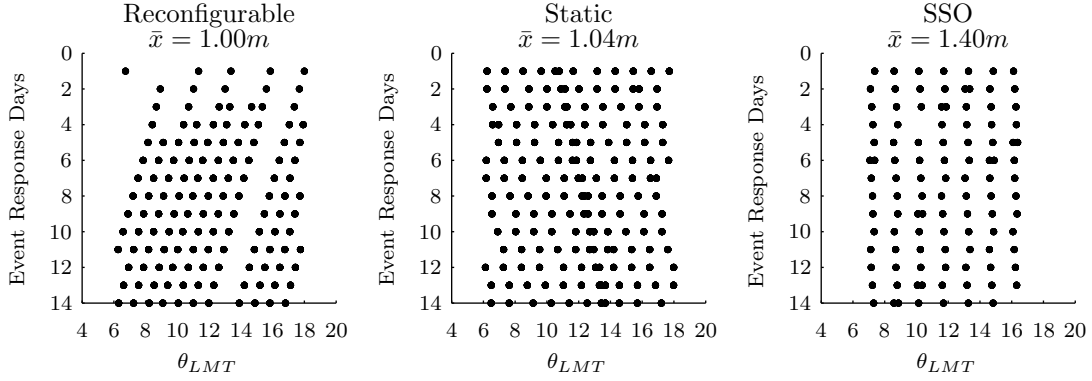
Figure 6-43: Daily coverage comparison between iso-cost reconfigurable, static, and SSO designs. The reconfigurable architecture provides coverage that is better matched to the desired temporal and spatial resolution

and provides coverage nearly every hour with an average GSD of $1.00m$ with a total normalized performance of $\tilde{P}/P_{max} = 0.71$ and a total cost of $C = \$761M$. The static constellation[8] features 36 satellites in as asymmetric Walker pattern with a total normalized performance of $\tilde{P}/P_{max} = 0.60$ and a total cost of $C = \$770M$. Despite having more than twice the total satellites, due to bunching of observations and a higher average GSD of $1.04m$, the static design performs worse than the reconfigurable constellation. The SSO constellation[9] features 35 satellites in an asymmetric Walker pattern with a total normalized performance of $\tilde{P}/P_{max} = 0.41$ and a total cost of $C = \$777M$. The SSO constellation costs more that both the reconfigurable and static constellations and performs far worse. The SSO constellation utilizes satellites inefficiently, and, despite having almost the same number of satellites as the static constellation, it provides far fewer coverage periods with much worse average GSD of $1.40m$. The SSO constellation provides nearly constant solar illumination for each of the seven orbit planes, as indicated by the vertical lines of observations, but both the static and reconfigurable constellations provide far more observations and the time difference between daily observations is small. Therefore, the primary benefit of SSO constellations is negated by the greater efficiency of both the static (using non-polar inclined orbits) and reconfigurable architectures.

Despite optimistic assumptions (\$10M FY2010 launch cost and a $24hr$ response time

---

[8] $h_{GOM} = 414.8km$, $N_p = 9$, $N_{sp} = 4$, $i = 122.1°$, $D = 0.265m$, $F = 5$, $\xi_\Omega = 0.44$
[9] $h_{GOM} = 452.9km$, $D = 0.213m$, $N_p = 7$, $N_{sp} = 5$

between event notification and satellite placement into RCO), the rapid launch architecture exhibits poor overall cost-effectiveness, except in the low performance region of the non-dominated front. This is due to not having a GOM maximum revisit time constraint which lower the 'entry cost' for rapid designs. The poor cost-effectiveness is caused by inefficient satellite utilization. Rapid launch designs launch satellites into an orbit with an inclination just above the event latitude to provide good event coverage. While the satellite provides efficient coverage for the current event, it will likely provide poor or no coverage for subsequent events.

6.7 Retaining Satellites in GOM

All of the results presented in the previous sections have assumed that all of the satellites in the reconfigurable constellation can be reconfigured to provide coverage for the current event. However, some situations may limit the number of satellites that a decision maker would want to commit to a single event response. The decision maker might want to preserve some level of partial global coverage during an event response, or might want to leave satellites in GOM, as a reserve, in case a second simultaneous event were to occur. While this is not the focus of this thesis, I have investigated how limiting the total number of satellites available to respond to each event changes the non-dominated design front. An additional parameter (ξ_R), representing the fraction of the total satellites in the constellation that are available for reconfiguration, was added to the simulation model. The maximum number of satellites that can be reconfigured is then equal to $\lceil N_T \xi_R \rceil$. Using this construction, $\xi_R = 1$ represents a fully reconfigurable designs, and $\xi_R = 0$ represents a static design. ξ_R values in between 0 and 1 should then yield non-dominated fronts in between the reconfigurable and static non-dominated fronts.

Figure 6-44 shows the non-dominated fronts for six ξ_R values using the restricted asymmetric pattern. Here we see that as ξ_R increases, the resulting non-dominated front sweeps from the static front to the reconfigurable front. Therefore, the value of reconfigurability drops as constraints are placed on the number of satellites that are allowed to reconfigure to support event response. Future work should investigate other ways to to incorporate the
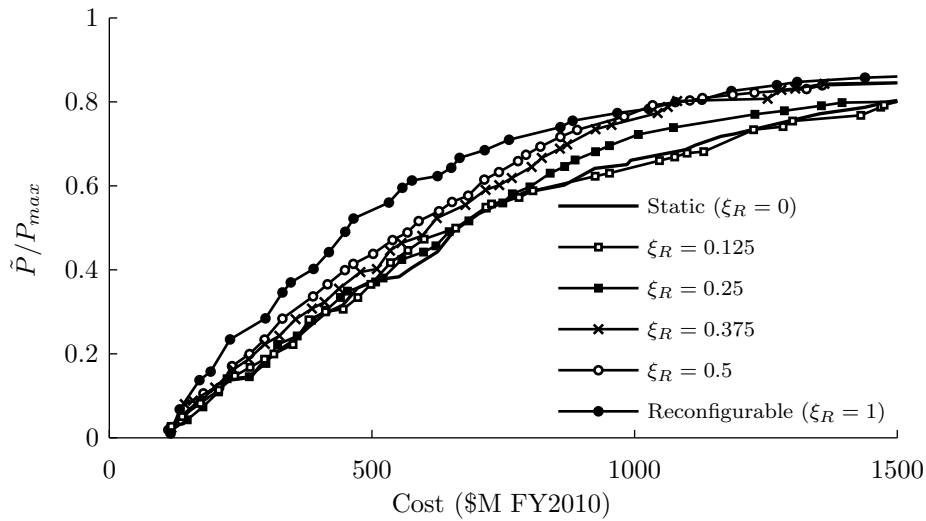
Figure 6-44: As the maximum number of satellites allowed to reconfigure for each event (expressed as a fraction of the constellation size) is reduced, the non-dominated front sweeps from the fully reconfigurable front to the static front

secondary objectives of maintaining partial global coverage and reserving satellites for a second simultaneous event response. One possible avenue to pursue would modify the satellite assignment optimization problem to consider the reduction in partial global coverage caused by maneuvering individual satellites into ROM.

6.8   Results Summary

This chapter has demonstrated that the constellation design and optimization framework introduced in this thesis can successfully find efficient constellation designs for a wide variety of system architectures and constellation patterns. Section 6.1 showed that, using symmetric patterns, reconfigurable constellations cost 20 to 70% less than iso-performance static constellations. This reduction in cost increases with increasing coverage requirements (temporal and spatial resolution), and when compared to static constellations, reconfigurable constellations provide increased cost-effectiveness over a wide range of parameter values. Section 6.2 showed that a layered pattern increases the cost-effectiveness of static constellations by around 10%, but does not increase the cost-effectiveness of reconfigurable constellations due to the loss in Ω phasing between satellites caused by differential orbital precession.

Section 6.3 illustrated that, when compared to symmetric or layered patterns, asymmetric patterns improve the cost-effectiveness of both reconfigurable and static constellations. Optmization using a fully-asymmetric pattern improved cost-effectiveness primarily due to asymmetric placement of orbit planes in Ω. This observation led to the development of two 'quasi'-asymmetric patterns that allow asymmetric placement of orbit planes in Ω, but impose regular spacing in Ω and M to reduce the number of design variables and improve optimization convergence. Section 6.4 showed that the restricted asymmetric pattern provides the most cost-effective reconfigurable designs and the asymmetric Walker pattern provides the most cost-effective static designs. Using these 'quasi'-asymmetric patterns, reconfigurable constellations were found to cost 20% to over 70% less than iso-performance static constellations.

Section 6.5 showed that reconfigurable designs provide better performance, in terms of all traditional performance metrics, than iso-cost static designs, and that reconfigurable designs tend to feature smaller constellation sizes with larger, more capable satellites, while iso-cost static designs tend to feature larger constellation sizes with smaller, less capable satellites. Section 6.6 compared the best static and reconfigurable designs to optimized sun-synchronous and rapid launch designs. The results show that these other traditional architectures are significantly less cost-effective than reconfigurable or even static architectures. Section 6.7 looked at how restricting the number of satellites available to respond to a single event affects the non-dominated front for the reconfigurable architecture. This analysis found that as the maximum number of satellites available for reconfiguration constraint decreases, the cost-effectiveness of the reconfigurable architecture decreases.

Chapter 7

Conclusions and Future Work

This thesis presents a new approach to designing and operating satellite constellations. By incorporating the flexible option of satellite reconfiguration, the ReCon concept improves system cost-effectiveness and gives operators the ability to change the system to respond to uncertain future conditions. This thesis introduces several tools to aid in the design, optimization, and operation of reconfigurable satellite constellations. The following section provides a brief summary of the work presented in this thesis. Section 7.2 lists specific contributions made to the field, Section 7.3 details the general conclusions drawn from this thesis, and Section 7.4 identifies several topics that should be considered in future research.

7.1   Thesis Summary

This thesis presents a new approach to providing cost-effective space based regional persistent surveillance, and introduces a framework to guide the design and optimization of these reconfigurable satellite constellations. Chapter 1 presents a comprehensive literature review that details the many flaws of conventional approaches to satellite constellation design. Chapter 2 then introduces the new proposed approach that avoids these flaws by widening the design space, explicitly considering uncertainty in future operating context, and utilizing state-of-the-art parallel computing resources to identify cost-effective reconfigurable (and static) designs. Chapter 3 explains the implementation of the detailed multidisciplinary simulation model, which computes the performance and cost of many different satellite constellation

architectures using varied constellation patterns. The simulation model balances the need for a detailed model that captures the coupling between system elements with the need for simulation efficiency. Chapter 4 presents the uncertainties considered in this thesis and the Monte Carlo simulation approach, which maps distributions of uncertain parameters to a distribution of constellation performance. Chapter 5 presents a novel multi-objective optimization algorithm that incorporates several state of the art multi-objective optimization techniques and is implemented on a large parallel computing cluster. Chapter 6 presents optimized reconfigurable and static constellation design, obtained using the developed satellite constellation design and optimization framework, and showed that reconfigurable designs cost 20 to 70% less than iso-performance static designs. Additionally, reconfigurable and static designs are shown to be more cost-effective than sun-synchronous or rapid launch architectures.

7.2 Contributions

This thesis:

1. Develops and demonstrates a comprehensive constellation design and optimization framework that uses state of the art multi-objective optimization techniques; is easily implemented on large cluster parallel computing resources; explicitly considers uncertainty in future operating conditions; concurrently optimizes pattern design, satellite design and operations design; and is broadly applicable to a wide range of constellation design problems.

2. Develops and demonstrates a detailed multi-disciplinary simulation model to calculate the performance and cost of a wide variety of constellation patterns for both static and reconfigurable architectures.

3. Develops and demonstrates an assignment optimization procedure to identify the suite of optimal reconfiguration options, enabling efficient decision making for reconfigurable satellite constellations.

4. Develops a new constellation coverage figure of merit that measures how well the system provides coverage with a desired temporal and spatial resolution, and avoids the problems observed with traditional metrics.

5. Finds that asymmetric patterns outperform symmetric patterns for both discontinuous coverage static and reconfigurable constellations, and proposes two new asymmetric patterns that outperform traditional patterns.

6. Successfully optimizes reconfigurable and static constellations under a wide range of pattern designs and operating parameters and finds that reconfigurable constellations cost 20 to 70% less than similarly performing static constellations for the scenarios studied.

7. Finds that optimized reconfigurable and static constellations are more cost-effective than optimized sun-synchronous and rapid launched designs for the scenarios studied.

7.3   Conclusion

This thesis presents methodology and tools to design, optimize, and operate reconfigurable satellite constellations capable of providing responsive space-based regional persistent surveillance. The developed framework avoids many limitations of previous research by focusing on detailed modeling, concurrent and multi-objective optimization, and uncertainty in future regional coverage needs. The results, presented in Chapter 6, show that reconfigurable constellation designs cost 20 to 70% less than similarly performing static constellation designs over a wide range of constellation patterns and operating parameters. The complete framework is applicable to a broad range of constellation optimization problems and is easily altered to accommodate different uncertain parameter distributions and varied objective functions.

Reconfigurable constellations are presented as a new approach to providing cost-effective space-based regional persistent surveillance. Enabled by maneuverable satellites, reconfigurable constellations provide focused regional coverage in times of need, which leads to fewer required satellites than traditional static constellation designs. Reconfigurable constellations

change coverage by transitioning satellites between two operational modes: one that provides partial global coverage and one that provides focused regional coverage. While these maneuvers necessitate satellites with increased ΔV capability, the ability to reconfigure the constellation increases the coverage provided by individual satellites leading to increased overall system cost-effectiveness.

This thesis develops and demonstrates a comprehensive constellation design and optimization framework to identify cost-effective reconfigurable constellation designs. The developed framework is novel and avoids many of the assumptions and simplifications made in past research. This improvement is accomplished by: explicitly considering uncertainty in future operating conditions; concurrently optimizing pattern design, satellite design, and operations design; and by investigating layered and asymmetric constellation patterns. The framework consists of three layers: the simulation layer, the Monte Carlo layer, and the multi-objective optimization layer. The simulation layer contains a detailed multi-disciplinary simulation model that calculates the performance and cost of a variety of constellation architectures using varied constellation patterns. The model captures the coupled interactions between system elements including pattern design, satellite design, reconfiguration design, and deployment strategy. The Monte Carlo layer samples uncertain parameter distributions and uses the simulation model to generate the performance distribution. The multi-objective optimization layer uses a modified version of the ϵ-NSGA-II evolutionary algorithm to find designs that maximize performance while simultaneously minimizing cost. This optimization algorithm provided fast and consistent convergence for all cases considered in this thesis, despite dealing with a discontinuous, non-linear objective space, and continuous, integer, and categorical variables. Additionally, the framework was implemented in parallel on a 1024-processor computing cluster to overcome the computational complexity caused by the detailed simulation model. This parallel processing capability allowed 85 different optimization cases to be investigated over the course of three months, and, using 256 processors, each case had an average optimization time of approximately three days. Enabled by fast optimization time, this thesis demonstrates a spiral design approach as the results from the fully asymmetric pattern spur the development and subsequent optimization of two 'quasi'-asymmetric patterns. By design, the framework accommodates a wide range of constellation

optimization problems, demonstrated in this thesis through the investigation of four distinct constellation architectures (reconfigurable, static, sun-synchronous, and rapid launch), and five different pattern types (symmetric, layered, asymmetric, restricted asymmetric, asymmetric Walker, and asymmetric layered).

A new figure of merit is introduced to measure how well a design meets desired persistence requirements, and introduces a process for identifying how decision makers, when responding to a regional event, should employ the flexible option of reconfigurability. The persistence metric directly measures how well the constellation provides the desired coverage with specified temporal and spatial resolution. The persistence metric takes a micro-scale view and computes the utility generated by each observation. In this case the utility is a function of the observation's temporal and spatial resolution. The total performance is then the sum of the utility generated by all individual observations. This thesis avoids skewing by statistical outliers, a problem observed with some traditional metrics, by using the new persistence metric. The automated optimal assignment process, also developed in this thesis, identifies the optimal set of reconfiguration options that simultaneously maximize event coverage and minimize propellant expenditure in their event response. As the effectiveness of a reconfigurable constellation is contingent on quick and informed decisions on when and how to employ the option of reconfigurability by decision makers, this is an important contribution. The assignment process concurrently optimizes assignment to find globally optimal solutions while determining how many satellites to reconfigure, the specific combination of satellites to reconfigure, how quickly to reconfigure each satellite, and which RGT orbit to place each reconfigured satellite. The assignment process also gives decision makers the option that maximizes future performance by balancing propellant use between satellites in the constellation and adjusting recommendations based on currently available propellant in the remaining system lifetime.

This thesis demonstrates that reconfigurable constellation designs cost 20 to 70% less than similarly performing static designs over a wide range of constellation patterns and operating parameters, which indicates that the value provided by reconfigurable constellations is robust to changing parameter values. This value of reconfigurability increases with increasing requirements for temporal and spatial resolution. The two new quasi-asymmetric patterns

introduced in this thesis outperformed symmetric and layered patterns for both architectures, with the restricted asymmetric pattern providing the best results for reconfigurable constellations, and the asymmetric Walker pattern providing the best results for the static architecture. These patterns feature asymmetry in the Ω placement of orbit planes, but allow for faster optimization by using regular spacing rules to reduce the number of design variables when compared to fully asymmetric patterns. The average value of reconfigurability, for performance from $\tilde{P}/P_{max} \geq 0.5$, was 27.5% for scenario 1 ($T = 1hr$, $X = 1m$), 40.2% for scenario 2 ($T = 1hr$, $X = 0.5m$), 48.4% for scenario 3 ($T = 0.5hr$, $X = 1m$), and 59.1% for scenario 4 ($T = 0.5hr$, $X = 0.5m$). When compared to iso-performance static designs, reconfigurable designs, with less than half the number of satellites, provide better overall performance in terms of persistence, average and maximum revisit time, mean response time, and GSD. Given that the static designs need more satellites, the maximum satellite constraint adversely affects static designs more than reconfigurable designs. When this constraint increased from 36 to 48 and 60 satellites, the average value of reconfigurability for scenario 1 dropped from 27.5% to 14.1% and 12.2% respectively. However, un-modeled operations cost could potentially have a greater effect on static designs, which would increase the value of reconfigurability. The maximum propulsion system mass fraction constraint was also active for reconfigurable designs, so increasing the constraint or reducing non-reconfiguration propellant use by employing electric propulsion would increase the value of reconfigurability.

Reconfigurable and static constellations are also shown to significantly outperform sun-synchronous and rapid launch architectures in all cases tested. Sun-synchronous constellations provide observations with constant solar illumination conditions, but sun-synchronous orbits require near polar inclinations, reducing the coverage provided by each satellite and causing poor overall cost-effectiveness. Additionally, reconfigurable or static constellations with short revisit times provide observations with near constant illumination conditions, negating some of the benefits of sun-synchronous constellations. When compared to static architectures, the rapid launch architecture provides better cost-effectiveness for low-cost, low-performance designs, but much worse cost-effectiveness for high-performance, higher-cost designs, and reconfigurable designs are much more cost-effective over the entire range of performance. The rapid launch architecture initially provides efficient coverage, but the

satellites provide little or no coverage for later events.

7.4 Future Work

This thesis develops and demonstrates a comprehensive, generalized approach to constellation design and optimization quickly able to find globally efficient designs, and shows that reconfigurable constellations can provide cost-effective regional persistent surveillance. However, the work presented here is only a starting point, and many promising avenues for further research are detailed below.

Improve models and expand design space

One promising avenue for future research is to refine the simulation model and expand the design space. Specific attention should be paid to improving the cost models, expanding analysis to include electric propulsion, and increasing simulation model computational efficiency. The current method for predicting FPA mass (and cost) would benefit substantially from a better model. Future work should try to obtain actual instrument properties for current Earth observation satellites and see how well the simple scaling implemented in this thesis matches this actual data. Additionally, future work could develop an operations and retirement cost model for both reconfigurable and static constellations. If the operations cost for reconfigurable constellations is significantly higher than static constellations, then the value of reconfigurability will likely decrease. However, if the operations cost is solely a function of the number of satellites, then the value of reconfigurability may increase as static designs tend to feature more satellites.

The simulation model should also be extended to include electric propulsion. Electric propulsion uses propellant mass more efficiently (higher I_{SP}), which would reduce propellant mass needed for deployment, station keeping, return to GOM maneuvers, and de-orbit maneuvers. This reduction in non-reconfiguration ΔV would allow the reconfiguration ΔV to increase while staying below the maximum propulsion system mass fraction constraint and would allow reconfigurable satellites to respond to more events. Additionally, electric-propulsion could potentially be used to perform slower reconfiguration maneuvers, and the choice between using chemical or electric propulsion could be added to the assignment op-

timization process. Electric propulsion could also reduce launch cost by allowing for more satellites to use shared launches due to improved maneuverability during deployment.

Additionally, improving the simulation model computational efficiency would allow for faster optimization time, a larger Monte Carlo sample size during optimization, and, with the inclusion of operations cost (explained earlier in this section), could potentially allow the maximum constellation size constraint to be increased or eliminated.

Use the framework and modify tools to study other objectives and mission scenarios

A second promising avenue for future research is to use the framework to study other objectives or mission scenarios including synthetic aperture radar and infrared imaging. This thesis considered an optical imaging mission where persistent coverage is desired for a number of events distributed around the globe and in time, and, when not responding to an event; the constellation would provide partial global coverage. Future work could investigate different objectives such as maintaining GOM coverage during event responses, investigating the tradeoff between spatial and temporal resolution, and changing how the event performance is calculated. Section 6.7 investigated restricting the number of satellites allowed to reconfigure to support a single event response as a way to retain some GOM performance and keep satellites in GOM in case a second, simultaneous event occurred. However, this strategy does not ensure that the satellites kept in GOM would provide good partial global coverage or would provide good ROM coverage for a future event. Instead, the optimal assignment process could be modified to add these additional objectives, giving decision makers more information about possible courses of action. The persistence metric presented in this thesis combined the temporal and spatial utility functions into a single utility function. Future work should also investigate the direct trade-off between these two objectives. One way to accomplish this would be to treat these objectives separately, optimizing the constellations with three objectives, and then analyzing the resulting surface of non-dominated designs to compare iso-cost designs in terms of spatial and temporal resolution.

All events considered in this thesis had the same duration and desired temporal and spatial resolutions. Instead, events could have a distribution of all these parameters, or different classes of events could be considered, each with different frequencies of occurrence. Also, the

266

event location probability distribution function should be changed to align with stakeholder objectives for a specific scenario. The analysis can also be extended to include other uncertain parameters like satellite failure rates and market uncertainty for the surveillance data products in the case of a commercial system.

Future work could also investigate: modifying the temporal utility function to provide some additional utility for oversampling; using a daily utility window based on solar elevation angle rather than the rectangular window used in this thesis, and including a discount rate on the daily performance where early observations have more utility than later observations. Providing additional utility for oversampling would be useful in a situation where a satellite cannot collect all the useful data in a single pass. The discount rate could represent the time to first image vs. persistent imaging over event duration tradeoff. For some situations, images collected in the first few hours or days would have a higher utility that images collected later.

With simple modifications, the framework could also be used to study missions other than optical imaging. For example, future work could look into a reconfigurable synthetic aperture radar (SAR) constellation capable of providing day/night and all weather data products. SAR satellites typically use low altitudes due to power limitations, and therefore, a reconfigurable SAR constellation providing persistent surveillance would likely be much more cost-effective than a static SAR constellation.

Further study the implementation challenges associated with reconfigurable constellations

A third avenue for future study is to further investigate the implementation challenges associated with reconfigurable constellations. One such challenge could arise if separate stakeholders handle satellite operations and payload tasking. In this case, fast communication between stakeholders is essential to reconfigure the constellation quickly.

The data downlink architecture is another implementation challenge for reconfigurable constellations. For missions where data latency is important, the framework could add in an objective or constraint on how long it takes data products to reach stakeholders on the ground. This may lower the value of reconfigurability since satellite-to-satellite crosslinking is more difficult in a reconfigurable constellation with a constantly changing orbital pattern. In this case, the simulation model could then directly model communication with ground

stations and satellite crosslinks, and the optimization process would find constellation designs with good coverage properties and fast data downlinking.

Future work should also utilize the optimal satellite assignment optimization algorithm to develop interactive decision support tools, providing decision makers with real time and interactive information to support reconfigurable constellation operations. As was explained in Section 3.5.4, the ability to make quick and well informed decisions is critical to ensuring effective use of a reconfigurable constellation.

Improve optimization tools

The fourth promising avenue for future work could improve and refine the tools employed in this thesis. The optimization routine could be improved in several ways. First, the observed parallel processing efficiency was around 50% meaning that optimization with 256 processors was around 130 times faster than an optimization on a single processor. As explained in Section 5.3, this loss in efficiency is likely caused by generational synchronization. To improve parallel implementation efficiency, future work should investigate moving the optimization algorithm to a stationary process, which eliminates generational synchronization. The optimization routine considered in this thesis maximized the median performance while not considering the variability of performance. Future work could extend this analysis by using a percentile away from the median or could penalize designs with high variation.

Appendix A

Detailed Results

A.1 Symmetric Pattern: Scenario 1

Figure A-1: Scenario 1 non-dominated front comparison with VoR

Table A.1: Non-dominated front design details

(a) Reconfigurable

$\tilde{P}$	C	$\frac{N_o}{N_d}$	Δalt	N_p	N_{sp}	i	F	D	ΔV_R	α_0
-	$M	-	km	-	-	deg	-	m	m/s	-
0.017	147	2	29.5	2	2	87.1	1	0.12	435	0.53
0.051	164	1	34.2	2	3	58.4	1	0.12	87	0.88
0.073	204	1	34.5	2	4	58.5	1	0.13	234	0.91
0.125	237	2	-15.9	3	2	58.6	2	0.18	498	0.03
0.134	247	2	-14.9	3	2	60.0	2	0.20	498	0.03
0.160	295	2	-18.1	4	2	58.6	3	0.18	497	0.05
0.201	318	2	-9.4	5	1	88.1	2	0.20	671	0.00
0.256	352	2	-9.9	5	1	87.7	3	0.25	667	0.00
0.298	417	2	-1.2	11	1	58.9	6	0.19	360	0.16
0.362	444	2	15.6	12	1	58.3	7	0.20	462	0.02
0.390	496	2	15.6	13	1	58.5	7	0.20	468	0.02
0.422	561	2	18.8	16	1	57.8	6	0.20	446	0.01
0.468	596	2	-6.8	11	1	58.6	9	0.29	463	0.01
0.510	624	2	19.2	12	1	57.9	0	0.29	501	0.03
0.532	649	2	19.9	12	1	57.8	0	0.31	499	0.03
0.583	687	2	6.6	21	1	57.9	8	0.22	469	0.00
0.624	719	2	6.7	21	1	57.9	9	0.24	467	0.00
0.640	768	2	-19.7	21	1	58.0	9	0.27	300	0.16
0.654	837	2	-19.7	21	1	58.3	16	0.28	295	0.17
0.707	866	2	19.8	21	1	58.1	16	0.29	464	0.02
0.728	889	2	18.7	21	1	57.8	14	0.30	454	0.02
0.753	924	2	19.0	21	1	57.8	14	0.31	458	0.01
0.766	983	2	20.1	22	1	57.8	15	0.31	456	0.01
0.786	1002	2	-18.6	23	1	57.7	12	0.31	458	0.03
0.811	1028	2	-13.9	24	1	59.4	23	0.31	461	0.00
0.826	1154	2	-4.6	25	1	57.8	23	0.34	523	0.00
0.829	1241	2	-13.9	30	1	59.4	27	0.31	416	0.00
0.865	1858	4	6.3	30	1	58.5	11	0.52	432	0.00
0.891	2453	4	11.9	33	1	57.0	7	0.64	436	0.00
0.910	6284	6	-15.0	35	1	57.4	2	1.06	418	0.00

(b) Static

$\tilde{P}$	C	h_{GOM}	N_p	N_{sp}	i	F	D
-	$M	km	-	-	deg	-	m
0.020	149	646	2	2	58.1	0	0.14
0.066	179	482	2	3	58.9	0	0.17
0.105	228	396	2	4	121.7	0	0.18
0.120	251	397	2	5	121.7	0	0.19
0.151	319	375	2	5	121.4	0	0.24
0.173	356	392	3	4	121.1	1	0.22
0.207	409	413	4	4	121.6	1	0.19
0.233	447	386	4	5	58.9	1	0.19
0.260	477	410	4	4	122.0	0	0.24
0.276	535	384	4	5	58.9	2	0.23
0.327	599	368	10	3	121.1	4	0.17
0.362	629	425	10	3	122.0	1	0.19
0.390	656	409	10	3	121.9	2	0.20
0.417	689	419	10	3	121.9	1	0.22
0.455	748	417	10	3	122.0	1	0.24
0.471	778	425	10	3	121.9	2	0.26
0.515	860	445	12	3	122.1	6	0.24
0.540	915	447	12	3	122.2	2	0.26
0.556	944	445	12	3	122.1	7	0.27
0.589	1026	473	12	3	121.7	6	0.29
0.606	1073	469	12	3	121.9	6	0.31
0.640	1183	553	12	3	122.6	1	0.34
0.672	1286	587	12	3	122.9	7	0.37
0.695	1371	628	12	3	123.0	5	0.41
0.718	1469	687	12	3	123.2	3	0.44
0.742	1646	696	18	2	123.0	11	0.44
0.777	1792	751	18	2	123.4	5	0.48
0.797	1936	822	18	2	123.6	14	0.52
0.826	2180	880	18	2	123.6	5	0.58
0.856	2505	967	18	2	123.7	14	0.66

A.2 Symmetric Pattern: Scenario 2

Figure A-2: Scenario 2 non-dominated front comparison with VoR

Table A.2: Non-dominated front design details

(a) Reconfigurable

$\tilde{P}$	C	$\frac{N_o}{N_d}$	Δalt	N_p	N_{sp}	i	F	D	ΔV_R	α_0
-	$M	-	km	-	-	deg	-	m	m/s	-
0.000	170	2	-32.3	2	3	57.9	0	0.15	1	0.70
0.026	214	1	-43.2	2	3	111.9	0	0.19	249	0.66
0.056	284	1	-50.0	2	3	116.4	0	0.28	228	0.74
0.096	322	2	-4.9	4	1	58.0	2	0.29	586	0.13
0.138	395	2	3.7	5	1	87.1	2	0.30	480	0.20
0.182	495	2	4.6	5	1	86.3	2	0.37	443	0.00
0.202	525	2	-4.8	5	1	86.3	2	0.41	443	0.00
0.247	626	2	14.0	11	1	58.7	4	0.31	465	0.02
0.273	661	2	12.9	11	1	58.3	4	0.34	446	0.00
0.298	719	2	-4.9	11	1	57.9	4	0.36	444	0.00
0.318	761	2	6.0	11	1	59.2	1	0.39	480	0.00
0.354	806	2	-4.9	11	1	57.9	4	0.42	444	0.05
0.370	835	2	11.6	11	1	58.0	4	0.44	444	0.00
0.413	886	2	13.2	12	1	57.4	4	0.45	444	0.01
0.436	952	2	11.6	13	1	58.0	4	0.44	487	0.00
0.461	1022	2	6.7	13	1	58.6	0	0.48	417	0.01
0.510	1078	2	-3.8	21	1	58.6	7	0.39	371	0.00
0.524	1093	2	-3.5	21	1	58.6	7	0.40	374	0.00
0.555	1147	2	-3.9	21	1	58.6	14	0.43	360	0.00
0.610	1250	2	13.9	21	1	57.7	11	0.47	448	0.00
0.653	1346	2	14.3	21	1	57.5	11	0.51	454	0.00
0.686	1428	2	14.1	21	1	57.5	11	0.54	449	0.00
0.696	1465	2	13.5	21	1	57.5	11	0.55	449	0.00
0.717	1508	2	-2.8	21	1	58.0	7	0.57	369	0.00
0.740	1574	2	-3.6	21	1	58.0	7	0.59	372	0.00
0.780	1738	2	6.7	24	1	57.7	8	0.59	432	0.00
0.793	1770	2	-4.8	24	1	57.9	7	0.60	501	0.00
0.817	1844	2	-2.9	24	1	57.8	18	0.62	495	0.00
0.830	2138	2	4.2	27	1	57.9	2	0.65	447	0.00
0.849	2763	2	16.5	33	1	58.6	2	0.73	433	0.00

(b) Static

$\tilde{P}$	C	h_{GOM}	N_p	N_{sp}	i	F	D
-	$M	km	-	-	deg	-	m
0.000	139	805	2	2	90.8	1	0.10
0.025	220	414	2	4	120.2	1	0.17
0.040	251	401	2	5	120.2	1	0.19
0.065	298	382	2	5	120.8	0	0.22
0.098	388	378	2	5	120.6	1	0.30
0.123	479	343	2	6	121.6	0	0.32
0.174	623	371	4	5	119.8	1	0.27
0.191	663	360	4	5	120.2	1	0.29
0.229	761	353	10	3	121.8	5	0.24
0.237	778	353	10	3	121.8	5	0.25
0.271	853	374	10	3	121.6	1	0.28
0.294	911	374	10	3	121.8	1	0.30
0.326	1007	391	10	3	121.8	9	0.33
0.352	1074	377	10	3	121.8	1	0.36
0.385	1163	377	10	3	121.8	8	0.39
0.415	1249	372	10	3	121.8	8	0.43
0.448	1349	380	11	3	121.6	9	0.42
0.468	1406	416	12	3	122.1	9	0.42
0.498	1525	426	12	3	121.9	9	0.46
0.529	1629	415	12	3	121.9	8	0.48
0.555	1797	399	12	3	121.8	9	0.53
0.587	1930	459	12	3	122.1	11	0.57
0.612	2090	481	12	3	122.4	6	0.60
0.641	2337	536	12	3	122.4	11	0.66
0.677	2606	564	35	1	121.9	34	0.69
0.700	2757	551	36	1	121.7	35	0.71
0.738	3258	663	18	2	122.9	3	0.81
0.772	4312	709	18	2	122.4	3	0.91
0.797	4945	818	18	2	123.8	3	1.02
0.819	5481	836	18	2	123.7	3	1.10

A.3 Symmetric Pattern: Scenario 3

Figure A-3: Scenario 3 non-dominated front comparison with VoR

Table A.3: Non-dominated front design details

(a) Reconfigurable

$\tilde{P}$	C	$\frac{N_o}{N_d}$	Δalt	N_p	N_{sp}	i	F	D	ΔV_R	α_0
-	$M	-	km	-	-	deg	-	m	m/s	-
0.000	125	6	-35.7	2	1	119.6	0	0.10	139	0.46
0.044	169	2	2.3	2	2	57.6	1	0.18	460	0.09
0.051	216	2	36.9	2	3	60.4	0	0.19	482	0.16
0.083	264	2	9.6	3	2	58.6	1	0.23	290	0.04
0.094	303	2	9.7	4	2	58.6	1	0.20	283	0.04
0.157	402	2	13.7	11	1	57.7	6	0.17	492	0.02
0.199	433	2	12.7	12	1	57.8	7	0.19	468	0.01
0.233	493	2	12.6	13	1	57.4	7	0.20	469	0.00
0.276	578	2	18.3	16	1	57.7	8	0.21	404	0.16
0.305	621	2	16.2	21	1	57.7	17	0.18	502	0.06
0.358	666	2	7.2	21	1	57.5	17	0.21	477	0.00
0.398	709	2	15.1	21	1	57.6	16	0.23	509	0.00
0.415	730	2	15.2	21	1	57.6	17	0.24	501	0.00
0.440	795	2	14.9	24	1	57.8	14	0.24	475	0.00
0.454	836	2	1.7	24	1	57.9	22	0.26	306	0.00
0.516	917	2	10.2	27	1	58.0	24	0.25	479	0.00
0.556	982	2	13.4	32	1	58.5	31	0.25	477	0.00
0.590	1032	2	13.1	32	1	58.5	31	0.26	481	0.00
0.615	1076	2	12.0	32	1	58.6	21	0.28	477	0.00
0.642	1121	2	11.9	32	1	58.7	28	0.29	481	0.00
0.656	1156	2	12.3	32	1	58.7	28	0.30	483	0.00
0.687	1193	2	-2.5	41	1	57.7	34	0.27	307	0.00
0.726	1257	2	-1.0	41	1	57.6	32	0.28	338	0.00
0.775	1348	2	-2.5	41	1	57.5	33	0.31	368	0.00
0.800	1421	2	3.2	44	1	58.6	34	0.31	323	0.00
0.819	1446	2	3.5	45	1	59.4	10	0.31	408	0.00
0.843	1553	2	4.9	48	1	58.0	35	0.31	385	0.00
0.872	2472	4	9.2	48	1	57.9	36	0.54	341	0.00
0.889	4241	6	-2.6	46	1	57.8	35	0.80	393	0.00
0.908	4545	6	0.5	47	1	58.0	30	0.84	398	0.00

(b) Static

$\tilde{P}$	C	h_{GOM}	N_p	N_{sp}	i	F	D
-	$M	km	-	-	deg	-	m
0.022	167	645	2	2	59.2	0	0.18
0.047	209	439	2	4	121.7	1	0.15
0.071	259	439	2	5	121.6	1	0.20
0.098	346	413	3	4	121.8	1	0.21
0.115	404	417	3	5	122.0	1	0.22
0.128	434	411	4	4	122.0	2	0.21
0.144	492	552	4	4	122.2	2	0.25
0.166	579	428	5	5	60.2	2	0.21
0.197	626	355	10	4	121.8	2	0.14
0.223	653	358	10	4	121.7	2	0.15
0.253	694	356	10	4	121.8	2	0.17
0.300	809	423	11	4	121.8	4	0.19
0.324	851	404	12	4	121.9	2	0.19
0.347	895	404	12	4	121.8	5	0.21
0.363	929	403	12	4	121.8	5	0.22
0.382	1015	450	12	4	120.4	7	0.25
0.408	1139	498	12	4	57.8	3	0.28
0.426	1207	501	12	4	57.9	3	0.29
0.445	1289	511	12	4	58.0	2	0.31
0.474	1431	583	12	4	57.7	7	0.35
0.500	1469	568	12	4	122.0	7	0.36
0.524	1560	658	14	3	122.5	0	0.41
0.556	1671	643	16	3	123.0	0	0.38
0.582	1789	716	16	3	123.2	6	0.42
0.602	1856	711	16	3	123.1	5	0.44
0.624	2009	785	16	3	123.4	13	0.47
0.648	2334	832	16	3	56.2	5	0.54
0.682	2562	965	22	2	122.6	0	0.58
0.720	2835	973	23	2	122.2	0	0.61
0.756	3112	1000	24	2	122.1	0	0.65

A.4 Symmetric Pattern: Scenario 4

Figure A-4: Scenario 4 non-dominated front comparison with VoR

Table A.4: Non-dominated front design details

(a) Reconfigurable

$\tilde{P}$	C	$\frac{N_o}{N_d}$	Δalt	N_p	N_{sp}	i	F	D	ΔV_R	α_0
-	$M	-	km	-	-	deg	-	m	m/s	-
0.000	139	3	-18.0	2	2	60.4	0	0.10	0	0.97
0.020	239	2	12.2	2	3	58.5	0	0.23	123	0.26
0.045	349	2	-9.4	5	1	58.5	3	0.25	374	0.00
0.061	396	2	-28.0	3	2	59.2	1	0.34	423	0.20
0.095	516	2	-14.9	6	1	62.6	2	0.36	422	0.02
0.132	598	2	-6.1	11	1	58.4	5	0.30	422	0.07
0.157	659	2	-6.4	12	1	59.0	0	0.32	379	0.00
0.191	762	2	-5.5	13	1	58.9	0	0.35	340	0.00
0.206	805	2	-12.2	11	1	58.5	2	0.42	468	0.05
0.260	951	2	-17.6	21	1	58.0	2	0.32	449	0.02
0.296	1015	2	-16.9	21	1	57.7	2	0.36	457	0.02
0.336	1079	2	-2.0	21	1	58.1	2	0.39	408	0.00
0.353	1133	2	-18.7	21	1	58.0	3	0.42	456	0.01
0.381	1216	2	-17.5	21	1	57.9	2	0.46	449	0.02
0.406	1302	2	-12.7	24	1	58.2	3	0.43	455	0.01
0.435	1371	2	-3.4	32	1	58.9	0	0.39	371	0.00
0.467	1434	2	1.3	31	1	58.0	1	0.42	405	0.00
0.491	1529	2	-3.4	35	1	58.0	33	0.40	381	0.00
0.536	1677	2	5.8	36	1	58.2	1	0.44	391	0.00
0.548	1725	2	-3.4	45	1	58.0	42	0.39	381	0.00
0.602	1849	2	-1.4	42	1	58.5	22	0.45	392	0.00
0.623	1916	2	-0.7	43	1	57.8	19	0.46	456	0.00
0.643	1980	2	-1.7	45	1	58.1	24	0.46	394	0.00
0.677	2081	2	0.7	44	1	57.5	39	0.49	338	0.00
0.704	2194	2	-5.0	44	1	58.1	12	0.52	440	0.00
0.733	2319	2	0.7	43	1	57.5	41	0.55	329	0.00
0.758	2397	2	0.7	44	1	57.5	42	0.56	329	0.00
0.799	2654	2	-3.1	46	1	57.7	14	0.59	362	0.00
0.816	2732	2	-7.9	45	1	59.0	23	0.62	428	0.00
0.847	3218	2	1.8	48	1	58.8	37	0.68	358	0.00

(b) Static

$\tilde{P}$	C	h_{GOM}	N_p	N_{sp}	i	F	D
-	$M	km	-	-	deg	-	m
0.000	153	534	2	3	61.1	0	0.10
0.020	224	407	2	3	121.5	0	0.21
0.036	291	356	2	5	121.5	0	0.21
0.060	415	353	2	5	121.5	0	0.31
0.079	526	362	3	5	121.7	1	0.29
0.113	697	364	4	5	121.5	1	0.30
0.151	828	365	10	4	121.7	9	0.23
0.168	886	357	10	4	121.6	9	0.24
0.200	1018	366	10	4	121.9	6	0.28
0.215	1079	365	10	4	121.9	3	0.30
0.240	1224	351	11	4	121.6	10	0.30
0.265	1299	357	12	4	121.6	11	0.31
0.302	1463	359	12	4	121.6	7	0.35
0.329	1604	380	12	4	121.7	1	0.39
0.347	1671	381	12	4	121.6	2	0.42
0.386	1854	413	44	1	122.1	2	0.44
0.410	1978	411	47	1	122.1	2	0.44
0.427	2070	421	47	1	121.9	2	0.47
0.465	2305	449	45	1	122.2	2	0.55
0.475	2446	502	45	1	121.0	2	0.58
0.504	2575	507	48	1	122.5	2	0.57
0.529	2788	489	48	1	121.7	2	0.61
0.556	3107	573	45	1	122.8	2	0.70
0.584	3367	563	48	1	122.1	2	0.71
0.609	3709	606	48	1	122.8	2	0.77
0.643	5148	823	23	2	123.5	3	0.95
0.658	5203	788	24	2	123.0	3	0.93
0.696	6216	824	24	2	123.3	3	1.01
0.712	6664	941	24	2	124.2	3	1.07
0.745	8615	909	24	2	123.8	3	1.14

A.5 Symmetric Pattern: Scenario 5

Figure A-5: Scenario 5 non-dominated front comparison with VoR

Table A.5: Non-dominated front design details

(a) Reconfigurable

$\tilde{P}$	C	$\frac{N_o}{N_d}$	Δalt	N_p	N_{sp}	i	F	D	ΔV_R	α_0
-	$M	-	km	-	-	deg	-	m	m/s	-
0.043	147	2	1.6	2	2	57.7	1	0.12	404	0.00
0.085	172	2	1.4	2	2	59.6	1	0.19	425	0.19
0.129	236	2	1.8	3	2	59.9	1	0.18	438	0.01
0.148	251	2	1.3	3	2	59.6	1	0.21	427	0.02
0.202	329	2	-13.8	5	1	92.2	1	0.22	580	0.04
0.242	358	2	15.2	5	1	97.0	4	0.26	568	0.05
0.284	387	2	-14.1	5	1	85.7	1	0.29	617	0.01
0.317	416	2	6.5	11	1	58.1	1	0.19	374	0.05
0.372	445	2	-0.9	11	1	58.2	1	0.22	338	0.05
0.393	463	2	-1.8	12	1	58.6	2	0.22	281	0.05
0.421	507	2	-1.7	13	1	57.9	4	0.22	300	0.05
0.442	519	2	-1.3	13	1	58.5	2	0.23	297	0.05
0.464	565	2	-13.1	11	1	57.8	0	0.27	506	0.00
0.486	588	2	-18.5	12	1	57.8	4	0.27	498	0.00
0.506	623	2	-4.9	12	1	60.4	6	0.30	365	0.02
0.534	644	2	-12.9	13	1	57.8	0	0.27	505	0.00
0.581	689	2	-5.8	21	1	58.6	3	0.23	356	0.03
0.634	718	2	-3.9	21	1	58.4	0	0.24	354	0.00
0.665	750	2	-5.2	21	1	57.9	3	0.26	361	0.00
0.701	838	2	-10.2	24	1	60.3	0	0.26	410	0.00
0.713	844	2	-10.2	24	1	58.0	2	0.26	410	0.00
0.763	899	2	-4.2	21	1	58.0	0	0.30	396	0.00
0.788	968	2	2.1	22	1	58.8	3	0.31	395	0.00
0.811	1017	2	7.1	23	1	59.0	6	0.32	347	0.00
0.837	1152	2	7.5	27	1	58.4	25	0.32	357	0.00
0.851	1295	2	7.1	35	1	59.0	10	0.32	347	0.00
0.860	1423	2	19.0	35	1	59.0	8	0.36	493	0.00
0.878	2007	4	-4.5	30	1	59.9	7	0.57	395	0.00
0.890	3289	4	3.7	36	1	59.2	0	0.77	477	0.00
0.909	4063	6	1.1	29	1	124.9	9	0.97	305	0.00

(b) Static

$\tilde{P}$	C	h_{GOM}	N_p	N_{sp}	i	F	D
-	$M	km	-	-	deg	-	m
0.017	145	593	2	2	114.6	1	0.12
0.043	178	462	2	3	119.5	1	0.12
0.086	207	395	2	3	120.3	0	0.18
0.113	236	358	2	4	121.6	0	0.19
0.162	327	394	3	4	119.4	1	0.19
0.189	356	387	3	5	119.5	1	0.19
0.216	414	368	3	5	120.1	2	0.22
0.239	441	410	4	4	121.8	2	0.21
0.255	465	375	4	4	120.6	3	0.23
0.285	529	398	5	4	121.8	1	0.21
0.308	566	372	5	4	120.6	4	0.23
0.341	628	398	6	4	120.4	3	0.21
0.372	656	474	12	2	121.2	3	0.23
0.396	705	379	12	3	121.2	7	0.17
0.428	740	402	12	3	120.7	5	0.19
0.446	760	395	12	3	120.7	5	0.20
0.467	799	456	12	3	121.1	5	0.22
0.505	836	439	12	3	121.7	5	0.23
0.524	868	438	12	3	121.5	5	0.24
0.570	977	474	12	3	121.2	3	0.28
0.578	994	474	12	3	121.2	3	0.28
0.621	1106	509	12	3	121.9	8	0.32
0.637	1178	550	12	3	121.2	7	0.34
0.668	1278	593	12	3	122.1	5	0.37
0.725	1529	705	12	3	122.1	2	0.46
0.742	1657	710	18	2	121.8	10	0.45
0.779	1780	732	18	2	123.3	3	0.48
0.816	2110	970	30	1	124.1	2	0.61
0.873	2497	995	33	1	123.0	2	0.66
0.887	2644	998	34	1	123.0	2	0.67

A.6 Symmetric Pattern: Scenario 6

Figure A-6: Scenario 6 non-dominated front comparison with VoR

Table A.6: Non-dominated front design details

(a) Reconfigurable

$\tilde{P}$	C	$\frac{N_o}{N_d}$	Δalt	N_p	N_{sp}	i	F	D	ΔV_R	α_0
-	$M	-	km	-	-	deg	-	m	m/s	-
0.021	116	2	-1.9	1	4	75.4	0	0.12	338	0.13
0.057	152	2	-47.6	1	5	60.5	0	0.19	1	0.98
0.111	230	2	1.7	3	2	66.7	1	0.17	432	0.08
0.135	279	2	-0.2	3	2	69.7	1	0.21	498	0.24
0.177	319	2	0.8	4	2	60.0	0	0.21	286	0.05
0.201	358	2	2.2	5	1	86.3	2	0.25	529	0.24
0.212	374	2	3.1	5	1	87.1	2	0.27	539	0.24
0.245	433	2	-0.4	11	1	58.8	0	0.20	285	0.04
0.269	466	2	-1.6	5	2	86.5	2	0.24	471	0.29
0.306	507	2	-2.4	5	2	86.8	2	0.28	329	0.18
0.338	553	2	-0.1	5	2	87.5	1	0.31	326	0.18
0.375	584	2	-0.2	11	2	58.5	0	0.19	309	0.03
0.405	635	2	0.4	12	1	58.5	11	0.30	344	0.05
0.500	671	2	0.4	21	1	58.3	19	0.22	342	0.06
0.537	718	2	8.4	21	1	57.5	16	0.24	338	0.14
0.552	759	2	-4.0	22	1	58.0	16	0.23	338	0.16
0.593	792	2	0.3	23	1	58.4	12	0.24	354	0.06
0.616	826	2	9.7	24	1	58.5	17	0.25	370	0.09
0.633	862	2	0.8	21	1	58.4	19	0.28	342	0.06
0.676	916	2	0.3	21	1	58.2	19	0.31	342	0.06
0.710	983	2	0.4	23	1	58.5	21	0.30	344	0.05
0.730	1019	2	-2.6	24	1	60.8	13	0.30	376	0.02
0.744	1105	2	-3.0	26	1	60.4	14	0.30	372	0.01
0.764	1153	2	-3.6	27	1	59.5	6	0.31	376	0.04
0.788	1266	2	11.5	32	1	58.5	24	0.34	371	0.07
0.802	1475	2	11.5	35	1	58.5	25	0.38	342	0.07
0.822	1509	2	-15.0	28	1	122.7	25	0.43	417	0.10
0.842	2022	4	12.5	35	1	56.1	12	0.54	332	0.07
0.853	2186	4	12.5	36	1	56.1	12	0.57	352	0.08
0.887	4132	6	-19.7	35	1	55.0	1	0.87	361	0.07

(b) Static

$\tilde{P}$	C	h_{GOM}	N_p	N_{sp}	i	F	D
-	$M	km	-	-	deg	-	m
0.024	153	576	2	2	83.9	1	0.15
0.066	200	413	2	4	120.3	1	0.13
0.110	239	403	2	4	121.4	1	0.19
0.142	306	373	2	5	121.1	1	0.22
0.174	358	422	3	4	121.5	2	0.22
0.226	435	404	4	4	121.5	1	0.20
0.265	519	377	4	5	121.3	2	0.21
0.280	544	396	4	5	121.3	2	0.23
0.299	595	453	12	2	121.4	0	0.19
0.327	629	459	11	2	121.5	3	0.22
0.394	719	405	11	3	121.3	3	0.19
0.415	740	423	11	3	121.5	3	0.20
0.463	797	407	11	3	122.1	4	0.22
0.483	831	437	11	3	122.2	4	0.24
0.512	866	422	12	3	122.1	3	0.24
0.535	917	441	12	3	121.7	4	0.25
0.550	940	447	12	3	122.2	4	0.26
0.569	980	441	12	3	122.1	3	0.27
0.608	1080	483	12	3	122.4	10	0.31
0.623	1141	492	12	3	122.4	4	0.32
0.650	1221	566	12	3	122.3	3	0.35
0.668	1308	567	12	3	122.0	3	0.38
0.697	1379	629	12	3	122.9	2	0.41
0.721	1527	677	12	3	122.6	4	0.45
0.744	1638	691	18	2	123.1	6	0.44
0.775	1782	745	18	2	123.2	10	0.48
0.798	1955	803	18	2	122.7	10	0.53
0.816	2089	963	32	1	122.9	2	0.56
0.849	2171	851	33	1	122.7	2	0.58
0.911	2497	954	36	1	123.6	2	0.65

A.7   Symmetric Pattern: Scenario 7

Figure A-7: Scenario 7 non-dominated front comparison with VoR

Table A.7: Non-dominated front design details

(a) Reconfigurable

$\tilde{P}$	C	$\frac{N_o}{N_d}$	Δalt	N_p	N_{sp}	i	F	D	ΔV_R	α_0
-	$M	-	km	-	-	deg	-	m	m/s	-
0.004	147	3	1.8	2	2	59.5	0	0.11	193	0.16
0.049	172	1	45.0	2	3	60.4	1	0.13	37	0.68
0.075	210	2	47.3	2	3	58.3	0	0.16	417	0.09
0.134	258	2	6.2	3	2	58.3	2	0.20	365	0.12
0.172	300	2	-0.6	4	1	61.8	0	0.25	342	0.01
0.184	313	2	-0.5	4	1	61.9	0	0.26	587	0.09
0.212	360	2	-0.5	4	1	61.9	0	0.32	587	0.13
0.236	409	2	2.2	5	1	57.9	3	0.30	343	0.09
0.286	443	2	10.9	11	1	57.8	0	0.18	384	0.12
0.333	474	2	5.2	11	1	57.8	2	0.21	317	0.07
0.349	494	2	-0.5	12	1	61.7	2	0.21	343	0.01
0.380	536	2	-2.2	13	1	61.0	1	0.20	365	0.05
0.404	557	2	-0.5	13	1	62.3	10	0.21	343	0.01
0.443	628	2	-4.6	11	1	57.9	1	0.28	341	0.06
0.465	655	2	10.4	16	1	57.9	4	0.22	385	0.07
0.474	674	2	-0.6	13	1	61.8	1	0.25	342	0.01
0.505	716	2	0.3	13	1	60.8	1	0.27	342	0.05
0.525	732	2	-0.4	13	1	60.8	1	0.28	342	0.05
0.551	775	2	-0.7	13	1	61.6	1	0.30	342	0.08
0.599	836	2	9.9	21	1	58.3	4	0.24	333	0.00
0.638	890	2	10.0	21	1	57.6	17	0.26	354	0.00
0.669	947	2	-9.9	22	1	57.5	6	0.26	348	0.00
0.718	1006	2	-1.7	21	1	57.8	12	0.29	350	0.00
0.746	1092	2	2.5	22	1	59.9	11	0.29	355	0.00
0.768	1129	2	-4.1	22	1	59.5	4	0.30	375	0.00
0.799	1189	2	6.1	23	1	60.0	21	0.31	414	0.00
0.817	1311	2	5.8	24	1	58.1	14	0.34	346	0.00
0.843	1599	2	12.2	32	1	57.8	30	0.35	341	0.00
0.868	2459	4	-1.3	29	1	58.3	0	0.56	344	0.00
0.894	4045	6	-10.0	33	1	57.5	2	0.77	326	0.00

(b) Static

$\tilde{P}$	C	h_{GOM}	N_p	N_{sp}	i	F	D
-	$M	km	-	-	deg	-	m
0.000	102	996	2	1	87.2	0	0.10
0.003	141	994	2	1	87.1	0	0.17
0.043	174	509	2	3	59.6	0	0.13
0.066	191	496	2	3	59.0	0	0.17
0.097	236	399	2	4	121.7	0	0.17
0.131	311	402	2	5	121.4	0	0.20
0.167	387	419	3	4	120.5	1	0.21
0.190	443	471	3	4	122.2	1	0.25
0.231	499	406	4	4	121.3	1	0.21
0.254	548	461	4	4	122.2	0	0.24
0.275	597	388	10	2	121.8	0	0.19
0.306	645	408	10	2	121.9	0	0.22
0.347	739	386	10	3	121.8	0	0.18
0.375	777	377	10	3	121.7	0	0.19
0.395	803	386	10	3	121.7	1	0.20
0.430	881	355	10	3	121.7	1	0.22
0.460	973	353	11	3	121.7	0	0.22
0.490	1062	438	11	3	120.3	4	0.25
0.525	1112	450	12	3	121.9	0	0.25
0.549	1191	443	12	3	121.3	0	0.26
0.574	1259	471	12	3	122.3	1	0.28
0.611	1388	510	12	3	122.5	0	0.31
0.636	1493	538	12	3	122.6	0	0.33
0.681	1796	670	16	2	122.9	6	0.41
0.700	1908	687	16	2	122.7	13	0.44
0.748	2124	688	18	2	123.2	13	0.44
0.765	2236	777	17	2	123.5	3	0.48
0.793	2464	819	18	2	123.4	3	0.51
0.820	2780	893	18	2	123.6	14	0.56
0.858	3304	972	18	2	123.8	14	0.65

A.8 Symmetric Pattern: Scenario 8
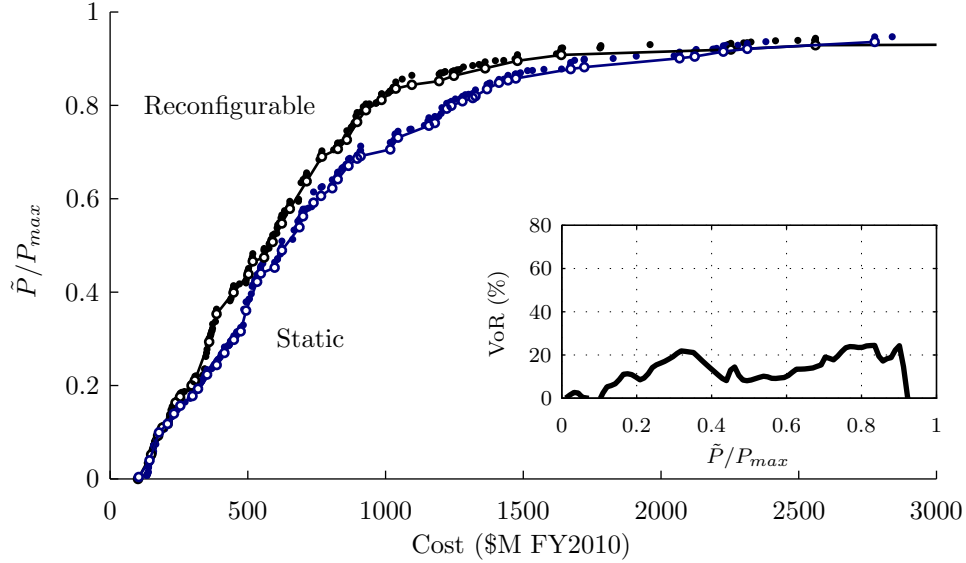
Figure A-8: Scenario 8 non-dominated front comparison with VoR

Table A.8: Non-dominated front design details

(a) Reconfigurable

$\tilde{P}$	C	$\frac{N_o}{N_d}$	Δalt	N_p	N_{sp}	i	F	D	ΔV_R	α_0
-	$M	-	km	-	-	deg	-	m	m/s	-
0.000	101	4	-50.0	2	1	113.4	1	0.10	0	0.02
0.052	149	2	-8.8	2	2	56.4	1	0.13	327	0.17
0.093	174	2	-11.0	2	2	58.5	1	0.19	477	0.21
0.110	190	2	-11.8	2	2	59.6	1	0.22	284	0.20
0.163	238	2	11.2	3	1	87.3	1	0.25	651	0.08
0.200	296	2	-14.7	4	1	56.1	0	0.25	560	0.20
0.211	308	2	4.9	4	1	57.1	0	0.27	395	0.18
0.294	360	2	12.2	10	1	55.9	1	0.18	440	0.06
0.353	386	2	12.0	10	1	55.8	1	0.21	449	0.06
0.399	448	2	-14.4	12	1	56.1	6	0.21	455	0.01
0.439	503	2	-13.5	13	1	57.3	2	0.21	464	0.14
0.466	518	2	-8.6	10	1	56.8	3	0.28	422	0.00
0.508	590	2	-3.8	12	1	57.3	4	0.27	399	0.06
0.547	624	2	-14.2	12	1	57.4	6	0.29	512	0.06
0.579	652	2	-15.7	12	1	57.5	2	0.31	531	0.00
0.637	713	2	-15.8	13	1	57.5	7	0.31	530	0.00
0.690	769	2	-14.1	21	1	58.1	0	0.27	316	0.07
0.707	827	2	-14.1	22	1	58.5	12	0.27	317	0.07
0.726	859	2	-12.7	21	1	58.3	12	0.29	314	0.07
0.764	897	2	-14.1	21	1	58.6	8	0.30	323	0.04
0.790	929	2	-12.7	21	1	56.9	16	0.32	393	0.01
0.812	985	2	-11.1	22	1	57.8	17	0.32	389	0.00
0.836	1037	2	-11.1	24	1	57.8	19	0.32	389	0.00
0.852	1194	2	-11.8	24	1	123.7	10	0.39	308	0.01
0.863	1248	2	-23.5	24	1	123.0	5	0.41	443	0.04
0.879	1362	2	-23.4	24	1	124.7	5	0.46	447	0.04
0.895	1479	2	-3.3	25	1	124.7	5	0.47	450	0.00
0.908	1638	2	-6.7	31	1	124.8	25	0.49	323	0.00
0.929	2561	3	-24.2	18	2	124.8	14	0.67	2	0.27
0.937	6730	6	13.9	32	1	54.2	10	1.20	344	0.00

(b) Static

$\tilde{P}$	C	h_{GOM}	N_p	N_{sp}	i	F	D
-	$M	km	-	-	deg	-	m
0.004	104	614	2	1	91.8	0	0.12
0.040	143	421	2	2	56.8	1	0.12
0.099	177	382	2	3	57.6	1	0.16
0.118	208	385	2	3	56.9	0	0.18
0.157	255	375	2	4	57.1	0	0.22
0.178	299	390	3	3	122.8	2	0.20
0.224	352	421	4	2	56.4	1	0.26
0.244	387	397	4	3	120.7	3	0.20
0.270	415	416	4	3	56.9	1	0.23
0.298	449	355	4	4	57.7	0	0.21
0.316	474	381	10	2	121.9	2	0.16
0.361	494	376	10	2	121.8	3	0.18
0.422	534	395	10	2	122.5	3	0.21
0.440	547	389	10	2	122.5	3	0.22
0.489	624	391	10	2	123.2	3	0.24
0.539	688	388	10	3	122.5	3	0.22
0.562	700	357	10	3	122.5	3	0.22
0.592	739	378	10	3	123.2	9	0.24
0.606	766	378	10	3	123.2	9	0.25
0.642	826	374	11	3	123.1	10	0.24
0.671	866	375	12	3	122.6	11	0.24
0.686	897	366	12	3	122.7	11	0.25
0.731	1045	364	12	3	122.8	6	0.29
0.757	1157	575	13	2	124.6	3	0.39
0.793	1222	559	14	2	124.5	3	0.39
0.809	1279	551	14	2	123.8	3	0.42
0.835	1369	559	16	2	124.5	3	0.40
0.858	1473	543	16	2	123.8	3	0.44
0.901	2067	698	17	2	54.4	11	0.58
0.915	2226	696	18	2	54.7	12	0.60

A.9 Symmetric Pattern: Scenario 9
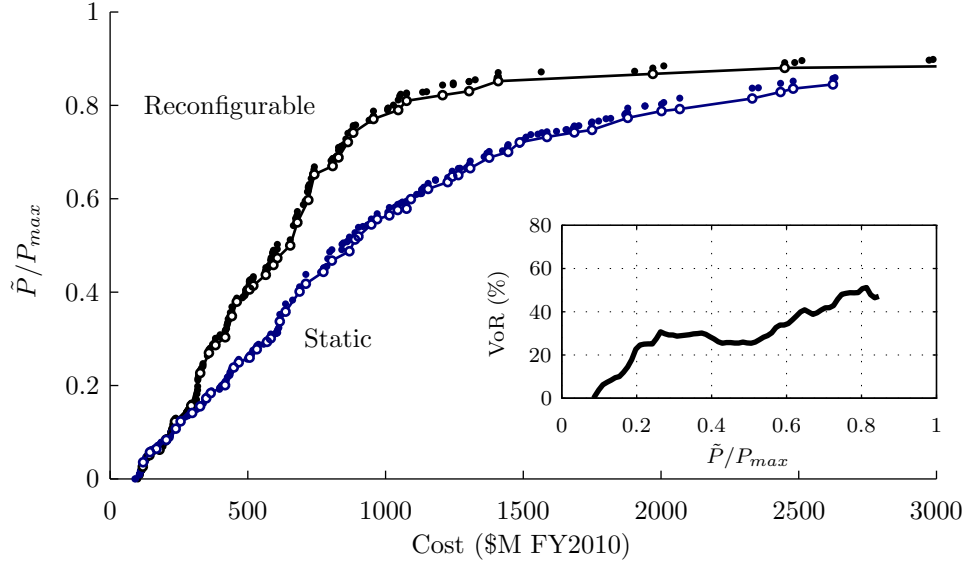
Figure A-9: Scenario 9 non-dominated front comparison with VoR

Table A.9: Non-dominated front design details

(a) Reconfigurable

$\tilde{P}$	C	$\frac{N_o}{N_d}$	Δalt	N_p	N_{sp}	i	F	D	ΔV_R	α_0
-	$M	-	km	-	-	deg	-	m	m/s	-
0.026	119	2	-50.0	1	5	62.1	0	0.12	7	0.32
0.051	143	2	-42.4	1	5	59.3	0	0.17	233	0.90
0.062	180	2	-23.7	1	6	59.4	0	0.21	30	1.00
0.084	203	2	-0.8	2	3	58.4	0	0.17	244	0.15
0.123	236	2	25.4	3	2	60.8	1	0.18	448	0.06
0.157	295	2	25.1	3	2	73.1	1	0.23	397	0.06
0.227	327	2	3.8	5	1	86.2	4	0.22	548	0.01
0.270	359	2	3.1	5	1	87.0	3	0.26	467	0.01
0.303	418	2	0.9	11	1	58.2	0	0.19	381	0.04
0.349	442	2	4.6	11	1	58.7	1	0.21	386	0.00
0.379	460	2	-5.6	12	1	59.2	8	0.22	342	0.09
0.406	506	2	4.3	13	1	57.9	1	0.21	373	0.00
0.437	565	2	-8.1	16	1	57.7	0	0.20	375	0.01
0.458	593	2	-3.4	11	1	58.0	2	0.29	401	0.10
0.473	607	2	-4.4	11	1	58.0	3	0.30	380	0.09
0.500	654	2	-2.7	18	1	61.8	5	0.22	295	0.00
0.549	680	2	-10.6	13	1	58.0	2	0.29	474	0.00
0.597	720	2	-8.5	21	1	57.7	1	0.24	475	0.00
0.652	742	2	-4.2	21	1	58.0	17	0.25	382	0.00
0.670	808	2	7.1	24	1	57.8	2	0.24	361	0.00
0.688	829	2	-5.4	21	1	58.0	17	0.27	402	0.00
0.721	863	2	-4.2	21	1	58.0	17	0.29	380	0.00
0.741	883	2	-2.7	21	1	58.3	1	0.30	378	0.00
0.771	956	2	-5.3	22	1	57.6	5	0.30	369	0.00
0.790	1046	2	-5.0	22	1	58.1	4	0.34	441	0.00
0.810	1076	2	-5.0	23	1	58.1	5	0.34	442	0.00
0.831	1303	2	-3.2	28	1	58.6	26	0.35	305	0.00
0.852	1409	2	-3.6	35	1	57.9	6	0.35	379	0.00
0.867	1970	4	-13.0	25	1	57.3	4	0.63	388	0.00
0.901	5937	6	-19.7	34	1	57.3	17	1.04	363	0.00

(b) Static

$\tilde{P}$	C	h_{GOM}	N_p	N_{sp}	i	F	D
-	$M	km	-	-	deg	-	m
0.036	120	483	1	4	58.5	0	0.15
0.057	145	434	1	5	58.6	0	0.18
0.084	204	379	1	6	58.2	0	0.24
0.108	238	449	2	4	57.9	0	0.20
0.141	298	360	2	5	58.5	1	0.22
0.155	327	358	2	6	58.7	1	0.22
0.184	365	393	3	5	58.0	2	0.20
0.239	449	370	4	5	58.3	3	0.19
0.260	507	397	4	5	58.9	2	0.21
0.293	569	380	4	6	58.6	1	0.22
0.337	616	401	10	3	58.4	3	0.18
0.401	688	415	10	3	58.2	6	0.22
0.418	711	410	10	3	58.1	6	0.23
0.443	774	394	12	3	58.4	9	0.21
0.468	805	419	12	3	58.1	8	0.22
0.488	869	457	11	3	58.3	5	0.26
0.513	889	446	12	3	58.3	6	0.25
0.545	949	451	12	3	58.3	6	0.27
0.564	1014	493	12	3	58.3	6	0.29
0.599	1092	513	12	3	57.7	6	0.31
0.621	1155	545	12	3	57.6	6	0.33
0.648	1242	570	12	3	58.0	8	0.36
0.665	1307	583	12	3	57.8	8	0.38
0.700	1445	705	12	3	58.0	6	0.43
0.721	1487	698	12	3	56.7	8	0.44
0.742	1685	781	12	3	58.2	8	0.50
0.773	1879	874	12	3	56.9	8	0.55
0.815	2331	980	18	2	57.5	15	0.62
0.829	2434	937	18	2	56.2	12	0.64
0.845	2624	988	18	2	56.3	12	0.68

A.10 Symmetric Pattern: Scenario 10a
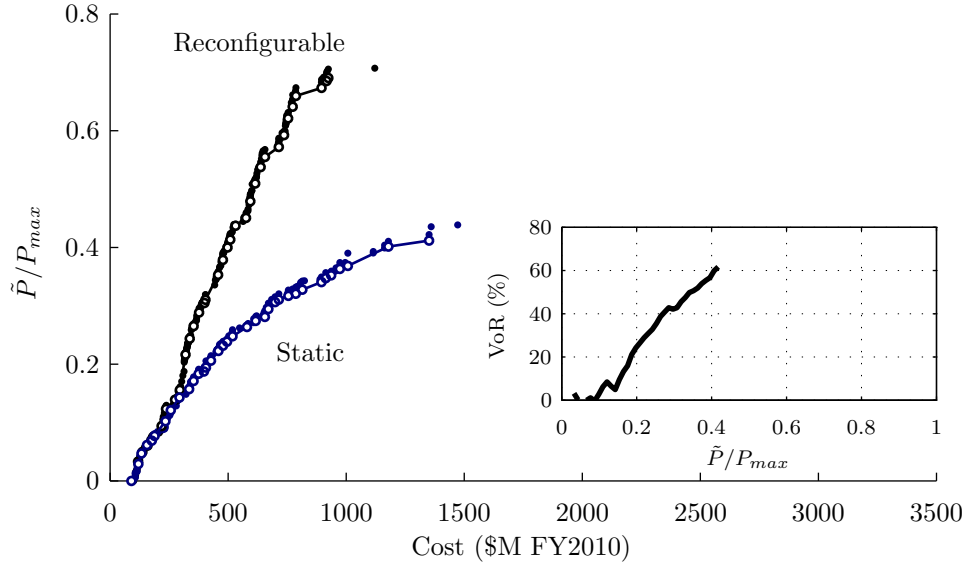
Figure A-10: Scenario 10a non-dominated front comparison with VoR

Table A.10: Non-dominated front design details

(a) Reconfigurable

$\tilde{P}$	C	$\frac{N_o}{N_d}$	Δalt	N_p	N_{sp}	i	F	D	ΔV_R	α_0
-	$M	-	km	-	-	deg	-	m	m/s	-
0.033	118	1	21.6	1	5	58.9	0	0.11	3	0.47
0.050	137	1	29.4	1	6	58.7	0	0.14	1	0.99
0.060	158	1	32.5	1	6	60.4	0	0.17	6	0.97
0.070	175	1	32.5	1	6	59.8	0	0.20	5	0.93
0.094	218	2	13.0	3	2	73.4	1	0.15	327	0.08
0.123	237	2	-0.4	3	2	77.6	1	0.19	261	0.23
0.139	275	2	1.2	3	2	88.6	1	0.21	224	0.27
0.156	295	2	13.0	3	2	73.4	1	0.24	327	0.08
0.216	319	2	1.2	5	1	86.5	3	0.21	468	0.05
0.244	337	2	0.7	5	1	86.2	2	0.23	473	0.10
0.265	354	2	1.8	5	1	86.7	2	0.26	439	0.00
0.288	377	2	1.6	5	1	86.4	2	0.28	445	0.01
0.305	400	2	6.7	5	1	88.3	4	0.31	533	0.00
0.353	458	2	4.2	7	1	87.1	4	0.24	474	0.01
0.379	478	2	7.1	7	1	87.1	5	0.26	509	0.05
0.400	497	2	6.8	7	1	86.0	5	0.28	511	0.06
0.413	509	2	7.0	7	1	86.0	5	0.29	511	0.05
0.437	531	2	-6.7	7	1	87.0	3	0.31	480	0.03
0.451	576	2	13.6	9	1	86.4	7	0.25	593	0.09
0.479	594	2	1.5	9	1	86.5	4	0.26	633	0.12
0.510	614	2	-2.7	9	1	87.6	5	0.28	556	0.13
0.538	638	2	6.0	9	1	86.5	8	0.30	577	0.14
0.555	656	2	7.4	9	1	87.1	5	0.31	474	0.09
0.572	715	2	0.1	11	1	88.1	8	0.27	579	0.01
0.592	737	2	-2.0	11	1	87.6	10	0.28	665	0.00
0.621	754	2	4.1	11	1	88.0	10	0.29	616	0.00
0.641	773	2	0.4	11	1	87.1	6	0.31	432	0.04
0.660	787	2	0.3	11	1	87.0	6	0.32	464	0.04
0.673	896	2	-2.2	11	1	87.8	8	0.33	484	0.00
0.690	924	2	-3.4	11	1	88.4	8	0.34	610	0.11

(b) Static

$\tilde{P}$	C	h_{GOM}	N_p	N_{sp}	i	F	D
-	$M	km	-	-	deg	-	m
0.000	90	851	1	3	63.1	0	0.10
0.029	120	460	1	5	58.8	0	0.12
0.047	133	443	1	5	57.9	0	0.16
0.062	156	480	1	4	57.9	0	0.23
0.077	188	341	1	6	59.0	0	0.21
0.081	201	341	1	7	59.0	0	0.21
0.102	234	340	2	4	58.7	1	0.18
0.121	257	428	2	5	58.0	0	0.20
0.124	265	434	2	5	59.1	0	0.20
0.143	294	370	2	5	121.8	0	0.22
0.157	335	461	3	4	120.9	1	0.20
0.171	354	448	3	4	120.6	0	0.22
0.184	375	447	3	4	120.5	1	0.24
0.194	406	452	4	3	122.1	1	0.22
0.206	427	450	4	3	121.7	1	0.24
0.223	459	529	4	3	122.6	1	0.27
0.239	495	458	4	3	122.1	1	0.29
0.248	519	497	4	3	121.8	1	0.31
0.264	580	521	4	3	122.5	3	0.33
0.274	617	631	4	3	123.0	2	0.35
0.294	670	661	4	3	123.0	1	0.39
0.306	699	667	4	3	123.0	1	0.42
0.317	755	752	4	3	122.9	3	0.46
0.328	814	750	4	3	122.8	3	0.49
0.341	895	811	4	3	122.9	1	0.54
0.347	914	887	4	3	123.0	1	0.55
0.356	957	967	4	3	124.0	0	0.57
0.368	1007	958	4	3	123.9	0	0.60
0.402	1179	992	6	2	121.5	2	0.63
0.412	1351	934	6	2	123.2	0	0.71

A.11 Symmetric Pattern: Scenario 10b
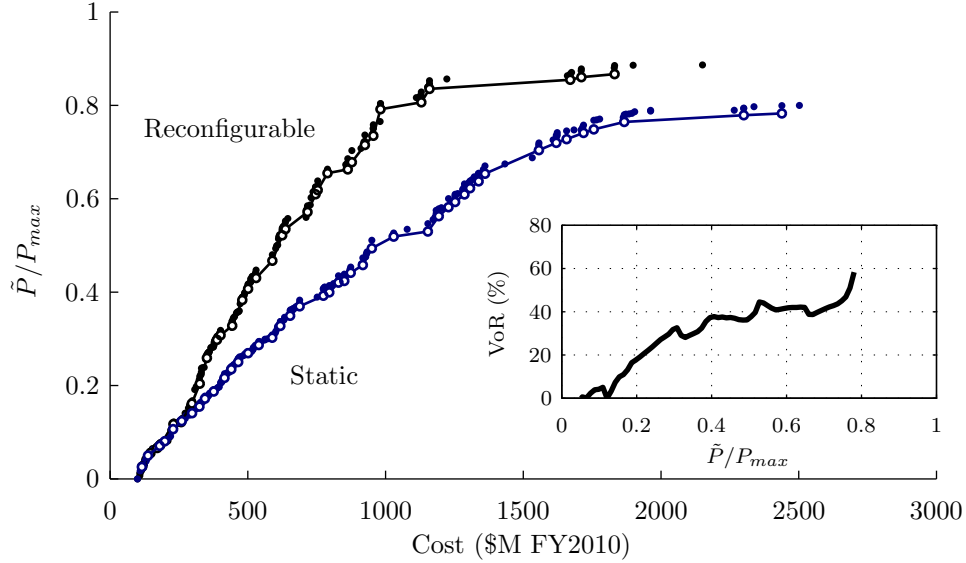
Figure A-11: Scenario 10b non-dominated front comparison with VoR

Table A.11: Non-dominated front design details

(a) Reconfigurable

$\tilde{P}$	C	$\frac{N_o}{N_d}$	Δalt	N_p	N_{sp}	i	F	D	ΔV_R	α_0
-	$M	-	km	-	-	deg	-	m	m/s	-
0.027	117	1	39.3	1	5	62.6	0	0.11	55	0.90
0.055	146	1	36.1	1	6	61.8	0	0.16	4	0.96
0.066	171	1	38.5	1	6	63.1	0	0.19	10	0.40
0.073	182	1	39.0	1	6	61.3	0	0.21	0	0.99
0.117	230	2	-1.8	3	2	87.8	1	0.18	164	0.15
0.162	297	2	2.0	3	2	87.1	1	0.24	216	0.31
0.204	325	2	4.2	5	1	85.8	3	0.22	372	0.14
0.259	352	2	-2.4	5	1	87.6	1	0.25	450	0.03
0.298	388	2	-5.6	5	1	86.5	4	0.29	500	0.05
0.308	401	2	-5.6	5	1	86.9	3	0.31	514	0.03
0.328	443	2	-5.0	7	1	86.4	4	0.23	438	0.00
0.383	480	2	6.4	7	1	86.4	3	0.26	575	0.04
0.407	501	2	-8.1	7	1	86.6	5	0.28	558	0.03
0.430	530	2	-12.9	7	1	87.0	5	0.31	531	0.14
0.467	589	2	-3.4	9	1	88.5	4	0.26	483	0.11
0.522	625	2	-6.1	9	1	87.0	7	0.29	452	0.08
0.535	637	2	2.2	9	1	87.0	7	0.30	452	0.17
0.572	717	2	-4.7	11	1	87.5	5	0.27	553	0.11
0.610	746	2	-0.7	11	1	87.5	2	0.29	460	0.09
0.618	754	2	-4.4	11	1	87.5	5	0.29	547	0.11
0.655	789	2	7.7	23	1	58.8	13	0.24	372	0.00
0.663	863	2	-0.7	13	1	88.0	3	0.29	460	0.09
0.678	878	2	-0.8	13	1	87.5	2	0.30	427	0.09
0.715	925	2	-3.8	22	1	57.6	11	0.29	369	0.01
0.735	956	2	7.5	22	1	57.7	6	0.30	368	0.01
0.792	982	2	7.7	23	1	57.5	12	0.30	372	0.00
0.807	1130	2	7.7	23	1	120.9	12	0.37	372	0.00
0.835	1160	2	2.2	24	1	121.0	4	0.37	395	0.00
0.855	1670	4	-15.7	24	1	123.9	12	0.57	351	0.03
0.867	1832	4	-16.4	24	1	123.6	13	0.62	345	0.03

(b) Static

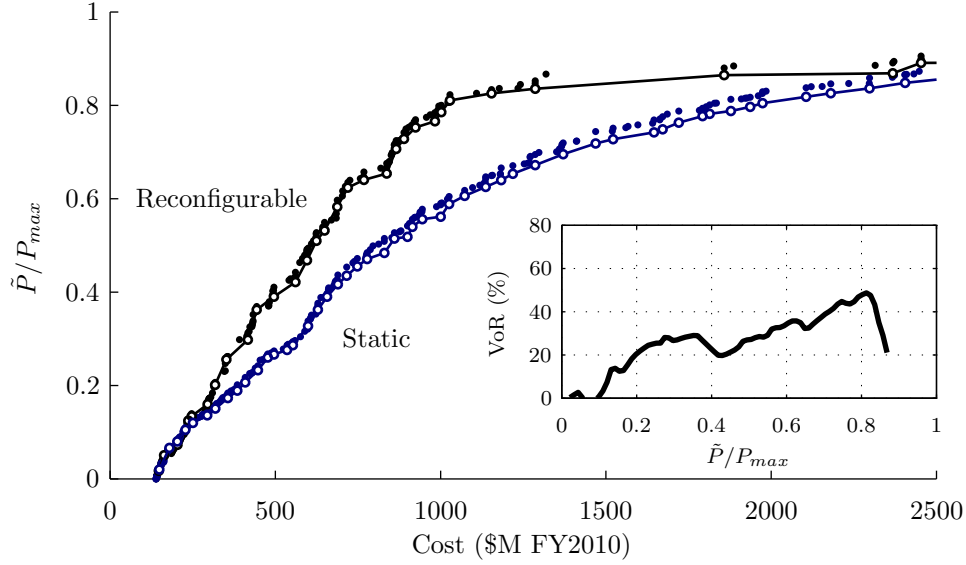| $\tilde{P}$	C	h_{GOM}	N_p	N_{sp}	i	F	D
-	$M	km	-	-	deg	-	m
0.026	115	470	1	4	88.1	0	0.13
0.050	138	387	1	6	121.0	0	0.14
0.081	198	372	1	6	119.7	0	0.23
0.107	229	397	2	4	121.8	0	0.18
0.124	260	396	2	5	118.7	0	0.20
0.155	324	402	3	4	121.3	2	0.19
0.187	376	404	3	4	121.0	0	0.24
0.216	415	364	4	4	121.9	2	0.19
0.235	440	378	4	4	121.2	0	0.21
0.250	465	419	4	4	121.3	0	0.23
0.287	540	370	4	5	121.2	0	0.23
0.302	589	426	5	4	121.8	1	0.25
0.328	618	383	6	4	120.9	1	0.21
0.349	654	431	6	4	121.2	1	0.23
0.392	774	567	12	2	121.6	10	0.26
0.400	796	522	11	2	121.7	4	0.29
0.420	829	450	24	1	57.8	22	0.26
0.458	917	587	11	2	122.1	9	0.34
0.494	950	559	12	2	122.1	3	0.34
0.519	1029	585	12	2	122.1	10	0.37
0.530	1154	575	12	2	122.1	10	0.43
0.563	1193	749	24	1	57.9	22	0.40
0.582	1229	775	23	1	56.7	21	0.43
0.609	1287	748	23	1	57.1	21	0.45
0.623	1307	762	24	1	58.2	22	0.45
0.654	1361	759	24	1	56.6	22	0.47
0.704	1557	903	24	1	55.9	22	0.54
0.720	1620	926	24	1	56.0	22	0.56
0.749	1756	967	24	1	55.9	22	0.60
0.768	1904	978	24	1	56.0	22	0.65

A.12 Symmetric Pattern: Scenario 11
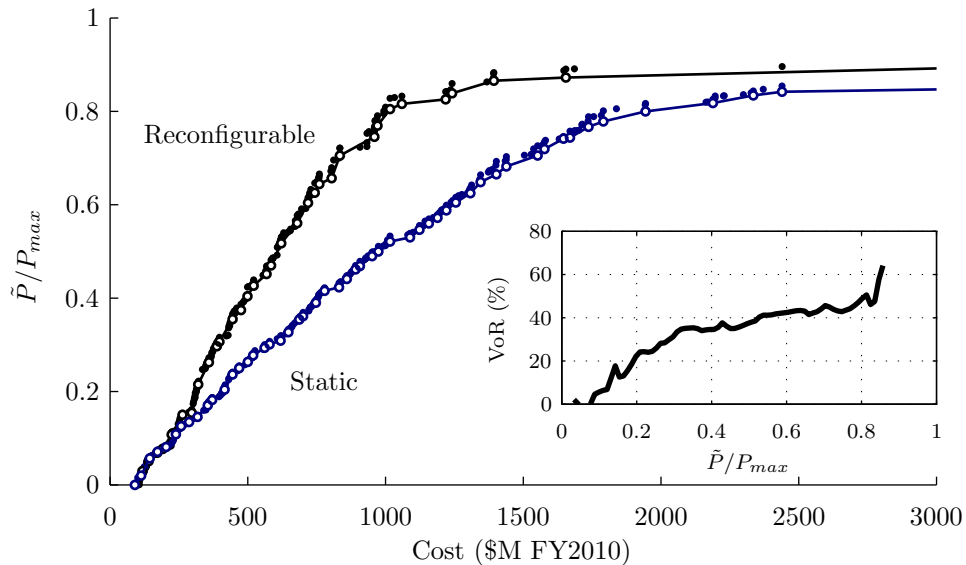
Figure A-12: Scenario 11 non-dominated front comparison with VoR

Table A.12: Non-dominated front design details

(a) Reconfigurable

$\tilde{P}$	C	$\frac{N_o}{N_d}$	Δalt	N_p	N_{sp}	i	F	D	ΔV_R	α_0
-	$M	-	km	-	-	deg	-	m	m/s	-
0.030	117	2	-21.7	1	4	67.4	0	0.13	161	0.08
0.051	140	1	34.2	1	6	62.3	0	0.15	1	0.06
0.069	171	1	27.2	1	6	60.8	0	0.19	4	0.79
0.108	224	2	0.5	3	2	57.7	1	0.17	215	0.02
0.150	263	2	-19.0	3	2	61.5	2	0.23	290	0.06
0.215	320	2	2.4	5	1	87.0	2	0.21	445	0.00
0.263	359	2	-19.8	5	1	87.4	2	0.25	672	0.03
0.297	388	2	1.1	5	1	87.6	1	0.29	434	0.00
0.355	445	2	10.4	12	1	57.5	6	0.20	360	0.08
0.374	475	2	-6.2	7	1	86.3	3	0.26	514	0.09
0.404	499	2	7.7	13	1	59.7	7	0.21	407	0.00
0.427	521	2	3.9	7	1	86.4	2	0.30	543	0.00
0.452	568	2	-23.1	12	1	58.9	4	0.25	754	0.01
0.470	585	2	-7.6	9	1	86.2	4	0.26	489	0.09
0.517	621	2	-8.0	9	1	86.9	4	0.28	646	0.06
0.561	679	2	-12.1	21	1	58.7	5	0.22	333	0.01
0.604	719	2	-14.8	21	1	57.8	4	0.24	323	0.01
0.626	743	2	-13.3	21	1	57.8	4	0.26	319	0.00
0.644	760	2	-13.0	21	1	58.6	4	0.26	352	0.01
0.657	804	2	-13.3	22	1	57.8	4	0.26	352	0.01
0.705	834	2	-1.7	23	1	57.5	5	0.26	328	0.00
0.746	960	2	23.2	22	1	59.0	20	0.30	604	0.00
0.769	971	2	-4.7	23	1	59.9	15	0.30	454	0.00
0.805	1016	2	-4.9	24	1	59.4	16	0.31	457	0.00
0.816	1059	2	-13.5	24	1	57.5	3	0.32	436	0.00
0.839	1242	2	-11.8	25	1	121.8	8	0.37	368	0.00
0.866	1393	2	-33.7	32	1	122.3	0	0.39	665	0.00
0.895	3185	6	-19.7	27	1	57.3	13	0.83	519	0.00
0.912	3587	6	-19.7	35	1	57.3	17	0.83	519	0.00
0.924	5975	6	-19.7	35	1	124.8	17	1.01	519	0.00

(b) Static

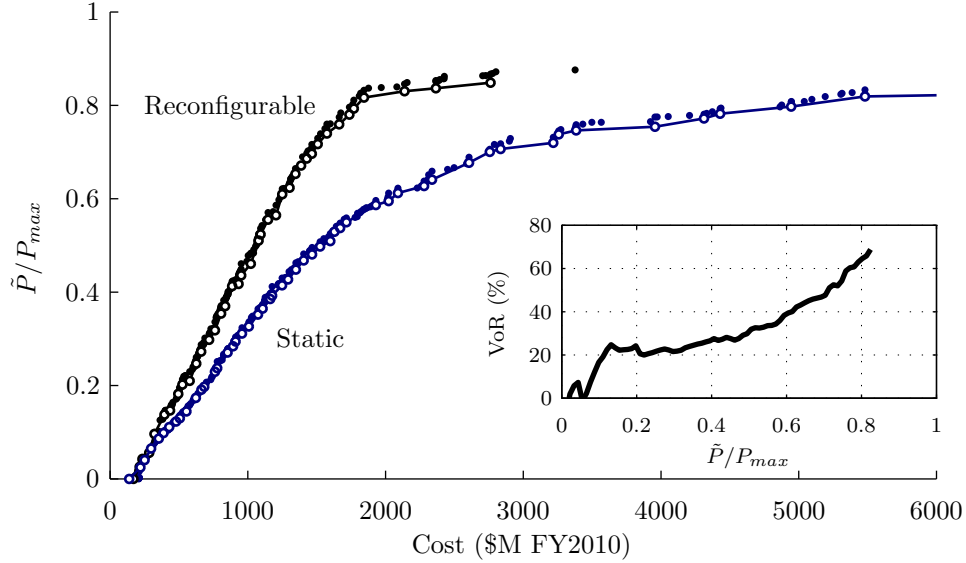| $\tilde{P}$	C	h_{GOM}	N_p	N_{sp}	i	F	D
-	$M	km	-	-	deg	-	m
0.000	90	656	1	3	60.6	0	0.10
0.020	113	656	1	3	60.6	0	0.15
0.057	144	429	1	5	59.6	0	0.18
0.071	172	342	1	6	59.2	0	0.19
0.108	239	360	2	4	58.9	1	0.19
0.126	258	380	2	5	58.9	0	0.19
0.170	355	413	3	5	59.1	1	0.19
0.182	371	420	3	5	59.1	1	0.21
0.237	445	350	4	4	121.5	1	0.21
0.250	469	409	4	5	58.0	2	0.20
0.278	520	355	4	5	121.5	1	0.21
0.309	619	401	6	5	58.9	1	0.18
0.354	687	359	5	6	95.9	2	0.22
0.390	747	417	7	5	88.6	3	0.20
0.416	779	427	7	5	90.6	3	0.21
0.423	831	389	7	5	94.3	5	0.21
0.462	891	410	7	5	89.2	4	0.24
0.490	951	421	7	5	90.6	4	0.26
0.521	1016	427	9	4	90.7	0	0.26
0.546	1123	461	9	4	90.4	3	0.27
0.588	1221	522	9	4	90.7	1	0.30
0.605	1255	519	9	4	90.4	4	0.31
0.649	1345	663	15	2	123.1	6	0.40
0.665	1402	689	16	2	122.9	14	0.41
0.705	1552	659	18	2	121.7	17	0.41
0.742	1646	738	17	2	123.1	8	0.46
0.767	1737	760	18	2	123.6	8	0.47
0.800	1944	815	18	2	123.6	16	0.53
0.818	2188	930	11	3	89.8	6	0.59
0.855	3874	995	11	3	89.4	8	0.94

A.13 Symmetric Pattern: Scenario 12
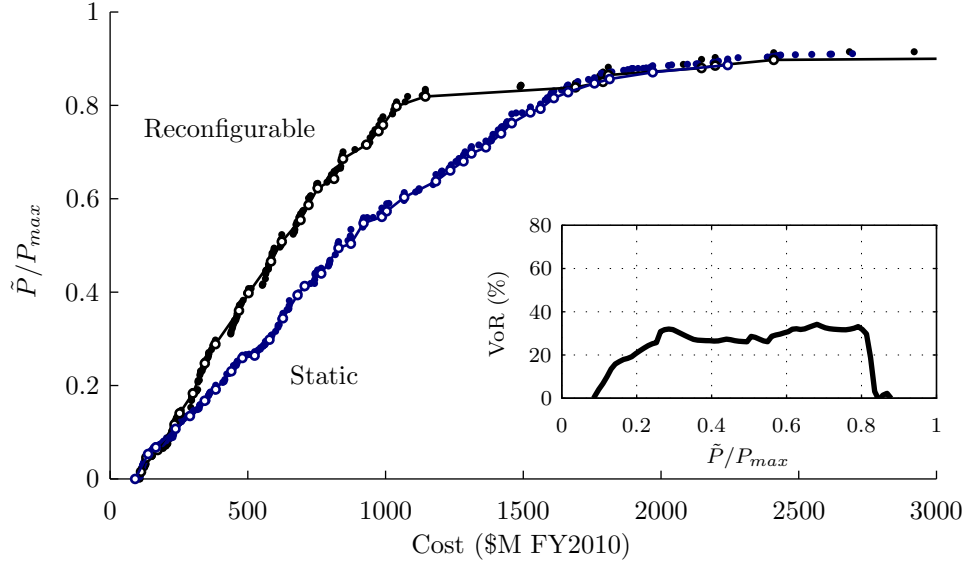
Figure A-13: Scenario 12 non-dominated front comparison with VoR

Table A.13: Non-dominated front design details

(a) Reconfigurable

$\tilde{P}$	C	$\frac{N_o}{N_d}$	Δalt	N_p	N_{sp}	i	F	D	ΔV_R	α_0
-	\$M	-	km	-	-	deg	-	m	m/s	-
0.015	112	2	10.6	1	4	78.6	0	0.11	215	0.27
0.046	132	1	50.0	1	5	59.5	0	0.15	24	0.72
0.062	172	1	50.0	1	5	59.5	0	0.20	415	0.54
0.117	234	2	-14.4	3	2	60.4	1	0.18	311	0.18
0.140	252	2	-3.2	3	2	59.1	1	0.21	382	0.20
0.183	301	2	10.1	4	1	59.1	0	0.26	439	0.00
0.248	344	2	-4.6	5	1	86.6	2	0.24	526	0.09
0.289	382	2	-0.9	5	1	87.5	2	0.28	519	0.10
0.360	468	2	-8.7	7	1	86.9	2	0.25	495	0.08
0.398	503	2	-18.9	7	1	87.5	1	0.28	661	0.09
0.466	584	2	-5.0	9	1	87.0	4	0.25	528	0.00
0.508	623	2	-19.0	9	1	87.3	1	0.28	693	0.09
0.555	691	2	-13.2	21	1	57.9	8	0.23	278	0.19
0.587	720	2	-14.2	21	1	57.6	8	0.24	282	0.18
0.622	754	2	-14.6	21	1	57.9	9	0.26	268	0.17
0.643	813	2	-19.7	21	1	57.7	2	0.26	435	0.00
0.686	846	2	-14.5	24	1	58.1	2	0.26	343	0.00
0.716	931	2	-14.6	21	1	58.0	2	0.31	343	0.19
0.745	975	2	-17.3	24	1	58.8	3	0.29	384	0.08
0.758	991	2	-11.3	23	1	57.8	10	0.31	300	0.08
0.798	1040	2	-16.9	24	1	60.0	6	0.31	418	0.01
0.819	1145	2	-14.0	26	1	59.7	6	0.32	416	0.00
0.824	1491	2	-1.3	15	2	87.5	1	0.34	219	0.20
0.839	1689	4	-15.8	25	1	122.7	2	0.54	421	0.00
0.850	1789	2	-0.1	26	1	120.7	0	0.56	298	0.00
0.865	1809	4	-6.7	28	1	58.5	12	0.53	392	0.00
0.880	2147	4	-0.5	36	1	123.1	3	0.56	271	0.00
0.885	2197	4	-0.5	36	1	56.4	3	0.58	271	0.00
0.897	2409	4	-0.5	36	1	123.1	13	0.62	271	0.00
0.913	6042	6	10.5	34	1	124.6	33	1.06	280	0.00

(b) Static

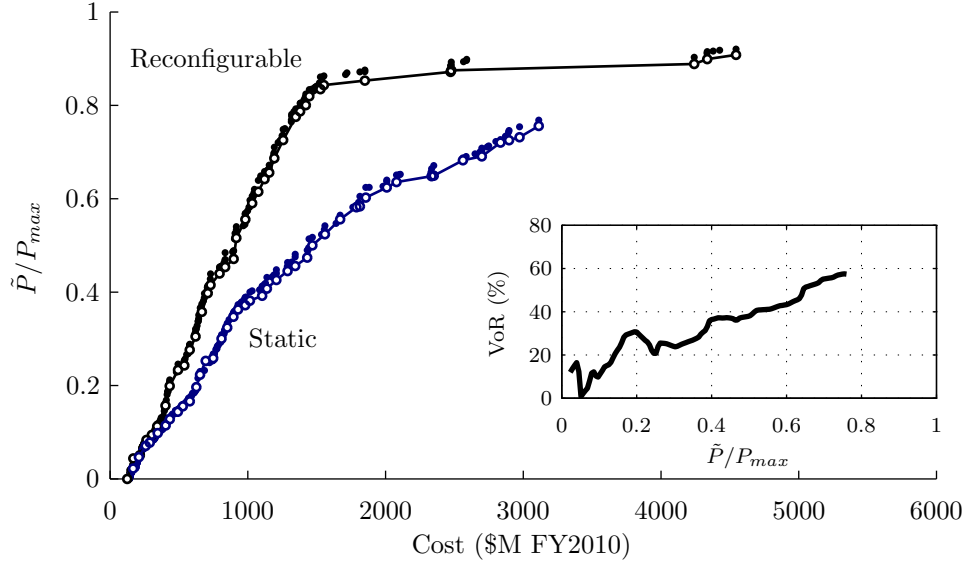| $\tilde{P}$	C	h_{GOM}	N_p	N_{sp}	i	F	D
-	\$M	km	-	-	deg	-	m
0.000	91	720	1	3	57.8	0	0.10
0.053	138	389	1	5	58.5	0	0.16
0.068	166	439	1	5	58.0	0	0.22
0.107	238	429	2	4	57.8	0	0.19
0.135	290	402	2	5	58.5	1	0.21
0.167	343	421	3	4	121.2	2	0.21
0.192	383	412	3	4	122.0	0	0.24
0.231	440	425	4	4	121.3	2	0.21
0.259	480	411	4	4	121.6	0	0.24
0.298	579	404	5	4	121.6	0	0.24
0.344	627	372	10	3	58.6	2	0.18
0.394	681	386	10	3	58.5	6	0.21
0.413	707	397	10	3	58.3	2	0.22
0.440	767	385	12	3	120.5	4	0.20
0.494	829	394	12	3	121.5	6	0.22
0.548	920	440	12	3	122.1	4	0.26
0.561	987	457	11	3	122.1	8	0.29
0.603	1068	498	12	3	122.2	4	0.30
0.637	1183	486	35	1	57.9	33	0.29
0.661	1235	545	36	1	57.4	34	0.30
0.680	1283	539	35	1	57.5	33	0.32
0.697	1312	537	35	1	57.6	33	0.33
0.710	1364	589	35	1	58.0	33	0.34
0.740	1420	590	35	1	57.4	33	0.36
0.762	1458	596	36	1	57.8	34	0.37
0.785	1526	602	36	1	57.3	34	0.39
0.816	1611	654	36	1	57.9	34	0.43
0.847	1758	713	36	1	59.0	34	0.47
0.871	1970	756	36	1	58.2	34	0.53
0.886	2242	826	36	1	63.1	34	0.55

A.14   Symmetric Pattern: Scenario 13

Figure A-14: Scenario 13 non-dominated front comparison with VoR

Table A.14: Non-dominated front design details

(a) Reconfigurable

$\tilde{P}$	C	$\frac{N_o}{N_d}$	Δalt	N_p	N_{sp}	i	F	D	ΔV_R	α_0
-	$M	-	km	-	-	deg	-	m	m/s	-
0.040	130	2	25.3	1	4	69.7	0	0.17	271	0.10
0.064	166	1	43.8	1	6	59.9	0	0.19	30	0.99
0.097	222	1	34.8	2	4	58.4	0	0.17	13	0.95
0.128	265	2	-2.4	4	1	110.7	2	0.20	518	0.00
0.201	312	2	1.2	5	1	86.7	1	0.20	426	0.05
0.262	351	2	1.2	5	1	86.7	1	0.25	426	0.05
0.304	399	2	-10.3	5	1	87.3	3	0.31	525	0.00
0.353	441	2	-10.3	12	1	57.9	10	0.20	448	0.01
0.390	484	2	1.6	7	1	87.2	1	0.27	453	0.07
0.447	539	2	-2.4	7	1	86.7	2	0.32	440	0.10
0.466	580	2	20.2	12	1	58.1	0	0.26	482	0.10
0.492	622	2	-15.2	12	1	58.8	11	0.29	405	0.11
0.542	663	2	-18.1	21	1	58.5	9	0.21	373	0.03
0.596	706	2	-15.4	21	1	58.4	0	0.23	430	0.00
0.620	765	2	-9.0	24	1	59.1	8	0.23	338	0.00
0.659	793	2	-2.7	24	1	59.3	13	0.24	338	0.00
0.714	855	2	-9.0	24	1	59.5	19	0.26	338	0.00
0.730	896	2	-17.5	21	1	58.5	9	0.30	373	0.03
0.765	940	2	-1.5	21	1	58.4	10	0.32	484	0.00
0.808	1020	2	8.4	24	1	58.9	6	0.31	506	0.00
0.812	1053	2	7.0	24	1	58.9	6	0.32	506	0.00
0.829	1193	2	-19.9	24	1	122.8	4	0.39	446	0.01
0.832	1272	2	-20.0	24	1	122.6	5	0.42	449	0.01
0.858	1348	2	-25.0	32	1	122.7	4	0.37	477	0.00
0.869	1426	2	-20.5	32	1	122.7	6	0.41	463	0.00
0.887	2174	4	-29.6	33	1	122.9	5	0.57	469	0.00
0.892	2335	4	-29.6	34	1	122.9	5	0.59	475	0.00
0.905	2789	4	-18.5	35	1	123.1	4	0.69	472	0.00

(b) Static

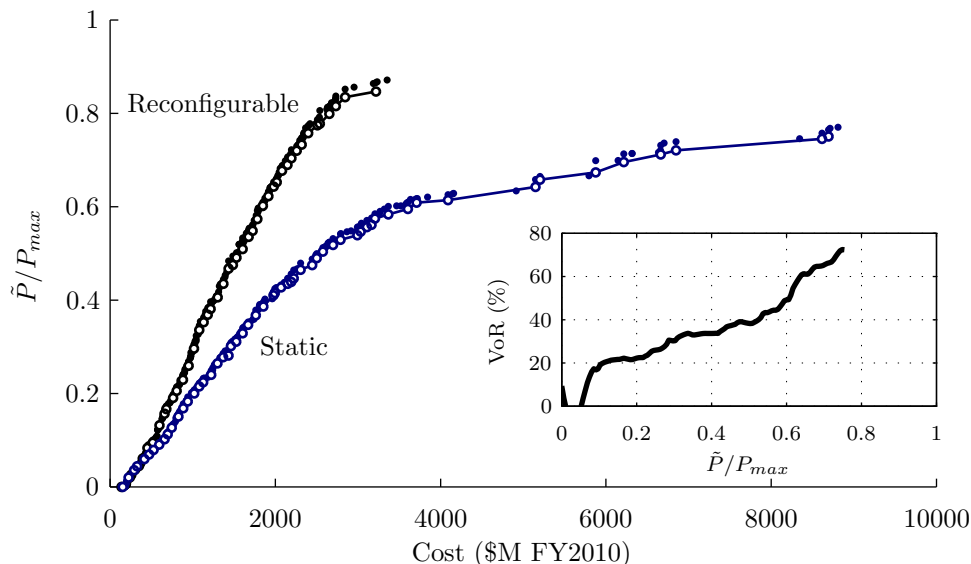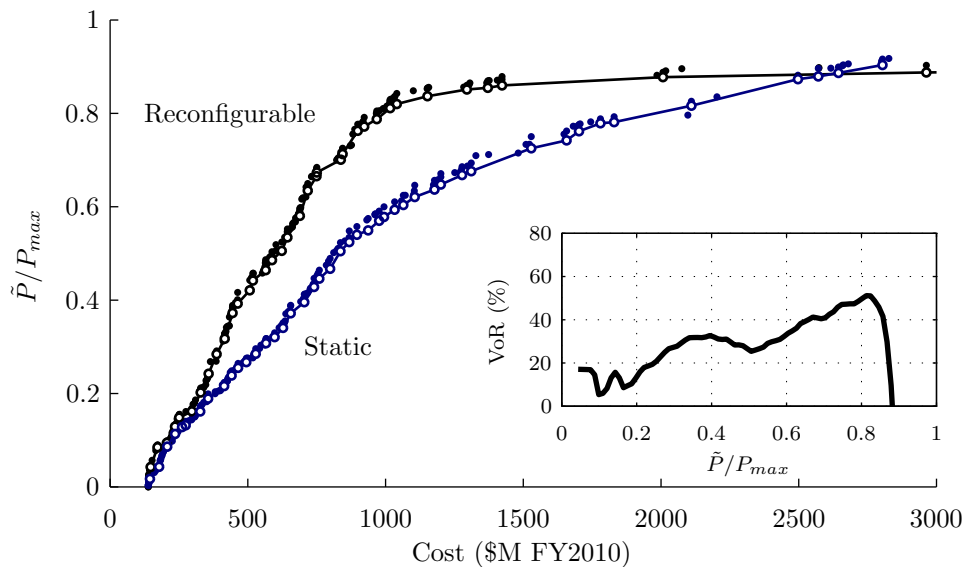| $\tilde{P}$	C	h_{GOM}	N_p	N_{sp}	i	F	D
-	$M	km	-	-	deg	-	m
0.044	125	387	1	5	121.6	0	0.13
0.067	170	365	1	6	116.7	0	0.19
0.118	247	389	2	5	120.7	1	0.18
0.140	291	384	2	5	121.5	1	0.22
0.189	377	398	3	4	121.3	1	0.24
0.220	422	394	4	4	121.4	0	0.20
0.257	475	397	4	4	121.4	0	0.24
0.310	561	414	10	2	122.1	2	0.23
0.363	624	418	10	3	122.0	4	0.19
0.397	660	405	10	3	122.0	2	0.20
0.456	742	418	10	3	122.0	1	0.24
0.481	788	417	10	3	122.0	2	0.26
0.522	866	399	12	3	121.7	8	0.24
0.563	943	426	12	3	122.0	2	0.27
0.571	962	435	12	3	122.2	7	0.27
0.588	1019	474	12	3	121.7	9	0.29
0.610	1104	491	12	3	121.4	5	0.32
0.628	1143	516	12	3	121.7	1	0.33
0.669	1253	576	12	3	122.6	9	0.36
0.686	1343	578	12	3	122.6	0	0.40
0.716	1429	635	36	1	123.0	2	0.36
0.753	1511	668	36	1	123.2	2	0.40
0.778	1546	671	36	1	123.2	2	0.41
0.799	1652	697	36	1	122.3	2	0.45
0.822	1744	704	36	1	123.0	2	0.47
0.838	1802	753	36	1	122.7	2	0.49
0.853	1925	802	36	1	121.5	2	0.52
0.876	2013	856	36	1	123.5	2	0.55
0.890	2141	893	36	1	123.5	2	0.58
0.909	2373	914	36	1	123.5	2	0.64

A.15 Symmetric Pattern: Scenario 14

Figure A-15: Scenario 14 non-dominated front comparison with VoR

Table A.15: Non-dominated front design details

(a) Reconfigurable

$\tilde{P}$	C	$\frac{N_o}{N_d}$	Δalt	N_p	N_{sp}	i	F	D	ΔV_R	α_0
-	$M	-	km	-	-	deg	-	m	m/s	-
0.000	96	5	-19.2	1	2	124.2	0	0.10	466	0.00
0.030	119	2	17.0	1	4	58.6	0	0.14	186	0.24
0.054	145	2	25.3	1	4	58.1	0	0.20	207	0.23
0.072	190	1	49.8	1	6	60.1	0	0.21	456	0.95
0.110	230	2	-7.7	3	2	67.1	2	0.17	283	0.24
0.151	292	2	-1.3	3	2	75.0	1	0.23	341	0.11
0.223	326	2	2.0	5	1	87.2	1	0.21	431	0.02
0.262	358	2	2.1	5	1	86.7	3	0.26	409	0.01
0.295	387	2	2.1	5	1	87.1	1	0.29	427	0.01
0.314	408	2	0.5	5	1	87.3	1	0.31	423	0.01
0.323	449	2	-1.0	7	1	88.4	0	0.23	402	0.02
0.380	488	2	-1.3	7	1	86.7	4	0.27	415	0.07
0.405	519	2	-1.2	7	1	86.8	2	0.30	401	0.08
0.431	536	2	-1.3	7	1	86.5	3	0.32	413	0.07
0.468	594	2	-1.2	9	1	86.7	1	0.26	400	0.04
0.519	625	2	-5.0	9	1	87.6	8	0.29	492	0.10
0.573	726	2	-7.7	11	1	87.2	4	0.27	560	0.12
0.609	751	2	11.1	11	1	87.8	4	0.29	557	0.09
0.626	766	2	10.8	11	1	88.4	1	0.30	559	0.10
0.653	805	2	8.3	23	1	59.9	7	0.24	459	0.00
0.681	827	2	-3.3	24	1	59.1	20	0.25	406	0.00
0.702	922	2	-2.3	13	1	88.4	1	0.33	399	0.02
0.741	979	2	-11.8	24	1	59.7	11	0.29	305	0.07
0.770	1019	2	-11.2	24	1	60.2	10	0.31	305	0.08
0.800	1101	2	-11.2	26	1	60.2	14	0.30	348	0.00
0.828	1183	2	10.8	23	1	122.4	7	0.39	402	0.00
0.842	1209	2	-5.4	24	1	122.2	23	0.39	430	0.00
0.855	1320	2	11.6	27	1	122.3	15	0.38	381	0.00
0.872	1461	2	10.8	33	1	122.4	10	0.39	402	0.00
0.895	6078	4	5.8	30	1	124.2	29	1.20	465	0.00

(b) Static

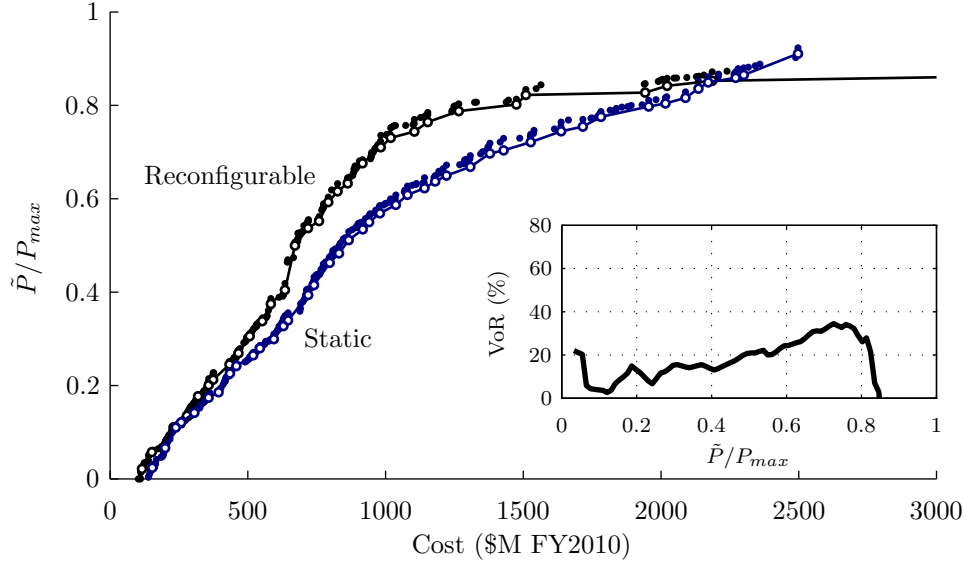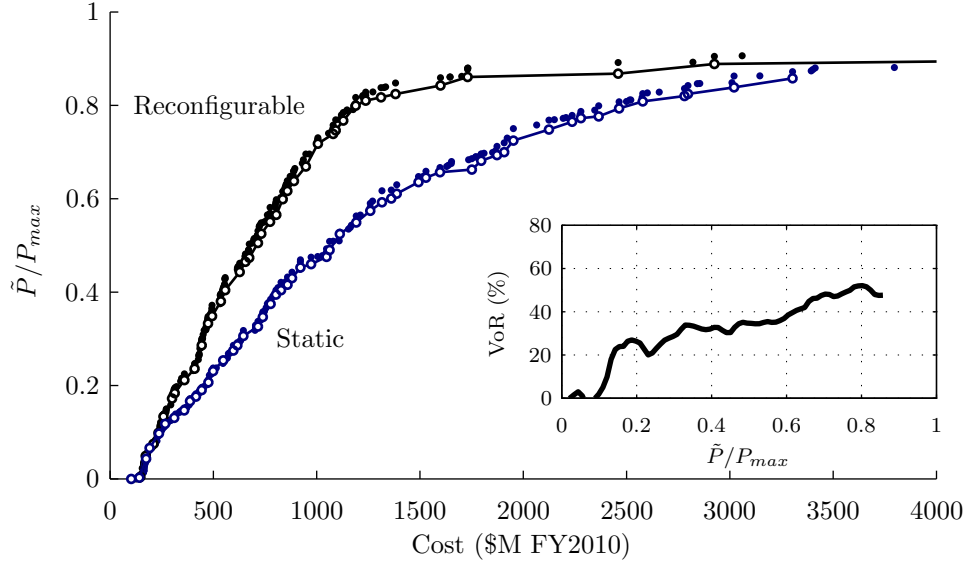| $\tilde{P}$	C	h_{GOM}	N_p	N_{sp}	i	F	D
-	$M	km	-	-	deg	-	m
0.012	108	498	1	4	121.4	0	0.10
0.062	155	425	1	5	120.6	0	0.19
0.091	216	410	2	4	121.7	1	0.16
0.121	251	372	2	5	121.2	0	0.18
0.151	316	369	2	5	121.8	1	0.23
0.177	364	419	3	4	120.3	2	0.23
0.220	432	412	4	4	120.1	2	0.20
0.247	469	446	4	4	122.1	1	0.23
0.294	568	392	4	5	121.9	0	0.24
0.333	638	427	6	4	121.8	2	0.22
0.346	661	440	6	4	121.6	2	0.23
0.392	736	380	7	4	122.0	3	0.22
0.406	802	389	6	5	60.5	0	0.24
0.432	851	379	8	4	120.2	5	0.23
0.468	907	394	9	4	121.4	6	0.21
0.498	947	383	9	4	121.9	6	0.23
0.524	1014	432	9	4	121.3	1	0.25
0.529	1044	482	9	4	91.2	1	0.27
0.557	1168	477	9	4	92.6	1	0.28
0.584	1222	508	9	4	89.5	4	0.30
0.621	1317	546	9	4	91.1	4	0.33
0.647	1404	598	9	4	88.8	1	0.36
0.665	1441	581	9	4	89.0	1	0.37
0.701	1557	659	9	4	90.5	5	0.41
0.714	1621	659	9	4	90.4	5	0.44
0.749	1812	758	9	4	90.7	6	0.49
0.766	1928	860	11	3	90.4	4	0.52
0.792	2044	878	11	3	90.6	4	0.55
0.820	2252	970	11	3	89.2	8	0.61
0.855	3042	995	11	3	89.7	8	0.80

A.16 Symmetric Pattern: Scenario 15

Figure A-16: Scenario 15 non-dominated front comparison with VoR

Table A.16: Non-dominated front design details

(a) Reconfigurable

$\tilde{P}$	C	$\frac{N_o}{N_d}$	Δalt	N_p	N_{sp}	i	F	D	ΔV_R	α_0
-	$M	-	km	-	-	deg	-	m	m/s	-
0.021	118	1	26.0	1	5	109.8	0	0.11	4	0.81
0.042	134	1	26.3	1	6	63.8	0	0.13	9	0.01
0.057	161	1	26.6	1	5	111.1	0	0.20	0	0.05
0.121	237	2	-0.7	3	2	67.5	1	0.18	254	0.12
0.142	290	2	-4.3	4	1	100.3	2	0.24	508	0.09
0.219	329	2	8.1	5	1	86.4	1	0.21	498	0.10
0.257	358	2	7.8	5	1	86.4	1	0.25	504	0.10
0.285	381	2	-2.0	5	1	86.9	4	0.28	484	0.16
0.315	417	2	-3.5	5	1	87.4	3	0.32	475	0.17
0.363	473	2	6.5	7	1	86.3	5	0.25	508	0.10
0.396	499	2	1.0	7	1	87.3	2	0.28	446	0.06
0.409	512	2	-2.6	7	1	86.5	5	0.29	506	0.09
0.430	569	2	10.5	9	1	86.4	7	0.23	500	0.10
0.476	594	2	0.6	9	1	86.7	2	0.26	526	0.06
0.509	624	2	-6.0	9	1	86.4	8	0.28	518	0.03
0.539	647	2	-3.2	9	1	86.5	1	0.30	496	0.03
0.561	673	2	4.4	9	1	86.9	7	0.32	446	0.07
0.594	744	2	1.7	11	1	87.4	10	0.28	440	0.14
0.629	775	2	1.8	11	1	87.2	10	0.30	449	0.06
0.661	803	2	0.4	11	1	87.3	9	0.32	443	0.01
0.711	917	2	-3.1	13	1	88.1	10	0.32	471	0.00
0.742	1041	2	-21.9	21	1	122.7	3	0.36	405	0.00
0.768	1096	2	-4.3	24	1	121.9	4	0.33	398	0.00
0.790	1138	2	-20.3	22	1	122.5	3	0.37	405	0.00
0.810	1169	2	-20.1	23	1	122.8	15	0.37	439	0.00
0.844	1229	2	-6.6	24	1	122.3	12	0.39	442	0.00
0.861	1375	2	-20.1	32	1	122.7	0	0.37	411	0.00
0.879	2024	2	24.7	35	1	122.2	0	0.53	456	0.00
0.887	3793	6	-38.7	18	2	124.6	8	0.81	410	0.02
0.912	4016	6	-20.5	35	1	124.6	15	0.87	403	0.02

(b) Static

$\tilde{P}$	C	h_{GOM}	N_p	N_{sp}	i	F	D
-	$M	km	-	-	deg	-	m
0.048	132	390	1	5	121.1	0	0.14
0.061	162	361	1	6	120.8	0	0.17
0.082	222	367	1	7	118.9	0	0.23
0.124	265	415	2	5	121.5	1	0.20
0.139	290	415	2	4	122.1	1	0.25
0.169	349	369	3	5	119.3	0	0.18
0.223	443	382	4	5	119.2	1	0.17
0.256	485	428	4	4	122.1	2	0.24
0.267	508	417	4	4	122.1	2	0.25
0.321	619	382	6	4	122.0	1	0.20
0.391	671	393	10	3	122.0	5	0.20
0.406	689	394	10	3	122.0	5	0.21
0.470	805	404	12	3	121.6	6	0.21
0.484	826	386	12	3	121.5	6	0.22
0.506	900	491	12	3	121.8	3	0.25
0.553	982	493	11	3	122.5	2	0.29
0.562	1018	514	12	3	122.3	7	0.28
0.602	1117	523	12	3	121.4	3	0.31
0.619	1158	507	12	3	121.4	3	0.32
0.639	1239	567	12	3	122.2	5	0.35
0.690	1392	645	12	3	123.1	3	0.40
0.692	1400	645	12	3	123.1	2	0.40
0.730	1514	588	35	1	121.9	2	0.39
0.756	1563	681	35	1	122.3	2	0.41
0.777	1611	692	36	1	122.7	2	0.42
0.805	1695	707	36	1	122.9	2	0.44
0.830	1863	825	34	1	123.7	2	0.51
0.866	2005	838	36	1	123.7	2	0.53
0.884	2123	869	36	1	124.0	2	0.56
0.905	2354	922	36	1	124.2	2	0.62

A.17 Layered Pattern: Scenario 1

Table A.17: Non-dominated front design details

(a) Reconfigurable

$\tilde{P}$	C	$\frac{N_o}{N_d}$	i_1	Δalt_1	$N_{p,1}$	$N_{sp,1}$	F_1	i_2	Δalt_2	$N_{p,2}$	$N_{sp,2}$	F_2	$\Delta\Omega_{key}$	ΔM_{key}	D	ΔV_R	α_0
-	$M	-	deg	km	-	-	-	deg	km	—	—	—	deg	deg	m	m/s	-
0.019	116	1	117.5	2	1	5	0	176.2	-15	-3	0	0	155	339	0.10	72	0.03
0.039	136	1	116.0	2	1	5	0	178.3	-11	-7	0	3	351	356	0.16	8	0.02
0.064	178	1	120.2	1	1	5	0	178.4	-14	-12	0	0	341	348	0.23	94	0.02
0.099	235	2	34.1	-1	1	2	0	109.7	-1	-18	4	0	99	97	0.24	178	0.37
0.116	266	2	37.4	-19	2	2	0	116.4	-37	-21	4	0	79	26	0.19	311	0.28
0.168	328	2	37.0	-0	2	2	0	110.7	-2	-31	3	0	98	86	0.28	150	0.35
0.191	344	2	61.5	8	5	1	3	169.2	-50	-35	0	2	175	67	0.25	339	0.04
0.235	385	2	61.9	-6	5	1	3	171.7	9	-43	0	0	232	111	0.29	490	0.02
0.284	418	2	62.4	-0	12	1	0	154.6	-46	-52	0	0	349	50	0.18	273	0.02
0.339	449	2	62.4	-1	12	1	0	155.3	-46	-62	0	0	349	145	0.21	272	0.02
0.367	480	2	58.1	-1	13	1	3	110.5	-49	-67	0	17	189	139	0.19	349	0.01
0.405	501	2	58.7	-0	13	1	3	155.9	-50	-74	0	17	233	142	0.21	348	0.00
0.428	513	2	58.1	-1	13	1	3	110.5	-49	-78	0	17	187	141	0.22	349	0.00
0.448	563	2	57.6	18	12	1	8	171.9	-49	-82	0	1	131	321	0.25	498	0.04
0.476	591	2	57.6	16	12	1	8	171.4	-49	-87	0	1	8	328	0.27	498	0.04
0.503	622	2	58.8	20	12	1	7	166.7	45	-92	0	1	39	341	0.29	514	0.04
0.561	690	2	59.7	19	13	1	10	134.1	-48	-102	0	22	39	70	0.30	515	0.04
0.631	747	2	57.9	-0	21	1	1	172.8	-17	-115	0	24	163	280	0.26	378	0.00
0.652	802	2	57.9	-0	22	1	1	172.9	-17	-119	0	24	163	281	0.26	378	0.00
0.673	827	2	57.6	18	24	1	16	171.9	-49	-123	0	0	12	321	0.25	394	0.00
0.689	880	2	57.6	11	25	1	16	171.9	-49	-125	0	2	12	321	0.25	394	0.00
0.743	920	2	57.9	-12	21	1	5	174.3	-47	-135	0	0	154	270	0.31	361	0.01
0.776	983	2	58.1	-12	24	1	6	179.4	-46	-141	0	0	242	288	0.29	357	0.00
0.808	1019	2	57.9	-8	24	1	10	179.8	-39	-147	0	0	251	294	0.31	446	0.00
0.827	1198	2	51.7	15	28	1	4	119.8	39	-151	3	0	297	233	0.33	329	0.00
0.872	1700	2	133.2	7	28	1	16	116.2	-28	-159	3	1	50	121	0.46	369	0.00
0.884	1762	2	132.4	6	29	1	17	116.5	-27	-161	3	0	49	128	0.46	367	0.00
0.908	6556	6	120.8	-20	26	1	21	138.0	-8	-165	2	2	276	125	1.17	454	0.00

(b) Static

$\tilde{P}$	C	i_1	$h_{GOM,1}$	$N_{p,1}$	$N_{sp,1}$	F_1	i_2	$h_{GOM,2}$	$N_{p,2}$	$N_{sp,2}$	F_2	$\Delta\Omega_{key}$	ΔM_{key}	D
-	$M	km	deg	-	-	-	deg	km	—	—	—	deg	deg	m
0.026	115	58.8	389	1	5	0	87.8	348	15	0	4	23	131	0.10
0.059	147	121.3	440	1	5	0	17.5	715	26	0	0	295	49	0.19
0.081	203	120.2	372	1	6	0	89.6	409	6	0	0	295	341	0.24
0.107	231	121.6	408	2	4	1	137.5	697	29	0	16	1	193	0.19
0.124	266	117.7	421	2	5	0	128.7	409	1	0	0	283	286	0.21
0.160	329	72.6	401	1	4	0	50.3	341	2	4	1	101	173	0.19
0.183	349	58.5	440	1	5	0	40.2	440	2	4	0	86	54	0.21
0.201	369	59.1	446	1	4	0	47.5	408	2	4	0	65	50	0.23
0.230	444	58.5	441	1	5	0	41.7	439	3	4	0	86	59	0.21
0.297	500	139.4	409	7	2	4	60.1	546	1	4	0	202	297	0.20
0.330	547	141.3	386	8	2	5	63.1	547	1	4	0	198	58	0.20
0.366	595	143.3	448	7	2	5	71.0	612	1	3	0	139	85	0.26
0.399	609	59.8	419	1	3	0	140.0	376	7	3	2	291	331	0.21
0.412	631	141.1	369	8	3	5	63.5	542	1	4	0	204	182	0.20
0.444	689	58.5	432	1	3	0	139.7	367	7	4	2	296	330	0.21
0.466	708	59.7	434	1	3	0	139.9	360	8	4	2	286	330	0.20
0.480	750	138.3	492	8	3	7	79.3	561	1	3	0	221	317	0.26
0.520	796	138.9	408	10	3	4	69.0	581	1	3	0	106	196	0.23
0.567	867	135.4	409	10	3	4	92.8	589	1	3	0	97	188	0.26
0.606	984	133.3	499	10	3	5	105.4	594	1	3	0	266	232	0.30
0.617	1012	133.9	503	10	3	5	100.0	598	1	3	0	268	228	0.31
0.633	1117	140.0	535	10	3	6	105.4	590	1	3	0	260	229	0.34
0.713	1289	138.5	581	17	2	16	122.3	585	1	2	0	39	341	0.36
0.733	1305	136.2	583	17	2	15	121.3	581	1	2	0	41	342	0.36
0.793	1470	134.8	650	17	2	3	102.2	702	1	2	0	206	218	0.42
0.810	2110	123.9	925	17	2	14	143.9	504	19	0	13	3	351	0.58
0.842	2274	123.8	919	18	2	15	148.2	495	20	0	13	5	343	0.61
0.844	2287	124.0	911	18	2	14	135.1	484	20	0	13	1	356	0.61

A.18 Layered Pattern: Scenario 2

Table A.18: Non-dominated front design details

(a) Reconfigurable

$\tilde{P}$	C	$\frac{N_o}{N_d}$	i_1	Δalt_1	$N_{p,1}$	$N_{sp,1}$	F_1	i_2	Δalt_2	$N_{p,2}$	$N_{sp,2}$	F_2	$\Delta\Omega_{key}$	ΔM_{key}	D	ΔV_R	α_0
-	$M	-	deg	km	-	-	-	deg	km	−	−	−	deg	deg	m	m/s	-
0.001	123	1	86.3	-8	1	5	0	107.2	48	-0	0	5	240	175	0.13	0	0.68
0.021	153	1	87.3	1	1	5	0	19.6	38	-4	0	0	272	14	0.19	40	0.66
0.062	299	2	68.1	46	1	4	0	40.8	19	-11	1	0	299	168	0.32	350	0.06
0.096	355	2	86.3	-2	5	1	4	138.6	11	-17	0	2	10	331	0.26	395	0.00
0.142	404	2	87.3	-8	5	1	1	132.4	7	-26	0	0	25	345	0.31	442	0.00
0.151	413	2	87.4	-8	5	1	1	132.4	-26	-27	0	0	25	235	0.32	442	0.00
0.169	485	2	87.1	-8	5	1	1	133.9	6	-31	0	0	24	347	0.35	442	0.00
0.213	539	2	86.1	0	5	1	2	148.8	-9	-39	0	0	12	330	0.42	388	0.02
0.241	616	2	58.1	-16	11	1	0	95.5	8	-44	0	5	97	276	0.31	467	0.00
0.275	658	2	57.6	-1	11	1	5	47.1	14	-50	0	12	15	215	0.34	415	0.00
0.320	719	2	86.9	-0	7	1	4	150.0	-10	-58	0	0	35	329	0.44	398	0.05
0.354	806	2	59.1	-9	11	1	4	94.9	8	-64	0	2	42	265	0.42	466	0.02
0.384	853	2	59.4	-3	11	1	3	137.0	7	-70	0	0	42	267	0.45	437	0.00
0.415	927	2	60.4	-1	13	1	7	160.9	3	-76	0	11	13	201	0.43	393	0.02
0.447	962	2	58.2	10	13	1	1	164.4	-34	-81	0	1	154	171	0.45	475	0.00
0.489	1045	2	58.3	-1	13	1	6	137.9	-4	-89	0	2	0	307	0.50	390	0.00
0.536	1118	2	57.9	-10	21	1	12	164.4	5	-98	0	3	51	49	0.41	447	0.00
0.593	1215	2	57.6	-7	21	1	12	158.5	-9	-108	0	7	33	55	0.46	412	0.00
0.611	1257	2	58.6	-5	21	1	7	172.2	-26	-111	0	1	94	86	0.47	437	0.00
0.639	1317	2	58.6	-4	21	1	12	160.4	33	-116	0	2	44	260	0.50	351	0.00
0.657	1392	2	58.6	-5	23	1	13	163.2	38	-120	0	1	47	244	0.48	381	0.00
0.689	1436	2	57.9	-2	21	1	18	154.8	11	-125	0	0	26	242	0.55	340	0.00
0.732	1571	2	57.9	-4	21	1	12	162.8	-29	-133	0	4	44	62	0.59	317	0.00
0.772	1673	2	57.5	-1	23	1	1	149.0	-1	-140	0	0	0	254	0.58	349	0.00
0.783	1738	2	58.5	-8	24	1	15	169.9	-5	-143	0	0	60	127	0.59	353	0.00
0.795	1763	2	57.9	-2	23	1	18	147.3	30	-145	0	0	76	329	0.61	355	0.00
0.834	2174	2	58.1	-7	29	1	22	97.6	-24	-152	0	0	118	181	0.63	391	0.00
0.848	2565	2	57.9	-3	35	1	28	29.5	-49	-154	0	5	39	61	0.67	494	0.00

(b) Static

$\tilde{P}$	C	i_1	$h_{GOM,1}$	$N_{p,1}$	$N_{sp,1}$	F_1	i_2	$h_{GOM,2}$	$N_{p,2}$	$N_{sp,2}$	F_2	$\Delta\Omega_{key}$	ΔM_{key}	D
-	$M	km	deg	-	-	-	deg	km	−	−	−	deg	deg	m
0.000	128	62.1	370	1	6	0	163.1	938	22	0	2	139	354	0.11
0.036	199	61.4	401	1	6	0	124.8	509	22	0	1	151	50	0.24
0.074	328	140.3	376	1	5	0	118.7	435	1	4	0	249	229	0.26
0.101	405	140.5	385	2	2	1	62.0	506	1	4	0	229	281	0.31
0.132	493	137.6	378	2	4	1	100.0	439	1	4	0	226	125	0.30
0.161	582	145.5	389	7	2	4	67.8	463	1	4	0	185	333	0.24
0.189	627	144.6	395	7	2	4	65.7	460	1	4	0	187	337	0.26
0.234	706	140.6	380	8	2	4	66.0	530	1	4	0	234	341	0.28
0.252	760	145.1	378	8	2	3	67.1	527	1	4	0	243	322	0.31
0.277	831	143.2	413	8	2	5	66.5	464	1	5	0	164	84	0.33
0.311	888	139.8	357	8	2	5	66.8	468	1	5	0	156	282	0.35
0.353	1002	145.1	389	8	2	5	65.2	467	1	4	0	159	343	0.43
0.380	1071	142.9	399	8	2	6	67.1	472	1	4	0	156	349	0.46
0.434	1180	141.2	372	8	3	2	90.7	571	1	5	0	173	284	0.41
0.470	1260	139.1	413	14	2	7	61.6	567	1	3	0	168	204	0.41
0.513	1394	142.9	411	14	2	6	61.4	558	1	3	0	168	0	0.45
0.528	1467	143.0	423	14	2	6	61.9	558	1	3	0	169	302	0.48
0.554	1550	143.0	411	14	2	7	60.7	561	1	3	0	167	3	0.50
0.586	1620	142.1	404	15	2	7	60.7	574	1	3	0	166	11	0.51
0.605	2037	38.6	428	29	1	10	57.8	620	3	2	0	159	164	0.56
0.649	2291	57.1	616	36	1	34	63.6	476	21	0	1	242	245	0.61
0.671	2390	57.8	612	36	1	34	63.6	474	21	0	1	240	245	0.63
0.696	2587	57.0	619	34	1	32	61.0	476	20	0	2	241	247	0.70
0.737	2729	57.4	547	36	1	34	63.1	464	2	0	0	354	204	0.71
0.764	2941	57.2	634	36	1	34	63.7	475	21	0	2	234	250	0.75
0.793	3199	58.9	646	36	1	34	70.5	480	21	0	4	194	356	0.80
0.817	3462	57.0	680	36	1	34	63.2	792	2	0	1	214	202	0.85
0.861	5578	60.2	717	36	1	34	8.9	391	20	0	4	352	302	1.11

A.19 Layered Pattern: Scenario 3

Table A.19: Non-dominated front design details

(a) Reconfigurable

$\tilde{P}$	C	$\frac{N_o}{N_d}$	i_1	Δalt_1	$N_{p,1}$	$N_{sp,1}$	F_1	i_2	Δalt_2	$N_{p,2}$	$N_{sp,2}$	F_2	$\Delta\Omega_{key}$	ΔM_{key}	D	ΔV_R	α_0
-	\$M	-	deg	km	-	-	-	deg	km	—	—	—	deg	deg	m	m/s	-
0.014	116	2	59.2	48	1	4	0	0.5	-34	-5	0	0	328	242	0.13	150	0.24
0.033	147	1	58.1	38	1	5	0	93.2	-43	-11	0	14	183	192	0.18	0	0.22
0.068	234	2	58.5	-4	3	2	1	165.0	22	-24	0	13	244	269	0.19	319	0.02
0.092	299	2	58.4	-1	4	2	1	169.7	23	-32	0	13	200	269	0.19	330	0.01
0.113	357	2	58.7	-7	5	1	2	80.9	5	-40	0	0	185	182	0.26	375	0.00
0.175	416	2	57.9	-20	12	1	4	129.8	-35	-61	0	18	78	264	0.17	493	0.05
0.222	455	2	58.4	-4	12	1	8	62.2	39	-78	0	0	75	116	0.21	390	0.00
0.266	565	2	58.8	-8	12	1	8	91.1	19	-93	0	8	187	276	0.25	491	0.10
0.285	580	2	58.4	-3	16	1	14	92.5	-1	-100	0	10	76	131	0.21	342	0.02
0.312	629	2	58.6	-18	21	1	12	97.0	4	-109	0	3	175	51	0.19	392	0.14
0.343	656	2	58.3	-16	21	1	3	157.3	37	-120	0	0	285	359	0.21	384	0.14
0.373	679	2	58.5	3	21	1	17	77.4	11	-131	0	10	56	305	0.22	393	0.00
0.390	749	2	58.0	-18	23	1	9	91.2	32	-137	0	0	55	19	0.22	508	0.14
0.413	762	2	58.5	-18	24	1	10	43.1	31	-145	0	0	191	182	0.22	507	0.08
0.447	808	2	59.1	-21	24	1	12	162.8	15	-157	0	1	223	269	0.24	501	0.07
0.467	831	2	58.3	-18	24	1	20	32.5	14	-163	0	1	230	298	0.25	462	0.07
0.500	898	2	58.9	-1	32	1	7	101.0	-49	-175	0	2	72	121	0.22	357	0.00
0.536	950	2	58.0	-19	31	1	11	20.4	4	-188	0	0	200	8	0.24	488	0.01
0.558	986	2	58.3	-18	32	1	8	83.6	-4	-195	0	2	227	298	0.25	465	0.07
0.575	1029	2	58.3	-13	32	1	10	74.7	-17	-201	0	2	159	85	0.26	430	0.00
0.615	1079	2	58.0	-19	32	1	12	56.0	3	-215	0	0	202	124	0.28	476	0.00
0.628	1101	2	58.0	-19	32	1	11	56.0	3	-220	0	0	202	0	0.29	485	0.00
0.662	1161	2	57.9	-18	32	1	11	56.9	0	-232	0	0	204	249	0.31	488	0.01
0.701	1272	2	58.3	-18	35	1	12	61.7	1	-245	0	0	204	228	0.31	515	0.01
0.718	1339	2	57.7	4	37	1	11	56.1	-17	-251	0	0	88	290	0.31	488	0.00
0.736	1424	2	58.0	-4	37	1	13	62.7	1	-258	0	1	127	250	0.33	497	0.00
0.761	1767	2	57.9	-5	35	1	11	56.2	-9	-267	1	0	7	221	0.31	502	0.00
0.822	3089	2	85.9	-4	36	1	28	61.2	32	-288	1	0	201	278	0.34	528	0.00

(b) Static

$\tilde{P}$	C	i_1	$h_{GOM,1}$	$N_{p,1}$	$N_{sp,1}$	F_1	i_2	$h_{GOM,2}$	$N_{p,2}$	$N_{sp,2}$	F_2	$\Delta\Omega_{key}$	ΔM_{key}	D
-	\$M	km	deg	-	-	-	deg	km	—	—	—	deg	deg	m
0.018	119	118.6	418	1	5	0	78.6	634	17	0	7	331	56	0.12
0.030	145	117.8	429	1	6	0	178.5	445	18	0	4	276	164	0.16
0.050	207	110.0	551	1	3	0	144.2	422	1	3	0	244	166	0.18
0.060	231	109.4	553	1	3	0	142.9	486	1	3	0	135	217	0.22
0.102	327	108.9	574	1	3	0	141.8	467	2	3	0	206	195	0.23
0.143	418	109.4	562	1	3	0	141.8	473	3	3	0	186	193	0.23
0.162	466	109.3	551	1	3	0	141.7	472	3	3	1	186	196	0.27
0.201	541	117.8	747	1	2	0	139.5	445	8	3	2	329	160	0.16
0.250	588	107.8	594	1	3	0	139.9	417	8	3	1	346	152	0.19
0.277	630	115.3	596	1	2	0	138.1	456	8	3	2	208	189	0.21
0.303	671	109.6	541	1	3	0	141.8	473	8	3	2	344	167	0.23
0.320	712	109.3	556	1	3	0	141.7	472	8	3	1	202	195	0.25
0.342	768	118.0	617	1	3	0	141.4	493	8	3	1	164	196	0.27
0.381	802	95.6	796	1	2	0	141.1	380	14	3	2	308	272	0.19
0.413	867	106.1	599	1	3	0	140.8	453	14	3	3	149	130	0.21
0.439	925	110.1	518	1	3	0	145.1	388	15	3	2	341	161	0.22
0.464	989	110.3	536	1	3	0	141.6	504	14	3	3	346	161	0.25
0.498	1010	107.3	562	1	3	0	142.2	440	15	3	4	134	126	0.25
0.508	1038	107.4	562	1	3	0	142.2	442	15	3	4	133	193	0.25
0.547	1159	106.6	552	1	3	0	142.3	472	15	3	4	134	195	0.28
0.594	1489	118.7	659	1	2	0	134.7	560	14	3	4	28	223	0.36
0.604	1574	114.6	621	1	3	0	139.6	699	12	3	6	277	138	0.43
0.626	1648	118.9	671	1	3	0	134.2	555	15	3	4	182	226	0.36
0.640	1680	106.6	647	1	3	0	137.2	647	14	3	6	332	195	0.41
0.673	1913	109.5	618	1	3	0	139.6	713	14	3	7	277	140	0.47
0.721	2279	114.5	789	1	2	0	137.3	859	13	3	10	337	125	0.58
0.750	2618	114.0	742	1	3	0	138.2	973	15	3	0	170	178	0.59
0.780	3134	110.9	778	1	3	0	133.4	987	15	3	0	335	135	0.63

A.20 Layered Pattern: Scenario 4

Table A.20: Non-dominated front design details

(a) Reconfigurable

$\tilde{P}$	C	$\frac{N_o}{N_d}$	i_1	Δalt_1	$N_{p,1}$	$N_{sp,1}$	F_1	i_2	Δalt_2	$N_{p,2}$	$N_{sp,2}$	F_2	$\Delta\Omega_{key}$	ΔM_{key}	D	ΔV_R	α_0
-	$M	-	deg	km	-	-	-	deg	km	−	−	−	deg	deg	m	m/s	-
0.000	130	1	118.8	2	1	5	0	50.0	3	-0	0	1	150	342	0.14	261	0.21
0.043	352	2	48.0	-18	1	4	0	63.7	-5	-15	3	0	121	354	0.32	193	0.24
0.075	449	2	120.7	36	1	2	0	50.0	-22	-26	1	2	28	116	0.33	475	0.14
0.084	502	2	120.9	29	1	2	0	49.9	-22	-29	1	2	27	117	0.32	475	0.12
0.130	580	2	120.9	-26	1	2	0	46.9	-21	-46	1	6	28	118	0.33	476	0.14
0.153	670	2	112.4	2	1	2	0	48.0	-7	-54	1	2	196	298	0.35	372	0.09
0.176	743	2	114.9	-2	1	2	0	46.9	-10	-62	1	0	186	360	0.44	335	0.14
0.198	795	2	121.3	-27	1	2	0	43.2	-21	-69	1	4	120	123	0.47	476	0.14
0.230	892	2	121.1	-26	1	2	0	50.0	-24	-81	1	8	31	118	0.32	481	0.13
0.245	943	2	117.1	-28	1	2	0	51.0	-6	-86	1	4	59	227	0.34	360	0.19
0.292	1039	2	117.7	-33	1	2	0	46.3	-20	-102	1	15	105	60	0.40	403	0.18
0.314	1100	2	115.5	-33	1	3	0	46.1	-20	-110	1	16	104	67	0.41	408	0.18
0.345	1153	2	113.8	-38	1	3	0	43.2	13	-121	1	5	129	150	0.37	314	0.14
0.390	1243	2	114.4	-41	1	3	0	43.3	12	-137	1	12	119	153	0.42	313	0.14
0.412	1315	2	97.3	-3	1	2	0	48.6	-19	-144	1	23	156	313	0.39	458	0.12
0.463	1414	2	102.4	6	1	2	0	51.7	-19	-162	1	19	152	348	0.43	448	0.08
0.501	1573	2	100.6	-39	1	3	0	48.7	-21	-176	1	11	54	126	0.42	496	0.11
0.529	1614	2	94.8	46	1	2	0	44.2	-18	-185	1	19	68	327	0.45	446	0.06
0.545	1725	2	118.7	6	1	2	0	52.0	-20	-191	1	20	146	338	0.53	392	0.11
0.583	1799	2	98.4	-34	1	3	0	46.7	-11	-204	1	25	186	196	0.50	432	0.00
0.613	1942	2	86.5	-18	1	3	0	46.6	-19	-214	1	14	186	212	0.52	388	0.08
0.627	1980	2	87.0	-18	1	3	0	46.7	-18	-219	1	14	189	213	0.53	389	0.06
0.656	2113	2	86.4	-18	1	3	0	46.6	-19	-230	1	14	204	197	0.55	419	0.08
0.681	2276	2	60.1	-16	36	1	14	175.4	-32	-239	0	0	15	353	0.60	410	0.01
0.721	2697	2	48.0	-18	36	1	15	88.9	-32	-252	8	0	73	339	0.61	431	0.01
0.740	4345	2	48.4	-15	36	1	26	116.4	-32	-259	10	0	10	356	0.82	416	0.00
0.784	4528	2	88.4	-19	35	1	23	89.3	-50	-274	10	0	1	263	0.66	571	0.00
0.799	4930	2	88.4	-19	35	1	23	89.7	-50	-280	10	0	318	262	0.73	566	0.00

(b) Static

$\tilde{P}$	C	i_1	$h_{GOM,1}$	$N_{p,1}$	$N_{sp,1}$	F_1	i_2	$h_{GOM,2}$	$N_{p,2}$	$N_{sp,2}$	F_2	$\Delta\Omega_{key}$	ΔM_{key}	D
-	$M	km	deg	-	-	-	deg	km	−	−	−	deg	deg	m
0.000	134	90.7	437	1	6	0	28.3	404	16	0	4	100	274	0.14
0.022	220	100.4	376	1	7	0	95.0	509	8	0	2	43	344	0.24
0.051	361	144.2	364	2	3	0	106.2	477	1	4	0	341	210	0.24
0.063	422	144.3	367	2	3	0	106.9	480	1	4	0	328	212	0.28
0.083	513	144.7	464	2	3	1	57.5	488	1	4	0	145	115	0.35
0.103	594	142.6	498	2	3	0	117.8	478	1	3	0	165	256	0.44
0.137	671	144.3	377	7	3	1	104.7	493	1	4	0	344	210	0.24
0.154	749	145.2	377	7	3	0	110.5	490	1	4	0	215	206	0.27
0.183	819	142.5	419	8	3	4	109.3	562	1	3	0	74	172	0.29
0.204	893	141.9	425	8	3	1	105.7	551	1	3	0	355	168	0.31
0.242	1023	141.8	424	8	3	4	105.0	558	1	3	0	358	168	0.36
0.273	1113	141.4	427	8	3	1	106.1	547	1	3	0	345	170	0.41
0.279	1221	139.2	362	9	4	1	121.9	620	1	5	0	261	122	0.32
0.329	1342	141.0	446	9	3	2	97.2	570	1	3	0	221	234	0.45
0.349	1456	142.0	410	12	3	4	97.3	574	1	3	0	164	356	0.39
0.399	1619	140.9	409	12	3	4	97.5	564	1	3	0	165	359	0.45
0.442	1669	140.6	374	15	3	7	73.3	529	1	3	0	12	360	0.41
0.470	1851	140.3	379	14	3	9	120.2	613	1	4	0	243	262	0.47
0.488	2172	143.7	441	14	3	4	112.1	597	1	3	0	152	181	0.53
0.546	2607	140.6	487	14	3	3	111.7	680	1	3	0	224	327	0.62
0.586	2962	141.2	540	15	3	0	116.6	730	1	3	0	140	45	0.66
0.603	3375	141.2	600	15	3	8	61.7	674	1	3	0	26	188	0.71
0.640	4029	141.4	611	15	3	4	112.0	670	1	3	0	42	322	0.78
0.669	4938	139.5	736	14	3	6	117.9	702	1	5	0	309	58	0.91
0.692	5152	139.6	694	15	3	0	118.9	765	1	3	0	97	44	0.93
0.718	6441	137.3	811	14	3	4	122.3	759	1	5	0	189	37	1.05
0.729	6828	142.5	853	15	3	0	124.0	892	1	3	0	216	14	1.08
0.742	8655	142.3	848	15	3	0	122.4	878	1	3	0	218	14	1.14

A.21 Restricted Asymmetric Pattern: Scenario 1
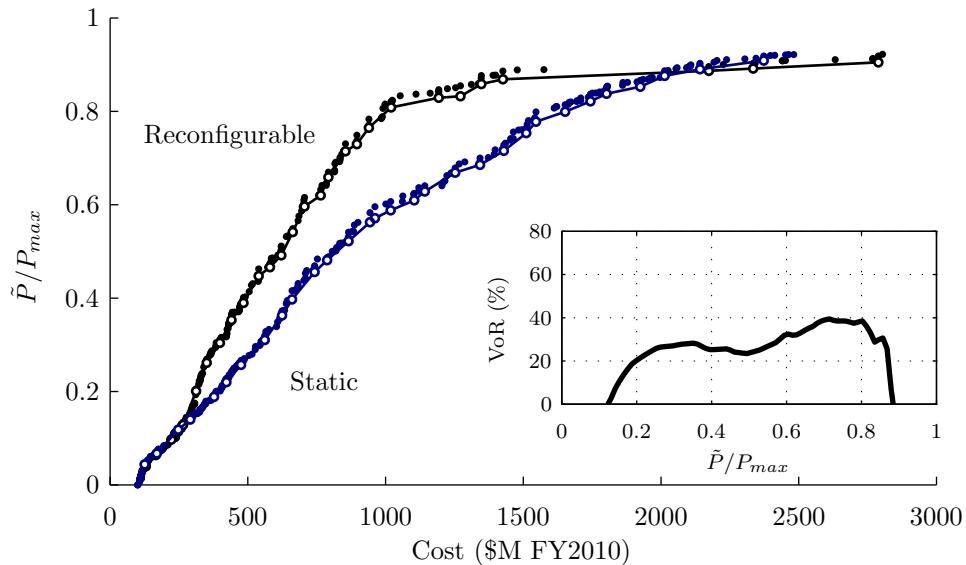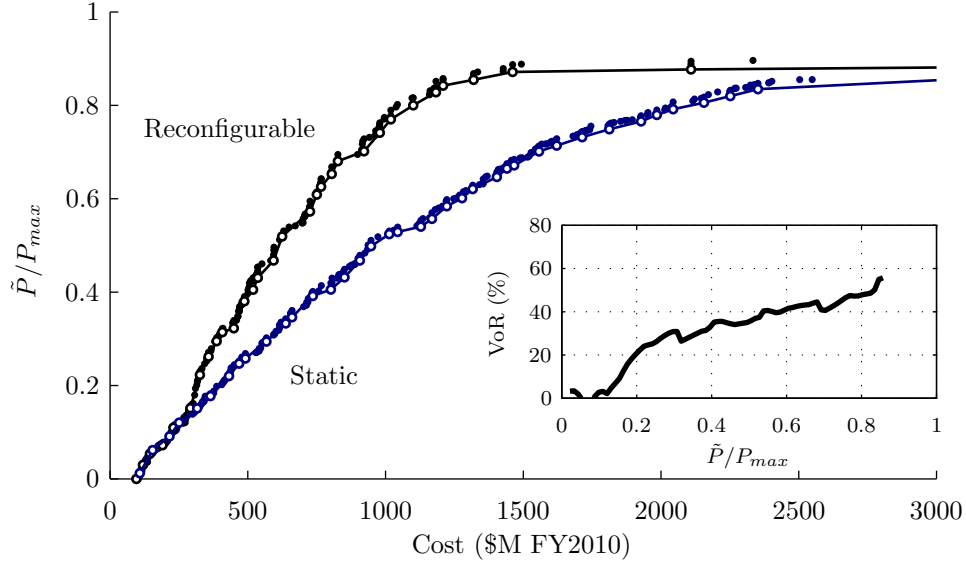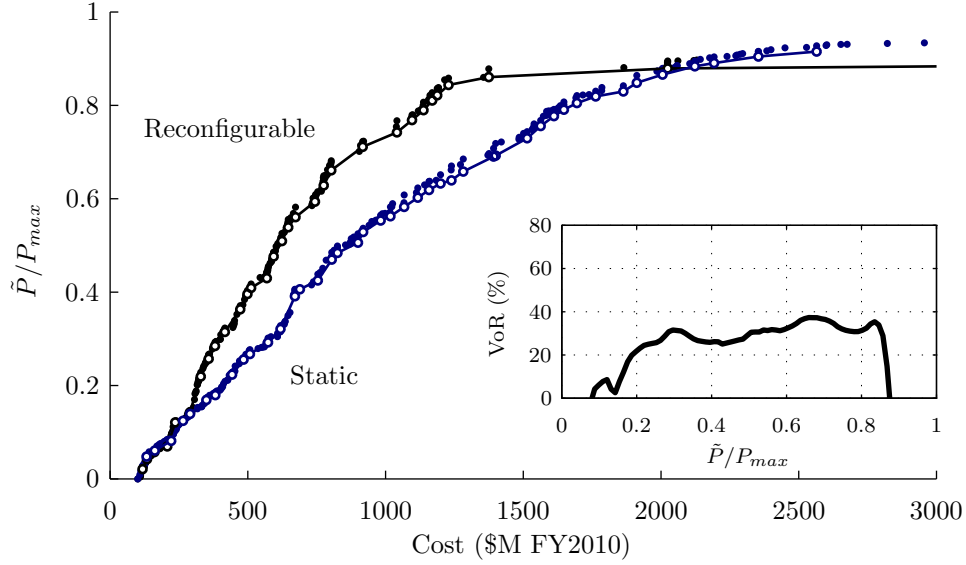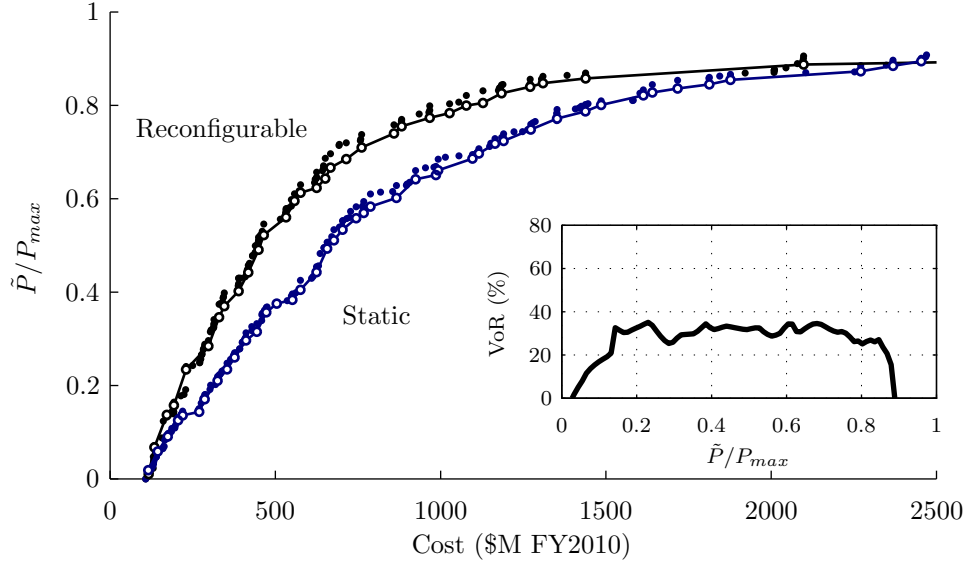

Figure A-17: Scenario 1 non-dominated front comparison with VoR

Table A.21: Non-dominated front design details

(a) Reconfigurable

$\tilde{P}$	C	$\frac{N_o}{N_d}$	Δalt	i	N_T	ξ_Ω	ΔM	D	ΔV_R	α_0
-	$M	-	km	deg	-	—	deg	m	m/s	-
0.010	117	3	25.0	60.9	4	0.02	238	0.13	138	0.21
0.068	134	2	15.6	62.0	4	0.06	1	0.17	428	0.25
0.137	172	2	9.0	61.7	4	0.19	16	0.18	490	0.20
0.158	193	2	9.4	61.7	5	0.19	16	0.18	489	0.19
0.234	230	2	-6.2	61.7	6	0.25	0	0.20	491	0.12
0.284	297	2	1.1	62.4	8	0.33	67	0.19	485	0.16
0.346	330	2	3.3	58.4	9	0.36	73	0.22	471	0.15
0.370	345	2	3.9	58.3	9	0.37	72	0.23	470	0.14
0.402	389	2	-3.3	62.8	10	0.41	12	0.22	491	0.09
0.442	418	2	-4.9	61.9	10	0.40	12	0.25	469	0.11
0.491	449	2	-2.8	60.3	12	0.49	0	0.24	464	0.14
0.522	465	2	-3.0	61.2	12	0.49	56	0.25	435	0.06
0.560	532	2	-6.8	59.0	11	0.45	210	0.30	506	0.00
0.595	558	2	-3.9	61.2	12	0.48	313	0.30	506	0.00
0.613	576	2	-4.5	61.7	12	0.49	305	0.31	504	0.00
0.623	625	2	-8.7	57.9	14	0.60	237	0.29	463	0.01
0.643	651	2	-9.4	58.0	14	0.59	168	0.30	463	0.00
0.667	667	2	-9.6	58.0	14	0.61	80	0.31	486	0.00
0.685	715	2	-10.8	57.9	15	0.62	330	0.32	529	0.00
0.710	761	2	12.1	60.1	16	0.65	294	0.31	501	0.00
0.740	859	2	-8.5	58.0	25	0.60	16	0.30	486	0.00
0.755	882	2	-8.5	58.0	25	0.60	18	0.31	486	0.00
0.773	967	2	-8.5	58.0	27	0.60	80	0.31	486	0.00
0.800	1078	2	-11.4	58.0	33	0.60	118	0.31	486	0.00
0.826	1184	2	-32.8	59.2	35	0.72	2	0.32	461	0.04
0.840	1271	2	10.6	58.1	35	1.00	7	0.31	516	0.00
0.848	1310	2	10.9	58.1	36	1.00	304	0.31	475	0.00
0.888	2098	4	-8.0	123.3	27	1.00	74	0.64	421	0.00
0.912	3933	6	8.9	125.1	30	1.00	102	0.93	425	0.00
0.924	4468	6	19.0	125.1	35	0.99	250	0.93	425	0.00

(b) Static

$\tilde{P}$	C	h_{GOM}	i	N_T	ξ_Ω	ΔM	D
-	$M	km	deg	-	—	deg	m
0.019	116	465	115.5	5	0.07	4	0.10
0.059	144	551	118.9	5	0.09	44	0.18
0.091	175	422	119.0	8	0.10	28	0.16
0.125	206	386	121.3	10	0.09	31	0.18
0.144	270	423	115.9	12	0.16	27	0.17
0.171	286	413	121.5	14	0.18	164	0.17
0.210	325	400	121.5	14	0.16	164	0.20
0.235	354	402	121.4	14	0.18	164	0.23
0.260	376	401	119.4	20	0.20	170	0.20
0.297	411	408	121.1	20	0.21	167	0.22
0.315	444	407	121.1	23	0.20	173	0.22
0.357	473	394	121.3	24	0.21	97	0.23
0.375	504	380	121.2	24	0.22	97	0.24
0.405	576	524	122.3	23	0.32	42	0.26
0.443	625	390	120.9	29	0.41	68	0.22
0.493	657	400	122.1	36	0.43	158	0.20
0.511	677	406	122.0	36	0.42	160	0.21
0.534	703	402	122.1	36	0.42	160	0.22
0.558	744	394	122.0	36	0.42	158	0.24
0.583	788	402	121.7	36	0.42	158	0.25
0.642	924	480	120.6	36	0.38	213	0.30
0.661	993	525	122.1	36	0.42	47	0.32
0.697	1116	560	121.6	35	0.51	46	0.34
0.718	1165	571	122.7	35	0.54	47	0.36
0.748	1273	644	121.5	35	0.51	165	0.40
0.772	1352	685	121.7	35	0.51	47	0.43
0.801	1486	691	121.1	36	0.54	166	0.44
0.828	1640	765	122.5	36	0.60	169	0.49
0.855	1877	871	122.5	36	0.60	170	0.55
0.885	2368	975	124.4	35	0.67	172	0.66

A.22 Restricted Asymmetric Pattern: Scenario 2
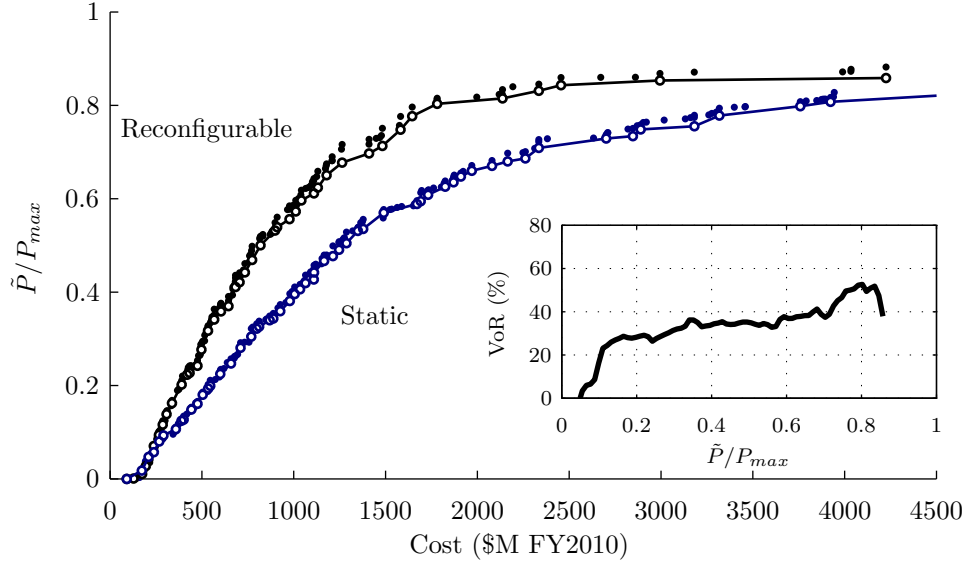
Figure A-18: Scenario 2 non-dominated front comparison with VoR

Table A.22: Non-dominated front design details

(a) Reconfigurable

$\tilde{P}$	C	$\frac{N_o}{N_d}$	Δalt	i	N_T	ξ_Ω	ΔM	D	ΔV_R	α_0
-	$M	-	km	deg	-	—	deg	m	m/s	-
0.000	91	3	5.0	61.2	3	0.00	240	0.10	94	0.07
0.001	128	1	25.4	59.6	6	0.00	62	0.11	76	0.42
0.027	195	1	19.8	64.2	8	0.03	197	0.18	360	0.27
0.070	238	2	2.5	58.1	6	0.23	111	0.22	294	0.00
0.094	266	2	-0.2	58.1	6	0.25	346	0.26	254	0.36
0.116	287	2	-0.3	58.1	6	0.25	344	0.28	257	0.11
0.139	308	2	-3.7	59.1	6	0.25	227	0.28	474	0.16
0.202	390	2	-3.7	59.9	6	0.24	225	0.37	473	0.15
0.223	420	2	-3.8	59.9	6	0.26	223	0.41	368	0.14
0.277	498	2	-7.5	60.8	9	0.38	358	0.34	462	0.16
0.317	533	2	-1.9	60.9	9	0.37	285	0.37	466	0.05
0.341	567	2	-0.6	61.0	9	0.39	345	0.41	403	0.03
0.359	604	2	3.1	59.1	9	0.38	290	0.44	404	0.04
0.411	683	2	-3.4	58.3	9	0.39	228	0.49	457	0.06
0.442	734	2	-3.2	58.8	12	0.49	229	0.43	445	0.00
0.469	774	2	-9.9	58.0	12	0.52	224	0.45	497	0.00
0.500	819	2	-3.9	59.6	12	0.50	209	0.48	458	0.06
0.532	898	2	-3.1	60.4	13	0.55	72	0.48	491	0.00
0.556	977	2	-5.0	58.5	12	0.48	197	0.56	472	0.07
0.573	1011	2	-6.5	57.8	14	0.61	144	0.52	439	0.01
0.611	1110	2	-6.7	58.1	14	0.58	275	0.56	412	0.03
0.650	1179	2	-5.5	58.6	14	0.58	294	0.60	420	0.02
0.677	1264	2	-5.7	58.1	15	0.62	285	0.61	418	0.00
0.697	1410	2	-10.3	57.6	18	0.76	76	0.60	381	0.00
0.713	1483	2	-10.2	57.6	18	0.76	76	0.63	382	0.00
0.748	1582	2	-4.1	58.7	18	0.75	253	0.66	486	0.00
0.777	1645	2	1.4	58.3	21	0.88	101	0.62	374	0.00
0.803	1781	2	-0.6	58.7	23	0.98	34	0.62	338	0.00
0.831	2335	2	-5.7	57.7	34	0.92	136	0.63	412	0.00
0.843	2455	2	-10.3	60.5	36	1.00	58	0.64	385	0.00

(b) Static

$\tilde{P}$	C	h_{GOM}	i	N_T	ξ_Ω	ΔM	D
-	$M	km	deg	-	—	deg	m
0.000	91	893	57.3	3	0.02	207	0.10
0.018	173	367	119.4	8	0.01	48	0.16
0.047	209	362	120.8	9	0.07	36	0.19
0.080	268	385	120.6	11	0.10	211	0.23
0.093	291	377	120.8	11	0.10	210	0.25
0.125	389	351	121.3	15	0.16	213	0.23
0.161	476	342	121.0	22	0.19	218	0.23
0.194	534	365	121.3	21	0.21	215	0.27
0.225	600	346	120.5	27	0.29	211	0.23
0.247	658	357	120.5	27	0.29	44	0.26
0.281	710	357	120.7	28	0.30	211	0.27
0.305	769	347	121.4	36	0.33	242	0.25
0.340	869	372	120.5	30	0.33	157	0.32
0.381	979	372	120.5	30	0.33	157	0.36
0.396	1005	382	121.1	36	0.41	28	0.32
0.427	1109	348	121.7	35	0.29	239	0.37
0.467	1166	348	121.8	35	0.32	239	0.39
0.491	1247	408	121.3	35	0.42	159	0.41
0.531	1349	412	121.2	36	0.41	163	0.44
0.570	1490	407	120.4	36	0.43	159	0.48
0.589	1671	491	122.4	36	0.44	168	0.53
0.609	1732	472	121.7	36	0.49	162	0.53
0.635	1870	470	121.4	36	0.47	165	0.56
0.670	2080	489	121.9	36	0.46	163	0.60
0.709	2335	518	122.6	36	0.52	164	0.66
0.729	2702	547	121.7	36	0.49	163	0.72
0.778	3318	659	121.9	36	0.58	166	0.83
0.798	3758	690	123.0	36	0.53	167	0.88
0.827	4767	749	122.5	36	0.62	167	0.99
0.848	5225	801	121.7	36	0.60	169	1.06

A.23 Restricted Asymmetric Pattern: Scenario 3

Figure A-19: Scenario 3 non-dominated front comparison with VoR

Table A.23: Non-dominated front design details

(a) Reconfigurable

$\tilde{P}$	C	$\frac{N_o}{N_d}$	Δalt	i	N_T	ξ_Ω	ΔM	D	ΔV_R	α_0
-	$M	-	km	deg	-	—	deg	m	m/s	-
0.036	126	2	3.4	64.0	5	0.08	203	0.12	472	0.00
0.080	171	2	-5.5	61.5	7	0.10	73	0.16	468	0.07
0.120	221	2	-6.6	59.4	7	0.20	147	0.17	483	0.02
0.161	267	2	0.4	58.5	7	0.18	126	0.23	493	0.03
0.212	298	2	-7.1	60.3	10	0.22	198	0.21	486	0.00
0.249	359	2	-12.3	60.0	10	0.21	0	0.26	482	0.02
0.289	397	2	-4.7	60.6	15	0.33	95	0.20	503	0.17
0.338	444	2	-11.4	58.9	15	0.35	320	0.23	477	0.00
0.357	467	2	-12.2	58.9	15	0.35	72	0.24	477	0.00
0.411	537	2	-3.2	59.0	15	0.33	322	0.29	507	0.00
0.431	577	2	-5.2	59.1	24	0.45	136	0.21	494	0.02
0.485	616	2	-5.0	61.9	20	0.42	284	0.26	494	0.01
0.500	661	2	3.5	60.6	20	0.40	226	0.28	482	0.00
0.532	709	2	3.4	60.4	20	0.40	227	0.30	483	0.00
0.553	730	2	2.6	61.4	24	0.51	205	0.26	495	0.00
0.599	803	2	-5.1	62.5	25	0.52	222	0.28	494	0.02
0.628	837	2	-0.3	59.1	25	0.56	276	0.29	435	0.00
0.655	937	2	-5.1	62.6	26	0.53	236	0.31	487	0.00
0.673	965	2	-5.4	62.5	27	0.56	233	0.31	487	0.00
0.713	1004	2	0.4	61.8	29	0.60	304	0.31	463	0.00
0.750	1159	2	-13.2	58.0	34	0.65	228	0.33	488	0.00
0.772	1302	2	-6.0	61.5	39	0.80	121	0.32	403	0.00
0.815	1438	2	2.8	60.5	45	0.95	293	0.31	451	0.00
0.825	1504	2	-5.2	59.4	46	0.97	149	0.31	449	0.00
0.839	1631	2	12.7	58.4	48	1.00	0	0.33	403	0.00
0.855	2449	4	-6.8	62.5	48	1.00	31	0.51	345	0.00
0.865	2513	4	-5.5	61.4	47	0.99	5	0.53	391	0.00
0.884	3352	4	3.8	57.2	48	1.00	337	0.70	389	0.00
0.897	4456	6	0.2	58.7	48	0.99	360	0.81	421	0.00
0.907	5672	6	6.4	55.1	48	1.00	339	0.92	364	0.00

(b) Static

$\tilde{P}$	C	h_{GOM}	i	N_T	ξ_Ω	ΔM	D
-	$M	km	deg	-	—	deg	m
0.022	125	458	121.5	5	0.02	65	0.14
0.045	177	532	121.2	9	0.08	204	0.16
0.084	221	391	120.2	14	0.10	120	0.15
0.114	269	391	120.2	19	0.10	120	0.16
0.138	352	476	119.7	16	0.10	79	0.25
0.168	405	359	119.2	30	0.20	193	0.15
0.194	446	372	118.5	30	0.19	59	0.18
0.209	465	354	120.0	29	0.18	194	0.19
0.245	532	391	119.2	36	0.19	202	0.20
0.268	574	383	119.2	43	0.19	240	0.19
0.296	613	402	120.3	37	0.27	196	0.20
0.321	654	371	120.8	44	0.28	240	0.19
0.348	702	411	121.8	42	0.31	242	0.22
0.376	739	379	120.8	48	0.30	78	0.21
0.409	881	380	120.9	47	0.35	238	0.24
0.440	939	470	120.3	48	0.30	81	0.27
0.464	948	473	121.5	48	0.30	81	0.27
0.489	1101	484	122.1	46	0.39	237	0.30
0.528	1201	541	122.6	47	0.36	240	0.32
0.549	1284	551	122.5	47	0.39	237	0.34
0.570	1395	602	122.1	47	0.38	123	0.37
0.591	1464	650	122.9	47	0.39	124	0.40
0.612	1522	662	122.9	48	0.38	124	0.41
0.639	1654	689	122.2	48	0.45	125	0.43
0.656	1767	724	121.5	48	0.44	124	0.46
0.675	1888	736	122.1	48	0.43	83	0.48
0.685	1964	804	123.3	48	0.51	126	0.49
0.723	2221	862	124.0	48	0.52	127	0.54
0.750	2698	991	124.3	48	0.66	129	0.61
0.777	2996	986	124.2	48	0.55	127	0.65

A.24 Restricted Asymmetric Pattern: Scenario 4

Figure A-20: Scenario 4 non-dominated front comparison with VoR

Table A.24: Non-dominated front design details

(a) Reconfigurable

$\tilde{P}$	C	$\frac{N_o}{N_d}$	Δalt	i	N_T	ξ_Ω	ΔM	D	ΔV_R	α_0
-	$M	-	km	deg	-	—	deg	m	m/s	-
0.000	108	4	-24.8	72.5	4	0.01	117	0.10	66	0.00
0.038	186	2	-2.6	59.6	5	0.10	37	0.23	383	0.05
0.059	264	2	-7.6	62.3	6	0.09	354	0.29	435	0.05
0.114	369	2	-4.0	58.0	9	0.21	140	0.28	464	0.01
0.151	448	2	8.5	58.4	10	0.21	296	0.33	423	0.00
0.179	502	2	1.8	62.1	10	0.21	294	0.37	424	0.02
0.214	588	2	-3.5	57.8	13	0.29	141	0.34	467	0.00
0.249	647	2	0.2	57.8	15	0.31	325	0.35	490	0.00
0.275	710	2	-2.1	58.4	13	0.29	305	0.43	512	0.00
0.325	809	2	7.6	58.0	17	0.38	152	0.39	482	0.00
0.367	886	2	6.9	58.2	20	0.46	186	0.39	487	0.00
0.401	941	2	6.8	60.5	20	0.45	164	0.42	486	0.00
0.442	1098	2	-3.4	62.0	21	0.45	46	0.46	492	0.04
0.490	1200	2	6.4	60.8	24	0.51	233	0.46	494	0.00
0.516	1227	2	-6.0	60.9	25	0.51	234	0.46	494	0.00
0.548	1414	2	-1.3	58.0	24	0.45	319	0.56	465	0.04
0.575	1479	2	1.1	59.9	24	0.49	337	0.56	465	0.00
0.587	1528	2	-12.6	60.1	24	0.51	175	0.57	479	0.04
0.609	1617	2	9.6	59.2	25	0.54	261	0.59	426	0.03
0.626	1694	2	-1.3	60.2	29	0.59	269	0.55	457	0.02
0.653	1796	2	13.9	59.2	27	0.56	148	0.60	482	0.02
0.722	2093	2	7.7	58.1	32	0.66	208	0.62	404	0.00
0.748	2362	2	15.0	61.3	37	0.76	158	0.62	482	0.02
0.770	2445	2	14.0	59.2	40	0.88	146	0.61	492	0.00
0.788	2572	2	14.3	59.0	41	0.88	144	0.62	481	0.00
0.808	2720	2	9.9	60.3	47	1.00	200	0.59	451	0.00
0.830	2983	2	13.6	58.8	47	1.00	26	0.64	504	0.00
0.858	4363	2	14.1	121.4	47	0.99	212	0.81	459	0.00
0.881	8993	4	7.1	121.9	46	0.99	262	1.20	328	0.00
0.896	9120	4	6.5	122.4	48	1.00	259	1.18	339	0.00

(b) Static

$\tilde{P}$	C	h_{GOM}	i	N_T	ξ_Ω	ΔM	D
-	$M	km	deg	-	—	deg	m
0.000	107	755	71.8	4	0.00	224	0.10
0.016	179	375	63.3	6	0.00	63	0.20
0.044	278	370	121.2	17	0.10	240	0.18
0.069	350	399	121.5	16	0.10	237	0.24
0.074	391	423	121.8	17	0.10	245	0.26
0.101	504	375	121.8	16	0.09	240	0.33
0.138	606	362	121.6	28	0.18	239	0.26
0.172	743	372	121.5	39	0.28	81	0.24
0.215	897	362	121.5	40	0.25	194	0.28
0.252	1046	369	121.5	40	0.26	200	0.32
0.271	1186	463	121.9	38	0.29	203	0.38
0.302	1264	454	121.8	39	0.30	202	0.41
0.316	1312	381	121.6	48	0.35	235	0.34
0.360	1494	373	121.7	48	0.35	235	0.39
0.381	1587	388	121.4	48	0.38	239	0.42
0.404	1708	389	121.4	48	0.35	239	0.45
0.414	1829	456	121.9	46	0.37	242	0.48
0.453	2175	493	121.9	47	0.39	246	0.54
0.472	2197	495	121.9	48	0.35	241	0.54
0.490	2480	548	121.0	47	0.42	201	0.60
0.533	2818	513	121.2	48	0.36	241	0.65
0.542	3080	547	121.5	47	0.41	202	0.69
0.559	3169	579	121.5	48	0.45	240	0.70
0.586	3707	599	122.5	48	0.49	202	0.77
0.611	4252	736	121.8	48	0.45	203	0.84
0.638	4833	724	123.2	47	0.46	202	0.90
0.668	6139	792	123.6	48	0.68	236	1.00
0.683	6509	891	123.9	48	0.68	246	1.05
0.721	8603	936	122.6	48	0.56	251	1.13
0.736	8960	964	122.8	48	0.57	253	1.17

A.25 Restricted Asymmetric: Limited Satellites Results

Table A.25: Non-dominated front design details

(a) $N_T \leq 12$

$\tilde{P}$	C	$\frac{N_o}{N_d}$	Δalt	i	N_T	ξ_Ω	ΔM	D	ΔV_R	α_0
-	$M	-	km	deg	-	−	deg	m	m/s	-
0.000	104	4	-46.7	120.1	3	0.00	239	0.12	2	0.97
0.033	119	2	-2.8	57.8	5	0.08	10	0.10	336	0.20
0.091	137	2	-2.3	58.6	5	0.11	179	0.15	361	0.13
0.128	177	2	-1.3	57.9	5	0.22	333	0.15	387	0.02
0.188	209	2	4.7	58.0	6	0.27	258	0.17	504	0.17
0.220	224	2	4.7	58.0	6	0.27	258	0.20	381	0.17
0.236	239	2	-7.2	57.7	6	0.23	301	0.22	478	0.06
0.255	250	2	5.3	57.9	6	0.26	256	0.23	393	0.17
0.280	275	2	5.5	57.8	6	0.26	33	0.26	395	0.17
0.295	294	2	-7.0	57.9	8	0.39	300	0.21	391	0.03
0.325	315	2	-6.5	60.1	9	0.39	273	0.21	370	0.00
0.338	320	2	-4.2	61.5	9	0.39	275	0.21	379	0.01
0.370	333	2	-0.1	61.0	9	0.38	193	0.22	367	0.19
0.384	348	2	-5.8	57.9	9	0.38	271	0.24	409	0.18
0.434	404	2	-6.1	59.3	9	0.38	273	0.27	415	0.12
0.448	412	2	-4.2	61.5	9	0.38	277	0.27	484	0.00
0.473	432	2	-10.9	61.8	11	0.46	360	0.24	490	0.00
0.507	458	2	-1.2	58.3	12	0.51	152	0.25	343	0.11
0.520	479	2	-0.1	58.3	12	0.54	161	0.27	336	0.17
0.568	540	2	-7.3	62.2	11	0.46	300	0.30	484	0.01
0.586	570	2	1.8	58.4	12	0.48	241	0.31	463	0.02
0.605	588	2	7.6	62.1	12	0.50	330	0.32	457	0.14
0.645	747	2	-0.5	87.2	11	0.47	279	0.29	416	0.04
0.665	758	2	-0.9	86.4	11	0.46	299	0.30	469	0.02
0.684	779	2	-0.5	87.2	11	0.47	279	0.32	416	0.04
0.699	789	2	0.7	86.5	11	0.46	300	0.32	461	0.04
0.720	822	2	-0.8	87.2	12	0.50	304	0.30	470	0.02
0.769	969	2	-2.4	87.0	12	0.51	337	0.33	471	0.12

(b) $N_T \leq 24$

$\tilde{P}$	C	$\frac{N_o}{N_d}$	Δalt	i	N_T	ξ_Ω	ΔM	D	ΔV_R	α_0
-	$M	-	km	deg	-	−	deg	m	m/s	-
0.058	120	2	9.3	58.7	4	0.10	156	0.13	360	0.09
0.089	136	2	9.2	58.9	4	0.09	151	0.17	361	0.09
0.102	159	2	-13.8	58.9	5	0.10	30	0.18	322	0.00
0.151	189	2	1.1	57.7	5	0.19	54	0.18	390	0.06
0.188	207	2	0.4	58.7	6	0.26	202	0.17	442	0.12
0.268	255	2	2.9	58.7	6	0.26	47	0.24	435	0.14
0.318	309	2	15.2	60.9	9	0.37	41	0.19	510	0.00
0.368	331	2	1.8	58.7	9	0.40	42	0.22	414	0.13
0.420	404	2	1.4	60.2	10	0.44	17	0.24	474	0.11
0.456	428	2	-2.5	59.9	11	0.48	100	0.24	429	0.20
0.494	453	2	-5.1	61.5	12	0.49	94	0.25	432	0.18
0.527	501	2	-1.7	61.0	11	0.47	106	0.28	428	0.18
0.554	524	2	-2.4	61.2	12	0.51	105	0.28	433	0.18
0.571	550	2	0.0	57.9	12	0.49	105	0.29	427	0.01
0.600	574	2	-1.6	58.9	12	0.51	98	0.31	439	0.18
0.624	623	2	8.3	58.2	14	0.58	6	0.28	501	0.00
0.644	641	2	-4.4	58.9	14	0.57	108	0.30	443	0.06
0.677	679	2	5.7	58.1	15	0.64	3	0.30	491	0.00
0.703	749	2	15.1	58.8	16	0.63	3	0.31	498	0.00
0.722	803	2	15.6	59.6	18	0.74	40	0.31	438	0.01
0.744	855	2	8.6	58.9	19	0.79	30	0.31	431	0.00
0.765	909	2	-13.4	58.9	21	0.90	30	0.31	444	0.00
0.786	990	2	16.9	59.3	21	0.85	69	0.34	511	0.00
0.812	1043	2	5.8	58.1	24	1.00	43	0.32	343	0.00
0.841	1198	2	11.6	122.5	24	1.00	219	0.39	398	0.00
0.858	1739	4	-18.0	122.5	24	0.99	220	0.59	357	0.06
0.877	2102	4	-5.0	123.0	24	0.99	216	0.69	414	0.00
0.895	4556	6	13.1	122.5	24	1.00	220	1.05	349	0.00

(c) $N_T \leq 48$

$\tilde{P}$	C	$\frac{N_o}{N_d}$	Δalt	i	N_T	ξ_Ω	ΔM	D	ΔV_R	α_0
-	$M	-	km	deg	-	−	deg	m	m/s	-
0.028	116	2	4.9	58.6	4	0.02	251	0.13	140	0.52
0.076	154	2	-19.5	59.0	7	0.11	52	0.13	445	0.01
0.118	176	2	-19.5	59.0	7	0.11	52	0.17	445	0.01
0.175	209	2	0.8	59.2	4	0.17	49	0.23	488	0.00
0.248	238	2	-2.3	59.0	6	0.26	57	0.22	441	0.02
0.287	266	2	-2.0	59.5	6	0.26	55	0.25	443	0.02
0.292	290	2	1.2	59.0	8	0.35	47	0.20	461	0.13
0.353	321	2	-0.1	59.1	9	0.40	51	0.21	429	0.12
0.399	349	2	-0.3	58.0	9	0.41	46	0.24	457	0.00
0.431	404	2	8.4	59.1	9	0.40	219	0.27	430	0.12
0.449	424	2	4.6	59.9	12	0.51	23	0.23	415	0.16
0.483	445	2	-3.5	59.1	9	0.40	44	0.30	428	0.12
0.492	475	2	8.5	59.1	9	0.40	204	0.32	465	0.12
0.516	501	2	-0.1	60.9	13	0.54	1	0.24	454	0.12
0.549	536	2	15.7	61.8	15	0.62	196	0.24	500	0.02
0.589	592	2	-0.1	60.8	13	0.55	3	0.28	454	0.11
0.605	616	2	8.0	60.9	13	0.54	4	0.30	454	0.07
0.665	660	2	11.7	58.9	14	0.59	89	0.31	482	0.08
0.701	772	2	13.0	58.9	16	0.63	97	0.32	493	0.07
0.749	910	2	21.3	59.1	21	0.85	44	0.30	528	0.05
0.764	964	2	-3.4	61.4	23	1.00	212	0.30	382	0.00
0.780	984	2	-4.3	61.4	23	1.00	254	0.30	382	0.00
0.801	1018	2	-4.3	61.4	24	1.00	254	0.31	382	0.00
0.831	1260	2	-42.0	58.0	42	0.83	7	0.30	474	0.08
0.853	1347	2	-37.4	58.0	43	0.84	27	0.31	474	0.00
0.870	1562	2	-25.8	59.5	47	0.96	123	0.32	430	0.00
0.897	1962	2	2.5	118.5	48	1.00	1	0.42	495	0.00
0.928	3238	4	-12.0	122.8	48	1.00	161	0.66	430	0.00

A.26 Restricted Asymmetric: Limited Reconfigured Satellites

Table A.26: Non-dominated front design details

(a) $\xi_R = 0.125$

$\tilde{P}$	C	$\frac{N_o}{N_d}$	Δalt	i	N_T	ξ_Ω	ΔM	D	ΔV_R	α_0
-	$M	-	km	deg	-	−	deg	m	m/s	-
0.027	118	2	-40.7	119.8	4	0.06	198	0.13	178	0.22
0.051	139	2	-14.7	119.8	4	0.05	198	0.19	169	0.23
0.082	173	2	-43.5	58.3	8	0.11	87	0.16	262	0.51
0.114	208	2	-43.8	57.9	8	0.10	87	0.21	262	0.62
0.148	239	2	-43.8	57.9	9	0.11	93	0.23	264	0.06
0.168	268	2	-43.8	58.0	9	0.21	94	0.20	263	0.06
0.187	296	2	-43.8	57.9	9	0.21	93	0.23	264	0.06
0.222	350	1	-34.1	119.2	17	0.19	211	0.19	131	0.99
0.281	380	1	-49.1	121.4	20	0.22	211	0.20	66	0.99
0.306	445	1	-49.1	121.4	21	0.23	212	0.21	68	0.99
0.334	473	1	-33.4	121.6	24	0.31	211	0.20	2	0.75
0.365	498	1	-35.7	121.0	29	0.30	214	0.18	16	0.40
0.417	535	1	-41.7	121.1	30	0.31	212	0.20	6	0.09
0.446	569	1	-41.3	121.1	30	0.31	212	0.22	6	0.03
0.473	599	1	-33.2	121.2	30	0.32	212	0.23	7	0.03
0.499	659	1	-37.6	122.0	32	0.31	213	0.24	0	0.68
0.549	717	1	-37.2	120.9	35	0.39	212	0.23	15	0.77
0.588	806	1	-44.2	122.0	36	0.42	38	0.26	19	0.86
0.623	925	1	40.9	120.7	35	0.39	214	0.30	17	0.84
0.660	1047	2	-38.2	120.4	34	0.47	165	0.33	0	0.84
0.669	1076	2	-38.1	120.4	34	0.47	163	0.33	19	0.83
0.734	1227	2	-45.5	122.6	35	0.54	52	0.37	354	0.15
0.768	1431	3	-48.8	121.6	34	0.49	48	0.45	190	0.84
0.787	1469	3	-40.9	120.3	36	0.59	48	0.44	0	0.96
0.823	1720	3	-49.6	120.8	36	0.57	48	0.51	169	0.99
0.853	1930	4	-49.4	122.8	36	0.61	73	0.56	1	0.49
0.880	2522	5	-47.7	122.4	33	1.00	22	0.65	339	0.95
0.915	2983	5	-46.8	122.3	34	0.99	22	0.74	2	0.99

(b) $\xi_R = 0.25$

$\tilde{P}$	C	$\frac{N_o}{N_d}$	Δalt	i	N_T	ξ_Ω	ΔM	D	ΔV_R	α_0
-	$M	-	km	deg	-	−	deg	m	m/s	-
0.015	116	3	-24.2	121.7	3	0.03	72	0.16	19	0.05
0.043	148	1	-23.9	119.9	8	0.09	92	0.11	172	0.77
0.074	178	1	-1.1	119.4	9	0.07	124	0.15	227	0.15
0.109	208	1	-1.6	122.1	9	0.09	178	0.19	227	0.65
0.141	224	2	21.4	58.0	9	0.11	158	0.21	274	0.29
0.177	298	2	-32.7	60.7	12	0.19	44	0.19	427	0.17
0.222	320	2	13.9	58.0	9	0.40	159	0.21	362	0.29
0.243	358	2	-22.5	58.2	13	0.29	182	0.19	207	0.32
0.280	385	2	-22.8	58.7	14	0.33	180	0.21	205	0.30
0.304	413	2	-22.8	58.3	13	0.29	182	0.24	208	0.29
0.334	440	2	-25.6	58.3	18	0.33	105	0.21	201	0.01
0.371	507	2	-32.4	57.7	17	0.33	123	0.25	395	0.14
0.425	557	2	-25.6	58.3	18	0.33	105	0.28	201	0.01
0.457	622	2	25.5	59.0	19	0.41	56	0.27	237	0.16
0.491	647	2	-24.3	57.6	25	0.40	43	0.25	172	0.20
0.517	685	2	-24.3	57.6	25	0.40	43	0.26	172	0.20
0.547	717	2	-25.5	57.7	25	0.56	98	0.25	199	0.00
0.581	767	2	-47.4	60.3	25	0.55	37	0.27	345	0.19
0.630	839	2	-47.4	60.3	30	0.55	37	0.27	345	0.19
0.646	867	2	-24.8	58.2	35	0.54	170	0.26	187	0.28
0.681	926	2	-25.3	58.2	34	0.52	161	0.28	200	0.30
0.722	1007	2	-25.2	59.7	35	0.53	168	0.30	225	0.31
0.739	1074	2	-24.8	58.4	35	0.55	167	0.32	186	0.30
0.770	1229	2	-23.9	121.7	35	0.54	164	0.37	242	0.31
0.798	1395	2	-23.3	122.4	36	0.68	161	0.41	230	0.22
0.832	1996	4	-30.7	124.0	34	0.96	22	0.55	210	0.96
0.874	2455	5	-40.8	124.0	31	0.99	22	0.67	11	0.89
0.900	2679	5	-41.9	123.7	34	0.99	22	0.68	1	0.88

(c) $\xi_R = 0.375$

$\tilde{P}$	C	$\frac{N_o}{N_d}$	Δalt	i	N_T	ξ_Ω	ΔM	D	ΔV_R	α_0
-	$M	-	km	deg	-	−	deg	m	m/s	-
0.024	118	1	-26.4	119.9	5	0.00	138	0.11	253	0.95
0.080	144	2	-11.2	59.7	5	0.10	38	0.17	197	0.19
0.089	159	2	-11.2	59.7	6	0.09	50	0.17	185	0.19
0.120	202	2	10.1	58.3	5	0.20	79	0.20	220	0.11
0.163	236	2	11.6	57.7	7	0.21	58	0.20	221	0.11
0.187	265	2	5.4	58.3	9	0.20	79	0.20	221	0.18
0.223	296	2	11.6	57.7	11	0.21	58	0.20	221	0.11
0.282	355	2	19.6	57.9	12	0.33	136	0.21	202	0.22
0.308	386	2	26.2	59.4	14	0.31	86	0.21	291	0.06
0.355	437	2	-19.2	59.5	14	0.33	29	0.24	283	0.05
0.395	478	2	-21.6	58.1	15	0.32	47	0.26	304	0.03
0.446	534	2	-27.8	58.0	19	0.41	55	0.23	343	0.04
0.481	596	2	-21.4	59.7	19	0.39	56	0.26	339	0.04
0.523	623	2	-25.0	60.9	19	0.42	46	0.27	344	0.00
0.555	678	2	22.3	58.6	20	0.45	95	0.29	271	0.16
0.590	716	2	22.7	58.0	20	0.48	94	0.31	325	0.12
0.619	766	2	-24.2	57.8	30	0.58	186	0.25	238	0.08
0.645	804	2	-24.5	58.5	30	0.58	112	0.26	239	0.08
0.666	823	2	-22.2	57.8	30	0.58	65	0.27	260	0.12
0.689	858	2	-21.8	57.8	30	0.58	67	0.28	256	0.12
0.735	926	2	-23.4	57.7	30	0.59	202	0.30	266	0.13
0.745	956	2	-22.2	57.8	30	0.58	65	0.31	260	0.12
0.773	1044	2	-22.2	58.0	35	0.67	71	0.30	278	0.18
0.802	1081	2	-22.5	58.0	35	0.67	71	0.31	263	0.14
0.829	1279	2	-45.9	121.9	35	0.63	154	0.37	505	0.02
0.858	2051	4	-28.9	121.3	34	0.76	62	0.56	270	0.13
0.895	3408	6	-28.3	124.9	36	1.00	130	0.79	274	0.00
0.912	4029	5	41.7	121.2	34	0.99	23	0.88	310	0.94

(d) $\xi_R = 0.5$

$\tilde{P}$	C	$\frac{N_o}{N_d}$	Δalt	i	N_T	ξ_Ω	ΔM	D	ΔV_R	α_0
-	$M	-	km	deg	-	−	deg	m	m/s	-
0.019	112	2	5.1	58.5	4	0.00	274	0.11	372	0.41
0.041	138	2	0.5	58.5	5	0.01	285	0.16	415	0.37
0.106	179	2	-24.6	58.5	5	0.19	223	0.15	389	0.04
0.171	234	2	-21.9	58.9	8	0.23	66	0.18	402	0.27
0.200	267	2	17.1	58.9	8	0.24	253	0.20	409	0.05
0.234	296	2	20.4	59.1	7	0.31	248	0.22	402	0.09
0.284	330	2	22.9	58.2	9	0.35	253	0.22	399	0.07
0.337	388	2	-20.9	59.1	11	0.47	356	0.21	331	0.04
0.366	415	2	-19.3	58.1	9	0.42	252	0.28	407	0.10
0.399	449	2	-18.2	58.8	12	0.55	223	0.24	397	0.13
0.414	465	2	-18.0	58.8	12	0.55	38	0.25	399	0.13
0.471	539	2	-29.5	60.3	15	0.62	117	0.24	415	0.12
0.516	589	2	-18.6	59.8	20	0.45	265	0.25	342	0.05
0.540	628	2	-20.9	60.1	20	0.42	281	0.26	412	0.15
0.562	652	2	-20.5	59.8	20	0.45	266	0.27	475	0.04
0.577	683	2	29.1	58.2	21	0.49	321	0.26	430	0.05
0.615	714	2	24.4	59.4	20	0.44	279	0.30	421	0.07
0.633	742	2	23.7	58.7	25	0.56	85	0.26	429	0.03
0.659	778	2	27.1	58.1	25	0.54	225	0.27	441	0.02
0.674	793	2	26.8	58.1	25	0.54	224	0.28	439	0.02
0.717	859	2	25.2	58.4	25	0.57	145	0.30	424	0.05
0.733	891	2	28.1	61.1	25	0.53	221	0.32	427	0.02
0.765	980	2	27.3	58.8	29	0.59	117	0.30	421	0.01
0.792	1034	2	-30.8	59.3	30	0.65	188	0.31	465	0.03
0.803	1105	2	-32.1	59.3	31	0.67	192	0.32	467	0.01
0.831	1327	2	22.0	60.3	36	0.68	70	0.34	419	0.02
0.858	1874	4	20.5	123.2	27	0.99	192	0.58	361	0.00
0.883	2267	4	20.2	124.2	36	1.00	206	0.59	361	0.00

A.27   Asymmetric Walker Pattern: Scenario 1
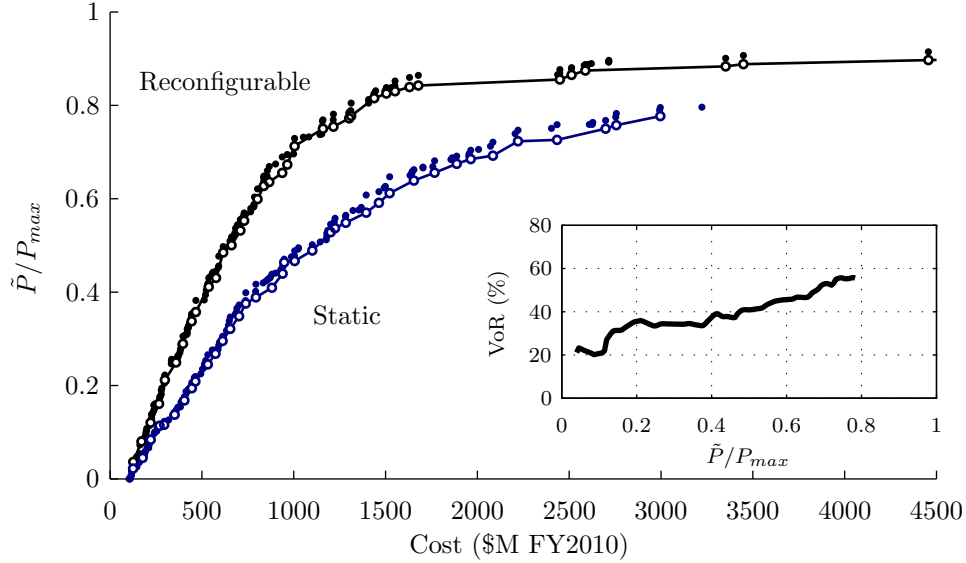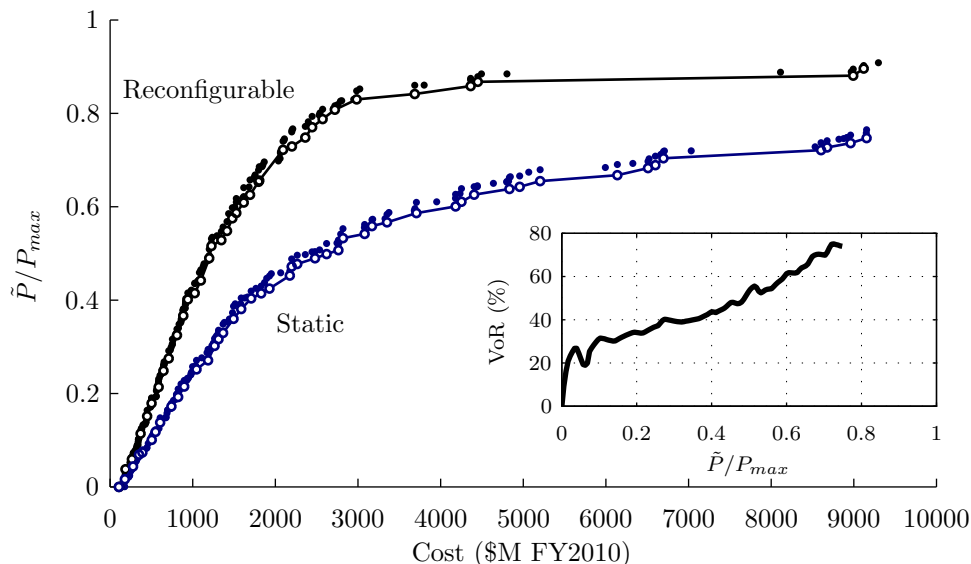

Figure A-21: Scenario 1 non-dominated front comparison with VoR

Table A.27: Non-dominated front design details

(a) Reconfigurable

$\tilde{P}$	C	$\frac{N_o}{N_d}$	Δalt	N_p	N_{sp}	i	ξ_Ω	F	D	ΔV_R	α_0
-	\$M	-	km	—	-	deg	—	—	m	m/s	-
0.025	115	2	-15.3	1	4	57.8	0.02	0	0.13	194	0.02
0.050	139	2	-48.7	1	5	61.0	0.36	0	0.17	17	0.05
0.066	175	2	-47.2	1	5	60.4	0.40	0	0.22	7	0.25
0.171	199	2	-11.7	5	1	60.2	0.19	1	0.19	521	0.09
0.203	226	2	-11.7	6	1	60.5	0.21	2	0.20	539	0.09
0.215	241	2	-11.7	5	1	60.1	0.19	1	0.24	525	0.09
0.295	289	2	-9.7	8	1	60.0	0.34	4	0.20	452	0.15
0.348	326	2	-6.3	9	1	58.2	0.35	2	0.21	508	0.09
0.380	344	2	-5.9	9	1	58.7	0.36	2	0.23	503	0.08
0.398	370	2	-8.4	9	1	58.0	0.35	3	0.26	427	0.03
0.404	409	2	-10.5	11	1	58.2	0.34	4	0.25	439	0.00
0.443	449	2	2.0	9	1	58.2	0.33	3	0.30	423	0.10
0.499	457	2	-6.8	12	1	59.2	0.56	5	0.25	429	0.11
0.530	536	2	4.8	11	1	62.8	0.44	7	0.30	365	0.01
0.561	546	2	5.7	12	1	59.7	0.50	0	0.29	359	0.02
0.589	580	2	4.7	12	1	61.0	0.50	0	0.32	359	0.02
0.634	652	2	0.4	14	1	60.9	0.55	7	0.31	348	0.00
0.685	748	2	-6.2	14	1	58.3	0.60	0	0.36	508	0.00
0.704	777	2	-6.7	18	1	58.8	0.71	4	0.30	400	0.00
0.715	807	2	-6.7	18	1	58.8	0.71	4	0.31	400	0.00
0.740	868	2	-19.2	25	1	61.3	0.55	13	0.31	361	0.07
0.757	940	2	-21.6	27	1	60.6	0.58	14	0.30	361	0.04
0.779	987	2	-23.1	29	1	61.2	0.62	15	0.31	366	0.04
0.791	1009	2	-22.1	29	1	61.2	0.61	15	0.31	366	0.04
0.811	1085	2	-28.4	34	1	57.7	0.67	18	0.31	378	0.06
0.838	1169	2	28.2	18	2	58.8	0.71	3	0.33	386	0.01
0.857	1733	4	-27.0	33	1	56.5	0.70	7	0.51	388	0.08
0.871	1851	4	-25.6	35	1	56.7	0.73	7	0.53	384	0.05
0.897	2376	4	-25.2	36	1	123.5	0.99	12	0.62	320	0.01
0.918	5853	6	-16.6	33	1	123.3	1.00	18	1.04	377	0.00

(b) Static

$\tilde{P}$	C	h_{GOM}	N_p	N_{sp}	i	ξ_Ω	F	D
-	\$M	km	—	-	deg	—	—	m
0.027	116	539	1	4	122.2	0.00	0	0.13
0.065	149	415	2	3	120.4	0.17	1	0.15
0.102	177	377	3	3	121.7	0.14	1	0.15
0.133	204	378	3	4	121.8	0.14	1	0.15
0.157	232	360	3	5	121.8	0.15	1	0.15
0.172	245	377	3	4	121.9	0.14	2	0.20
0.204	294	422	3	4	121.3	0.14	1	0.24
0.220	327	362	4	4	120.8	0.19	1	0.19
0.245	348	380	6	4	121.2	0.28	5	0.14
0.296	382	394	6	4	120.4	0.27	2	0.17
0.337	419	392	6	4	120.8	0.29	2	0.20
0.391	481	383	6	4	121.5	0.30	2	0.23
0.425	537	415	8	4	121.3	0.38	5	0.19
0.457	565	393	8	4	120.9	0.37	3	0.20
0.498	592	374	9	4	122.0	0.41	3	0.20
0.526	626	380	9	4	121.3	0.40	3	0.21
0.536	653	401	9	4	120.9	0.44	4	0.22
0.568	711	414	9	4	121.2	0.44	5	0.25
0.587	736	426	9	4	121.9	0.44	1	0.25
0.612	783	434	9	4	121.2	0.44	4	0.27
0.639	896	483	9	4	120.7	0.42	5	0.30
0.656	936	493	9	4	121.7	0.41	5	0.32
0.680	996	536	12	3	121.9	0.53	1	0.32
0.731	1165	633	12	3	122.4	0.52	2	0.37
0.752	1203	634	12	3	122.4	0.53	2	0.38
0.790	1319	673	12	3	122.4	0.52	2	0.43
0.803	1404	677	12	3	121.6	0.51	2	0.45
0.829	1748	821	12	3	113.7	0.53	3	0.52
0.853	1965	858	12	3	121.4	0.59	3	0.57
0.880	2790	966	12	3	111.0	0.57	3	0.70

A.28 Asymmetric Walker Pattern: Scenario 2

Figure A-22: Scenario 2 non-dominated front comparison with VoR

Table A.28: Non-dominated front design details

(a) Reconfigurable

$\tilde{P}$	C	$\frac{N_o}{N_d}$	Δalt	N_p	N_{sp}	i	ξ_Ω	F	D	ΔV_R	α_0
-	$M	-	km	–	-	deg	–	–	m	m/s	-
0.000	130	3	-8.5	1	3	58.5	0.98	0	0.20	148	0.10
0.030	179	2	-10.2	3	2	58.8	0.09	2	0.20	356	0.03
0.043	212	2	-21.6	7	1	62.8	0.08	0	0.23	344	0.01
0.118	268	2	3.6	6	1	59.5	0.26	3	0.25	410	0.07
0.146	311	2	2.9	6	1	59.6	0.27	3	0.28	409	0.07
0.164	332	2	2.9	6	1	59.6	0.27	3	0.31	410	0.07
0.214	391	2	1.4	6	1	58.0	0.28	1	0.37	415	0.06
0.236	420	2	1.4	6	1	58.1	0.28	1	0.40	414	0.06
0.266	479	2	1.5	9	1	60.0	0.38	6	0.33	400	0.06
0.296	531	2	-6.2	8	1	60.9	0.34	4	0.40	415	0.10
0.357	582	2	0.6	9	1	60.5	0.39	5	0.42	434	0.07
0.394	667	2	1.3	11	1	59.7	0.46	7	0.40	408	0.05
0.439	718	2	-2.3	12	1	59.7	0.52	6	0.42	392	0.02
0.463	758	2	5.1	12	1	60.5	0.50	6	0.44	463	0.00
0.490	804	2	5.1	12	1	60.5	0.51	9	0.47	458	0.00
0.535	892	2	14.7	12	1	60.1	0.50	9	0.52	507	0.03
0.561	945	2	-1.3	12	1	59.3	0.49	6	0.55	406	0.01
0.579	1012	2	17.1	14	1	59.7	0.57	7	0.51	510	0.00
0.606	1058	2	16.7	14	1	59.6	0.58	7	0.54	511	0.00
0.615	1096	2	13.2	14	1	60.4	0.61	10	0.55	478	0.01
0.645	1152	2	11.4	15	1	60.8	0.62	12	0.56	495	0.02
0.671	1194	2	15.3	15	1	58.9	0.61	11	0.58	507	0.03
0.680	1245	2	18.5	15	1	60.6	0.62	12	0.60	503	0.02
0.731	1454	2	17.0	18	1	60.5	0.70	14	0.61	517	0.00
0.758	1607	2	0.7	20	1	59.3	0.83	6	0.62	397	0.00
0.777	1650	2	0.4	21	1	59.2	0.88	6	0.62	393	0.00
0.806	1807	2	-0.9	24	1	58.9	0.99	0	0.61	382	0.00
0.825	2135	2	1.7	26	1	58.9	1.00	6	0.66	388	0.00
0.845	2899	2	47.2	36	1	59.3	0.69	35	0.73	539	0.05
0.861	4659	2	6.1	36	1	58.0	1.00	8	0.95	431	0.00

(b) Static

$\tilde{P}$	C	h_{GOM}	N_p	N_{sp}	i	ξ_Ω	F	D
-	$M	km	–	-	deg	–	–	m
0.000	90	613	1	3	58.5	0.00	0	0.10
0.000	127	368	1	6	63.7	0.56	0	0.11
0.040	197	350	1	6	59.4	0.58	0	0.23
0.086	264	349	3	4	120.4	0.14	1	0.21
0.108	312	352	3	4	120.4	0.15	1	0.25
0.156	437	366	5	4	121.4	0.24	3	0.23
0.185	489	362	5	4	121.5	0.24	2	0.25
0.211	538	358	6	4	121.6	0.26	3	0.25
0.244	615	358	6	4	121.6	0.26	3	0.28
0.270	652	351	6	5	121.0	0.29	2	0.26
0.295	718	366	9	4	121.1	0.38	3	0.24
0.326	787	351	9	4	121.2	0.35	3	0.26
0.351	840	377	9	4	121.6	0.37	3	0.28
0.372	895	354	9	4	121.2	0.35	3	0.30
0.429	1025	356	9	4	121.3	0.38	3	0.33
0.455	1108	348	9	4	121.5	0.36	3	0.36
0.485	1166	356	9	4	121.3	0.38	3	0.38
0.511	1217	367	9	4	121.0	0.37	3	0.41
0.559	1364	397	9	4	121.2	0.38	3	0.46
0.586	1611	496	12	3	121.2	0.48	1	0.51
0.622	1737	486	12	3	121.2	0.48	1	0.55
0.640	1798	474	12	3	120.9	0.47	1	0.56
0.660	2016	487	12	3	121.1	0.49	1	0.59
0.701	2324	509	12	3	121.1	0.49	1	0.66
0.719	2422	550	12	3	122.3	0.50	1	0.68
0.751	2949	620	12	3	121.2	0.53	1	0.76
0.778	3559	669	12	3	123.0	0.58	1	0.84
0.806	3971	709	12	3	122.0	0.58	2	0.91
0.828	4965	741	12	3	122.3	0.59	2	1.02
0.854	6825	873	12	3	116.7	0.57	3	1.14

A.29 Asymmetric Walker Pattern: Scenario 3
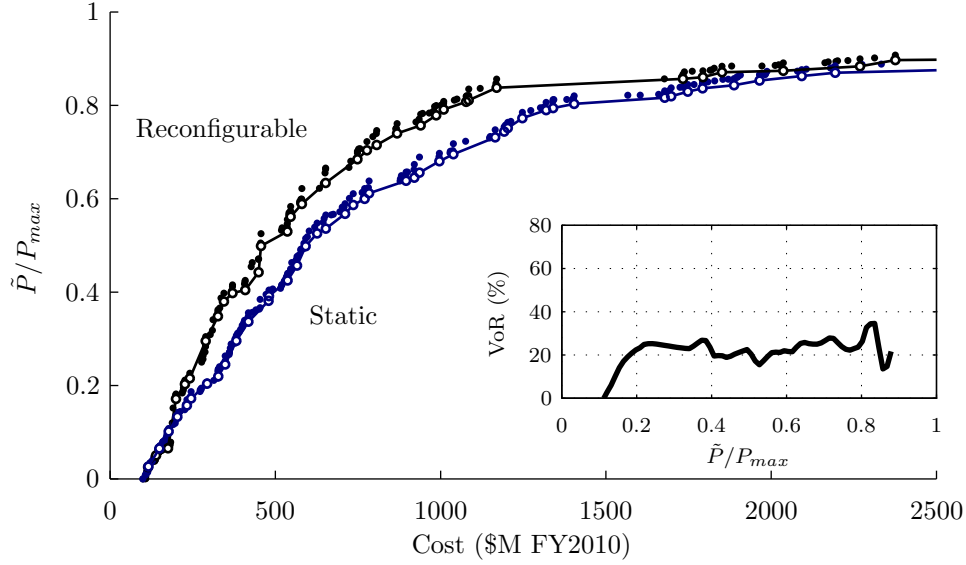

Figure A-23: Scenario 3 non-dominated front comparison with VoR

Table A.29: Non-dominated front design details

(a) Reconfigurable

$\tilde{P}$	C	$\frac{N_o}{N_d}$	Δalt	N_p	N_{sp}	i	ξ_Ω	F	D	ΔV_R	α_0
-	$M	-	km	—	-	deg	—	—	m	m/s	-
0.030	124	2	10.4	5	1	59.1	0.07	0	0.12	470	0.00
0.077	166	2	-3.0	5	1	62.8	0.08	2	0.19	441	0.05
0.095	182	2	-6.0	6	1	63.8	0.09	1	0.20	460	0.09
0.157	252	2	2.5	9	1	59.6	0.19	2	0.18	405	0.05
0.206	294	2	-2.0	10	1	58.0	0.21	5	0.21	487	0.16
0.216	319	2	-1.2	10	1	61.8	0.20	6	0.23	495	0.01
0.267	375	2	-6.0	14	1	59.2	0.32	7	0.19	425	0.01
0.313	415	2	-4.7	15	1	58.2	0.33	7	0.21	428	0.11
0.330	444	2	0.3	15	1	60.4	0.32	1	0.23	386	0.06
0.382	502	2	-3.8	15	1	60.8	0.33	0	0.27	424	0.01
0.419	540	2	-4.5	20	1	58.0	0.43	11	0.22	489	0.06
0.440	583	2	-7.6	23	1	58.8	0.44	12	0.22	499	0.16
0.486	625	2	-5.2	19	1	58.0	0.40	11	0.27	489	0.12
0.508	670	2	-4.5	24	1	59.6	0.44	13	0.25	486	0.04
0.527	708	2	-8.1	24	1	61.3	0.50	18	0.25	457	0.10
0.566	752	2	-6.6	25	1	57.8	0.53	10	0.26	422	0.00
0.583	784	2	-6.6	25	1	59.9	0.52	10	0.27	498	0.11
0.621	833	2	-5.2	25	1	59.7	0.53	6	0.29	480	0.09
0.648	882	2	-5.0	25	1	60.0	0.54	3	0.31	485	0.07
0.690	984	2	-13.9	29	1	58.3	0.60	15	0.30	471	0.08
0.701	1011	2	-11.7	30	1	57.7	0.61	15	0.31	481	0.08
0.725	1134	2	-11.9	32	1	57.9	0.64	16	0.32	475	0.04
0.738	1243	2	-12.4	35	1	58.8	0.70	8	0.33	474	0.05
0.773	1294	2	-16.1	40	1	58.0	0.76	27	0.32	439	0.05
0.802	1529	2	-19.6	47	1	58.2	0.87	38	0.34	413	0.04
0.815	1627	2	-20.0	43	1	122.1	0.88	16	0.37	475	0.04
0.828	1700	2	-21.6	48	1	121.9	0.89	2	0.38	474	0.04
0.848	2221	2	-4.6	24	2	87.2	0.50	3	0.33	374	0.18
0.859	2260	2	-4.5	24	2	87.1	0.50	3	0.34	377	0.18
0.868	3739	2	-4.4	24	2	87.3	0.50	4	0.63	392	0.17

(b) Static

$\tilde{P}$	C	h_{GOM}	N_p	N_{sp}	i	ξ_Ω	F	D
-	$M	km	—	-	deg	—	—	m
0.017	119	520	1	4	60.9	0.28	0	0.14
0.045	165	385	4	2	121.9	0.11	2	0.14
0.062	202	414	2	5	58.7	0.13	1	0.18
0.097	249	379	3	5	58.4	0.12	1	0.17
0.115	294	441	4	5	59.3	0.11	2	0.18
0.149	335	383	5	5	58.8	0.12	2	0.17
0.167	373	417	5	5	58.0	0.11	2	0.20
0.217	458	417	8	4	120.9	0.23	3	0.18
0.234	499	416	7	5	120.4	0.22	3	0.19
0.254	538	415	8	5	59.5	0.23	3	0.19
0.275	575	414	8	5	59.4	0.23	3	0.20
0.283	626	393	9	5	59.6	0.19	5	0.20
0.324	667	480	22	2	121.3	0.30	8	0.20
0.344	708	465	21	2	121.6	0.28	8	0.23
0.367	760	481	22	2	121.6	0.28	8	0.24
0.385	836	513	19	2	121.7	0.30	7	0.28
0.427	866	408	48	1	121.6	0.38	32	0.24
0.452	1015	578	16	3	122.6	0.34	1	0.28
0.496	1088	551	16	3	122.6	0.34	1	0.29
0.537	1277	583	15	3	122.6	0.33	1	0.37
0.551	1389	580	48	1	57.2	0.39	32	0.37
0.583	1496	627	48	1	122.3	0.49	32	0.38
0.619	1669	793	22	2	123.3	0.43	9	0.46
0.628	1739	816	22	2	123.3	0.42	9	0.47
0.650	1782	801	23	2	123.2	0.42	9	0.47
0.676	1962	811	47	1	123.0	0.47	32	0.49
0.684	2020	837	47	1	123.3	0.48	32	0.51
0.723	2418	948	47	1	123.6	0.49	32	0.58
0.742	2578	959	48	1	123.9	0.52	34	0.59
0.762	3002	999	48	1	122.9	0.51	34	0.65

A.30 Asymmetric Walker Pattern: Scenario 4
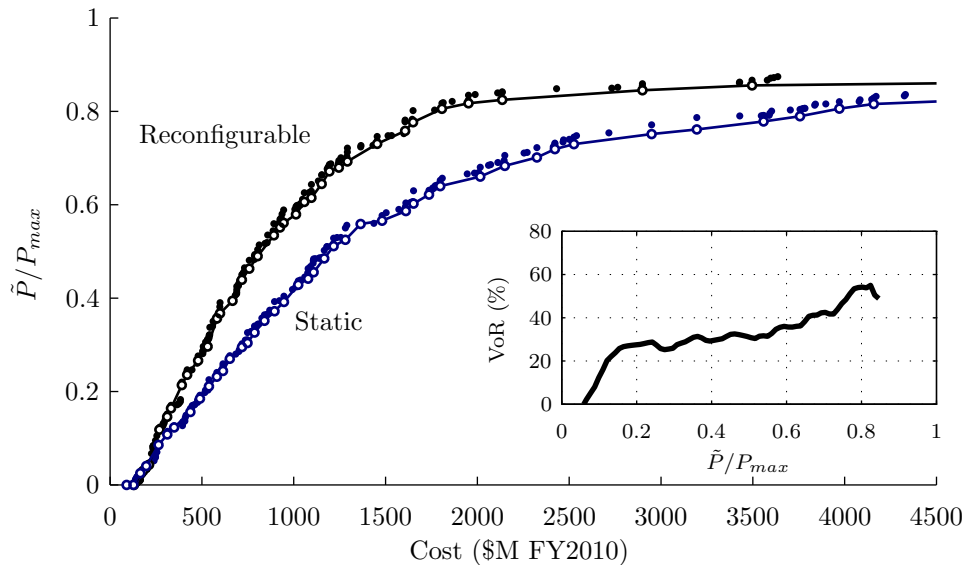

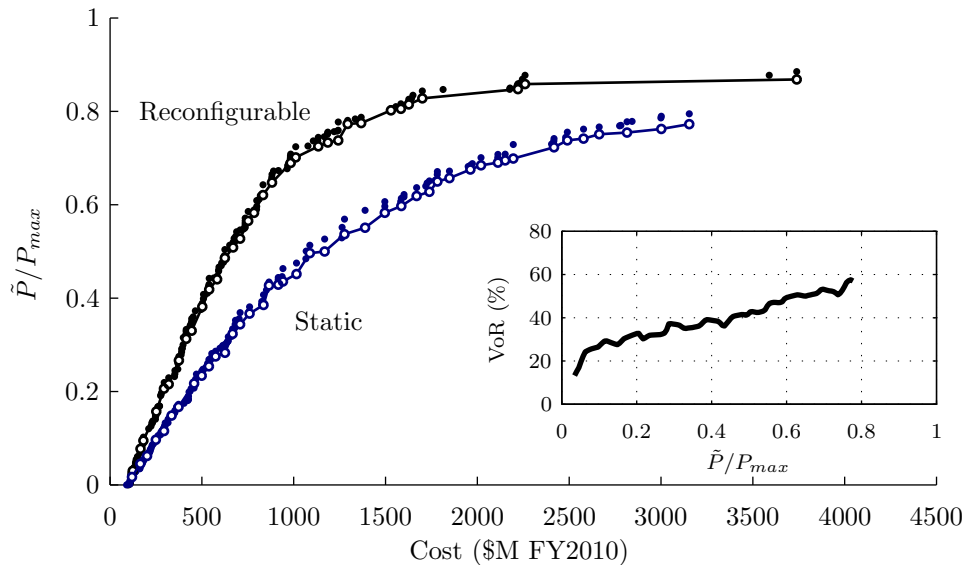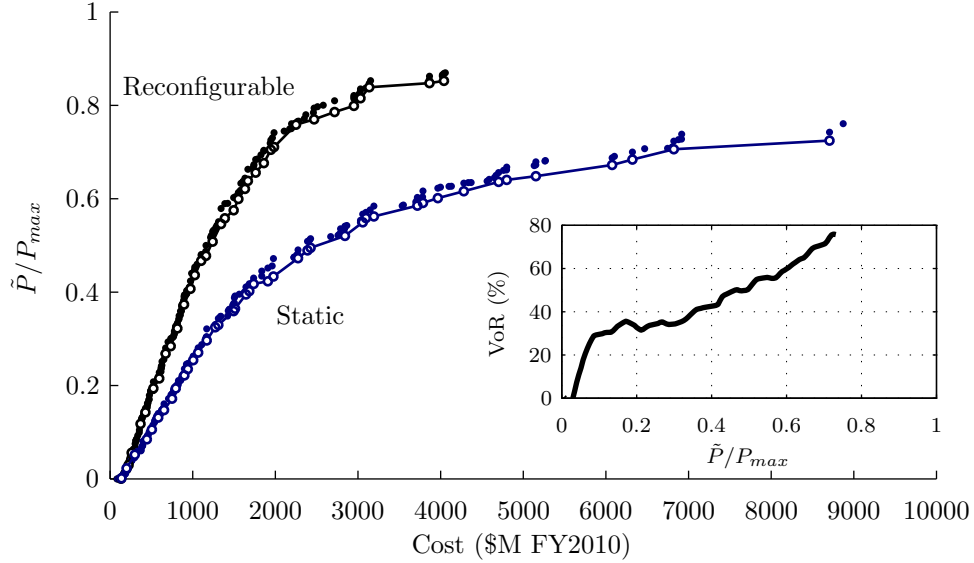Figure A-24: Scenario 4 non-dominated front comparison with VoR

Table A.30: Non-dominated front design details

(a) Reconfigurable

$\tilde{P}$	C	$\frac{N_o}{N_d}$	Δalt	N_p	N_{sp}	i	ξ_Ω	F	D	ΔV_R	α_0
-	$M	-	km	–	-	deg	–	–	m	m/s	-
0.000	133	2	-2.6	1	4	93.7	0.18	0	0.17	287	0.36
0.030	224	2	-0.5	6	1	63.2	0.16	5	0.20	431	0.00
0.056	261	2	-8.1	6	1	61.3	0.21	2	0.25	427	0.00
0.118	369	2	-5.5	10	1	60.1	0.23	2	0.27	497	0.03
0.143	428	2	2.5	9	1	59.4	0.20	5	0.33	471	0.00
0.194	524	2	-2.5	10	1	59.8	0.21	9	0.40	482	0.17
0.215	595	2	-1.8	10	1	61.3	0.21	8	0.45	486	0.26
0.268	672	2	-5.1	15	1	58.9	0.35	1	0.37	455	0.01
0.284	733	2	-7.6	14	1	60.0	0.29	6	0.43	465	0.02
0.322	814	2	-3.7	17	1	59.0	0.37	1	0.39	471	0.01
0.374	895	2	-4.0	19	1	59.7	0.44	14	0.41	466	0.02
0.407	973	2	-2.9	20	1	60.8	0.42	6	0.44	472	0.00
0.436	1025	2	-6.0	20	1	61.5	0.42	5	0.46	480	0.00
0.467	1103	2	-5.9	20	1	58.2	0.44	6	0.49	503	0.00
0.478	1161	2	-9.8	25	1	60.6	0.56	7	0.43	477	0.00
0.508	1242	2	12.1	25	1	59.7	0.53	22	0.46	486	0.04
0.546	1343	2	-5.0	25	1	59.2	0.54	15	0.50	483	0.00
0.558	1389	2	12.1	25	1	59.7	0.54	16	0.52	486	0.04
0.575	1495	2	14.1	26	1	60.2	0.54	16	0.52	486	0.00
0.600	1553	2	-17.7	29	1	59.5	0.59	5	0.51	523	0.01
0.621	1632	2	-16.3	29	1	59.6	0.57	5	0.53	516	0.00
0.638	1668	2	-2.0	28	1	58.7	0.58	22	0.55	495	0.00
0.656	1762	2	14.4	29	1	60.1	0.59	13	0.57	511	0.02
0.676	1860	2	14.2	29	1	58.9	0.59	13	0.60	515	0.01
0.705	1945	2	15.8	30	1	59.4	0.64	19	0.61	500	0.00
0.759	2250	2	-5.8	35	1	59.4	0.72	34	0.62	476	0.00
0.786	2716	2	-16.1	40	1	61.9	0.80	0	0.66	509	0.00
0.815	3030	2	1.6	25	1	86.9	0.52	1	0.67	531	0.00
0.839	3136	2	-4.2	48	1	61.6	0.98	4	0.66	432	0.00
0.848	3865	2	2.7	24	2	87.0	0.50	11	0.66	331	0.17

(b) Static

$\tilde{P}$	C	h_{GOM}	N_p	N_{sp}	i	ξ_Ω	F	D
-	$M	km	–	-	deg	–	–	m
0.001	137	496	1	5	104.8	0.53	0	0.17
0.023	199	393	2	4	59.5	0.10	1	0.20
0.052	299	358	3	4	59.6	0.09	2	0.24
0.085	445	387	10	2	121.3	0.22	1	0.24
0.106	506	376	11	2	121.8	0.22	2	0.25
0.131	583	367	14	2	121.3	0.21	2	0.25
0.147	653	393	14	2	121.3	0.20	2	0.28
0.172	749	378	14	3	121.3	0.21	2	0.25
0.194	795	355	15	3	121.3	0.34	0	0.23
0.222	899	348	24	2	120.1	0.29	3	0.25
0.235	941	348	24	2	120.0	0.29	3	0.26
0.254	1006	348	24	2	121.7	0.29	3	0.28
0.271	1066	359	24	2	121.9	0.29	3	0.29
0.297	1169	356	24	2	121.9	0.29	4	0.32
0.325	1273	389	24	2	121.9	0.30	4	0.35
0.359	1494	353	23	2	121.6	0.30	4	0.41
0.395	1644	409	23	2	121.9	0.35	8	0.45
0.418	1737	411	24	2	122.0	0.34	8	0.46
0.473	2274	496	16	3	119.9	0.40	0	0.56
0.489	2389	489	24	2	122.4	0.45	7	0.58
0.521	2842	522	16	3	121.0	0.45	1	0.65
0.550	3057	563	16	3	122.7	0.48	0	0.68
0.562	3192	553	16	3	122.4	0.41	0	0.71
0.585	3718	630	16	3	120.5	0.38	1	0.76
0.601	3966	632	16	3	120.6	0.38	1	0.79
0.636	4701	721	16	3	121.7	0.45	1	0.87
0.648	5152	763	16	3	121.5	0.43	1	0.93
0.672	6076	782	16	3	121.2	0.43	1	0.99
0.684	6321	761	16	3	122.7	0.43	1	1.02
0.706	6822	899	24	2	124.0	0.99	0	1.09

A.31 Asymmetric Walker: Limited Satellites Results

Table A.31: Non-dominated front design details

(a) $N_T \leq 12$

$\tilde{P}$	C	h_{GOM}	N_p	N_{sp}	i	ξ_Ω	F	D
-	\$M	km	—	-	deg	—	—	m
0.000	99	772	3	1	112.9	0.00	2	0.10
0.029	118	444	1	4	86.5	0.28	0	0.14
0.045	133	374	1	6	120.9	0.10	0	0.13
0.051	143	407	1	6	61.5	0.72	0	0.16
0.082	165	387	2	4	120.5	0.13	1	0.15
0.098	180	386	2	4	120.5	0.13	1	0.17
0.114	193	390	3	4	121.9	0.13	1	0.14
0.133	207	390	3	4	121.9	0.13	1	0.16
0.146	219	386	3	4	120.5	0.13	1	0.17
0.165	237	380	3	4	119.7	0.14	1	0.19
0.173	255	470	3	4	122.2	0.15	1	0.21
0.202	323	450	12	1	120.9	0.22	2	0.22
0.214	342	448	12	1	121.0	0.22	2	0.24
0.225	357	444	12	1	120.8	0.22	2	0.25
0.235	386	460	12	1	120.8	0.21	2	0.27
0.272	476	574	6	2	122.7	0.22	3	0.33
0.306	554	663	12	1	122.9	0.21	2	0.39
0.311	563	663	12	1	122.9	0.21	2	0.39
0.324	613	660	12	1	122.6	0.35	2	0.39
0.349	688	760	12	1	123.3	0.36	1	0.44
0.358	719	718	12	1	122.7	0.32	4	0.46
0.374	824	792	12	1	123.3	0.36	1	0.49
0.394	829	901	12	1	123.9	0.29	5	0.53
0.413	899	903	12	1	123.8	0.34	2	0.57
0.424	966	905	12	1	123.8	0.34	2	0.60
0.438	1063	977	12	1	124.1	0.36	2	0.62
0.443	1103	985	12	1	124.2	0.37	2	0.64
0.466	1698	998	12	1	124.5	0.36	5	0.88

(b) $N_T \leq 24$

$\tilde{P}$	C	h_{GOM}	N_p	N_{sp}	i	ξ_Ω	F	D
-	\$M	km	—	-	deg	—	—	m
0.034	120	400	1	5	60.7	0.13	0	0.12
0.057	143	426	1	5	121.8	0.31	0	0.18
0.089	169	363	3	3	121.4	0.13	2	0.13
0.131	205	367	3	4	121.5	0.13	2	0.15
0.150	219	363	3	4	121.3	0.15	1	0.17
0.179	263	367	3	4	121.3	0.13	0	0.21
0.206	294	352	4	4	121.5	0.13	2	0.20
0.228	329	361	4	4	121.5	0.13	3	0.23
0.254	354	369	6	3	121.8	0.28	3	0.19
0.303	388	362	6	4	121.8	0.30	3	0.17
0.326	411	369	6	4	121.8	0.28	3	0.19
0.344	426	390	6	4	121.6	0.30	3	0.20
0.381	476	390	6	4	121.4	0.26	1	0.23
0.422	567	440	8	3	121.5	0.37	1	0.25
0.450	615	452	8	3	121.8	0.37	6	0.27
0.471	655	451	8	3	121.8	0.36	7	0.28
0.486	705	484	8	3	120.8	0.37	6	0.31
0.513	762	539	8	3	122.7	0.32	1	0.33
0.535	809	533	8	3	122.5	0.34	1	0.35
0.564	906	642	8	3	122.3	0.35	2	0.39
0.586	1012	681	8	3	119.2	0.40	2	0.42
0.608	1108	756	8	3	119.0	0.39	2	0.46
0.623	1168	768	8	3	118.4	0.38	2	0.48
0.640	1294	841	8	3	118.2	0.38	2	0.53
0.662	1422	931	8	3	118.5	0.41	2	0.57
0.690	1521	956	23	1	124.3	0.45	11	0.60
0.712	1705	978	24	1	124.1	0.45	12	0.64
0.731	1824	967	24	1	124.1	0.47	11	0.68

(c) $N_T \leq 48$

$\tilde{P}$	C	h_{GOM}	N_p	N_{sp}	i	ξ_Ω	F	D
-	\$M	km	—	-	deg	—	—	m
0.028	118	429	1	5	120.8	0.31	0	0.11
0.068	149	403	2	3	121.0	0.13	1	0.15
0.093	174	399	3	3	120.4	0.13	1	0.15
0.133	206	421	3	4	121.9	0.14	1	0.16
0.163	233	403	3	4	122.0	0.14	2	0.19
0.182	264	407	3	5	121.9	0.14	2	0.19
0.205	318	403	3	6	121.7	0.14	2	0.21
0.248	349	359	5	4	121.7	0.23	2	0.17
0.301	384	409	6	4	122.0	0.28	2	0.18
0.329	410	359	6	4	121.9	0.27	1	0.19
0.357	445	374	6	4	121.9	0.29	2	0.21
0.380	469	402	6	4	121.5	0.28	2	0.23
0.412	508	375	6	5	121.1	0.29	1	0.21
0.468	567	399	9	4	121.2	0.41	2	0.19
0.516	630	385	9	4	120.6	0.39	1	0.21
0.531	654	397	9	4	120.7	0.41	0	0.23
0.571	705	380	9	4	120.9	0.42	0	0.24
0.598	748	409	9	4	121.1	0.43	3	0.26
0.635	804	400	11	4	121.2	0.50	3	0.23
0.673	837	392	12	4	121.6	0.50	5	0.23
0.718	925	429	12	4	121.8	0.52	5	0.25
0.736	988	455	12	4	121.8	0.52	5	0.27
0.760	1045	434	12	4	121.4	0.55	5	0.28
0.794	1196	505	12	4	121.3	0.54	6	0.32
0.822	1395	538	12	4	121.5	0.52	6	0.37
0.855	1461	587	15	3	122.8	0.62	2	0.39
0.878	1630	604	16	3	122.7	0.63	2	0.41
0.904	1895	702	16	3	120.3	0.65	3	0.47

(d) $N_T \leq 60$

$\tilde{P}$	C	h_{GOM}	N_p	N_{sp}	i	ξ_Ω	F	D
-	\$M	km	—	-	deg	—	—	m
0.029	118	419	1	5	121.2	0.61	0	0.11
0.060	148	424	1	5	59.0	0.53	0	0.19
0.088	168	359	2	4	119.1	0.12	1	0.15
0.131	206	351	3	4	120.7	0.14	1	0.15
0.161	240	380	3	4	119.6	0.12	1	0.19
0.180	297	402	6	3	121.4	0.29	5	0.14
0.221	323	401	6	3	121.4	0.27	4	0.17
0.261	359	432	6	3	121.9	0.29	2	0.20
0.291	379	424	6	4	122.1	0.29	2	0.17
0.320	409	431	6	4	121.9	0.30	1	0.19
0.363	444	418	6	4	122.1	0.29	2	0.21
0.394	510	419	7	4	122.0	0.34	2	0.20
0.405	520	423	7	4	122.1	0.31	3	0.21
0.448	565	417	8	4	122.0	0.34	2	0.21
0.487	589	420	9	4	120.3	0.41	4	0.20
0.515	618	424	9	4	120.8	0.39	3	0.21
0.572	712	433	9	4	121.7	0.42	3	0.25
0.605	772	420	11	4	121.0	0.46	4	0.22
0.637	802	413	11	4	120.0	0.46	5	0.23
0.657	835	412	12	4	119.9	0.46	6	0.23
0.700	891	415	12	4	122.1	0.50	4	0.24
0.748	1007	441	12	4	119.2	0.49	5	0.27
0.771	1042	385	15	4	119.3	0.61	5	0.23
0.798	1146	368	15	4	119.3	0.62	5	0.25
0.842	1289	470	14	4	120.9	0.60	5	0.30
0.865	1348	486	15	4	120.6	0.62	7	0.30
0.885	1421	482	15	4	120.8	0.61	7	0.31
0.914	1951	646	18	3	122.9	0.66	5	0.45

A.32 Sun-Synchronous Architecture Results

Table A.32: Non-dominated front design details

(a) Scenario 1

$\tilde{P}$	C	h_{GOM}	N_p	N_{sp}	D
-	$M	km	−	-	m
0.017	116	485	1	5	0.11
0.042	136	485	1	5	0.16
0.061	175	443	1	5	0.22
0.093	235	433	2	5	0.17
0.125	296	433	2	5	0.22
0.163	353	412	3	5	0.19
0.190	420	363	4	5	0.16
0.232	467	413	4	5	0.20
0.269	538	393	5	5	0.18
0.285	561	413	5	5	0.20
0.306	623	413	5	5	0.22
0.341	654	403	6	5	0.20
0.390	743	402	7	5	0.19
0.406	777	453	7	5	0.21
0.441	837	381	6	6	0.23
0.468	919	461	9	4	0.23
0.492	952	461	9	4	0.24
0.526	1013	462	9	4	0.26
0.553	1137	462	9	4	0.28
0.593	1213	488	9	4	0.30
0.631	1336	515	9	4	0.34
0.660	1498	659	9	4	0.39
0.686	1551	659	9	4	0.41
0.718	1746	727	11	3	0.46
0.745	2001	794	12	3	0.50
0.766	2408	956	16	2	0.58
0.799	2548	952	17	2	0.58
0.826	2704	955	18	2	0.59

(b) Scenario 2

$\tilde{P}$	C	h_{GOM}	N_p	N_{sp}	D
-	$M	km	−	-	m
0.000	107	758	1	4	0.10
0.004	156	359	1	8	0.13
0.034	218	345	1	9	0.20
0.079	354	365	2	6	0.25
0.099	427	365	2	6	0.30
0.132	530	365	3	6	0.27
0.174	668	365	4	6	0.26
0.186	704	365	4	6	0.28
0.229	838	365	5	6	0.28
0.254	913	365	5	6	0.30
0.284	1007	365	6	6	0.28
0.319	1110	365	6	6	0.31
0.351	1220	365	6	6	0.35
0.373	1289	365	6	6	0.37
0.403	1389	381	6	6	0.41
0.434	1488	364	7	5	0.43
0.465	1612	392	7	5	0.47
0.493	1755	413	7	5	0.52
0.525	1897	462	9	4	0.52
0.559	2056	461	9	4	0.56
0.598	2315	542	9	4	0.62
0.621	2452	515	9	4	0.65
0.649	2742	542	9	4	0.72
0.682	3109	605	12	3	0.76
0.717	3666	663	12	3	0.86
0.743	4895	871	17	2	1.04
0.771	5179	878	17	2	1.09
0.806	5548	880	18	2	1.10

(c) Scenario 3

$\tilde{P}$	C	h_{GOM}	N_p	N_{sp}	D
-	$M	km	−	-	m
0.009	114	443	1	5	0.10
0.027	148	414	1	5	0.19
0.062	268	413	2	5	0.21
0.070	312	412	2	5	0.24
0.095	375	413	3	5	0.21
0.124	476	413	4	5	0.21
0.146	553	365	4	6	0.21
0.171	634	402	6	5	0.19
0.191	713	383	7	5	0.18
0.211	754	383	7	5	0.20
0.230	827	382	8	5	0.19
0.257	917	382	9	5	0.19
0.278	986	495	9	5	0.22
0.306	1109	433	8	5	0.27
0.320	1139	402	9	5	0.25
0.346	1225	433	9	5	0.27
0.370	1423	557	24	2	0.26
0.392	1495	557	24	2	0.28
0.415	1578	563	24	2	0.30
0.437	1650	561	24	2	0.32
0.460	1792	683	22	2	0.39
0.487	1875	673	22	2	0.42
0.504	1984	611	24	2	0.41
0.536	2193	748	15	3	0.44
0.555	2279	748	16	3	0.43
0.576	2346	751	16	3	0.45
0.598	2469	748	16	3	0.48
0.621	2745	887	15	3	0.57

(d) Scenario 4

$\tilde{P}$	C	h_{GOM}	N_p	N_{sp}	D
-	$M	km	−	-	m
0.000	107	874	1	4	0.10
0.006	166	358	1	8	0.15
0.034	353	358	2	8	0.21
0.056	457	365	2	6	0.32
0.080	609	364	3	6	0.31
0.103	766	365	3	6	0.39
0.136	926	365	5	6	0.31
0.159	1053	365	6	6	0.30
0.182	1182	365	7	6	0.29
0.209	1332	365	8	6	0.29
0.245	1550	381	7	6	0.40
0.268	1705	363	9	5	0.39
0.294	1847	392	9	5	0.44
0.312	1979	393	9	5	0.47
0.334	2204	498	24	2	0.47
0.371	2458	493	24	2	0.52
0.395	2659	504	24	2	0.56
0.415	2859	550	24	2	0.60
0.440	3295	665	16	3	0.65
0.465	3516	663	16	3	0.69
0.500	3898	630	12	4	0.79
0.515	4049	663	16	3	0.77
0.543	4451	727	16	3	0.84
0.580	4982	751	16	3	0.91
0.596	5271	793	16	3	0.95
0.621	6719	864	16	3	1.02
0.646	7186	863	16	3	1.08
0.673	8971	964	16	3	1.17

A.33 Rapid Launch Architecture Results

Table A.33: Non-dominated front design details

(a) Scenario 1

$\tilde{P}$	C	h_{GOM}	N_T	N_E	Δi	D
-	\$M	km	−	-	−	m
0.017	52	427	1	2	0.64	0.15
0.051	88	392	3	2	0.32	0.14
0.083	117	408	3	2	0.58	0.21
0.099	150	530	4	3	0.31	0.23
0.129	173	391	5	2	0.87	0.23
0.151	204	424	7	2	0.46	0.21
0.163	215	428	7	2	0.79	0.22
0.187	259	429	9	2	0.98	0.22
0.239	329	439	11	2	0.71	0.25
0.267	385	456	13	2	0.75	0.25
0.283	413	448	13	2	0.62	0.27
0.316	479	388	17	2	0.81	0.25
0.348	539	415	19	2	0.82	0.26
0.357	557	432	19	2	0.82	0.27
0.373	619	529	17	2	0.87	0.33
0.394	685	567	17	2	0.85	0.36
0.408	730	495	22	2	0.82	0.31
0.424	756	501	23	2	0.85	0.31
0.447	837	506	25	2	0.90	0.32
0.466	916	663	21	2	0.78	0.42
0.490	1029	740	21	2	0.79	0.47
0.511	1115	593	29	2	0.85	0.39
0.546	1312	675	31	2	0.88	0.44
0.565	1491	800	29	2	0.71	0.52
0.576	1559	799	31	2	0.72	0.52
0.606	1889	866	34	2	0.93	0.58
0.621	2231	1000	32	2	0.69	0.68
0.636	2490	1000	36	2	0.85	0.69

(b) Scenario 2

$\tilde{P}$	C	h_{GOM}	N_T	N_E	Δi	D
-	\$M	km	−	-	−	m
0.008	59	349	1	2	0.41	0.17
0.035	116	358	3	2	0.44	0.21
0.049	145	376	3	2	0.52	0.26
0.072	205	368	5	4	0.06	0.27
0.095	258	382	5	4	0.48	0.33
0.113	317	405	7	2	0.85	0.33
0.134	385	343	9	1	0.32	0.32
0.159	444	387	9	2	0.67	0.38
0.179	504	371	9	2	0.65	0.43
0.205	560	373	13	2	0.64	0.36
0.223	613	349	13	2	0.75	0.40
0.255	695	397	15	2	0.71	0.41
0.268	759	383	19	2	0.67	0.35
0.302	846	344	19	2	0.72	0.41
0.312	894	383	19	2	0.72	0.44
0.337	1007	412	19	2	0.89	0.50
0.362	1110	408	21	2	0.70	0.50
0.380	1199	358	25	2	0.85	0.47
0.402	1341	390	25	2	0.79	0.53
0.426	1471	402	29	2	0.70	0.52
0.451	1760	501	29	2	0.65	0.60
0.467	1845	411	35	2	0.71	0.55
0.491	2061	477	33	2	0.83	0.63
0.509	2309	503	36	2	0.85	0.66
0.537	2923	669	31	2	0.75	0.85
0.556	3243	671	35	2	0.86	0.86
0.591	4286	789	35	2	0.85	1.03
0.597	4948	841	32	2	0.90	1.18

(c) Scenario 3

$\tilde{P}$	C	h_{GOM}	N_T	N_E	Δi	D
-	\$M	km	−	-	−	m
0.007	49	368	1	2	0.79	0.13
0.031	89	368	3	2	0.79	0.13
0.040	106	469	3	2	0.43	0.19
0.068	141	491	4	3	0.26	0.22
0.088	171	422	4	3	0.83	0.26
0.103	235	591	4	3	0.77	0.35
0.123	254	374	9	4	0.80	0.21
0.145	290	441	10	3	0.63	0.23
0.157	322	395	13	3	0.79	0.20
0.185	379	444	13	3	0.78	0.25
0.198	412	409	16	3	0.58	0.22
0.214	446	430	16	3	0.62	0.25
0.226	476	438	16	3	0.63	0.26
0.258	561	451	19	3	0.71	0.27
0.292	650	429	25	3	0.87	0.25
0.319	773	471	25	3	0.76	0.30
0.332	823	494	28	3	0.60	0.29
0.346	859	456	28	3	0.90	0.30
0.377	998	511	31	3	0.74	0.32
0.379	1023	472	31	3	0.83	0.33
0.398	1102	492	35	3	0.80	0.32
0.420	1215	566	34	3	0.83	0.37
0.432	1299	636	34	3	0.81	0.40
0.446	1411	699	35	3	0.90	0.43
0.468	1588	789	34	3	0.80	0.49
0.495	1825	836	34	3	0.92	0.56
0.506	2035	951	34	3	0.84	0.61
0.519	2368	981	36	4	0.85	0.67

(d) Scenario 4

$\tilde{P}$	C	h_{GOM}	N_T	N_E	Δi	D
-	\$M	km	−	-	−	m
0.006	69	346	1	2	0.84	0.21
0.039	154	374	4	3	0.81	0.24
0.052	198	341	5	4	0.78	0.25
0.070	262	370	5	4	0.73	0.33
0.090	359	374	9	4	0.78	0.31
0.108	424	372	10	3	0.29	0.33
0.132	517	400	10	3	0.55	0.42
0.138	555	380	13	3	0.93	0.36
0.164	656	408	13	3	0.91	0.43
0.175	720	379	19	3	0.76	0.34
0.191	777	467	16	3	0.88	0.44
0.214	863	407	19	3	0.80	0.43
0.223	918	406	19	3	0.90	0.45
0.240	1003	406	22	3	0.74	0.44
0.271	1146	341	28	3	0.72	0.41
0.279	1200	387	25	3	0.83	0.48
0.297	1311	400	28	3	0.74	0.48
0.314	1428	384	31	3	0.68	0.48
0.328	1510	379	31	3	0.80	0.50
0.350	1605	402	34	3	0.88	0.50
0.368	2071	456	33	3	0.89	0.63
0.390	2112	477	34	3	0.89	0.63
0.397	2220	508	34	3	0.92	0.66
0.418	2854	633	32	3	0.90	0.82
0.435	2952	616	34	3	0.90	0.81
0.452	3537	681	34	3	0.78	0.92
0.464	3930	759	34	3	0.75	0.99
0.481	4806	931	33	4	0.71	1.14

Bibliography

[1] O. Abdelkhalik and D. Mortari. Orbit design for ground surveillance using genetic algorithms. *Journal of Guidance Control and Dynamics*, 29(5):1231–1235, 2006. `doi: 10.2514/1.16722`.

[2] O. Abdelkhalik, D. Mortari, and K. J. Park. Satellite constellation design for earth observation. In *15th AAS/AIAA Space Flight Mechanics Meeting, Copper Mountain, CO*, 2005.

[3] Osama Mohamed Omar Abdelkhalik. *Orbit design and estimation for surveillance missions using genetic algorithms*. Doctoral dissertation, Texas A&M University, 2005.

[4] W. S. Adams and L. Rider. Circular polar constellations providing continuous single or multiple coverage above a specified latitude. *Journal of the Astronautical Sciences*, 35(2):155–192, 1987.

[5] Nigeria and space technology, 2011. Retrieved on 05/11/2014 from http://www.africanglobe.net/africa/nigeria-space-technology/.

[6] R. B. Agrawal and K. Deb. Simulated binary crossover for continuous search space. *Complex Syst.*, pages 115–148, 1995.

[7] J. Agte, N. Borer, and O. de Weck. Design of long-endurance systems with inherent robustness to partial failures during operations. *Journal of Mechanical Design*, 134, 2012. `doi:10.1115/1.4007574`.

[8] Y. T. Ahn and D. B. Spencer. Optimal reconfiguration of a formation-flying satellite constellation. In *Decision and Control, 2005 and 2005 European Control Conference. CDC-ECC '05. 44th IEEE Conference on*, pages 66–71, 2002. `doi:10.1109/CDC. 2005.1582132`.

[9] Annual global climate and catastrophe report: Impact forecasting-2013, 2014. Retrieved on 08/05/2014 from http://thoughtleadership.aonbenfield.com/Documents/20140113_ab_if_annual_climate_catastrophe_report.pdf.

[10] A. Arias-Montano, C. Coello Coello, and E. Mezura-Montes. Multi-objective evolutionary algorithms in aeronautical and aerospace engineering. In *Evolutionary Computation, IEEE Transactions on*, volume 16, pages 662–694. IEEE, 2012. `doi: 10.1109/TEVC.2011.2169968`.

[11] M. Asvial, R. Tafazolli, and B. G. Evans. Modified gsc for hybrid satellite constellation. *Electronics Letters*, 38(20):1216–1217, 2002. `doi:10.1049/el:20020809`.

[12] M. Asvial, R. Tafazolli, and B. G. Evans. Non-geo satellite constellation design with satellite diversity using genetic algorithm. In *20th AIAA International Communication Satellite Systems Conference and Exhibit, Montreal, Canada*, 2002. `doi:10.2514/6.2002-2018`.

[13] M. Asvial, R. Tafazolli, and B. G. Evans. Genetic hybrid satellite constellation design. In *21st International Communications Satellite Systems Conference and Exhibit, Yokohama, Japan*, 2003. `doi:10.2514/6.2003-2283`.

[14] M. Asvial, R. Tafazolli, and B. G. Evans. Satellite constellation design and radio resource management using genetic algorithm. In *Communications, IEE Proceedings-*, volume 151, pages 204–209. IET, 2004.

[15] ATK / Lockheed Martin. Athena Mission Planner's Guide, 2012.

[16] M. E. Avendano, J. J. Davis, and D. Mortari. The lattice theory of flower constellations. In *Proceedings of the 2010 Space Flight Mechanics Meeting Conference. San Diego, CA*, 2010.

[17] A. H. Ballard. Rosette constellations of earth satellites. *Aerospace and Electronic Systems, IEEE Transactions on*, AES-16(5):656–673, 1980. `doi:10.1109/TAES.1980.308932`.

[18] David Barnhart. SeeMe, Broad Agency Announcement, 2012.

[19] Ashok D. Belegundu and Tirupathi R. Chandrupatla. *Optimization concepts and applications in engineering*. Cambridge University Press, 2011.

[20] D. C. Beste. Design of satellite constellations for optimal continuous coverage. *Aerospace and Electronic Systems, IEEE Transactions on*, AES-14(3):466–473, 1978. `doi:10.1109/TAES.1978.308608`.

[21] N. T. Bliss, R. Bond, J. Kepner, H. Kim, and A. Reuther. Interactive grid computing at lincoln laboratory. *Lincoln Laboratory Journal*, 16(1):165, 2006.

[22] Christian Bruccoleri. *Flower constellation optimization and implementation*. Doctoral dissertation, Texas A&M University, 2007.

[23] I. A. Budianto and J. R. Olds. A collaborative optimization approach to design and deployment of a space based infrared system constellation. In *2000 IEEE Aerospace Conference Proceedings, Vol 1*, pages 385–393, 2000. `doi:10.1109/AERO.2000.879415`.

[24] I. A. Budianto and J. R. Olds. Design and deployment of a satellite constellation using collaborative optimization. *Journal of Spacecraft and Rockets*, 41(6):956–963, 2004. `doi:10.2514/1.14254`.

[25] Irene Arianti Budianto. *A collaborative optimization approach to improve the design and deployment of satellite constellations.* Doctoral dissertation, Georgia Institute of Technology, 2000.

[26] Fg to launch 34m-pound nigeriasat-2, -x july 7, 2011. Retrieved on 05/11/2014 from http://www.businessdayonline.com/NG/index.php/news/76-hot-topic/ 23546-fg-to-launch-34m-pound-nigeriasat-2-x-july-7.

[27] Sergio Camacho-Lara. Current and future gnss and their augmentation systems. In J. N. Pelton, S. Madry, and S. Camacho-Lara, editors, *Handbook of Satellite Applications.* Springer Publishing Company, Incorporated, New York, NY, 2013.

[28] M. Cardin, W. J. Nuttall, R. De Neufville, and J. Dahlgren. Extracting value from uncertainty: A methodology for engineering systems design. In *17th Symposium of the International Council on Systems Engineering, San Diego, CA, United States*, 2007.

[29] Michel-Alexandre Cardin. Facing reality: Design and management of flexible engineering systems. Master's dissertation, Massachusetts Institute of Technology, 2007.

[30] D. Casanova, M. Avendano, and D. Mortari. Necklace theory on flower constellations. In *Spaceflight Mechanics*, volume 140, February 13-17 2012.

[31] D. Casanova, M. Avendano, and D. Mortari. Optimizing flower constellations for global coverage. In *AIAA/AAS Astrodynamics Specialist Conference, Minneapolis, Minnesota*, 13-16 August 2012. `doi:10.2514/6.2012-4805`.

[32] Mathieu Chaize. Enhancing the economics of satellite constellations via staged deployment and orbital reconfiguration. Master's dissertation, Massachusetts Institute of Technology, 2003.

[33] Jeng-Shing Chern, J. Ling, and Shui-Lin Weng. Taiwan's second remote sensing satellite. *Acta Astronautica*, 63(11):1305–1311, 2008.

[34] John Clarkson and Claudia Eckert. *Design process improvement: a review of current practice*, section 7, pages 174 – 197. Springer, 2005.

[35] T. Co, J. Black, and C. Zagaris. Responsive satellites through ground track manipulation using existing technology. *Journal of Spacecraft and Rockets*, 50(1), 2013. `doi:10.2514/6.2011-7262`.

[36] Carlos A. Coello Coello, Gary B. Lamont, and David A. Van Veldhuisen. *Evolutionary algorithms for solving multi-objective problems.* Springer, 2007.

[37] W. A. Crossley, A. M. Cook, D. W. Fanjoy, and V. B. Venkayya. Using the two-branch tournament genetic algorithm for multiobjective design. *AIAA journal*, 37(2):261–267, 1999. `doi:10.2514/2.699`.

[38] W. A. Crossley and E. A. Williams. Simulated annealing and genetic algorithm approaches for discontinuous coverage satellite constellation design. *Engineering Optimization*, 32(3):353–371, 2000. `doi:10.1080/03052150008941304`.

[39] A. da Silva Curiel, L. Boland, J. Cooksley, M. Bekhti, P. Stephens, W. Sun, and M. Sweeting. First results from the disaster monitoring constellation (dmc). *Acta Astronautica*, 56(1):261–271, 2005.

[40] I. Das and J. E. Dennis. Normal-boundary intersection: A new method for generating the pareto surface in nonlinear multicriteria optimization problems. *SIAM Journal on Optimization*, 8(3):631–657, 1998. `doi:10.1137/S1052623496307510`.

[41] P. Davies, F. Chizea, A. Cawthorne, A. Carrel, L. Gomes, A. da Silva Curiel, and Sir Martin Sweeting. Commissioning of the NigeriaSat-2 high resolution imaging mission. In *26th AIAA/USU Conference on Small Satellites, Logan, Utah, 13-16 August 2012*, 2012.

[42] J. J. Davis, M. E. Avendano, and D. Mortari. Elliptical lattice flower constellations for global coverage. In *AAS 10-173, AAS/AIAA Space Flight Mechanics Meeting Conference, San Diego, CA*, Feb. 8-12 2010.

[43] Jeremy John Davis. *Constellation reconfiguration: Tools and analysis.* Doctoral dissertation, Texas A&M University, 2010.

[44] R. de Neufville. Real options: Dealing with uncertainty in systems planning and design. *Integrated Assessment*, 4(1):26–34, 2003. `doi:10.1076/iaij.4.1.26.16461`.

[45] R. de Neufville, O. de Weck, J. Lin, and S. Scholtes. *Identifying real options to improve the design of engineering systems*, pages 75–98. CRC press Boca Raton, FL, 2009.

[46] R. de Neufville, K. Hodota, J. Sussman, and S. Scholtes. Real options to increase the value of intelligent transportation systems. *Transportation Research Record: Journal of the Transportation Research Board*, 2086(1):40–47, 2008. `doi:10.3141/2086-05`.

[47] Richard de Neufville and Stefan Scholtes. *Flexibility in Engineering Design.* The MIT Press, Cambridge, MA, 2011.

[48] Peter B. de Selding. Enhancedview contract awards carefully structured, nga says, 2010. Retrieved on 05/11/2014 from http://www.spacenews.com/article/enhancedview-contract-awards-carefully-structured-nga-says.

[49] O. De Weck, R. De Neufville, and M. Chaize. Staged deployment of communications satellite constellations in low earth orbit. *Journal of Aerospace Computing, Information, and Communication*, 1(3):119–136, 2004. `doi:10.1.1.164.124`.

[50] O. De Weck, C. M. Eckert, and P. J. Clarkson. A classification of uncertainty for early product and system design. In *Proceedings of the 16th International Conference on Engineering Design (ICED'07), 2007-8-28 to 2007-8-31, Paris, France*, pages 159–160, 2007.

[51] O. L. De Weck, U. Scialom, and A. Siddiqi. Optimal reconfiguration of satellite constellations with the auction algorithm. *Acta Astronautica*, 62(2):112–130, 2008. `doi:10.1016/j.actaastro.2007.02.008`.

[52] K. Deb and D. Deb. Analyzing mutation schemes for real-parameter genetic algorithms. Technical Report KanGAL report 2012016, Kanpur Genetic Algorithms Laboratory, Indian Institute of Technology Kanpur, 2012.

[53] K. Deb and H. Jain. Self-adaptive parent to mean-centric recombination for real-parameter optimization. Technical Report KanGAL report 2011001, Kanpur Genetic Algorithms Laboratory, Indian Institute of Technology Kanpur, 2011.

[54] K. Deb, D. Joshi, and A. Anand. Real-coded evolutionary algorithms with parent-centric recombination. In *Evolutionary Computation, 2002. CEC'02. Proceedings of the 2002 Congress on*, volume 1, pages 61–66. IEEE, 2002. `doi:10.1109/CEC.2002.1006210`.

[55] K. Deb and A. Kumar. Real-coded genetic algorithms with simulated binary crossover: Studies on multimodel and multiobjective problems. *Complex Syst.*, 9(6):431–454, 1995.

[56] K. Deb, M. Mohan, and S. Mishra. A fast multi-objective evolutionary algorithm for finding well-spread pareto-optimal solutions. Technical Report KanGAL report 2003002, Kanpur Genetic Algorithms Laboratory, Indian Institute of Technology Kanpur, 2003.

[57] K. Deb, A. Pratap, S. Agarwal, and T. Meyarivan. A fast and elitist multiobjective genetic algorithm: NSGA-II. *Evolutionary Computation, IEEE Transactions on*, 6(2):182–197, 2002. `doi:10.1109/4235.996017`.

[58] K. Deb, A. Sinha, and S. Kukkonen. Multi-objective test problems, linkages, and evolutionary methodologies. In *Proceedings of the 8th annual conference on Genetic and evolutionary computation*, pages 1141–1148. ACM, 2006.

[59] F. J. Dietrich. The globalstar satellite cellular communication system design and status. In *17th AIAA International Communications Satellite Systems Conference and Exhibit, Yokohama, Japan*, pages 229–234, 1998. `doi:10.2514/6.1998-1213`.

[60] Maxx Dilley. *Natural disaster hotspots: a global risk analysis*, volume 5. World Bank Publications, 2005.

[61] A. Dinardi and M. Persson. High performance green propulsion (HPGP): A flight-proven capability and cost game-changer for small and secondary satellites. In *26th AIAA/USU Conference on Small Satellites, Logan, Utah, 13-16 August 2012*, 2012.

[62] Jean-Phillipe Donnio. The satellite encyclopedia. Retrieved on 11/08/2013 from http://www.tbs-satellite.com/tse/online/index_alpha.html.

[63] William L. Dunn and J. Kenneth Shultis. *Exploring Monte Carlo Methods*. Elsevier, Amsterdam, Netherlands, 2011.

[64] T. A. Ely, W. A. Crossley, and E. A. Williams. Satellite constellation design for zonal coverage using genetic algorithms. In *Spaceflight Mechanics 1998*, volume 99 of *Advances in the Astronautical Sciences*, pages 443–460, 1998.

[65] T. A. Ely, W. A. Crossley, and E. A. Williams. Satellite constellation design for zonal coverage using genetic algorithms. *Journal of the Astronautical Sciences*, 47(3-4):207–228, 1999.

[66] eoPortal. Satellite missions database. Retrieved on 11/07/2013 from https://directory.eoportal.org.

[67] S. Eves and A. Cawthorne. Redefining the word "responsive" in ors. In *7th Responsive Space Conference, Los Angeles, CA*, 2009.

[68] S. Eves, A. Cawthorne, P. Davies, A. Baker, A. da Silva Curiel, and M. Sweeting. Reading the fine print from orbit... In *ESA Special Publication*, volume 660, page 86, 2008.

[69] S. Eves and M. Taylor. Thinking at the constellation level. In *9th Responsive Space Conference, Los Angeles, CA*, 2010.

[70] S. Ferguson, A. Siddiqi, K. Lewis, and O. De Weck. Flexible and reconfigurable systems: Nomenclature and review. In *ASME 2007 International Design Engineering Technical Conferences and Computers and Information in Engineering Conference, Las Vegas, Nevada*, 2007. doi:10.1115/DETC2007-35745.

[71] M. Ferringer, R. Clifton, and T. Thompson. Constellation design with parallel multi-objective evolutionary computation. In *AIAA/AAS Astrodynamics Specialist Conference and Exhibit, Keystone, Colorado*, 21-24 August 2006. doi:10.2514/6.2006-6015.

[72] M. Ferringer, D. Spencer, R. Clifton, T. Thompson, and P. Reed. Pareto-hypervolumes for the reconfiguration of satellite constellations. In *AIAA/AAS Astrodynamics Specialist Conference and Exhibit, Honolulu, Hawaii*, 2008. doi:10.2514/6.2008-6611.

[73] M. P. Ferringer, R. S. Clifton, T. G. Thompson, D. B. Spencer, R. G. Melton, P. M. Reed, W. A. Crossley, and V. L. Coverstone. Efficient and accurate evolutionary multi-objective optimization paradigms for satellite constellation design. *Journal of Spacecraft and Rockets*, 44(3):682–691, 2007. doi:10.2514/1.26747.

[74] M. P. Ferringer and D. B. Spencer. Satellite constellation design tradeoffs using multiple-objective evolutionary computation. *Journal of Spacecraft and Rockets*, 43(6):1404–1411, 2006. doi:10.2514/1.18788.

[75] M. P. Ferringer, D. B. Spencer, and P. Reed. Many-objective reconfiguration of operational satellite constellations with the large-cluster epsilon non-dominated sorting genetic algorithm-ii. In *Evolutionary Computation, 2009. CEC'09. IEEE Congress on*, pages 340–349. IEEE, 2009.

[76] Matthew Phillip Ferringer. *General framework for the reconfiguration of satellite constellations.* Doctoral dissertation, The Pennsylvania State University, 2009.

[77] E. Fleming, J. Lafleur, and J. Saleh. Response surface equations for expendable launch vehicle payload capability. In *AIAA SPACE 2009 Conference & Exposition, Pasedena, California*, 2009. `doi:10.2514/6.2009-6656`.

[78] C. M. Fonseca and P. J. Fleming. Genetic algorithms for multiobjective optimization: Formulation, discussion and generalization. In *ICGA*, volume 93, pages 416–423, 1993.

[79] Center for International Earth Science Information Network CIESIN Columbia University and Centro Internacional de Agricultura Tropical CIAT. Gridded population of the world, version 3 (gpwv3): Population density grid, future estimates, 2005. URL: Retrievedon01/07/2014fromhttp://sedac.ciesin.columbia.edu/data/set/gpw-v3-population-density-future-estimates.

[80] E. Frayssinhes. Investigating new satellite constellation geometries with genetic algorithms. In *AIAA/AAS Astrodynamics Conference, San Diego, CA*, 1996. `doi:10.2514/6.1996-3636`.

[81] E. Fricke and A. P. Schulz. Design for changeability (DfC): Principles to enable changes in systems throughout their entire lifecycle. *Syst. Engin.*, 8(4), 2005. `doi:10.1002/sys.20039`.

[82] E. R. George. Optimization of satellie constellations for discontinuous global coverage via genetic algorithms. In *Astrodynamics 1997*, volume 97 of *Advances in the Astronautical Sciences, Pt. 1*, pages 333–346, 1997.

[83] GITA announces 2004 board of directors, 2004.

[84] Jean Dickinson Gibbons and Subhabrata Chakraborti. *Nonparametric statistical inference.* Chapman and Hall/CRC, 5th edition, 2010.

[85] M. A. Gleyzes, L. Perret, and P. Kubik. Pleiades system architecture and main performances. In *International Archives of the Photogrammetry, Remote Sensing and Spatial Information Sciences, Volume XXXIX-B1, XXII ISPRS Congress*, 2012.

[86] D. E. Goldberg. Using time efficiently: Genetic-evolutionary algorithms and the continuation problem. Technical report, Illinois Genetic Algorithms Laboratory, University of Illinois at Urbana-Champaign, 1999.

[87] M. Guelman and A. Kogan. Electric propulsion for remote sensing from low orbits. *Journal of Guidance, Control, and Dynamics*, 22(2):313–321, 1999. `doi:10.2514/2.4380`.

[88] H. Habib-Agahi, J. Mrozinski, and G. Fox. NASA instrument cost/schedule model. In *Aerospace Conference, 2011 IEEE*, pages 1–19, 2011. `doi:10.1109/AERO.2011.5747633`.

[89] Hamid Habib-Agahi, Joe Mrozinski, George Fox, and Gary Ball. Nasa instrument cost model for explorer-like mission instruments: Nicm-e. In *AIAA SPACE 2013 Conference & Exposition, San Diego, California*, 2013.

[90] D. Hadka, K. Madduri, and P. Reed. Scalability analysis of the asynchronous, master-slave borg multiobjective evolutionary algorithm. In *Parallel and Distributed Processing Symposium Workshops & PhD Forum (IPDPSW), 2013 IEEE 27th International*, pages 425–434. IEEE, 2013. `doi:10.1109/IPDPSW.2013.160`.

[91] D. Hadka and P. Reed. Diagnostic assessment of search controls and failure modes in many-objective evolutionary optimization. *Evolutionary Computation*, 20(3):423–452, 2012. `doi:10.1162/EVCO_a_00053`.

[92] D. Hadka and P. Reed. Borg: An auto-adaptive many-objective evolutionary computing framework. *Evolutionary computation*, 21(2):231–259, 2013. `doi:10.1162/EVCO_a_00075`.

[93] Gerald J. Hahn and William Q. Meeker. *Statistical intervals: A guide for practitioners*. John Wiley & Sons, 1991. `doi:10.1002/9780470316771`.

[94] J. M. Hanson, M. J. Evans, and R. E. Turner. Designing good partial coverage satellite constellations. In *AIAA Astrodynamics Conference, Portland, Oregon*, 1990.

[95] J. M. Hanson, M. J. Evans, and R. E. Turner. Designing good partial coverage satellite constellations. *Journal of the Astronautical Sciences*, 40(2):215–239, 1992.

[96] J. M. Hanson and A. N. Linden. Improved low-altitude constellation design methods. *Journal of Guidance Control and Dynamics*, 12(2):228–236, 1989. `doi:10.2514/3.20395`.

[97] R. Hassan and R. de Neufville. Design of engineering systems under uncertainty via real options and heuristic optimization. Retrieved on 05/10/14 from http://www.researchgate.net/publication/228634248_Design_of_engineering_systems_under_uncertainty_via_real_options_and_heuristic_optimization/file/3deec525139ad5c269.pdf, 2006.

[98] R. Hassan, R. De Neufville, and D. McKinnon. Value-at-risk analysis for real options in complex engineered systems. In *Systems, Man and Cybernetics, 2005 IEEE International Conference on*, volume 4, pages 3697–3704. IEEE, 2005. `doi:10.1109/ICSMC.2005.1571721`.

[99] E. Hayes. A method for selecting satellite constellations to minimize revisit time. In *26th Aerospace Sciences Meeting, AIAA, Reno, NV*, 1988.

[100] R. Hopkins. Long-term revisit coverage using multi-satellite constellations. In *AIAA/AAS Astrodynamics Conference, Minneapolis, Minnesota*, Aug. 15-17 1988. `doi:10.2514/6.1988-4276`.

[101] Delta 2 rocket launches quintet of iridium satellites, 2002. Retrieved on 07/28/2014 from http://www.spaceflightnow.com/delta/d290/.

[102] B. Jackson. Performance of meshed comb constellations for minimizing target revisit time. In *1998 IEEE Aerospace Conference Proceedings, Vol 5*, pages 59–69, 1998. `doi:10.1109/AERO.1998.685792`.

[103] Cyrus D. Jilla. *A multiobjective, multidisciplinary design optimization methodology for the conceptual design of distributed satellite systems*. Doctoral dissertation, Massachusetts Institute of Technology, 2002.

[104] Edward Jurkevics. Digitalglobe raises $355 million in debt issue, next imaging satellite worldview-2 now all-systems-go. Retrieved on 05/11/2014 from http://seekingalpha.com/instablog/391378-edward-jurkevics/1774-digitalglobe-raises-355-million-in-debt-issue-next-imaging-satellite-worldview-2-now-all-system 2009.

[105] H. Keller and H. Salzwedel. Link strategy for the mobile satellite system iridium. In *Vehicular Technology Conference, 1996. Mobile Technology for the Human Race., IEEE 46th*, volume 2, pages 1220–1224, 1996. `doi:10.1109/VETEC.1996.501506`.

[106] H. D. Kim, H. Bang, and O. C. Jung. Genetic design of target orbits for a temporary reconnaissance mission. *Journal of Spacecraft and Rockets*, 46(3):725–728, 2009. `doi:10.2514/1.41620`.

[107] H. D. Kim, O. C. Jung, and H. Bang. A computational approach to reduce the revisit time using a genetic algorithm. In *Control, Automation and Systems, 2007. ICCAS '07. International Conference on*, pages 184–189, 2007. `doi:10.1109/ICCAS.2007.4406905`.

[108] I. Y. Kim and O. L. De Weck. Adaptive weighted-sum method for bi-objective optimization: Pareto front generation. *Structural and multidisciplinary optimization*, 29(2):149–158, 2005. `doi:10.1007/s00158-004-0465-1`.

[109] H. Kita, I. Ono, and S. Kobayashi. Multi-parental extension of the unimodal normal distribution crossover for real-coded genetic algorithms. In *Evolutionary Computation, 1999. CEC 99. Proceedings of the 1999 Congress on*, volume 2. IEEE, 1999. `doi:10.1109/CEC.1999.782672`.

[110] F. Knight. Concept of operations for operationally responsive space". In *4th Responsive Space Conference, Los Angeles, CA*, 2006.

[111] J. D. Knowles and D. W. Corne. Approximating the nondominated front using the pareto archived evolution strategy. *Evolutionary computation*, 8(2):149–172, 2000. `doi:10.1162/106365600568167`.

[112] J. B. Kollat and P. M. Reed. The value of online adaptive search: a performance comparison of NSGAII, ε-NSGAII and εMOEA. In *Evolutionary Multi-Criterion Optimization*, volume 3410, pages 386–398. Springer, 2005. `doi:10.1007/978-3-540-31880-4_27`.

[113] H. J. Kramer. *Observation of the Earth and its Environment: Survey of Missions and Sensors*. Springer, 2002.

[114] J. Krueger, D. Selva, M. Smith, and J. Keesee. Spacecraft and constellation design for a continuous responsive imaging system in space. In *AIAA SPACE 2009 Conference & Exposition, Pasadena, California*, 14-17 September 2009. `doi:10.2514/6.2009-6773`.

[115] J. M. Lafleur, E. S. Fleming, and J. H. Saleh. Response surface equations for expendable launch vehicle payload mass capability. *Journal of Spacecraft and Rockets*, 49(1):185–189, 2012. `doi:10.2514/1.48714`.

[116] Elisabeth Lamassoure. A framework to account for flexibility in modeling the value of on-orbit servicing for space systems. Master's dissertation, Massachusetts Institute of Technology, 2001.

[117] T. J. Lang. Symmetric circular orbit satellite constellations for continuous global coverage. In *Astrodynamics 1987 : proceedings of the AAS/AIAA Astrodynamics Conference held August 10-13, 1987, Kalispell, Montana*, volume 65, pages 1111–1132, 1987.

[118] T. J. Lang. Optimal low earth orbit constellations for continuous global coverage. In *Astrodynamics 1993 : proceedings of the AAS/AIAA Astrodynamics Conference held August 16-19, 1993, Victoria, British Columbia, Canada*, volume 85, pages 1199–1216, 1993.

[119] T. J. Lang. A parametric examination of satellite constellations to minimize revisit time for low earth orbits using a genetic algorithm. *Advances in the Astronautical Sciences*, 109:625–640, 2001.

[120] T. J. Lang. Walker constellations to minimize revisit time in low earth orbit. In *Spaceflight Mechanics*, volume 114 of *Advances in the Astronautical Sciences, Pt. 1*, pages 427–442, 2003.

[121] T. J. Lang and J. M. Hanson. Orbital constellations which minimize revisit time. *Advances in the Astronautical Sciences*, 54:1071–1086, 1984.

[122] M. Laumanns, L. Thiele, K. Deb, and E. Zitzler. Combining convergence and diversity in evolutionary multiobjective optimization. *Evolutionary computation*, 10(3):263–282, 2002. `doi:10.1162/106365602760234108`.

[123] J. C. Leachtenauer, W. Malila, J. Irvine, L. Colburn, and N. Salvaggio. General image-quality equation: GIQE. *Applied Optics*, 36(32):8322–8328, 1997. `doi:10.1364/AO.36.008322`.

[124] Jijun Lin. *Exploring Flexible Strategies in Engineering Systems Using Screening Models*. Doctoral dissertation, Massachusetts Institute of Technology, 2008.

[125] A. Long, M. Richards, and D. E. Hastings. On-orbit servicing: A new value proposition for satellite design and operation. *Journal of Spacecraft and Rockets*, 44(4):964–976, 2007. `doi:10.2514/1.27117`.

[126] R. D. Luders. Satellite networks for continuous zonal coverage. *American Rocket Society Journal*, 31:179–184, 1961. `doi:10.2514/8.5422`.

[127] D. M. Ma and W. C. Hsu. Exact design of partial coverage satellite constellations over oblate earth. *Journal of Spacecraft and Rockets*, 34(1):29–35, 1997. `doi:10.2514/2.3188`.

[128] Donald H. Martin. *Communication Satellites*. The Aerospace Press, El Segundo, CA, 2000.

[129] M. Martinez-Sanchez and James E. Pollard. Spacecraft electric propulsion-an overview. *Journal of Propulsion and Power*, 14(5):688–699, 1998. `doi:10.2514/2.5331`.

[130] P. Massatt and W. Brady. Optimizing performance through constellation management. In *Crosslink, Summer 2002, The Aerospace Corporation, El Segundo, CA*, pages 17–21, 2002.

[131] D. Mortari. Flower constellations for future space missions. In *Satellite Telecommunications (ESTEL), 2012 IEEE First AESS European Conference on*, pages 1–7. IEEE, 2012. `doi:10.1109/ESTEL.2012.6400116`.

[132] D. Mortari, O. Abdelkhalik, and C. Bruccoleri. Synodic and relative flower constellations with applications for planetary explorations. *Advances in the Astronautical Sciences, 05-151*, 2005.

[133] D. Mortari, M. De Sanctis, and M. Lucente. Design of flower constellations for telecommunication services. *Proceedings of the IEEE*, 99(11):2008–2019, 2011. `doi:10.1109/JPROC.2011.2158766`.

[134] D. Mortari and M. P. Wilkins. Flower constellation set theory. Part i: Compatibility and phasing. *Aerospace and Electronic Systems, IEEE Transactions on*, 44(3):953–962, 2008. `doi:10.1109/TAES.2008.4655355`.

[135] D. Mortari, M. P. Wilkins, and C. Bruccoleri. Constellation design using flower constellations. *The Journal of the Astronautical Sciences*, 52(1,2):107–127, 2004.

[136] T. Mosher. Applicability of selected multidisciplinary design optimization methods to conceptual spacecraft design. In *Proceedings of the 6th AIAA ISSMO Symposium on Multidisciplinary Analysis and Optimization, Bellevue, Washington*, 1996.

[137] T. Mosher. Spacecraft design using a genetic algorithm optimization approach. In *Aerospace Conference, 1998 IEEE*, volume 3, pages 123–134. IEEE, 1998. `doi:10.1109/AERO.1998.685783`.

[138] T. J. Mosher. *Improving spacecraft design using a multidisciplinary design optimization methodology.* Doctoral dissertation, University of Colorado at Boulder, 2000.

[139] G. V. Mozhaev. The problem of the continuous earth coverage and the kinematically regular satellite networks. i. *Cosmic Research*, 10(6):833–840, 1972.

[140] G. V. Mozhaev. The problem of the continuous earth coverage and the kinematically regular satellite networks. ii. *Cosmic Research*, 11(1):52–61, 1973.

[141] G. V. Mozhaev. Capabilities of kinematically regular satellite systems with symmetry groups of the second type in the problem of continuous single coverage of the earth. *Cosmic Research*, 43(3):205–212, 2005.

[142] I. Nann, D. Izzo, and R. Walker. A reconfigurable mars constellation for radio occultation measurements and navigation. In *4th International Workshop on Satellite Constellation and Formation Flying, Sao Jose dos Campos, Brazil*, pages 14–16, 2005.

[143] Pegasus xlhessi: Last-minute decisions in flight-based launch, 2007. NASA Case Studies GSFC-1019C-1.

[144] NASA Headquarters Cost Analysis Division. *NASA Cost Estimating Handbook*, 2008 edition, 2008.

[145] A. J. Nebro, J. J. Durillo, M. Machín, C. A. Coello Coello, and B. Dorronsoro. A study of the combination of variation operators in the NSGA-II algorithm. In *Advances in Artificial Intelligence*, pages 269–278. Springer, 2013. `doi:10.1007/978-3-642-40643-0_28`.

[146] Dan Newman. Vulture II, DARPA BAA, 2009.

[147] Orbital Sciences Corporation. Taurus Launch System Payload User's Guide, Release 4.0, 2006.

[148] Orbital Sciences Corporation. Pegasus User's Guide, Release 7.0, 2010.

[149] Orbital Sciences Corporation. Delta IV Launch Service User's Guide, June 2013.

[150] Orbital Sciences Corporation. Minotaur IV, V, VI User's Guide, Release 2.0, 2013.

[151] M. Oxfort. The rapideye mission. In *WGISS-24 Host Workshop*, 2007.

[152] Sung Wook Paek. Reconfigurable satellite constellations for geo-spatially adaptive earth observation missions. Master's dissertation, Massachusetts Institute of Technology, 2012.

[153] G. Palmerini. Polar elliptic orbits for global coverage constellations. In *AAS/AIAA Astrodynamics Conference, Scottsdale, Arizona*, 1994. `doi:10.2514/6.1994-3720`.

[154] G. Palmerini. Design of global coverage constellations based on elliptical orbits. In *AAS/AIAA Astrodynamics Conference, San Diego, California*, 1996. `doi:10.2514/6.1996-3637`.

[155] D. J. Pate, M. D. Patterson, and B. J. German. Optimizing families of reconfigurable aircraft for multiple missions. *Journal of Aircraft*, 49(6):1988–2000, 2012. `doi:10.2514/1.C031667`.

[156] R. Patel and M. Raghuwanshi. Multi-objective optimization using multi parent crossover operators. *Journal of Emerging Trends in Computing and Information Sciences*, 2(2):33–39, 2010.

[157] D. J. Pegher and J. A. Parish. Optimizing coverage and revisit time in sparse military satellite constellations: A comparison of traditional approaches and genetic algorithms. Master's dissertation, Naval Postgraduate School, 2004.

[158] Joseph M. Piwowar. The satellite morgue, 2010. Retrieved on 05/11/2014 from http://uregina.ca/piwowarj/Satellites/Morgue.html.

[159] G. E. Pollock, J. W. Gangestad, and J. M. Longuski. Responsive coverage using propellantless satellites. In *Responsive Space Conference (RS6). Los Angeles, CA. AIAA Paper RS6-2008-2002*, 2008.

[160] M. Pontani and P. Teofilatto. Satellite constellations for continuous and early warning observation: A correlation-based approach. *Journal of Guidance, Control, and Dynamics*, 30(4):910–920, 2007. `doi:10.2514/1.23094`.

[161] A. V. Rao, A. E. Scherich, S. Cox, and T. E. Mosher. A concept for operationally responsive space mission planning using aeroassisted orbital transfer. In *Responsive Space Conference (RS6). Los Angeles, CA. AIAA Paper RS6-2008-1001*, 2008.

[162] P. Reed, B. S. Minsker, and D. E. Goldberg. Simplifying multiobjective optimization: An automated design methodology for the nondominated sorted genetic algorithm-ii. *Water Resources Research*, 39(7), 2003. `doi:10.1029/2002WR001483`.

[163] P. M. Reed, J. B. Kollat, M. P. Ferringer, and T. G. Thompson. Parallel evolutionary multi-objective optimization on large, heterogeneous clusters: An applications perspective. *Journal of Aerospace Computing, Information, and Communication*, 5(11):460–478, 2008. `doi:10.2514/1.36467`.

[164] A CEOS Disaster SBA Team GEO DI-06-09 Report. Use of satellites for risk management, volume i, 2008.

[165] Calculating response time statistics. personal communication with R. C. Thompson, October 9, 2013.

[166] E. Riddle. Use of optimization methods in small satellite systems analysis. In *12th AIAA/USU Conference on Small Satellites, Logan, Utah*, 1998.

[167] L. Rider. Optimized polar orbit constellations for redundant earth coverage. *Journal of the Astronautical Sciences*, 33(2):147–161, 1985.

[168] D. Roos, R. de Neufville, F. Moavenzadeh, and S. Connors. The design and development of next generation infrastructure systems. In *Systems, Man and Cybernetics, 2004 IEEE International Conference on*, volume 5, pages 4662–4666. IEEE, 2004. `doi:10.1109/ICSMC.2004.1401267`.

[169] A. M. Ross, D. H. Rhodes, and D. E. Hastings. Defining changeability: Reconciling flexibility, adaptability, scalability, modifiability, and robustness for maintaining system lifecycle value. *Syst. Engin.*, 11(3):246–262, 2008. `doi:10.1002/sys.20098`.

[170] E. T. Ryan, D. R. Jacques, and J. M. Colombi. An ontological framework for clarifying flexibility-related terminology via literature survey. *Syst. Engin.*, 16(1):99–110, 2013. `doi:10.1002/sys.21222`.

[171] J. H. Saleh, E. S. Lamassoure, D. E. Hastings, and D. J. Newman. Flexibility and the value of on-orbit servicing: New customer-centric perspective. *Journal of Spacecraft and Rockets*, 40(2):279–291, 2003. `doi:10.2514/2.3944`.

[172] G. Salgado, S. Abbondanza, R. Blondel, and S. Lannelongue. Constellation availability concepts for galileo. In *Proceedings of the 17th International Technical Meeting of the Satellite Division of The Institute of Navigation (ION GNSS 2004), Long Beach, CA*, pages 616–623, 2004.

[173] Sam L. Savage. *The flaw of averages: Why we underestimate risk in the face of uncertainty*. Wiley, 2012.

[174] Uriel Scialom. Optimization of satellite constellation reconfiguration. Master's dissertation, Massachusetts Institute of Technology, 2003.

[175] A. Siddiqi, O. L. De Weck, and K. Iagnemma. Reconfigurability in planetary surface vehicles: Modeling approaches and case study. *Journal of the British Interplanetary Society*, 59:450–460, 2006.

[176] A. Siddiqi, J. Mellein, and O. L. De Weck. Optimal reconfigurations for increasing capacity of communication satellite constellations. In *46th AIAA/ASME/ASCE/AHS/ASC Structures, Structural Dynamics, and Materials Conference, Austin, Texas*, 2005. `doi:10.2514/MSDM05`.

[177] Afreen Siddiqi. *Reconfigurability in space systems: architecting framework and case studies*. Doctoral dissertation, Massachusetts Institute of Technology, 2006.

[178] M. J. Soppet. ResCon: A conceptual architecture for a responsive space constellation. In *AIAA Responsive Space 2010*, 2010.

[179] Low-cost replacements for Ikonos, QuickBird, 2010. Retrieved on 05/11/2014 from http://www.spacenews.com/article/low-cost-replacements-ikonos-quickbird.

[180] SpaceX. Falcon heavy. Retrieved on 05/11/2014 from http://www.spacex.com/falcon-heavy.

[181] SpaceX. Falcon 9 Launch Vehicle Payload User's Guide, Rev. 1, 2009.

[182] R. A. Spores, R. Masse, S. Kimbrel, and C. McLean. GPIM AF-M315E propulsion system. In *49th AIAA/ASME/SAE/ASEE Joint Propulsion Conference & Exhibit, San Jose, California, 15-17 July 2013*, 2013.

[183] N. Srinivas and K. Deb. Muiltiobjective optimization using nondominated sorting in genetic algorithms. *Evolutionary computation*, 2(3):221–248, 1994. `doi:10.1162/evco.1994.2.3.221`.

[184] R. P. Srivastava. Time continuation in genetic algorithms. Technical Report IlliGAL Report No. 2001021, Illinois Genetic Algorithms Laboratory, University of Illinois at Urbana-Champaign, 2002.

[185] SSTL. Xenon propulsion system datasheet. Retrieved on 11/07/2013 from http://www.sstl.co.uk.

[186] H. P. Stahl. Survey of cost models for space telescopes. *Optical Engineering*, 49(5):053005–053005–8, 2010. `doi:10.1117/1.3430603`.

[187] H. P. Stahl. Survey of cost models for space telescopes. *Optical Engineering*, 49(5), 2010. `doi:10.1117/1.3430603`.

[188] H. P. Stahl, T. Henrichs, A. Luedtke, and M. West. Update on multivariable parametric cost models for ground and space telescopes. In *Proc. SPIE 8442, Space Telescopes and Instrumentation 2012: Optical, Infrared, and Millimeter Wave, 844224*, 2010. `doi:10.1117/12.926363`.

[189] H. P. Stahl, T. Henrichs, A. Luedtke, and M. West. Update on parametric cost models for space telescopes. In *Proc. SPIE 8146, UV/Optical/IR Space Telescopes and Instruments: Innovative Technologies and Concepts V, 81460F*, 2011. `doi:10.1117/12.894085`.

[190] H. P. Stahl, K. Stephens, T. Henrichs, C. Smart, and F. A. Prince. Single-variable parametric cost models for space telescopes. *Optical Engineering*, 49(7), 2010. `doi:10.1117/1.3456582`.

[191] Dannie Stamp. Iridium satellite. NASA GSFC Systems Engineering Seminar, Aug 2 2005, 2005.

[192] R. Storn and K. Price. Differential evolution–a simple and efficient heuristic for global optimization over continuous spaces. *Journal of global optimization*, 11(4):341–359, 1997. `doi:10.1023/A:1008202821328`.

[193] W. H. Tam, M. J. Debreceni, M. S. Hersh, and C. D. Nye. Low cost derivative tanks for spacecraft and launch vehicles (updated as of may 2012), 1999. Retrieved on 05/11/2014 from http://www.psi-pci.com/Technical_Paper_Library/AIAA%2099-2831%20Diaphragm%20Tank%20Updated%20List%20May%202012.pdf.

[194] Y. Tang, P. Reed, and T. Wagener. How effective and efficient are multiobjective evolutionary algorithms at hydrologic model calibration? *Hydrology and Earth System Sciences Discussions*, 10(2):289–307, 2006.

[195] Nick T. Thomopoulos. *Essentials of Monte Carlo Simulation*. Springer, 2013.

[196] S. T. Thurman and J. R. Fienup. Analysis of the general image quality equation. In *Proc. SPIE 6978, Visual Information Processing XVII, 69780F*, 2008. `doi:10.1117/12.777718`.

[197] S. Tonetti. Optimization of flower constellations: Applications in global navigation system and space interferometry. In *47th AIAA Aerospace Sciences Meeting including The New Horizons Forum and Aerospace Exposition, Orlando, Florida*, 2009. `doi:10.2514/6.2009-205`.

[198] S. Tsutsui, M. Yamamura, and T. Higuchi. Multi-parent recombination with simplex crossover in real coded genetic algorithms. In *Proceedings of the genetic and evolutionary computation conference*, volume 1, pages 657–664, 1999.

[199] A. Turner. Constellation design using walker patterns. In *AIAA/AAS Astrodynamics Specialist Conference and Exhibit, Monterey, California*, 2002. `doi:10.2514/6.2002-4636`.

[200] G. Tyc, J. Tulip, D. Schulten, M. Krischke, and M. Oxfort. The rapideye mission design. *Acta Astronautica*, 56(1):213–219, 2005.

[201] M. H. Ullock and A. H. Schoen. Optimum polar satellite networks for continuous earth coverage. *AIAA Journal*, 1(1):69–72, 1963. `doi:10.2514/3.1471`.

[202] Y. Ulybyshev. Near-polar satellite constellations for continuous global coverage. *Journal of Spacecraft and Rockets*, 36(1):92–99, 1999. `doi:10.2514/2.3419`.

[203] Y. Ulybyshev. Satellite constellation design for complex coverage. *Journal of Spacecraft and Rockets*, 45(4):843–849, 2008. `doi:10.2514/1.35369`.

[204] Y. Ulybyshev. Geometric analysis and design method for discontinuous coverage satellite constellations. In *AIAA/AAS Astrodynamics Specialist Conference, Minneapolis, Minnesota*, 2012. `doi:10.2514/6.2012-4803`.

[205] United Launch Alliance. Atlas V Launch Services User's Guide, 2010.

[206] David A. Vallado. *Fundamentals of Astrodynamics and Applications, Fourth Edition*. Springer, 2013.

[207] L. G. Vargo. Orbital patterns for satellite systems. *Advances in the Astronautical Sciences*, pages 709–725, 1960.

[208] L. Viscito, D. Chattopadhyay, and A. M. Ross. Combining pareto trace with filtered outdegree as a metric for identifying valuably flexible systems. In *7th Conference on Systems Engineering Research, Loughborough, UK*, 2009.

[209] L. Viscito and A. M. Ross. Quantifying flexibility in tradespace exploration: Value weighted filtered outdegree. In *AIAA SPACE 2009 Conference & Exposition, 14 - 17 September 2009, Pasadena, California*, 2009.

[210] S. D. Vtipil and B. Newman. Designing a constrained optimal orbit for earth observation satellites based on user requirements. In *AIAA/AAS Astrodynamics Specialist Conference, Toronto, Canada*, 2010.

[211] S. D. Vtipil and B. Newman. Determining an earth observation repeat ground track orbit for an optimization methodology. *Journal of Spacecraft and Rockets*, 49(1):157–164, 2012. `doi:10.2514/1.A32038`.

[212] J. G. Walker. Circular orbit patterns providing continuous whole earth coverage. Technical Report 70211, Royal Aircraft Establishment, 1970.

[213] J. G. Walker. Some circular orbit patterns providing continuous whole earth coverage. *Journal of the British Interplanetary Society*, 24:369–384, 1971.

[214] J. G. Walker. Continuous whole-earth coverage by circular-orbit satellite patterns. Technical Report 77044, Royal Aircraft Establishment, 1977.

[215] T. Wang and R. De Neufville. Real options "in" projects. In *9th Real Options Annual International Conference, Paris, France*, 2005.

[216] T. Wang and R. de Neufville. Identification of real options "in" projects. In *4th Conference on Systems Engineering Research, Los Angeles, CA*, 2006.

[217] D. Werner. Lockheed targets 2014 for athena 2 rideshare debut. *Space News*, 2012. Retrieved on 05/11/2014 from http://www.spacenews.com/article/lockheed-targets-2014-athena-2-rideshare-debut.

[218] J. R. Wertz. Coverage, responsiveness, and accessibility for various "responsive orbits". In *3rd Responsive Space Conference, Los Angeles, CA*, 2005.

[219] J. R. Wertz. ORS mission utility and measures of effectiveness. In *6th Responsive Space Conference, Los Angeles, CA*, volume 28, 2008.

[220] J. R. Wertz, J. T. Collins, S. Dawson, H. J. Koenigsmann, and C. W. Potterveld. Autonomous constellation maintenance. In *Mission Design & Implementation of Satellite Constellations, Proceedings of an International Workshop, held in Toulouse, France, November 1997*, pages 263–273, 1997. `doi:10.1007/978-94-011-5088-0_25`.

[221] James Richard Wertz, David F. Everett, and Jeffery John Puschell. *Space Mission Engineering: The New SMAD*. Microcosm Press, 2011.

[222] M. P. Wilkins, C. Bruccoleri, and D. Mortari. Constellation design using flower constellations. In *Advances in the Astronautical Sciences, 04-208*, Feb. 9-13 2004.

[223] M. P. Wilkins and D. Mortari. Flower constellation set theory part ii: Secondary paths and equivalency. *Aerospace and Electronic Systems, IEEE Transactions on*, 44(3):964–976, 2008. `doi:10.1109/TAES.2008.4655356`.

[224] E. A. Williams, W. A. Crossley, and T. J. Lang. Average and maximum revisit time trade studies for satellite constellations using a multiobjective genetic algorithm. In *Spaceflight Mechanics 2000*, volume 105 of *Advances in the Astronautical Sciences, Pt. 1*, pages 653–666, 2000.

[225] E. A. Williams, W. A. Crossley, and T. J. Lang. Average and maximum revisit time trade studies for satellite constellations using a multiobjective genetic algorithm. *Journal of the Astronautical Sciences*, 49(3):385–400, 2001.

[226] Graham Woan. *The Cambridge handbook of physics formulas*. Cambridge University Press, 2000.

[227] W. Yao, X. Chen, Y. Huang, and M. van Tooren. On-orbit servicing system assessment and optimization methods based on lifecycle simulation under mixed aleatory and epistemic uncertainties. *Acta Astronautica*, 87:107–126, 2013. `doi:10.1016/j.actaastro.2013.02.005`.

[228] P. Yarbrough. Operations concept for the world's first commercially licensed low-earth orbiting mobile satellite service. In *16th International Communications Satellite Systems Conference, Washington, DC*, 1996. `doi:10.2514/6.1996-1049`.

[229] B. T. C Zandbergen. Mass data for specific spacecraft propulsion systems. Retrieved on 01/14/2014 from http://www.lr.tudelft.nl/en/organisation/departments/space-engineering/space-systems-engineering/expertise-areas/space-propulsion/system-design/analyze-candidates/dry-mass-estimation/chemical-systems/sc-propulsion-mass-data/.

[230] Aimin Zhou, Bo-Yang Qu, Hui Li, Shi-Zheng Zhao, Ponnuthurai Nagaratnam Suganthan, and Qingfu Zhang. Multiobjective evolutionary algorithms: A survey of the state of the art. *Swarm and Evolutionary Computation*, 1(1):32–49, 2011. `doi:10.1016/j.swevo.2011.03.001`.

[231] S. Zhou, Y. Cao, J. Zhou, X. Hu, C. Tang, L. Liu, R. Guo, F. He, J. Chen, and B. Wu. Multiobjective evolutionary algorithms: A survey of the state of the art. *Science China Physics, Mechanics and Astronomy*, 55(12):2290–2299, 2012. `doi:10.1007/s11433-012-4942-z`.

[232] E. Zitzler, M. Laumanns, and L. Thiele. SPEA2: Improving the strength pareto evolutionary algorithm. Technical Report TIK-Report 103, Eidgenössische Technische Hochschule Zürich (ETH), Institut für Technische Informatik und Kommunikationsnetze (TIK), 2001.

[233] E. Zitzler and L. Thiele. Multiobjective evolutionary algorithms: A comparative case study and the strength pareto approach. *Evolutionary Computation, IEEE Transactions on*, 3(4):257–271, 1999. `doi:10.1109/4235.797969`.